Extreme Ultraviolet Spectroscopy of the Solar Corona

Giulio Del Zanna

A thesis submitted in
partial fulfilment
of the requirements
for the degree of
Doctor of Philosophy.

Centre for Astrophysics
University of Central Lancashire

July 1999

Declaration

The work presented in this thesis was carried out in the Centre for Astrophysics, University of Central Lancashire. Unless stated otherwise, it is the original work of the author.

While registered for the degree of Doctor of Philosophy, the author has not been a registered candidate for another award of the University. This thesis has not been submitted in whole, or in part, for any other degree.

Giulio Del Zanna
1999

Abstract

New Extreme Ultra-Violet (EUV) observations of the solar corona, obtained by the Coronal Diagnostic Spectrometer (CDS) instrument on board the NASA/ESA Solar and Heliospheric Observatory (SOHO) are presented. The CDS instrument for the first time has provided the opportunity of observing a large number of emission lines from a wide range of ions of different elements. The spectral and spatial resolution of the CDS instrument has allowed the simultaneous application of a wide range of spectroscopic diagnostic techniques to determine the temperature distribution, densities and elemental abundances in the solar plasma. A differential emission measure (DEM) diagnostic technique has been used to infer the temperature structure and the element abundances. The importance of including DEM effects in the element abundance analysis is demonstrated. A complete in-flight cross-calibration between all the CDS detectors (NIS and GIS, 150-785 Å), is presented here for the first time. The level of accuracy and completeness of the CHIANTI atomic database, used throughout this thesis, has allowed the identification of the many hundreds of spectral lines observed in the CDS spectra, resulting in several new line identifications. An assessment of the GIS solar spectra is presented, showing that, in spite of complexities, GIS spectra are useful for diagnostic analyses. Many discrepancies (in particular with the Li-like ions) between theory and CDS observations are highlighted. It is shown that some of these may be explained by inaccurate ionization equilibrium calculations. Coronal hole densities, temperatures, $DEMs$, and relative element abundances from both off-limb (plume and inter-plume regions) and on-disc observations are derived and compared with quiet sun values. These included (August 1996) a large equatorial hole, the Elephant's Trunk, probably the best example of a coronal hole observed by SOHO. Coronal hole densities in both coronal ($N_e \simeq 1\text{x}10^8$ cm^{-3}) and transition region ($N_e \simeq 1\text{x}10^{10}$ cm^{-3}) plasma were found to be about a factor of 2 lower than in the quiet sun, with much lower emission measures at temperatures above 10^6 K. Moreover, in the transition region, the cell-centres in both coronal holes and quiet sun regions show consistently higher densities (factor of 2) compared to those in the network. Relative element abundances show approximately photospheric values for the coronal holes, with an indication of element abundance variation (neon in particular) with the supergranular structure. On-disc EUV observations of coronal hole plumes have been performed. This allowed a spectroscopic characterisation of plumes to be obtained for the first time, leading to the first identification of a low-latitude plume near sun-centre. Plumes are shown to be quasi-isothermal structures, with temperatures $T \simeq 7 - 8\text{x}10^5$ K. Abundance analyses (using transition region lines) reveal a small FIP effect in these plumes, together with a decreased Ne/O abundance ratio (compared to photospheric).

Contents

Chapter 1

Introduction

The solar corona is the tenuous outer atmosphere of the Sun which is revealed to the human eye during a total solar eclipse, or with space observations. The visible spectrum of the solar corona has two major components: a continuum (the K-corona), due to Thomson scattering of photospheric light by the free electrons in the corona; and weak absorption lines (corresponding to the Fraunhofer lines - the F-corona), superimposed on a continuum emission. The latter is due to scattering by interplanetary dust particles in the immediate vicinity of the Sun. In addition, emission lines of highly-ionised atoms (e.g. the green coronal line Fe XIV 5303 Å and the red Fe X 6374 Å) are also observed. Their visibility clearly indicates the presence of million-degree plasma in the solar corona. From white light coronagraph observations, and using a model for the distribution of electrons in the corona following *van de Hulst* (1950), it is possible to estimate the electron density, which has values of the order of 10^8 cm^{-3}. Hence, even before the advent of space-based observations, ground-based data had revealed that the solar corona is mainly composed of high-temperature and low-density plasma. Due to its characteristics, this plasma is mostly optically thin and emits principally in X-rays and in the Extreme Ultra-Violet (EUV, 100-900 Å) region of the spectrum, and detailed studies therefore require observations from space.

For a general introduction to the Sun and the solar atmosphere, see, e.g.: *Athay* (1976); *Phillips* (1992); *Mariska* (1992); *Golub and Pasachoff* (1997).

The solar corona has been studied in more detail since the early 1960s using data from a number of rocket flights. Detailed studies started with Skylab, which observed the solar corona with various instruments from June 1973 to February 1974. Skylab's data together with a number of rocket flights and Yohkoh observations, have been the main observational source of information for our understanding of the solar corona, until 1996. In December 1995, the NASA/ESA Solar and Heliospheric Observatory (SOHO), one of the four major cornerstones of the ESA's Horizon 2000 project, was launched successfully.

It makes continuous observations of the Sun using 12 complementary instruments that allow for the first time a wide range of simultaneous observations at different wavelengths. It has greatly extended the limited information on the solar corona that was previously available.

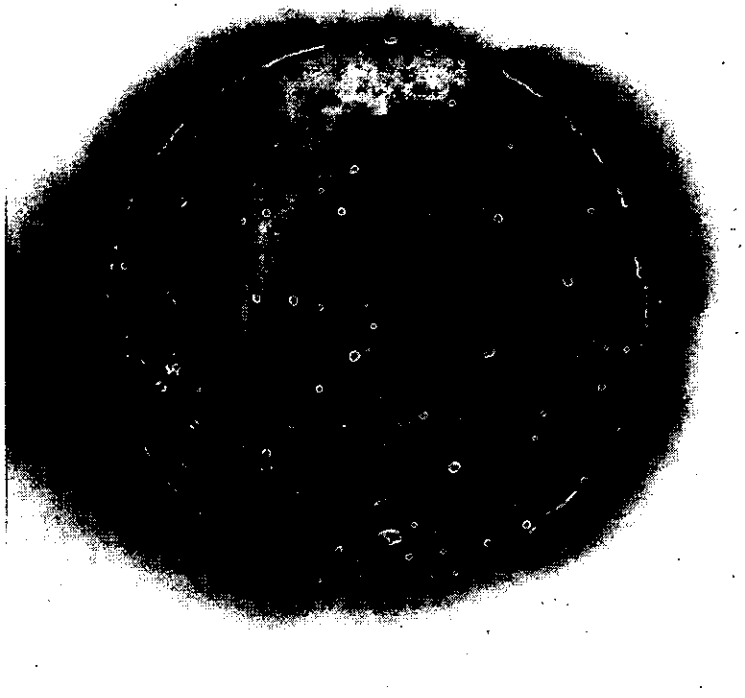

Figure 1.1: An EUV (195 Å) negative image of the solar corona taken on the 25th August 1996, during solar minimum conditions, with one of the instruments on the Solar and Heliospheric Observatory.

When imaged in the EUV (Figure 1.1), the solar corona shows a wide range of different structures, that magnetograms show to be magnetically linked to the underlying and cooler regions of the solar atmosphere, the chromosphere and the photosphere. Between the chromosphere and the corona there is a thin and complex region, the transition region, where the temperature dramatically increases, and which is highly dynamic (for some models of the transition region, see, e.g., *Gabriel*, 1976; *Athay*, 1982).

Most of the corona appears to have a diffuse nature (at modest spatial resolutions) and is referred to as 'quiet sun (QS)'. This quiet corona, which has a mixed-polarity magnetic field, is filled everywhere with small 'bright points (BP)'. Then, in regions with enhanced magnetic field (which in the corresponding visible photosphere appear as sunspots), bright 'active regions (AR)' form, with a multitude of extended loop structures.

The other large-scale structures of the solar outer atmosphere are the coronal holes, which appear as dark features in EUV and soft X-ray images. At the photospheric level, they

correspond to a prevalence of unipolar magnetic fields. During solar minimum, the Sun's large-scale magnetic field structure is similar to a dipole, and coronal holes extend over the north and south polar regions, where the magnetic field is mostly unipolar. Occasionally, coronal holes also form in equatorial regions, as shown in Figure 1.1, and described in Chapter 4 of this thesis. Inside polar coronal holes, large-scale ray-like extended features are usually observed, at various wavelengths. Due to their appearance they are named coronal hole plumes.

In the equatorial regions, cusp-like structures form and extend out to large distances: these are called streamers. At even greater distances, the main coronal plasma effect is a stream of fast particles (300-800 km/s) that pervades the solar system: the solar wind. In general, there are many features of the solar outer atmosphere that have been defined and characterized in various ways, in relation to observations with various instruments. It should be borne in mind that these characterisations sometimes merely reflect the limitations in temporal, spectral, or spatial resolution, or areal coverage of the observations performed.

When imaged in lines emitted at temperatures between 100 000 K and a million degrees, in the transition region, the solar atmosphere shows the same pattern as in the chromospheric lines. Magnetograms and measurements of velocity fields show that this pattern is related to the convective motions at the solar surface, which are organised in supergranular cells (about 30 000 Km across, and not to be confused with the smaller photospheric granules), and where magnetic flux is pushed by the plasma motions from the cell-centres toward their boundaries (the so-called network).

The main underlying characteristic of the solar corona is the important role played by the magnetic field in forming and keeping in place all the observed structures. This is because the ratio between gas pressure and magnetic pressure $\beta \ll 1$, i.e. the static structures and the dynamics of the coronal plasma are dominated by the magnetic field. The time evolution of coronal structures is in some way linked to the evolution of the photospheric magnetic field. This surface field is created by dynamo processes acting in the solar interior, which are related to convective motions and are difficult to model.

Although coronal magnetic fields have not been measured directly, there is a large body of evidence suggesting that over large scales streamers represent regions of closed magnetic field, and that the magnetic field lines in the coronal holes open out to interplanetary space. One of these pieces of evidence has been the identification of coronal holes as the sources of the high-speed ($\simeq$ 800 km/s) solar wind (*Krieger et al.*, 1973; *Nolte et al.*, 1976), thereby raising interest in the study of coronal holes. This interest has been renewed in recent years since the launch of the Ulysses probe in October 1990. This has produced

new in-situ measurements of the solar wind, for the first time out of the ecliptic plane, confirming that the polar holes are the source of the steady high-speed solar wind. Ulysses has also recently shown that the high-speed solar wind fills most of interplanetary space and has fairly constant characteristics, and should therefore be easier to model, compared with the highly-variable low-speed ($\simeq$ 400 km/s) wind that streams out of the equatorial regions (streamer belt). For this reason, considerable interest has developed recently in studying the high-speed solar wind and coronal holes. This is one of the reasons why the work presented in this thesis will mainly focus on coronal holes, although there are many fascinating and unexplained phenomena in the solar corona.

It is also interesting to study plumes, for many reasons. First, they are the only stable observable structures within coronal holes, and although they fill only a small percentage of the solid angle subtended by coronal holes, their contribution to the observed emission along the line of sight is usually significant and important to assess. Secondly, because of their morphology, it is generally assumed that plumes trace the open field lines of the coronal holes and it is therefore important to assess the relationship between plumes and the fast solar wind. Any solar wind model should account for the presence of plumes.

One would expect to derive from the observational data various physical parameters to describe the status of the plasma. These should include for example the elemental abundances, particle velocities and distribution functions, ionic and electron temperatures, densities and magnetic field strengths as a function of space and time. Only in-situ measurements by spacecraft can provide direct information for such parameters. Otherwise, the plasma's physical parameters have to be inferred from remote measurements, i.e. from observations of the solar radiation. Great efforts have been made by various authors to derive values of such parameters from the observations. In particular, EUV spectroscopic observations can provide information on the basic plasma parameters such as temperature, density, element abundances, and flow velocities. Many interesting results have been produced, with the aid of models and various assumptions. These assumptions must always be borne in mind when estimating the values of the deduced physical parameters, and added to the uncertainties in the observations and in the atomic data.

Among the various interesting results, a detailed examination of the Sun's upper atmosphere has revealed that coronal element abundances vary between different solar regions, and are different from their photospheric values, and from those of the solar wind composition. It seems that there is a correlation between the coronal abundances and the first ionization potential (FIP) of the various elements. Low-FIP ($\leq$ 10 eV) elements tend to be more abundant in the corona, relative to those with a high FIP. A large number of papers, often with conflicting conclusions, have been published on this subject (see the

reviews by *Meyer*, 1985; *Meyer*, 1993; *Feldman*, 1992a; *Feldman et al.*, 1992b; *Mason*, 1995; *Saba*, 1995; *Meyer*, 1996; *Mason*, 1992; *Phillips*, 1997a). Plumes are particularly interesting in that they represent an extreme case of particular element abundances, in the sense that large FIP biases have been reported from EUV observations close to the limb (*Widing and Feldman*, 1992).

Many theoretical models have been produced to try to explain observations of the solar corona, and although limited by various simplifications, assumptions and the contemporary computational methods, they have been successful in various cases. However, they have failed to satisfactorily answer many general questions, and in particular:

- why is the solar corona a million degrees hotter than the underlying atmosphere ? It is widely accepted that coronal heating takes place when magnetic energy is supplied to the corona, but how and where this is dissipated is still not known;
- why are there variations of chemical abundances in the corona, and what is their relationship with the magnetic field ?
- what is the structure of the transition region, and its relation to the corona ?
- how and where is the solar wind created and accelerated ?
- why do we see coronal holes in the EUV ? Their lower EUV emission is thought to be due to their lower densities and temperatures, even though accurate measurements have been absent. When observed in transition-region lines, the coronal holes are almost indistinguishable from the other regions of the Sun;
- why do coronal holes form, and what is their chemical composition ?
- what is the relationship between coronal holes and plumes ? Are plumes the source of the high speed solar wind ?
- are plumes cooler or hotter than the inter-plume regions ?

Most of these (and many more) questions are still unanswered, for many different reasons. First, the adopted models usually assume various simplifications which might not be justified. In general, the difficulty of the theoretical models in representing the observed structure and dynamics of the solar corona resides in its complexity and in the inter-relations (not yet understood) between the various atmospheric phenomena together with their relation to both the solar interior and the solar wind.

Secondly, the complexity of coronal observations and analysis means that further and more accurate observations are required, including direct measurement of coronal magnetic fields. The EUV region of the spectrum is still relatively unexplored, and many additional uncertainties arise from calculations used in the theory, instrument calibrations and uncertainties in the adopted atomic physics.

Our knowledge of coronal holes is even more limited than that of the corona as a whole. For example, prior to SOHO only one set of EUV spectroscopic data for a coronal hole region existed (*Vernazza and Reeves*, 1978). These data were from the Skylab Harvard College Observatory (HCO) instrument, mounted on the Apollo Telescope Mount (ATM), and until 1996 they were the best source of information about coronal holes in the EUV wavelength range, although the spectral resolution was poor.

SOHO was designed to provide, amongst other things, new observational constraints on the corona and to study in particular the quiet sun around solar minimum. These conditions are the most favourable for studies of polar coronal holes, because they are then at their greatest extent and because of the relative lack of large loop structures. However, projection effects from quiet-sun material along the line of sight can strongly affect both off-limb (see e.g. the comments of *Habbal, Esser, and Arndt*, 1993) and on-disc coronal hole observations.

SOHO has produced a wealth of data and has changed our view of the Sun in so many respects already, and most of the present physical models are being modified or reconsidered in light of the new exciting observations. In particular SOHO observations have already shown the highly dynamic and inhomogeneous structure of the solar corona.

The present research project

The aim of the present research project was to advance our understanding of the solar corona by studying especially coronal holes and their boundaries, using ground-based and SOHO data, and in particular the Coronal Diagnostic Spectrometer (CDS) data. The CDS instrument offered, for the first time, the opportunity of observing emission lines produced by a wide range of temperatures with sufficient spectral resolution to apply spectroscopic diagnostic techniques. The project mainly consisted of: planning CDS coronal hole observations and executing them at the SOHO operations centre, Goddard Space Flight Centre, U.S.; analysing the data, implementing methods with software in IDL (Interactive Data Language); and researching the atomic physics of the CDS spectral lines, in order to determine values for the plasma parameters.

Layout of the thesis

The thesis is organized as follows. Section 1.1 gives an introduction to the theoretical plasma emission, and how temperatures, densities and elemental abundances of the plasma can be obtained from EUV observations. It also introduces the definition of differential emission measure (DEM) and how the multithermal plasma distribution can be studied. Different spectroscopic diagnostic methods are briefly described, leading to a review of coronal observations which is given in Section 1.2. Section 1.2 summarizes observations and theories of the solar corona, with particular reference to coronal holes. It includes a brief description of some of the most recent results from SOHO. This review concentrates on the observational constraints to the models, and how these constraints have been determined, rather than on the theories themselves.

Chapter 2 describes the various diagnostic techniques and the software developed by the author to derive the values of physical parameters from CDS observations. A critical evaluation of the various methods found in the literature is also given. In particular, Section 2.5 presents a re-analysis of Skylab coronal hole spectral data, and compares different methods to deduce differential emission measure and element abundances. Section 2.6 presents a critical discussion of previous work on element abundances.

Chapter 3 describes the CDS instrument and outlines those aspects that limited the possible observations and complicated the data analysis. Then, the CDS data calibration is discussed and new calibrations presented, starting with a description of various preliminary tasks undertaken. The sequence of new CDS observations, planned and executed in order to cross-calibrate the CDS detectors, are fully described. The full CDS line identifications and comparisons of different observations with theoretical calculations are also given in this Chapter.

Chapter 4 details the new CDS observations that were planned and executed in order to study coronal holes, including both on-disc and off-limb observations of polar holes, and on-disc observations of low-latitude holes. The observations were mainly carried out during August 1996, February 1997 and September-October 1997, during solar minimum and the initial rise towards the next maximum. A short description is also given of the methods and software developed for data analysis.

Chapter 5 reports results in terms of morphological descriptions, temperatures, densities and elemental abundances for a selection of the observed coronal structures. First, the general differences in terms of temperatures and densities, between quiet sun and coronal hole regions, as derived from 1996 to 1998 observations, are presented. Then, results from some of the near Sun centre 1996 observations in coronal hole and quiet sun areas are

presented and compared.

Chapter 6 is dedicated to on-disc and off-limb coronal hole and plume observations and results. First, the results from the on-disc observations of polar holes are presented and compared to those given in Chapter 5. Secondly, off-limb plume and inter-plume regions are examined in detail, giving examples of 'contamination' from background diffuse non-coronal hole emission. Finally, results from on-disc observations of polar plumes are presented.

Chapter 7 draws together the main results and conclusions of the work, in order to define and characterise coronal holes and plumes in comparison with the quiet sun regions, within the wider range of observed coronal structures.

1.1 An introduction to the theory of emission from coronal plasmas

The *standard model* for coronal emission is adopted in this thesis (see, e.g., *Dere et al.*, 1997, and below for a short description). The best available atomic data have been used, as stored in the CHIANTI databases. The CHIANTI atomic database and analysis software (*Dere et al.*, 1997) is the result of an international collaboration (USA/Italy/UK) to provide a comprehensive dataset for ions of astrophysical interest seen in the wavelength region $\lambda > 50$ Å. Additional information about the CHIANTI atomic database can be found at the CHIANTI homepage:

`http://wwwsolar.nrl.navy.mil/chianti.html`

The Arcetri database (*Landi and Landini*, 1998), produced at the Arcetri Observatory, Italy, has been used for those transitions not included in the CHIANTI database, and as a cross-check. Information on the Arcetri database can be found at:

`http://www.arcetri.astro.it/science/chianti/chianti.html`

The standard model has many assumptions, the main ones being that the plasma is optically thin, hot ($T \geq 10^4$), in a steady state, and in ionization equilibrium. A plasma is in ionization equilibrium when the processes that contribute to the formation of the ions can be decoupled from those affecting the level balance within that ion. These assumptions considerably simplify the analysis of EUV observations. When the plasma is optically thin, it is not necessary to solve the radiative transport equations, in the sense that the observed

emission is directly related to the state of the plasma. The results of the theoretical calculations that follow these adopted assumptions will be shown to explain the observed CDS spectra in this thesis with an accuracy often better than the estimated errors on the atomic calculations or the observations. This confirms that for most spectra analysed here, the standard model is applicable.

Another assumption in the standard model is that the particles (electrons and ions) are in thermal equilibrium (i.e. they have a Maxwellian distribution function). This assumption appears justified, since the relaxation time for e-e collisions is $\tau_{ee} \simeq 0.01\ T^{3/2}\ N_e^{-1} = 0.01$ s for $T = 10^6$ K and $N_e = 10^9$ cm^{-3}. The ions also become thermal, after a time longer by the factor $(m_i/m_e)^{1/2} \simeq 43$. After the same time factor, both species are thermalised, and only one temperature need be used: $T = T_e = T_i$. This certainly does not hold for the solar wind, as for example Helios observations have shown (*Marsch*, 1991), and there is an ongoing debate on whether the thermal assumption is in fact valid in the corona, since recent SOHO observations of the upper corona indicate much higher ion temperatures (and different ones for each ion), compared to the electron temperature.

The prevalent atomic processes that take place in the transition region and corona, and the adopted assumptions, are now briefly summarised. Complete descriptions of the emission from coronal plasmas can be found in relevant textbooks and review papers (see e.g. *Mariska*, 1992; *Mason and Monsignori Fossi*, 1994). The main processes are ionization, recombination, excitation and de-excitation. In low density plasmas the collisional excitation and de-excitation processes take place on time scales much shorter than ionization and recombination. Hence collisional excitation dominates ionization and recombination in the populating of the excited states. This allows the low-lying level population mechanisms to be treated separately from the ionization and recombination processes. Radiative excitations are rare due to the weak radiation field. The same applies to stimulated emission. Therefore for permitted transitions the levels are mainly excited by collisions and de-excited by spontaneous radiative decay. In the following, Z_n^{+r} indicates the element of atomic number Z which is r times ionized, in the excited state n, in the sense that n identifies the level, ordered in increasing energy, starting from the ground level $n = 1$ for the ionized state r. $N(Z^{+r})(cm^{-3})$, or more simply N_r will indicate the number density of ion Z^{+r} (i.e. the number of particles per unit volume).

The intensity $I(\lambda_{ij})$ of an optically thin spectral line of wavelength λ_{ij} (frequency ν_{ij}) is:

$$I(\lambda_{ij}) = \frac{1}{4\pi} \int_h P_{ji}\ dh = \frac{h\nu_{ij}}{4\pi} \int_h N_j(Z^{+r})\ A_{ji}\ dh \quad [\text{ergs cm}^{-2}\ \text{s}^{-1}\ \text{sr}^{-1}] \tag{1.1}$$

where i, j are the lower and upper levels, P_{ji} is the bound - bound emissivity (power per unit volume), A_{ji} is the spontaneous radiation transition probability, $N_j(Z^{+r})$ is the number density of the upper level j of the emitting ion, and h is the line-of-sight coordinate. If instead of the intensity, the flux (as, e.g. in whole sun or star observations) is observed, then a similar definition holds, with the integral of the power over the volume of the emitting plasma. Since for allowed transitions we have $N_j(Z^{+r})A_{ji} \sim N_e^2$, the intensity is usually rewritten using the identity:

$$N_j(Z^{+r}) \equiv \frac{N_j(Z^{+r})}{N(Z^{+r})} \frac{N(Z^{+r})}{N(Z)} \frac{N(Z)}{N_{\rm H}} \frac{N_{\rm H}}{N_e} N_e \tag{1.2}$$

where the various terms are defined as follows.

- $N_j(Z^{+r})/N(Z^{+r})$ is the population of level j relative to the total $N(Z^{+r})$ number density of the ion Z^{+r} and is a function of the electron temperature and density. In the coronal model, where every level is collisionally excited from the ground level by the electrons and de-populated via spontaneous emission, $N_j(Z^{+r})$ is proportional to N_e, for allowed transitions. The number density population of level j is calculated by solving the statistical equilibrium equations for a number of low lying levels and including all the important collisional and radiative excitation and de-excitation mechanisms:

$$\begin{aligned} \frac{dN_j}{dt} = & \sum_{i<j} N_i R_{i,j} + \sum_{i>j} N_i A_{i,j} + \sum_{i>j} N_i N_e C^e_{i,j} + \sum_{i<j} N_i N_e C^e_{i,j} \\ & - N_j(\sum_{i<j} A_{j,i} + \sum_{i>j} R_{j,i} + N_e \sum_{i<j} C^e_{j,i} + N_e \sum_{i>j} C^e_{j,i}) \end{aligned} \tag{1.3}$$

  * C^e ($\mathrm{cm}^{-3}\ \mathrm{s}^{-1}$) are the electron collisional excitation rate coefficients.

  * $R_{j,i}$ (s^{-1}) are the stimulated absorption rate coefficients, proportional to the mean intensity of the radiation field.

  * $A_{j,i}$ (s^{-1}) are the spontaneous radiation transition probabilities.

  In practice, because of the short time scales of the relevant processes, it is always assumed that the plasma is in a steady state ($\frac{dN_j}{dt} = 0$). The set of Equations 1.3 is then solved for a number of low lying levels, with the additional requirement that $N(Z) = \sum_j N_j$.

  In the CHIANTI database the processes included are electron excitation and de-excitation, and spontaneous radiative decay. The proton collisional coefficients could also be considered as an additional term, but are not yet included in CHIANTI. The stimulated emission can be neglected in an optically thin plasma.

- $N(Z^{+r})/N(Z)$ is the ionization ratio, and is predominantly a function of temperature.

  Various processes can affect the ionization balance. Since the plasma is optically thin, most of the radiation escapes, the plasma is not in local thermodynamic equilibrium (LTE), and the main processes that regulate the ionization balance are spontaneous radiative recombination, di-electronic recombination and collisional ionization. By considering the detailed balance equations that relate successive ionization stages for these processes, and requiring that the population of ions in a given state is constant with time, it is possible to derive for each state the ratio of two successive ionization stages $N_{Z,r+1}/N_{Z,r}$, which is mainly a function of the temperature, and only slightly depends on the electron density through the rate coefficients. With the additional condition $N(Z) = \sum_r N_{Z,r}$, it is possible to derive the ionization ratio. Many ionization equilibrium calculations have been published in the past, but none include density effects. The most recent ones are those of *Arnaud and Rothenflug* (1985), *Landini and Monsignori Fossi* (1991), *Arnaud and Raymond* (1992), *Mazzotta et al.* (1998).

- $N(Z)/N_{\rm H} \equiv Ab(Z)$ is the element abundance relative to hydrogen.

- $N_{\rm H}/N_e$ is the hydrogen abundance relative to the electron density. This ratio is usually in the range $\sim 0.8-0.9$. H and He, at coronal temperatures, are fully ionized. If we neglect the contribution of the heavier elements to the electron density ($\leq 1\%$), and assume fully ionized H and He, the only parameter that changes this ratio is the relative abundance of He, which is not yet well established. If we assume the *Meyer* (1985) abundances, $\rm N_H/N(He)$=10 , $N_{\rm H}/N_e = 0.83$; whilst for log ($\rm N_H/N(He)$)=1.2, $N_{\rm H}/N_e = 0.89$.

The intensity of a spectral line can then be written in the form:

$$I(\lambda_{ij}) = \int_h Ab(Z) C(N_e, T, \lambda_{ij}) N_e N_H dh \tag{1.4}$$

with the *contribution function* C given by:

$$C(N_e, T, \lambda_{ij}) = A_{ji} \frac{h\nu_{ij}}{4\pi} \frac{N_j(Z^{+r})}{N_e N(Z^{+r})} \frac{N(Z^{+r})}{N(Z)} \quad (erg\ cm^3\ s^{-1}) \tag{1.5}$$

The *contribution function* contains all of the relevant atomic physics parameters and for most of the transitions has a narrow peak in temperature, and therefore effectively confines the emission to a limited temperature range. In the literature there are various definitions

of *contribution functions*, depending on which terms are included. Aside from constant terms, sometimes the elemental abundance and/or $N_H/N_e = 0.8$ and/or the term $1/4\pi$ are included in the definition, for example. Throughout this thesis, we will refer to both the contribution functions $C(T, \lambda_{ij}, N_e)$ and to $G(T, \lambda_{ij}, Ab(Z), N_e) \equiv Ab(Z)\, C(T, \lambda_{ij}, N_e)$, i.e. the contribution functions that contain the abundance factor. Also, since the contribution functions will be calculated at fixed density values, and the abundances are independently chosen, in many cases we will simply refer to the functions $C(T)$ and $G(T)$.

At this point, there are many assumptions that can be made, in order to simplify the expression for the intensity. One of the major problems in trying to interpret EUV spectra is that the intensity of the observed spectral line is related to the sum of all the photons emitted into the line of sight. One of the problems is that the current spatial resolution of the EUV instruments is not sufficient to specify the plasma distributions along the line of sight. For example, the same emission can be produced by a low-density plasma occupying a large volume, or by a high-density plasma distributed over only a small fraction of the line of sight.

If a unique relationship exists between N_e and T, a differential emission measure $DEM(T)$, a function of only the plasma temperature, can be defined (*Withbroe*, 1978):

$$\int_T DEM(T)dT = \int_h N_e\ N_H dh \tag{1.6}$$

i.e.

$$DEM(T) = \ N_e N_H \frac{dh}{dT} \qquad [cm^{-5}K^{-1}] \tag{1.7}$$

For example, if we assume that the plasma pressure along the line of sight is constant, then from the perfect-gas law $N_e^2 \sim (P^2/T^2)$, and the electron density is only a function of temperature, and the $DEM(T)$ can be defined. The DEM gives an indication of the amount of plasma along the line of sight that is emitting the radiation observed and has a temperature between T and $T + dT$. The DEM is related to the conductive flux and gives information about the structure of the atmosphere.

With this definition, the intensity integral becomes:

$$I(\lambda_{ij}) = Ab(Z) \int_T\ C(T, \lambda_{ij}, N_e)\ DEM(T)\ dT, \tag{1.8}$$

assuming that the abundance of the element $Ab(Z)$ is constant over the line of sight. We therefore have a system of Fredholm integrals of the first species to be inverted,

in order to deduce the DEM from a set of observed intensities. More details on the inversion techniques used in the present work can be found in Chapter 2. The integral inversion method has also the advantage that at the same time the DEM distribution and the elemental abundances can be obtained, using a large number of line intensities. This minimizes the effects of errors in observation or theory associated with single lines. Further refinements and considerations of the integral inversion problem, and extensions with the use of an emission measure differential in both temperature and density, can be found in *Craig and Brown* (1976), *Doschek* (1984), *Almleaky et al.* (1989), *Newton et al.* (1995), and *Hubeny and Judge* (1995).

Once the differential emission measure DEM is known, the total emission measure EM can be calculated, integrating the DEM over the whole temperature range:

$$EM \equiv \int_h N_e N_H dh = \int_T DEM(T)\, dT \qquad [\mathrm{cm}^{-5}] \tag{1.9}$$

Sometimes the total emission measure is defined as $EM = \int N_e^2 dh = \int DEM(T) dT$, with the differential emission measure defined as $DEM(T) = N_e^2 (dT/dh)^{-1}$. Following *Pottasch* (1963), various approximations and methods have been introduced in order to approximate the DEM and to deduce elemental abundances, as reviewed in Chapter 2. One method is to define for each observed line an average emission measure $< EM >$, while another is to define for each observed line an averaged $< DEM >$, in order to simplify the inversion of (1.8).

1.1.1 Temperature determination

A first estimate of the plasma electron temperature can be obtained by noting the presence or absence of EUV lines emitted by ions having different ionization equilibrium temperatures. Coronal temperatures can also be estimated from the intensity ratio of pairs of EUV lines, if their contribution function does not depend on density, and assuming an isothermal plasma ($T = T_0$) along the line of sight. If the lines are formed at similar temperatures, it can be assumed that they are emitted by the same spatial structures along the line of sight. The intensity of a line, from a region of constant abundance, can then be written:

$$I_{\lambda_{ij}} = Ab(Z)C(T_0) \int DEM(T)\, dT = Ab(Z)C(T_0) \quad EM \tag{1.10}$$

and therefore the total emission measure can be estimated. From the ratio of two lines of different ions, T_0 can be estimated. The best method is to use lines of the same element and

similar ionization stage, in order to make the temperature determination independent of element abundance variations. Examples that apply to CDS will be given in Chapter 2. It should be stressed that the temperatures derived in this way are isothermal temperatures assuming ionization equilibrium. It should also be kept in mind that if the plasma is not homogeneous, the lines emitted by different ions will be generated in different spatial regions, and therefore their ratio has no real meaning except as an average value.

A more direct determination of an isothermal electron temperature, that is not dependent on ionization equilibrium assumptions, can be obtained from the intensity ratio of two allowed transitions to the ground level g of the same ion, from upper levels j and k having significantly different excitation energies E_{gj} and E_{gk}. In fact, if $(E_{gk}-E_{gj})/kT >> 1$, the intensity ratio is temperature-dependent, and assuming that the lines are emitted by the same isothermal volume with the same electron density, an isothermal temperature can be directly deduced from the intensity ratio. This method is difficult to apply because usually the wavelengths of the two transitions are hundreds of Å apart, and therefore the lines need to be observed by different instruments, which must then have a rigorous relative intensity calibration. Temperature-dependent ratios of this type include, for example: O V [629/172], O V [1218/629], and O VI [1032/173]. Examples that apply to CDS observations will be given in Chapter 2.

However, if the plasma distribution along the line of sight is multithermal, as can be expected in most cases, especially for on-disc observations, a more detailed temperature description is obviously needed. This can be obtained from EUV spectroscopic observations via the DEM distribution.

1.1.2 Electron density estimates

An average electron density N_e can be deduced from the total emission measure $< EM >$ and an estimate of the dimension Δh along the line of sight of the emitting plasma (or the volume $V = A_s \Delta h$, with A_s being the observed projected area), assuming that the elemental abundances are known: $< N_e^2 > \sim < EM > / \Delta h$. In most cases, when the $< N_e^2 >$ are compared to the $< N_e >^2$ values that are calculated from direct measurements of the average (along the line of sight) density $< N_e >$ in the transition region, large discrepancies are found. This has been interpreted (*Dere et al.*, 1987) as due to the transition region having a filamentary structure, so that most of the plasma occupies only a small fraction (the filling factor) of the observed volume.

By contrast, no assumption about the size of the emitting volume or the elemental abundances is needed when estimating N_e from density-sensitive line ratios for the same ion.

However, such results still represent an average along the line of sight. The intensity ratio of two lines can become density-sensitive when the two lines have a different dependency on the electron density. For example, for allowed lines the intensity $I_{j,i} \sim N_e^2$ while for forbidden and intersystem lines collisional de-excitation becomes an important de-populating mechanism and the intensity $I_{j,i} \sim N_e$. In general, a ratio of two such lines can therefore be a good density diagnostic, although a temperature dependence can also produce a change in the ratio. There are many cases in which the temperature dependence is so low, and the calculation is performed at the temperature of maximum formation of the ion. Examples that apply to CDS observations will be given in Chapter 2.

Previous estimates of coronal densities have produced a large scatter in the values (see e.g. the SERTS observations, *Brosius et al.*, 1996). Such discrepancies may well be due to uncertainties in the atomic physics or in the instrument calibration, or they could be related to the complexity of structures emitting along the line of sight. In fact, if the plasma is inhomogeneous, different line ratios can easily produce different density values, as *Doschek* (1984) pointed out.

In general, densities deduced from lines emitted at different temperatures should not be expected to be the same, since there is fine structure in the solar corona. This fact has not been fully recognised by many authors. In 'normal' conditions, the density decreases with height. Since the emission is proportional to $N_e{}^2$, this means that most of the emission will come from the denser (and lower) regions. However, there are many cases where this is not true. For example, if one observes a hot loop in an active region that extends high into the corona, one would expect to measure higher densities from high-temperature lines, because of the contribution from the loop, and lower densities from cooler lines, coming from the other regions in the line-of-sight.

1.1.3 General considerations of the plasma equations

For completeness, this Section introduces some general definitions. Given the high temperature and low density, the coronal plasma follows the perfect gas law:

$$P = \frac{k}{\mu m_H}\rho T = k(N_e T_e + N_i T_i) = 2NkT \tag{1.11}$$

where μ is the mean atomic weight, the average mass per particle in units of proton mass m_H. $\mu = 0.5$ for a plasma of fully ionised hydrogen, while $\mu = 0.62$ for a plasma composed of hydrogen and helium, with a helium abundance $N_{H_e}/N_H = 0.1$. The last equality holds only for a single-fluid plasma, where all the particles have the same temperature

($T = T_e = T_i$ and $N = N_e = N_i$) . The equation of motion for a fluid element (without the viscosity terms) is:

$$\rho \frac{d\vec{v}}{dt} = -\nabla P + \frac{\vec{J}}{c} \wedge \vec{B} + \rho \vec{g} \tag{1.12}$$

where $d/dt = \partial/\partial t + \vec{v}\mathrm{x}\nabla$ is the Lagrangian derivative along the the path, $\vec{J}$ is the current density, $\vec{B}$ the magnetic field, $\vec{g}$ is the gravity acceleration. When the velocity of the fluid element is negligible, compared to the velocity of propagation of sound and magnetic waves, and the velocity of free fall, the equation can be simplified:

$$\frac{dP}{ds} = \rho g \cos\theta \tag{1.13}$$

with $\vec{g} = -g\vec{e}_z$, s the coordinate along the field line that has an angle θ with the vertical $\vec{e}_z$, and $ds\cos\theta = dz$. Using the perfect gas law:

$$P(z) = P_o exp\left(-\int_0^z \frac{dz'}{L_P(z')}\right) \tag{1.14}$$

and $L_P = RT(z)/\mu g$ is the pressure scale-height for a single-fluid plasma. In many cases, L_P is much less than the magnetic scale-length, and therefore a constant pressure can be assumed. If the plasma is also isothermal, the density scale-height is the same as the pressure one, and

$$\frac{N(z)}{N(R_\odot)} = \exp\left[-\frac{\mu m_H g_\odot R_\odot}{kT}\left(1 - \frac{R_\odot}{z}\right)\right] \tag{1.15}$$

For a two-fluid plasma, the same equation holds (*Guhathakurta and Fisher*, 1998), with $T = (T_e + T_i)/2$. With these assumptions, is therefore possible to deduce a scale-height temperature T_h from the measured density profiles (*Guhathakurta et al.*, 1992).

The temperature variation along the field lines can be deduced from the heat equation (when the entropy is conserved), considering a flux tube with a cross-section area A:

$$-\nabla\mathrm{x}\vec{F}_c = \tfrac{1}{A}\tfrac{d}{ds}\left(\chi_o T^{5/2} A \tfrac{dT}{ds}\right) = E_R(T) - E_H(T) \tag{1.16}$$

that is simply a balance between thermal conduction $\nabla\mathrm{x}\vec{F}_c$, radiative losses $E_R(T)$ and heating processes $E_H(T)$. χ_o is the coefficient of conduction (*Spitzer*, 1965). The thermal conduction is very efficient along the field lines; the heating function is usually parameterised; the radiative loss function for the coronal plasma is:

$$E_R = N^2\Lambda(T) = \frac{P^2}{4k^2T^2}\Lambda(T) \quad erg\ cm^{-3}\ s \tag{1.17}$$

where $\Lambda(T)$ is the sum of all the emissivities of the coronal lines (total power per unit emission measure). Once the DEM distribution and the $\Lambda(T)$ are calculated, the total luminosity $L = \int_T DEM(T)\ \Lambda(T)\ dT$ emitted by the plasma can be derived. Once the DEM is known, it is straightforward to deduce the temperature gradient along the line of sight, assuming that the temperature is a single-valued function, and to deduce the temperature, once a value for the pressure is fixed.

1.2 Previous observations of the solar corona

1.2.1 Ground and space observations of the solar corona

The main observations of the solar corona consist of X-ray and EUV observations, radio brightness measurements and brightness and polarization of the white-light emission. The photospheric magnetic fields are provided as magnetograms, and the distribution of sunspots indicates the level of magnetic activity. Magnetograms, H_α, Ca H and K images, have been and continue to be provided by many ground based observatories.

Many observatories around the world take daily observations of the solar corona. For example, the Mauna Loa Solar Observatory K-coronameter has provided white-light data since 1965. Infrared observations in the absorption line of He I (10830 Å) have been taken continuously since 1977 with the Vacuum Solar Telescope at the Kitt Peak National Observatory, and are also provided by other observatories (e.g. Pic du Midi).

Observations in the visible part of the spectrum are particularly interesting in the green and red coronal lines Fe XIV 5303 Å and Fe X 6374 Å , since their intensity is lower in coronal holes (especially Fe XIV), whereas intensities of other lines, (e.g. H_α and Ca II K) and the continuum are not reduced. Coronal-line intensity measurements at 1.15 $R_\odot$ are carried out daily at the National Solar Observatory at Sacramento Peak (NSO/SP), New Mexico. Fe XIII 10798 and 10747 Å , Si X 14301 Å are also observed (*Penn and Kuhn*, 1994).

Solar radio observations are provided for example by the Nobeyama and Nancay radioheliosCopes.

Space observations pre-SOHO

Many rocket flights and satellites have provided EUV observations of the solar corona. Some of them are listed in Table 1.1. After some early rocket flights, the first series of small satellites were the Orbiting Solar Observatories (OSO). The main sources of EUV

Table 1.1: Some space-borne instruments that observed the solar corona in EUV.

Instrument	Dates	λ [Å]	$\delta\lambda$[Å]	δS (arc sec)	$\delta t(s)$	FOV	references
OSO IV	1968	300-1400	3.2	60	900 full scan	1x1	*Reeves and Parkinson* (1970)
Rocket	1969	50-300	0.25	-	-	integrated Sun	*Malinovsky and Heroux* (1973)
LASP (rocket)	1969	60-385					*Behring et al.* (1972)
OSO V	1969	25-400	~ 0.4		900 full scan	integrated Sun	*Kastner et al.* (1974)
OSO V	1969	280-370 465-630 760-1030	integrated	none	2	integrated Sun	*Kastner et al.* (1974)
OSO VI	1969	280-1390	3.2	35	900 full scan	1x1	*Noyes* (1971); *Reeves and Parkinson* (1970)
OSO VII	1972	150-400	0.85	20	120	5x5	*Kastner et al.* (1974, 1976)
Rocket	1973	140-873	0.17	-	-	disc centre	*Firth et al.* (1974)
LASP (rocket)	1973	160-770	0.06	-	-	-	*Behring et al.* (1976)
Skylab S-O55 (HCO)	1973-4	280-1350	1.6	5	~ 330	5x5	*Reeves and Parkinson* (1970); *Vernazza and Reeves* (1978)
Skylab SO82-A (NRL)	1973-4	171-630	0.1	$\geq$ 2 slit-less	none	full Sun images	*Feldman* (1987); *Dere* (1978a)
Skylab SO82-B (NRL)	1973-4	970-3940	0.04-0.08	slit 2x60			*Bartoe et al.* (1977)
CHASE	1985	160-1344	0.25-0.4	15	few sec.	3x1 max	*Breeveld et al.* (1988)
NIXT	1988	63.5	wide band	2-3	none	full Sun images	*Golub et al.* (1990)
MSSTA (rocket)	1991	40-2800	few bands	0.7	none	full Sun images	*Walker et al.*, (1993)
SERTS	1989-	235-450 (170-225 IIo)	0.06	6	none	5x8	*Brosius et al.* (1998a)

data for twenty years have been the instruments flown on Skylab (1973-1974). Three Skylab workshops summarised the main findings: on coronal holes and the solar wind (*Zirker*, 1977); solar flares (*Sturrock*, 1980); and solar active regions (*Orrall*, 1981). Coronal brightness and polarization using a broad bandpass have been measured by the white light coronagraph (WLC) on Skylab. These data have been used by various authors to deduce coronal densities (see below).

One of the main instruments was the Harvard College Observatory EUV spectrometer S-O55 (HCO), on the Apollo telescope mount (ATM). The Skylab HCO spectrometer had good spatial resolution in the 280 Å - 1350 Å range, but low spectral resolution ($\simeq$ 1.6 Å). This limited the information that could be extracted from these data and might explain why many studies based on these data have produced conflicting results. In the standard grating position, the instrument scanned six wavelengths typical of chromospheric to coronal temperatures: Lyα (1216 Å, $T \simeq 2\text{x}10^4$); C II (1336 Å, $T \simeq 3.5\text{x}10^4$); C III (977 Å, $T \simeq 7\text{x}10^4$); O IV (554 Å, $T \simeq 1.5\text{x}10^5$); O VI (1032 Å, $T \simeq 3\text{x}10^5$) and Mg X (625 Å, $T \simeq 1.1\text{x}10^6$). With other grating positions, spectroheliograms of the lines Ne VII (465 Å, $T \simeq 5\text{x}10^5$) and Si XII (521 Å, $T \simeq 1.8\text{x}10^6$) were also recorded. The good spatial resolution of the HCO spectrometer enabled *Vernazza and Reeves* (1978) to produce a list of line intensities for different solar regions. As already mentioned, these data include the *only* coronal hole spectra in that wavelength range obtained before SOHO.

Skylab observed many mid-latitude coronal holes, classified by *Nolte et al.* (1976) as CH 1,2,.... The principal one (CH 1) was already formed when Skylab started its observations, and is known as the 'Italy boot-shaped' coronal hole, due to its famous appearance. It extended N-S from the north pole to southern latitudes, and passed the central meridian on November 21-22 1973. No other such elongated coronal holes were observed by Skylab. The photospheric magnetic field was predominantly of positive polarity within the coronal hole, the same as the north pole and the polarity of the *following* parts of northern-hemisphere active regions. It was surrounded by predominantly negative polarity. A magnetogram taken one rotation before the first Skylab CH 1 observation showed an active region (at $\sim 15°S$) with positive *leading* polarity. Therefore, the unipolar region probably formed from the decay of the active region flux (*Timothy et al.*, 1975; *Wang and Sheeley*, 1993).

After Skylab, the Coronal Helium Abundance Spacelab Experiment (CHASE) on the Spacelab 2 Mission was a specific mission to determine the helium abundance from the ratio of He II 304 Å to Lyman-α 1218 Å, on the disc and off the limb.

In addition, rocket borne EUV spectrometers were developed at the University of Colorado. The first high resolution images of the Sun using the multi-layer technique were obtained

in 1987 by *Walker et al.* (1988) at around 171-175 Å(Fe IX, Fe X) and at 256 Å (He II, Fe XXIV). In 1989, *Golub et al.* (1990) obtained an image with a normal incidence X-ray telescope (NIXT), with a filter centred at around 63.5 Å (Mg X, Fe XVI). The Multi Spectral Solar Telescope Array (MSSTA) was first flown in 1991 (*Walker et al.*, 1993) and produced sub-arc-second resolution (0.7") images in Lyman-α and Fe XII (193 Å) and 1.5" images in Fe XIV (211 Å).

The Solar EUV Rocket Telescope and Spectrometer (SERTS), developed at the Goddard Space Flight Center, has been flown several times since 1989, and has produced both non overlapping spectroheliograms and stigmatic spectra (slit 4.9′ by 7") of the same solar region. SERTS has observed many quiet sun and active regions, but has not observed coronal holes. Given its high spectral resolution, and an overlap with the wavelengths observed by CDS, the SERTS observations are particularly important, especially for instrument calibration purposes. A re-examination of the SERTS 1989 observation (SERTS-89) is presented in Chapter 3.

Finally, it should be noted that many other satellites and instruments have observed the solar corona, and in particular coronal holes at both X-rays and UV wavelengths. For example, Yohkoh is a successful satellite that has observed the solar corona in X-rays, with four instruments. It was mainly designed to study energetic phenomena such as flares, and not coronal holes. Various High Resolution Telescope and Spectrometer (HRTS) rockets, developed at the Naval Research Laboratory (NRL), have observed in the UV the solar transition region. The sixth one, flown on November 20th, 1988 observed a coronal hole on the disc.

EUV line lists and identifications.

Despite the large number of observations of the solar corona, very few EUV spectral observations have been sufficiently complete and accurate to allow extensive line lists and identifications to be made. The most important studies for direct comparison with CDS are listed here.

Malinovsky and Heroux (1973) were among the first to apply the *Pottasch* (1963) emission measure method to confirm or reject previous identifications in the 50-300 Å range, using an integrated Sun spectrum with 0.25 Å resolution taken with a grazing-incidence spectrometer flown on a rocket in 1969.

Firth et al. (1974) give a line list in the 140-870 Å range, based on U.K. rocket observations, with 0.17 Å resolution.

Behring et al. (1976) present a high-resolution (0.06 Å) spectrum in the 160-770 Å range

of the entire Sun, taken with a rocket flight. The lines were identified based on their position, and the intensities were only approximate.

Dere (1978a) presented a list of line identifications based on all the flare observations of the NRL SO82-A instrument aboard Skylab, in the 171-630 Å range, with 0.1 Å resolution. This list is therefore biased toward high-temperature lines. *Dere* (1982) presents an extensive list of lines from spectra of active regions observed with the same NRL SO82-A instrument.

The SERTS-89 observation has been described by *Thomas and Neupert* (1994), including a useful line list in the 170-450 Å range, based on high resolution well calibrated spectra. More details can be found in Chapter 3, where this observation is re-analysed.

Space observations: SOHO

Details of the SOHO project and its instruments can be found in a special issue (Vol. 162) of the Solar Physics journal (1995). More information on the publicly-available data and software databases can be found on the World Wide Web:

`http://sohowww.nascom.nasa.gov/`

The 12 instruments on SOHO are:

- SUMER (Solar Ultraviolet Measurements of Emitted Radiation) is a normal incidence spectrometer in the 500 to 1610 Å band, with high spatial resolution (1.2-1.5″) and high spectral resolution ($\frac{\lambda}{d\lambda}$ = 19 000 to 40 000). Doppler velocities and line broadenings can be measured down to 1 km/s separately for each spatial resolution element.

- The CDS instrument, described in *Harrison et al.* (1995), consists of two instruments: a Normal Incidence Spectrometer (NIS) and a Grazing Incidence Spectrometer (GIS), which overall cover the 151-785 Å spectral region [with two channels in normal incidence (NIS 1, NIS 2) and four channels (GIS 1, GIS 2, GIS 3, GIS 4) in grazing incidence] at moderate resolution (0.35-0.5 Å). CDS can observe coronal diagnostic lines on the disc, unlike SUMER. More details on CDS, including data reduction methods, can be found in Chapter 3.

- UVCS (Ultraviolet Coronagraph Spectrometer) can perform spectroscopic observations between 2 and 10 $R_\odot$ from sun centre and produces line profiles of Lyα, O VI,

Fe XII and many other ions. It allows a determination of proton velocity distribution, proton outflow velocity, electron temperature, and ion outflow velocities and densities.

- EIT (Extreme ultraviolet Imaging Telescope) is a normal-incidence, multi-layer telescope which covers the full solar disc (1024 x 1024 pixels with a field of view of 45'x45'). Subfield images can be created in four band-passes: Fe IX 171 Å, Fe XII 195 Å, Fe XV 284 Å and He II 304 Å. The pixel resolution is 2.6″.

- LASCO (Large Angle and Spectrometric Coronagraph Experiment) is a set of three coronagraph telescopes that image the solar corona in white light from 1.1 $R_\odot$ to 30 $R_\odot$ (C1: 1.1 to 3 $R_\odot$; C2: 1.5 to 6 $R_\odot$; C3: 3.5 to 30 $R_\odot$).

- VIRGO (Variability of solar IRradiance and Gravity Oscillations) has two types of active cavity radiometers that are measuring the spectral irradiance and radiance variations on time scales down to minutes. These monitor the solar irradiance (formerly known as the *solar constant*).

- GOLF (Global Oscillations at Low Frequencies) measures doppler shifts of sodium absorption lines, deducing mean disc line-of-sight velocities, to study p and g modes of the solar non-radial oscillations.

- MDI (Michelson Doppler Imager) images the Sun on a 1024 x1024 CCD camera through a series of increasingly narrow filters (Michelson interferometers) and polarizers, giving a full-width-half-maximum (FWHM) bandwidth of 100 mÅ centred on Ni I 6768 Å. Velocity and magnetic field line-of-sight components and continuum intensity can be determined once per minute, with a resolution of 4″ over the whole disc. A higher resolution is also achievable with a smaller field of view.

- SWAN (Solar Wind ANisotropies) measures Lyman alpha UV light scattered by interplanetary H I, in order to determine the large scale solar wind distribution.

- Particle instruments study the solar wind and the solar energetic particles (SEP): COSTEP (Comprehensive Supra-thermal and Energetic Particle Analyzer); CELIAS (Charge, Element, and Isotope Analysis System); ERNE (Energetic and Relativistic Nuclei and Electrons experiment).

1.2.2 General coronal hole characteristics

Following the first EUV observations, coronal holes were defined (*Reeves and Parkinson*, 1970) as those areas with much lower (by factors up to 10) intensities of coronal lines (e.g., Mg X 625 Å). It should be noted that such a simple definition of coronal hole areas can be

misleading. In fact, the so-called *filament channels* also appear as thin long regions of low intensity in coronal lines. Filament channels are usually (but not always) associated with stable dark H_α chromospheric features. Characteristic features that differentiate *filament channels* from coronal holes, are: (1) X-ray arches cross over a channel but diverge in a coronal hole; and (2) *filament channels* lie along neutral lines.

In the lines emitted from the transition region, it is difficult to recognize coronal holes. Studies based on Skylab and HRTS data (*Huber et al.*, 1974; *Dere et al.*, 1989) have shown that transition region lines have almost the same intensity distribution inside and outside coronal holes, with the only difference that the brightest supergranular cell boundaries (network) are depressed in coronal holes (by about 50 %). Transition region lines produce limb-brightened rings that in coronal hole areas are both elevated (10-15") and wider (5-8" in width), compared to the quiet sun regions (*Withbroe and Noyes*, 1977). This observation has been interpreted in the sense of a larger range of heights over which the lines are formed, and therefore indicates a lower temperature gradient in coronal holes. As a result, the heat flux conducted from the corona to the transition zone is much smaller (by an order of magnitude) in the holes than in the quiet sun.

In chromospheric lines, coronal holes are once again clearly visible. For example, in the EUV He I and He II emission lines, the network within the holes is about 50% of the intensity of the quiet sun. Because chromospheric lines do not have the problem of foreground emission that coronal lines have, they can be used to trace the hole boundaries. In the visible part of the spectrum, the network areas show stronger He I absorption both inside and outside coronal holes, while the cell centres have lower He I absorption. On the average, coronal hole areas have lower He I (10830 Å) absorption than the other areas, and therefore the equivalent width of this line has become a commonly used diagnostic for defining coronal holes. It is interesting to note that in transition region lines, coronal holes sometimes show large jets of plasma (*macrospicules*), that are not visible in the quiet sun. Macrospicules differ from the H_α spicules in that their average width, height and lifetime are all much greater, and also that they tend to be radial, whilst spicules have no preferred inclination.

Bocchialini and Vial (1996) analysed the profiles observed by the OSO-8 spectrometer inside and outside of the equatorial coronal hole which was at the centre of the solar disc between 27 and 29 November, 1975. After separating coronal hole and quiet sun profiles and taking an average, they found stronger Hydrogen L_α (40 %) and Mg II k profiles (25 %)in the coronal hole, compared to the quiet sun. Network L_α intensities, on the other hand, are very similar. This result is rather surprising, and at variance with other Skylab observations (e.g. *Vernazza and Reeves*, 1978).

In terms of physical parameters, previous coronal hole observations (see the reviews of *Habbal, Esser, and Arndt*, 1993; *Withbroe*, 1988; *Hara et al.*, 1994), based primarily on Skylab data, have shown coronal holes to be regions of lower coronal density and temperature. However, the various results are not in very good agreement with each other, and are not as precise as the theoretical solar wind models require (*Habbal, Esser, and Arndt*, 1993). More details on how coronal hole densities and temperatures have been estimated are given in the following Sections.

Coronal hole area, distribution and rotation

He I 10830 Å observations during the period 1978-1991 have been used by various authors (e.g. *Insley et al.*, 1995) to study the distribution of coronal holes. This large dataset has shown that in the declining phase of the solar cycle and at solar minimum, the polar coronal holes dominate, and have equator-ward extensions, while there are but few low-latitude coronal holes. Around solar maximum, on the other hand, mid-latitude coronal holes dominate, and have a large spread in latitude. The time variation of the distribution of mid-latitude holes follows the same equator-ward trend as the sunspots. In addition, the mid-latitude coronal holes exhibit significant differential rotation, although not as pronounced as that observed for sunspots. However, the equator-ward extensions of polar coronal holes show no differential rotation.

Timothy et al. (1975) using Skylab data, deduced that although the structures that delineate the hole boundary change significantly, coronal holes rotate almost rigidly, with only a slight distortion due to the solar differential rotation. The rotation rate is almost equal to that of the sunspot equatorial rotation. After the Skylab era, other coronal holes were observed, some of which showed significant differential rotation (*Wang and Sheeley*, 1993), while others (*Tsuneta and Lemen*, 1993, from Yohkoh observations) apparently did not.

The boundaries of coronal holes change in short timescales and those are related to appearances or disappearances of bright points, according to *Kahler and Moses* (1990). These authors explain the boundary changes using a magnetic reconnection scenario. In particular, *Wang and Sheeley* (1993) explain the formation of the Skylab CH 1 in terms of an interaction between the axisymmetric polar field and the non-axisymmetric photospheric flux, in the form of a decaying active region located at low southerly latitude. In general, it is therefore concluded that equatorial coronal holes rigidly rotate during the declining phase of a solar cycle, when an active region erupts at low latitudes and interacts with the polar fields. Conversely, during the rising and maximum phases of the cycle, non-axisymmetric photospheric flux tends to be present at higher latitudes, and coronal holes tend to shear and rotate differentially at the local photospheric rate.

1.2.3 Temperatures

Coronal hole temperatures have previously been estimated using various methods assuming an isothermal plasma. *Habbal, Esser, and Arndt* (1993) review the range of temperatures that have been deduced from remote (e.g., spectroscopic) measurements of coronal holes, within a distance of 1.6 $R_\odot$, and they also review the accuracy to which these temperatures have been determined. *Withbroe* (1988) also reviews coronal hole temperature measurements, and those are critically discussed below. Apart from the in-situ measurements, all others can be usefully separated into those observations made on the disc, and those made above the limb. Observations above the limb have the advantage that physical parameters like temperature and density can be measured as a function of the radial distance. However, care must be taken to allow for foreground and background quiet Sun emission along the line of sight (see, e.g., *Esser et al.*, 1995), which (on the other hand) can be a small effect for on-disc observations.

Temperatures from in-situ charge state measurements

Empirical constraints on the temperatures at the "freezing-in radius" have been derived from charge state measurements at 1 AU. The freezing-in radius is the distance from the Sun centre where the expansion time of the solar wind equals the equilibrium timescale between the ions. Various assumptions must be made in order to deduce such temperatures, e.g.: assumptions about the expansion model, the charge state distribution, the elemental abundances, the distribution function of the electrons and the relative flow speed of the different charge states. *Galvin et al.* (1984) found a value of 1.3 ± 0.2 MK at 1.5 $R_\odot$ from CNO ions, while *Ipavich et al.* (1986) derived values of 1.3 ± 0.3 MK at 1.5 $R_\odot$ from CNO ions and 1.4 ± 0.2 MK at 3 $R_\odot$ from Fe ions. For recent results from Ulysses SWICS data and models, see *Ko et al.* (1997).

Temperatures above the limb from white light observations

Analyses of white-light coronagraph observations have been used to derive the radial density profile from the measured intensity of the polarized brightness of the K corona, following *van de Hulst* (1950). Assumptions about the F corona contribution and the density distribution along the line of sight produce additional uncertainties in the densities. Then the temperature can be derived, assuming an isothermal atmosphere in hydrostatic equilibrium. Clearly, the deduced temperatures can only be rough estimates.

Temperatures from Lyα profiles

Several coronagraph experiments (e.g. Spartan, SOHO/UVCS) have provided temperatures above polar coronal holes from Lyα profiles (see, e.g., *Withbroe et al.*, 1986; *Kohl et al.*, 1980). The spectral line profiles, at the distances observed by these instruments, have two components. The resonantly scattered, relatively narrow component provides empirical constraints on the electron and proton temperatures. The weaker, electron scattered component is wider and related to the electron density and temperature. This method provides effective temperatures rather than kinetic temperatures, and therefore the reported values can be used as upper limits to the temperature of the coronal plasma.

Limb observations from EUV intensities

Many early studies, instead of directly measuring temperatures, deduced them from observations of radial intensity profiles off-limb, and an appropriate model. For example, *Krieger et al.* (1973) inferred a temperature of 1.3 x10^6 K at a distance 1-1.14 $R_\odot$ in a south polar coronal hole using X-ray images of a rocket flight on 1970 November 24. They deduced X-ray intensities from photographic densities, and from these they derived the density scale height and finally the temperature, assuming an isothermal spherically symmetric model. *Mariska* (1978) derived the off-limb temperature of a polar coronal hole on 14th August 1973 (near solar minimum), using the spectroheliograms of the HCO instrument on Skylab. The radial intensity profile of five EUV lines of different elements were fitted with an empirical model that assumes an isothermal corona in hydrostatic equilibrium. The derived parameters are the density (1.7 x10^8 cm^{-3}) and conductive flux (6 x10^4 ergs cm^{-2} s^{-1}) at the base of the corona which was assumed to be 1.03 $R_\odot$, together with a coronal temperature of 1.1 x10^6 at 1.08 $R_\odot$. The model then yields a temperature of 7.6 x10^5 K at 1.03 $R_\odot$. A *DEM* analysis was also performed.

Other studies have derived isothermal temperatures from line ratios, but in most cases lines emitted by different elements were used, and this limits the accuracy of the temperatures inferred. For example, *Habbal, Esser, and Arndt* (1993) present some estimates of off-limb temperatures, from analysis of 1973 December 13 Skylab S-O55 spectroheliograms, using intensity ratios of the lines Mg X (625 Å), Ne VII (465 Å), and O VI (1032 Å). These were limb observations of a south polar coronal hole and its neighboring quiet regions. The authors assert that there is very little contamination from quiet region emission along the line of sight. They obtain a temperature range of 7.8-9.3 x 10^5 K, between 1.02 and 1.07 $R_\odot$ for the coronal hole, and 9.4 x 10^5 - 1.2 x 10^6 K for the quiet regions bordering it, where this quoted range in temperatures is due to inhomogeneities within the coronal hole itself. The authors carefully take account for possible abundance variations. They varied

the theoretical abundances of the three observed elements (Mg, Ne, O), to obtain the best agreement between abundances and temperature. This was probably the most accurate pre-SOHO work, in terms of temperature measurements based on EUV lines, and it gives an idea of how the paucity of data affected the attempted measurements.

Guhathakurta et al. (1992) derived temperatures from the intensity ratio of two Fe XIV lines: the 173 Å line recorded by a rocket; and the green 5303 Å line from ground-based observations. They found an average coronal temperature of 1.34 x 10^6 K for a south polar coronal hole and 1.27 x 10^6 K for a north polar coronal hole, at 1.15 $R_\odot$, during the 1988 March 17-18 solar eclipse. They also deduced temperatures from density scale heights deduced from contemporaneous white light coronagraph observations, but these values (0.95 and 1.1 x 10^6 K) are not in agreement with the previous ones.

Esser et al. (1995) analysed daily intensity measurements at 1.15 $R_\odot$ of the green Fe XIV 5303 Å and red Fe X 6374 Å lines. Their main finding is that the coronal hole temperatures derived using the line ratio technique vary by more than 0.8 x 10^6 K over the time interval of the observations which covered about four solar rotations. They also discuss how the regions surrounding the coronal holes might influence the temperature gradient in the coronal holes.

Disc observations and emission measure analysis

Direct EUV observations on the disc have been rare, and so on-disc temperatures of coronal holes were also scarce. For example, using OSO-4 data, *Munro and Withbroe* (1972) found a coronal hole temperature of 1.05 x10^6 K, assuming constant electron pressure and temperature gradient.

The most complete description of the distribution of plasma at different temperatures is given by a DEM analysis. Only a few DEM analyses have been performed on coronal hole EUV spectra (*Munro and Withbroe*, 1972; *Raymond and Doyle*, 1981b; *Dere and Mason*, 1993; *Doschek*, 1997a; *Mason et al.*, 1997).

Raymond and Doyle (1981b) derived a DEM from the 'Italy' coronal hole observed by Skylab, using the averaged cell-centre and network intensities of *Vernazza and Reeves* (1978). See Chapter 2 for a re-analysis of these data.

Doschek (1997) have deduced emission measures using high-resolution NRL S082-B Skylab spectra of different regions (including coronal holes). In this case the information was limited by the fact that only transition region lines in a restricted temperature range ($3x10^4 - 2.5x10^5$ K) were observed at the limb.

Temperatures from filter ratio techniques

Finally, temperatures have also been estimated by many authors from soft X-ray or EUV broad-band filter images, this method uses the intensity ratio of two filters in which emission comes mainly from plasma at distinct temperatures for the respective two filters. For example, *Hara et al.* (1994) estimate the temperatures of a large coronal hole that extended to both northern and southern hemispheres, with the filter ratio technique of *Tsuneta et al.* (1991), applied to the Soft X-ray Telescope (SXT) aboard Yohkoh. The estimated coronal hole temperatures are 1.8-2.4 x 10^6 K, almost the same values as those derived for quiet regions. The Yohkoh X-ray filter ratio technique therefore yields coronal hole temperatures around 2 MK (as confirmed by *Hara*, 1997), a result that contradicts other estimates (e.g. by almost a factor of two higher than from EUV spectra). This fact has puzzled many researchers. Yohkoh observes coronal X ray emission from a broad range of plasma temperatures above 1x10^6 K, and with a sensitivity biased toward hotter emission in the 3–6x10^6 K range. A possible explanation for the apparent discrepancy is then the presence of hot material in the line of sight.

In general, these *filter ratio techniques should be avoided*, if possible, for a variety of reasons. First, the lines that contribute to the emission observed through one filter, will not normally be formed at the same temperatures, and hence might not be emitted by the same spatial regions: the filter does not then sample isothermal plasma. Secondly, the lines in a broad-band emission, might derive from different elements (as is the case for the Yohkoh filters), and therefore assumptions about element abundances have to be made, thus increasing the uncertainty in what is already only an average temperature.

1.2.4 Densities

The density measurements that differentiate between coronal holes and plumes will be described in Section 1.2.6. Most studies (e.g., *Munro and Jackson*, 1977; *Guhathakurta et al.*, 1993; *Guhathakurta and Holzer*, 1994) have estimated the electron density following the *van de Hulst* (1950) method.

Many other authors have derived densities from the intensity gradients in off-limb observations. For example, *Mariska* (1978), as already explained, derived a density of 1.7x10^8 cm^{-3} for the 14th August 1973 polar coronal hole, a value remarkably close to the values subsequently derived by SOHO.

Other recent studies have determined the temperature and density structure of the solar corona from a combination of K-coronal and polarization brightness (from eclipse or coro-

nagraph observations), the green and red coronal forbidden lines, and EUV images from a sounding rocket (e.g. *Guhathakurta et al.*, 1996).

Crude estimates of densities have also been obtained from the emission measure method. For example, *Hara et al.* (1994) estimated the total emission measure of a coronal hole from Yohkoh observations, and found values in the range $10^{25.5}$ - $10^{26.2}$ cm^{-5}, about ten times smaller than those of quiet regions. Therefore, if their deduced temperatures and EM values are correct, it follows that the observed lower soft X-ray intensity of the coronal hole regions is due to a density that is lower by a factor of 3 compared with the quiet regions.

However, as mentioned above, the most accurate method is to use density-sensitive ratios of lines emitted from the same ion. In the past, very few such EUV observations have been performed, and none successfully used coronal lines to deduce coronal hole densities, before SOHO was launched. *Dwivedi and Mohan* (1995a) estimated the electron density in a coronal hole using the Mg VIII density-sensitive theoretical line ratio [436.62 / 430.47], and Skylab HCO data, to find an electron density $N_e = 3.4\text{x}10^7$ cm^{-3} for the coronal hole, compared to $N_e = 5.8\text{x}10^7$ cm^{-3} for the quiet sun, using the *Vernazza and Mason* (1978) data. However, the HCO data were affected by blending, as the same authors pointed out.

It is only with SOHO that, for the first time, line-ratio techniques have been fully applied to obtain coronal hole densities. *Doschek et al.* (1997b) applied a ratio technique to coronal lines (Si VIII and S X) in SUMER off-limb observations. They found the coronal hole densities to be systematically lower than those in the quiet sun, by a factor of about 2. Similar results, based on a much more complete data set, were found during this thesis work, as described in Chapter 5. *Laming et al.* (1997a) also present off-limb SUMER observations, and deduce densities from various coronal line ratios. More recently, *Warren and Hassler* (1999) accurately measured off-limb densities at a height between 10″ and 20″ from the limb, using many lines from SUMER, and found densities $N_e \simeq 10^{8.35}$, with a small scatter.

Regarding measurements of electron densities at lower heights, i.e. from lines emitted at lower temperatures in the transition region it should be noted that before SOHO even quiet-sun results were very rare, and had large uncertainties. This was due to the low spectral resolution and low sensitivity of the previous instruments. *Munro and Withbroe* (1972) were among the first to attempt a measurement of transition region densities in coronal holes using OSO IV spectra and the C III 1176/977 Å density-sensitive ratio. As the authors reported, the data did not allow a reliable measurement of the density. However, some coronal hole areas were found to have densities a factor of two to three lower than the quiet sun regions. *Dupree et al.* (1976) analysed Skylab HCO data and

found significant variations in the C III 1176/977 Å ratio, for different solar regions, with an average value for the quiet sun of 0.29, yielding a density $N_e = 4.6\text{x}10^9$ cm^{-3}. A trend for higher densities in the cell centres was also found, although in the quiet sun regions the uncertainty was large. *Vernazza and Reeves* (1978) derived densities from the same C III 1176/977 Å lines observed by the Skylab HCO instrument, but found $N_e \simeq 1\text{x}10^{10}$ cm^{-3} from the averaged spectra, with no differences between coronal holes and quiet sun. Moreover, differences were found between the cell centres and network regions, but this time with the network having larger (by about a factor of two) densities than the cell centres, in contradiction to the previous analyses done by *Dupree et al.* (1976). However, the density sensitivity of this C III ratio is small and furthermore C III could be affected by some opacity effects.

Various authors used the Skylab NRL S082-B to deduce densities. However, only observations close to the limb could be used for density diagnostics. *Doschek et al.* (1978) presented densities for coronal holes and the quiet sun close to the limb, using C III, O III, and Si IV lines, finding an averaged value $N_e \simeq 1.9\text{x}10^{10}$ cm^{-3} for the quiet sun regions, with no differences in the polar coronal hole, except in one case where a lower density (by a factor of 2) was found. *Cook and Nicolas* (1979) also derived densities for coronal holes and the quiet sun from Skylab NRL S082-B observations close to the limb, using C III, Si III and Si IV lines, finding densities in the range $N_e = 3\text{x}10^9 - 2\text{x}10^{11}$ cm^{-3}, with most of the values at the limb $N_e \simeq 1\text{x}10^{10}$ cm^{-3}, and with no differences between quiet sun and polar coronal holes. Recently, *Doschek* has re-analysed some of the NRL S082-B observations, comparing the results that are obtained using different instrument calibration, and using more recent atomic data. The results from O V, Si III, C III showed discrepancies, that moreover could not be easily explained by a wrong calibration. Densities had a large scatter of values around $N_e \simeq 1\text{x}10^{10}$ cm^{-3}, depending on the ratio and/or the instrument calibration adopted, with the coronal hole having consistently lower values.

Cook et al. (1995) present O IV and Si IV density diagnostics in the UV range applied to solar and stellar spectra. From HRTS and Skylab S082-B observations of the quiet sun and active regions, but not coronal holes. Large discrepancies were also found there, with one O IV ratio producing a value of $N_e = 5\text{x}10^9$ cm^{-3} for the quiet sun region. *Keenan et al.* (1995) present new calculations for O V diagnostics and apply the 1371.29 Å / 1218.35 Å ratio to HRTS and Skylab S082-B observations at the limb, of coronal hole, quiet sun, and active regions. a density $N_e = 3\text{x}10^{10}$ cm^{-3} for a coronal hole region observed by the Skylab instrument was found, with no differences from the quiet sun values. In terms of transition region pressures, the values that can be found in the literature (see, e.g., *Dere et al.*, 1982) are about $P_e = 1\text{x}10^{15}$ cm^{-3} K for the quiet sun.

Recently, many results based on SOHO have started to be published. The results obtained during this thesis work are described in Chapter 5. *Young and Mason* (1997) use O IV and Mg VII lines to estimate densities in bright transition regions. *Pinfield et al.* (1999) presents the first detection of an O V forbidden line and use it to deduce $N_e \simeq 10^{8.5}$ for the quiet sun. *Doschek et al.* (1998a) presents densities derived from the O V 759.441 and 761.128 Å lines observed at the limb by SUMER, and finds densities inside coronal holes ($N_e = 2 - 3\text{x}10^9$), a factor of two lower than in the quiet sun. No differentiation between cell-centres and network regions was possible, because the lines were observed at the limb in this case.

1.2.5 Element abundances

A large number of papers (and reviews, see above), have been written on this subject, and there are still differences of opinion on the reality and importance of the FIP effect. (Recall that different solar structures show different element abundances, and these appear to be related to the first ionization potential of the elements, with the low-FIP ($\leq$ 10 eV) elements tending to have higher abundances. Articles that deal with solar abundance determinations and models include these by: *Mariska* (1980); *Veck and Parkinson* (1981); *Widing et al.* (1986); *Widing and Feldman* (1989, 1992, 1993); *Feldman and Widing* (1990, 1993); *Schmelz* (1993); *Laming et al.* (1995); *Geiss* (1995); *Schmelz et al.* (1996); *Fludra and Schmelz* (1995); *Grevesse and Anders* (1991); *Peter* (1998); *Grevesse and Sauval* (1998) and *Grevesse and Sauval* (1999). Photospheric abundances of most elements are relatively well determined (with uncertainties of the order of 15%), although values are continuously changing (see, e.g. the photospheric C, N, O abundances that in the recent study of *Grevesse and Sauval*, 1998, are about 20% lower than the previously quoted values). The photospheric abundances of the noble gases (as e.g. Ne and Ar) are not directly measured (because absorption lines of these elements are not present in the photospheric spectra). Their values are derived from carbonaceous meteorites, and therefore have large uncertainties.

The coronal values are still very uncertain, because they depend critically on the method of derivation. Most relative abundances have been measured in situ by various spacecraft studying the solar wind, or else with EUV spectroscopic techniques (which rely on the accuracy of the atomic physics). In general it has been found, from direct observations, that low-speed solar wind (SSW) and gradual Solar Energetic Particle events (SEP) show a permanent large scale FIP effect (of the order of 4-5), while in the high-speed solar wind (HSSW), no significant FIP-bias has been measured. This has also been confirmed by Ulysses observations of the Mg/O ratio (*Geiss*, 1995).

In almost all papers that derive element abundances using X-EUV spectroscopy, a large scatter of values is found. In some cases, for a few elements there are large deviations from the 'canonical' photospheric values. For example active regions show FIP effect factor from 0 to 4-5. Table 1.2 lists the most commonly used representative sets of 'standard' coronal and photospheric values, as used in this thesis.

The recent SOHO results have not solved the abundance problems, and if anything are creating more confusion on this subject. A critical review of the different EUV spectroscopic methods, with a re-analysis of Skylab data, is given in Chapter 2. It is found that crude approximations have been applied in many cases, and some important effects neglected, such as the presence of *DEM* distributions in the plasma. *Schmelz* (1993) is one of the few authors that apply a *DEM* method to X-ray spectra of solar flares to deduce relative element abundances, finding enhancements in the Ne/O and S/O abundance ratios, relative to their photospheric values.

Table 1.2: *Coronal (*Feldman *et al., 1992b) and photospheric (*Grevesse and Anders, *1991) element abundances. Note that these photospheric abundances have been adopted as reference values throughout this thesis. The FIP values are from* Martin and Wiese *(1996).*

Z	Element	Coronal	Photospheric	FIP (eV)
1	H	12.0	12.00	13.59
2	He	10.9	10.90	24.59
6	C	8.59	8.60	11.26
7	N	8.0	8.00	14.53
8	O	8.89	8.93	13.62
9	F	-	4.56	17.42
10	Ne	8.08	8.09	21.56
11	Na	6.93	6.33	5.14
12	Mg	8.15	7.58	7.65
13	Al	7.04	6.47	5.99
14	Si	8.1	7.55	8.15
15	P	-	5.45	10.49
16	S	7.27	7.21	10.36
17	Cl	-	5.50	12.97
18	Ar	6.58	6.56	15.76
19	K	-	5.12	4.34
20	Ca	6.93	6.36	6.11
21	Sc	-	3.10	6.56
22	Ti	-	4.99	6.83
23	V	-	4.00	6.75
24	Cr	-	5.67	6.77
25	Mn	-	5.39	7.43
26	Fe	8.1	7.67	7.90
27	Co	-	4.92	7.88
28	Ni	6.84	6.25	7.64
29	Cu	-	4.21	7.73
30	Zn	-	4.60	9.39

Schmelz et al. (1996) report anomalous Ne/O abundance variations, by about a factor of two, both below and above the 'standard' coronal value of 0.15 for the relative abundance

of these two high-FIP elements.

The Helium abundance is not reliably determined from X-EUV observations. In the HSSW and SSW the He abundance is very variable but on the average is 2-3 times lower than the photospheric value.

Coronal hole abundances have only been estimated by a few authors. In general, they do not show significant FIP effects. Coronal hole plumes are a special case, in the sense that large FIP biases have been reported (*Widing and Feldman*, 1992), from a single EUV observation close to the limb of the brightest polar plume observed by Skylab. Analysis of plume abundances should therefore be useful to test theoretical models that try to explain the FIP effect (see e.g. *Peter*, 1998).

Feldman and Widing (1993) found that Ne/Mg is lower in open field regions than in closed field regions, but there is a large scatter in the values they obtained. Assuming a Ne/Mg photospheric ratio of 3.39, and a constant pressure of 1.2 x $10^{15} cm^{-3} K$ in the transition region, and therefore a density of 3 x 10^9 for the selected ions, they found Ne/Mg values in the ranges 1.5-2 and 1.8-4.6 for the coronal holes and quiet regions respectively. *Habbal, Esser, and Arndt* (1993) used intensity ratios of three spectral lines from coronal hole images recorded by Skylab S-O55 on 1973 December 13, to derive O, Ne and Mg abundances. They found the values: $A_b(\mathrm{O}) = 8.96$, $A_b(\mathrm{Ne}) = 8.2$, and $A_b(\mathrm{Mg}) = 7.65$ (on the usual log scale where $A_b(\mathrm{H}) = 12$).

Very recently, some results from SOHO observations have been published.
Young and Mason (1997) have found large variations in Mg/Ne from CDS active region observations. *Feldman et al.* (1998) present SUMER off-limb observations which confirm a relative FIP effect of a factor of about 4 between a quiet sun streamer region and above the north coronal hole, assuming that the plasma was isothermal. However, it has to be pointed out that they used lines from different ions, and found that '*the Ne VIII, Na IX, Mg X lines, all of which belong to the Li-like isoelectronic sequence, appear to indicate a systematic lower effective FIP bias value than the rest of the lines*'. Since they used the O VI 1032 Å to normalize all the other lines, and since O VI *is* also of the same isoelectronic sequence, their result should be treated with caution. Examples of the particular behavior of the Li-like ions have also been found during the course of the present work, and these are presented later in this thesis. *Doschek et al.* (1998b) has also recently presented SUMER off-limb observations in the quiet sun (streamer) and polar coronal hole regions but they analysed lines of Si VII and Ne VII as representatives of low- and high-FIP elements. Surprisingly, they found photospheric values for Si/Ne (i.e. no FIP effect) in the streamer regions, and *an enhancement* of Si/Ne (i.e. 'anti-FIP' effect) in a coronal hole inter-plume region. However this last result was only a factor of 2, which is within the overall

uncertainty deriving from the atomic physics and the observational errors.

It would be useful to determine the individual elemental abundance values (relative to hydrogen), but these are difficult to measure in the corona. In principle, they can be determined by Solar Energetic Particle (SEP) measurements, or by spectroscopic measurements, by comparison of line intensities with either hydrogen continuum emission (which is always contaminated by some scattered background intensity), or with the resonantly scattered hydrogen emission lines observed in the corona. However, the errors in these methods mean there is some uncertainty as to whether the observed variations are in fact due to a depletion of high-FIP elements or an enhancement of low-FIP elements. This is a long-standing issue in solar physics. *Veck and Parkinson* (1981) were the first to compare line intensities and hydrogen continuum emission and found that the low-FIP elements seem to have their photospheric values, and that high-FIP elements are *depleted*. *Fludra and Schmelz* (1995) applied a *DEM* analysis on the same solar flare spectra examined by *Schmelz* (1993), combining the line information with hydrogen continuum data. They found high-FIP elements *depleted*, compared with their photospheric values, with a gradual FIP-effect. Direct measurements of inner-shell Fe lines have also shown (*Phillips et al.*, 1994, 1995) that the coronal Fe abundance is equal to the photospheric one, within a factor of two, and therefore if the FIP effect exist, it is a *depletion* of the high-FIP elements. Other papers (see, e.g., *Meyer*, 1993; *Reames*, 1995, from SEP analysis) point in the opposite direction, i.e. they found that low-FIP elements are *enhanced* in the corona, while high-FIP elements retain typically the photospheric abundances (and therefore are *not depleted*). More recently, *Raymond et al.* (1997) have used SOHO/UVCS data to determine absolute abundances in the high coronal streamer regions, from a comparison of emission lines and H I scattered light. They found that high-FIP elements are *depleted* even by factors of ten, in the core of an equatorial streamer (but with large spatial variations).

Regarding possible explanations for the observed FIP effect, it has been suggested (e.g. *Meyer*, 1993) that this depletion is occurring at the chromospheric level ($T \leq 10^4$ K) where the low-FIP elements are more easily ionized by electron collisions. In fact, the FIP effect implies an ion-neutral fractionation, and this can take place only at those temperatures, where the ions are only partially ionized. Then, in the presence of open magnetic field lines these ions can drift out into the corona to become more ionized. For closed magnetic structures, the ions would be trapped. Therefore, the abundances observed in the open field regions would reflect the production rates of the first ions at the coronal base, while those of the closed regions would be similar to the photospheric values. However, the recent SOHO data seem to introduce more questions, instead of solving the long-standing problems. For example, there have been independent indications (*Raymond et al.*, 1997, from

UVCS data; *Feldman et al.*, 1998, from SUMER observations) of gravitational settling, which makes ions of heavier elements behave differently from the other ones, thus casting doubt on the whole physical reason for the creation of the observed element abundance variations.

Another process that can affect element abundance variations is ambipolar diffusion (see *Mariska*, 1992, p. 184). In the lower transition region, the electrons are more mobile, because of the presence of a large number of neutral atoms. This will create an electric field and enhance the diffusion of the ions. This process is dependent on ionic charge, not on FIP.

1.2.6 Coronal plumes

Solar coronal plumes are common features and they originate in coronal holes. They appear as ray-like, extended (up to few solar radii) structures in white-light eclipse coronagraph images of the polar regions (see, e.g., *van de Hulst*, 1950; *Saito*, 1965), and as shorter spikes in EUV images (e.g. *Ahmad and Withbroe*, 1977; *Widing and Feldman*, 1992; *Walker et al.*, 1993), at X-rays (*Ahmad and Webb*, 1978), and possibly also at radio wavelengths (*Gopalswamy et al.*, 1992). It is important to study plumes because they are the only stable observable structures within coronal holes, where the heating and acceleration processes lead to the formation of the fast solar wind (FSW).

In EUV, plumes have been known to be visible only in emission lines that form over a narrow range of temperatures (e.g. *Widing and Feldman*, 1992), with emission from ions that form at temperatures above a million degree almost absent.

DeForest et al. (1997) showed that plumes seen in white light and in the EUV are the same physical objects, tracing plume structures from the lower corona up to 15 $R_{\odot}$. Plumes have been shown to diverge super-radially, with an expansion factor ~ 10 (*DeForest et al.*, 1997 and references therein). They are stable structures, lasting from a few hours to more than one day, and tend to be recurrent, i.e. appear and disappear at the same locations (*Lamy et al.*, 1997). They are usually rooted in the boundaries of chromospheric cells (see, e.g., *Wang and Sheeley*, 1995b; *DeForest et al.*, 1997), where there is a concentration of unipolar flux of the same sign as that of the ambient coronal hole. In many cases a small concentration of opposite magnetic flux is found at these sites, (*Wang et al.*, 1997), suggesting that magnetic reconnection plays an important role in the formation and evolution of plumes (*Wang*, 1998). On the other hand, not all magnetic flux concentrations on network junctions inside coronal holes have plumes associated with them.

Because of their morphology, it is generally assumed that plumes trace the open field lines

of the coronal holes. They would therefore be expected to exist in low-latitude coronal holes as well as in polar holes. A few such observation have been claimed (*Wang and Sheeley*, 1995a; *Woo*, 1996). *Del Zanna and Bromage* (1999a) - see Chapter 5 in this thesis - report the first detection by SOHO of a low latitude plume visible on the disc.

These features are also particularly interesting because they present an extreme case of particular element abundances, as explained above.

Prior to SOHO, it was not possible to clearly distinguish characteristics of plumes and ambient coronal hole (inter-plume) regions. Density and temperature measurements were mostly based on Skylab and coronagraph data, and were only very approximate determinations. Densities were usually estimated from the plume brightness in Thomson scattered white light coronagraph observations, applying the *van de Hulst* (1950) technique. For example, *Fisher and Guhathakurta* (1995) presented densities of polar coronal holes and plumes extending from 1.16 to 5 $R_\odot$, as a function of the radial distance. They showed that plumes have shallower density gradients, and need to be 3-5 times denser than their surroundings, in order to explain these white light coronagraph observations. Temperatures were usually only estimated from intensity gradients of EUV emission lines, assuming hydrostatic equilibrium and ionization equilibrium, which were shown to be reasonable approximations (*Widing and Feldman*, 1992).

In the reminder of this Section, the main observational results are re-evaluated (in chronological order), followed by comments on the theoretical models used to interpret them.

pre-SOHO observations.

Saito (1965) presents white-light observations of plumes. With the assumptions that plumes are isothermal and in hydrostatic equilibrium a temperature of 1.2×10^6 K was found.

Ahmad and Withbroe (1977) presented Skylab observations of three off-limb polar plumes seen with the HCO instrument. Intensity profiles across the observed plumes, at a fixed radial distance from the Sun, suggest that the density distribution across them can be represented by a gaussian profile. Also, the intensity ratios of Mg X/O VI lines show a marked decrease in the plumes (with constant values inside them), suggesting that plumes contain cooler material than their surroundings and have a constant temperature across their width. Radial profiles of the Mg X/O VI intensity ratio along the plumes, in the range 1.03-1.11 $R_\odot$, show a tendency to increase from 0.3 to about 0.8. Assuming a relative Mg/O abundance of 0.079, these authors derived the associated isothermal temperature increase, with values $T \simeq 1.1 \times 10^6$ K. A calculation was performed by the author using

more recent atomic data (CHIANTI), assuming that only the transitions Mg X 624.941 and O VI 1031.91 contributed to the observed lines, gives a different range of temperatures (T = 8.3x10^5 , 9.3x10^{5}K), for a Mg/O abundance of 0.079. In fact, much of the uncertainty in the derived temperature is in the relative abundance. The Mg/O abundance that *Ahmad and Withbroe* (1977) adopted is quite high, compared with 0.045 for photospheric (*Grevesse and Anders*, 1991), or 0.18 for coronal abundances (*Feldman et al.*, 1992b). Assuming a photospheric abundance, for example, increases the temperatures T = 8.9x10^5 to 1.15 x10^6 K. Thus, the plume temperatures deduced from *Ahmad and Withbroe* (1977) were probably overestimated. The density along the plumes was estimated from the temperature profiles and so, given the large uncertainties in the derivation of the temperature, their density estimates should be treated with caution.

Ahmad and Webb (1978) presented Skylab S-054 X-ray images of polar plumes seen off-limb. Following *Ahmad and Withbroe* (1977), they assume a gaussian shape for the density distribution. Using some assumptions (e.g. that plumes are isothermal along the line of sight), they deduce radial profiles of the electron pressure, between 1.04 and 1.1 $R_\odot$. These curves are well fitted with a model that assumes hydrostatic equilibrium and an isothermal temperature along the plumes of 7.9x10^5 K. They then reject the model because this temperature is too low compared to those derived by *Saito* (1965) and *Ahmad and Withbroe* (1977).

Walker et al. (1993) analysed some plume X-ray images obtained by multi-layer optics. Compared to Skylab observations, these have better spatial resolution ($\sim$ 1.5″), and extend up to 0.6 $R_\odot$ off the limb. They could only estimate plume temperatures and densities from the scale height of the intensity in one filter image, together with the application of a model which assumed that plumes have higher densities and slightly higher temperatures than the inter-plume regions. Hence, their deduced temperature and densities are very approximate.

Widing and Feldman (1992) analysed the brightest polar plume observed by the Skylab S082-A spectroheliograph at the limb, on 1973 December 11. They measure the intensities at plume centre of various lines (Ne VI, VII, Mg VI-VIII, Na VIII, Ca IX,X), at different heights above the limb. They derived a hydrostatic temperature for each ion, assuming hydrostatic equilibrium to relate temperature and density, and relating the measured intensities with the density. They found good agreement between this temperature and the temperature of maximum emission in ionization equilibrium. This agreement suggests that the plume could be approximated by a multi-thermal structure, with each ion emitting under hydrostatic and ionization equilibrium conditions. Outflow velocities in the range 10-20 km s^{-1} were consistent with their data. The electron density derived from the Mg

VIII [436.7/430.5] ratio has a large scatter around $N_e = 10^9 cm^{-3}$ and does not show the decline toward higher altitudes that is derived from the intensity measurements. A comparison of this mean value with the average density derived from the Mg VIII EM suggests a 0.3 filling factor for that plume. Finally, *Widing and Feldman* (1992) performed an average line differential emission measure (DEM_L) analysis (see Chapter 2, below for a definition), using the line intensities as measured at two heights. This analysis was used to derive relative element abundances, and it represents the only one made on plumes. Their result is that this plume had an Ne/Mg abundance ratio 10 times smaller than the photospheric ratios, thus this plume showed an FIP effect of 10. *Widing and Feldman* (1992) also found that the Ca/Mg and the Na/Mg ratio do not differ by more than a factor of 2 from the corresponding photospheric values.

Wang and Sheeley (1995a) have identified in the Skylab S082-A EUV images some plume-like features inside low-latitude coronal holes undergoing either east or west limb passage. Like the polar plumes, these diffuse structures are prominent in the Mg IX (368 Å) images and rarely visible in the Ne VII (465 Å) images, probably because of the lower temperature of formation of Ne VII and the reduced Ne/Mg abundance ratio in the plumes. Also, at the base of the plumes, compact network enhancements (within the weak background emission of the coronal hole) are visible in the Ne VII, He II (465, 304 Å), and sometimes other coronal lines. A plume was observed during its movement inward from the limb; its lifetime was more than one day but less than two; the associated hot emission (Fe XV 284 Å) near the base remained strong for more than 11 hours, and began to fade after 22 hours. Although these authors only present a few cases, it could be concluded that coronal plumes with similar characteristics can occur in regions of open magnetic field lines at *any* latitude, from polar regions to equatorial ones.

Wang and Sheeley (1995b) use a theoretical model to show how the appearance of coronal plumes varies, depending on their orientation relative to the line of sight. In their model, plumes are aligned along open magnetic field lines, which are calculated using a potential field method. Hydrostatic equilibrium is also assumed. The simulations show that plumes would appear as diffuse objects when viewed projected on the disc. With the aid of this simulation, those authors identified various plumes at different latitudes in a coronal hole seen , in Mg IX (368 Å) spectroheliograms from Skylab S082-A, and also located underlying network features in the corresponding Ne VII (465 Å) and He II (304 Å) images. When the base of the plumes was visible (in Mg IX) against the disc, intense network features within their base areas were always found, but the converse did not hold: not every Ne VII or He II bright point had an associated Mg IX plume. An analysis of a lower latitude hole, observed on 1974 January 15, compared with a simultaneous high-resolution magnetogram, showed that the plumes occurred in the vicinity of mixed

magnetic polarity regions, although not every magnetic bipole had a plume associated with it. Mixed polarity was present wherever neon and helium enhancements occurred in the coronal hole.

Woo (1996) reported the detection of low-latitude plumes using Ulysses radio ranging observations. *Fisher and Guhathakurta* (1995) estimated densities of south and north polar coronal holes and rays extending from 1.16 to 5 $R_\odot$, as a function of the radial distance. The densities were derived by applying the van de Hulst technique to the 1993 April 11-12 observations obtained with the white-light coronagraph aboard the Spartan 201-01 spacecraft, together with the ground-based K-coronameter on Mauna Loa, Hawaii. Coronal rays appeared as coherent structures at much higher altitudes (5 $R_\odot$) than previously observed.

Theoretical models.

Since the high-speed solar wind originates from open field regions, a full solar wind theory should also explain the observed properties of coronal plumes. Various solar wind-plume models have been proposed (see *Wang*, 1994, *Velli et al.*, 1994 and *Del Zanna*, 1997, for some of the most recent ones) but they all suffer from a lack of observational constraints, in particular on the temperature of the plumes.

Wang (1994) developed a model of steady and radial mass flow of a single-fluid within a polar plume, exemplified as a flux tube with constant section. A two-component heating source in the energy conservation equation was assumed. In addition to the "global" heating (with damping length $H_m \sim R_\odot$), required to drive the high-speed wind from the plume and inter-plume regions, the model showed that a large amount of energy must be dissipated over a scale $H_b \ll R_\odot$, in order to produce the high plasma densities observed in the plumes ($N_e \geq 10^9$ cm^{-3}). This concentrated heating gives rise to a steep temperature gradient with a local temperature maximum just above the plume base, while at greater distances the plume is cooler than the inter-plume regions. Although the mass flux densities are higher within the plumes, the inter-plume regions occupy most of the polar hole area and are therefore the main source of the high-speed polar wind.

Velli et al. (1994) presented a solar wind model which takes into account the possible origin of fast solar wind streams in coronal plumes. They model the solar wind as a combination of warm, dense plumes immersed in a cooler and less dense solar wind. Their model shows plumes expanding beyond 10 $R_\odot$ and having larger β than the inter-plume regions. *Del Zanna* (1997) solved a self-consistent ideal 2-D MHD steady model that took into account pressure, inertial and gravity forces, under the assumptions of azimuthal

symmetry around the plume axis and constant temperature along the field lines in a low-beta plasma. This model reproduces basic plume features such as the super-radial expansion near the plume base.

SOHO observations

Many problems concerning coronal plumes were therefore unsolved at the time of SOHO's launch. For example, it was not entirely clear whether plumes were cooler or hotter than their surroundings, nor whether plumes are not the source of the high speed solar wind. The results for element abundances suggest that plumes are not the source of the high speed solar wind.

SOHO spectroscopic observations have sufficient spatial and spectral resolution to allow a more accurate characterisation of plumes than was previously possible. Some recent results are summarised here.

Wilhelm et al. (1998) presented SOHO SUMER off-limb (in the range 1.03 - 1.6 $R_\odot$) spectroscopic observations of plume and inter-plume regions. They estimated temperatures and densities using Mg IX and Si VIII line ratios. Plume temperatures are approximately constant around $T = 780\ 000$ K and then decrease at higher radial distances, while inter-plume temperatures were found to increase over the same height range. Densities of both plume and inter-plume regions start at $N_e \simeq 1\text{x}10^8$ cm^{-3} and then decrease with height, with plumes having shallower gradients.

Although these adopted line ratio techniques are among the most accurate for determining temperatures and densities from EUV spectra, the *Wilhelm et al.* (1998) results are severely limited by the fact that plumes and inter-plume regions were compared using data over a time span of six months, and at different spatial locations.

SUMER (e.g., *Hassler*, 1997) and UVCS (*Noci et al.*, 1997, *Kohl et al.*, 1997) off-limb observations have shown that the spectral line widths in the inter-plume lanes are larger than in the plumes, indicating lower temperatures in plumes as a possible explanation.

EIT images were used by *DeForest et al.* (1997) to estimate plume temperatures in the range $1 - 1.5\text{x}10^6$ K, finding higher temperatures in the inter-plume lanes (but by no more than 30%).

The new SOHO results therefore all suggest that plumes are slightly cooler and denser, and that the high-speed wind is likely to stream out of the inter-plume regions. In this thesis (Chapters 5 and 6) new results obtained from CDS observations are presented, confirming these early SOHO findings.

Chapter 2

Critical discussion of spectroscopic diagnostic techniques and their application to CDS data

CDS was designed with sufficient spectral resolution to enable EUV spectroscopic diagnostic techniques in determining coronal plasma parameters (density, temperature and abundance). In this chapter, the main diagnostic methods are described and compared, explaining the choice of techniques employed in this thesis.

The adopted methods and the software that was developed are described, with details of the recommended techniques and line selection for use with CDS. All the comments are based on the experience gained during the last three years from the analysis of a large number of CDS spectra and from comparisons with spectral data from other instruments in the same wavelength range, mainly the Skylab data and high-resolution SERTS data. Here only a summary of the main diagnostics that were found to be more appropriate for use with CDS are presented. A description of CDS, and the full CDS line identification and comparison of observations with theoretical calculations are given in Chapter 3. Examples of spectra and the assessment of line blending is also given in Chapter 3.

The main density and temperature diagnostics based on line ratio techniques are presented in Sections 2.1 to 2.3, while Section 2.4 describes the method developed to derive the differential emission measure (DEM).

Section 2.5 focuses on a critical discussion of emission measure (and differential emission measure) techniques and the evaluation of element abundances. This is based on a re-analysis of the Skylab coronal hole spectral data. Various concepts and definitions that will be used in the remainder of this thesis are also explained here. Some interesting results of this re-analysis are presented, revealing departures from previous results which casts some doubt on the applicability of ionization equilibrium for ions of the Li-like sequence.

Section 2.6 contains a critical discussion (with examples and a re-analysis of Skylab data) of previous work on element abundances, showing how various effects can change the results, in particular showing the importance of the inclusion of the thermal distribution along the line of sight (the DEM) in the calculations for the element abundances, something that has been neglected in the past in most cases. A discussion of the potential of CDS spectra for element abundance analysis is also presented.

2.1 Electron density diagnostics

CDS observations can be used to estimate average electron densities along the line of sight, using density-sensitive ratios of lines emitted from the same ion.

Theoretical calculations for EUV lines, useful for coronal hole and quiet region density diagnostics, have been presented, in some cases together with comparisons with observations, by a large number of authors. Also many review papers have been written on the subject. A useful long bibliography of spectroscopic diagnostics in the EUV-UV, organised by isoelectronic sequence, is given by *Keenan* (1996). Some of the most useful publications about density diagnostics in the CDS wavelength range are now briefly mentioned. *Dwivedi and Raju* (1980) present density diagnostics for Mg VIII and Si X lines. *Mason and Monsignori Fossi* (1994) present a review paper on spectroscopic diagnostics for solar and stellar plasma. *Masai* (1994) studied O V (and Fe XXII) density diagnostics for application to tokamak plasma, pointing out the diagnostic capabilities for these ions. *Keenan et al.* (1994) present O V diagnostics applied to solar observations. *Dwivedi and Mohan* (1995a) present Mg VIII calculations applied to coronal hole Skylab observations. *Dwivedi and Mohan* (1995c) present Ne V and Mg V diagnostics with solar applications. *Foster et al.* (1997) analyse various Mg VIII line ratios and compare them with Skylab observations; *Mason et al.* (1997) apply spectroscopic diagnostics to CDS observations for the first time. Finally, many papers have been written on applications of the SERTS-89 observations presented by *Thomas and Neupert* (1994). For example, *Brickhouse et al.* (1995) have presented an analysis of the Fe ions, including density diagnostics, while *Del Zanna et al.* (1995) have previously produced a more complete differential emission measure analysis using many ions of different elements. *Young et al.* (1998) have recently presented a complete analysis, including recalibration, of the SERTS-89 spectrum, with a description of the density diagnostics used. *Dwivedi et al.* (1998) have also presented a list of diagnostics to be applied to the SERTS-89 spectrum.

A large effort was spent in checking which of the many proposed diagnostics were applicable to CDS, or if there were new ones not proposed by previous authors, in order to select

the most useful ones. A set of CHIANTI routines that calculate the level populations and present the ratio of lines of the same ion, calculated at constant temperature, have been used for this purpose. In the majority of cases, the CHIANTI calculations were found to be in agreement with the other calculations found in the literature. A set of IDL routines were written by the author to convert the observed ratio values with their errors to density values, performing spline interpolation between the theoretical points. Although a full critical description of the various density diagnostics is beyond the scope of this Chapter, there are some key points that are worth considering.

1. It has to be noted that all the density diagnostics used in this thesis calculate the line ratios at the temperature of maximum ionization fraction, and some degree of approximation is therefore introduced. Figure 2.1 shows the density-sensitive Si IX ratio calculated at three temperatures ($T = 10^6$ K is the temperature of maximum ionization fraction for Si IX), showing that these temperature variations do not appreciably affect the ratio.

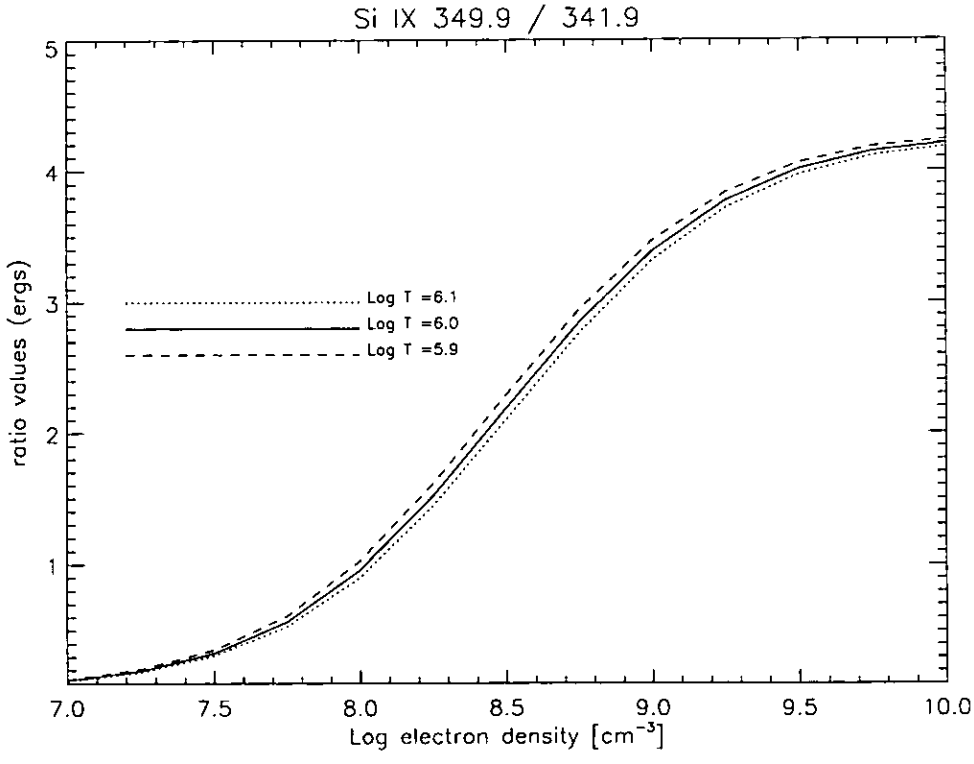

Figure 2.1: *The density-sensitive Si IX ratio and its variation with temperature.*

2. The process of photoionization, that is not included in the CHIANTI routines, can have some effects on the density estimation. The radiation that comes from the solar photosphere can excite transitions between levels in the ground configuration of ions in the corona, mainly affecting the level balance calculations for very low densities

($N_e \leq 10^8$ cm^{-3}, see *Young*, 1998t). The effect is stronger close to the photosphere, and tends to die out with height because of the decrease of the photospheric radiation field with distance. This decrease can be accounted for by estimating a geometric dilution factor that is a function of height above the photosphere. Si IX should be affected more than other ions.

Photoionization has not been taken into account in this thesis, partly because of the difficulty in estimating the height of the emitting plasma for on-disc observations, where all the plasma at all heights in principle contributes to the observed emission. The introduction of the photoionization would have the effect of lowering the electron densities derived from the observations (possibly by up to 30-40% for Si IX), so the densities derived from Si IX in this thesis should be treated as upper values, in cases when $N_e \leq 10^8$ cm^{-3}. A possible estimate of the real importance of the photoionization process for this issue can be given comparing densities obtained by transitions that can be affected with those that are not, in off-limb observations. It should be noted that no obvious effects due to photoionization were found in the spectra analysed, if we except a coronal hole off-limb observation (see Section 6.2).

3. Many density diagnostics proposed in the literature involve ratios of lines emitted by different elements (*Dwivedi and Mohan*, 1995b; *Dwivedi and Mohan*, 1995c). In view of the fact that small differences in contribution functions can be very important indeed, and in view of the uncertainties of the elemental abundance evaluations, it was felt that these diagnostics should *not* be used.

4. As already mentioned, the various line ratios usually produce a large scatter of values, and it is therefore important to confirm any density estimate with other estimates based on the maximum possible number of different line ratios. Also, there are some well known density ratios that produce results which strongly disagree with those derived from ions that are emitted at similar temperatures.

5. Most of the observed diagnostic lines are very weak, which makes the data analysis difficult.

6. Then last, but not least, is the fact that many proposed diagnostic ratios are affected by blending which varies depending on the type of source observed, and which is particularly strong at the moderate resolution of CDS.

Table 2.1 presents a list of useful line ratios available with CDS, while Figure 2.2 shows how some of these ratios vary with density. Only the principal usable ratios are listed, involving pairs of lines seen by the same spectrometer and detector. In fact, the use of pairs seen by different spectrometers is severely limited by any time variability of the

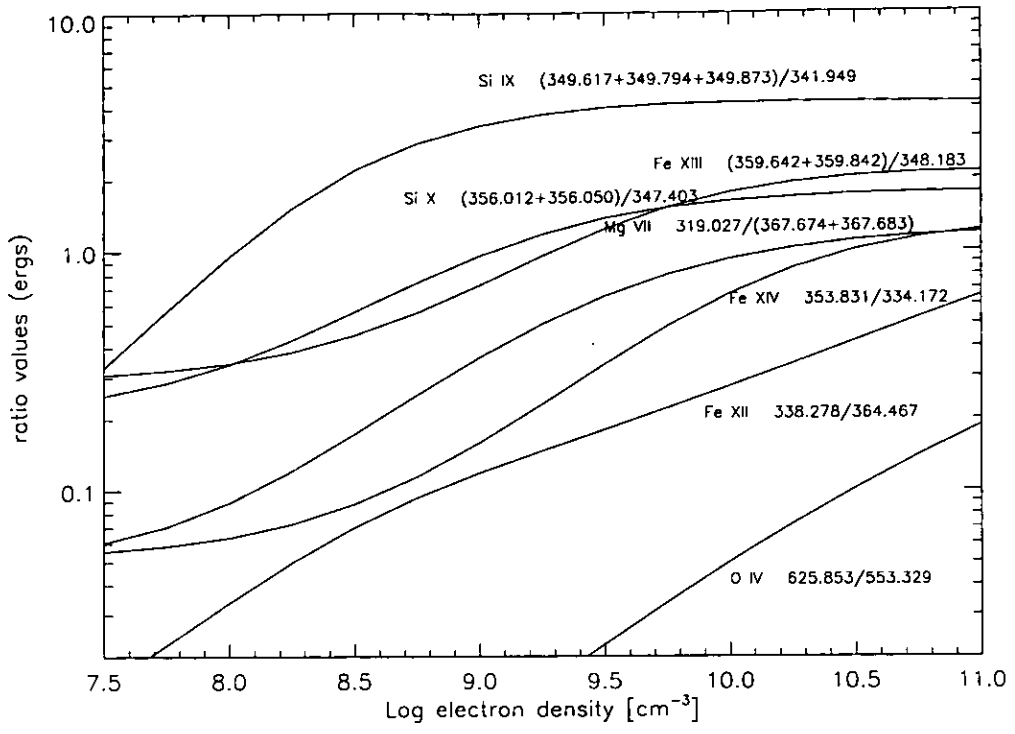

Figure 2.2: *Some useful density-sensitive line ratios observed by CDS.*

Table 2.1: *Density sensitive line ratios observed by CDS, ordered by the temperature of maximum of the contribution functions shown in column 4, calculated with the ionization equilibrium calculations of* Arnaud and Rothenflug *(1985). The ranges for which the ratios can be used are shown in column 5. The numbers in parentheses indicate the number of transitions that compose the self-blends. The lines indicated with a (!) have problems in either their observation or in the atomic physics. The lines indicated with a (*) are the best selection within a wider choice. The detectors in parentheses indicate that the lines are also visible in second order. N means NIS, and G means GIS; the NIS and GIS channels are described in Chapter 3.*

Ion	Ratio (Å)	Detector	log T_{max}	log N_e
O IV	625.853 (!) / 608.397 (*)	N 2	5.27	8.0 – 11.0
Mg VII	319.027 (!) / 367.7 (2) (*)	N 1	5.81	7.0 – 10.0
Mg VII	280.737 / 434.700 (*)	G 3	5.81	7.0 – 10.0
Mg VIII	315.038 / 317.038	N 1	5.91	7.0 – 8.5
Mg VIII	315.038 / 313.754	N 1	5.91	7.0 – 8.5
Mg VIII	436.7 (2) / 430.465	G 3	5.91	7.0 – 9.0
Si IX	349.9 (3) / 341.949	N 1 (G 4)	6.02	7.5 – 9.5
Si IX	345.100 / 341.949	N 1 (G 4)	6.02	7.5 – 9.5
Si IX	349.9 (3) / 345.100	N 1 (G 4)	6.02	7.5 – 9.5
Fe X	175.3 (2) (!) / 174.534 (*)	G 1	6.04	9.0 – 11.0
Fe X	324.763 (!) / 345.722	N 1	6.04	7.0 – 10.0
Si X	356.0 (2) / 347.402	N 1 (G 4)	6.12	8.0 – 10.0
Fe XII	338.278 (!) / 364.467 (!) (*)	N 1 (G 4)	6.16	7.0 – 12.0
Fe XIII	359.6 (2) (!) / 348.18	N 1 (G 4)	6.21	8.5 – 10.5
Fe XIII	320.8 (!) / 348.18	N 1	6.21	7.0 – 10.0
Fe XIII	203.8 (2) / 202.044	G 1	6.21	8.5 – 10.5
Fe XIV	353.83 (!) / 334.17	N 1 (G 4)	6.25	9.0 – 11.0

source and by cross-calibration uncertainties. Many of the ratios are formed between a density-sensitive line and a relatively insensitive one, choosing the brightest and the least affected by blends, which is close in wavelength to the other line (to reduce calibration errors, discussed further in Chapter 3).

The ranges for which the ratios can be used are also shown in Table 2.1, but this does not mean that all the ratios are usable in all cases. Ions like Fe XIII that emit above a million degrees, for example, are simply not seen in coronal holes or in very quiet regions of the Sun. Most of the ratios can be reliable or not depending on the source region observed, because of blending with different lines, either emitted at lower or higher temperatures. The lines indicated with a (!) have problems in either their observation or in the atomic physics. This is based on experience gained in analysing different source regions (e.g. on-disc, off-limb, coronal holes, quiet sun, active regions) with the different detectors, and on the best possible line identification, with *DEM* analysis of the various regions. Chapter 3 describes some example spectra in detail. Note that most of the reliable density-sensitive ratios are in NIS 1, although in many cases they can be seen in second order in GIS 4.

Comments on the lines in Table 2.1

O IV

The O IV 625.9 Å line is very weak and in the wing of the Mg X 624.9 Å line, but is more visible when the Mg X intensity is reduced, as in coronal holes. This line is density-sensitive and has previously been used in the study of transition region brightenings (*Young and Mason*, 1997). This line could be partly blended with the second order Fe XIII 312.872 Å, but due to the low NIS sensitivity in second order (see Chapter 3), this is only likely to be a problem in active region spectra. The other O IV lines seen in NIS 2 are all strong lines (seen at 553.329, 554.513, 555.263 Å), usually with good agreement between them. O IV 608.4 Å was selected because it is closest to the 625.9 line. Note that an error in the CHIANTI database concerning this, and the line at 609.829 Å, has been discovered and corrected in version 2.

Mg VII

CDS observes many Mg VII lines, of which only two are strongly density-sensitive, at 319.027 and 280.737 Å. The ratio of the 319.027 Å line to any of the three other lines observed in NIS 1, one at 363.772 Å, one at 365.2 Å(self-blend of 365.176 + 365.234 + 365.243 Å), and one at 367.7 Å(self-blend of 367.674 + 367.683 Å) would be a good density diagnostic, but should be used with caution, for many reasons. First, the 319.027 Å is weak (except in plumes or similar low-temperature objects) and can be blended with Ni XV

319.063 Å line, if high-temperature plasma is present along the line of sight . Secondly, the other three lines are very close to other lines, and their measurement is difficult, including the 367.7 Å line, which is the brightest of the three and close to the brightest line of all in the NIS 1 detector, the Mg IX 368 Å line. Thirdly, the 319.027 Å line is quite distant in wavelength from the other lines, and a correct intensity calibration is crucial. The 280.737 Å line is observed in GIS 3. The ratio of this line with any of the relatively bright lines observed in the same detector at 434.7 (434.72 + 434.917), 429.14, 431.2 (431.188 + 431.313) Å is also a good density diagnostic.

Mg VIII

Mg VIII lines are observed in various CDS detectors. The two ratios of the lines visible in NIS 1 are only weakly density-sensitive. The 436.7 (436.735+436.672) Å/ 430.465 Å ratio is one of the best diagnostic ratios that are present in the GIS.

Si IX

CDS observes many Si IX lines, but only those visible in NIS 1 are usable, because those seen in GIS 2 are affected by *ghosts* (see Chapter 3). The lines visible in NIS 1 are seen at 341.949, 345.1, and 349.9 Å. The last is a complex self-blend of three transitions. These lines are free of blends and close in wavelength.

Fe X

The Fe X 175.3 Å line is not strong and lies close to the bright Fe X 174.534 Å so its intensity is not well determined. Its ratio to any of the lines at 174.534, 177.242, 184.543 Å is a good density diagnostic. The Fe X 324.763 Å line is weak and this is the first time it is identified, to the author's knowledge.

Si X

CDS observes many Si X lines, but only the two visible in NIS 1 can be used. They are free from blends and were found to give densities in close agreement with those derived from Si IX. The line at 356.0 Å (a self-blend of two transitions) lies close to other lines, so its intensity must be carefully measured.

Fe XII

Most of the Fe XII lines are observed in NIS 1 and GIS 1. Among them, CHIANTI predicts only a few density-sensitive lines, while all the others have emissivities that vary only slightly with density. Of the three brightest density-sensitive lines, one is seen in GIS 1 at 186.8 Å(a blend of the 186.851 and 186.884 Å lines), while the other two fall in the NIS 1 wavelength range, at 335.339 and 338.278 Å. Unfortunately, the first line at 186.8

Å in normal quiet sun conditions is blended with an Fe VIII 186.6 Å line (Arcetri spectral code), and is therefore not generally usable. In some cases, such as in plumes, where the thermal plasma distribution is biased toward lower temperatures, the Fe VIII 186.6 Å line even becomes dominant.

Only in active region spectra can the contribution from the Fe VIII line be neglected. The derived density is found to be significantly higher than that derived from other ions, as was recently confirmed with high-resolution SERTS observations (*Brosius et al.*, 1998). In their work, the Fe XII ratios 186.8/195.1 and 196.6/193.5 both give much higher densities ($\log N_e = 10.0 \pm 0.2$) compared to the densities derived from Fe X, Fe XI, Fe XIII, Fe XIV ($\log N_e \simeq 9.4 \pm 0.2$).

Now, considering the lines observed in NIS 1, the 335.339 Å line predicted by CHIANTI has never been identified, since the much stronger Mg VIII 335.253 Å and Fe XVI 335.41 Å lines are too close in wavelength, even for the highest resolution spectrometers. CHIANTI adopts for Fe XII the energy levels of *Jupen et al.* (1993), who present new Fe line identifications based on a detailed comparison of solar, beam-foil, tokamak and laser-produced high-resolution spectra. They reject the identification of the 335.06 Å line, given by *Thomas and Neupert* (1994) (and also found in all the previous literature), and predict an Fe XII line at 335.33 Å. The contribution of this Fe XII line to the observed blend was always assumed to be negligible, probably because most of the EUV spectra analysed were of active regions or obtained during relatively high solar activity, when the Fe XVI 335.41 (the strongest line of the doublet) becomes one of the brightest lines in the whole spectral region. However, our CDS observations indicate that this line *does exist* and gives a non-negligible contribution (as shown in Chapter 3).

In any case, we are left only with the bright Fe XII 338.278 Å line for a density diagnostic. The ratio of the bright Fe XII 338.278 Å with any other Fe XII line observed in NIS 1 would be excellent, as shown in Figure 2.2, since it spans a large density range. The lines that can be used in conjunction with the 338.278 Å line are at 346.852, 352.106 and 364.467 Å. The brightest Fe XII 364.467 Å is partly blended with the Si XI 364.497 Å line, which is only seen in active region spectra, not in coronal holes or the quiet sun. It is possible to estimate the Si XI contribution to the observed line, from the intensities of the other Si XI lines seen in the spectra. The Fe XII 352.106 Å is partly blended with an Al VII 352.149 Å line, while the 346.852 Å line should be free of blends.

However, the ratio of the 338.278 Å line to any of these three lines also gives very high densities at odds with those derived from other ratios. This is not a new result, as it has been observed in many other cases in SERTS spectra (*Brosius et al.*, 1996; *Young et al.*, 1998), but has been explained by the presence of an unidentified line blend. Now, the

high spectral resolution of the SERTS spectra (compared to CDS) and also the fact that all the other observed density-sensitive Fe XII lines produce high densities, favours the alternative hypothesis that there is something wrong in the Fe XII theoretical calculations. This point has relevance in the discussion of the NIS 1 calibration and the discussion on the identification of the 335.339 Å line given in Chapter 3.

In conclusion, the Fe XII 338.278 Å line *can* be used for density diagnostics in conjunction with any other Fe XII line seen in the same detector, *but* bearing in mind that it is giving overestimated densities.

Fe XIII

The Fe XIII 359.7 Å(359.642 + 359.842 Å) line is close to the Ne V 359.382 Å line, and therefore can be reliably used only in off-limb or active region observations. The same applies to Fe XIII 320.809, which is blended with O III 320.976 Å and Mg IV 320.994 Å.

Fe XIV

Fe XIV has always been a problem in EUV spectroscopy. Although tens of bright Fe XIV lines are present in EUV spectra, especially in active regions, disagreement between observations and theory has been reported by numerous authors. Only very recently, new calculations (*Storey et al.*, 1999) have shed some light on the Fe XIV problem.

One density diagnostic ratio is reported, but should be used with caution, since the Fe XIV 353.83 Å becomes blended with an Ar XVI 353.920 Å line in active region spectra.

Some other density-sensitive ratios with problems

Now, follow some comments on a few of the many density-sensitive lines that are visible in the CDS wavelength range but which present a series of problems.

Ne V 416.194 / 481.3 (or Ne V 416.843 / 481.3) is not easily usable, because the 481.3 Å line is difficult to fit, being almost at the edge of GIS 3, and because it is a blend with a second order Fe XIII line.

CDS observes various O V 2s 2p ^{3}P – 2p^2 ^{3}P transitions around 760 Å (760.444, 758.675, 762.002, 759.439, 760.225, 761.126 Å from the brightest to the weakest) seen in GIS 4, and the strong 629.73 Å line in NIS 2. The ratio of any of the lines seen in GIS 4 with the 629.73 Å line is a good density diagnostic in the range $N_e = 10^{10} - 10^{12}$, but unfortunately the fact that these lines are observed by the two different spectrometers prevents their use. In fact, the O V lines exhibit repeated brightenings, so these lines can be used for diagnostics only if observed simultaneously, which is not possible with CDS. The 761.126 Å line is

also a good density-diagnostic in conjunction with any of the other lines of the multiplet, but is very weak and, with the GIS resolution, in the wing of the bright 760.444 Å line. Only SUMER is able to clearly separate these lines, allowing this ratio to be used to derive densities (*Doschek et al.*, 1998a).

The Mg IX 443.973, 448.293, 439.176, 441.199, 443.403 Å lines (ordered from the brightest to the weakest) are density-sensitive at densities lower than 10^9 and their ratio with any of the lines (368.070, 706.060, and 749.551 Å) could be used as a diagnostic. Unfortunately, aside from calibration problems, these lines are weak and partly blended with first and second order lines, which limits their use.

The Fe XI 308.548 Å line is density-sensitive and could be used in conjunction with e.g. the 369.153 Å line, but it is a weak line, at the edge of NIS 1, probably blended, and in the case of GIS 2, probably affected by *ghosting* problems (see Chapter 3).

Concluding comments

Although the CDS instrument potentially has many density-diagnostic capabilities, unfortunately for various reasons only some of these can be reliably used. Most of them are observed in the NIS 1 channel, which has a low sensitivity and suffers from scattered light (see Chapter 3 for details). The lines observed by the GIS have large uncertainties because of various anomalies and detector effects (see Chapter 3 for details).

Many of the usable density-sensitive lines are emitted at high temperatures, and are hardly visible in coronal holes. Here, sufficient signal-to-noise can only be achieved at the expense of spatial and/or temporal resolution. The Si IX [349.9 Å/ 341.9 Å] ratio is the best density diagnostic for typical coronal hole densities. This ratio varies by a factor of 2 over a variation in density of a factor of 6, (at $N_e \simeq 2 \cdot 10^8$ cm^{-3}). These lines have the added advantage that they are close in wavelength and any error due to the instrumental calibration is minimized. Other line ratios mostly used in this thesis for coronal densities are Si IX [349.9 Å/ 345.1 Å] and Si X [356. Å/ 347.4 Å] . Transition region densities have been estimated principally using the Mg VII [319.0 Å/ 367.7 Å] and the O IV [625.9 Å/ 608.4 Å] ratios.

2.2 The *L-function* method of determining electron density

This diagnostic method allows an evaluation of density and of possible errors in the relative intensity calibration of lines seen at different wavelengths at the same time, comparing

lines emitted by the same ion. This method is described by *Landi et al.* (1997a). Briefly, a reasonable assumption is that the *contribution function* can be written in the form:

$$G_{ij}(T, N_e) = f_{ij}(T, N_e)g(T) \tag{2.1}$$

where $g(T)$ is the temperature dependence that mainly comes from the ionization equilibrium and for each ion is the same for all the lines. If an effective temperature T_{eff} is defined:

$$LogT_{eff} = \frac{\int g(T)\ DEM(T)\ logT\ dT}{\int g(T)\ DEM(T)\ dT} \tag{2.2}$$

the function $L_{ij}(N_e)$ (hereafter *L-function*) can be defined as the ratio between the observed line intensity $I_{\rm ob}$ and $G_{ij}(T_{eff}, N_e)$, calculated as a function of N_e at the temperature T_{eff}:

$$L_{ij}(N_e) = \frac{I_{\rm ob}}{G_{ij}(T_{eff}, N_e)} \tag{2.3}$$

The diagnostic method relies on the observation that if all the L-functions of the same ion, calculated with the line fluxes derived from a well-calibrated spectrum, are displayed in the same diagram versus the electron density, all the curves should meet in a common point $(N_e^\star, L(N_e^\star))$. Moreover, the L-functions of density-independent lines should be superimposed. An example of this behaviour is shown in Figure 2.3. It is important to note also that unsplit multiplets of the same ion share this common behavior. The first step is to calculate a DEM. The second step is to compute the effective temperature T_{eff}, which depends on the DEM distribution, for each line of each of the ions. The third step is to display the L-functions at that effective temperature versus electron density in order to verify line overlapping (for density independent lines) or proper crossing (for density dependent ones).

When this procedure is applied to a set of density-sensitive observed lines, the electron density of the emitting plasma may be found. It is possible that some L-functions do not cross the meeting point. In this case, one possible cause is an intensity calibration problem. Thus, it is possible to define an intensity correction factor for all the lines whose L-functions do not intersect at the common crossing point. Lines of the same ion which are observed in more than one spectral window can therefore be used for inter-calibration purposes. This method is particularly useful because it is not strongly dependent on the DEM distribution, and at the same time allows an evaluation of the electron density and the relative calibration to be made, using any number of lines, thereby reducing possible errors compared with using only line ratios.

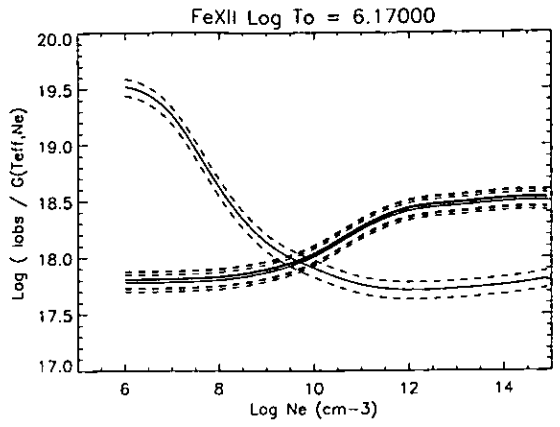

Figure 2.3: *Fe XII lines observed in CDS NIS 1 spectral range. The nearly coincident curves are from lines observed at 346.8 Å, 352.1 Å and 364.4 Å while the crossing transition is observed at 338.2 Å. In each case the dashed lines correspond to the error bars. Courtesy of E. Landi.*

2.3 The electron temperature evaluation. The isothermal case

Estimates of coronal temperatures (averages over the line of sight) can be obtained from ratios of lines emitted by ions of the same element and close ionization stage, assuming that the plasma is isothermal. As already mentioned in Chapter 1, many works have used lines emitted by *different elements*, because of the paucity of the observed spectral lines, introducing extra uncertainties due to abundance estimation. As for the density case, many works have been published on the subject of electron temperature evaluation. A review of some methods is given in *Mason and Monsignori Fossi* (1994), while the above cited work of *Keenan* (1996) gives a useful bibliographical list.

Once the isothermal assumption is made, it is straightforward to deduce from a line ratio a temperature T_*, since the intensity ratio I_1/I_2 is directly equal to the ratio of the contribution functions:

$$\frac{I_1}{I_2} = \frac{C_1(T_*, N_e)}{C_2(T_*, N_e)} \tag{2.4}$$

Any ratios of lines of ions of close ionization stage can be used for this purpose, as long as the lines are not density-sensitive, otherwise the derived temperature T_* becomes density-dependent. A set of IDL routines has been written by the author to calculate the contribution functions, take into account possible blends, and calculate the ratio of $C(T)$s and the temperature from input intensities. Figure 2.4 shows as an example the contribution functions of a Mg VII and a Mg IX line, and how their ratio varies with temperature.

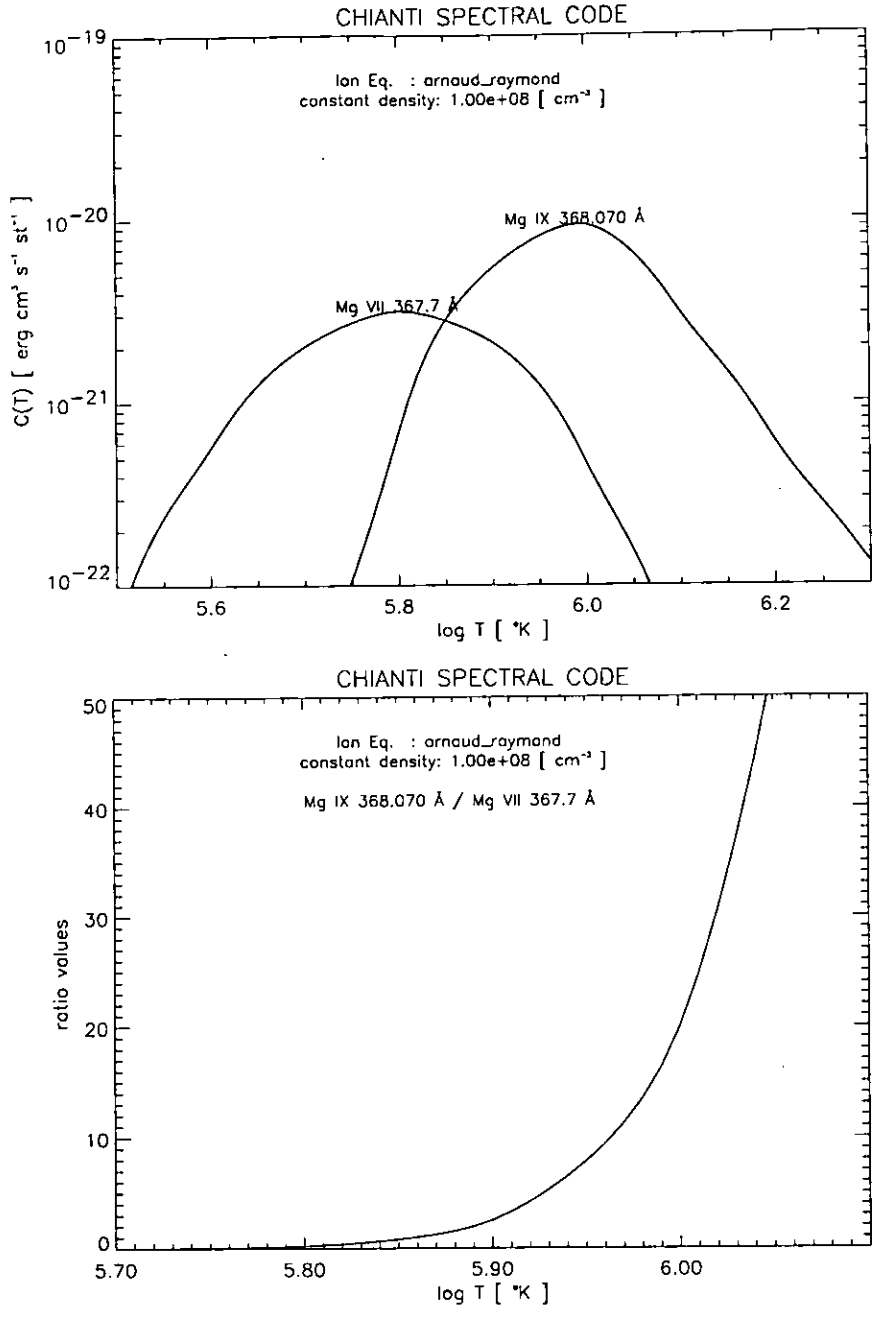

Figure 2.4: *Contribution functions of two Mg VII (a self-blend of two transitions) and Mg IX lines with their ratio, calculated with* Arnaud and Raymond *(1992).*

Different line ratios are expected to give different temperatures, if the plasma distribution is not isothermal. If the plasma distribution along the line of sight is multithermal, as can be expected especially in the case of on-disc observations, isothermal temperatures are only a crude approximation and a more complete description of the distribution of plasma at different temperatures can only be given by the *DEM* distribution.

Given the fact that CDS observes many emission lines of the same element for different ionization stages, it is possible to choose many useful ratios as temperature diagnostics, using bright lines that are not (or only slightly) density-sensitive. Examples will be given throughout this thesis. Since the emission in high-temperature lines inside coronal holes is very low, the best lines to use are those that are formed at temperatures around a million degrees or lower, for example, [Mg X 624.9 Å/ Mg IX 368.0 Å] and [Mg IX 368.0 Å/ Mg VII 367.7 Å] .

Aside from the cited possible errors due to density and element abundance uncertainties, which can easily be avoided by careful choice of lines, there is one substantial source of error that surprisingly has always been neglected in the EUV literature, except in a few cases. This is the validity of the adopted ionization equilibrium. In fact, the use of different ionization equilibrium calculations produces significantly different results. An example is shown in Figure 2.5.

A more direct way to deduce electron temperatures is to use the ratio of two lines of the same ion. There are only very few cases in which there is a temperature dependence between two lines emitted in the same EUV spectral region. In fact, usually the lines fall at very different wavelengths, as explained in Chapter 1, and are observed by different instruments, increasing the uncertainty in the derived values. An investigation of the lines observed by CDS has shown that Mg IX and Si XI are probably the only ions suitable for this purpose. Some useful Mg IX and Si XI ratios are shown in Figure 2.6.

The ratio of the Si XI 580.9 Å to either the Si XI 303.3 Å (seen in second order in NIS 2) or the Si XI 604.15 Å is temperature-sensitive. The difficulties in using these lines are the following: the 580.9 Å line is partly blended in on-disc observations with O II; the 303.3 Å line on-disc is in the wings of the strong He II 303.8 Å line seen in second order; the use of the 303.3 Å line requires an accurate second order calibration; the 604.15 Å line is weak. Furthermore, the Si XI emission is in practice absent in coronal holes, and very weak in quiet sun conditions.

The Mg IX 368.070, 706.060, and 749.551 Å lines are basically density-insensitive but have a different temperature dependence. Therefore, any combination of any two of these three lines is a good temperature diagnostic. The 706.060, and 749.551 Å lines are seen in GIS 4,

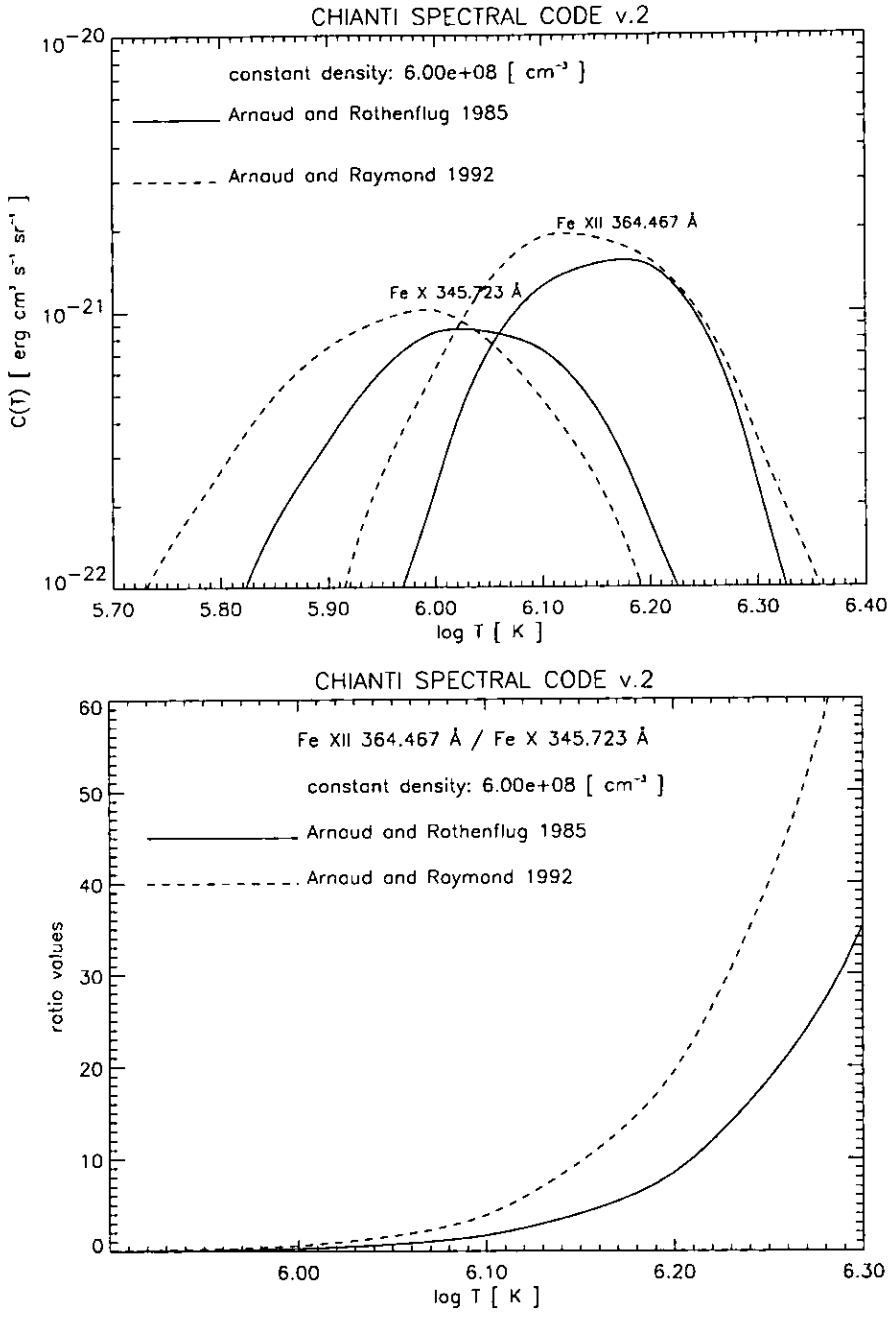

Figure 2.5: *Contribution functions of two iron lines and their ratio, for different ionization equilibria. Note how the ratio is different.*

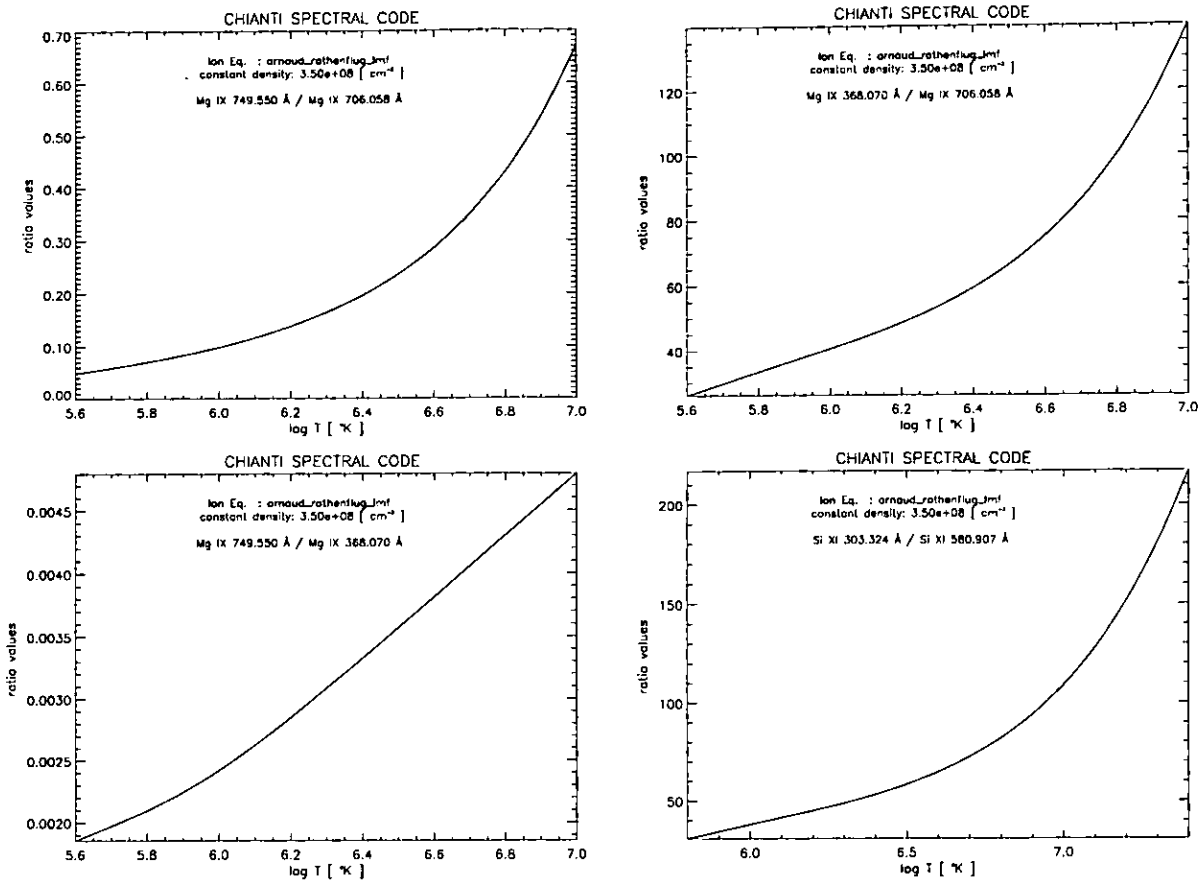

Figure 2.6: *Some useful Mg IX and Si XI temperature ratios, calculated with* Arnaud and Rothenflug *(1985).*

and have been already used as a temperature diagnostic in coronal holes (*Wilhelm et al.*, 1998). GIS 4 also observes a weak line at 694.005 Å that is strongly density-dependent above 10^8 cm^{-3} and also temperature-dependent, but is blended with the much stronger Si IX 345.1 Å seen in second order. Unfortunately, the 749.551 Å line is very weak, and the 706.06 Å line is very close to other lines, making the intensity of the line difficult to measure. The 368.07 Å line is seen in NIS 1 in first order and in GIS 4 in second order, and has the best counting statistics of the three Mg IX lines. The use of the 368.07 Å line is therefore strongly dependent on the inter-calibration between NIS 1 and GIS 4, and the second order calibration of GIS 4.

Details on the calibration and the possible use of the Si XI and Mg IX lines will be given in Chapter 3.

2.4 The electron temperature evaluation. The *DEM* method

The CDS instrument for the first time offers the opportunity of observing a large number of emission lines emitted over a large temperature range, thus enabling a more complete *DEM* analysis to be performed than ever before. An example of the span of temperatures covered simultaneously by a wide range of ions observed by CDS is shown in Figure 2.7. Skylab's S082A instrument was capable of observing a large range of ions but was limited by the overlapping in wavelength, while other instruments like the SERTS rockets had limited spatial information (typically only one slit position). This is why a large effort was put into developing methods of *DEM* analysis for this thesis.

The *DEM* analysis has also been used in this thesis to deduce relative element abundances. For each element, it is possible to deduce a *DEM* in the temperature interval for which there are observed emission lines, assuming that the element abundance does not vary along the line of sight. Since the lines observed by CDS are produced by a large number of ions (see e.g. Table 4.2) that cover a large temperature range, it is possible to deduce a *DEM* curve for each element, and to determine element relative abundances, aligning the *DEM* curves of the different elements. More details on how the *DEM* method can be applied will be given in Section 2.5.3 with a practical example, in Section 2.6, and in the following Chapters.

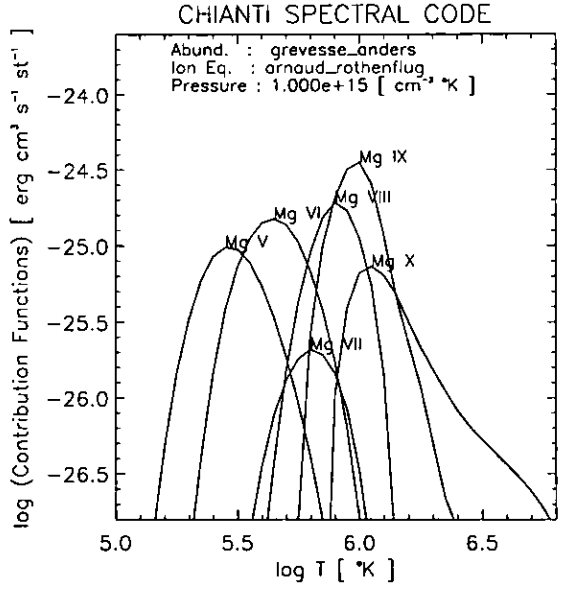

Figure 2.7: *The contribution functions for various ionization stages of Mg: Mg V (353.09 Å), Mg VI (349.1 Å- multiplet), Mg VII (363.77 Å), Mg VIII (315.04 Å), Mg IX (368.07 Å), Mg X (624.94 Å) calculated at constant pressure and with the* Arnaud and Rothenflug *(1985) ionization equilibrium.*

There are various methods of obtaining the differential emission measure. The inversion problem itself is not simple and requires some assumptions about the nature of the solution. A series of workshops was sponsored in 1990/91 to study differential emission measure techniques (*Harrison and Thompson*, 1992). It was found that most codes eventually gave consistent results, but that the DEM derived depends rather critically on the methods used to constrain the solution and the errors in the observed intensities and atomic data.

It is advisable to select a number of well resolved, unblended lines which are not density sensitive, emitted by various elements over a wide temperature interval. Appropriate values of the pressure (or density) and the elemental abundances must be chosen according to the region of the Sun being observed. The pressure value can be obtained once the values of the temperature and the density are estimated.

The inversion technique developed to calculate the DEM

The moderate CDS spectral resolution does not allow all the lines to be resolved. Therefore, a method to take into account all the theoretical lines that might contribute to each observed line had to be developed. If the elemental abundances are assumed constant over the emission volume, for every observed line in a wavelength bin $\Delta\lambda$, the flux observed can be written :

$$I^{ob}_{\Delta\lambda} = \int G_{\Delta\lambda}(T)\ DEM(T)\ dT \tag{2.5}$$

Where $G_{\Delta\lambda}(T)$ is the sum of the contribution functions of all the theoretical lines $G_{\Delta\lambda}(T) = \sum_{\lambda_{ij}} G(T, \lambda_{ij}, N_e)$ within $\Delta\lambda$.

Once the line fluxes $I^{ob}_{\Delta\lambda}$ are measured and the contribution functions $G_{\Delta\lambda}(T)$ are calculated, there are various methods to deduce the differential emission measure.

A set of IDL routines was written in order to evaluate the DEM distributions, using the CHIANTI database. Because of the large number of emission lines observed by the spectroscopic instruments on board SOHO, in particular CDS, there was a need for a semi-automatic set of programs that could allow a quick analysis of the data. A complete set of routines was written, documented and then released for public use into the CDS software. The main routine is called CHIANTI_DEM (see the CDS software note No. 50, *Del Zanna et al.*, 1997 for a description).

A far more complex set of IDL routines was also written for use in this thesis, and is briefly outlined below. The main differences between this and the routines released for public use are more flexibility and interactive control over the various parameters of the

fit, and also in the way the fitting is performed. These IDL routines were also used for the intensity calibration work described in Chapter 3, and accepted as input line intensities in *photon-events*, rather than physical units ($ergs\ cm^{-2}s^{-1}sr^{-1}$). The main input to these routines is a file that lists, for each observed line:

- the observed wavelength $\lambda_{\rm ob}$ [Å].
- The observed flux I_{ob} and the corresponding error σ_{ob}.
- The value of $\Delta\lambda$ [Å], corresponding to the spectral resolution of the instrument at that wavelength.
- The identification of the line.
- A flag to indicate if the line is to be used in the fit or not and another one to indicate if the line is a first order line (free from second order contributions) or a second order line (free from first order contributions).

Having read the observed intensities, the routines proceed as follows. First, in the case of GIS lines, a reconstruction of the lines that were *ghosting* is performed (see Chapter 3). Then, the appropriate intensity calibration is applied, converting the intensities to $ergs\,cm^{-2}s^{-1}st^{-1}$, for the first order lines and the second order ones, separately. After this, the CHIANTI database is searched for all the theoretical lines that may have contributed to the observed lines, i.e. that have a theoretical wavelength $\lambda_{\rm th}$ in a $\lambda_{\rm ob} \pm \delta\lambda$ interval. For each line the contribution function $C(T, \lambda_{ij}, N_e)$ is calculated using one ionization equilibrium calculation, either at constant pressure or at constant electron density. This is done in various ways, either directly reading the database or reading files of $C(T, \lambda_{ij}, N_e)$ already prepared, in order to save computing time. The $C(T, \lambda_{ij}, N_e)$ values are calculated for the temperature interval log(T)= 4.0 - 8.0 in steps of log(T) = 0.1. If a constant pressure is selected, $C = C(T, \lambda_{ij}, P/T)$, i.e. for each line the contribution function at the temperature T_i is calculated at an electron density N_e equal to the ratio of the pressure and the temperature T_i. The $C(T, \lambda_{ij}, N_e)$ values corresponding to the observed lines are then stored in an output file, that is used for subsequent DEM evaluations. This method was chosen, because it allowed a fast re-calculation of the DEM changing various parameters (e.g. the element abundances or the lines used in the fit) without having to start again and read the CHIANTI database, which can take a long time (of the order of 20 minutes for a typical set of observations). Also, in some cases some transitions can be missed by this automatic procedure, for example if the wavelength calibration was not very accurate, and have to be subsequently added manually. On the other hand, sometimes some contributions have to be removed.

Once the $C(T, \lambda_{ij}, N_e)$ are calculated, an abundance file is read, containing the values of the elemental abundances, relative to hydrogen. It is possible to change these values. Then the $G(T, \lambda_{ij}, N_e)$) are calculated, multiplying each theoretical line by the abundance factor. It is then possible to check which theoretical lines are contributing to each blend. This is an important step, since in many cases, depending on the density and chemical composition of the plasma along the line of sight , different theoretical lines contribute most to the observed line (see e.g. Figure 2.8 for an example). The same check is performed later during the fit, because in many cases the temperature distribution is the major effect.

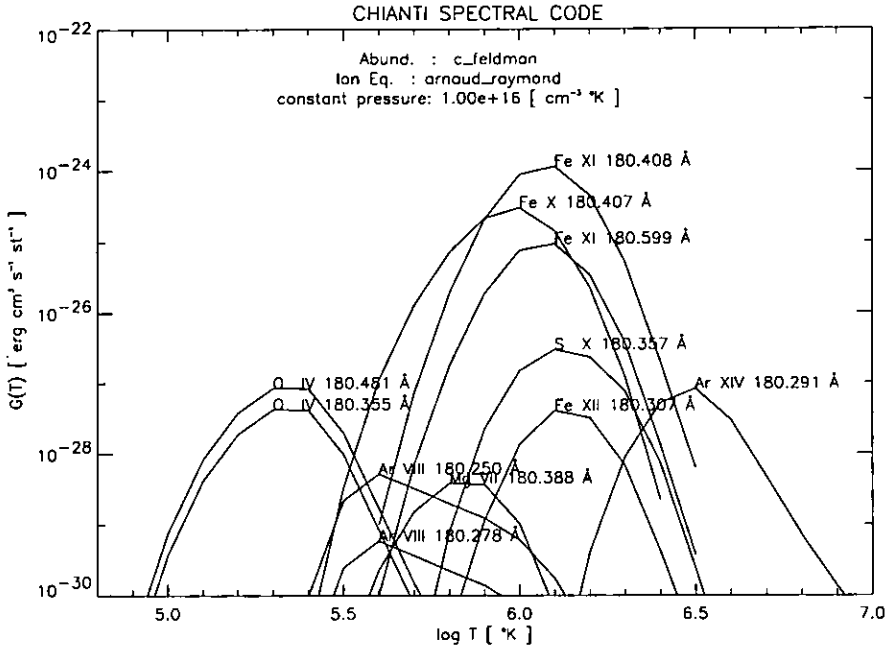

Figure 2.8: *The contribution functions of lines contributing to the observed emission line at 180.4 Å.*

The total contribution function for each observed line is then calculated summing all the theoretical contributions with the abundance factors: $G_{\Delta\lambda}(T) = \sum_{\lambda_{ij}} A_b(X) \cdot C(T, \lambda_{ij}, N_e)$. The inversion of the system of eqns.(2.5) can then start. The numerical inversion procedure used to evaluate the DEM function is an application of the 'maximum entropy method', as described in *Monsignori Fossi and Landini* (1991). The DEM function is assumed to be a cubic spline with a limited number of selected reference ('mesh') points. The smoothness of DEM distribution depends on the number of selected mesh points, which are chosen at those temperatures where there are constraints from observations. This procedure has the advantage to give only positive DEM values and proved to be quickly converging. The fitting program has been modified in order to allow the search for the best solution for each single mesh point, with the possibility of adjusting interactively the number and position of the mesh points. The solution (i.e. the DEM distribution) strongly

depends on the correct intensity calibration, the lines used and the adopted element abundances. Since the contribution functions are for each case calculated at the appropriate pressure (or density), also most of the lines that have a slight density-dependence are usually well fitted. Once an appropriate DEM is found, it is then possible to calculate the CDS synthetic spectra, including all the second order contributions, in order to check if, overall, the spectra are well represented or not. This process is usually repeated a few times, adjusting the mesh points and the element abundances to produce the best agreement between observed and calculated intensities.

Regarding possible errors in the estimation of the DEM values, it has been shown by *Dere* (1978b) that if the DEM is approximated with a non-negative smooth function, then the solutions have errors that are not significantly greater than the errors in the spectral data, in the temperature ranges where there are observational constraints. In the regions with limited observational constraints, the DEM values can have large errors, as shown by *Jakimiec et al.* (1984).

2.5 A comparison of various emission measure methods, using Skylab coronal hole data

There are many emission measure methods and definitions to be found in the literature, which can create confusion. For example, in some cases, column emission measures instead of volume emission measures are used. In this Section, the main methods that can be found in the literature are explained, bearing in mind that in each paper the practical definitions are usually different. This is accomplished by applying the DEM analysis described above to a set of data and making a comparison with other methods, to clarify the differences, which in some cases are subtle. At the same time the practical description of how the DEM is applied and of how the results are presented will be given, with various definitions that then will be used in the remainder of this thesis. This is particularly important, since the DEM inversion method will be applied to the CDS data both for calibration and for plasma diagnostic purposes in the following chapters.

In order to present a comparison that is independent of atomic data and instrument calibration, the method is applied to the published Skylab data of *Vernazza and Reeves* (1978), using the same atomic data (CHIANTI v.2) that are used in the analysis of CDS data. As already mentioned, the *Vernazza and Reeves* (1978) data were among the best sources of EUV spectra before SOHO, and have been accurately calibrated in intensity and used by a large number of authors. Only rocket flights such as SERTS have similar accuracy in calibration with a much better resolution, compared to that ($\simeq$ 1.6 Å) of the

HCO instrument on-board Skylab. The SERTS data are not used here for the comparison because of the more restricted temperature coverage of the observed lines.

Vernazza and Reeves (1978) produced line intensities for different solar regions. The averaged values for the coronal hole cell centres have been selected for the comparison, so the results can also be useful for various reasons. First, it is interesting to compare the coronal hole DEM derived using the latest atomic data, with previous results. Then, it will be possible to compare this result with that derived from SOHO/CDS data, using the same atomic data, and to point out similarities and differences in where the model fails to reproduce the observations.

The averaged intensities of most of the published lines have been used, in some cases correcting the observed wavelength in order for the automatic routine to find the correct theoretical lines. This has been necessary since the HCO wavelength calibration was poor ($\simeq$ 1-2 Å), of the order of the resolution. A $\Delta\lambda = 1.1 \simeq 0.7 \times FWHM$(Å), was chosen to ensure that all the significant theoretical contributions would be included. A 10% error on all the observed intensities has been adopted. While this error is reasonable for most of the bright lines, it might be low for the other ones, in particular for those at the shorter wavelengths, where the intensity calibration becomes more uncertain. The contribution functions have been calculated at constant pressure $P = 2 \times 10^{14}\mathrm{cm}^{-3}$ K with the ionization equilibrium calculations of *Arnaud and Rothenflug* (1985). The inversion technique described above was applied to these data in order to derive the DEM. As a starting point, photospheric abundances of *Grevesse and Anders* (1991) were used, but some element abundances were then slightly changed, as described below. These abundances are referred to as the *adopted abundances* for this work, and are the photospheric except for Ne, Ca and Na, for which the values were increased from the photospheric ones by 0.2, 0.2, 0.4 (in logarithmic scale), respectively.

Only some *selected* observed lines emitted by different ions are shown here, for clarity, bearing in mind that many other lines (most of which are in agreement with the selected ones) were included. Figure 2.9 shows the composite contribution functions G(T) for these lines (see Table 2.2 for the identifications), showing the large temperature coverage, which is only limited at high temperatures, where no reliable lines were observed. It also shows that some of the G(T) are *not* sharply peaked, because of the ionization equilibrium, as is the case for some ions like Si III and O VI, or because of blending, as in the case of Mg IX. In many cases the G(T) are even double-peaked, with peaks at low and high temperatures as is the case of the Ca X - C III blend observed at 574.2 Å. In such complex cases, which are quite common, it is not easy to find the contribution of each line to the blend, because it strongly depends on the DEM values around the temperature of the maximum of the

C(T) of each contributing line (log T_{max} = 5.8 for Ca X and log T_{max} = 5.0 for C III), and on the relative element abundance, so only a proper DEM and abundance analysis can give the correct answer. Figure 2.9 also shows that in some cases, such as the pairs O III, Ne III and O IV, Ne IV the contribution functions have almost the same temperature dependence, and therefore are suitable for element abundance analysis, as described in Section 2.5.3.

Recalling that the theoretical intensity of a line can be written (see Chapter 1), assuming constant abundances along the line of sight as

$$I_{\rm th} = A_b(Z) \int_h C(T, N_e)\ N_e N_H\ dh = A_b(Z) \int_T C(T, N_e)\ DEM(T)\ dT \qquad (2.6)$$

the solution to the inversion problem is to use the observed intensities $I_{\rm ob}$ and derive at the same time the element abundances $A_b(Z)$ and the differential emission measure DEM.

2.5.1 Some historical approaches. The EM_L, EM_T, DEM_L approximations

In the past, various approaches have been used to obtain estimates of emission measure distribution and element abundances A_b(Z).

The emission measure loci approach

One direct approach is to plot the ratio $I_{\rm ob}/G(T)$ for each line as a function of temperature and consider the loci of these curves to constrain the shape of the emission measure distribution. In fact, for each line and temperature T_i the value $I_{\rm ob}/G(T_i)$ represents an upper limit to the value of the *line emission measure* EM_L (Equation 2.8, below) at that temperature, assuming that all the observed emission $I_{\rm ob}$ is produced by plasma at temperature T_i. An example of such an approach applied to solar EUV spectra can be found in *Judge et al.* (1995).

The $I_{\rm ob}/G(T)$ curves for the selected lines of the coronal hole spectrum are displayed in Figure 2.10. An examination of the Figure shows already the main expected characteristics of an emission measure from on-disc observations, i.e. a minimum at lower transition region temperatures, and a maximum around a million degrees.

Note that with the adopted abundances the O III/Ne III and O IV/Ne IV curves overlap almost exactly, which confirms that the relative adopted O/Ne abundance is correct.

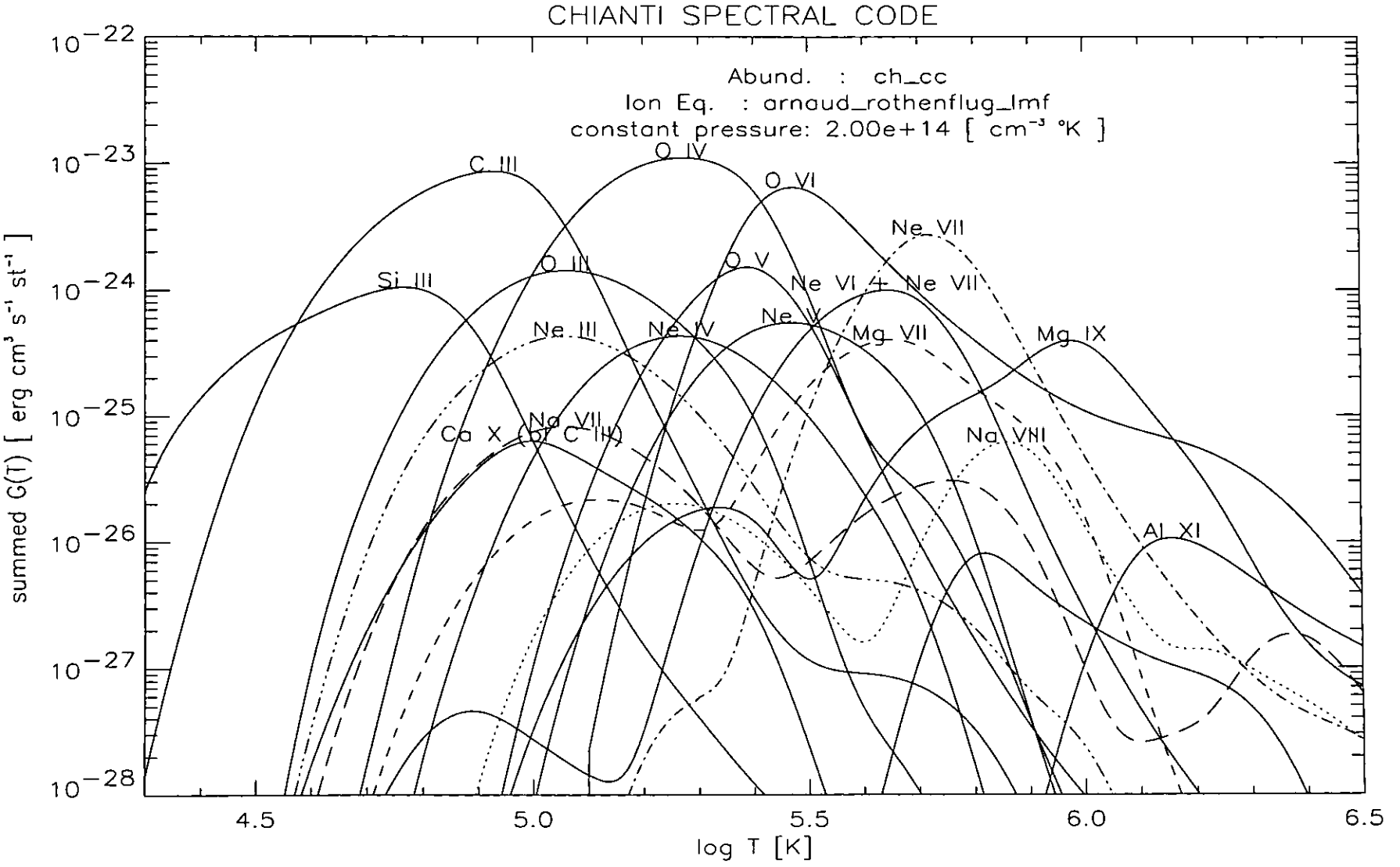

Figure 2.9: *Contribution functions $G(T)$ of the selected observed lines, calculated with the adopted abundances.*

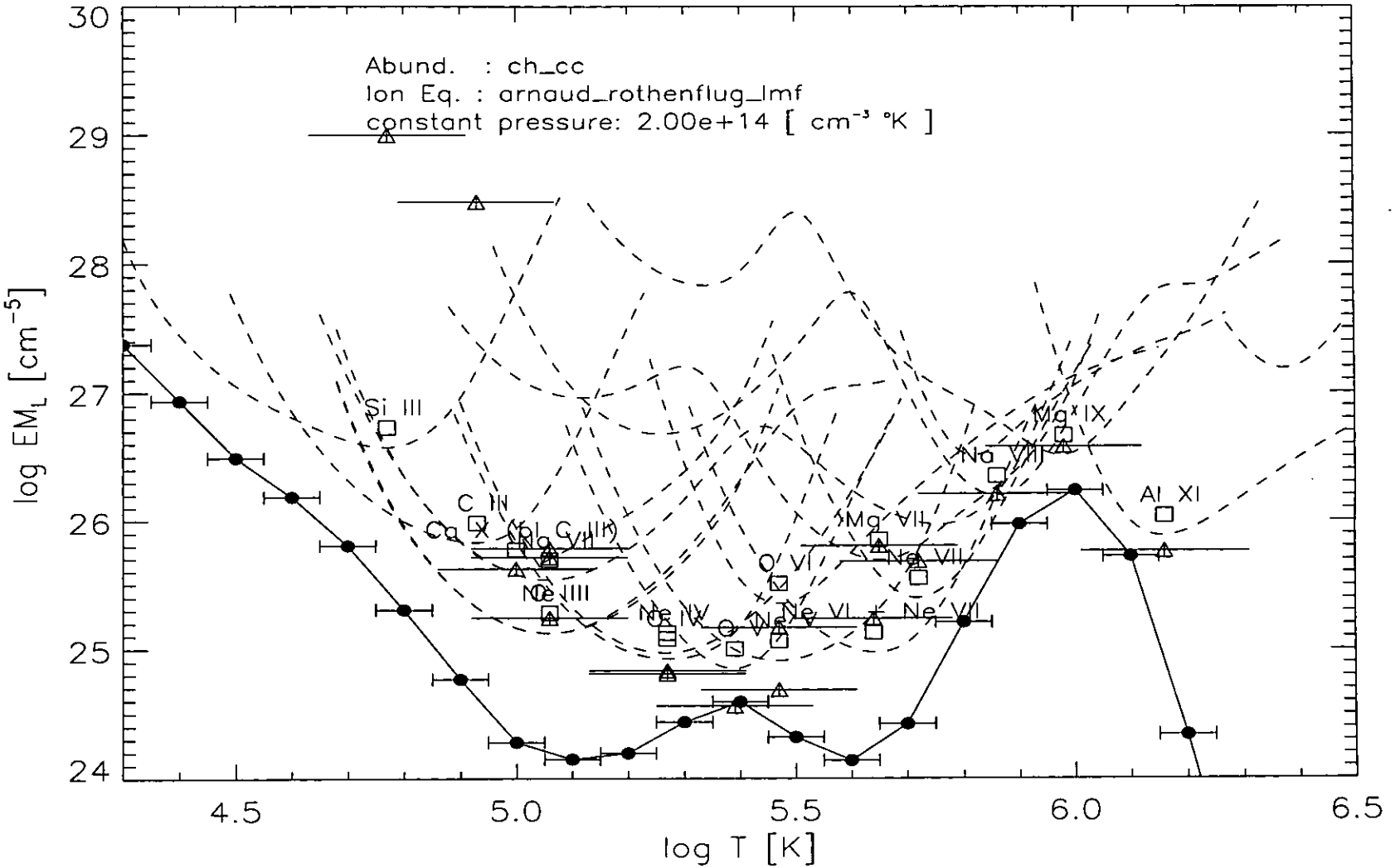

Figure 2.10: *The emission measure values of the selected observed lines, calculated with the adopted abundances. Values of* EM_L Pottasch *(1963) are represented by squares, while the EM(0.3) values* (Jordan and Wilson, *1971) are triangles, both plotted at the temperature* T_{max}. *The horizontal bars of the EM(0.3) values are* $\Delta logT = 0.3$ *K wide. Filled circles represent the* EM_T *values calculated from the DEM. The horizontal bars refer to the adopted* $\Delta logT = 0.1$ *K for the calculation of the* EM_T *values.*

The *Pottasch* approach

Following *Pottasch* (1963), many authors (e.g. *Dupree*, 1972) have approximated the above expression (Equation 2.6) by removing an averaged value of C(T) from the integral:

$$I_{\rm th} = A_b(Z) \ < C(T) > \int_h N_e N_H dh \tag{2.7}$$

A suitably defined volume *line emission measure* EM_L can therefore be defined, for each observed line of intensity I_{ob}:

$$EM_L \equiv \frac{I_{\rm ob}}{A_b(Z) \ < C(T) >} \quad [{\rm cm}^{-5}] \tag{2.8}$$

Now, the crude approximation applied by *Pottasch* (1963) was to take $C(T) = 0$ when $C(T)$ is less than one-third of its maximum value, and equal to a constant value otherwise. For T_1, T_2 such that $C(T_1) = C(T_2) = \frac{1}{3}C(T_{\rm max})$, define:

$$C_P(T) = \begin{cases} C_0 & T_1 \leq T \leq T_2 \\ 0 & T < T_1, \quad T > T_2 \end{cases} \tag{2.9}$$

and requiring that

$$< C(T) >= \frac{\int C(T) dT}{|T_2 - T_1|} \tag{2.10}$$

gives $< C(T) >= 0.7 \ C(T_{\rm max})$. Since each spectral line is emitted from a volume V, over a temperature range $T_2 - T_1 = \Delta T$ around the temperature $T_{\rm max}$ corresponding to the peak value of its contribution function, $C(T_{\rm max})$, *Pottasch* (1963) and following authors have produced figures of the *line emission measures*, multiplied by the corresponding abundance value:

$$A_b(Z) \ EM_L = \frac{I_{\rm ob}}{0.7 \ C(T_{\rm max})} \tag{2.11}$$

plotted at the temperature $T_{\rm max}$. The relative abundances of the elements are derived in order to have all the *line emission measures* of the various ions lie along a common smooth curve. This is of course possible only for the observed elements and once one element abundance is fixed.

The *line emission measures* EM_L calculated with this approximation, using the adopted abundances for the selected lines of the coronal hole spectrum are displayed as squares in Figure 2.10.

The *Jordan and Wilson* approximation

Jordan and Wilson (1971) adopted the *Pottasch* (1963) approach but proposed a different approximation, assuming that $C(T)$ has a constant value over a narrow temperature interval $\Delta logT = 0.3$ around $C(T_{\max})$:

$$C_J(T) = \begin{cases} C_0 & |\log T - \log T_{\max}| < 0.15 \\ 0 & |\log T - \log T_{\max}| > 0.15 \end{cases} \tag{2.12}$$

and requiring that

$$\int C(T)dT = \int C_J(T)dT \tag{2.13}$$

so that

$$C_0 = \frac{\int C(T)\ dT}{T_{\max}(10^{+0.15} - 10^{-0.15})} = \frac{\int C(T)\ dT}{0.705\ T_{\max}} \tag{2.14}$$

and thus deducing the relative *line emission measure* EM_L, sometimes indicated by EM(0.3), to make clear that the contributions are calculated over a temperature interval $\Delta logT = 0.3$. This approximation has been used by various authors (for example by *Widing et al.*, 1986, to derive the element abundances of an erupting prominence observed by Skylab).

Values of EM(0.3)for the coronal hole spectrum are displayed in Figure 2.10 as triangles, together with their $\Delta logT = 0.3$ intervals. The agreement with the values deduced from the *Pottasch* (1963) approximation is reasonable for the few lines that are sharply peaked, but is poor for the other ones. It is also evident that, for most of the lines, the emissivities outside the $\Delta logT = 0.3$ interval are *not* negligible.

A way to compare the emission measures derived from these two most commonly used approximations is to calculate some emission measure values as a function of temperature directly from the differential emission measure values, after the DEM has been calculated. As usual, an emission measure has to be defined over some temperature interval ΔT. For each temperature T_i it is therefore possible to define an emission measure value EM_T:

$$EM_T(T_i) \equiv \int_{T_i - \frac{\Delta T}{2}}^{T_i + \frac{\Delta T}{2}} DEM(T)dT \tag{2.15}$$

These EM_T points have been calculated from the DEM distribution (Figure 2.12) with a $\Delta logT = 0.1$, and are displayed in Figure 2.10 with filled circles. It is quite obvious that neither of the two approximations above is a good representation of the emission measure derived from the DEM.

A different approach. The DEM_L method

A different approach was proposed by *Widing and Feldman* (1989). The idea is to rewrite Equation 2.6 in terms of differential emission measure :

$$I_{\rm th} = A_b(Z) \int_T C(T, N_e)\ N_e N_H \frac{dh}{dT} dT \tag{2.16}$$

and to extract from the integral an averaged value of the DEM of the line, that in this thesis is termed the *line differential emission measure* DEM_L:

$$DEM_L \equiv \left\langle N_e N_H \frac{dh}{dT} \right\rangle \quad [cm^{-5} K^{-1}] \tag{2.17}$$

such that for each line of observed intensity I_{ob}:

$$DEM_L \equiv \frac{I_{\rm ob}}{A_b(Z) \int_T C(T) dT} \tag{2.18}$$

A plot of the $A_b(Z)\ DEM_L = I_{\rm ob} / \int_T C(T) dT$ values displayed at the temperatures T_{max} gives the differential emission measures of the observed lines, and at the same time can be used (*Widing and Feldman*, 1989) to deduce relative element abundances, adjusting them in order to have a continuous sequence of the $A_b(Z)\ DEM_L$ values.

The DEM_L values for the coronal hole spectrum, calculated with the adopted abundances, are shown in Figure 2.11 at the temperatures T_{max}. This figure shows a minimum of the DEM_L values around log T=5.4, a maximum at a million degrees, and an exact overlap of the Ne III, O III and Ne IV, O IV points, confirming the validity (by using this method) of the adopted relative Ne/O abundance.

This DEM_L approach has been used and reported in almost all the works on element abundance analysis, after *Widing and Feldman* (1989). The method is quick to apply, since it only requires for each line an integration of the contribution function, and apparently gives the correct answer in term of abundance analysis. In reality, it will be shown below that **this method should not be applied to deduce a DEM distribution**, because it is inherently wrong, **nor to deduce elemental abundances**, except in particular cases.

2.5.2 Results of the DEM approach, basic definitions and comparison with the DEM_L method.

The DEM approach assumes that a DEM can be defined, and that it is a smooth function of temperature, which is a basic assumption (well accepted in the literature). The current

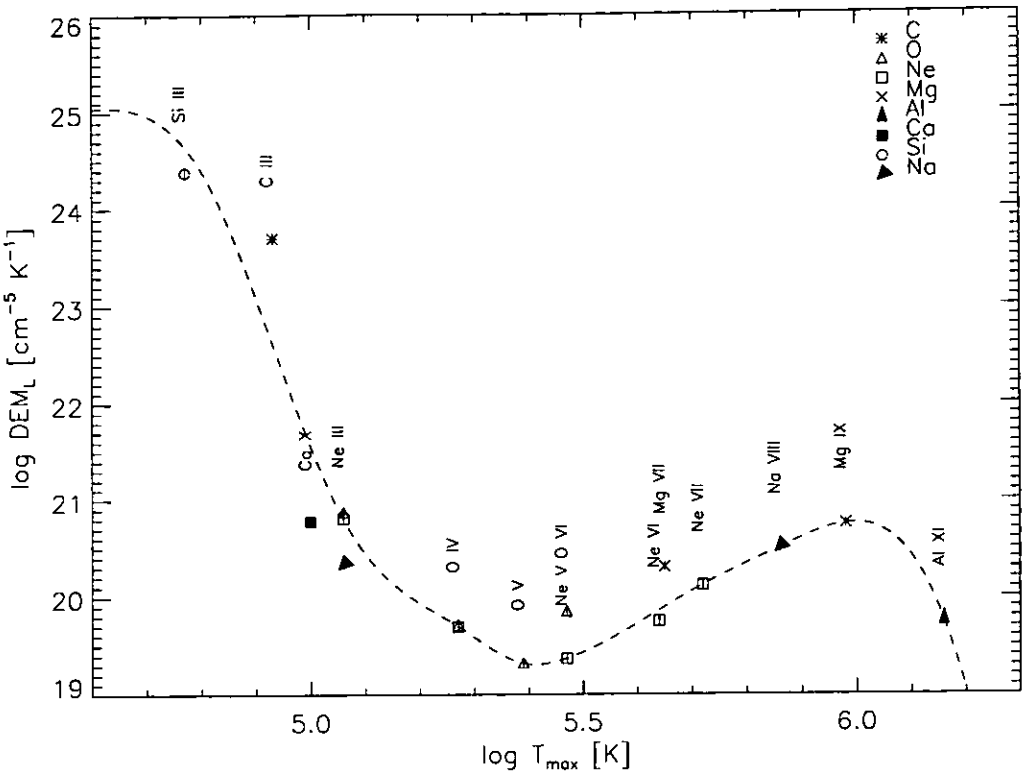

Figure 2.11: *Line differential emission measures DEM_L of selected lines with Skylab data, with the adopted abundances. A 'trial' DEM is plotted as a dashed line. Note that the O III, Ne III and O IV, Ne IV points overlap.*

EUV instruments have such a spatial resolution (of order 2″) that any small-scale features on the Sun have a diffuse aspect. Also, since the emission is optically thin, the sum of all the contributions along the line of sight blurs any contribution from possible filamentary structures.

Figure 2.12 shows the *DEM* distribution of the Skylab coronal hole cell-centre data, found with the inversion technique. The mesh points, indicated with triangles, are positioned at the temperatures where there are good constraints, i.e. well-observed lines that are emitted at those temperatures. In this case, the high-temperature tail of the *DEM* distribution is not directly constrained. On the other hand, the absence of observed high-temperature lines in the spectrum is itself an excellent constraint on the upper limits of the *DEM* distribution at high-temperatures. Any higher values of the *DEM* at temperatures above 10^6 K would make high-temperature lines observable above the noise. The low-temperature tail of the *DEM* distribution is directly constrained by low-temperature lines but should be treated with caution, since some opacity effects may come into play.

Now, some definitions that will be used throughout the rest of this thesis: a theoretical

Table 2.2: *Selected lines of the averaged coronal hole spectrum of* Vernazza and Reeves *(1978), with the adopted abundances.*

Ion	λ_{th} (Å)	λ_{ob} (Å)	Transition	I_{ob}	I_{th}/I_{ob}	+/-	log T_{eff}	log T_{max}	frac
With the adopted abundances									
Si III	1206.499	1206.5	3s2 $^1S_0$ - 3s.3p $^1P_1$	393.6	1.33	0.19	4.53	4.77	
C III	977.017	977.0	2s2 $^1S_0$ - 2s2p $^1P_1$	579.4	0.99	0.14	4.73	4.93	
O III	599.597	599.6	2s22p2 $^1D_2$ - 2s2p3 $^1D_2$	19.0	1.02	0.14	4.99	5.06	
Ne III	489.495	489.3	2s2 2p4 $^3P_2$ - 2s 2p5 $^3P_2$	5.7	1.06	0.15	5.06	5.06	0.56
Ne III	488.9		2s2 2p4 $^3P_1$ - 2s 2p5 $^3P_0$					5.06	0.15
Ne III	490.3		2s2 2p4 $^3P_0$ - 2s 2p5 $^3P_1$					5.06	0.15
Ne III	489.6		2s2 2p4 $^3P_1$ - 2s 2p5 $^3P_1$					5.06	0.11
O IV	554.513	554.5	2s2 2p $^2P_{3/2}$ - 2s 2p2 $^2P_{3/2}$	92.7	0.98	0.14	5.30	5.27	0.55
O IV	554.1		2s2 2p $^2P_{1/2}$ - 2s 2p2 $^2P_{1/2}$					5.27	0.22
O IV	555.3		2s2 2p $^2P_{3/2}$ - 2s 2p2 $^2P_{1/2}$					5.27	0.11
O IV	553.3		2s2 2p $^2P_{1/2}$ - 2s 2p2 $^2P_{3/2}$					5.27	0.11
Ne IV	543.892	543.8	2s2 2p3 $^4S_{3/2}$ - 2s 2p4 $^4P_{5/2}$	4.0	0.93	0.13	5.32	5.27	
O V	760.444	760.0	2s.2p $^3P_2$ - 2p2 $^3P_2$	10.7	1.07	0.15	5.40	5.39	0.69
O V	759.4		2s.2p $^3P_0$ - 2p2 $^3P_1$					5.39	0.17
O V	760.2		2s.2p $^3P_1$ - 2p2 $^3P_1$					5.39	0.13
Ne V	572.331	572.3	2s22p2 $^3P_2$ - 2s2p3 $^3D_3$	4.5	1.16	0.16	5.49	5.47	0.85
Ne V	572.1		2s22p2 $^3P_2$ - 2s2p3 $^3D_2$					5.47	0.14
Na VII	491.951	491.9	2p $^2P_{3/2}$ - 2s.2p2 $^2D_{5/2}$	2.8	0.97	0.14	5.69	5.78	0.42
Ne III	491.0		2s2 2p4 $^3P_1$ - 2s 2p5 $^3P_2$					5.06	0.41
Ca X	574.010	574.2	3s $^2S_{1/2}$ - 3p $^2P_{1/2}$	2.6	0.82	0.12	5.72	5.82	0.53
C III	574.3		2s2p $^1P_1$ - 2s3d $^1D_2$					4.98	0.35
Ne VI	562.803	562.0	2s2 2p $^2P_{3/2}$ - 2s 2p2 $^2D_{5/2}$	9.4	1.20	0.17	5.76	5.63	0.66
Ne VII	561.7		2s2p $^3P_2$ - 2p2 $^3P_2$					5.72	0.22
O VI	1031.912	1032.0	1s2 2s $^2S_{1/2}$ - 1s2 2p $^2P_{3/2}$	145.9	0.65	0.09	5.81	5.47	
Ne VII	465.220	465.2	2s2 $^1S_0$ - 2s2p $^1P_1$	68.1	1.03	0.15	5.87	5.72	
Mg VII	434.917	434.6	2s22p2 $^3P_2$ - 2s2p3 $^3D_3$	19.9	0.79	0.11	5.88	5.80	0.67
Ne VI	435.6		2s2 2p $^2P_{3/2}$ - 2s 2p2 $^2S_{1/2}$					5.64	0.21
Mg VII	434.7		2s22p2 $^3P_2$ - 2s2p3 $^3D_2$					5.81	0.10
Na VIII	411.166	411.2	2s2 $^1S_0$ - 2s.2p $^1P_1$	9.6	0.93	0.13	5.93	5.86	
Mg IX	368.070	368.2	2s2 $^1S_0$ - 2s.2p $^1P_1$	127.3	0.94	0.13	5.98	5.98	
Al XI	550.031	550.0	1s2.(^{1}S).2s $^2S_{1/2}$ - 1s2.(^{1}S).2p $^2P_{3/2}$	0.8	0.95	0.15	6.07	6.16	
With the photospheric abundances of *Grevesse and Anders* (1991)									
Ne III	489.495	489.3		5.7	0.67	0.09	5.08	5.06	0.56
Ne III	488.9							5.06	0.15
Ne III	490.3							5.06	0.15
Ne III	489.6							5.06	0.11
Ne IV	543.892	543.8		4.0	0.59	0.08	5.32	5.27	
Ne V	572.331	572.3		4.5	0.73	0.10	5.49	5.47	0.85
Ne V	572.1							5.47	0.14
Ne III	491.040	491.9		2.8	0.48	0.07	5.62	5.06	0.52
Na VII	492.0							5.78	0.33
C III	574.279	574.2		2.6	0.66	0.10	5.64	4.98	0.43
Ca X	574.0							5.82	0.42
Ne VI	562.803	562.0		9.4	0.76	0.11	5.76	5.63	0.66
Ne VII	561.7							5.72	0.22
Ne VII	465.220	465.2		68.1	0.65	0.09	5.87	5.72	
Mg VII	434.917	434.6		19.9	0.73	0.10	5.89	5.80	0.73
Ne VI	435.6							5.64	0.14
Mg VII	434.7							5.81	0.11
Na VIII	411.166	411.2		9.6	0.38	0.05	5.93	5.86	

line is considered a **principal** line if it *contributes at least 10% of the total theoretical I_{th} intensity*; an observed line is considered a **blend** *if its emission is composed of at least two principal lines*; an observed line is considered a **self-blend** if all the **principal** lines are of the same ion. Note that with these definitions the same observed line can be considered a blend of different lines or not depending on the importance of the contribution from the various lines, which in turn depends on the DEM distribution (i.e. on the type of observed source on the Sun), the element abundance, and on the ionization equilibrium used. Examples of observed lines that become blends of different principal lines under different conditions will be given throughout this thesis. A line will be termed **well-reproduced** if the calculated intensity $I_{\rm th}$ equals the observed intensity $I_{\rm ob}$, within the errors.

Table 2.2 shows the details of the selected lines with the adopted abundances and, for comparison, some of the results with photospheric abundances which were used as a starting point.

Note that all the Tables presented in this thesis have the following contents and abbreviations:

- the observed wavelength λ_{ob} in column (3).
- The identification (ion and theoretical wavelength λ_{th}) of *only* the lines that were found to contribute to the observed line, in columns (1, 2). Only *principal* lines are shown.
- The configuration and term of the lower and upper level, in column (4).
- The observed flux I_{ob} ($ergs\ cm^{-2}s^{-1}sr^{-1}$) in column (5).
- The ratio between the theoretical I_{th} and the observed flux I_{ob}, with an estimated error, in columns (6,7). The theoretical I_{th} is calculated summing up all the contribution functions from all the lines in the blend, and integrating the product with the DEM distribution (Equation 2.6). The error is the combination of the observed error (see Chapter 3) and an assumed 10% error on the calculated values.
- The *effective temperature* $\rm T_{eff}$ of the line, as a $\log_{10}$ value, in column (8). The effective temperature $\rm T_{eff}$ is defined:

$$T_{\rm eff} = \frac{\int T\ G(T)\ DEM(T)\ dT}{\int G(T)\ DEM(T)\ dT} \tag{2.19}$$

  i.e. is an averaged temperature, weighted by the DEM distribution.

- The T_{max} value of the transition as a $\log_{10}$ value, in column (9), calculated as the temperature of the maximum of the contribution function.
- The fraction, *frac*, the calculated intensity of each transition contributed, to the total theoretical I_{th} intensity of the line, in column (10). Only principal lines are shown.
- (*bl*) indicates when a line is a blend.
- A number in parentheses indicates the number of self-blends.
- IIo indicates a line seen in second order.

The lines in Table 2.2 are ordered by the *effective temperature* T_{eff}. Table 2.2 shows that even with the conservative errors adopted, most of the lines are well represented within the errors, with a few exceptions, one of which is the O VI line, for which more comments will be given later. Table 2.2 also shows that most of the selected lines are blends, a feature common to most of the lines, due to the poor spectral resolution of the HCO instrument.

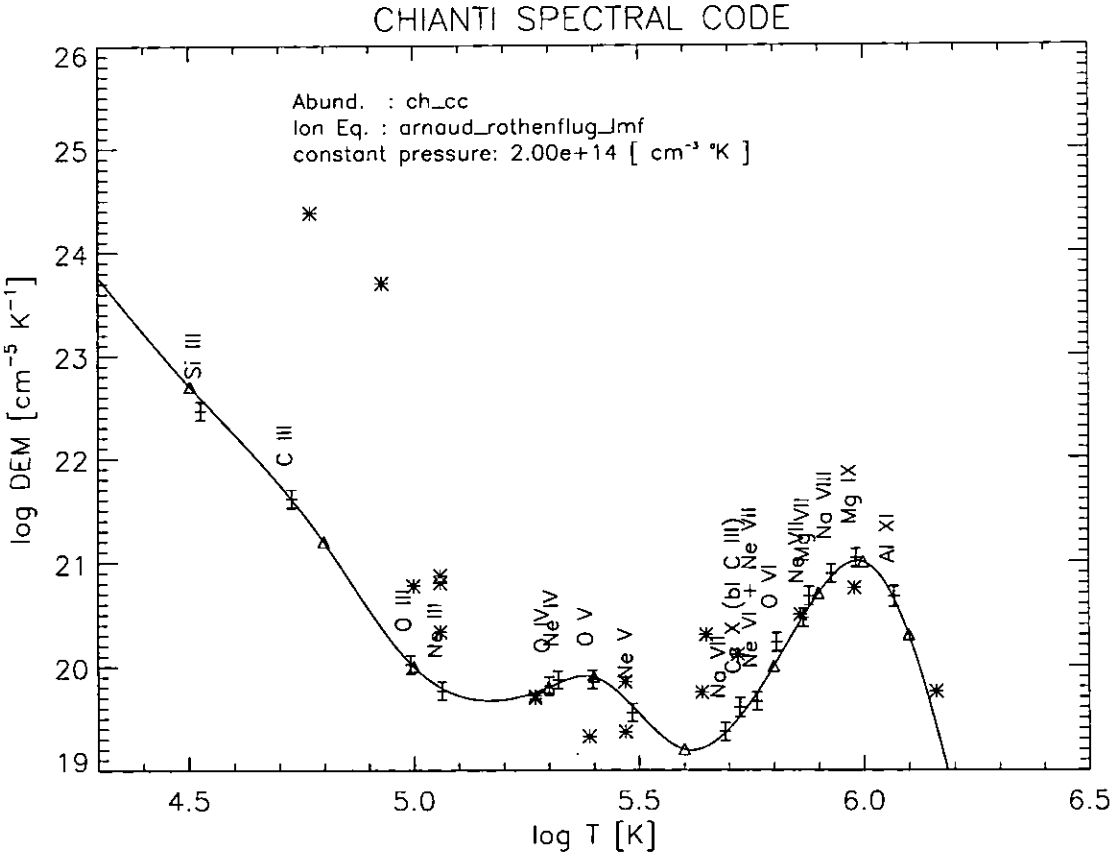

Figure 2.12: *The DEM distribution (continuous line) calculated with the adopted abundances, with the mesh points indicated by triangles. The points with the error bars (labelled with the ion) are plotted at the temperature T_{eff}. Also reproduced with the * symbol are the line differential emission measures DEM_L values of Figure 2.11.*

A comparison of the effective temperature T_{eff} and the maximum temperature T_{max} of the principal lines is instructive. For example, the maximum of the G(T) for the Si III 1206.5 Å line is at log T=4.77 K, but the G(T) of this line is very broad, as shown in Figure 2.9. Since the DEM distribution has a steep increase toward low temperatures, the contribution to the *emissivity* $G(T)\ DEM(T)$ from temperatures $T < T_{max}$ is very important indeed, and in fact the effective temperature log T_{eff}=4.53. A similar case is seen for O VI 1032 Å a line with very broad G(T), but this time the steepening of the DEM distribution is toward higher temperatures, which means that this time most of the observed O VI emissivity comes from plasma at temperatures higher than the maximum of the G(T) (in fact log T_{eff}=5.81 while log T_{max}=5.47). This also explains why the O VI lines are still visible in off-limb observations, while all the other lines that have peaks of their G(T) around log T_{max}=5.5 (as Ne V) are not seen at all. This *shows how graphs that show quantities such as* DEM_L *as a function of* T_{max} *can be misleading.* The effective temperature T_{eff} instead gives a much better indication of where the bulk of the emissivity of the lines comes from, at least in some cases.

In order to have a visual representation of the data in Table 2.2, each experimental data point is plotted in Figure 2.12 at the effective temperature T_{eff} and at a value equal to the product $DEM(T_{eff})\times(I_{ob}/I_{th})$. *The DEM is therefore not strictly speaking a fit through the points.* The same type of representation is also adopted in the rest of this thesis.

The error bars refer to the combination of observational and theoretical (10%) errors and give an idea of the uncertainties in the derived DEM values. In the same figure 2.12 the EM_L values of Figure 2.11 are also plotted as asterisks, for a direct comparison. This comparison gives a better idea of the large differences in the ordinate values on the one hand, and on the differences between T_{eff} and T_{max} on the other. The worst cases are those of the blends that are composed of principal lines that have peaks in their G(T) at different temperatures, such as the Ca X – C III blend, where the maximum of the total G(T) is at log T_{max}=5, i.e. where the C III line has maximum emissivity. In fact, with the adopted abundances, the G(T) of C III is higher than the G(T) of Ca X. But the DEM distribution is such that the emissivity of the Ca X (that peaks at log T_{max}=5.8) becomes stronger than that of the C III line, resulting in log T_{eff}=5.7. Only a few lines have $T_{max} \simeq T_{eff}$ when T_{max} can be safely used to indicate the region of maximum emission. The reasons for this can be various, but in most cases this happens when: a) such lines have G(T) almost equal (except for a scaling factor); b) *and* most of their G(T) is at temperatures where the DEM distribution is relatively flat, as is the case of the self-blends Ne III, O IV, O V, Ne V. More details of these lines can be found in the following Section.

This explains why the DEM_L method fails when used to estimate the differential emission

Table 2.3: *Some of the selected lines of the averaged coronal hole spectrum of* Vernazza and Reeves *(1978), with the theoretical intensities* I_{th} *calculated with the adopted abundances and with the trial DEM curve derived from the* DEM_L *values of Figure 2.11.*

Ion	λ_{th} (Å)	λ_{ob} (Å)	I_{ob}	I_{th}/I_{ob}	+/-	log T_{eff}	log T_{max}	frac
Si III	1206.499	1206.5	393.6	604.91	86.25	4.66	4.77	
O III	599.597	599.6	19.0	632.44	89.44	4.80	5.06	
O IV	554.513	554.5	92.7	10.37	1.47	4.93	5.27	0.50
O IV	554.1						5.27	0.20
O IV	555.3						5.27	0.10
O IV	553.3						5.27	0.10
O V	760.444	760.0	10.7	0.57	0.08	5.40	5.39	0.69
O V	759.4						5.39	0.17
O V	760.2						5.39	0.13
Ne VII	465.220	465.2	68.1	1.73	0.25	5.80	5.72	
Mg IX	368.070	368.2	127.3	0.67	0.10	5.98	5.98	0.81

measure and the element abundances. When trying to use it to estimate a DEM, this method is inherently wrong because it first assumes that for each emission line the DEM is a constant in temperature (and therefore can be extracted from the integral, Equation 2.6), and then pieces together these values to reconstruct a smooth curve. This simply does not work, even if emission lines with narrow G(T) are used. This can already be seen by the large differences between the DEM_L and DEM values in Figure 2.12. To give a quantitative idea on the differences, which are striking, a smooth curve joining the DEM_L values has been taken as a trial DEM curve (the dashed line in Figure 2.11) and the G(T) of the observed lines folded with it (Equation 2.6), to calculate the theoretical values. The results are shown in Table 2.3. Lines that are in the region of steep DEM gradient such as the Si III 1206.5 Å line are overestimated by a factor of 600. Even lines that do not have a wide G(T) such as the O IV 554.5 Å line *and* are emitted over a region where the DEM gradient is small, are overestimated by large factors (up to 10). The DEM_L therefore gives an **incorrect** differential emission measure distribution.

2.5.3 The element abundances evaluation. Comparison of the DEM with the DEM_L method.

With the DEM method the element abundances are found by adjusting their values until the maximum number of lines from different ions follow the same DEM curve. Once one absolute element abundance is fixed, all the other element abundances can be adjusted, aligning the DEM curves of the different elements.This is only possible if there is sufficient temperature overlap for the different elements and the element abundances are assumed not to vary within the observed volume (i.e. not to vary with temperature). **In this case, as in the rest of this thesis, unless otherwise stated, the abundance of oxygen**

has been fixed at the photospheric value $10^{8.93}$ (*Grevesse and Anders*, 1991), and all the other element abundances have been found relative to this. Note that in the recent study of *Grevesse and Sauval* (1998), the oxygen photospheric value has been lowered to $10^{8.83}$.

For example, for the averaged coronal hole spectrum of *Vernazza and Reeves* (1978), the adopted Ne/O relative element abundance was obtained by deriving a DEM curve from the O III, O IV, O V lines, and requiring an overlap with the DEM curve obtained from the Ne lines (Ne III, Ne IV, Ne V, Ne VI, Ne VII). This resulted in an increase over the photospheric Ne abundance ($10^{8.09}$) of $10^{0.2}$=1.6, while keeping the O abundance equal to the photospheric value. The abundances of Ca and Na were modified in the same way. However, the Ca abundance determination is based on only one line, Ca X 574Å which was blended with a C III line, and so should be treated with caution. The Na abundance was found using two lines, the Na VII (blended) line at 491.9 Å and the bright Na VIII 411.2 Å line.

To have a quantitative idea of the effects of the differences between the adopted and photospheric abundances, theoretical intensities have been calculated for the Ne, Ca, Na lines with the photospheric abundances of *Grevesse and Anders* (1991) and the same DEM, and the results reported in Table 2.2. The ratio $I_{\rm th}/I_{\rm ob}$ clearly shows that these lines are *not* well reproduced. These points are also displayed in Figure 2.13, for a visual confirmation of the need to modify the Ne, Ca, and Na abundances. The same Figure 2.13 also shows the line differential emission measures DEM_L values derived with the photospheric abundances. While nothing can really be said about the blended lines, because of the already mentioned differences between $T_{\rm eff}$ and $T_{\rm max}$, the EM_L values of the O III – Ne III and O IV – Ne IV also show the need to vary the Ne/O abundance. So, both the DEM method and the EM_L method give the same result, in this case. This happens because:

a) such lines have G(T) almost equal (except for a scaling factor) and $T_{\rm eff} = T_{\rm max}$;

b) most of their G(T) is at temperatures where the DEM distribution is relatively flat.

In fact, given two elements X_1 and X_2, the ratio of the observed intensities can be written:

$$\frac{I_1}{I_2} = \frac{A_b(X_1) \int\limits_T C_1(T, N_e)\ DEM(T)\ dT}{A_b(X_2) \int\limits_T C_2(T, N_e)\ DEM(T)\ dT} \tag{2.20}$$

from which the relative element abundance $A_b(X_1)/A_b(X_2)$ can be deduced, from the observed intensity ratio I_1/I_2, once the DEM distribution is known. Only when the two lines have similar $C(T)$ and the DEM distribution is relatively flat would one expect that

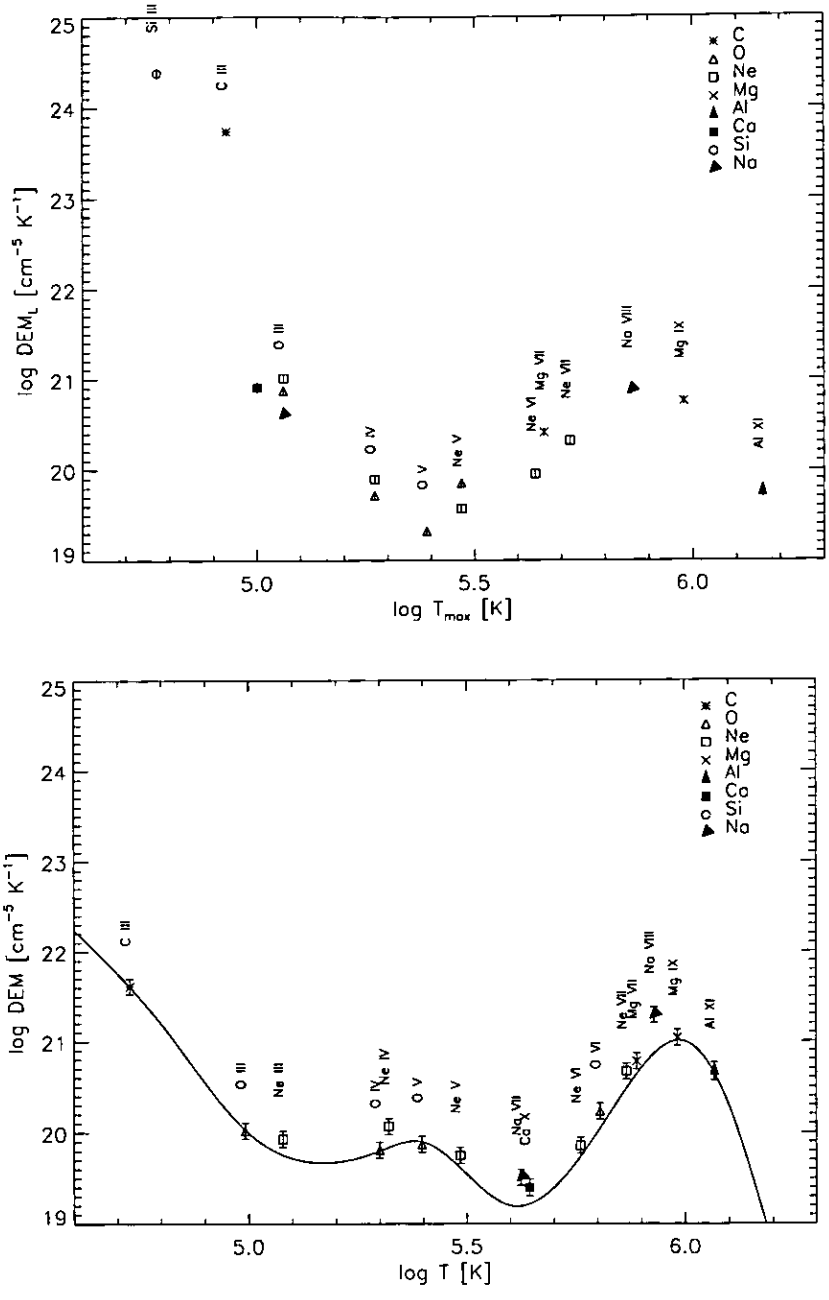

Figure 2.13: *Line differential emission measures DEM_L of the selected lines (top), and DEM with the* Grevesse and Anders *(1991) abundances (bottom), showing the need to modify them for some elements (Ne, Na, and Ca).*

the DEM factors out from the integrals:

$$\frac{\int_T C_1(T,N_e)\ DEM(T)\ dT}{\int_T C_2(T,N_e)\ DEM(T)\ dT} = \frac{\int_T C_1(T,N_e)\ dT}{\int_T C_2(T,N_e)\ dT} \tag{2.21}$$

If the above equality holds, then it is possible to deduce the relative abundances directly from the observed intensities and the contribution functions, because:

$$\frac{A_b(X_1)}{A_b(X_2)} = \frac{I_1 \cdot \int_T C_2(T,N_e)\ dT}{I_2 \cdot \int_T C_2(T,N_e)\ dT} = \frac{DEM_L(X_2)}{DEM_L(X_1)} \tag{2.22}$$

i.e. the DEM method and the DEM_L method are equivalent. In any other case, the two methods can be expected to produce different results. There are many cases in which it is possible to observe lines emitted by ions of different elements that have similar contribution functions $C(T)$, from which relative element abundances have been derived in the past (see Section 2.6 for some examples), assuming the DEM_L method and neglecting what is termed here and in the rest of this thesis 'the DEM effect' on the element abundance derivation. The DEM effect is particularly important when the emissivity $C(T)\ DEM(T)$ of a line peaks at temperatures where there is a non-negligible DEM gradient and Equation 2.21 does not hold. In the averaged coronal hole spectrum of *Vernazza and Reeves* (1978) the DEM distribution is such that the DEM effect can be important at temperatures $logT < 5$ and $logT > 5.6$, but in other spectra the DEM distribution can be very different. The DEM effect becomes particularly important at certain temperatures. In particular, the region $5.5 < logT < 5.8$ is very important for the determination of the FIP effect, because most of the EUV low- and high-FIP lines are emitted in that temperature range, and the DEM effect plays an important role. Section 2.6 discusses this issue and gives some examples.

2.5.4 Discussion of the results and comparison with previous analyses

It is beyond the scope of this chapter to provide a full description of the data analysis and results on the averaged coronal hole spectrum, although interesting. However, before concluding this Section, some general comments on the science rather than the methods are worth noting, in particular because some of the results are relevant in the remainder of this thesis.

First, the DEM method has shown that blending is the major problem when analysing the HCO data. Most of the lines not presented are serious blends, where the principal lines are from different ions and elements. Also, most of the lines at shorter wavelengths could not

be well reproduced, which is probably due to intensity calibration errors at wavelengths below 400 Å as also reported by *Warren et al.* (1998), who recently re-analysed the quiet sun data of *Vernazza and Reeves* (1978), performing a DEM analysis. The Mg IX 368 Å line is the strongest line at shorter wavelengths, and has been used in the present work, while it has been rejected by other analyses of the HCO data (*Raymond and Doyle*, 1981b; *Warren et al.*, 1998).

The shape of the DEM and the element abundances

The DEM of the averaged cell-centre coronal hole spectrum is slightly different from that obtained by *Raymond and Doyle* (1981b), reproduced in Figure 2.14. They calculated the EM_T values, integrating the DEM over $logT = 0.1$ intervals, and therefore the comparison should be made with the EM_T values shown in Figure 2.10.

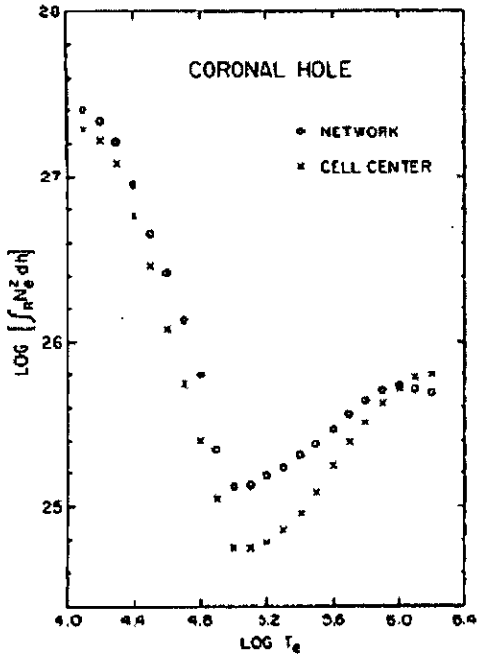

Figure 2.14: *The emission measure distribution (EM_T values) for the coronal hole network and cell centre of* Raymond and Doyle *(1981b), derived from the* Vernazza and Reeves *(1978) data.*

The EM_T values at lower and higher temperatures are basically the same, as is also true for the minimum at $logT = 5.0 - 5.2$. The small increase around $logT = 5.4$ is mainly due to O V lines, while the second minimum around $logT = 5.6$ is mainly required by the Ne V lines. These differences might be due to the improved atomic data used, or to differences in element abundances, while differences in the adopted pressures for the calculation of the contribution functions can be ruled out (although *Raymond and Doyle*

(1981b) do not specify the adopted values). *Raymond and Doyle* (1981b) refer to the previous paper *Raymond and Doyle* (1981a), where contribution functions are calculated with abundances that are close to photospheric. Their adopted log values in their analysis were : He (10.93); C(8.55); N(7.96); O (8.63); Ne(7.60); Mg(7.65); Si(7.65); S(7.20). As well as a departure in the O abundance from the photospheric value (8.93), they took the O/Ne relative abundance to be 10.7. The adopted abundance ratio from the present analysis is $10^{8.93-8.09+0.2}$=4.37, a factor 2.4 lower, which explains part of the difference in the *DEM* distribution. In any case, it should be noted that *Raymond and Doyle* (1981b) did not use the Ne III, Ne IV, Ne V, Ne VI lines, and their *DEM* at $logT = 5.0 - 5.6$ K is constrained by O III, O IV, O V, O VI lines. It is therefore not surprising to find differences, because of the different atomic data used, and the line selection and element abundances. This type of difference will be encountered elsewhere in this thesis, and is typical of the state of the art in the field.

The problem with the Li-like ions and other lines

Table 2.4: Some other lines of the averaged coronal hole spectrum of *Vernazza and Reeves* (1978), with the adopted abundances.

Ion	λ_{th} (Å)	λ_{ob} (Å)	Transition	I_{ob}	I_{th}/I_{ob}	+/-	log T_{eff}	log T_{max}	frac
N II	916.011	915.5	2s2 2p2 $^3P_1$ - 2s 2p3 $^3P_2$	18.7	0.89	0.13	4.55	4.73	0.31
N II	915.6		2s2 2p2 $^3P_0$ - 2s 2p3 $^3P_1$					4.73	0.25
N II	916.0		2s2 2p2 $^3P_1$ - 2s 2p3 $^3P_0$					4.73	0.25
N II	916.0		2s2 2p2 $^3P_1$ - 2s 2p3 $^3P_1$					4.73	0.19
O II	718.610	718.0	2s22p3 $^2D_{3/2}$ - 2s2p4 $^2D_{5/2}$	10.6	5.43	0.77	4.65	4.82	0.56
O II	718.5		2s22p3 $^2D_{5/2}$ - 2s2p4 $^2D_{3/2}$					4.82	0.36
N III	991.577	991.4	2s2(^{1}S)2p $^2P_{3/2}$ - 2s 2p2 $^2D_{5/2}$	24.4	0.94	0.13	4.79	4.98	
S IV	1062.661	1062.7	3s2.(^{1}S).3p $^2P_{1/2}$ - 3s.3p2 $^2D_{3/2}$	2.1	0.21	0.03	4.94	5.05	
N IV	765.147	764.3	2s2 $^1S_0$ - 2s 2p $^1P_1$	38.2	0.53	0.07	5.09	5.18	0.69
N III	764.4		2s2 2p $^2P_{3/2}$ - 2s 2p2 $^2S_{1/2}$					5.01	0.20
N III	763.3		2s2 2p $^2P_{1/2}$ - 2s 2p2 $^2S_{1/2}$					5.01	0.11
S VI	933.378	933.1	3s $^2S_{1/2}$ - 3p $^2P_{3/2}$	5.8	0.20	0.03	5.45	5.27	
N V	1238.821	1238.8	1s2 2s $^2S_{1/2}$ - 1s2 2p $^2P_{3/2}$	24.0	0.35	0.05	5.58	5.27	
C IV	419.713	419.5	1s2 2p $^2P_{3/2}$ - 1s2 3s $^2S_{1/2}$	11.2	0.08	0.01	5.74	5.08	0.51
C IV	419.5		1s2 2p $^2P_{1/2}$ - 1s2 3s $^2S_{1/2}$					5.08	0.26
Ca X	419.8		3p $^2P_{3/2}$ - 3d $^2D_{5/2}$					5.82	0.18
Mg X	609.793	609.6	1s2.(^{1}S).2s $^2S_{1/2}$ - 1s2.(^{1}S).2p $^2P_{3/2}$	10.0	5.32	0.75	5.91	6.04	0.73
O IV	609.8		2s2 2p $^2P_{3/2}$ - 2s 2p2 $^2S_{1/2}$					5.27	0.26
Ne VIII	770.409	770.4	1s2 2s $^2S_{1/2}$ - 1s2 2p $^2P_{3/2}$	19.8	6.77	0.96	5.94	5.79	
Mg X	624.941	624.7	1s2.(^{1}S).2s $^2S_{1/2}$ - 1s2.(^{1}S).2p $^2P_{1/2}$	2.4	8.48	1.20	6.02	6.04	

Table 2.4 shows the identifications and results for some other lines in the same spectrum, based on the adopted values of pressure, element abundances, and *DEM*. The first striking result is the behaviour of the Li-like ions, compared to the others. In fact, N V and C IV are **underestimated**, while Ne VIII and Mg X are **overestimated**, both by large factors. The S VI 933.3 Å (Na-like) is also **underestimated**, but this could be due to an

underestimation of the S abundance. In fact, other S lines (S IV) are also underestimated. No correction was made to the S abundance, because only a few S lines were observed.

Raymond and Doyle (1981b) do not report any such problems, and actually state that '*a good agreement is found between lines of different isoelectronic sequences*', but in reality, to constrain the million-degree peak of the *DEM* they only used Li-like lines (O VI, Ne VIII, Mg X, Si XII, S XIV), with the exception of Ar VII and Ca X (see Figure 4 of their paper. No comparison with the other sequences was presented by *Raymond and Doyle* (1981b).

Anomalous behaviour of the Li-like ions, together with those of the Na-like isoelectronic sequence, compared to the other sequences, was first discovered by *Dupree* (1972), using OSO-IV quiet sun data (with even lower spectral resolution than ATM), although it has been neglected in most of the subsequent literature on solar EUV spectroscopy, except in a few cases that are mentioned below.

Judge et al. (1995) present a *DEM* analysis of solar spectra with no spatial resolution (the Sun was observed as a star) and a spectral resolution of 1 Å, based on satellite and rocket data. The spectra were well calibrated, with a photometric accuracy of 15%. With the *DEM* analysis, *Judge et al.* (1995) found that '*very significant and systematic differences exist between the line intensities of the Li and Na isoelectronic sequences formed below 3* $\times 10^5$ *K and those of the other sequences*', and note '*the absence of a discrepancy in the coronal Li-like ions Mg X, Ne VIII*'.

Judge et al. (1995) used the photospheric abundances and performed a *DEM* analysis on the observed lines of the ions C II, Si III, C II, N III, Si IV, O III, C IV, O IV, N V, O VI, Ne VII, Ne VIII, Mg IX, Mg X, i.e. only a limited number of lines were used. However, considering first the Li-like lines, they found C IV, N V, and O VI lines **underestimated** by factors of 2 to 5.

Although they state no discrepancy for the Ne VIII lines, their $I_{\rm th}/I_{\rm ob}$=1.8, a factor much higher than the stated uncertainties in the calibration as well as the fact that all the other lines are reproduced within 20%. Furthermore, only two lines (Ne VII and Mg IX, Be sequence) were used to constrain the peak of the *DEM*, and any of their conclusions on the high-temperature lines should be treated with caution. However, considering those two lines, it seems that their *DEM* is underestimated at higher temperatures. If this underestimation is taken into account, then $I_{\rm th}/I_{\rm ob}$=2.2.

The other Li-like coronal line they used was the bright Mg X 609.8 Å line, for which they state $I_{\rm th}/I_{\rm ob}$=1.07. In reality, this line is a strong blend with an O IV line that is not reported in the paper. If the O IV contribution was indeed neglected, it could easily

account for more than 30% of the observed intensity (see Chapter 3 for examples), and with the probable underestimation of the DEM, $I_{\rm th}/I_{\rm ob}$ must be at least 1.7, again an **overestimation** as for the Ne VIII. Regarding the Na sequence, only Si IV was observed, with an **underestimation** by a factor of 2.

In conclusion, the observations presented by *Judge et al.* (1995) are found here to be in agreement with the behaviour of the Li-like ions in this analysis of the coronal hole spectrum, and will be further confirmed in the next Chapter from SOHO/CDS observations. The author agrees on the question posed by *Judge et al.* (1995): '*Why are these results so striking, and yet earlier work failed to identify these systematic effects ?*'; and with the comment that '*the implications are likely to be far-reaching*'. In fact, the probable cause for this effect is a departure from equilibrium, which can be explained with the long timescales of the dielectronic recombination from the He-like ions. If this is true, the large body of work in solar and stellar coronal physics, based on Li-like ions, will have to be revisited.

Recently, *Warren et al.* (1998) also re-analysed the *Vernazza and Reeves* (1978) quiet sun spectral intensities with a DEM method, recent atomic data and coronal abundances. They also found an **underestimate** of the low-temperature Li- and Na-like O VI, N V, S VI lines by factors 2-4. As in *Raymond and Doyle* (1981b), they used the higher temperatures lines of Li- and Na-like ions to determine the $DEM(T)$ around 10^6 K, and therefore no disagreement with the other isoelectronic sequences could be found for those lines. All the other lines were discarded because of the larger uncertainties at the shorter wavelengths. The unfortunate situation in which most of the bright and well-calibrated high-temperature lines observed by the HCO instrument were from Li- and Na-like ions is not repeated in the CDS instrument which does observe high-temperature lines of different isoelectronic sequences. More details on the findings from CDS observations can be found in the following Chapters.

Finally, aside from the Li- and Na-like problems, the examined coronal hole spectrum also showed that many other ions could not be well represented, some of which (such as C II) are emitted at such low temperatures that opacity effects come into play. Another case is O II, which is **overestimated** by a factor of 5. *Warren et al.* (1998) also found an overestimation for the quiet sun data, but only by a factor of 2. The blend N III-N IV at 764 Å is underestimated by a factor of 2. These inconsistencies are found also from CDS spectra, as explained in the following Chapter, which confirms the fact that these findings are not instrument-dependent but are due to incorrect atomic physics or wrong model assumptions.

2.6 The element abundance evaluation. Critical discussion of previous work and assessment of the CDS possibilities

One of the main unresolved issues in the solar corona is the FIP effect and the determination of the coronal abundances. It is therefore important to explain what method was used to derive element abundances, and compare it with the methods that have been previously used.

The ratios of lines emitted by ions of different elements, but having similar contribution functions, were used as proxies for abundance variations, while the differential emission measure analysis was used to deduce relative element abundances (as explained in Section 2.4).

In the past, using Skylab observations, only a limited number of lines could be used unambiguously (due to the characteristics of the overlapping spectroheliograms), and most of the abundance determinations were based on line ratios at the rings of the limb-brightening. The most commonly used ratios were those of Mg VI/Ne VI and Ca IX/Ne VII lines (*Widing and Feldman*, 1989). In particular, most of the abundance determinations found in the literature are based on Mg VI/Ne VI lines, because one is from a low-FIP element (Mg) and the other from a high-FIP element (Ne), and there was much interest in the FIP effect. Although intensity ratios of lines of these ions do show large variations, depending on the structures observed (and presumably on the topology of the magnetic field (*Sheeley*, 1996)), it is not straightforward to deduce from them variations in relative elemental abundances, since various effects can change the observed ratios as well. The most important ones are the *DEM* effect and the result of density analyses along the line of sight.

Although the possibility of the presence of the *DEM* effect has been pointed out by some authors, as was the possibility of casting serious doubts on the elemental abundance work (*Phillips*, 1997a), only a few abundance analyses include a full *DEM* analysis (*Schmelz*, 1993; *Fludra and Schmelz*, 1995; *Del Zanna and Bromage*, 1999a).

The Mg VI contribution functions are slightly skewed toward higher temperatures, compared to the Ne VI ones, as Figure 2.15 shows. The ratio of the contribution functions (also Figure 2.15) shows how the differences increase above temperatures of $10^{5.7}$ K. These kinds of differences are much more pronounced for other pairs of ions, such as Ca IX and Ne VII, or Mg VII and Ne VII, and therefore any effects present in the Mg VI / Ne VI ratios would also be present, and much more important, for these other ions.

The lines emitted by the Mg VI and Ne VI ions have C(T) that peak at temperatures

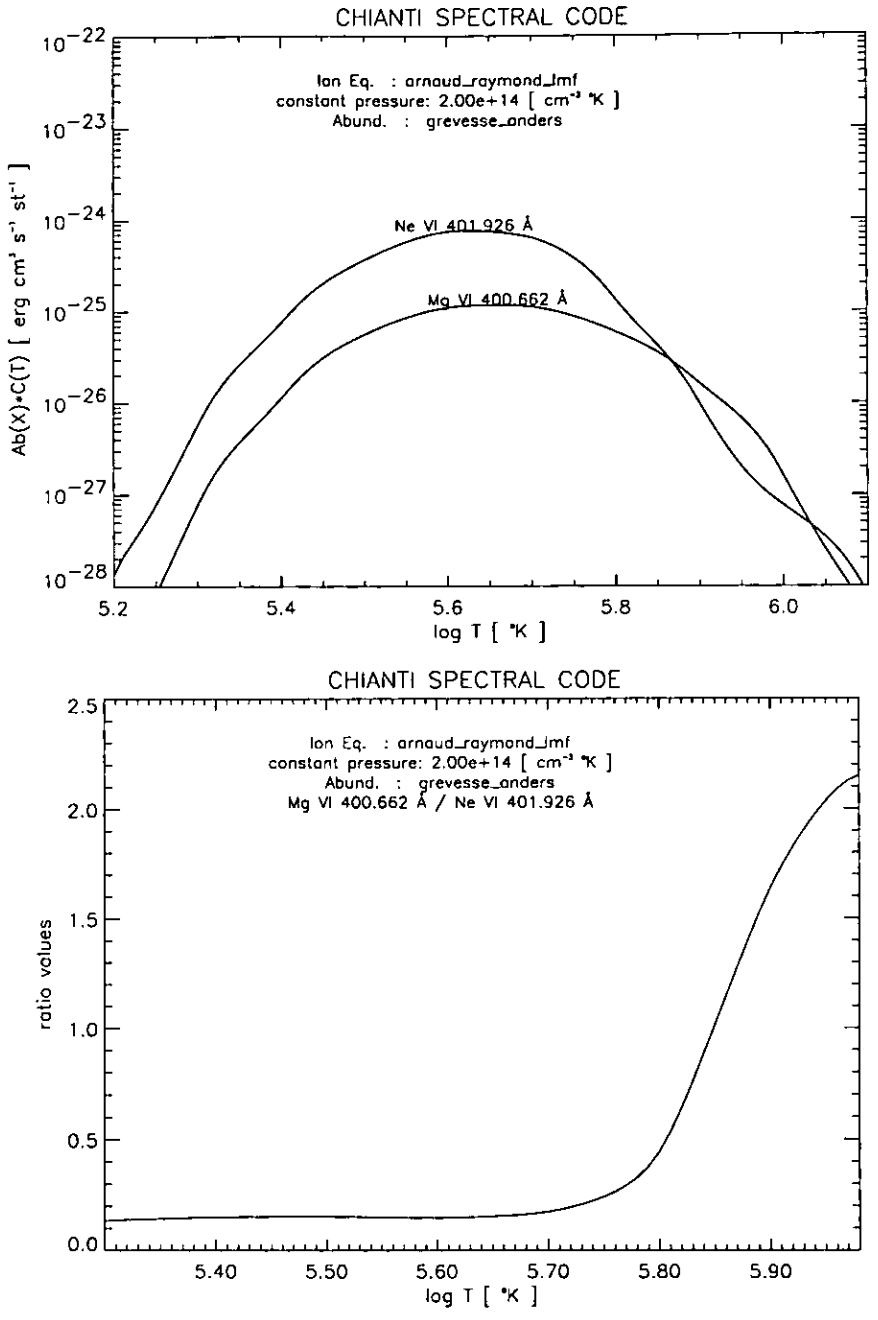

Figure 2.15: *Contribution functions of the two Mg VI 400.666 Å and Ne VI 401.926 Å lines and their ratio, calculated at constant pressure* $P_e = 2\ 10^{14}$ *[cm*$^{-3}$ *K], with the ionization equilibrium calculations of* Arnaud and Rothenflug *(1985) and photospheric abundances (*Grevesse and Anders, *1991).*

where the DEM gradient is large in most of the solar observations, and is particularly large for low-temperature structures such as plumes (see Chapter 5). Therefore, these small differences in the contribution functions are amplified when forming the integrals and the relation 2.21 does not hold; the DEM_L method gives the wrong answer. Neglecting the shape of the DEM curves when calculating the Ne/Mg relative abundances using Ne VI and Mg VI ions has the effect of underestimating the Ne/Mg relative abundance, thus overestimating the FIP effect. Any inaccuracy in the ionization equilibrium calculations (or departures from equilibrium) could also be amplified by this DEM effect.

Density variations can also change the observed Mg VI / Ne VI intensity ratios, since most of the Mg VI lines are density-dependent (while the Ne VI are not). In theory, if one can independently measure an electron density pertaining to the region where the Mg VI lines are emitted (in the transition region), then it is possible to accurately calculate the Mg VI emissivities at that density and remove any uncertainty due to density variations. But unfortunately, transition region densities are very difficult to measure, because in the EUV only a few weak density-sensitive lines are observed. The few values previously reported in the literature have a large scatter around typical values of $N_e \simeq 10^9$ cm^{-3} (from Mg VII).

Another source of uncertainty is the fact that when calculating the contribution functions the source region might be better represented with a constant pressure along the line of sight, instead of a constant density. Ideally, if enough density estimates at different temperatures are available, one should calculate the contribution functions $C(T, N_e)$ with an appropriate density-temperature model, although other effects can still come into play (*Doschek*, 1984). The issue of constant pressure or constant density in the transition region is still an open one, in the sense that there have not been sufficient observational constraints to indicate which is better.

It is useful to see to what extent different densities or pressures can affect the observed ratios. A particular group of Mg VI-Ne VI lines (around 400 Å) has been chosen as an example, because these lines have been widely used in the past (*Sheeley*, 1996), due to the fact that they are close in wavelength and possible calibration errors are much reduced. The line intensities have been calculated at different densities and pressure values, for different DEM distributions, as an exercise to see how these effects change the theoretical ratios.

The group of lines is: Mg VI (399.281, 400.666, 403.31 Å) and Ne VI (399.821, 401.136, 403.255, 401.926 Å). The ratios of these lines, calculated using CHIANTI, compared to the brightest ones in each group (Mg VI 403.31 Å and Ne VI 403.255 Å) are (Mg: 0.35, 0.67, 1.); (Ne: 0.20, 0.38, 0.22, 1.), i.e. the same values that can be deduced from Table 1

in *Widing and Feldman* (1993). These ratios are the same for different densities, because the Ne VI lines are not density-dependent, and the Mg VI lines all have the same density dependence. This confirms the consistency between the atomic data used by other authors in the past (*Widing and Feldman*, 1993) and those used in the present work.

Table 2.5: *Table of theoretical intensity ratios for the Mg VI 400.666 Å /Ne VI 401.926 Å, and Ne VI 401.926 Å /Mg VI (+ Ne VI) 403.3 Å, assuming a relative abundance A_b (Ne/Mg) = 0.5, for a pressure $P_e = 10^{14}$ (cm^{-3} K), different densities N_e (cm^{-3}) and: a) without the consideration of a DEM; b) with a plume DEM (*Del Zanna and Bromage, *1999b); c) with a quiet sun (network) DEM (*Del Zanna and Bromage, *1999a). The values calculated in* Widing and Feldman *for $N_e = 10^{10}$ and those presented by* Sheeley *(1996) are also displayed for comparison in the last two columns.*

	$P_e = 10^{14}$	$N_e = 10^8$	$N_e = 10^{10}$	$N_e = 10^{10}$ *Widing and Feldman* (1993)	*Sheeley* (1996)
			Mg VI 400.666 Å /Ne VI 401.926 Å		
(a)	1.42	1.50	0.90	0.97	1.00
(b)	2.91	3.03	1.76	-	-
(c)	2.18	2.28	1.34	-	-
			Ne VI 401.926 Å /Mg VI (+ Ne VI) 403.3 Å		
(a)	0.43	0.40	0.65	-	0.61
(b)	0.22	0.21	0.36	-	-
(c)	0.29	0.28	0.46	-	-

Two ratios have been selected, from the various possible combinations, the Mg VI 400.666 Å / Ne VI 401.926 Å and Ne VI 401.926 Å / Mg VI (+ Ne VI) 403.3 Å. While the use of the first ratio is preferred, since the lines are unblended, the second is used more in the literature, since the Mg VI 403.31 Å line is the brightest in the group, although blended with Ne VI 403.255 Å. The moderate CDS spectral resolution makes the evaluation of the Mg VI 400.666 Å line difficult, due to the proximity of other lines.

The effects that different *DEM* distributions and different densities have on these two theoretical Mg/Ne intensity ratios were studied, calculating the ratios for a pressure $P_e = 10^{14}$ (cm^{-3} K), typical of coronal holes, and for densities $N_e = 10^8$ and 10^{10} (cm^{-3}), assuming a relative Ne/Mg abundance A_b (Ne/Mg) = 0.5, with different *DEM* distributions. The adopted densities are extreme values, in the sense that previous density estimates of the quiet sun (at the Mg VI temperatures) have produced values within this range. It is therefore to be expected that the possible variations in density affecting the observed ratios are well within the range $N_e = 10^8 - 10^{10}$.

Table 2.5 shows the results. Case (a) is when the *DEM* is neglected in the calculation of the ratio (Equation 2.22). Case (b) is with a plume DEM (*Del Zanna and Bromage*,

1999b), which represents an extreme case, because the steepening of the DEM curve is exactly where the differences between the Mg VI and Ne VI C(T) are maximum, and the DEM effect is greatest. Case (c) is with a more 'normal' quiet sun (network) DEM (*Del Zanna and Bromage*, 1999a). The values calculated in *Widing and Feldman* (1993) for $N_e = 10^{10}$ and those presented by *Sheeley* (1996) are also displayed for comparison.

Table 2.5 shows that the DEM effect is more important than the density effect, and that the values the ratios have with different DEM distributions are quite different from the values stated by *Widing and Feldman* (1993) and *Sheeley* (1996) (and used in all the literature on this topic, for that matter), where no DEM effect was taken into account. It is therefore possible, if not probable, that some of the previous results on elemental abundances, if based on Mg VI/Ne VI lines, produced an underestimate of the Ne/Mg relative abundance of up to a factor of three. Work based on different pairs of lines (e.g. Mg VII/Ne VII) can have produced much larger underestimates.

Some of the published Skylab data, that were used to produce estimates of element abundances, were re-analysed, to see if the DEM effect played a role in those observations. This re-analysis of old Skylab data has shown that in most cases using the full DEM analysis made little difference. Only a couple of examples are briefly discussed here, because they are instructive.

The first is the *Widing and Feldman* (1992) work on off-limb observations of a plume. This is the only work of abundance analysis on plumes ever published. In this work, which focused on the brightest plume observed by Skylab, *Widing and Feldman* (1992) derive a Ne/Mg relative abundance of 0.36, one of the lowest values observed. Although a complete DEM analysis on the same data was not possible, since only a few lines in a restricted temperature range were reported, a limited DEM analysis on those data has indicated that the correct relative Ne/Mg abundance is about a factor of two higher. The DEM and the DEM_L methods are therefore *not* equivalent in this case, as expected, for the reasons explained above. More details on coronal hole plume elemental abundances can be found in Chapters 5 and 6.

The second example is based on the re-analysis of the published data of an erupting prominence observed by Skylab and presented by *Widing et al.* (1986). The contribution functions have been calculated at the same constant density $N_e = 10^{10}$ adopted in their paper. Also the same element abundances, derived in their paper were used, with the only difference that *Widing et al.* (1986) present their results in terms of abundances relative to Mg, while in the present work the abundances are given relative to H, assuming a Mg/H relative abundance of $4\text{x}10^{-5}$. An estimated 10% error on the published values is reported on the data points. Figure 2.16 shows the comparison of the line emission

measures DEM_L and DEM analysis. The DEM in Figure 2.16 shows a peak around the temperatures where the Mg VI and Ne VI lines have maximum emissivities, and therefore at those temperatures the gradient in the DEM is small, and the two methods agree, as one would expect.

The potential of CDS for determining abundances

Unfortunately, all the low temperature lines (log T $\leq$ 5.5 K) observed by CDS/NIS are from high-FIP elements (e.g. N, O, Ne), while all the high temperature lines (log T $\geq$ 5.9 K) are from low-FIP elements (e.g. Mg, Ca, Fe, Si, Al), and the FIP effect is therefore difficult to study. However, considering first these two groups of elements, separately, the number of observed lines and their temperature overlap is good enough to determine quite accurately their relative abundances. For example, the same O III, O IV, O V and Ne III, Ne IV, Ne V lines observed by Skylab are observed by CDS, with a much better resolution, and the O/Ne relative abundance can easily be checked as already shown. Furthermore, these lines are mostly density-insensitive and are observed by the same detector (NIS 2), therefore reducing any calibration problems. The same applies to high-temperature lines, which CDS observes mostly in NIS 1 and the GIS detectors. The number of observed lines is so large that density-insensitive lines can be used, and the determination of the relative abundances is not a problem.

The scaling between high and low-FIP elements can be achieved using low-FIP low-temperature lines and high-FIP high-temperature lines, that overlap in temperature. Unfortunately, NIS observes only a few of these, one Mg VI line at 349.2 Å and three Mg VII lines in NIS 1, and a few Ne VI and Ne VII lines visible in NIS 2. The Mg V lines (NIS 1) are excluded because they are very weak and mostly blended. The determination of the FIP effect is problematic: 1) because there are only a few such lines, and they are visible in different detectors, thus making the relative intensity calibration between NIS 1 and NIS 2 a crucial issue (see Chapter 3 for a complete discussion); 2) these lines fall in the temperature range $logT = 5.6 - 5.8$, where the differential emission measure usually has a steep increase and the shape of the DEM curve affects the abundance determination most, as already explained; and 3) some of these lines are slightly density-sensitive.

The Mg VI line at 349.2 Å is a blend of four Mg VI transitions which are only slightly density-dependent at low densities (their total emissivity varies by 40% in the interval $N_e = 1 \cdot 10^8 - 1 \cdot 10^9$ cm^{-3}). This Mg VI line has the further complication of being blended with a density-dependent coronal line, Fe XI at 349.046 Å . However, the Fe XI contribution can be safely neglected when observing coronal holes and the quiet sun on the disc, and the Mg VI 349.2 Å line can be used in conjunction with the Ne VI 562.8

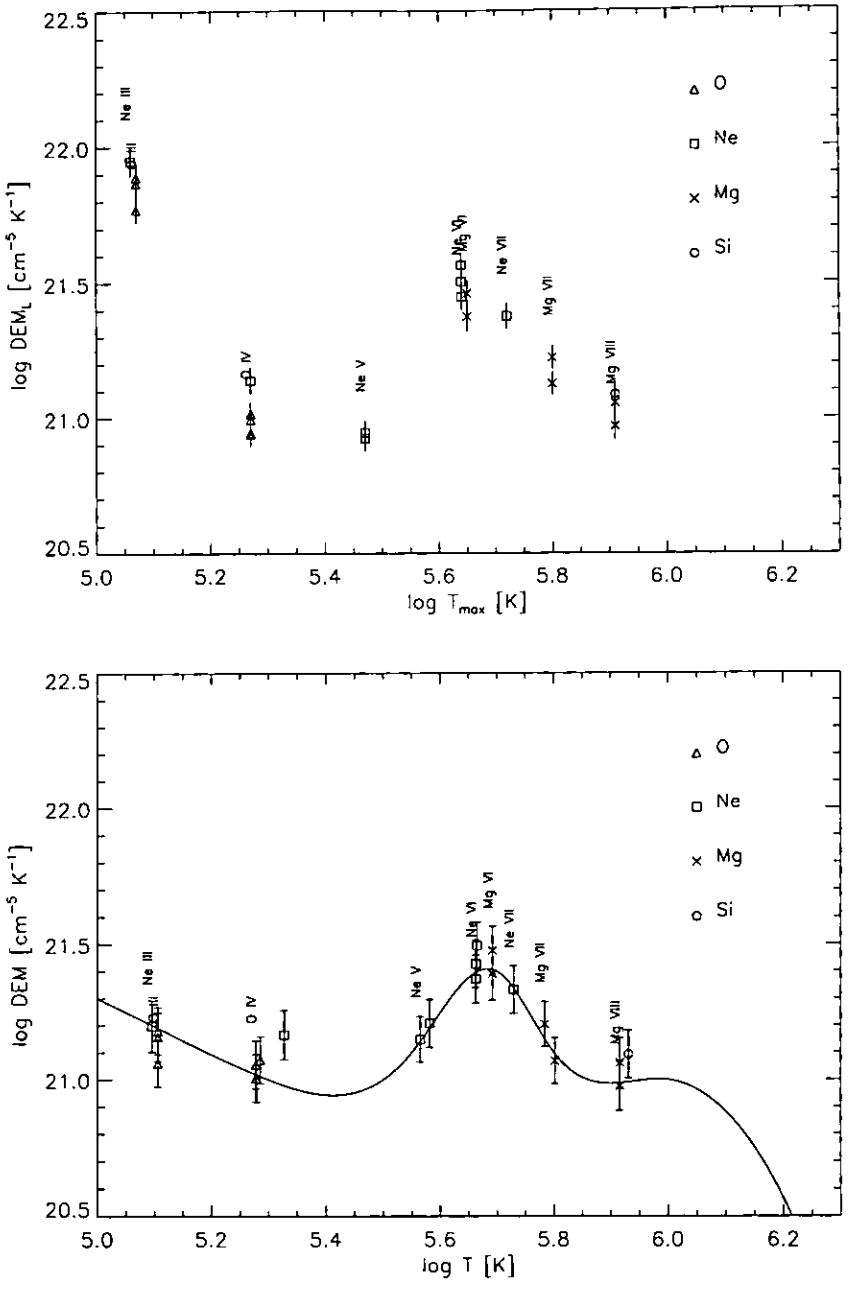

Figure 2.16: *Top: The line differential emission measures DEM_L of the lines of an erupting prominence (*Widing *et al., 1986), plotted at the temperature $T_{\max}$. Bottom: The DEM distribution corresponding to the same lines as above.*

Å when searching for a FIP effect in the solar features observed. The contribution of the Fe XI 349.046 Å line to the observed line can be estimated by combining theory and observations. In fact, at $N_e \simeq 2 \cdot 10^8$ cm^{-3}, the intensity of the Fe XI 349.046 Å line is 1/20 of the intensity of the Fe XI 341.113 Å line, which is observed un-blended. Even in the cell centre regions, where the Mg VI intensity is low, on average the contribution of the Fe XI 349.046 Å line to the blend was found to be less than 5 % for coronal hole observations. In any case, the Fe XI contribution was included in the calculation of the $G(T, N_e)$.

As for the previous example, this Mg VI/ Ne VI ratio is also strongly affected by the *DEM* effect. For example, assuming the photospheric abundances of *Grevesse and Anders* (1991), a constant pressure of $4 \cdot 10^{14}$ (cm^{-3} K), and a constant *DEM* distribution, it is found from eqn. 2.20 that the theoretical intensity ratio I[Mg VI 349.17 Å/ Ne VI 562.8 Å] = 0.35. If the contribution functions are folded with a quiet sun *DEM* distribution for the cell centres (e.g. Figure 6 in *Del Zanna and Bromage*, 1999), the ratio increases to a value of 0.54, while if a coronal hole *DEM* for the cell centres (same figure) is used the ratio has a value of 0.66. Therefore, small variations in this Mg VI/Ne VI intensity ratio may be due, not just to real changes in the Mg/Ne relative abundance, but also to a change in the DEM distribution.

Given the fact that only a few lines were available for analysis of the FIP effect from CDS/NIS observations, a large effort has been made to perform and analyse CDS/GIS observations to be used in support of the NIS observations, whenever possible. The CDS/GIS observes many useful lines for such an analysis, as for example the group of Mg VI, Ne VI lines around 400 Å previously mentioned, and many other lines of ions that extend the overlapping region between the high-FIP and the low-FIP ions observed (e.g. the Ca IX 466 Å and Ne VII 465 Å lines). The use of different ions from different isoelectronic sequences is very important because it can help to indicate where the atomic physics may be in disagreement with the observations.

Unfortunately, the analysis of GIS spectra is very complex, for example some of the useful lines can be affected by *ghosts* or second order lines. The use of GIS lines for abundance analysis therefore strongly depends on an assessment of the performance of the GIS detectors, which will be described in the next Chapter.

Chapter 3

The CDS instrument. Data analysis and calibration

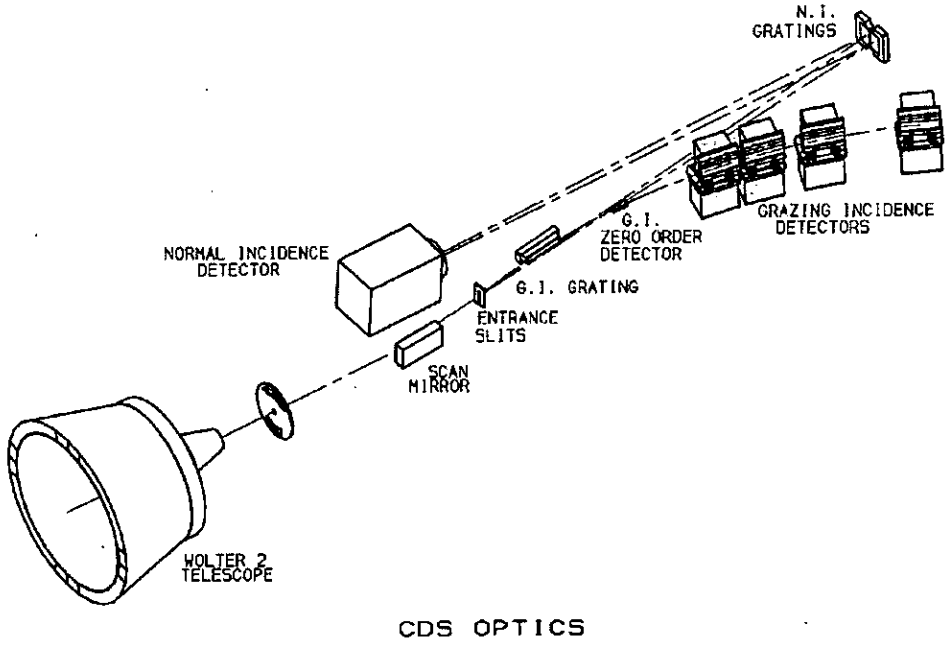

Figure 3.1: *The optical layout of the CDS instrument (from the WWW).*

The CDS instrument and data analysis are described in *Harrison et al.* (1995) and in the CDS software notes, available on the WWW. Since there is no user guide to CDS observations, the descriptions of the instrument characteristics that are given in this Chapter can be regarded as complementary (with examples) to those that can be found in the various software notes, although they reflect the personal experience and methods of data analysis adopted by the author, and should not be regarded as comprehensive.

The CDS instrument (Figure 3.1) consists of a Wolter-Schwartzschild type II grazing incidence telescope, a scan mirror, a set of different slits, and two spectrometers that do not observe simultaneously, the normal incidence spectrometer (NIS) and the grazing incidence spectrometer (GIS).

The slits provide various fields of view (2″x2″, 4″x4″, 2″x240″, 4″x240″, 90″x240″, 8″x50″) and are normally oriented along the solar N-S direction.

Any position on the Sun is commonly indicated by two coordinates, Solar X and Solar Y, also used to indicate the centres of the pointing of any CDS observation. Solar X is given in arc sec from the disc centre along the East-West (E-W) direction, while Solar Y indicates arc sec from the disc centre along the South-North (S-N) direction. Note that 1″ corresponds on the Sun to 700 km.

The NIS is composed of two normal incidence gratings that disperse the light into the NIS detector, known as the viewfinder detector subsystem, or VDS. The gratings are slightly tilted, in order to produce two wave-bands (NIS 1: 308 – 379 Å and NIS 2: 513 – 633 Å; note that in this thesis abbreviations such as N 1 and N 2 are also used) on the same detector, one on top of the other (see Figure 3.2). The spectral resolution is $\simeq$ 0.35 Å for NIS 1 and $\simeq$ 0.5 Å for NIS 2. Second order lines have been observed only in NIS 2.

The NIS can provide monochromatic images of the solar field of view. This is accomplished with the *rastering* of a region, moving a mirror and producing contiguous images of one of the long slits. The rastering is performed from west to east (being the normal alignment of CDS with the slits in the solar N-S direction). More details of the NIS spectral characteristics, performance and data analysis are given in Section 3.1.

The grazing incidence spectrometer (GIS) has a grazing incidence spherical grating that disperses the incident light to four microchannel plate (MCP) detectors placed along the Rowland Circle (GIS 1: 151 – 221 Å, GIS 2: 256 – 341 Å, GIS 3: 393 – 492 Å and GIS 4: 659 – 785 Å; note that in this thesis abbreviations such as G 1 or G1 are used). The spectral resolution of the GIS detectors is about 0.5 Å. Many second order lines have been observed in GIS 3 and GIS 4.

The GIS is astigmatic, focusing the image of the slit along the direction of dispersion but not perpendicular to it. Images of the Sun are obtained using a pinhole slit and combining movements of the slit and of the scan mirror. Normally, the movements are such that an area of the Sun is rastered in a zig-zag pattern, starting from south to north and from west to east (in normal CDS alignment). More details of the GIS spectral characteristics, performance and data analysis are given in Section 3.2.

The pointing to any location is accomplished through two mechanisms, one external and one internal. The first is achieved with the use of external legs, that move the whole CDS instrument at 45 degrees to the N-S and E-W directions, with about 2″ steps. The overall pointing accuracy of the CDS instrument has been *at best* 10″. This meant that in many cases small target sources have been 'missed', that corrections for the solar rotation are very limited, and that accurate measurements need analysis (e.g. cross-correlations of the observation with large field of view images) to identify the real pointing.

The solar rotation produces an apparent movement of any feature of about 10″ in an hour at the sun centre. Considering that the typical duration of a CDS observation is one hour, rastering over a region of the order of one arc min, the solar rotation is often a non-negligible effect in observations near sun-centre, and is further complicated by the differential rotation of the solar corona.

CDS has feature tracking software, which moves the entire instrument, but since the accuracy of the movements is much less than the spatial resolution, it is not generally recommended. CDS software note #45 details the limitations, but in short these are:

1) The minimum E-W movement is approximately 2″.

2) the actual movement may often be 2″ ±2″ with the result that the effect may be 'worse than doing nothing', depending on what effect was intended.

3) The default interval for updating the pointing is 600 seconds. If an individual raster duration is less than this, no correction will ever occur.

The internal movement is more accurate because it is done via the movement of the scan mirror and the slits, with 2″ steps, and has a negligible error. It is limited to 4' in either direction.

Telemetry constraints usually make it necessary to pre-select a number of NIS wavelength windows to be extracted on-board from the spectra, before the data are telemetered to the ground.

An advantage of the GIS over the NIS is that it is possible to record spectra with short exposure times. In fact, with normal CDS telemetry the four GIS spectra can be down-loaded in about 13s. Telemetry is therefore not a limitation for GIS, and the entire GIS wavelength range can be telemetered (and actually should, to have the possibility to then *deghost* the spectra, see Section 3.2). Observations are instead limited by the necessary exposure time to achieve sufficient signal. This exposure time is of the order of hundreds of seconds for coronal holes, much higher than the telemetry time.

An important aspect of the planning of CDS observations comes in the designing of the *'studies'* to be run by the instrument. Each CDS study is a sequence of commands to be sent to the spacecraft, containing pointing, exposure times, movements of the mirror and/or the chosen slit, and various telemetry instructions (for example the specifications of the extraction windows for the NIS). Chapter 4 describes the CDS studies that were used and those that had to be designed and developed to study coronal holes. More details of the main CDS characteristics that are of particular importance for the planning of observations are also described in Chapter 4.

Since the CDS was new, it took almost two years before a correct approach to the data analysis was found, and before the proper software either became available or was developed by the author. As an example, during the first year of the mission, in 1996, there were no suitable IDL routines to perform a gaussian multi-fit of the spectra, and some of the data analysis was done using IRAF packages. Therefore, most of the data have had to be re-analysed more than once, as often happens during a learning process when analysing new data. In the following Sections 3.1 and 3.2, some aspects of the standard CDS data analysis reduction are covered, while more general software developed by the author for the analysis of the coronal hole observations is described in Chapter 4.

The CDS wavelength region is rich in emission lines but is relatively unexplored. A large effort was devoted to the identification of the more than 500 lines present in the spectra, to writing automatic IDL routines for multiple line-fitting of all the lines present in the spectra, and to finding the most useful ones for the various diagnostic purposes.

Because of the moderate resolution of CDS, the presence of second order lines and the various instrumental effects that will be described later, an analysis of CDS spectra of several different solar regions (e.g. active regions, quiet sun, coronal hole, plumes, on-disc, off-limb) was needed to achieve a correct identification of the lines. In fact, many lines observed by CDS are blends and in most of cases different lines become predominant in different solar regions.

Also, it was important to develop a diagnostic method to be used for the line identification. The *DEM* and abundance evaluation method already described in Chapter 2 was employed. It is interesting to note that very few works have presented solar EUV line identifications that are *not* simply based on line positions, but rather on diagnostic methods as used in this thesis. *Malinovsky and Heroux* (1973) were among the first to apply a diagnostic method (*Pottasch*, 1963) to confirm or reject previous identifications in the 50-300 Å range, using an integrated Sun spectrum with 0.25 Å resolution taken with a grazing-incidence spectrometer flown on a rocket in 1969.

Comparison with higher resolution spectral data also helped assessment of line identification and blending. As described in Chapter 1, there have been only a few studies that could be used for this purpose (*Malinovsky and Heroux*, 1973; *Firth et al.*, 1974; *Behring et al.*, 1976; *Dere*, 1978a; *Dere*, 1982), which observed the entire sun and/or active regions. Aside from these, the most useful studies are those based on the SERTS flights, mainly the 1989 flight (*Thomas and Neupert*, 1994; *Young et al.*, 1998) and the 1995 one (*Brosius et al.*, 1998a; *Brosius et al.*, 1998b).

The importance of CDS/GIS observations for abundance analysis was the motivation for the large and original effort by the author in analysing GIS spectra. To obtain a better understanding of the in-flight behaviour of the GIS detectors, three early (two first-light) GIS observations representative of different types of coronal emission were analysed: an active region, the quiet Sun and a coronal hole. The main goals of this work, presented in Section 3.3, were to identify the principal emission lines, study the characteristics of spectra of different regions, evaluate which lines could be used to perform density and temperature diagnostics, and check the wavelength and intensity calibration. This work contributed to one of the papers that described the first science results from CDS (*Mason et al.*, 1997).

3.1 The normal incidence spectrometer

The VDS detector is mainly composed of a microchannel plate and a 1024x1024 pixels charge coupled device (CCD), composed of four square sections. The CCD was orientated with its columns parallel to the slit alignment. Therefore, any pixel Y position should represent a single Solar Y point, while the grating dispersion is along the pixel X coordinates. In reality, the CDS alignment is more complex, as shown in Figure 3.2 and described below.

A pixel in the detector Y direction corresponds to 1.68″. The extent in Y of the long slits (240″) is therefore 143 pixels on the detector. A pixel in the detector X direction corresponds to about 0.07 Å for NIS 1 and 0.11 Å for NIS 2.

Unfortunately, the NIS spectra contain a large scattered light (*'background'*) component when observed on the solar disc. The NIS 1 spectral region, where CDS has many potential diagnostic lines, is the most affected. This scattered light produces a spatially and wavelength-dependent background component in the spectra, and is most intense in the network spectra, as shown in Figure 5.5.

Typically, in the NIS 1 channel, the scattered light component is a factor of 2 higher in the network areas than in the cell centre areas. The background level can be of the order of

the peak intensity of most of the NIS 1 lines (see, e.g., Figure D.1) in coronal hole regions, and also in the quiet sun. The background determination provides the major uncertainty in line intensity measurements. This scattered light is also strongly wavelength-dependent in some areas (as can be seen in many of the spectra presented in this thesis), in particular in bright regions of the network. Because of this, in general only results from comparison of lines close in wavelength were relatively free from such an uncertainty, and in any case this diffuse background component should be carefully removed.

During the first year of analysis , the data were first intensity-calibrated, and the lines subsequently fitted. Because of the wavelength-dependence of the calibration, it was difficult to correctly subtract the diffuse background component. Because of this, and because the intensity calibration was uncertain, it was then decided to perform the fit directly on the photon-event spectra. This also allowed a more appropriate evaluation of the errors, and the possibility of applying different intensity calibrations to the data.

In the following, the procedure that was used to analyse the NIS data is outlined, specifying some aspects of the CDS data reduction.

Subtraction of the CCD bias

This is accomplished by the CDS routine VDS_DEBIAS. All rasters used by the author were designed to include four VDS background windows in the corners of the CCD. Average CCD readout biases are removed from each of the four CCD sections. The error associated with this step is small when compared to the scattered light. Raw data from the VDS detector are in 'ADC' (Analog to Digital Conversion) units. After applying VDS_DEBIAS, the units of the data are 'DEBIASED-ADC'.

Cosmic ray removal

An effect that strongly constrains the observations is the presence of cosmic ray hits. Exposure times cannot be too long, otherwise cosmic rays literally wipe out the use of large fractions of the spectra. Various software routines are available to automatically 'flag' cosmic ray hits with 'missing' values, but an interactive check is highly recommended, although this takes a very long time if the number of exposures and extraction windows is large. The CDS routine CDS_CLEAN_IMAGE was used by the author, together with XCDS_COSMIC. Figure 3.2 shows some cosmic ray hits flagged as missing with this software. Often, the number of cosmic ray hits is such that a line profile in one exposure is lost and no line intensity can be deduced. Therefore, it is highly recommended to raster small regions on the sun a few times, clean the single spectra from the cosmic rays, and then

Table 3.1: *The burn-in factors for some lines, as applied by the standard CDS software, for two dates one year apart. Note the increase of the correction with time and that in 1997 the brightest line in NIS 2 already had a 40% in peak intensity depression. The wavelengths correspond to the predicted position of the lines for the observations on 1st Sept 1997 (there is a time-dependent wavelength calibration).*

Line	Detector	1st Sept 1997	1st Sept 1996
Fe XVI (bl) 335.407 Å	NIS 1	0.141	0.095
Fe XI 341.117 Å	NIS 1	0.005	-
Si X 347.390 Å	NIS 1	0.080	-
Si X 356.023 Å	NIS 1	0.081	0.006
Fe XVI 360.763 Å	NIS 1	0.165	0.093
Fe XII 364.456 Å	NIS 1	0.096	0.051
Mg IX 368.086 Å	NIS 1	0.226	0.146
O III 525.863 Å	NIS 1	0.104	0.050
He I 537.108 Å	NIS 2	0.161	0.112
O IV 554.499 Å	NIS 2	0.236	0.146
He I 584.370 Å	NIS 2	0.419	0.321
O III 599.620 Å	NIS 2	0.124	0.082
Mg X (bl O IV) 609.818 Å	NIS 2	0.268	0.158
Mg X 624.990 Å	NIS 2	0.189	0.099
O V 629.819 Å	NIS 2	0.369	0.274

average the spectra. In this way, the effect of the cosmic rays is removed (unless cosmic rays hit the same emission line at the same spatial position along the slit). Another way of reducing the effect of the cosmic rays is to spatially average the line profiles.

Corrections for flat-fielding, burn-in and nonlinear effects, using VDS_CALIB

The flat field of the detector presents variations of only a few percent. However, before the spectra are divided by the appropriate parts of the flat field, the burn-in correction is added to the flat field. The VDS detector sensitivity decreases with time in the most strongly illuminated areas (i.e. in the centres of the brightest lines), because of local gain depression (*burn-in*). This has been monitored since launch using wide slit observations. The line profiles are reconstructed, adding to the flat field some gaussian 'absorption' profiles with a predicted width, position, and normalized peak intensity. Table 3.1 shows some of the lines that need such a correction. Note how the correction changes with time, and how considerable it is. For example, the He I 584 Å line, the brightest in these detectors, had already in September 1997 a burn-in of 40%. This correction is accurate (to a few percent) only for the bright and un-blended lines.

VDS_CALIB, after dividing the spectra by the flat field, corrects the exposure time and divides it into the data to give the ADC count rate. The correction to the exposure time is

due to the electronic shuttering, which makes each exposure slightly longer (0.1165 seconds for the normal VDS operating voltage). VDS_CALIB also applies a correction for non-linear effects at high count rates (ADC counts per photon, a function of the voltage).

Then, the VDS throughput is divided into the data to convert from DEBIASED-ADC count-rate to photon-events/pixel/s. The term "photon-events" refers to those EUV photons which actually interact with the detector. For the subsequent data analysis, it is useful to also have the spectra in photon-events/pixel and so the output from VDS_CALIB is multiplied by the 'corrected' exposure time.

Correction for geometric distortions, using VDS_ROTATE

Unfortunately, it is not possible to make in-flight adjustments to CDS to correct for, e.g. distortion during launch. This has resulted in a series of effects, that can only be partially corrected for during the data analysis.

First, it seems that the NIS instrument is not in focus. In fact, the line widths created by the 2″ and 4″ slits appear to be about the same, and much larger (by factors $\sim$ 2) than in pre-flight measurements. No correction is possible.

Another optical factor to take into account in the data analysis is the fact that the centres of the various slits are not co-aligned, which has the consequence that images taken will not be aligned in the Y-direction. However, images taken with different slits by the author show that the 4″x4″ and the 4″x240″ slits are co-aligned, in accordance with results based on other work (D. Pike, priv. comm.), which have shown for the other slits misalignments of up to 4″.

Then, the spectra are slanted, in the sense that the dispersion direction is tilted relative to the rows of the VDS CCD, with different angles for NIS 1 and NIS 2, as shown in Figure 3.2. This is the main effect. On top of this, the spectral lines appear to be tilted relative to the dispersion direction (i.e. the angle they for with the dispersion direction is not 90 degrees, and varies). The slant of the spectra complicates the planning of a CDS 'study' and data analysis. A correction for the slant and tilt of the lines can be done in two ways, one during the data planning and one in the analysis (by the routine VDS_ROTATE).

During the planning of a CDS 'study', the CDS routine MK_RASTER makes the following adjustment. If a study is designed with specific data extraction windows then the windows are positioned on the detector at different row positions to allow for the slant. Using this method, data extracted at any of the wavelength windows are co-spatial on the Sun to

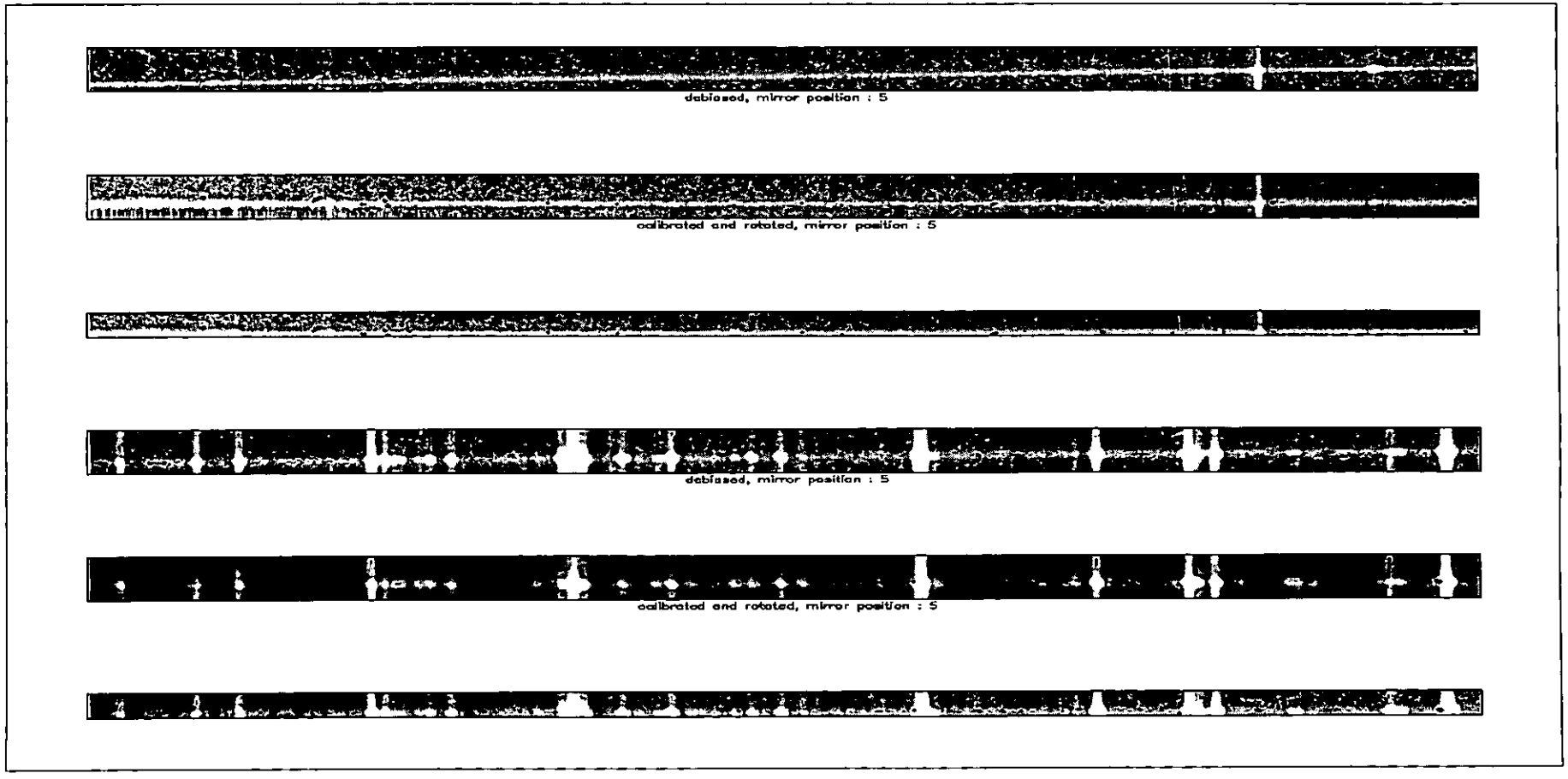

Figure 3.2: *The NIS spectra, showing the effects of the slant of the spectra and the cosmic rays. First three spectra, from top to bottom: a NIS 1 de-biased spectrum; the same spectrum with the cosmic rays flagged as missing data, calibrated using VDS_CALIB (and NIS_CALIB), and rotated (using VDS_ROTATE); the previous spectrum, but with the unusable spatial areas (top and bottom rows) removed. The bottom three figures show the NIS 2 spectra. The particular exposure shown here was taken during a brightening in a spatially-localized region of the network. The bright stripe across the spectra is caused by enhanced emission in all the emission lines, plus by scattered light, and clearly shows the slant of the spectra, that is more pronounced in NIS 1. Note that a large portion of the spectra (along the slit) is lost after the correction for the slant is applied.*

within one pixel in Y. The usual extraction window height is 143 pixels, corresponding to 240″.

For studies that use the full default extraction window the correction for slant has to be applied during data analysis, and it is important in the planning phase to extend the Y-size so that a sufficiently large area of the detector is extracted, to cover the full rotated spectrum. In the data analysis, VDS_ROTATE is used to rotate the entire NIS 1 and NIS 2 spectra to correct for the slant and tilt. In this category there are two further types of CDS 'studies', one that extracts the full spatial positions along the slit (as done in the spectral atlases) and one with a shortened extraction along the slit (case shown in Figure 3.2). In the case of spectral atlases, two windows of 1024x160 pixels are extracted. VDS_ROTATE pivots around the centre of the data. There is a difference in the height of the unrotated data for NIS1 and NIS2, where the first is 160 pixels in height, and the second is only 153 pixels. Therefore, NIS1 data pivots around vertical pixel 79.5, while NIS2 data pivots around pixel 76. Thus, there is a 3.5 pixel difference in the positions due to that effect. VDS_ROTATE then cuts the two spectra to 143 pixels, although two arrays of 1024x160 pixels are given in output. In the other case, with shortened extraction along the slit, there is no difference in the height of the unrotated data for NIS1 and NIS2, and the spectra are rotated around the centre of the data.

In any case, the slant of the two channels is such that about 30″ along the slit direction is lost, if one is interested in having all the NIS spectral information at the same spatial position. Figure 3.2 shows the rotated NIS 1 and NIS 2 spectra.

The tilt of the lines can be partially corrected for by applying the routine VDS_ROTATE to the spectra, or by adjusting the wavelength calibration.

The NIS wavelength calibration also has some peculiar aspects. The wavelength calibration requires a 'scan mirror correction', which appears to be different for different observations. Then, the NIS wavelength calibration has been found to be a function of the CDS optical bench temperature (D. Pike, priv. comm.), which continuously changes depending on the solar illumination, and which has been observed to cause shifts of up to a pixel (0.1 Å), which for a strong line such as O V 629 Å corresponds to a velocity of 56 km/s.

Even after all the possible tilt and wavelength corrections, the line profiles are not strictly gaussian, and residuals to gaussian fits show peculiar spatial patterns still not explained. Recently, *Haugan* (1999) has suggested that a possible explanation for some of these features is an asymmetric tilted point spread function.

In conclusion, NIS does not have an accurate 'standard' wavelength calibration, and therefore, in the absence of any reference wavelength scale, most absolute wavelength measure-

ments are subject to various uncertainties. Also, the NIS shows a series of geometrical effects that are not well understood and are difficult to explain, and can only be partially corrected for.

Spatial resolution and binning along the slit

It has to be noted that the resolution of the instrument (FWHM of the Point Spread Function or PSF) is at least 5–6″. Therefore, the pixel resolution (1.68″) along the slit is much less than the spatial resolution, and the spectra can be binned without losing any spatial information. Binning over two pixels was applied to all the NIS data during the analysis. This not only reduces by a factor of two the data volume, but is also useful in reducing the effect of the cosmic rays, since it is an averaging process.

Alternatively, binning can be implemented on-board as has been done for some CDS studies developed by the author (see Table 4.1), to reduce the telemetry time.

Line-fitting

Line intensities were obtained by using multiple-line-fitting IDL routines (CFIT package, *Haugan*, 1997) on the spectra, assuming gaussian profiles, and removing the *'background'* by fitting polynomials.

The CFIT package has many advantages, compared to many other line fitting packages found in the literature (and tested). It is very flexible, in the sense that any type of line profile and/or background, with any number of parameters can be fitted; any number of lines can be fitted over a wavelength region (although large numbers considerably slow the process); the parameter's values can be allowed to vary within some fixed ranges, or can be kept constant; each fitted line's parameters can be checked and modified interactively. The fit is performed with a non-linear weighted least squares fit, optimizing an initial user-supplied set of parameters in order to find the best agreement between the chosen model function and the observed data.

Many IDL routines have been written by the author to apply the routines of the CFIT package to different types of observations. For example, in some cases each CDS NIS 'study' is composed of a scan with the long slit in the X-direction, giving two spatial dimensions. The data to be analysed is in this case a 'cube'. In other cases, there can be a time dimension to be added, or only one spatial dimension, if one is interested in the line variation along only one spatial direction. In any case, the fit is actually done for a one-dimensional spatial-temporal dimension at a time, i.e. on a single spectrum, intensities versus wavelengths.

Gaussian profiles have been assumed for the analysis of NIS spectra, and therefore the parameters are the peak intensity I_0, the central wavelenghth, and the full width of half maximum $FWHM$. In many cases lines are closely spaced, and a proper de-blending can only be done if ranges for the positions and widths are given. Only 'real' lines that have a width at least equal to the instrument resolution are fitted.

Since different CDS 'studies' extract different spectral ranges, routines that could automatically analyse any type of NIS data were written. This was done first by writing a database with the parameters (values, minimum and maximum range, for a total of about 1500 values) of all the lines observed by NIS in all solar regions examined, a total of more than 165 lines.

Then, two sub-types of fitting routines had to be written, one to analyse full spectral data, and one for the 'windowed' data. In fact, the line fitting programs cannot cope with too many lines to fit, and the full spectral data had to be fitted in sections. The windowed data, on the other hand, have to be merged whenever possible, to allow a better evaluation of the background.

In either of these two sub-types of fitting routines, the fit on the background is performed first. To do so, all the pixels that correspond to regions where lines are expected are flagged with weights=0., and the routine therefore attempts a polynomial fit to the remaining pixels. This is done for the full spectral data over the whole spectral range, before dividing the spectra into sections for the fit of the lines.

Then, the integrated line intensities are estimated from the background-subtracted spectra by summing pixel values. This first estimate is very close to the final value that is provided by the gaussian fit for well separated lines, if a correct position and width of the line are given. This has been checked on many test cases.

After this, the peak intensities are estimated and given to the line fitting routine, with the position and $FWHM$ as an initial value, to speed the fitting process; this can take a long time (of the order of an hour on a Digital workstation for a typical medium-size NIS raster). The background can be allowed to vary. Then the fit is interactively checked, adjusting some parameters as necessary. This is also time-consuming. The parameters are then saved in IDL save files, together with the processed data and various information. This is the first step of the analysis completed.

Error estimates.

The various noise sources associated with the NI spectrometers are described in *Thompson* (1997). As well as Poisson noise associated with the photons which interact with the detector, there is another source of noise due to the fluctuation in the amount of amplification in the detector system, known as the pulse height distribution (PHD). This latter effect can be assumed to be comparable to the Poisson noise. Other sources of noise are only detector-dependent. The readout noise R has been found to vary from 0.62 to 0.83 photon-events/pixel, and therefore has an effect only at low light levels. A value of 0.7 is assumed in this work.

If N is the total number of photon-events in a line, the Poisson noise is $\sqrt{N}$, and assuming that the PHD component is comparable, and adds in quadrature, the total photon noise is $\sigma_N = \sqrt{2 * N + R^2 * n_{pix}}$, where n_{pix} is the number of pixels being summed over and R is the readout noise per pixel. In reality, the main source of error (not mentioned in *Thompson*, 1997) in determining intensities in NIS spectra is the scattered light in the detector, and what we want to measure is the intensity of each background-subtracted line $I = N - B$, where B is the total background intensity over the line. The noise associated with the background is again $\sigma_B = \sqrt{2 * B + R^2 * n_{pix}}$ and the error on the intensity I is therefore

$$\sigma_I = \sqrt{\sigma_N^2 + \sigma_B^2} = \sqrt{2 * (I + B) + R^2 * n_{pix} + 2 * B + R^2 * n_{pix}} \tag{3.1}$$

In the case of n_{avg} spectra averaged, we have to divide σ_I by $\sqrt{n_{avg}}$.

Another way to determine the error on the intensity is directly from the errors on the parameters of the fit. All the line profiles have been assumed to be gaussian, and the total intensity in the line has been derived from the peak amplitude I_0 and the line full-width-half-maximum $FWHM$ (in pixels):

$$I = \frac{1}{2}\sqrt{\frac{\pi}{\ln 2}}\ I_0\ \ FWHM \tag{3.2}$$

Since the fitted peak amplitude I_0 and the $FWHM$ are not statistically independent, in the sense that too high $FWHM$ favors too low I_0 and vice versa, the error on the intensity σ_I has been calculated from:

$$\frac{{\sigma_I}^2}{I} = \frac{1}{2}\left[\frac{{\sigma_{I_0}}^2}{I_0} + \frac{{\sigma_{FWHM}}^2}{FWHM}\right] \tag{3.3}$$

In most cases, the errors derived from (3.3) are very similar to those from (3.1). Unless stated, the errors derived from the parameters (3.3) are those presented in this thesis.

The intensity calibration

The CDS routine NIS_CALIB performs the conversion from photon-events/pixel/s to the calibrated default units 'photons/cm^2/sec/arcsec^2'. The conversion factor from arcsec^2 to steradians is simply $(\pi/(180\times 60^2))^2 \simeq 2.35\times 10^{-11}$, while the conversion from photons to ergs is $hc/\lambda \simeq 1.986\times 10^{-8}/\lambda$, where λ is in Ångstroms. There are several factors which determine this final conversion of the data from photon-events to absolute units.

1. The absolute sensitivity $ef(\lambda)$ [counts/photons] as a function of wavelength.

   The absolute sensitivity of the NI spectrographs is a combination of the reflectivity of the primary mirror, the secondary mirror and the scan mirror, the efficiencies of the gratings, and the quantum sensitivity of the VDS detector. The wavelength dependence of absolute sensitivity is therefore a combination of the wavelength dependence of all these various factors. The sensitivities were measured on the ground at only a few wavelengths (see Figures 3.28, 3.29, and 3.30). See the calibration Section 3.4.10 for more details.

2. The telescope aperture $A_t(k)$ [cm^2].

   $A_t(k)$ is a function of the scan mirror position (k), because as the scan mirror moves, the two NIS gratings are 'seeing' apertures of different sizes.

   The variations, around a median value of 27–28 cm^2 (for NIS 1–2) are considerable ($\sim$ 20%) over the full extent of the scan mirror positions (4′). The CDS routine GET_EFF_AREA provides the pre-flight values of $A_t(k)$, and these have been confirmed by in-flight measurements (W. Thompson, priv. comm.).

3. Angular width of the slit.

   The values are well known.

4. The exposure time.

Note that, unless stated otherwise: all the NIS spectra presented in this thesis are in photon-events; the spectral line intensities in the Figures are in phot s^{-1} cm^{-2} $arcsec^{-2}$; the intensities in the Tables are in ergs s^{-1} cm^{-2} sr^{-1}; the intensity ratio values, both in Tables and in Figures, are obtained from the intensities in ergs s^{-1} cm^{-2} sr^{-1}, and therefore, for clarity reasons, are indicated as 'ratio values (ergs)'. The errors in the intensities do not include all the systematic errors that can come from all the correction and calibration factors above-mentioned, of which the main one is the error in the instrument sensitivities, discussed below.

3.2 The grazing incidence spectrometer

The GIS detectors (*Breeveld*, 1992; *Breeveld*, 1996) are composed of a stack of micro-channel plates (MCPs), and a spiral anode (SPAN) to read the position and charge of the electron cloud created by the MCPs. The reading is converted with an 8-bit analogue to digital converter (ADC) which outputs data at (x, y) position values (known as GIS raw data). The (x, y) values form a spiral in cartesian coordinates (see Figure 3.3), which contains all the one-dimensional spectral information (the GIS being astigmatic, no more information is needed). The wavelength varies with distance along the spiral and the width of each *arm* is related to the noise in the electronics.

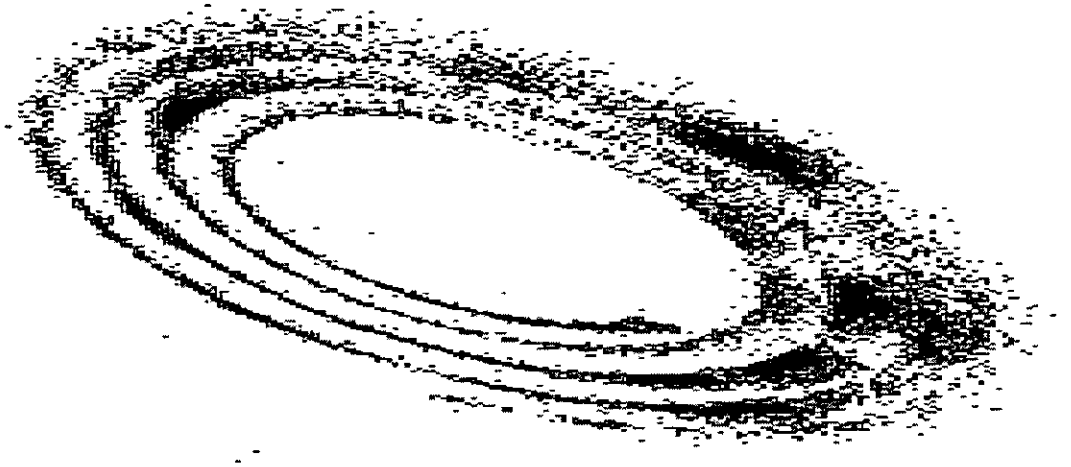

Figure 3.3: *The spiral pattern of a GIS observation (courtesy of R. Bentley).*

A set of parameters, called a look up table (LUT) is produced for each detector, fitting this spiral pattern, in order to convert the signal produced by the photon events to an array of 2048 spectral data points as a function of wavelength.

Because the gain in the micro channel plates is sensitive to the intensity, the voltages applied to each detector are adjusted depending on the slit used and the solar conditions (active or quiet sun), creating different spiral patterns, each requiring a different set of LUTs.

Because it takes too long to telemeter to the ground the raw data, this is done only once in

a while to generate the LUTs. Normally the raw data are converted on-board by applying a set of LUTs, uniquely identified by a number *GSET_ID*, to the raw data. Various sets of LUTs are stored on-board for use, and loaded before the GIS starts exposing (it takes about half an hour). It is important, during planning, to select the correct set of LUTs (i.e. GSET_ID number) for the type of observation, otherwise the telemetered spectra are not usable.

The GIS spectra have various effects that must be carefully considered before starting any data analysis. Some effects are typical of any MCP detector, and are electronic dead times, short term gain depression and long term gain depression.

The GIS operates by sending a continuous stream of event positions to the Command and Data-Handling System (CDHS). The various electronic dead-times are such that any events occurring within about 10 ms of each other will be rejected, and higher rates will render the data meaningless.

Short term gain depression occurs when count rates per pixel are above 40. In this situation, the MCP cannot re-charge fast enough to provide full gain for every event, and the data are not usable.

Long term gain depression is an *ageing* effect, a reduction in detector sensitivity over a long time interval due to continued illumination. The applied high voltage can be increased to compensate for the decrease in the MCP gain with time. However, the gain depression will be greatest at the position of the brightest lines so a wavelength-dependent effect will remain. Corrections for flat field and long term gain depression were not included in reduction of data for this thesis since they are not yet available. It is known, however, that these corrections are small.

Some other effects are very peculiar, and are related to the finite number of bits employed in the ADCs, and the noise of the electronics, that create distortions in the spiral pattern and wrong encoding by the LUTs. These are *fixed patterning* and *ghosts*, and are described in detail in the following two Sections. Some of the results presented in these two Sections are based on the analysis of GIS observations described in Section 3.4.4, and are also partially reported as contribution of the author in *Landi et al.* (1999a).

3.2.1 Fixed patterning and line profiles

The profiles of the GIS lines are predominantly instrumental. They are corrupted by the superposition of a *spiky* effect on the whole spectrum, referred to as *fixed patterning*. Counts falling near the boundary of a pixel can be shifted to neighbouring pixels, producing

narrow spikes and troughs in the profiles of the emission lines. Weaker lines can appear swamped by this effect. Figure 3.4*a* shows a portion of the GIS 1 spectrum, as an example. It is not only impossible to define a line profile, but even hard to recognise the presence of weak lines. Fixed patterning *should not alter* the total counts recorded in an emission line; it merely displaces some of them.

It is evident that it is necessary to apply some kind of correction in order to restore the original line profiles and to clean weak lines without altering the total intensity of the lines. This is important since a fixed patterned line profile is an obstacle to any fitting routine, which tries to adapt a selected analytical line profile to the input data. This is particularly important in the case of unresolved blending of lines. Strong departures from smooth profiles cause additional uncertainties in the evaluation of line intensities, and moreover can make it impossible even to fit weak lines.

Since it is impossible to rebuild the original pixel intensities from the observed spectrum, a smoothing technique, which does not change the total count-rates, is the only 'correction' that can be applied.

Many smoothing methods are available. In order to evaluate the effect that a smoothing procedure has on the GIS spectra, three different methods have been applied to a spectrum, and their effects compared. This was done by applying the same line fitting procedure to the smoothed spectra, and comparing the derived intensities with those obtained by simply summing up the pixel intensities over the entire 'line profile'. Since the fixed patterning is expected to simply shift counts to neighbouring pixels, summing the pixel values should give the most accurate measurement of the intensity of an un-blended, well isolated line, because it is independent of the type of line profile adopted. Unfortunately, the moderate resolution of the GIS does not allow this to be applied for most of the lines.

The three different methods chosen are: boxcar filtering with 3 pixel width, convolution with a gaussian function with a 2 pixel-wide σ, and Fourier filtering of proper width. The widths of the filtering kernels were chosen in order to reasonably smooth the GIS spectra, with the smallest broadening of the line profiles. In Figure 3.4 a comparison between the original GIS 1 spectrum and the results of the three smoothing procedures is reported between 169 Å and 176 Å.

It is possible to see that the shape of the spectrum is much improved by all three smoothing procedures. It is important to note however that the 3-pixel boxcar smoothing (Figure 3.4*b*) is not able to remove completely the effects of fixed patterning, though these are greatly reduced, and produces double peaked line profiles, more evident for most of the GIS 1 lines and less pronounced in the lines observed in the other spectral windows.

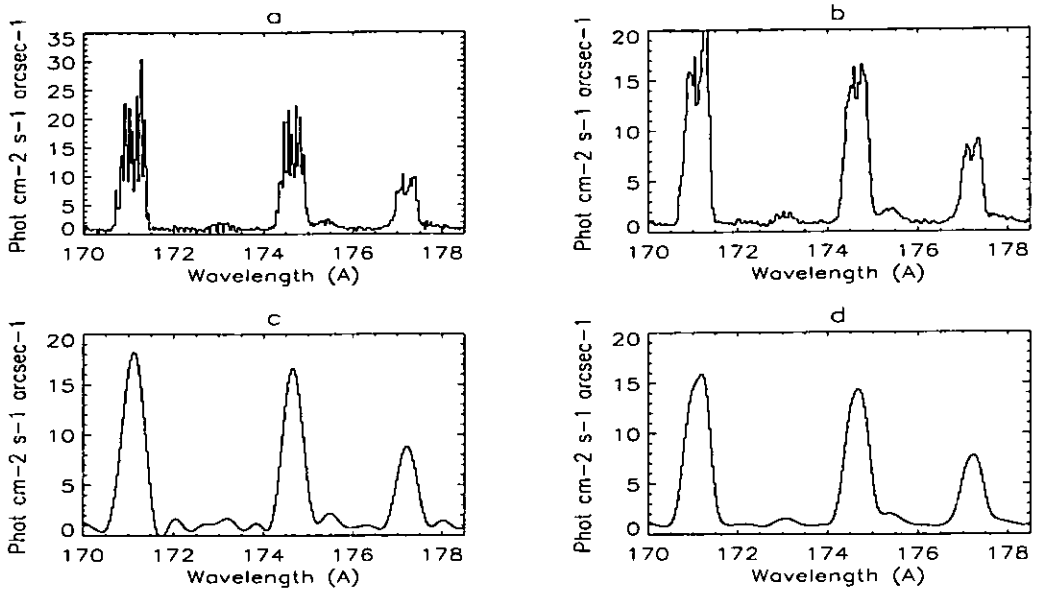

Figure 3.4: *Effects of different smoothing procedures applied to a portion of the GIS 1 active region spectrum.* a*: original spectrum;* b*: box-smoothed spectrum;* c*: Fourier-filtered spectrum;* d*: Gaussian-convolved spectrum.*

Fourier filtering (Figure 3.4*c*) produces nearly gaussian line profiles and a very clean spectrum, but alters the background, making it very difficult to distinguish weak spectral features as real lines or spurious effects produced by the smoothing procedure.

The gaussian convolution is able to clean line profiles (Figure 3.4*d*), and the resulting lines are close to gaussian-shaped profiles (as expected), with a flat background.

Line profiles.

However, various tests done on all the GIS spectra have shown that none of the smoothing procedures is able to provide gaussian profiles, unless a significant loss of spectral resolution is accepted, increasing the widths of the kernels. Moreover, these tests have also shown that, whichever smoothing procedure is applied, *each line in the GIS spectra presents a slightly different (and wider) smoothed profile.* The GIS 1 is the worst channel in this respect, where many lines are double-peaked.

Some of these (unexplained) effects must be due to the MCPs or to some distortions related to the optics. In fact, pre-flight observations (*Bromage et al.*, 1996) did show the fixed patterning effect, but not anomalous line profiles. Also, the line widths were narrower (by about a factor of 2, see the comparison in *Landi et al.*, 1999a) than those that are observed in-flight, even after including a broadening correction due to the fact that the ground calibration used a narrow-beam source of EUV radiation. It is therefore possible that distortions took place during flight, some of which might be common to the NIS, which has

also shown larger in-flight line widths and various geometrical effects, as already described. Another explanation for the anomalous line profiles can be found in the fact that the line positions were observed to shift depending on which part of the aperture is illuminated, an effect reported in *Bromage et al.* (1996) (see Figure 24) and measured scanning the aperture with the narrow-beam source. Since the Sun fully illuminates (usually) the aperture, the resulting observed line profile would be a superposition of different line profiles shifted between each other. Double-peaked line profiles can therefore be created. In addition to these profile anomalies, there are some variations of the line widths along each detector as expected, due to the configuration of the detectors (which are flat) along the curved Rowland Circle.

In conclusion, the GIS line profiles (that in any case are instrumental) are anomalous and therefore the spectral resolution of the GIS depends on the type of smoothing adopted to reduce the effects of the fixed patterning.

Comparison of different smoothing procedures.

In order to quantitatively compare the three different smoothing procedures, it is necessary to use a line fitting routine that adapts a known line profile to the observed spectral lines, to obtain the line intensities. Due to the complexity of the GIS line profiles, the adopted method has been to use gaussian profiles. First, the line fitting routines of CFIT (see above) and ADAS (*Summers et al.*, 1996) packages have been applied (in collaboration with E. Landi) to the same dataset, to evaluate the effect a different line fitting routine has on the results. A general agreement was found, with differences between the results smaller than $\simeq 5\%$ for the strongest lines. These differences were ascribed to the different evaluation of background in the two packages, which results in larger differences for weaker lines. It is worth noting that the GIS background emission results from a combination of true continuum emission, scattered light, detector effects (some of which are present at the edges, others that are related to ghosting, see below), and a contribution from weak emission lines. A proper evaluation of the background emission will only be possible when detector effects have been removed through proper flat-fielding.

The CFIT package was used to deduce line intensities, positions and widths for GIS spectra filtered with the three smoothing procedures. Table 3.2 reports the results in terms of line intensities and widths for some lines of the GIS 1 'raw' and smoothed spectra.

The same linear background has been adopted for the four spectra. This choice is suggested by the fact that the boxcar filtered spectrum and the gaussian convolved spectrum have a nearly identical background. The Fourier filtered spectrum instead alters the background more significantly. Table 3.2 shows that there is good agreement between the intensities

Table 3.2: *Comparison of fitting results. In the first column are the results of fitting the original spectrum, then the results from the three spectra smoothed using different methods. In the last column the results from the sum of counts from the original spectrum is given. The same background was imposed in all 4 cases.*

Ion	Wavelength (Å)	Original sp.	Boxcar sm.	Fourier sm.	Gauss sm.	Sum of counts
		Line widths (pixels)				
Fe IX	171.07	0.49±0.01	0.51±0.01	0.52±0.01	0.54±0.01	-
O VI	173.00	0.65±0.11	0.65±0.07	0.65±0.07	0.65±0.07	-
Fe X	174.53	0.47±0.01	0.49±0.01	0.51±0.01	0.51±0.01	-
Fe X	177.24	0.47±0.02	0.61±0.02	0.65±0.02	0.65±0.02	-
Fe XI	180.41	0.45±0.01	0.45±0.01	0.50±0.01	0.48±0.01	-
O VI	184.00	0.60±0.06	0.60±0.05	0.37±0.05	0.60±0.05	-
Fe X	184.54	0.49±0.01	0.38±0.01	0.51±0.02	0.41±0.01	-
Fe XII	186.87	0.50±0.01	0.52±0.01	0.51±0.01	0.56±0.01	-
Fe X	190.00	0.51±0.02	0.59±0.02	0.57±0.03	0.57±0.02	-
Fe XII	192.39	0.60±0.01	0.65±0.01	0.65±0.03	0.65±0.02	-
Fe XII	193.52	0.40±0.01	0.43±0.01	0.41±0.01	0.46±0.01	-
Fe XII	195.12	0.42±0.00	0.42±0.00	0.41±0.01	0.46±0.01	-
Fe XIII	196.54	0.60±0.03	0.50±0.04	0.46±0.01	0.54±0.04	-
Fe XIII	200.02	0.51±0.01	0.54±0.03	0.53±0.01	0.57±0.04	-
Fe XIII	201.13	0.44±0.01	0.46±0.02	0.46±0.01	0.49±0.02	-
Fe XIII	202.04	0.44±0.00	0.45±0.02	0.47±0.00	0.47±0.02	-
Fe XIII	203.80	0.40±0.00	0.41±0.01	0.46±0.00	0.46±0.01	-
Fe XIV	211.32	0.52±0.02	0.49±0.02	0.50±0.01	0.52±0.52	-
		Line intensities (phot $s^{-1}cm^{-2}arcsec^{-2}$)				
Fe IX	171.07	2996±54	3372±60	3635±62	3538±57	3567±61
O VI	173.00	154±23	187±22	199±22	196±21	212±18
Fe X	174.53	2257±51	2453±59	2557±60	2487±54	2591±52
Fe X	177.24	1228±58	1561±54	1653±53	1599±48	1530±40
Fe XI	180.41	1993±46	2042±50	2259±54	2126±48	2192±48
O VI	184.00	147±14	188±15	121±16	184±15	261±18
Fe X	184.54	744±20	633±20	790±36	645±20	740±29
Fe XII	186.87	1189±23	1279±24	1319±37	1318±24	1300±37
Fe X	190.00	387±15	480±17	491±27	474±17	465±23
Fe XII	192.39	939±24	1042±25	1020±56	797±25	1005±33
Fe XII	193.52	1359±24	1418±25	1409±37	1427±26	1418±39
Fe XII	195.12	1809±27	1866±28	1883±41	1897±28	1872±44
Fe XIII	196.54	303±16	342±28	346±6	363±28	354±21
Fe XIII	200.02	270±5	284±20	290±5	292±21	275±19
Fe XIII	201.13	477±6	489±26	494±6	496±27	505±24
Fe XIII	202.04	851±8	939±36	980±9	970±38	981±33
Fe XIII	203.80	987±8	1266±38	1357±10	1327±40	1306±37
Fe XIV	211.32	615±26	748±30	798±29	786±786	764±29

derived from the smoothed spectra and those derived by the total sum of counts, with differences smaller than 5 % in most cases, with the only exception being lines shortward of 180 Å for which the double peaked profile is most pronounced. The smoothing procedures therefore all provide values close to the correct ones.

On the other hand, the results of the line fitting on a raw spectrum are such that intensities are usually reduced, with differences up to 25 %, showing how it is important to smooth the spectra before any fit is done and a gaussian fitting profile is used.

The agreement between the results obtained from each of the smoothed spectra is always better than 10 %. Only a few very weak lines show greater differences between the Fourier filtered spectrum and the other two due to strong background alteration. The line widths are also slightly different for the various smoothing procedures, while the line positions are very similar.

Unless otherwise stated, the smoothing adopted for the GIS data is a convolution with a gaussian profile of $\sigma = 2$ pixels.

3.2.2 Ghosts

For some lines, the cluster of photon events will tend to spread across to the neighbouring arms of the spiral. This happens when the width of the spiral is broadened by electronic noise. This effect tends to occur only in those regions where the spiral arms are close together, and can lead to spreading to one of the adjacent arms (or both). Now, once a set of LUTs is applied to the data on-board, i.e. a particular spiral pattern is assumed appropriate for the data, the original information is lost. In terms of counts versus wavelength, this means that a portion of the counts belonging to a line can be shifted into different parts of the telemetered spectrum, giving rise to spurious spectral lines if they fall in a spectral region void of lines, or providing extra intensity to already existing spectral lines. Henceforth we will refer to a spectral line whose intensity is enhanced in this way as *ghosted (or contaminated) line*, while the lines whose counts have been partially shifted toward other regions of the spectrum will be referred to as *ghosting (or parent) lines*. The counts shifted by this effect will be called *ghosts*, while the process will be called simply *ghosting*.

Since the spreading can only occur toward one or the other side of a spiral arm, each line can generate no more than two ghosts. When the spreading occurs toward the outer arm, a ghost is created at a lower wavelength, in the so-called red-shifted spectrum. Conversely, when part of the counts of a line are read into the inner arm, a ghost is created at a higher wavelength (in the so-called blue-shifted spectrum). Note that the definitions of

red-shifted and blue-shifted GIS spectra do not have any relation to physical blue- or red-shifts, nor these spectra are simply 'shifted' (in fact, they are compressed or expanded in the wavelength scale). This notation, commonly used in GIS-related documentation, is simply used to indicate in which arm of the spiral ghosting occurs.

For each application of a given set of LUTs, ghosts will appear in the same positions. Once the applied LUTs are known, it is therefore possible to deduce which regions of the spectrum are unlikely to be affected by them, and to predict where ghosts might appear. It is therefore theoretically possible to *deghost (or reconstruct)* the spectra, i.e. add to each line the intensity lost by the creation of a ghost.

A large number of GIS spectra has been analysed, using software developed by the author, in order to assess the ghosting problem, since it severely affects any scientific use of the GIS spectra. Indeed, because of the ghosting problem, very few people have attempted any use of the GIS spectra, despite their great potential for plasma diagnostics.

Unfortunately, the situation is quite complex, for many reasons.

- First, different LUTs (i.e. spectra with different GSET_ID) produce different ghosting.
- Then, *there are no general rules that can be applied to deghost the spectra.*

  One example is that the boundaries of the regions where ghosts are expected to appear are not sharp, in the sense that there are ghosts that are created also in other regions. On the other hand, there are regions where ghosting is predicted to occur, but has not been observed. Another example is the fact that when ghosting occurs, it does in random proportions. Sometimes ghosts are only a few percent of the ghosting line, while in other cases they are much brighter than the parent line, i.e. almost all the intensity of the ghosting line appears in a ghost. It is therefore not possible to, say, analyse GIS spectra without correcting for ghosting, assuming some uncertainty level. Some lines appear to create two ghosts, while others only create one ghost. For the GSET_ID=42 case it appears that most of the lines produce red-shifted ghosts, rather than blue-shifted, although some produce both. The only positive note is that apparently only the brightest lines in each detector tend to create ghosts, even though it is difficult to exclude any ghosting of weak lines, masked in the noise of the spectra.

  Examples of ghosts, ghosting lines, contaminated lines, both contaminated and ghosting lines, red-shifted and/or blue-shifted ghosts, etc., and the possible reconstructions that were applied to the GIS spectra presented in this thesis are given in the rest of

this thesis in the form of labels in the spectra and in Tables. Note that although most of the ghosting in the GIS spectra has similar patterns for different GSET_IDs, the amount of it varies by large factors, and the examples provided here should only be used as an indication of where the problems are.

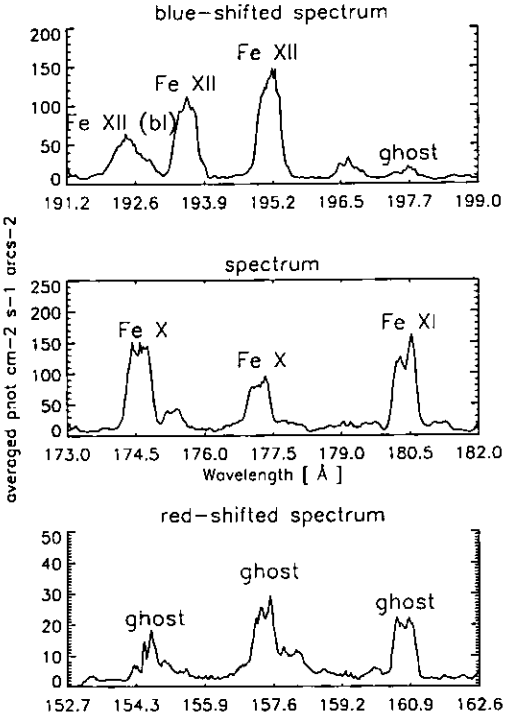

Figure 3.5: *A GIS 1 ghosting region.*

Only when a ghost appears in a region of the spectrum free of lines, is it possible to reconstruct the depleted line from which it came. Usually it is very difficult to distinguish between the ghost and any real lines with which it is blended.

For this reason only an extensive analysis of a large number of different GIS spectra can help in the ghost identification. An example of the sort of problems and how corrections can be applied, is given here. Figure 3.5 displays in the middle a portion (173-182.5 Å) of a GIS 1 spectrum. Using the geometry of the spiral pattern that was adopted to create the spectrum, the blue- and red-shifted spectra have been constructed from the observed spectrum. The spectral regions where ghosts were expected, in the blue- and red-shifted spectra, are displayed above and below the original spectrum, with the appropriate wavelength scale.

In this type of plot, a ghost would appear in one of the two shifted spectra at a position corresponding to where a line appears in the original spectrum. It is possible to see that the three spectral features observed in the bottom spectrum are *ghosts* of the three bright

Fe X 174.5 Å, Fe X 177.2 Å and Fe XI 180.4 Å lines. This is clear because no emission lines are expected to be visible in the 150–162 Å spectral region, for the type of source observed. It is therefore possible in this case to reconstruct the three ghosting lines, adding the ghosts' intensities to each parent line.

In the blue-shifted spectrum the ghosting problem seems to produce three contaminated lines: Fe XII 192.4 Å, Fe XII 195.1 Å and the Fe XIII 197.4 Å. In this case, a simple reconstruction is not possible. In fact, a great complication in the GIS spectra is that ghosted lines can be themselves the source of ghosts, ghosting into the very same region that created their contamination (*'cross-ghosting'*). In the example shown in Figure 3.5, the Fe XII 192.4 Å line can itself ghost into its red-shifted correspondent, i.e. contaminate the Fe X 174.5 Å line, increasing the confusion in this spectral range.

In conclusion, an examination of many GIS spectra has suggested the following method to try and tackle the ghosting problem in the GIS spectra. Initially, no correction to ghosting is made. [A different approach has been suggested by *E. Breeveld* (1998, priv.comm.), who developed CDS software to interactively move the intensities of 'presumed' ghosts (i.e. unidentified lines that appear in areas likely to be affected by ghosts) back to their parent line. The main limitation of the method proposed by *E. Breeveld* is that ghosts can be confused (or blended) with real emission lines. In any case, no correction should be applied to contaminated lines. There are many examples in which, depending on the type of solar source observed, ghosts can be blended with other real lines. Such examples are described in Section 3.4.6].

The presumed ghosts should then be treated as real lines, and their intensity measured. Then, a *DEM* analysis should be performed, using a selection of suitable lines. GIS synthetic spectra can then be created, and compared to the observed ones. This will immediately show the presence of the principal isolated ghosts, and will give an indication of the contaminated or ghosting lines. Ghost identification is also supported by the analysis of the position of the lines, in the original spectrum and in the blue- and red-shifted spectra. Examples will be given in Section 3.4.6. Corrections can then be applied to both the ghosting and ghosted lines. Even in the case of cross-ghosting, it is theoretically possible to apply some corrections, at least when the lines that cross-ghost are from ions for which an independent way of measuring their emission measure exists.

The drawbacks of this method are that it is time-consuming and that it relies on the accuracy of atomic physics and intensity calibration, that in some cases can have uncertainties of the same order as the ghosting. In any case, a complete reconstruction of the GIS spectra is not always possible. Note, on the other hand, that a blind exclusion of all the GIS lines possibly affected by a ghosting problem would leave only very few lines usable.

Table 3.3: *The coefficients for the GIS wavelength calibration, derived for two GSET_ID.*

	GSET_ID =42
GIS 1	151.23139, 0.031265225, 2.148844E-06, -7.9808423E-10, 2.0195808E-13
GIS 2	255.34898, 0.041980195, -2.6495787E-06, 1.3628225E-09, -5.8074565E-14
GIS 3	392.15063, 0.046712395, 7.634996E-07, -3.388151E-10, 2.2388279E-13
GIS 4	657.01778, 0.062105382, -6.019735E-06, 4.5349149E-09, -7.16958E-13
	GSET_ID =47
GIS 1	150.992, 0.0327321, -1.64271E-08, 3.75398E-10
GIS 2	256.491, 0.0412557, -1.44149E-06, 7.60522E-10
GIS 3	393.535, 0.0452287, 2.25383E-06, -3.88733E-10
GIS 4	657.343, 0.0599007, -1.78422E-06, 1.52401E-09

3.2.3 The wavelength calibration

The wavelength-to-pixel relation for the GIS spectra is a complex function, that depends on many factors. First, it depends on the slit used and on the LUT applied to convert the spiral pattern into a one-dimensional spectrum. Therefore, each GIS spectrum with a different GSET_ID number requires a different wavelength calibration. Also, the noise created by the electronics introduces distortions (*R. Bentley*, priv. comm.). Then, the wavelength calibration depends on the dispersion from the grating and the fact that the detectors are flat, and not curved, along the Rowland circle.

In the pre-flight calibration (*Bromage et al.*, 1996; *Lang et al.*, 1999) a quadratic relation for the wavelength calibration was assumed. Early in-flight spectra were fitted for different LUTs to obtain a revised set of quadratic wavelength calibrations (*B. Bromage*, priv. comm.) and these are available in the CDS software. This quadratic relation is sufficiently accurate for the central parts of the detectors, but is increasingly inaccurate toward the edges of all the detectors, reaching offsets of more than 1 Å, an unacceptably large value.

The above-mentioned complexity of the GIS wavelength calibration makes any attempt to describe it in terms of a polynomial very difficult. However, for simplicity in the data analysis, and since high accuracies are unattainable, given all the other complications in terms of line profiles, polynomial fits to various datasets have been made. Table 3.3 presents the coefficients that were found by the author, and that have been applied to the GIS observations presented in this thesis. These coefficients give reasonable accuracies (usually to better than one-half the resolution) over the whole detectors.

3.2.4 The intensity calibration

As for the NIS case, there are several factors which determine the conversion of the data to absolute units.

1. The absolute sensitivity $ef(\lambda)$ [counts/photons] as a function of wavelength, which is a combination of the efficiencies of the optics, grating, and detectors. As in the NIS case, intensity calibrations were obtained on the ground for a limited number of lines within each detector (see Figure 3.30). To refine this, and to determine post-launch changes, an in-flight calibration was required. More details can be found in Section 3.4.10.

2. The telescope aperture A_t [cm^2]. Contrary to the NIS case, there is no measurable variation with the scan mirror position (*Bromage et al.*, 1996). In any case, even if some dependence were present, it would be negligible, because the GIS rasters are in most cases very small (i.e. the scan mirror is moved only few times). An averaged value of 25.5 cm^2 is adopted.

3. The geometric area available at the slit, which depends on which slit is used.

4. The exposure time, which is measured accurately and only needs a small correction for dead times.

Software to calibrate the GIS spectra in intensity was written by the author.
Note, as in the NIS case, that unless stated otherwise: all the GIS spectra presented in this thesis are in 'corrected' counts, or counts/s; the spectral line intensities in the Figures are in phot s^{-1} cm^{-2} $arcsec^{-2}$; the intensities in the Tables are in ergs s^{-1} cm^{-2} sr^{-1}; the intensity ratio values, both in Tables and in Figures, are obtained from the intensities in ergs s^{-1} cm^{-2} sr^{-1}, and therefore, for clarity reasons, are indicated as 'ratio values (ergs)'. The errors in the intensities do not include all the systematic errors that can come from all the correction and calibration factors above-mentioned of which the main ones are: the error in the instrument sensitivities, discussed below; contaminations due to the ghosting problem.

3.3 The first-light GIS observations

Table 3.4 lists some of the main characteristics of the first-light observations that were analysed. Single spectra were extracted, averaging the total number of exposures in each observation. Figures 3.6, 3.7, 3.8 show the averaged spectra of these observations. Spectra are smoothed over 3 pixels, to reduce the fixed pattern. Note the large differences in the spectra (that are plotted on different scales), in terms of both absolute intensity and the relative intensities between lines emitted by different ions, which clearly indicates completely different temperature distributions.

Second order lines were found to be present in GIS 3 and GIS 4, and are particularly prominent in the active region spectrum. The spectra have been calibrated in wavelength and in intensity, and a multiple gaussian line fit (with a linear background) was performed using standard IRAF programs, to deduce line intensities.

Table 3.4: *The GIS first-light observations. The type of observed region, the CDS fits file name, the day of observation, the slit used, the number of exposures of the rasters (averaged), the exposure time, the GSET_ID number, and the type of observation are displayed.*

Region	file	day	slit	# exp.	t exp.	GSET_ID	type
Active (AR)	s110r00	28/02/96	2″x2″	50	10s	19	first light
Quiet Sun (QS)	s132r00	04/03/96	2″x2″	225	50s	22	spectral atlas
Coronal hole (CH)	s90r00	25/02/96	2″x2″	20	500s	16	first light

The ground-based calibration for GIS was used as a starting point, but some variations in the sensitivity of the GI detectors were expected to have occurred since launch, so it was important to check them, and to assess the values for the second order sensitivities.

The adopted sensitivities for the first order (second order) were: GIS 1: 1.4e-4 (1.4e-5); GIS 2: 2.4e-4 (2.4e-5); GIS 3: 3.4e-4 (2.7e-5); GIS 4: 0.5e-4 (1.e-5). These values were deduced comparing the intensities of density-insensitive lines emitted by the same ion and observed in different detectors. These results were preliminary. In particular, no wavelength-dependent effects were considered. To help with the complex identification of the lines, check the calibration and the contribution of the second order lines, a differential emission measure analysis was performed. The Arcetri inversion technique (*Monsignori Fossi and Landini*, 1991) and the CHIANTI (version 0.9) database were used in order to deduce the differential emission measure . The continuum (visible in the GIS 4) was calculated with the Arcetri code, with the *Feldman et al.* (1992b) abundances and a log N_e=9. Densities of the three spectra were estimated mainly using Fe XIII 203.83 Å / 202.04 Å, and the contribution functions were therefore calculated at the following constant pressures: $1 \cdot 10^{16}$ (AR);$2 \cdot 10^{15}$ (QS); $1 \cdot 10^{14}$ (CH).

Adjustments were made to the elemental abundances to obtain consistency among spectral lines from different elements. The photospheric (*Grevesse and Anders*, 1991) abundances were used to deduce the DEMs for the coronal hole and quiet sun observations, with the following element abundances varied (values are log differences from the starting values): C (+0.6), N(+0.3), O(+0.2), S(+0.5) for the quiet sun observation; C (+0.7), N(+0.3), O(+0.25), Ne(-0.05), S(+0.5) for the coronal hole observation. The coronal (*Feldman et al.*, 1992b) abundances were found more appropriate for the AR observation. The following element abundances were varied (values are log differences from the starting

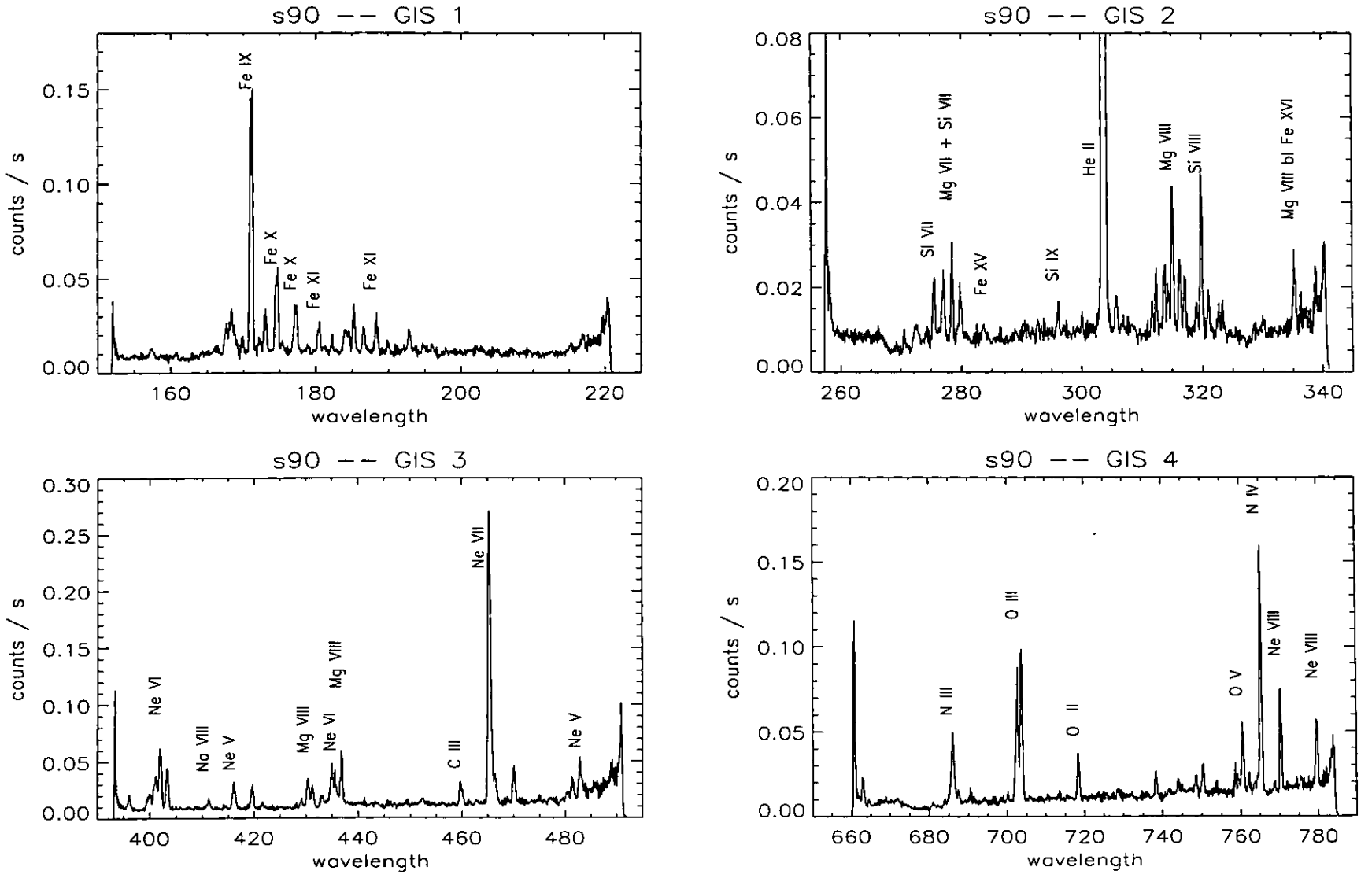

Figure 3.6: *The first light GIS spectra of a coronal hole (s90)*

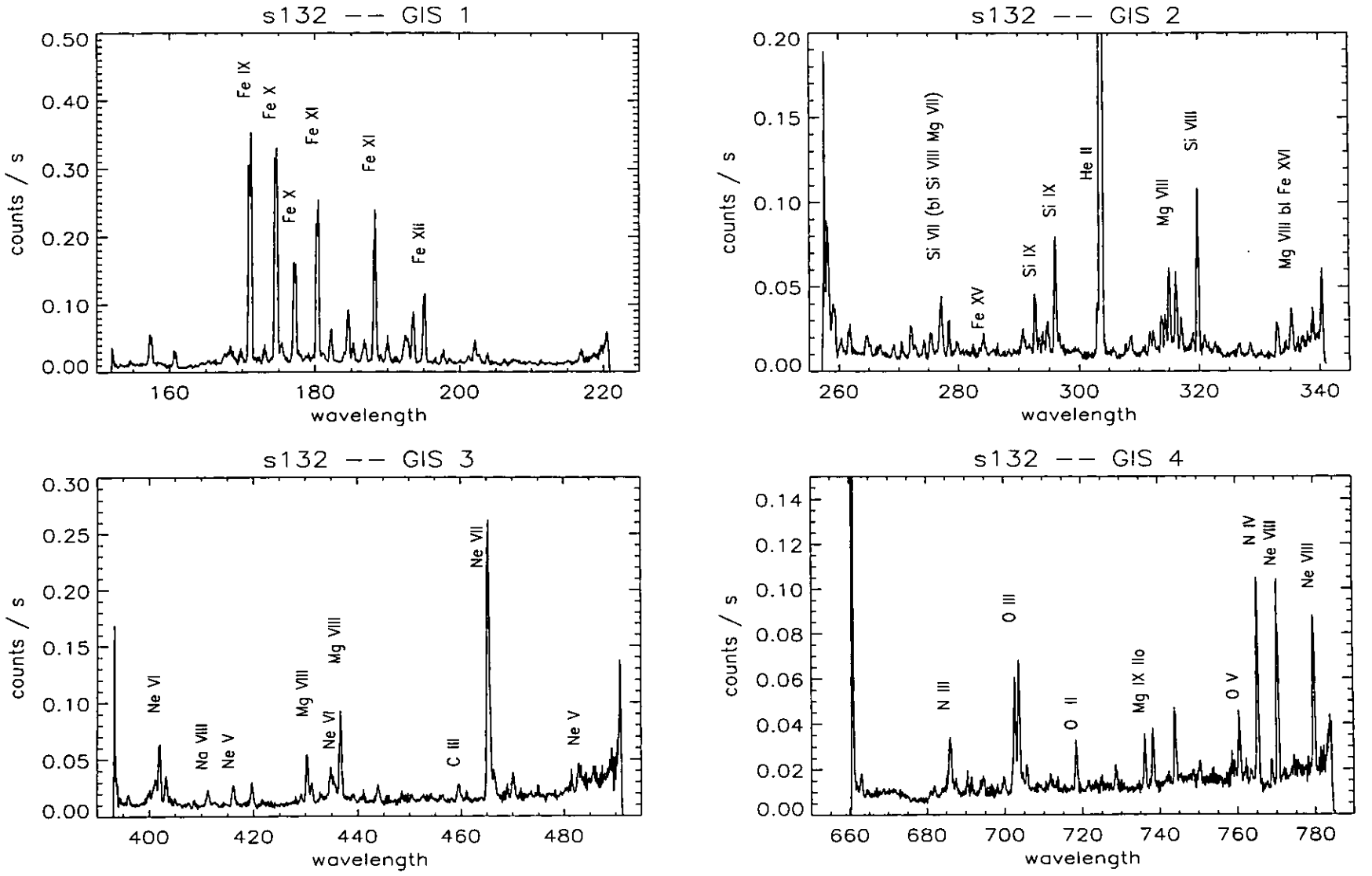

Figure 3.7: *One of the first series of GIS spectra of a quiet sun (s132) region.*

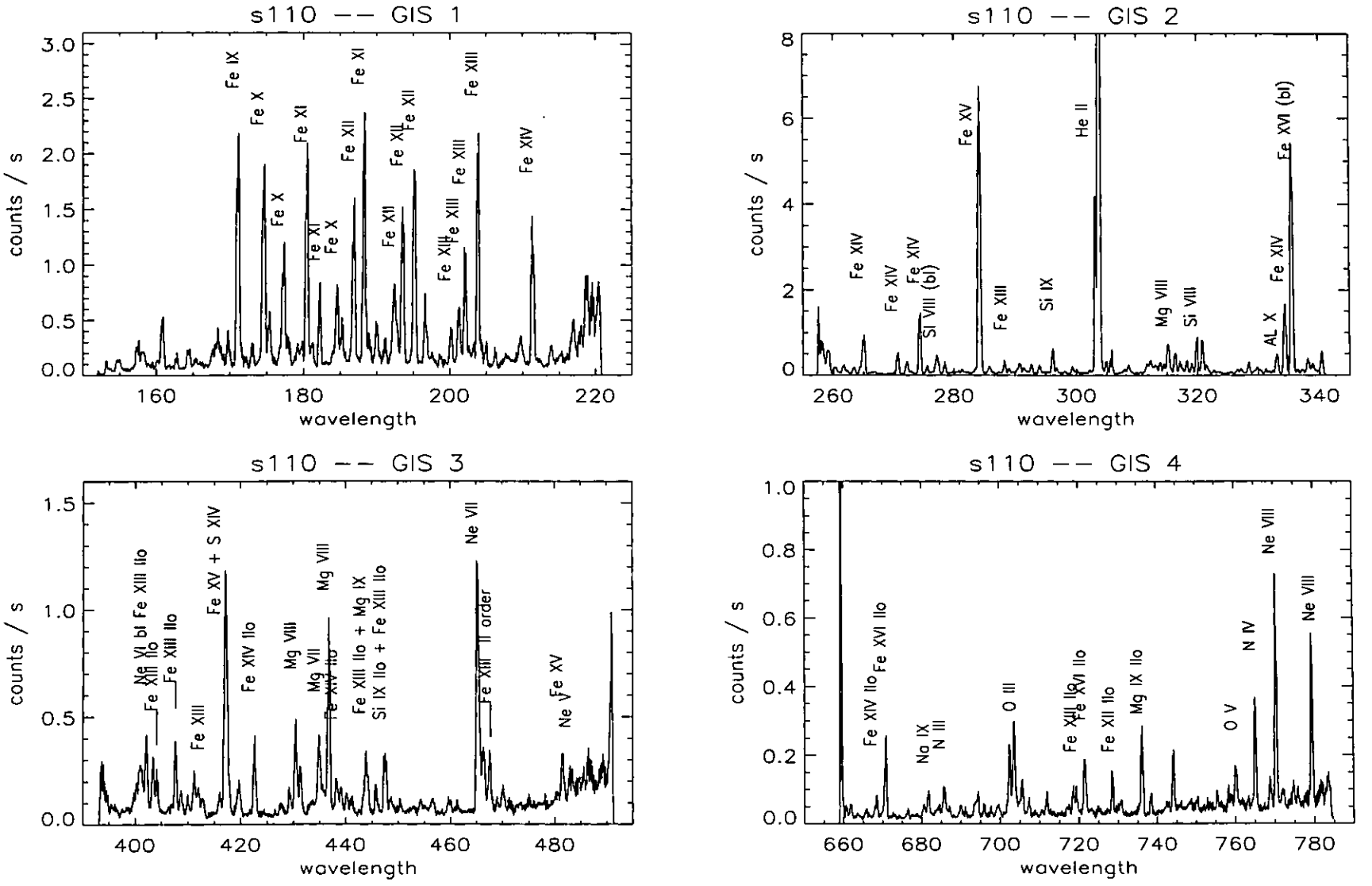

Figure 3.8: *The first light GIS spectra of an active region (s110).*

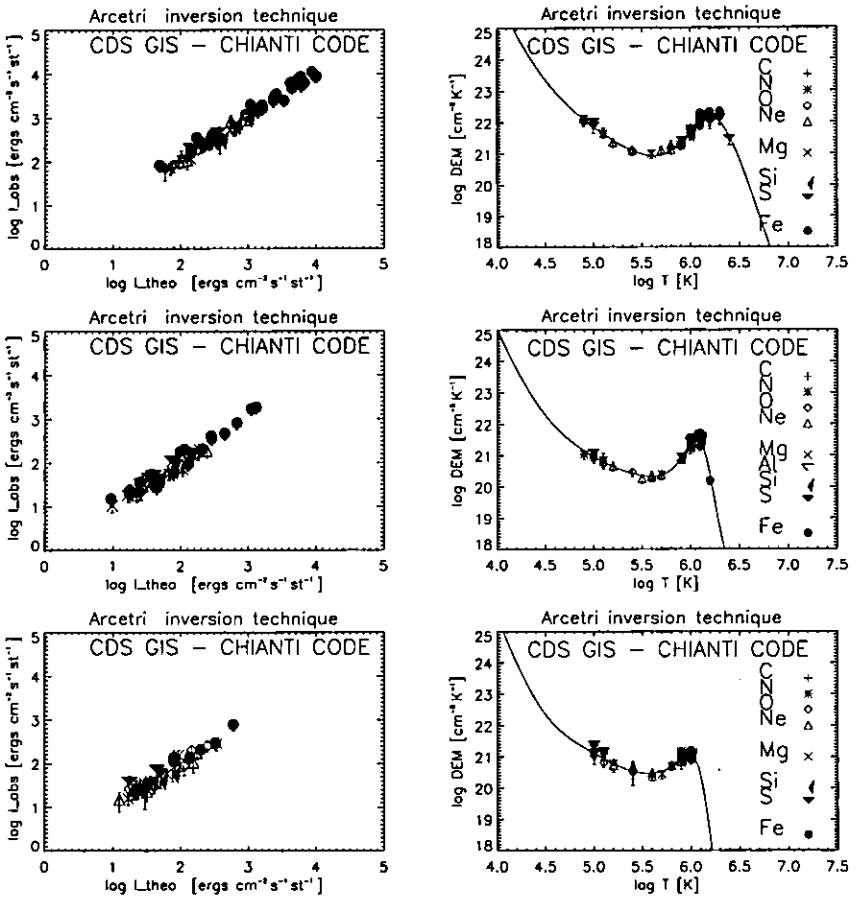

Figure 3.9: *The derived DEMs (right hand plots) and comparison of observed ($LogI_{obs}$) and theoretical ($LogI_{theo}$) intensities (left hand plots) for an active region, the quiet Sun and a coronal hole. (top to bottom).*

values): C (+0.6),N(+0.1),S(+0.1).

The DEM analysis shown in Figure 3.9 confirms a difference between the elemental abundances of different regions. The low temperature region (Log T $\sim$ 4.5) is constrained by the continuum, which is seen at longer wavelengths. The high temperature region (Log T $\sim$ 6.5 - 7) is constrained by the absence of high temperature lines. The highest temperature lines used (from Fe XV, Fe XVI and S XIV), were visible in the quiet Sun and active region spectrum, and were used to determine the drop in the DEM at high temperatures. We note that the DEM falls rapidly in the coronal hole spectrum. This is constrained by the lack of any Fe XIII lines - in particular the lines at 202Å and 203.8Å and any other higher Fe ionization stages.

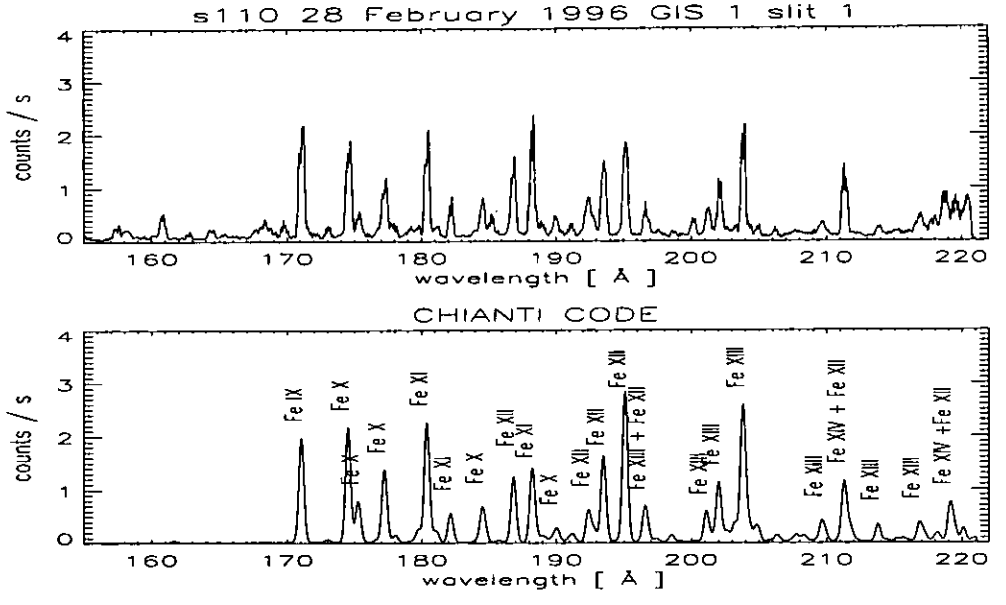

Figure 3.10: *The observed (top) and synthetic (bottom) GIS 1 spectra of the active region observation.*

With the adopted DEM distributions and calibration values, most of the spectral lines have a 30-40% agreement between the theoretical and observed intensities (see the left hand plots of Figure 3.9). Synthetic spectra of the three regions were then created, including the second order lines and the continuum. In Figure 3.10 and Figure 3.11 we show as examples, comparisons of the observed and synthetic spectrum for the active region spectrum for the GIS 1 and GIS 3 wavelength bands. The GIS 1 wavelength band is dominated by a sequence of iron lines from Fe IX - Fe XIV. These are well reproduced by the CHIANTI synthetic spectra. The GIS 3 spectrum is also well represented, with many second order lines, some of which are blended with first order lines.

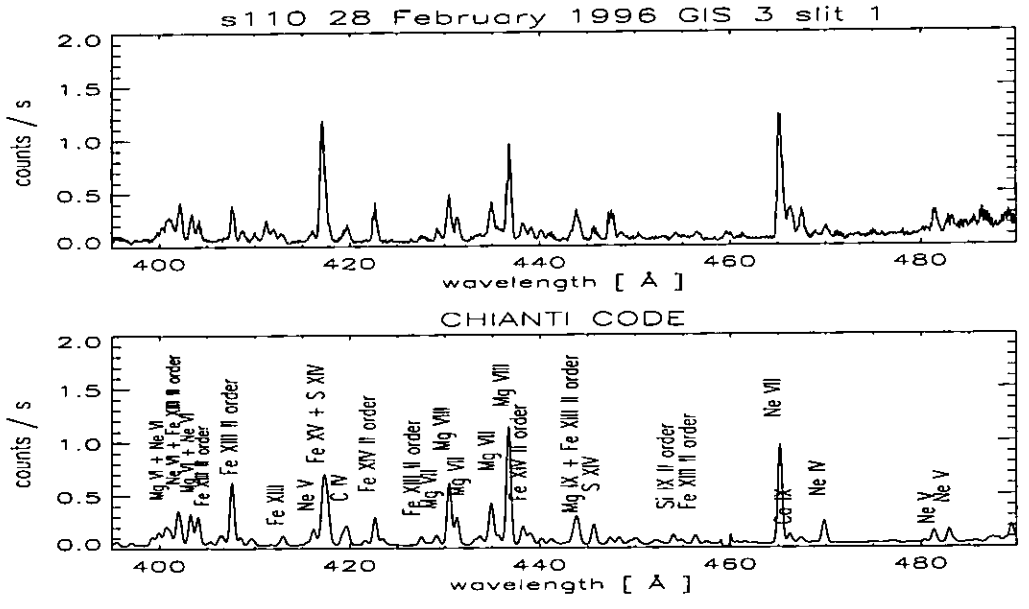

Figure 3.11: *The observed (top) and synthetic (bottom) GIS 3 spectra of the active region observation.*

3.4 The calibration of the CDS instrument

Intensity calibration is a fundamental requirement for any scientific use of spectral data, but obtaining such information is not an easy undertaking in the extreme ultraviolet spectral range. A history of the CDS calibration is now summarised, to clarify this important issue.

- A pre-flight calibration was performed (*Bromage et al.*, 1996), producing an absolute calibration for both NIS and GIS. However, these measurements did not provide the full relative sensitivity function along each NIS and GIS detector. It provided an initial measure of the mean sensitivity of each detector and a basis for absolute calibration of the instrument.

- The *Bromage et al.* (1996) values, together with a theoretically derived wavelength dependence and a preliminary correction (based on in-flight measurements), produced the sensitivities stored for public use in the CDS data analysis software until December 1998. This NIS calibration will be referred as the the *NIS first standard calibration.* It is shown in detail in Figures 3.28, 3.29, and discussed in Sections 3.4.8 and 3.4.9, below.

- The NIS first standard calibration was found to require corrections by various authors (see, e.g., *Landi et al.*, 1997a), the main one being the need to increase the NIS 1 sensitivity, relative to NIS 2, by some factor. *Landi et al.* (1997a) proposed a factor between 2.5 and 5. Note that such *large uncertainty* in the NIS 1/NIS 2 calibration significantly affects the determination of the FIP effect (because the diagnostic lines are observed by different detectors). It can also affect emission measure (or DEM) analysis, since almost all low-temperature lines are seen in NIS 2, while most of the high-temperature lines are observed only in NIS 1.

- An in-flight cross-calibration between the NIS and a rocket flight launched in May 1997 has recently been presented by *Brekke et al.* (1999). This study has produced *absolute* values of the NIS sensitivities, for both NIS 1 and NIS 2. For NIS 2, it was possible to estimate a coarse wavelength-dependence (which turned out to be different from the predicted pre-flight one, see Figure 3.29 in Section 3.4.9 below). For NIS 1, only one reliable measurement at one wavelength was possible (see Section 3.4.8 below for a discussion).

- A revised pre-flight calibration for both GIS and NIS has recently been presented (*Lang et al.*, 1999). This revised pre-flight calibration (see Figures 3.28, 3.29, for NIS and Figure 3.30 for the GIS values, and discussion below) suggests a different

NIS calibration, both in *absolute* and relative (between NIS 1 and NIS 2) terms. The revised value of the absolute sensitivity at 584 Å(NIS 2) is in agreement with the in-flight value of *Brekke et al.* (1999). The other values are not.

- A *NIS second standard* calibration, based on the results of *Brekke et al.* (1999) and *Lang et al.* (1999) was proposed in December 1998 and implemented in the CDS data analysis software. It is also shown in Figures 3.28, 3.29, and discussed below.

- No measurements (except for a pre-flight one) of the second order NIS 2 sensitivities were available. It will be shown here how many second order lines are seen in NIS 2.

- No measurements of the GIS second order sensitivities were available. Most of the observed lines in GIS 2 and GIS 3 are either second order lines or blends with second order lines.

- No GIS standard calibration was provided in the CDS data analysis software (until recently).

It should be noted that the uncertainties in the pre-flight calibration ($\sim$ 15%) and in the cross-calibration work of *Brekke et al.* (1999) [$\sim$ 15-25%] are relatively large, and moreover only limited wavelength dependence has been sufficiently measured for the NIS 1 channel, which is most important in terms of diagnostics. Also, the ground calibration may not be directly applicable to the in-flight observations, for many reasons:

- The pre-flight calibration was based on spectra taken on the ground nearly two years before launch (in March 1994). A comparison with the CDS spectra taken in-flight shows that the CDS instrument has suffered many changes, probably during launch, that have already been mentioned. The main ones are lower resolution for both NIS and GIS, and a large scattered light contribution in the NIS 1 channel.

- The detectors on the ground were illuminated by a narrow-beam calibration source, while in-flight they are fully-illuminated by the Sun.

- Because of the presence of MCPs in both the NIS and GIS detectors, a decrease in their sensitivity was expected, due to the exposure to solar radiation, in particular during the first few months of operations (which in fact has been observed).

- The same exposure to solar radiation, produces effects that change the detectors' characteristics with time, known as the long-term gain depression (i.e. the burn-in in the bright NIS lines).

- Other important variations in time are related to a decreased reflectivity of the telescope's mirrors, the scan mirror and the gratings, which can be due to deposits on the various surfaces and can cause decreased sensitivities for all the CDS detectors. Such effects have become even more evident in the recent CDS spectra, after the dramatic SOHO loss of contact in 1999.

From all the above, it is clear that *an in-flight calibration of all the CDS detectors was necessary*, and in the absence of any on-board equipment, the only possibility was to use the solar emission as the calibration source (which causes a lot of problems, as described in Section 3.4.6). The aim of the work presented here was to find a relative calibration that could represent most of the brightest lines observed in all the CDS detectors within a 20-30% accuracy.

The CDS *absolute* intensity calibration is not the main concern here, since a change in the absolute intensity calibration would merely have the effect of changing the scaling of quantities such as the DEM values. What is important is to find the *relative* intensity calibration, i.e. the intensity calibration as a function of wavelength for the various channels. In fact, most of the diagnostic lines fall at different wavelengths and a different calibration has the effect of changing absolute values of densities, temperatures and element abundances.

In all the following work it will be assumed that all the above-mentioned factors that contribute to the intensity calibration of both NIS and GIS are correct and do not vary in time (a reasonable assumption), while all the relative values of the sensitivities will be allowed to vary and deduced from in-flight observations. An absolute reference point for the sensitivity was chosen at the He I 584 Å line $ef = 4.75\text{x}10^{-4}$ *[counts/photon], in accordance with the* Lang *et al. (1999) and* Brekke *et al. (1999) values. All the other values of the sensitivities, for both the NIS and GIS channels, and for the first and second order, have been obtained relative to that point, using the diagnostic method. The results are shown in Figure 3.30. These calibration values are used throughout this thesis, unless explicitly stated otherwise.*

3.4.1 The diagnostic method for the CDS calibration

The diagnostic method

The best way to find the relative intensity calibration (and any changes with time), is to compare the observed intensities (taken at different times) with theoretical values, for those groups of lines whose ratios are expected to be independent of the observed source. The

calibration is adjusted in order to obtain agreement between the observed and theoretical intensities.

First, ratios of lines emitted by the same ion are examined. The results are therefore independent of the element abundance *and* the thermal distribution along the line of sight of the source (i.e. the DEM values). The first ratios to examine are branching ratios (i.e. ratios of lines that share a common upper level), that are equal to the ratios of the radiative transition probabilities, which are well known. Then, ratios of density-insensitive lines are also used. For each ion, in fact, there are groups of transitions, usually originating from the same upper level, that have nearly the same density dependence so that any ratio formed from these lines is density-independent.

The procedure is then applied to all the other observed lines, examining ion by ion, to obtain a relative calibration over the entire wavelength range. When agreement is found between the results obtained by the use of many lines of different ions, one can be sure that the calibration is correct. In order to make full use of this diagnostic method for calibration purposes, given the uncertainties in the atomic data and the observed intensities, it is essential to use as many lines emitted by the same ion as possible.

This method is not new, and has already been applied a few times in the past. For example, *Neupert and Kastner* (1983) apply this method for an in-flight calibration of the OSO V and OSO VII EUV spectrometers, in the 150-400 Å range. Recently, this method was successfully applied (*Brosius et al.*, 1998b) to calibrate the Solar EUV Rocket Telescope and Spectrometer observations in 1995 (SERTS-95), using averaged active region and quiet sun spectra, and CHIANTI (version 1.01, except for Fe XIV). SERTS-95, compared to the previous SERTS flights, had an enhanced second order sensitivity and recorded high-resolution (0.03 Å) spectra in the 171-225 Å range in second order and in the 235-335 Å range in first order.

Applicability of the method

A large effort was spent for this thesis on calibration issues, analysing and planning new CDS observations in order to apply the calibration method. This was needed since the coronal hole spectra are not suitable for calibration purposes, because of the low signal. There is no space here to describe all of them, and only examples will be given. Table C.1 presents a list of some of the observations designed by the author, together with B. Bromage, for calibration purposes.

Many NIS and GIS observations of different solar regions have been analysed, and the calibration method applied. These are the main reasons:

- the need to observationally assess the blending of the lines, for all the CDS channels. In fact, as it will become clear, many 'calibration' lines are blended with other lines, and only by observing completely different regions, can the contributions from the blending lines be ruled out, without having to rely on theoretical predictions to remove the intensity of the blending line. For example, the bright 610 Å line is a strong blend of Mg X and O IV transitions, and only in off-limb observations does the O IV contribution become negligible. Many of these cases are present in the NIS spectra, and will be described in detail.

- The need to independently assess ghosting in the GIS spectra. For example, a ghost will disappear if the parent line does, as low-temperature lines do in off-limb observations. In other cases it is difficult to assess the presence of a ghost because it contaminates a line, and it is only when this line is not emitted by the observed solar region (again a cool line in off-limb observations, for example), that the observed 'line' can be identified as a 'pure ghost'. Examples of all these cases will be given.

- The need to assess the importance of the 'background' intensity in the NIS and GIS spectra. As mentioned, in the NIS spectra this component is mainly due to scattered light and disappears in off-limb observations. In GIS spectra, the main background component is due to true He and H continua, which also disappear off-limb.

3.4.2 Layout of the rest of Section 3.4

In order to help with the complexity of line identification, test the latest atomic data available, and to find which 'calibration' lines are suitable for the CDS calibration, a complete *DEM* analysis has been performed on the SERTS-89 observation (*Thomas and Neupert*, 1994). This is presented in Section 3.4.3.

Many GIS observations have been analysed to study the GIS peculiar characteristics. Only some examples will be given in this thesis. A GIS detailed study of two different observations was performed, to give a preliminary assessment of the ghosts and to check the pre-flight relative intensity calibration of the GIS channels. This work contributed to the published work of *Landi et al.* (1999a), and is briefly described in Section 3.4.4. In the same Section, a revision of that work (using more recent atomic data) is also presented.

Many NIS observations, on disc and off-limb, were analysed, for the internal calibration of the NIS detectors alone. They are described in Section 3.4.5.

One of the main outcomes of the above-mentioned analyses has been the realisation that for both NIS and GIS instruments only a few reliable (i.e. not blended, not affected by

instrumental effects or atomic physics problems) calibration lines emitted by the same ion are observed in each detector. Actually, only for a few detectors is it possible to produce at least two values of the sensitivity. This strongly limits the application of the diagnostic method for calibration purposes. *The potential of the diagnostic method is therefore achieved only when all the NIS and GIS detectors are calibrated at the same time, with the use of the full CDS wavelength range.*

In a detailed survey, all the available CDS observations, including those that were made for the purpose of calibrating the CDS against other instruments (including rocket flights), were found to be unsuitable for a proper application of the diagnostic method, and hence for a cross-calibration of the CDS detectors. This was for many different reasons (e.g. low S/N, paucity of extracted NIS lines, temporal variability of the solar region observed, lack of sufficient spatial overlapping region between the NIS and the GIS rasters, due to solar rotation).

Since NIS and GIS detectors do not observe simultaneously, special NIS-GIS observing sequences were therefore carefully planned, executed and analysed by the author and B. Bromage. These are described in Section 3.4.6. Most of these observations were performed at the solar limb. Section 3.4.6 also presents some examples of the analysis that was done to assess any time variability of the relative CDS calibration during 1997. The constancy in time and space of the ratios of the lines selected for calibration is also illustrated with some typical examples. These NIS-GIS sequences were used for both internal NIS and GIS calibration, and in particular for the cross-calibration of all the CDS detectors. Some results are already presented in Section 3.4.6.

Among all the NIS-GIS observations analysed, two have been selected as examples for the following Sections, to be used not only for calibration purposes but also to present for the first time typical NIS and GIS near-simultaneous spectra of the quiet sun. They are an on-disc (October 16 1997) and an off-limb (May 4 1997) observation, extracted from two series of NIS-GIS observations at the solar limb.

Although most of the calibration lines used here have only a minor dependence on density and temperature, some sensitivity is still present, and is therefore important to calculate the contribution functions of these lines at the correct density (or pressure). The values of densities and temperatures of the two regions selected as examples are presented in Section 3.4.7, where it is also shown that the use of a different calibration does not significantly affect the derived values.

Specific software was written by the author in order to apply this calibration method to CDS observations. This method, given the complexity of having 9 different wavelength

regions (including the second order, and with only a few pre-flight measurements for some of them) to cross-calibrate at the same time, has been applied in stages, taking into account many different observations.

There is no space here to describe all the various steps in great detail. However, a description of how the method has been applied to assess the NIS 1 internal calibration (Section 3.4.8) and then the NIS 2 first order internal calibration (Section 3.4.9) is presented. These internal calibrations are completely independent.

Then, all the NIS and GIS channels, including the second orders, have been calibrated against each other, using the diagnostic calibration method. Some of the lines used for this cross-calibration are described in detail in Section 3.4.10, where the final results are presented and compared with the other calibration studies.

Finally, the *DEM* analyses of the two example observations are presented, and used to illustrate a series of points. First, the off-limb *DEM* analysis is presented in Section 3.4.11. The relatively simple plasma structure (almost isothermal) of this observation allowed discrepancies between lines emitted by different ions to be highlighted. This is used for a double purpose. First, it shows that the most up-to-date second NIS standard calibration fails to represent some of the observed lines well, and at the same time confirms the calibration presented here. Secondly, it shows how different ionization equilibrium calculations affect the calculated intensity of the lines. The full line lists and identification of the lines is then presented. This also confirms that the calibration presented here explains most of the observed emission. The *DEM* analysis of the on-disc observation of October 16 1997 is finally presented in Section 3.4.12, together with a full line list of the identified lines.

3.4.3 The SERTS-89 spectrum

The active region SERTS-89 observation (*Thomas and Neupert*, 1994) has represented a landmark in EUV solar spectroscopy for several years. Unfortunately, *Thomas and Neupert* (1994) presented line identifications based only on the positions of the lines, and misidentified some of them. *Del Zanna et al.* (1996) produced a differential emission measure analysis using some ions of different elements. *Brickhouse et al.* (1995) also presented a differential emission measure analysis, but based only on the Fe ions, while *Young et al.* (1998) have recently corrected and introduced new line intensities and identifications, comparing observed and theoretical line ratios, ion by ion. *Dwivedi et al.* (1998) have presented a list of diagnostic lines, based on the SERTS-89 spectrum.

Since most of the lines present in the SERTS-89 list are also visible in the CDS spectrum,

the SERTS-89 observation, with its high spectral resolution and quality, has been used here to help the identification and blending of some of the CDS lines, and to assess the quality of the atomic data used subsequently to calibrate the CDS instrument.

The calibrated intensities of *Thomas and Neupert* (1994), plus those of *Young et al.* (1998) have been used together with CHIANTI v.2 (including the recent Fe XIV calculations by *Storey et al.*, 1999). A *DEM* analysis was performed on all these lines, and a full line list of this spectrum, with identifications based on a *DEM* method, is presented here for the first time. The contribution functions have been calculated at constant $N_e = 2\text{x}10^9$ cm^{-3}, using the *Arnaud and Rothenflug* (1985) ionization equilibrium (for all the ions) and photospheric abundances (*Grevesse and Anders*, 1991), except for the following elements (with logarithmic differences from the photospheric values indicated in parentheses): Na (+0.3), Al (+0.3), S (-0.4). It is to be noted that a need for an increase in the Al abundance, relative to the other low-FIP elements, was also found by *Falconer et al.* (1997).

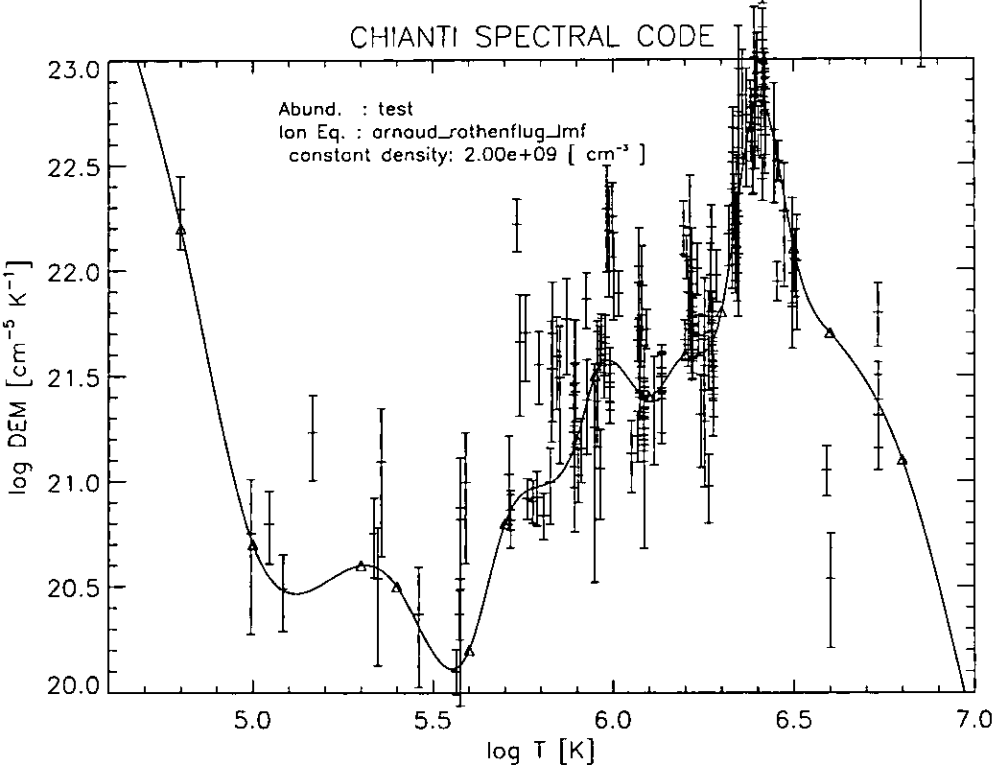

Figure 3.12: *The derived DEM for the SERTS-89 active region spectrum.*

Figure 3.12 shows the derived *DEM* which is well constrained at high temperatures. Table A.1 presents the results for all the lines that have been identified, ordered in temperature. In most cases, agreement with the corrections and new identifications presented by *Young et al.* (1998) was found. However, some new identifications, or corrections to inaccurate ones (even at the high resolution of SERTS, blending is still present in some

cases) are presented in Table A.1. The fact that the majority of the lines, including Fe XIV, are well reproduced (within 10%) confirms the high quality of the atomic data. The new Fe XIV calculations evidently solve a long-standing problem with the Fe XIV lines (see e.g. *Young et al.*, 1998 and references therein).

Many lines are not so well reproduced, but this can be simply explained in some cases. For example, when lines are density-dependent. In fact, a single averaged density fails to reproduce all the density-sensitive lines, as already shown by all the previous studies of this spectrum. Furthermore, no particular trend, as a decrease with the temperature of formation of the ions, can be found. Another example is for the lines that were seen in second order, where the calibration was more uncertain. *Young et al.* (1998) propose a correction (up to a factor of 2) in the calibration at wavelengths above 400 Å. The analysis presented here confirms a need for a correction, but at longer wavelengths, above 430 Å, as constrained by Mg VIII, Mg VII, Ne VI lines. It should be noted that if the correction proposed by *Young et al.* (1998) is applied, then all the Mg IX lines around 440 Å would no longer be in agreement with the bright Mg IX 368 Å line. The lines of C IV and Ar XVI are underestimated and overestimated by large factors, a confirmation of the problem with the Li-like ions, introduced in Chapter 2.

Other groups of lines are in disagreement as a whole, as is the case of the Mg V lines, which are in agreement among themselves, but not with all the other lines. This disagreement can not be due to an element abundance problem, since the the other Mg lines are well represented. For example, the Mg VI lines are in excellent agreement with the Ne VI lines, confirming that for that active region spectrum there was no FIP effect. Finally, many other single lines are not well represented, and for which a change in the smooth calibration adopted by *Thomas and Neupert* (1994), or variations of element abundance with height, or a different atomic physics, would be required.

Some of the peculiar characteristics found from the analysis, can be ascribed to the complexity and inhomogeneity of the large region where the average spectrum was obtained. It is therefore important to keep in mind that for calibration purposes it is best to observe a simple region, possibly having uniform characteristics, such as temperature and density.

3.4.4 A GIS internal intensity calibration study

GIS spectra of an active region and of a region of quiet sun were analysed, in order to apply a new *L-function* diagnostic technique, already used for a preliminary NIS calibration *Landi et al.* (1997a). This plasma diagnostic technique has been used to check the pre-flight relative intensity calibration of the four GIS windows. The analysis of the obser-

vations was also used to assess the in-flight characteristics of the GIS detectors. This work was done in collaboration with E. Landi, and has led to the *Landi et al.* (1999a) paper, where details can be found. Here, only a brief description of the analysis is given. This work led to the selection of a number of lines which were found not to be significantly affected by ghosting, and so could and so can be reliably used for plasma diagnostics with GIS in further studies.

The active region spectrum has been re-analysed for this thesis, by the author, using new atomic data and different ionization equilibrium calculations. This re-analysis is described below, since this spectrum was also used to assess the GIS new calibration presented below.

The GIS study presented in *Landi et al.* (1999a)

The Arcetri Spectral Code (*Landi and Landini*, 1998a) was used for this data analysis. The ionization equilibrium of *Arnaud and Raymond* (1992)has been adopted for the iron ions, while the *Arnaud and Rothenflug* (1985) data were used for the other elements and those of *Landini and Monsignori Fossi* (1991) for the minor elements.

Two full spectral GIS atlases were analyzed, one emitted by a solar active region (AR), and the other in quiet sun (QS) conditions. Both of them were obtained by rastering over a 30″x30″area on the solar disk with 15 mirror positions and 15 slit positions using the 2″x2″slit. For each of the resulting 225 exposures of both sets of spectra the exposure time was 50s. The quiet sun observation was obtained between 18:26 UT and 21:38 UT on September 2nd 1996. The corresponding data file for this observation is s4552, and its GSET_ID number is 41. The active region spectrum was taken after the quiet sun observation, starting at 22:42 UT and ending at 01:54 UT on September 3rd 1996. Its GSET_ID is 47. The data file for the active region observation is s4554. It is important to keep in mind that the spectra analysed had GSET_ID=41 and 47 and therefore the ghosting analysis that allowed a selection of usable lines to be made can in principle only be applied to other observations having the same GSET_IDs. The two spectra were taken on the same day in order to eliminate any possible long term time variation of the GIS intensity calibration between one observation and the other, so that the results obtained from the two spectra could be directly compared.

Spatially averaged spectra were formed, in order to increase the signal to noise ratio. Monochromatic images of the rastered areas on the Sun were obtained by summing up the pixel intensities of the brightest lines. These were examined for inhomogeneity in the emitting regions, before spatially averaging the spectra. This is necessary because, as noted by *Landi et al.* (1997a), the L-functions will cross each other only if the emitting plasma

is homogeneous. If there are inhomogeneities it is possible that some departures of the L-functions from the expected behavior may occur due to lines emitted in different solar conditions, making it more difficult to determine possible intensity calibration problems.

The emission appeared fairly uniform over the QS region, and there was no evidence of significant inhomogeneities, while the AR images showed large variations in the intensity in the hottest lines, revealing a very complex morphology, the structure varying with temperature. A map of the intensity ratio of two Fe XIII strongly density-sensitive lines 202.0 Å / 203.8 Å also indicated considerable variations in electron density. As a result, only an area with a restricted range of density values (Fe XIII ratio values between 1.2 and 1.4) was used to form an average AR spectrum. This selected region broadly covered the hottest part of the total emitting area, and had an averaged electron density $\simeq 10^{9.4}\ cm^{-3}$.

This preliminary study of the spectra was done assuming constant sensitivities for each channel, and with values equal to the averaged values of the pre-flight (*Bromage et al.*, 1996) calibration. Only few lines were de-ghosted. In the GIS spectra there are only a few ions whose lines are observed in more than one window and which can be used for calibration purposes: Mg VII; Mg VIII; Mg IX; Fe X; Fe XII; Fe XIII; Fe XV. These lines have been used for checking the relative intensity calibration of the GIS instrument. No evident indications for a modification of the pre-flight intensity calibration (*Bromage et al.*, 1996) were found. More details of the results can be found in *Landi et al.* (1999a).

The revision of the active region spectrum

The study of the active region spectrum has been revised, using: 1) new atomic data (CHIANTI v.2 plus recent Fe XIV calculations, *Storey et al.*, 1999); 2) the *Arnaud and Rothenflug* (1985) ionization equilibrium for all the ions, except the minor elements for which *Landini and Monsignori Fossi* (1991) was used; 3)a constant density $N_e = 2\text{x}10^9$ cm^{-3}; 4) coronal abundances (*Feldman et al.*, 1992b).

These data have been used for calibration purposes because many bright high-temperature lines are observed. These lines have been used to constrain part of the GIS 3 and GIS 4 second order calibration, presented below in Figure 3.30. Furthermore, a *DEM* analysis has been performed on the calibrated data, and synthetic spectra created and compared to the observations, to show how well this calibration reproduces the observed lines.

The *DEM* is shown in Figure 3.13. Figures 3.14 and 3.15 show the averaged spectra. The main lines, the main ghosts, and those high-temperature lines that are otherwise not visible in the quiet sun and coronal hole spectra (that are presented elsewhere in this thesis), are labelled.

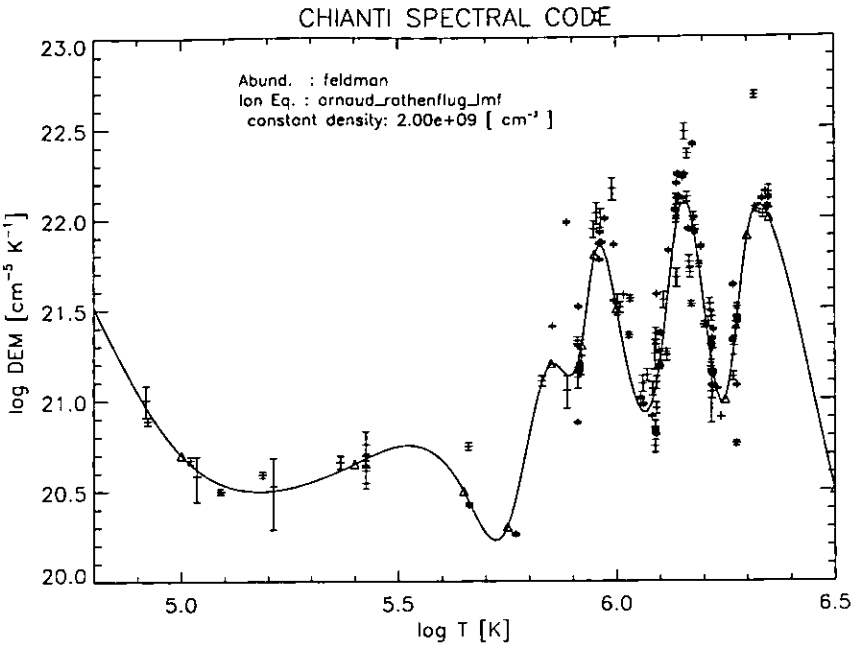

Figure 3.13: *The derived DEM for the active region spectrum of September 2nd 1996. Note the high-temperature peak.*

Table 3.5 presents the results for a selected group of lines, mainly high-temperature lines, and those used for the calibration, with in addition some particular ones. Some of the lines have been reconstructed, i.e. the ghost intensity added to them, while others still have partial, unremovable ghosting. Note:

- The observed lines are well represented, including most of the Fe XIV ones (without the new Fe XIV calculations of *Storey et al.*, 1999, discrepancies of factors of 2 or more are found).
- The second order lines are also well represented. Some of the second order lines are seen also in first order, allowing a direct check of the second order sensitivity.
- The Li-like lines of Na IX and Ne VIII are about a factor of 2 weaker than predicted by theory, while the S XIV lines (445.7 Å) are about a factor of 7 weaker, another example of the problems with the Li-like ions.
- The Fe XV 417.26 Å line is much brighter than expected, especially taking into account the fact that this line, at the moderate GIS resolution, is blended with a S XIV 417.66 Å line that is probably overestimated by a factor of 7. The problem with the Fe XV 417.26 Å again is a well known one (see e.g. *Young et al.*, 1998).

Figures 3.14 and 3.15 also contain synthetic spectra that have been produced (with software written by the author) taking into account the derived DEM, the abundances, and

the first and second order calibration (Figure 3.30). The synthetic profiles have been produced by convolution with assumed gaussian profiles of constant width across each channel, and therefore are not exactly comparable with the observed profiles, because of the peculiar GIS line profile characteristics. However, these comparisons give a direct and visible idea of the quality of the adopted assumptions and the completeness of the CHIANTI atomic database. Such comparisons are very rarely found in the literature, where instead results are presented only for a selected group of lines.

Visual inspection of Figures 3.14 and 3.15 shows many interesting aspects: the edge effects; the continuum emission in GIS 3 and GIS 4 (which is not reproduced in the synthetic spectra); the ghosts of the brightest lines; the complexity of GIS 3 and GIS 4 spectra, where ghosts, ghosting lines, first order and second order lines all contribute significantly.

Table 3.5: *Line List for the active region spectrum of September 2nd 1996.*

Ion	λ_{th} (Å)	λ_{ob} (Å)	Transition	I_{ob}	I_{th}/I_{ob}	+/-	Det	log T_{eff}	log T_{max}	frac	
Fe XII	192.393	192.4	3s2.3p3 $^4S_{3/2}$ - 3s2.3p2(3p).3d $^4P_{1/2}$	1359.9	0.84	0.08	G 1	6.18	6.16		
Fe XII	193.521	193.5	3s2.3p3 $^4S_{3/2}$ - 3s2.3p2(3p).3d $^4P_{3/2}$	3752.5	0.86	0.09	G 1	6.18	6.16		
Fe XII	195.118	195.1	3s2.3p3 $^4S_{3/2}$ - 3s2.3p2(3p).3d $^4P_{5/2}$	5495.5	0.98	0.10	G 1	6.18	6.16		
Fe XII	196.648	196.6	3s2.3p3 $^2D_{5/2}$ - 3s2.3p2(1d).3d $^2D_{5/2}$	1093.8	0.63	0.06	G 1	6.19	6.16	0.59	[1]
Fe XIII	196.54		3s2 3p2 $^1D_2$ - 3s2 3p 3d $^1F_3$						6.21	0.40	
Fe XIII	200.022	200.1	3s2 3p2 $^3P_1$ - 3s2 3p 3d $^3D_2$	870.4	0.73	0.07	G 1	6.22	6.21		
Fe XIII	201.128	201.2	3s2 3p2 $^3P_1$ - 3s2 3p 3d $^3D_1$	1527.8	0.57	0.06	G 1	6.22	6.21		
Fe XIII	202.044	202.1	3s2 3p2 $^3P_0$ - 3s2 3p 3d $^3P_1$	3042.6	1.03	0.10	G 1	6.22	6.21		
Fe XI	202.706	202.7	3s2.3p4 $^1D_2$ - 3s2.3p3(2d*).3d $^1P_1$	350.0	0.94	0.10	G 1	6.14	6.11		
Fe XIII	203.828	203.8	3s2 3p2 $^3P_2$ - 3s2 3p 3d $^3D_3$	4081.2	0.80	0.08	G 1	6.22	6.21	0.75	
Fe XIII	203.797		3s2 3p2 $^3P_2$ - 3s2 3p 3d $^3D_2$						6.21	0.25	
Fe XIII	204.263	204.3	3s2 3p2 $^3P_1$ - 3s2 3p 3d $^1D_2$	337.3	1.11	0.12	G 1	6.22	6.21		
Fe XII	206.371	206.1	3s2.3p3 $^2D_{3/2}$ - 3s2.3p2(1s).3d $^2D_{3/2}$	253.4	0.90	0.10	G 1	6.18	6.16		
Fe XIII	209.919	209.6	3s2 3p2 $^3P_2$ - 3s2 3p 3d $^3P_1$	777.2	1.24	0.13	G 1	6.22	6.21	0.55	
Fe XIII	209.621		3s2 3p2 $^3P_1$ - 3s2 3p 3d $^3P_2$						6.21	0.45	
Fe XIV	211.32	211.3	3s2 3p $^2P_{1/2}$ - 3s2 3d $^2D_{3/2}$	2435.3	1.07	0.11	G 1	6.28	6.25		[2]
Fe XIII	213.771	213.9	3s2 3p2 $^3P_2$ - 3s2 3p 3d $^3P_2$	390.2	1.11	0.12	G 1	6.22	6.21		
Si VIII	216.915	216.9	2s22p3 $^2D_{5/2}$ - 2s2p4 $^2P_{3/2}$	562.3	0.95	0.11	G 1	6.10	5.91	0.41	
Fe XIII	216.834		3s2 3p2 $^1D_2$ - 3s2 3p 3d $^3D_2$						6.21	0.24	
Fe XIII	216.869		3s2 3p2 $^1D_2$ - 3s2 3p 3d $^3D_3$						6.21	0.14	
Fe IX	217.101		3p6 $^1S_0$ - 3p5.3d $^3D_1$						5.94	0.12	
Fe XVI	262.984	263.4	3p $^2P_{3/2}$ - 3d $^2D_{5/2}$	226.4	1.10	0.12	G 2	6.34	6.34		
Fe XIV	264.78	264.9	3s2 3p $^2P_{3/2}$ - 3s 3p2 $^2P_{3/2}$	1261.2	1.11	0.11	G 2	6.28	6.25		
Fe XIV	270.507	270.8	3s2 3p $^2P_{3/2}$ - 3s 3p2 $^2P_{1/2}$	169.9	4.45	0.46	G 2	6.28	6.25		[3]
Fe XIV	274.2	274.5	3s2 3p $^2P_{1/2}$ - 3s 3p2 $^2S_{1/2}$	1498.4	0.97	0.10	G 2	6.28	6.25		
Si VII	275.353	275.7	2p4 $^3P_2$ - 2s.2p5 $^3P_2$	203.2	1.18	0.12	G 2	5.91	5.77	0.87	
Si VII	275.667		2p4 $^3P_1$ - 2s.2p5 $^3P_1$						5.77	0.13	
Si X	277.255	277.2	2p $^2P_{3/2}$ - 2s.2p2 $^2S_{1/2}$	553.0	1.20	0.12	G 2	6.08	6.13	0.51	
Si VIII	277.054		2s22p3 $^2D_{5/2}$ - 2s2p4 $^2D_{5/2}$						5.90	0.30	
Mg VII	277		2s22p2 $^3P_1$ - 2s2p3 $^3S_1$						5.81	0.16	
Fe XV	284.16	284.2	3s2 $^1S_0$ - 3s3p $^1P_1$	7765.0	1.01	0.10	G 2	6.32	6.29		
S XI	285.822	285.8	2s22p2 $^3P_1$ - 2s2p3 $^3D_2$	190.3	0.84	0.09	G 2	6.27	6.24	0.71	
S XI	285.587		2s22p2 $^3P_1$ - 2s2p3 $^3D_1$						6.24	0.28	
Al IX	286.377	286.5	2s2.2p $^2P_{3/2}$ - 2s.2p2 $^2P_{1/2}$	34.2	0.70	0.10	G 2	6.06	6.03		
S XII	288.434	288.1	2s2.2p $^2P_{1/2}$ - 2s.2p2 $^2D_{3/2}$	236.5	0.92	0.09	G 2	6.33	6.32	0.83	
Ni XVI	288.166		3s2 3p $^2P_{1/2}$ - 3s 3p2 $^2D_{3/2}$						6.39	0.17	
Fe XIV	289.148	288.8	3s2 3p $^2P_{3/2}$ - 3s 3p2 $^2S_{1/2}$	126.1	0.87	0.09	G 2	6.28	6.25		
Mg VIII	315.039	314.9	2p $^2P_{3/2}$ - 2s.2p2 $^2P_{3/2}$	822.5	0.99	0.10	G 2	5.96	5.91		[4]
Si VIII	319.826	319.6	2s22p3 $^4S_{3/2}$ - 2s2p4 $^4P_{5/2}$	675.0	1.09	0.11	G 2	5.99	5.91		[5]
Fe XIII	320.809	320.5	3s2 3p2 $^3P_2$ - 3s 3p3 $^3P_2$	410.9	0.94	0.09	G 2	6.23	6.20		
Fe XIII	321.4	321.3	3s2 3p2 $^3P_2$ - 3s 3p3 $^3P_1$	131.9	0.82	0.08	G 2	6.22	6.20		
Fe XV	327.011	326.9	3s3p $^3P_2$ - 3p2 $^1D_2$	73.3	1.06	0.11	G 2	6.32	6.29		
Al X	332.789	333.0	2s2 $^1S_0$ - 2s.2p $^1P_1$	316.1	0.75	0.08	G 2	6.16	6.09		[6]
Fe XIV	334.172	334.4	3s2 3p $^2P_{1/2}$ - 3s 3p2 $^2D_{3/2}$	1031.0	1.01	0.10	G 2	6.27	6.24		[7]
Fe XVI	335.41	335.6	3s $^2S_{1/2}$ - 3p $^2P_{3/2}$	3608.6	0.89	0.09	G 2	6.35	6.34		[8]

[1] + ghost 211.3 Å
[2] ghosting 196.5 Å
[3] ghosting ?
[4] reconstructed
[5] reconstructed
[6] ghosting 316 Å
[7] ghosting 317 Å
[8] reconstructed

Table 3.5: *(continued)*

Ion	λ_{th} (Å)	λ_{ob} (Å)	Transition	I_{ob}	I_{th}/I_{ob}	+/-	Det	log T_{eff}	log T_{max}	frac	
Mg VIII	339.006	339.3	2p $^2P_{3/2}$ - 2s.2p2 $^2S_{1/2}$	194.7	0.96	0.10	G 2	5.97	5.92		
Fe XIII	202.044	403.8	3s2 3p2 $^3P_0$ - 3s2 3p 3d $^3P_1$	3043.9	1.02	0.10	G 3	6.22	6.21		
Fe XIII	203.828	408.0	3s2 3p2 $^3P_2$ - 3s2 3p 3d $^3D_3$	2956.7	1.10	0.11	G 3	6.22	6.21	0.75	
Fe XIII	203.797		3s2 3p2 $^3P_2$ - 3s2 3p 3d $^3D_2$						6.21	0.25	
Fe XV	417.258	417.1	3s2 $^1S_0$ - 3s3p $^3P_1$	524.2	0.79	0.08	G 3	6.34	6.29	0.58	
S XIV	417.66		1s2.2s $^2S_{1/2}$ - 1s2.2p $^2P_{3/2}$						6.44	0.40	
Fe XIV	211.32	422.4	3s2 3p $^2P_{1/2}$ - 3s2 3d $^2D_{3/2}$	2521.3	1.04	0.11	G 3	6.28	6.25		
Fe XIII	213.771	427.2	3s2 3p2 $^3P_2$ - 3s2 3p 3d $^3P_2$	314.4	1.37	0.18	G 3	6.22	6.21		
Mg VIII	430.465	430.1	2p $^2P_{1/2}$ - 2s.2p2 $^2D_{3/2}$	227.6	1.22	0.12	G 3	5.96	5.91		
Mg VII	431.313	431.0	2s22p2 $^3P_1$ - 2s2p3 $^3D_2$	123.7	1.10	0.11	G 3	5.91	5.80	0.78	
Mg VII	431.188		2s22p2 $^3P_1$ - 2s2p3 $^3D_1$						5.80	0.22	
Mg VIII	436.735	436.6	2p $^2P_{3/2}$ - 2s.2p2 $^2D_{5/2}$	521.0	0.99	0.10	G 3	5.96	5.91		
S XIV	445.7	445.8	1s2.2s $^2S_{1/2}$ - 1s2.2p $^2P_{1/2}$	10.8	7.33	1.37	G 3	6.39	6.44		
Ne VII	465.22	464.8	2s2 $^1S_0$ - 2s2p $^1P_1$	405.8	0.63	0.06	G 3	5.85	5.72		
Fe XIV	467.395	467.0	3s2 3p $^2P_{3/2}$ - 3s 3p2 $^4P_{3/2}$	121.6	0.42	0.04	G 3	6.27	6.24		
Ne IV	469.823	469.4	2s2 2p3 $^2D_{5/2}$ - 2s 2p4 $^2D_{5/2}$	22.3	0.90	0.11	G 3	5.37	5.28	0.56	
Ne IV	469.875		2s2 2p3 $^2D_{3/2}$ - 2s 2p4 $^2D_{3/2}$						5.28	0.37	
Al X	332.789	665.9	2s2 $^1S_0$ - 2s.2p $^1P_1$	542.5	0.43	0.06	G 4	6.16	6.09		
Fe XIV	334.172	668.4	3s2 3p $^2P_{1/2}$ - 3s 3p2 $^2D_{3/2}$	1126.7	0.92	0.11	G 4	6.27	6.24		
Fe XVI	335.41	670.8	3s $^2S_{1/2}$ - 3p $^2P_{3/2}$	3631.4	0.90	0.09	G 4	6.35	6.34		
Na IX	681.721	681.8	1s2.2s $^2S_{1/2}$ - 1s2.2p $^2P_{3/2}$	50.2	1.71	0.19	G 4	6.11	5.92		
Fe XI	341.113	682.4	3s2.3p4 $^3P_2$ - 3s.3p5 $^3P_1$	142.6	0.78	0.14	G 4	6.14	6.10		
N III	684.998	684.8	2s2 2p $^2P_{1/2}$ - 2s 2p2 $^2P_{3/2}$	7.0	0.91	0.20	G 4	4.92	5.01		
N III	685.817	685.8	2s2 2p $^2P_{3/2}$ - 2s 2p2 $^2P_{3/2}$	38.3	1.15	0.13	G 4	4.92	5.01	0.72	
N III	685.515		2s2 2p $^2P_{1/2}$ - 2s 2p2 $^2P_{1/2}$						5.01	0.28	
Fe X	345.723	691.4	3s2.3p5 $^2P_{3/2}$ - 3s.3p6 $^2S_{1/2}$	275.0	0.87	0.11	G 4	6.08	6.04		
Na IX	694.147	694.4	1s2.2s $^2S_{1/2}$ - 1s2.2p $^2P_{1/2}$	22.9	1.86	0.23	G 4	6.12	5.92		
O III	702.897	702.8	2s22p2 $^3P_1$ - 2s2p3 $^3P_2$	51.3	0.95	0.11	G 4	5.02	5.04	0.42	
O III	702.821		2s22p2 $^3P_1$ - 2s2p3 $^3P_0$						5.04	0.32	
O III	702.891		2s22p2 $^3P_1$ - 2s2p3 $^3P_1$						5.04	0.26	
O III	703.854	703.8	2s22p2 $^3P_2$ - 2s2p3 $^3P_2$	76.9	1.10	0.12	G 4	5.09	5.04	0.74	
O III	703.848		2s22p2 $^3P_2$ - 2s2p3 $^3P_1$						5.04	0.24	
Mg IX	706.058	705.7	2s2 $^1S_0$ - 2s.2p $^3P_1$	81.7	0.61	0.06	G 4	6.03	5.98		
Fe XVI	360.761	721.3	3s $^2S_{1/2}$ - 3p $^2P_{1/2}$	1989.7	0.78	0.08	G 4	6.35	6.34		
Fe XII	364.467	728.7	3s2.3p3 $^4S_{3/2}$ - 3s.3p4 $^4P_{5/2}$	685.7	0.88	0.10	G 4	6.18	6.16		
Mg VII	367.674	735.4	2s22p2 $^3P_2$ - 2s2p3 $^3P_2$	191.4	1.19	0.20	G 4	5.91	5.81	0.77	
Mg VII	367.683		2s22p2 $^3P_2$ - 2s2p3 $^3P_1$						5.81	0.23	
Mg IX	368.07	736.0	2s2 $^1S_0$ - 2s.2p $^1P_1$	2485.5	0.90	0.09	G 4	6.06	5.98	0.89	[9]
Fe XIII	368.171		3s2 3p2 $^3P_2$ - 3s 3p3 $^3D_3$						6.20	0.11	
Fe XI	369.153	738.2	3s2.3p4 $^3P_1$ - 3s.3p5 $^3P_2$	416.3	0.30	0.04	G 4	6.14	6.10		[10]
N II	746.984	746.7	2s2 2p2 $^1D_2$ - 2s2 2p 3s $^1P_1$	5.8	0.94	0.41	G 4	5.21	4.77		
O V	758.675	758.6	2s.2p $^3P_1$ - 2p2 $^3P_2$	15.8	1.11	0.23	G 4	5.43	5.39		
O V	759.439	759.4	2s.2p $^3P_0$ - 2p2 $^3P_1$	15.9	0.84	0.17	G 4	5.43	5.39		
O V	760.444	760.5	2s.2p $^3P_2$ - 2p2 $^3P_2$	61.0	1.02	0.12	G 4	5.43	5.39	0.84	
O V	760.225		2s.2p $^3P_1$ - 2p2 $^3P_1$						5.39	0.16	
O V	762.002	762.0	2s.2p $^3P_2$ - 2p2 $^3P_1$	14.1	1.16	0.27	G 4	5.43	5.39		
N IV	765.147	765.3	2s2 $^1S_0$ - 2s 2p $^1P_1$	99.7	0.81	0.09	G 4	5.19	5.18		[11]
Ne VIII	770.409	770.7	1s2 2s $^2S_{1/2}$ - 1s2 2p $^2P_{3/2}$	339.5	1.83	0.19	G 4	6.09	5.79		[12]
Mg VIII	772.26	772.0	2p $^2P_{3/2}$ - 2s.2p2 $^4P_{5/2}$	38.3	0.68	0.10	G 4	5.95	5.90		[13]
Ne VIII	780.324	780.3	1s2 2s $^2S_{1/2}$ - 1s2 2p $^2P_{1/2}$	186.9	1.66	0.17	G 4	6.09	5.79		
Mg VIII	782.338	782.2	2p $^2P_{3/2}$ - 2s.2p2 $^4P_{3/2}$	23.8	0.64	0.11	G 4	5.95	5.90		

[9] reconstructed
[10] + ghost 765.3 Å
[11] ghosting 369.1 Å
[12] reconstructed
[13] reconstructed

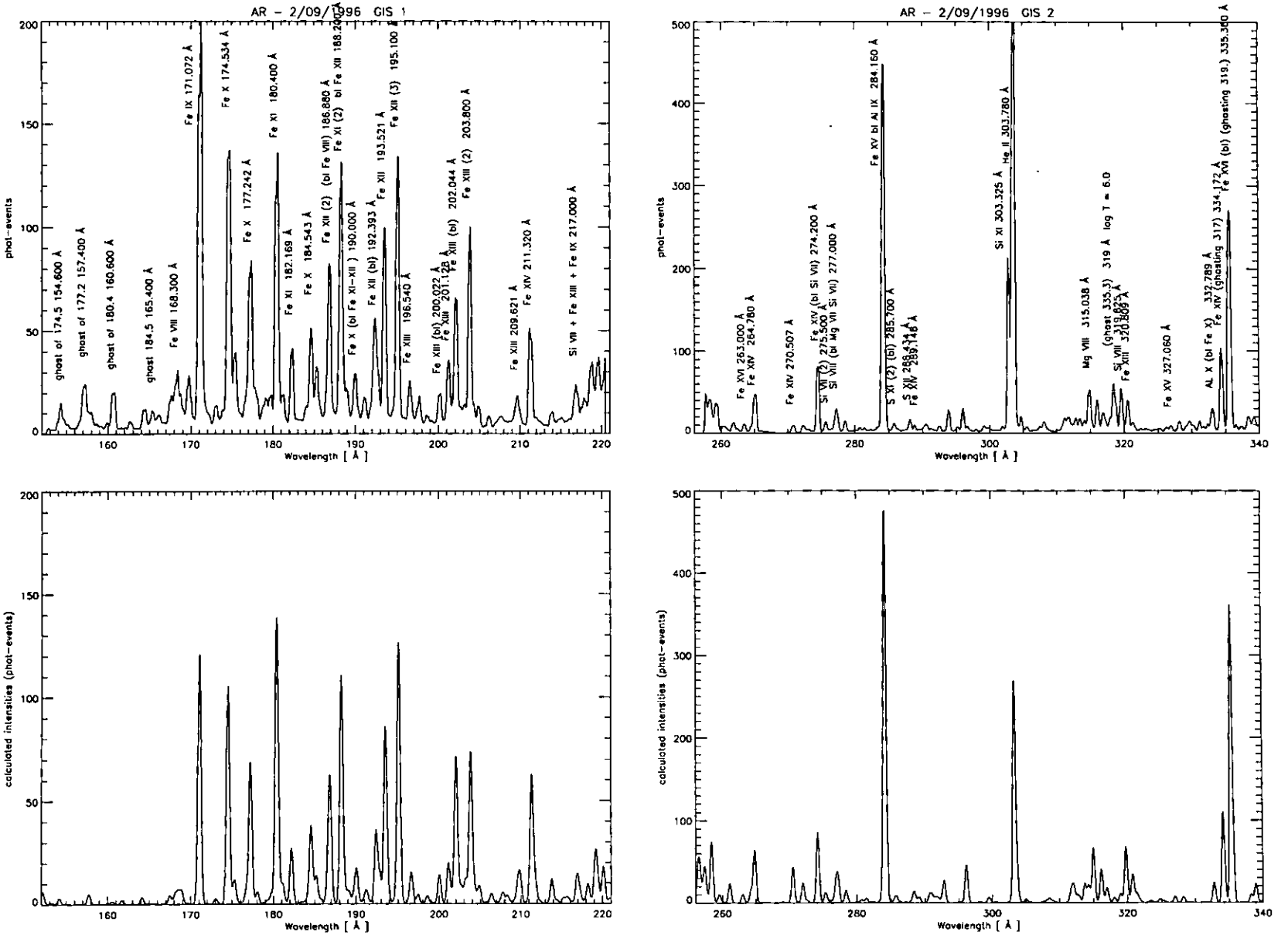

Figure 3.14: *Top: the GIS 1 and GIS 2 spectra of the active region - September 2nd 1996. Bottom: the corresponding synthetic spectra.*

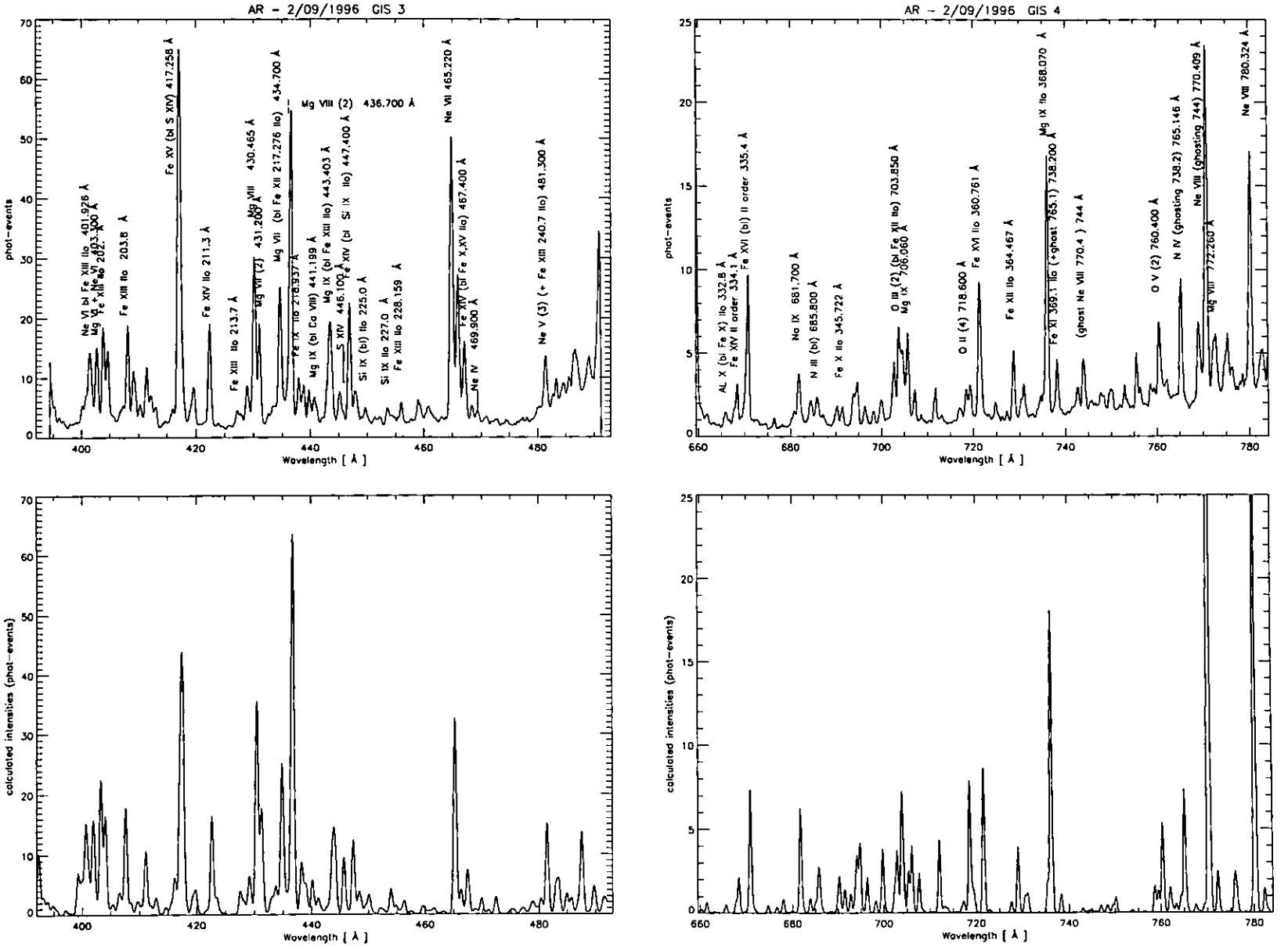

Figure 3.15: *Top: the GIS 3 and GIS 4 spectra of the active region - September 2nd 1996. Bottom: the corresponding synthetic spectra.*

3.4.5 The NIS observations for the internal intensity calibration

The following observations were selected for the internal NIS calibration:

1. An on-disc active region spectral atlas (NISAT study) on the 25th September 1997.
2. Two quiet sun spectral atlases (NISAT studies) at sun centre, on June 22nd 1997 and 19th October 1997.

These types of spectral atlases are routinely performed (see Table C.1 for details). These observations, made in June, September and October were selected, since most of the other NIS-GIS observations that are used for the NIS-GIS cross-calibration were done during those periods. Other observations have been analysed, in collaboration with S. Parenti, and the results confirm those presented in this Chapter. Below, only the the active region observation of 25th September 1997 is presented. The two other NISAT observations are 'normal' observations of the quiet sun.

The on-disc active region observation of 25th September 1997

Monochromatic images of the active region rastered by NIS on the 25th September 1997 were created. Three regions having slightly different characteristics have been selected for creating averaged spectra and subsequent analysis. In all the selected regions the high-temperature lines are the strongest lines in the spectra. In particular, the Fe XVI doublet seen in these NIS 1 (at 335.4 and 360. Å) spectra is particularly important for calibration purposes. In fact, these lines are not density-dependent and the agreement between observations and theory has already been tested in many different (solar and stellar) works. As already mentioned in Chapter 2, in normal quiet sun conditions the Fe XVI lines are very weak and the 335.4 line is mainly Mg VIII (plus a previously unidentified Fe XII line, see below), and not Fe XVI. In the examined spectra, the Mg VIII lines are very weak, as the Fe XII are, compared to the Fe XVI lines, and the 335.4 line is basically all Fe XVI.

Since the results of the *DEM* analyses of the various regions are very similar, only one is presented here, chosen because the high-temperature lines are not too strong, and the lower temperature ones still have a good signal. Figures 3.16 and 3.17 show the NIS averaged spectra of the chosen area. Note the strong scattered light background intensity, in particular in the NIS 1 spectrum. A complete *DEM* analysis on the NIS line intensities measured from the spectra shown in Figures 3.16 and 3.17 has been performed. The contribution functions (CHIANTI v.2 plus recent Fe XIV calculations, *Storey et al.*, 1999) have been

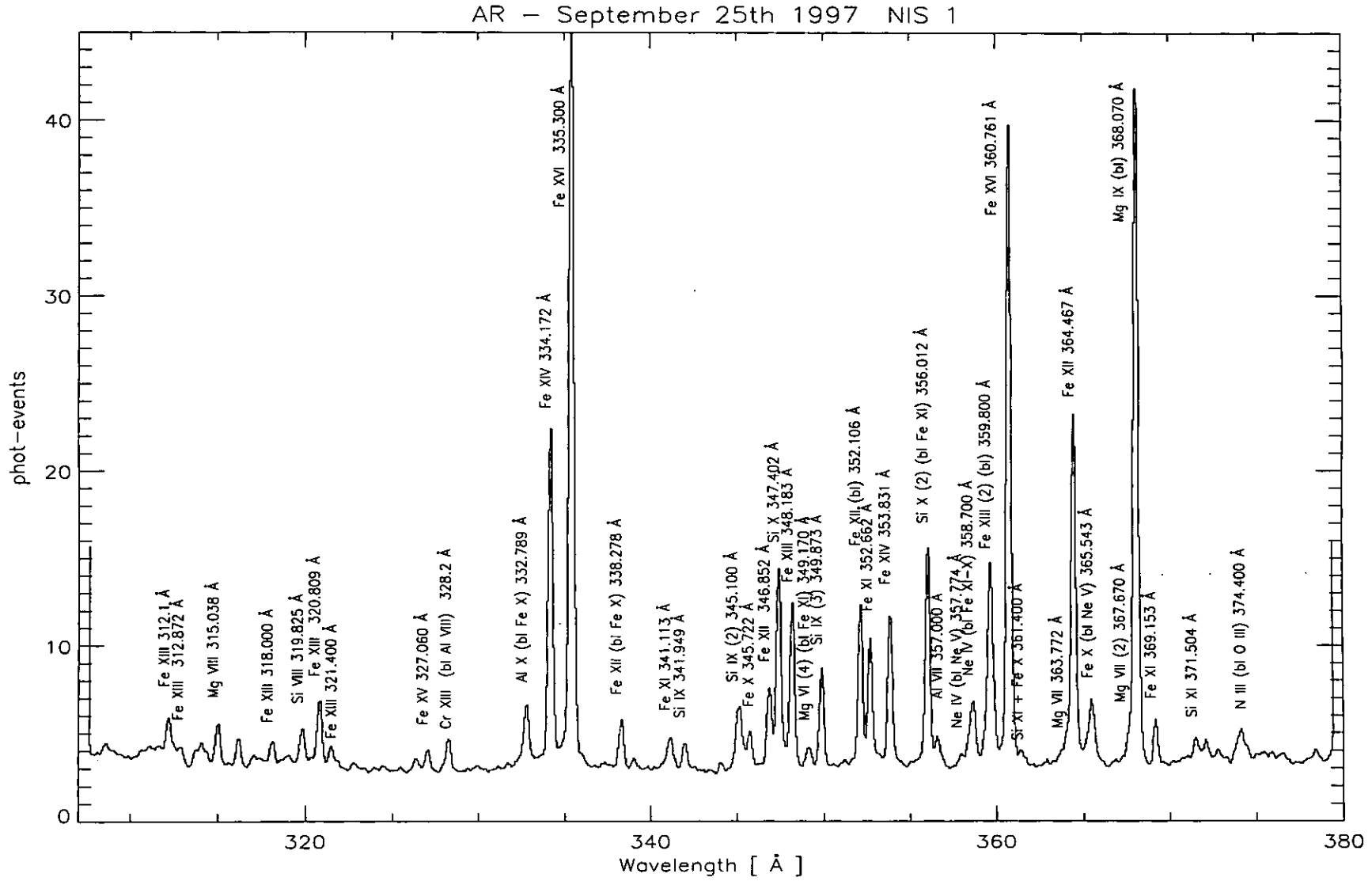

Figure 3.16: *The NIS 1 averaged spectrum of one of the examined areas of the active region observation of September 25 1997.*

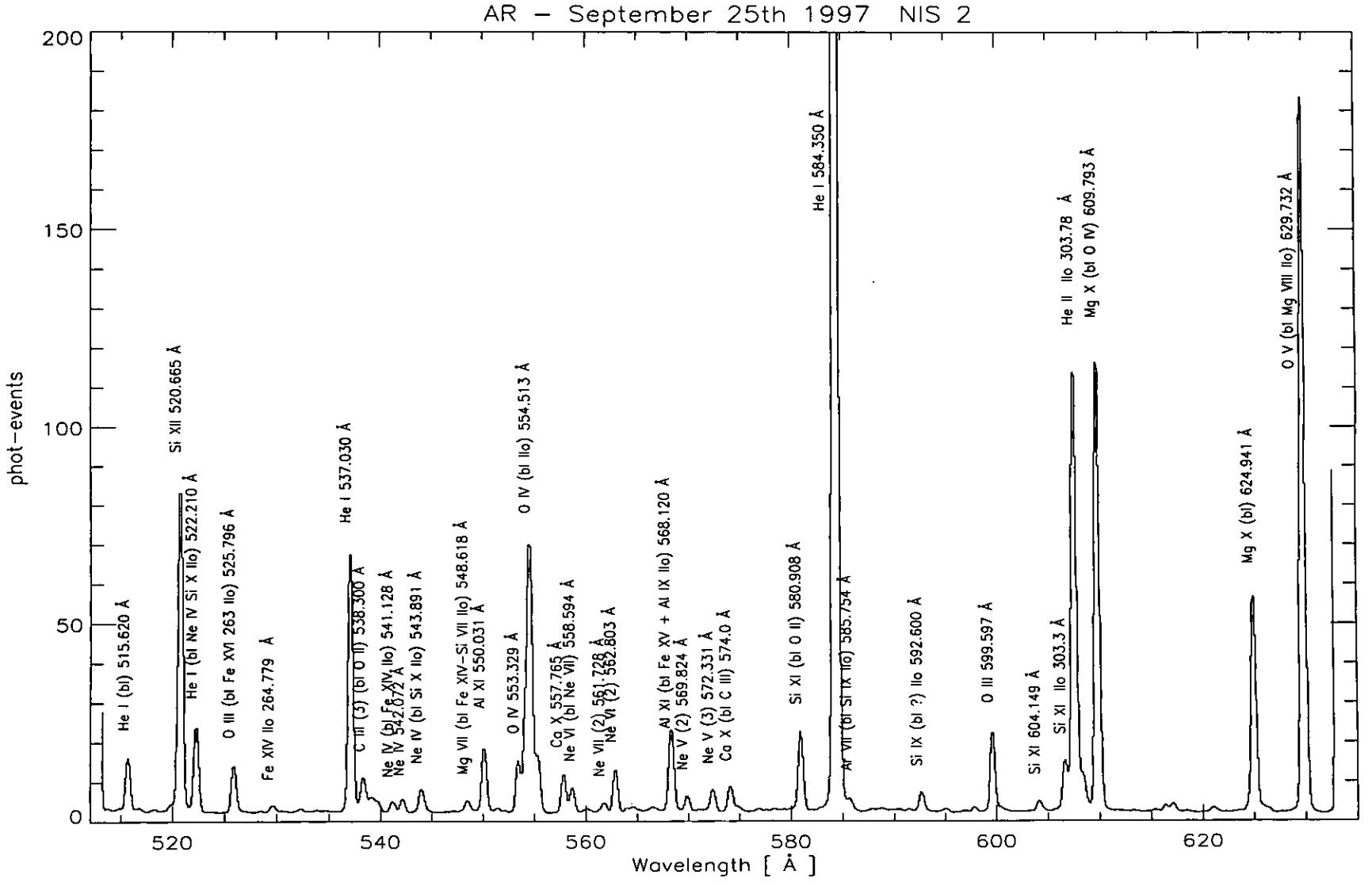

Figure 3.17: *The NIS 2 averaged spectrum of one of the examined areas of the active region observation of September 25 1997.*

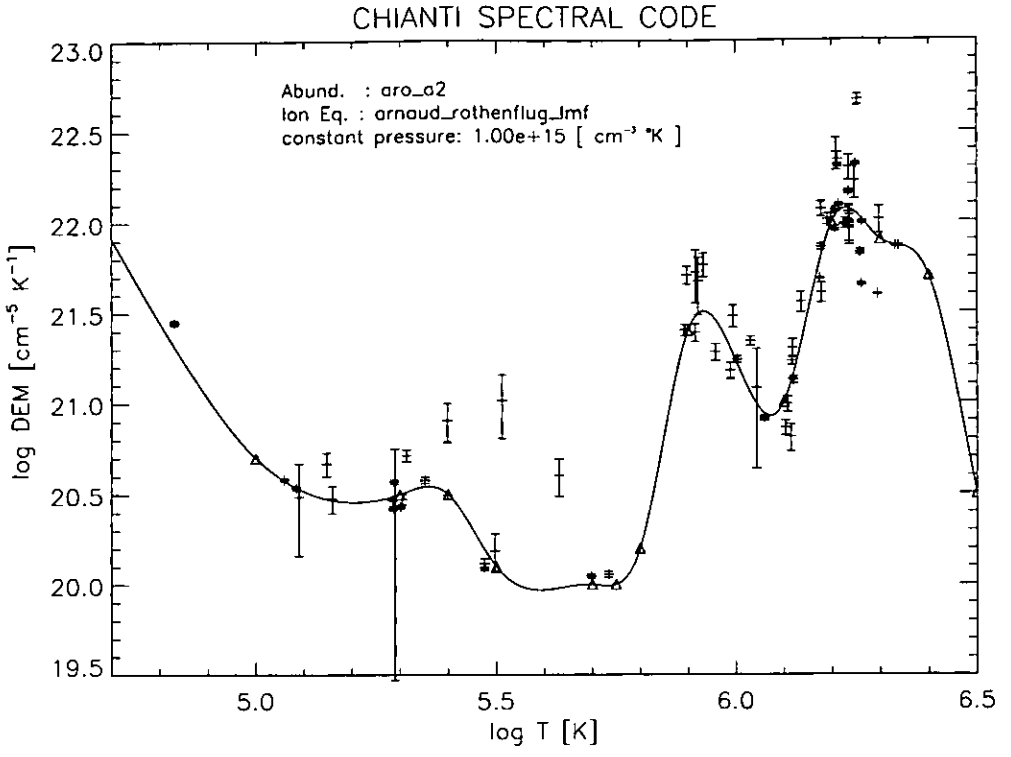

Figure 3.18: *The derived DEM for the on-disc active region observation of 25th September 1997. Note the 'usual' peak at 10^6 K, and the high-temperature peak.*

calculated at constant $N_e = 2\text{x}10^9$ cm^{-3}, using the *Arnaud and Rothenflug* (1985) ionization equilibrium (for all the ions) and photospheric abundances (*Grevesse and Anders*, 1991), except for the following elements (with logarithmic differences indicated in parentheses): Ne (+0.2), Al (+0.3), Ca (+0.7).

Figure 3.18 shows the *DEM* for this region, while Table 3.6 presents the results for a small selection of lines. Note:

- the 335.4 Å line intensity is only from Fe XVI. In the other regions within the raster that have been examined, the Fe XVI 335.4/ 360. Å ratio was found to be constant. The Fe XVI 335.4/ 360. Å ratio is therefore used to constrain the sensitivity ratio in NIS at those wavelengths (see Section 3.4.8 below).

- Many bright high-temperature lines, usually not seen in quiet sun or coronal hole NIS spectra, are observed (e.g., Fe XIII, Fe XV, Si XI). Many of these high-temperature lines are also contributing in second order to the NIS 2 spectrum. However, except the lines indicated in Figure 3.17, they are all blended with the strong transition region lines that are visible in NIS 2. For a better examination of them, off-limb spectra are needed.

- The higher-than-photospheric Ne and Al abundances. The Al abundance is the same as that one derived for the SERTS-89 spectrum. The high Ca abundance is based only on Ca X, and is dubious.
- The discrepancy for the Mg V ions, the same as seen in the SERTS-89 spectrum.
- The overestimation (by a factor of 2) of the Li-like Al XI and Si XII.

Table 3.6: *Some of the lines of the active region spectrum of September 25th 1997.*

Ion	λ_{th} (Å)	λ_{ob} (Å)	Transition	I_{ob}	I_{th}/I_{ob}	+/-	Det	log T_{eff}	log T_{max}	frac
O II	538.32	538.3	2s22p3 $^2D_{3/2}$ - 2s2p4 $^2P_{3/2}$	30.0	0.74	0.08	N 2	4.83	4.87	0.42
C III	538.31		2s2p $^3P_2$ - 2s3s $^3S_1$						4.96	0.29
C III	538.147		2s2p $^3P_1$ - 2s3s $^3S_1$						4.96	0.18
O III	599.597	599.6	2s22p2 $^1D_2$ - 2s2p3 $^1D_2$	70.7	0.99	0.10	N 2	5.06	5.06	
O III	525.796	525.9	2s22p2 $^1D_2$ - 2s2p3 $^1P_1$	30.6	1.01	0.10	N 2	5.08	5.07	
O III	374.435	374.5	2s22p2 $^3P_2$ - 2s22p3s $^3P_1$	3.9	1.10	0.59	N 1	5.09	5.11	0.49
N III	374.434		2s2 2p $^2P_{3/2}$ - 2s2 3d $^2D_{5/2}$						5.08	0.45
O III	374.075	374.1	2s22p2 $^3P_2$ - 2s22p3s $^3P_2$	17.2	0.64	0.11	N 1	5.15	5.11	0.60
O III	374.005		2s22p2 $^3P_0$ - 2s22p3s $^3P_1$						5.11	0.15
N III	374.198		2s2 2p $^2P_{1/2}$ - 2s2 3d $^2D_{3/2}$						5.08	0.12
O III	374.164		2s22p2 $^3P_1$ - 2s22p3s $^3P_1$						5.11	0.12
O III	597.817	597.8	2s22p2 $^1S_0$ - 2s2p3 $^1P_1$	4.4	0.98	0.19	N 2	5.16	5.07	
O IV	554.513	554.6	2s2 2p $^2P_{3/2}$ - 2s 2p2 $^2P_{3/2}$	237.0	1.04	0.10	N 2	5.28	5.27	
O IV	553.329	553.4	2s2 2p $^2P_{1/2}$ - 2s 2p2 $^2P_{3/2}$	42.1	1.16	0.12	N 2	5.29	5.27	
O IV	608.397	608.4	2s2 2p $^2P_{1/2}$ - 2s 2p2 $^2S_{1/2}$	44.0	0.84	0.09	N 2	5.29	5.27	
O III	373.805	373.8	2s22p2 $^3P_1$ - 2s22p3s $^3P_2$	2.3	1.05	0.95	N 1	5.29	5.11	
O IV	555.263	555.3	2s2 2p $^2P_{3/2}$ - 2s 2p2 $^2P_{1/2}$	43.1	1.17	0.12	N 2	5.30	5.27	
Ne IV	542.073	542.1	2s2 2p3 $^4S_{3/2}$ - 2s 2p4 $^4P_{3/2}$	11.1	1.07	0.13	N 2	5.30	5.27	
Ne IV	541.128	541.2	2s2 2p3 $^4S_{3/2}$ - 2s 2p4 $^4P_{1/2}$	9.4	0.63	0.08	N 2	5.31	5.27	
Ne IV	543.892	544.0	2s2 2p3 $^4S_{3/2}$ - 2s 2p4 $^4P_{5/2}$	20.9	0.92	0.10	N 2	5.35	5.27	
Ne IV	357.832	358.0	2s2 2p3 $^2D_{3/2}$ - 2s 2p4 $^2P_{1/2}$	20.4	0.40	0.10	N 1	5.40	5.30	0.65
Ne V	357.954		2s22p2 $^3P_0$ - 2s2p3 $^3S_1$						5.49	0.35
O V	629.73	629.8	2s2 $^1S_0$ - 2s.2p $^1P_1$	581.7	1.02	0.10	N 2	5.40	5.39	
Ne V	569.824	569.9	2s22p2 $^3P_1$ - 2s2p3 $^3D_2$	11.1	1.20	0.14	N 2	5.48	5.47	0.76
Ne V	569.753		2s22p2 $^3P_1$ - 2s2p3 $^3D_1$						5.47	0.24
Ne V	572.331	572.4	2s22p2 $^3P_2$ - 2s2p3 $^3D_3$	16.5	1.26	0.14	N 2	5.48	5.47	0.86
Ne V	572.098		2s22p2 $^3P_2$ - 2s2p3 $^3D_2$						5.47	0.14
Ne V	359.382	359.2	2s22p2 $^3P_2$ - 2s2p3 $^3S_1$	17.2	0.84	0.22	N 1	5.50	5.49	
Mg V	355.329	355.4	2p4 $^3P_1$ - 2s.2p5 $^3P_2$	11.8	0.11	0.04	N 1	5.51	5.46	
Mg V	353.092	353.1	2p4 $^3P_2$ - 2s.2p5 $^3P_2$	18.1	0.24	0.06	N 1	5.63	5.46	
Ne VI	562.803	562.9	2s2 2p $^2P_{3/2}$ - 2s 2p2 $^2D_{5/2}$	33.7	0.90	0.09	N 2	5.70	5.63	
Ne VI	558.594	558.7	2s2 2p $^2P_{1/2}$ - 2s 2p2 $^2D_{3/2}$	21.4	0.86	0.09	N 2	5.73	5.63	0.84
Ne VII	558.609		2s2p $^3P_1$ - 2p2 $^3P_2$						5.72	0.16
Ne VII	561.728	561.7	2s2p $^3P_2$ - 2p2 $^3P_2$	9.8	0.87	0.11	N 2	5.89	5.72	
Ne VII	564.528	564.5	2s2p $^3P_2$ - 2p2 $^3P_1$	5.9	0.47	0.07	N 2	5.90	5.72	
Mg VII	367.674	367.7	2s22p2 $^3P_2$ - 2s2p3 $^3P_2$	33.7	1.23	0.19	N 1	5.92	5.81	0.77
Mg VII	367.683		2s22p2 $^3P_2$ - 2s2p3 $^3P_1$						5.81	0.23
Mg VII	363.772	363.8	2s22p2 $^3P_0$ - 2s2p3 $^3P_1$	13.8	0.57	0.20	N 1	5.92	5.81	
Al VII	356.888	356.9	2s22p3 $^4S_{3/2}$ - 2s2p4 $^4P_{5/2}$	13.7	0.66	0.24	N 1	5.92	5.78	
Ne VII	559.948	560.1	2s2p $^3P_0$ - 2p2 $^3P_1$	4.5	0.55	0.10	N 2	5.93	5.72	
Mg VIII	315.039	315.0	2p $^2P_{3/2}$ - 2s.2p2 $^2P_{3/2}$	96.4	1.51	0.22	N 1	5.96	5.91	
Si VIII	319.826	319.8	2s22p3 $^4S_{3/2}$ - 2s2p4 $^4P_{5/2}$	104.5	1.33	0.19	N 1	5.99	5.91	
Fe XI	349.046	349.1	3s2.3p4 $^3P_1$ - 3s.3p5 $^3P_0$	36.2	0.61	0.10	N 1	5.99	6.11	0.38
Mg VI	349.163		2s2.2p3 $^2D_{5/2}$ - 2s.2p4 $^2D_{5/2}$						5.65	0.30
Mg VI	349.124		2s2.2p3 $^2D_{3/2}$ - 2s.2p4 $^2D_{3/2}$						5.65	0.23
Ca X	574.01	574.1	3s $^2S_{1/2}$ - 3p $^2P_{1/2}$	19.9	0.95	0.10	N 2	6.00	5.82	0.87
C III	574.279		2s2p $^1P_1$ - 2s3d $^1D_2$						4.98	0.10
Fe XI	358.621	358.6	3s2.3p4 $^3P_0$ - 3s.3p5 $^3P_1$	98.2	0.51	0.06	N 1	6.03	6.10	0.43
Ne IV	358.686		2s2 2p3 $^2D_{5/2}$ - 2s 2p4 $^2P_{3/2}$						5.30	0.19
Si XI	358.652		2s.2p $^3P_1$ - 2p2 $^3P_2$						6.20	0.18
Ne V	358.484		2s22p2 $^3P_1$ - 2s2p3 $^3S_1$						5.49	0.17
Al VIII	325.292	325.4	2p2 $^3P_1$ - 2s.2p3 $^3P_2$	13.4	0.81	0.52	N 1	6.04	5.92	0.29
Al VIII	325.276		2p2 $^3P_1$ - 2s.2p3 $^3P_0$						5.92	0.29
Al VIII	325.338		2p2 $^3P_1$ - 2s.2p3 $^3P_1$						5.92	0.24
P XI	325.516		2p $^2P_{3/2}$ - 2s.2p2 $^2D_{5/2}$						6.24	0.14
Ca X	557.765	557.8	3s $^2S_{1/2}$ - 3p $^2P_{3/2}$	31.2	1.06	0.11	N 2	6.06	5.82	
Si XI	365.433	365.5	2s.2p $^3P_2$ - 2p2 $^3P_2$	43.6	1.45	0.20	N 1	6.10	6.20	0.40
Fe X	365.543		3s2.3p5 $^2P_{1/2}$ - 3s.3p6 $^2S_{1/2}$						6.04	0.39
Ne V	365.603		2s22p2 $^1D_2$ - 2s2p3 $^1P_1$						5.49	0.21
Fe X	345.723	345.7	3s2.3p5 $^2P_{3/2}$ - 3s.3p6 $^2S_{1/2}$	50.9	1.15	0.16	N 1	6.11	6.04	
Si XI	365.433	365.3	2s.2p $^3P_2$ - 2p2 $^3P_2$	25.9	1.97	0.38	N 1	6.11	6.20	0.49

Table 3.6: *(continued)*

Ion	λ_{th} (Å)	λ_{ob} (Å)	Transition	I_{ob}	I_{th}/I_{ob}	+/-	Det	log T_{eff}	log T_{max}	frac
Mg VII	365.234		2s22p2 $^3P_1$ - 2s2p3 $^3P_2$						5.81	0.18
Mg VII	365.176		2s22p2 $^3P_1$ - 2s2p3 $^3P_0$						5.81	0.17
Mg VII	365.243		2s22p2 $^3P_1$ - 2s2p3 $^3P_1$						5.81	0.13
Si IX	345.124	345.1	2s22p2 $^3P_1$ - 2s2p3 $^3D_2$	115.7	0.79	0.09	N 1	6.12	6.03	0.79
Si IX	344.951		2s22p2 $^3P_1$ - 2s2p3 $^3D_1$						6.03	0.20
Si IX	341.949	342.0	2s22p2 $^3P_0$ - 2s2p3 $^3D_1$	48.2	0.69	0.11	N 1	6.12	6.03	
Mg IX	368.07	368.1	2s2 $^1S_0$ - 2s.2p $^1P_1$	479.6	1.04	0.10	N 1	6.12	5.98	0.73
Fe XIII	368.171		3s2 3p2 $^3P_2$ - 3s 3p3 $^3D_3$						6.20	0.27
Si IX	349.873	349.9	2s22p2 $^3P_2$ - 2s2p3 $^3D_3$	110.9	1.10	0.12	N 1	6.12	6.03	0.88
Si IX	349.794		2s22p2 $^3P_2$ - 2s2p3 $^3D_2$						6.03	0.11
Cr XIII	328.267	328.3	3s2 $^1S_0$ - 3s.3p $^1P_1$	68.8	0.60	0.10	N 1	6.14	6.19	0.58
Al VIII	328.185		2p2 $^3P_2$ - 2s.2p3 $^3P_2$						5.92	0.28
Mg X	609.793	609.8	1s2.(1s).2s $^2S_{1/2}$ - 1s2.(1s).2p $^2P_{3/2}$	443.1	1.26	0.13	N 2	6.17	6.04	0.88
O IV	609.829		2s2 2p $^2P_{3/2}$ - 2s 2p2 $^2S_{1/2}$						5.27	0.12
Fe XI	341.113	341.1	3s2.3p4 $^3P_2$ - 3s.3p5 $^3P_1$	61.9	0.55	0.08	N 1	6.18	6.10	
Fe XI	352.662	352.7	3s2.3p4 $^3P_2$ - 3s.3p5 $^3P_2$	142.0	0.90	0.10	N 1	6.18	6.11	
Al X	332.789	332.8	2s2 $^1S_0$ - 2s.2p $^1P_1$	131.9	0.83	0.10	N 1	6.19	6.09	
Fe XII	346.852	346.9	3s2.3p3 $^4S_{3/2}$ - 3s.3p4 $^4P_{1/2}$	104.5	0.92	0.10	N 1	6.20	6.16	
Si X	356.012	356.0	2p $^2P_{3/2}$ - 2s.2p2 $^2D_{5/2}$	211.7	1.17	0.12	N 1	6.21	6.13	0.88
Si X	356.05		2p $^2P_{3/2}$ - 2s.2p2 $^2D_{3/2}$						6.13	0.12
Si X	347.403	347.4	2p $^2P_{1/2}$ - 2s.2p2 $^2D_{3/2}$	223.7	0.93	0.10	N 1	6.21	6.13	
Si XI	361.412	361.4	2s.2p $^3P_0$ - 2p2 $^3P_1$	24.0	0.46	0.10	N 1	6.21	6.20	0.74
Fe X	361.406		3s2.3p4(3p).3d $^4F_{7/2}$ - 3s.3p5(3p*).3d $^4F_{7/2}$						6.04	0.21
Si XI	580.907	580.9	2s2 $^1S_0$ - 2s.2p $^3P_1$	60.2	0.55	0.06	N 2	6.21	6.19	
Fe XII	338.278	338.3	3s2.3p3 $^2D_{5/2}$ - 3s.3p4 $^2D_{5/2}$	76.6	0.51	0.07	N 1	6.21	6.16	
Fe XII	364.467	364.5	3s2.3p3 $^4S_{3/2}$ - 3s.3p4 $^4P_{5/2}$	286.4	0.92	0.09	N 1	6.21	6.16	
Mg X	624.941	625.0	1s2.(1s).2s $^2S_{1/2}$ - 1s2.(1s).2p $^2P_{1/2}$	196.7	1.23	0.12	N 2	6.22	6.04	
Fe XIII	320.809	320.8	3s2 3p2 $^3P_2$ - 3s 3p3 $^3P_2$	160.8	1.21	0.15	N 1	6.23	6.20	
Fe XIII	359.642	359.7	3s2 3p2 $^3P_1$ - 3s 3p3 $^3D_2$	250.1	0.81	0.08	N 1	6.23	6.20	0.73
Fe XIII	359.842		3s2 3p2 $^3P_1$ - 3s 3p3 $^3D_1$						6.20	0.26
Fe XIII	318.128	318.1	3s2 3p2 $^1D_2$ - 3s 3p3 $^1D_2$	68.5	0.59	0.11	N 1	6.23	6.20	
Fe XIII	312.109	312.2	3s2 3p2 $^3P_1$ - 3s 3p3 $^3P_1$	124.1	1.04	0.14	N 1	6.24	6.20	
Fe XIII	312.872	312.8	3s2 3p2 $^3P_1$ - 3s 3p3 $^3P_0$	50.0	1.18	0.29	N 1	6.24	6.20	
Fe XIII	348.183	348.2	3s2 3p2 $^3P_0$ - 3s 3p3 $^3D_1$	165.4	1.21	0.13	N 1	6.24	6.20	
Fe XIII	321.4	321.5	3s2 3p2 $^3P_2$ - 3s 3p3 $^3P_1$	47.4	1.28	0.27	N 1	6.24	6.20	
Si XI	371.503	371.6	2s.2p $^3P_2$ - 2p2 $^3P_1$	13.6	0.67	0.15	N 1	6.25	6.20	
Si XI	303.324	606.7	2s2 $^1S_0$ - 2s.2p $^1P_1$	2807.9	0.54	0.06	N 2	6.25	6.20	
Si XI	604.147	604.2	2s.2p $^1P_1$ - 2p2 $^1D_2$	13.3	0.24	0.03	N 2	6.25	6.20	
Fe XIV	353.831	353.8	3s2 3p $^2P_{3/2}$ - 3s 3p2 $^2D_{5/2}$	168.0	1.55	0.16	N 1	6.26	6.24	
Al XI	550.031	550.1	1s2.(1s).2s $^2S_{1/2}$ - 1s2.(1s).2p $^2P_{3/2}$	54.7	2.29	0.23	N 2	6.26	6.16	
Fe XIV	334.172	334.2	3s2 3p $^2P_{1/2}$ - 3s 3p2 $^2D_{3/2}$	611.8	1.03	0.11	N 1	6.26	6.24	
Si XII	520.665	520.7	1s2.2s $^2S_{1/2}$ - 1s2.2p $^2P_{1/2}$	204.6	2.06	0.21	N 2	6.29	6.26	
Fe XV	327.011	327.0	3s3p $^3P_2$ - 3p2 $^1D_2$	50.7	0.78	0.15	N 1	6.30	6.29	
Fe XVI	335.41	335.4	3s $^2S_{1/2}$ - 3p $^2P_{3/2}$	1347.8	1.01	0.10	N 1	6.33	6.34	
Fe XVI	360.761	360.8	3s $^2S_{1/2}$ - 3p $^2P_{1/2}$	630.6	1.00	0.10	N 1	6.34	6.34	

3.4.6 The observations for the NIS-GIS cross-calibration

The rationale for special observing sequences

We have already pointed out the need for near-simultaneous NIS and GIS full-wavelength observations. With this in mind, the main issues when using the Sun as a CDS calibration source are the following:

- Temporal variability. It is important to be able to estimate where and how much the solar variability considerably changes the line intensities. Knowing where and when such variations take place is better than just trying to keep the exposure times down as much as possible, because then the signal would be too poor. To do this, first, it is better to observe diffuse quiet regions rather than, for example, active regions, because the variations would be less anyway. Second, a series of repeats of NIS and GIS rasters reveal where intensity variations have taken place (if any). This can then be used to decide which data can be used/integrated.

- Raster sizes. The raster sizes should be small enough to keep the total duration of the observation as short as possible. A bigger area should be scanned by NIS, and a smaller one by GIS which takes longer.

- The solar rotation. As already mentioned, the solar rotation is such that accurate overlaying of different observations is difficult, if they are made near disc centre. Also, the fact that the accuracy of the pointing is less than the spatial resolution, complicates the situation.

- Good signal. To get sufficient signal-to-noise while keeping the time between the NIS and GIS exposures as short as possible, either spatial areas have to be averaged or the exposure time has to be sufficient without this. Also, the wider ($4''$) slits are to be preferred because of the higher signal they produce, considering that this advantage is not gained at any expense of spectral resolution.

- The location and the spatial variability. In on-disc observations, it is important to be able to cross-correlate the GIS and NIS data to get co-alignment (and correct for the solar rotation), and to compare intensities of the lines that are emitted by the same spatial regions, avoiding irregularly varying areas. To do this, there is a need to have a sufficiently large spatial region covered, and some sort of structure to get a good correlation (e.g. the solar limb, a bright point, a network boundary).

  Looking at the limb (or just off, at the limb brightening) instead gives a structure to check that the pointing for the NIS and GIS rasters is the same. The effects of the

solar rotation are reduced by the large line-of-sight path, which also produces signals that are several times higher than those of the on-disc observations, which increases the signal-to-noise and allows smaller exposure times to be used. The scattered light and the continuum also disappear from the spectra in off-limb observations, leaving much cleaner spectra to analyse.

Observation sequences and data analysis

The CDS studies that were used for calibration purposes are listed in Table 4.1, and the observations performed and analysed are shown in Table C.1. Some preliminary observations on the disc were made in collaboration with M. Landini and E. Landi of the Arcetri Observatory, Italy. These used the ARC_CALN/v3 and ARC_CALG/v1 studies, repeated successively on the same region near disc centre. The drawback of these observations was that the area rastered by the GIS was larger than that observed by NIS, and count-rates were low. The observations performed on March 3rd 1997 were analysed, but were not fully usable for calibration purposes because many brightenings occurred in network regions, in all the successive observations and because of the solar rotation. Other on-disc observations were performed with the UCLAN_N1/v1 and ARC_CALG/v1 studies, in which only the NIS 1 channel and a few lines observed in NIS 2 were extracted. This was done to focus on the overlapping region between the NIS 1 and the GIS 2 channels.

The NIS observations that were developed for the observations at the limb are small rasters of full spectra using the 4″x 240″slit. The CDS study name is ARC_CALN/v3, covering an area of 32″x70″. After rotating the spectra, this reduces to 32″in X and about 40″in Y. With an exposure time of 45s, it takes less than 13m to raster the whole area. The GIS observation used the CDS study DEM_GIS/v2, where the 4″x4″slit is rastered in order to cover a 24″x 24″region with 36 spatial positions. The total duration is just under 13m, with a 20s exposure time. The ARC_CALN and DEM_GIS were repeated in succession about five times, without changing the pointing, for a total duration of about 2 hours.

The observations analysed in detail were performed on May 4th (two sets of observations), June 20th, October 1st, October 16th 1997. Most of the observations have been completely successful in terms of pointing, telemetry, good signal, and reduced time variability. Only a very few 'typical' results have been selected as examples from this very large dataset, for presentation here.

The standard corrections (e.g. cosmic ray removal and de-tilt for the NIS case) already described were applied to the data. Then, special software was written to deal with such a complex case, with a total of 40 (8x5) NIS exposures and 180 (36 x5) GIS spectra, for

each set of 5 successive NIS and GIS rasters analysed. In short, this software allowed an evaluation of the temporal variations, and the possibility to select spatial areas and different observations in order to produce GIS and NIS averaged spectra emitted by the same spatial regions at times when intensity variations were at a minimum. Figure 3.19 shows as an example a sequence of GIS rasters over a region on the quiet west limb observed on May 4th 1997. This figure already shows that this region was very quiet. The NIS rasters were performed at the same position, alternating with the GIS ones.

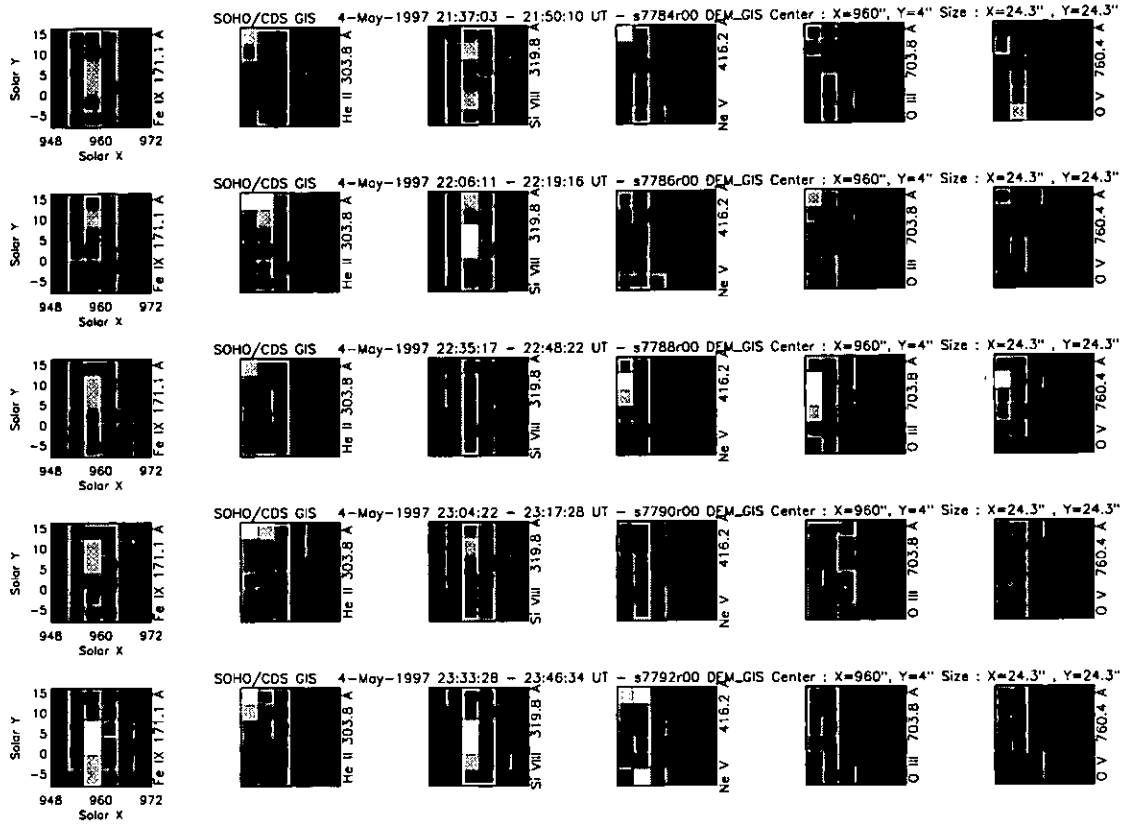

Figure 3.19: *Monochromatic images in few selected lines observed with the DEM_GIS study at the limb, on May 4th 1997. The images for each line are plotted with the same intensity scale, showing only marginal intensity variations in time.*

In order to increase the signal, and reduce the effect of the cosmic rays, averaged GIS and NIS spectra for each mirror position (i.e. for each Solar X) and for each observation (file) have been averaged selecting a spatially overlapping region along Solar Y. These spectra were fitted, and figures such as Figure 3.20 inspected in order to judge if there were observations with brightenings. Indeed some cases were found, and the corresponding files excluded. For example, only three successive NIS and GIS rasters were used for the May 4th observation, while only four NIS and GIS rasters were usable for the October 16th observation.

Once this was established for all the observations, an analysis of the time-averaged spectra

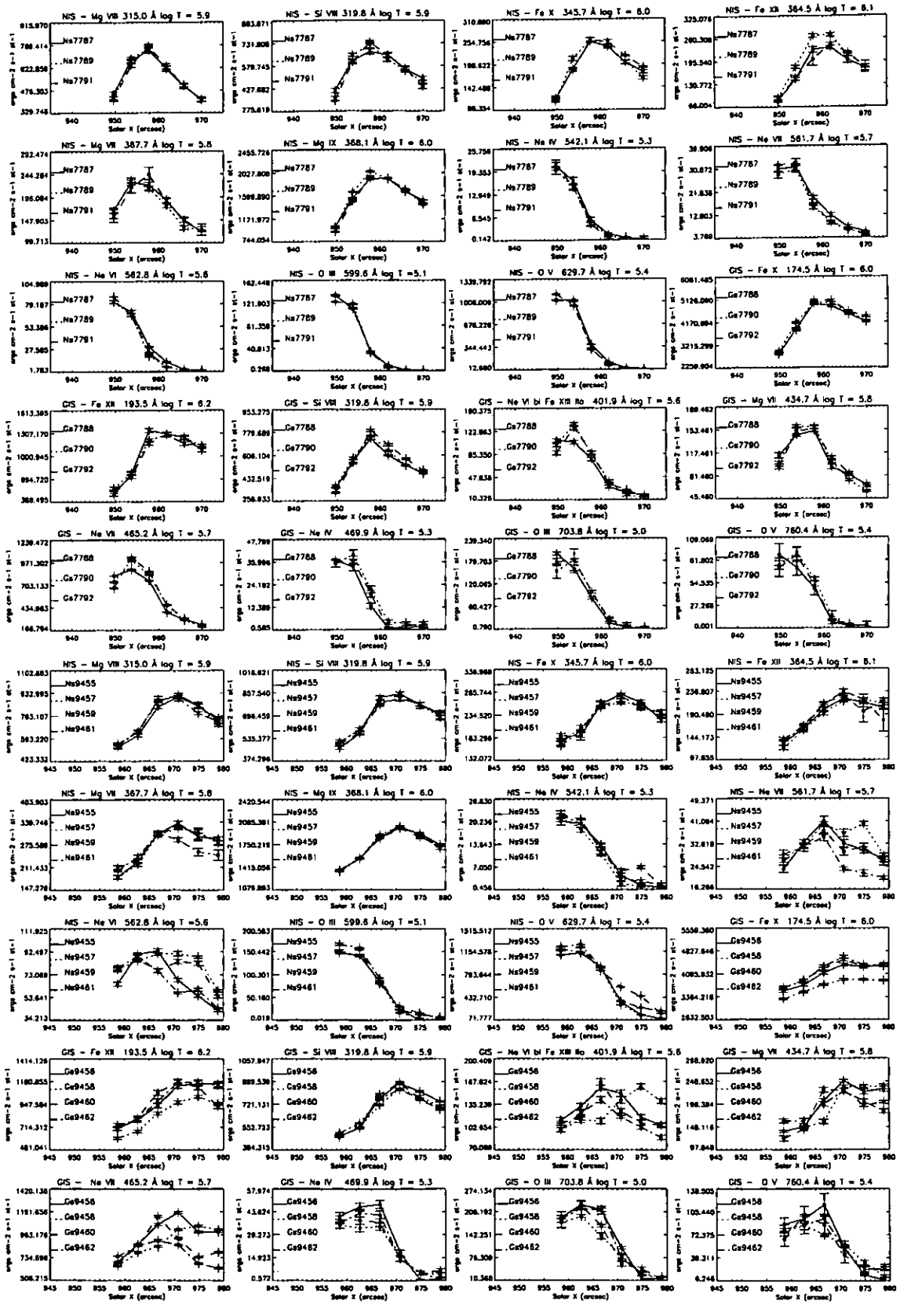

Figure 3.20: *Some intensities of NIS and GIS lines, as a function of position across the limb and time – May 4th (upper five rows) and October 16th (below), 1997. Note the limb brightening in some lines and the rapid disappearance of the 'cool' transition region lines just off-limb.*

was performed, with accurate line fitting and background subtraction, for a few spatial positions, typically one on the disc, and one off the limb. The diagnostic method was then applied to each of these many spectra, typically for each date, one on-disc and one off-limb, and the information from the two data sets combined, to find the relative calibration for each NIS and GIS channel. It was expected that the calibration would not depend on the position, in particular since the overall intensities of all the coronal lines did not change by large factors, see Figure 3.20. The only position-dependent factor is the aperture at the telescope, which was taken into account (although this correction is only about 2% for the NIS, given the small region rastered). First, however, some direct comparisons between the various observed lines were done, and are described below.

The overlapping regions between the CDS channels

The CDS detectors contain some overlapping spectral regions, where the same emission lines are observed in two channels, either in first or second order. Examples are NIS 1 (330-379 Å) with GIS 4 (second order), and NIS 1 with GIS 2 (308-340 Å), shown in Figures 3.21 and 3.22. These figures show the series of spectra superimposed, on the same scale, and demonstrate visually that temporal variations were small. The main variation is due to the scattered light in the NIS 1 channel, that is particularly evident in Figure 3.22. This comparison also shows the evident presence of ghosts in the GIS spectra. Some of the lines such as the Fe XVI blend at 335.4 Åare almost completely ghosting, and 'disappear'. It should be noted that this spectral region and these types of quiet sun observations are not the worst example, of ghosting and scattered light effects.

Direct comparisons of the line intensities give a measure of the relative calibration between the different channels. An example is given in Figure 3.23, which shows the ratio of Mg VIII and Si VIII line intensities as observed in the NIS 1 and GIS 2. These ratios have been calculated leaving out only the sensitivity factor in the intensity calibration (i.e. taking into account the other different factors between the NIS and GIS calibration), and are therefore a direct measure of the relative sensitivity. The NIS channel around 319.8 Å has a sensitivity about a factor 0.12 lower than GIS 2. Also, the same ratios for all the different dates examined have the same averaged value, meaning that **the relative calibration at 320 Å between NIS 1 and GIS 2 has not changed over six months**, which is an important result. The same applies for the other possible combinations of channels. Figure 3.23 also shows the ratio between Mg IX 368 Å, the (usually) brightest line in NIS 1, and in second order in GIS 4. Again, the ratios have not shown appreciable variations in all the spectra examined.

A puzzling aspect that was apparent in all the observations is a tendency for the ratios

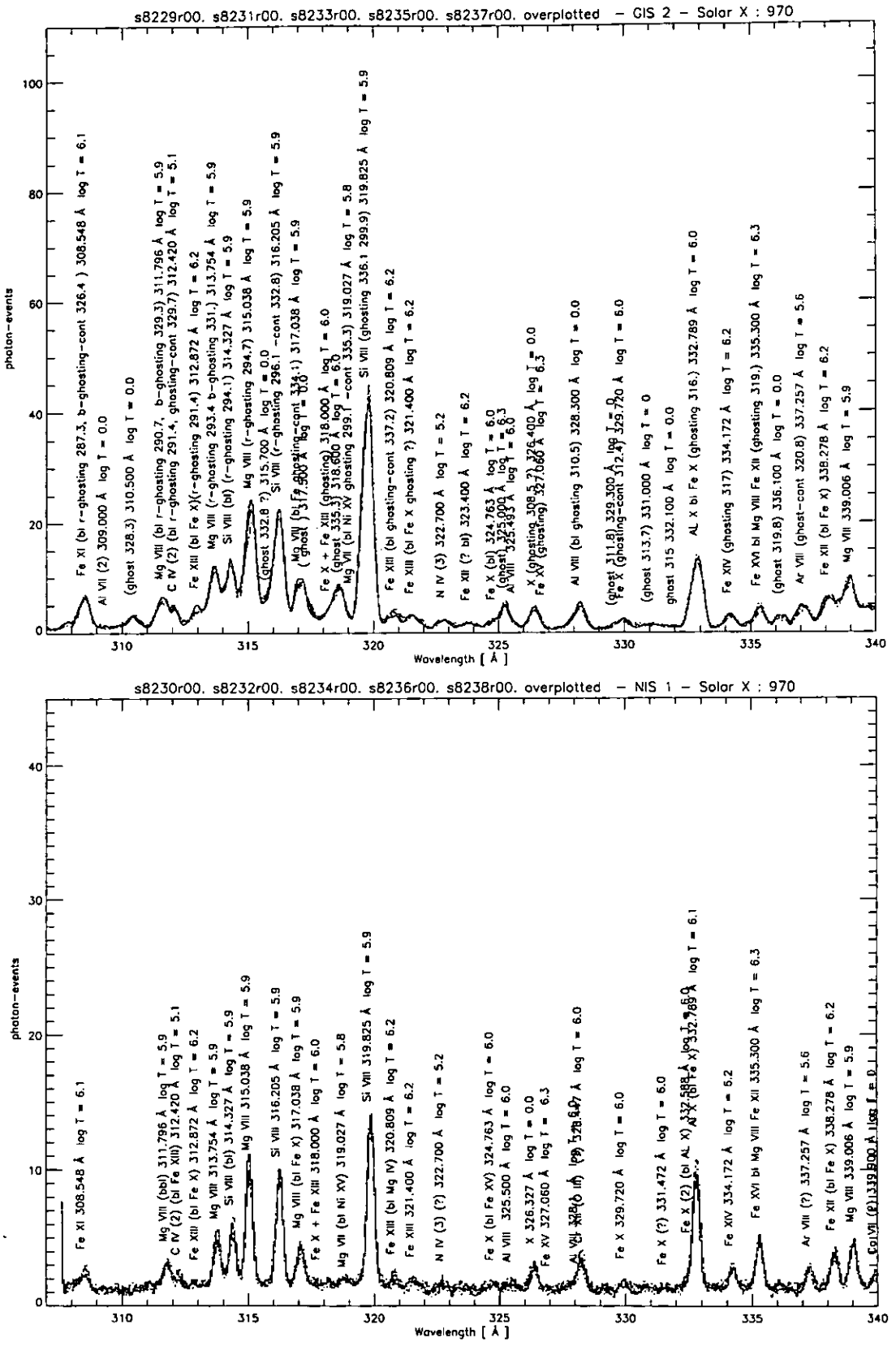

Figure 3.21: *The off-limb GIS and NIS spectra overlaid – 20th June 1997. Only the overlapping region is plotted. Note: (1) the small variation in time; (2) the large differences between the spectra, some of which can be ascribed to ghosting, other to different intensity calibration curves; (3) in particular how some of the GIS lines are depressed due to ghosting; (4) the ghosts that are present in the GIS spectrum.*

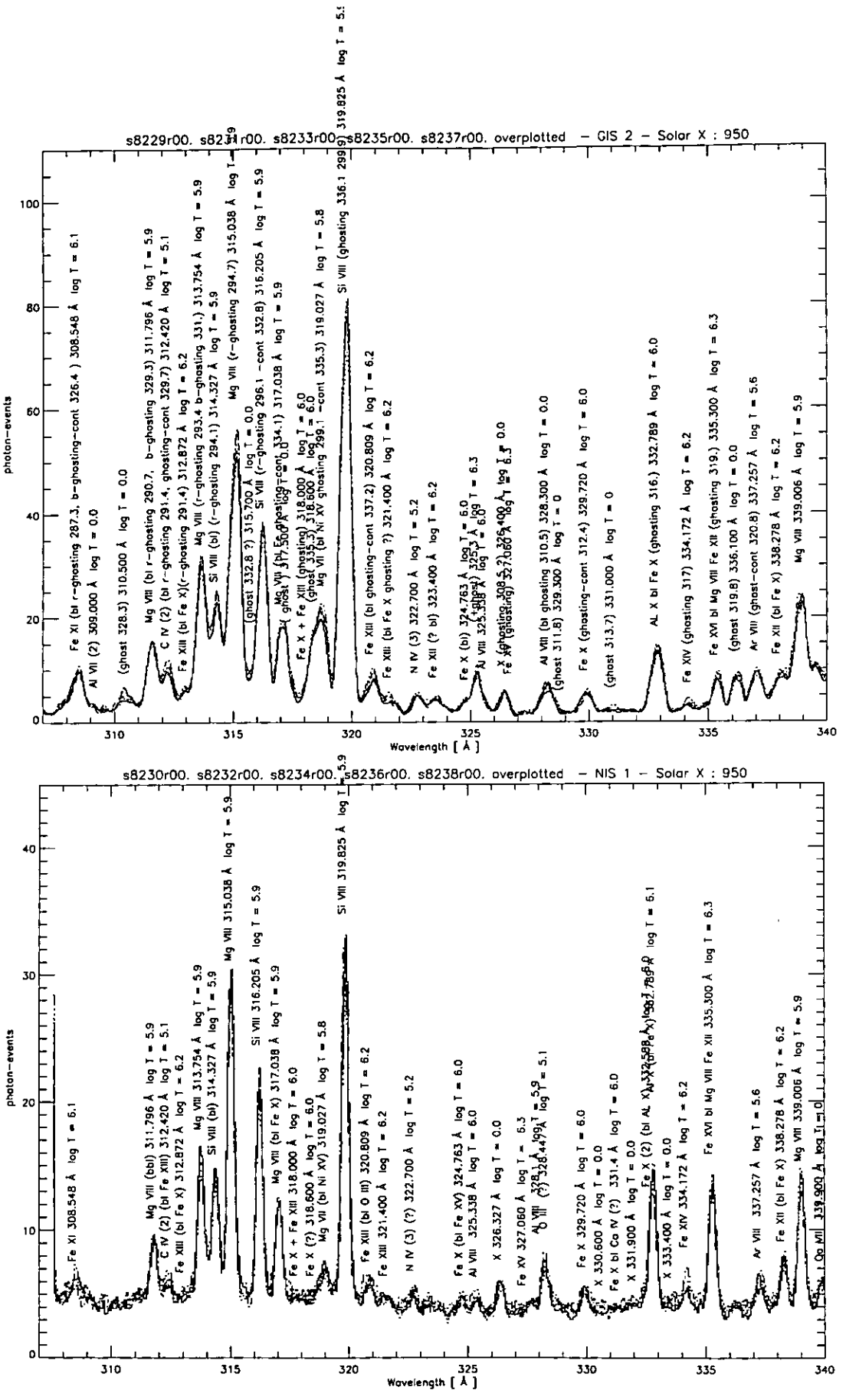

Figure 3.22: *The on-disc GIS and NIS overlapping region, as in Figure 3.21 – 20th June 1997. Note the higher background in the NIS spectrum.*

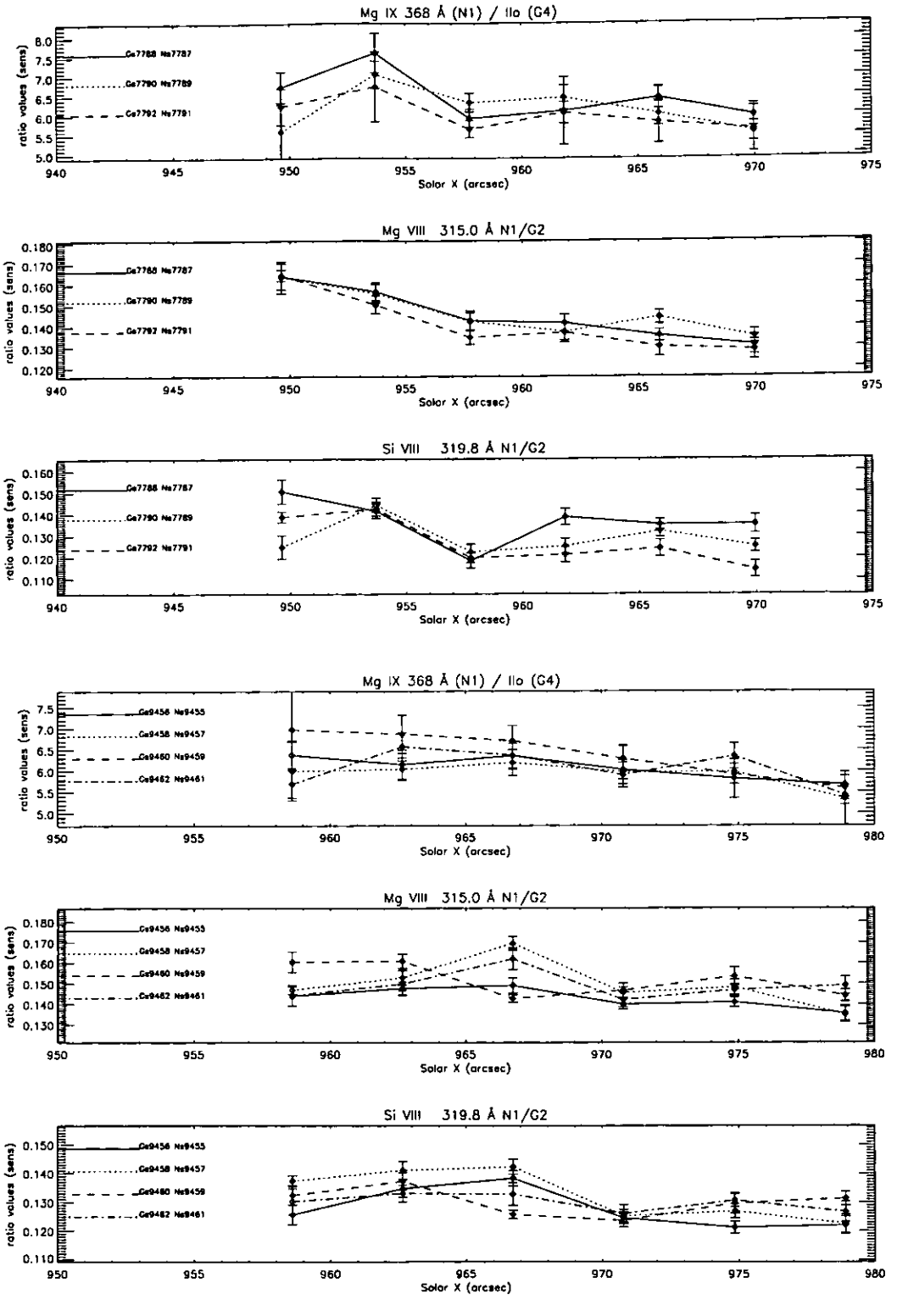

Figure 3.23: *The intensity ratios (calculated leaving out only the sensitivity factor) of the same lines observed in the NIS and GIS spectra – May 4th (upper three plots) and October 16th (below), 1997. Note: (1) how close the ratio values are for the two different dates, which is a direct confirmation of the fact that the relative sensitivities between the NIS 1 and GIS 2 (and NIS 1 and GIS 4, from the Mg IX 368 Å) channels have not significantly changed between May and October 1997; (2) a tendency for the ratios to be different on the disc; (3) that NIS 1 sensitivity at 319.8 Å is about a factor 0.12 lower than the GIS 2 one; (4) that the fact that the sensitivity ratio at 315 Å is higher implies a different wavelength dependence for the NIS 1 and GIS 2 sensitivities in that wavelength region.*

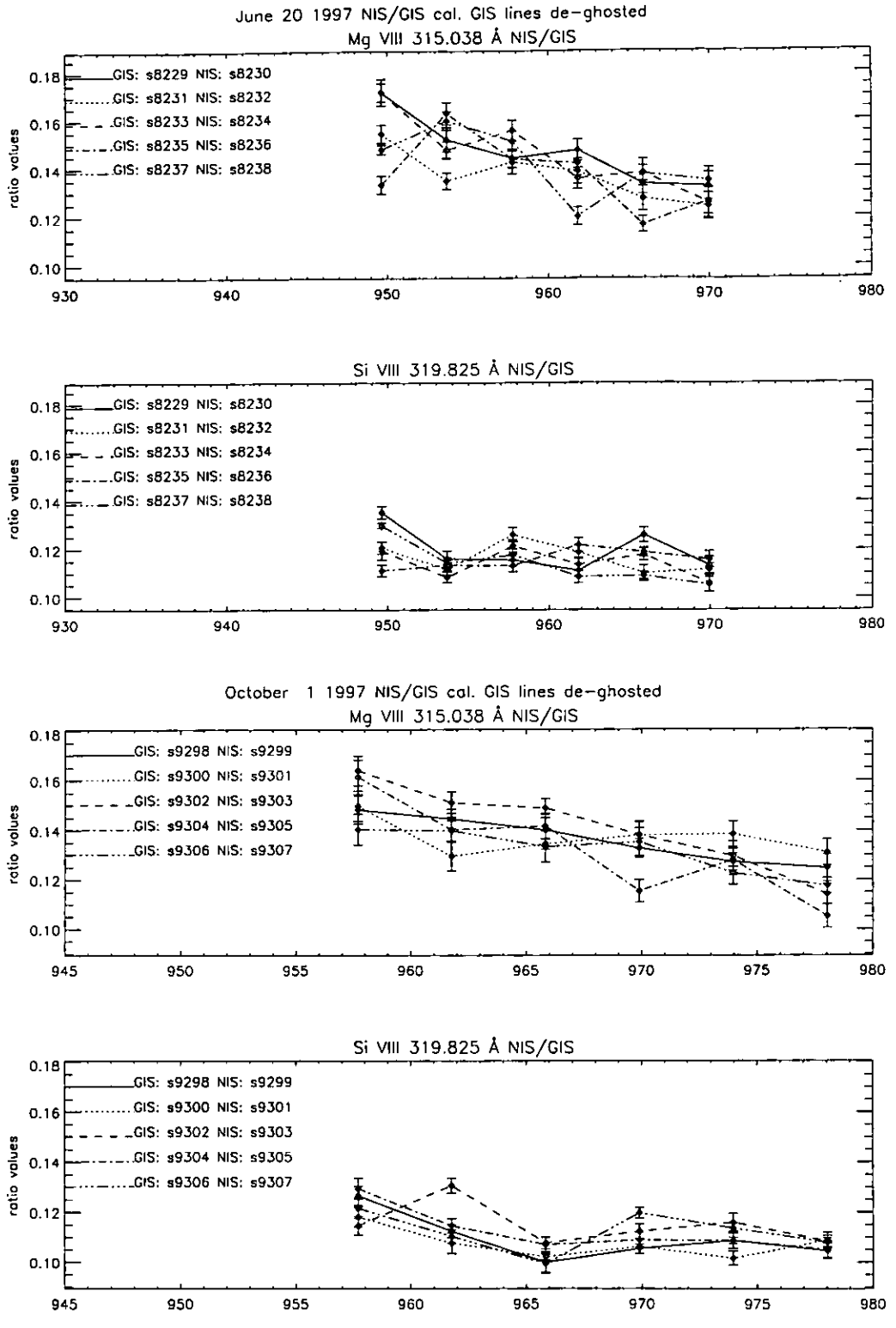

Figure 3.24: *The intensity ratios (calculated leaving out only the sensitivity factor) of the same lines observed in the NIS and GIS spectra – June 20th (upper two plots) and October 1st (below), 1997. Note that the relative sensitivities are the same as in Figure 3.23 (within the errors and the time variations) and that also in this case the sensitivity appears to be different between the on-disc and off-limb case.*

to be different on the disc, as partly shown in Figures 3.23 and 3.24. In general, all the NIS line intensities appear to be consistently shifted by a 10% as a whole, in respect to the other lines seen in the other CDS detectors. Apparently, the NIS 1 sensitivity varies between the on-disc and the off-limb observation by this amount. This effect will need a more complete analysis to be assessed. A brief discussion of it can be found in Section 3.4.8 below.

The lines of the same ion seen in different channels

Another step in the calibration was the analysis of temporal and spatial variations of all the principal lines observed in all the spectra, to find for each ion the best un-blended and not too density-sensitive lines, and for each date the best set of data. Figures 3.25,3.26, and 3.27 show some examples. These lines can be grouped in three classes:

1. Coronal lines. These lines appear in all the CDS spectra with the same characteristics. Some of these are shown by the constancy in space and time of their ratio values (see Figure 3.25).

2. Transition region (cool) lines. These lines are 'crucial' for a relative calibration of the NIS 1 and NIS 2 channels. In fact, as already mentioned, most of the NIS 1 lines are coronal lines, and most of those observed by NIS 2 are transition region ones, and these two channels can only be properly calibrated with the use of the GIS spectra, that observe both transition region and coronal lines in each channel, in particular in GIS 3. Unfortunately, some of these lines are partly density-dependent and, more important, present large intensity variations in time (on time-scales of minutes), and only a careful temporal analysis allows these lines to be used for calibration purposes. Figure 3.26 shows some of these ratios.

3. Blended lines. Among the brightest lines in the CDS spectra are the doublets, which are useful for calibration purposes, but that unfortunately, in most cases are blended with other lines. We have already seen the Fe XVI 335.4 complex case. Other examples are Al XI, Ca X and Mg X, the strongest lines in NIS 2 off-limb spectra which are blended with cool lines, as is evident from Figure 3.27. Therefore, only off-limb observations of these lines can be used for calibration purposes (unless the contribution from the cool line is theoretically removed, as many authors have done in the literature). The Ne VIII doublet of bright lines is not blended, but is shown in Figure 3.27 for comparison. These lines do not show appreciable spatial variation, and therefore show that if departures from the optically thin limit are present, they are very small, because the Ne VIII ratio is close to 2 (see *Doschek et al.*, 1981). On

the other hand, *Doschek et al.* (1998b) have found (from SUMER spectra) this ratio to have values of $\simeq$ 1.4 at the limb in coronal holes, with an implication of opacity effects. It is also assumed that no opacity effect is present in the other doublets, and indeed the CDS intensity calibration has been adjusted in order for these ratios to be 2 in the off-limb spectra.

Ghosting and the reconstruction of some lines

Some ghosts have been definitively identified, and the lines reconstructed. Table 3.4.6 presents an example of some of the ghosting reconstruction applied to a GIS observation, i.e. a list of some of the brightest 'pure' ghosts found, in which case it was possible to directly deghost some of the lines. The most impressive example of a ghost is the line at 744 Å, the ghost of the Ne VIII 770.409 Å. Typically, the intensity of these ghosts is more than 40% that one of the observed line. A reconstruction of the line permits to achieve an agreement with the other Ne VIII 780.324 Å line. The counts of each ghost have been transferred to the relative parent line. In some cases, a parent line created both red and blue-shifted ghosts. In many cases, these parent lines are contaminated by ghosts of other lines, and therefore their restored intensity should be taken with caution.

More complete reconstructions have been performed for the time-averaged spectra. More information on ghosting can be found in the Appendix, where some sample quiet sun on-disc and off-limb spectra are presented. Other examples of ghosting will be given throughout this thesis.

The NIS and GIS spectra of the quiet sun observations

Figures C.1, C.2, C.3, C.4, C.5, C.6 show the averaged off-limb CDS spectra of one of the two sets of May 4th 1997 observations. The pointing was sufficiently high above the limbs that all the transition region lines are completely absent. Also the stray light is almost absent, as can be judged by the disappearance of the bright chromospheric lines (e.g. the He I lines). These spectra are therefore very suitable for a study of the quiet sun off-limb spectra. Almost all the hundreds of lines have been identified with the diagnostic method, and are indicated in the figures.

Figures C.11, C.12, C.13, C.14, C.15, C.16 show the averaged on-disc CDS spectra of the October 16th 1997 observations.

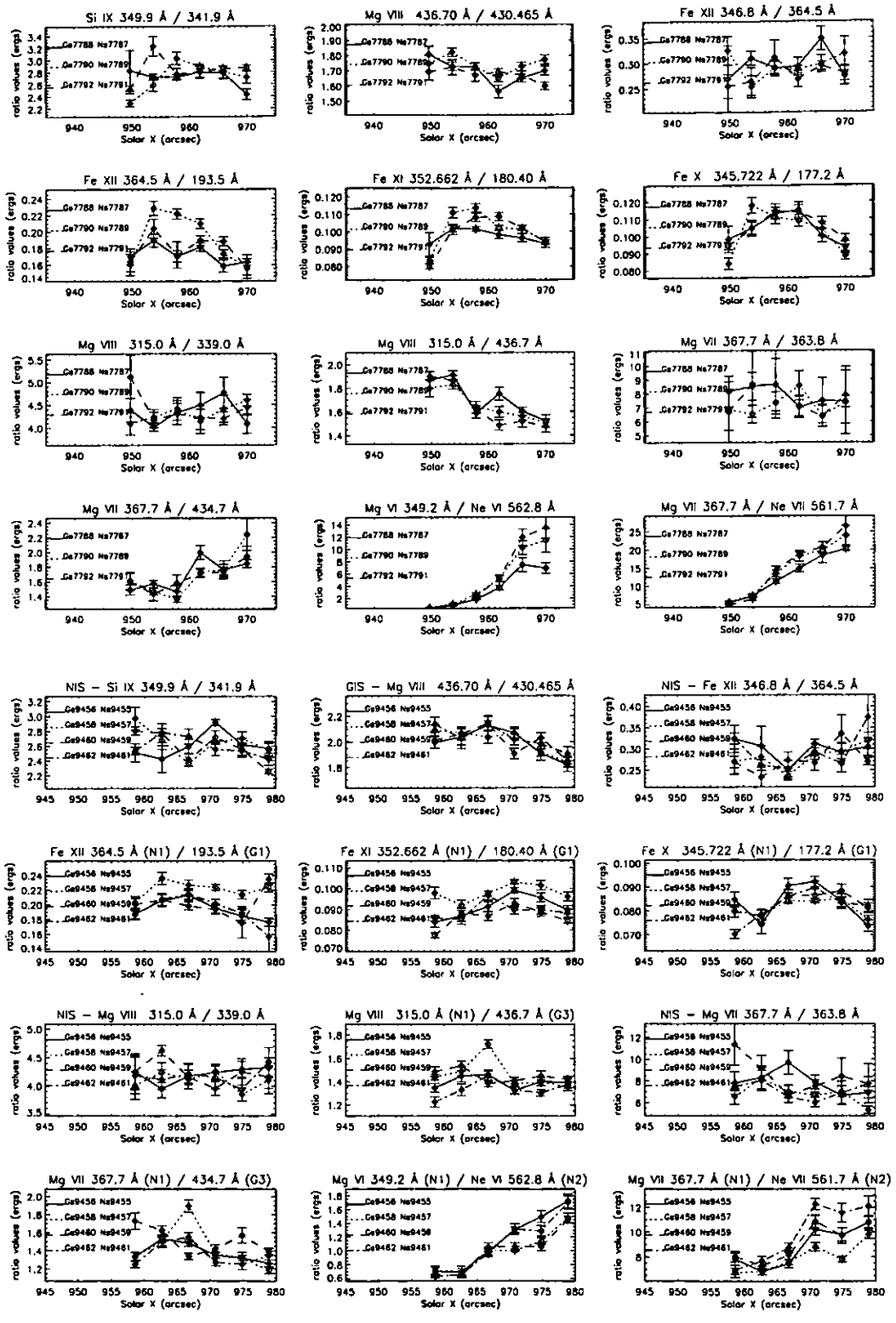

Figure 3.25: *Some intensity ratios of NIS and GIS lines, useful for the NIS/GIS cross-calibration, and for internal calibration within each detector – May 4th (upper four rows) and October 16th (below), 1997. The same intensity calibration has been applied for the two dates. Note: (1) that the density is fairly constant, as shown by the Si IX and Mg VIII ratios (first two figures on the left top corner); (2) that the relative sensitivities between the presented lines, originating from the same ion, and seen either within the same channel or in different ones, is relatively constant in time and in space (middle figures), and are therefore usable for calibration purposes; (3) that lines originating from different ions, as the Mg VI/Ne VI and Mg VII/Ne VII, are not usable for calibration purposes, as their ratio spatially varies by large factors (last two figures, bottom right).*

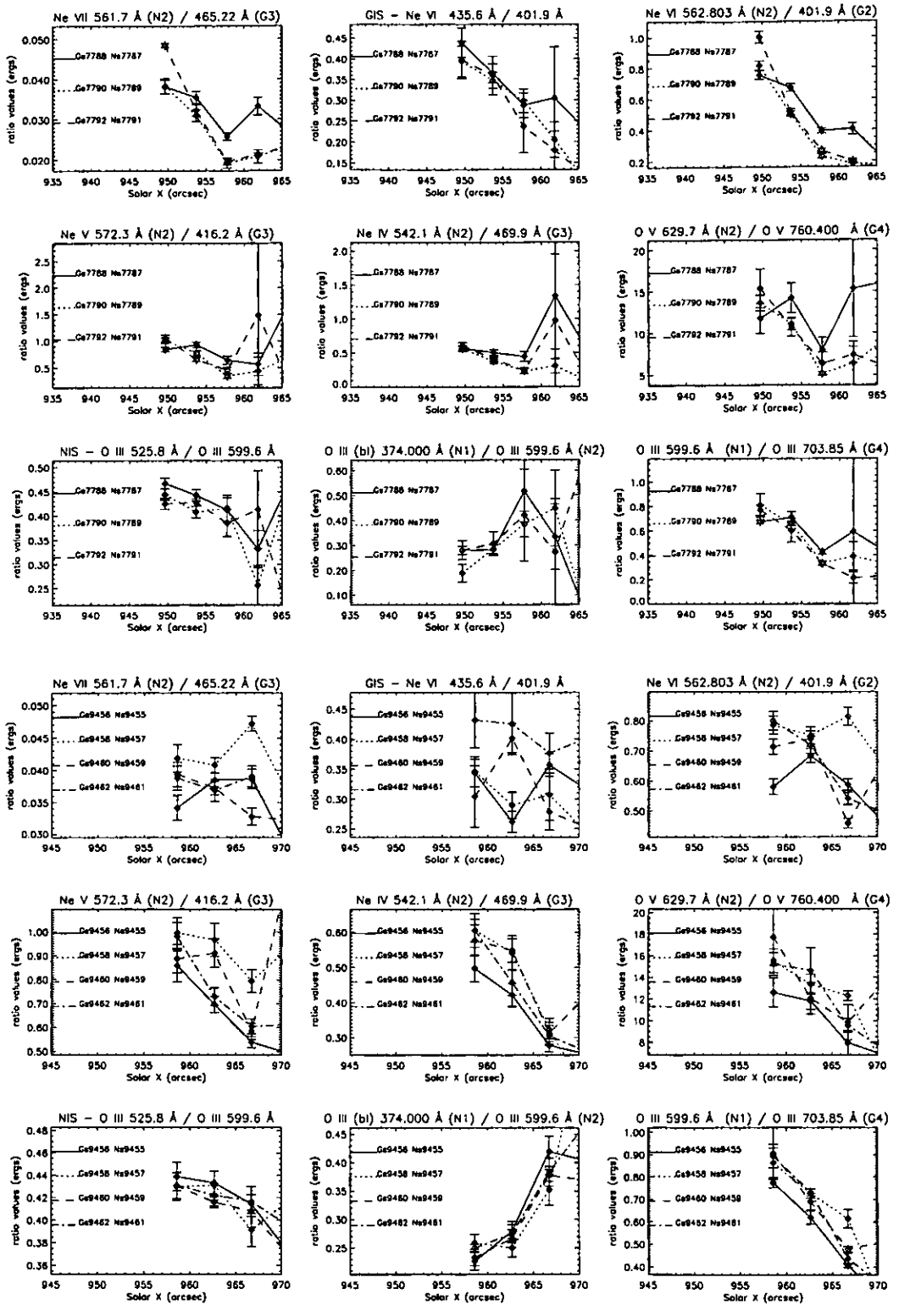

Figure 3.26: *Some ratios of intensities of NIS and GIS transition region lines, useful for the NIS/GIS cross-calibration, and for internal calibration within each detector – May 4th (upper three rows) and October 16th (below), 1997. The same intensity calibration has been applied for the two dates. Note: (1) how temporal variations are small, considering that these cool lines alway present large intensity variations; (2) how close the ratio values are for the two different dates, confirming that the relative sensitivities for the lines shown have been constant in time. These lines (among other not shown here) are therefore suitable for relative calibration purposes, for these observations. Only the values on the disc were used for the calibration (the first point, at Solar X* $\simeq$ *950″, 960″), since these lines disappear above the limb, see Figure 3.20.*

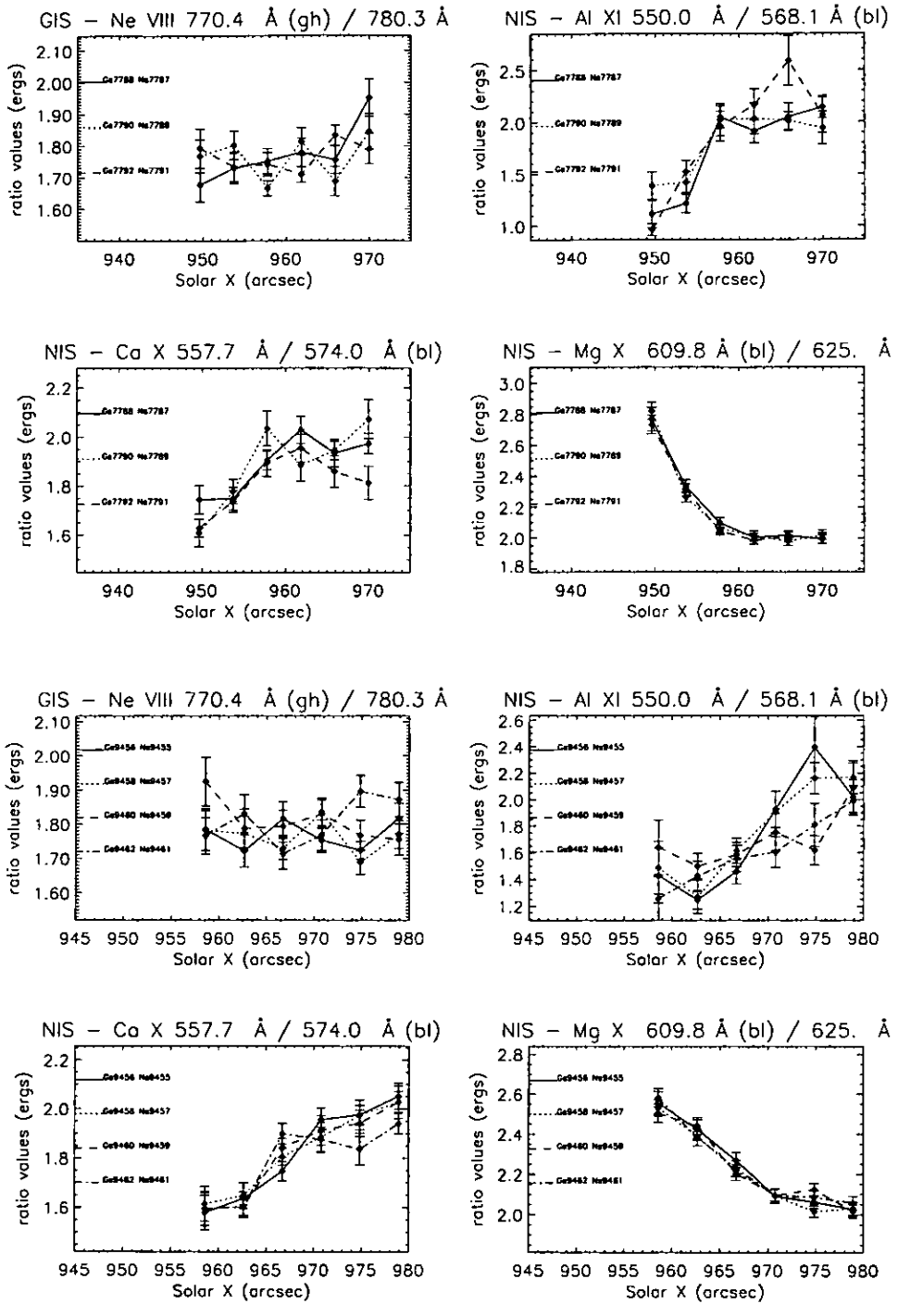

Figure 3.27: *The intensity ratios of the doublets (Li- and Na-like) seen in NIS and GIS – May 4th (upper four figures) and October 16th (below), 1997. The same intensity calibration has been applied for the two dates. The Al XI, Ca X and Mg X are the strongest lines in NIS 2 off-limb spectra and are useful for the internal calibration of NIS 2. Note: (1) the GIS line at 770.4 Å has been reconstructed from ghosting (by 40-70%); (2) that the Ne VIII ratio do not show much variation across the limb, suggesting small (if any) opacity; also, that the ratio value is close to the theoretical value of 2; (3) that in all the other three ratios one of the transition is strongly blended with an on-disc line, and is only off-limb that the blend disappears, and the ratios level toward the theoretical value of 2.*

Table 3.7: *Some of the ghosting reconstruction applied to the GIS observation s7792r00 (a) of May 4th, 1997 and s9462r00 (b) on October 16th, 1997. Each column gives the amount of correction applied for each of the six spatial locations. The corrections applied to the other spectra are similar to the (a) and (b) cases. The averaged positions of the ghost and ghosting lines are indicated. Then, for each spatial position, the ratio of the intensity of the ghost with that one of the ghosting line (in counts) is presented, together with the intensity of the ghosting line (in counts), in brackets. Note that the correction for ghosting is important for many lines. Some lines (Fe XVI 335.4 Å, and Mg VIII 436.7 Å) have been corrected twice, while some (Si VIII 319.8 Å) have been corrected for both the red- and blue-shifted ghosts. Also note that the amount of ghosting varies with the intensity of the ghosting line, for each observation, and that for some reasons ghosting was much higher for the October 16th observations (all the NIS-GIS observations presented in this Section had the same GSET_ID applied).*

ghost (157.24 Å) of Fe X 177.25 Å						
(a)	0.34 (727)	0.40 (1059)	0.43 (1345)	0.41 (1325)	0.40 (1212)	0.34 (1163)
(b)	0.63 (856)	0.70 (887)	0.74 (1039)	0.79 (1029)	0.74 (1026)	0.64 (1056)
ghost (160.63 Å) of Fe XI (bl Fe X) 180.47 Å						
(a)	0.20 (952)	0.22 (1314)	0.24 (1901)	0.24 (1976)	0.24 (1796)	0.21 (1722)
(b)	0.36 (1121)	0.39 (1239)	0.41 (1407)	0.40 (1556)	0.40 (1542)	0.35 (1561)
ghost (294.05 Å) of Si VIII 314.36 Å						
(a)	0.31 (146)	0.31 (224)	0.32 (311)	0.30 (284)	0.27 (256)	0.29 (216)
(b)	0.38 (200)	0.45 (219)	0.47 (276)	0.46 (323)	0.50 (300)	0.45 (263)
ghost (294.80 Å) of Mg VIII 315.1 Å						
(a)	0.28 (456)	0.35 (726)	0.37 (946)	0.33 (793)	0.29 (682)	0.25 (586)
(b)	0.49 (576)	0.50 (657)	0.55 (807)	0.57 (919)	0.56 (782)	0.45 (759)
ghost (296.99 Å) of Mg VIII (bl) 317.09 Å						
(a)	0.63 (123)	0.77 (202)	0.65 (300)	0.64 (270)	0.60 (218)	0.58 (186)
(b)	0.89 (176)	1.06 (172)	1.20 (226)	1.13 (243)	1.06 (230)	0.80 (255)
ghost (300.08 Å) of Si VIII 319.77 Å						
(a)	0.05 (533)	0.07 (872)	0.05 (1321)	0.04 (1179)	0.03 (999)	0.03 (837)
(b)	0.07 (808)	0.07 (915)	0.08 (1182)	0.07 (1350)	0.07 (1232)	0.05 (1154)
ghost (336.24 Å) of Si VIII 319.77 Å						
(a)	0.06 (559)	0.08 (931)	0.05 (1387)	0.03 (1221)	0.03 (1031)	0.04 (864)
(b)	0.08 (864)	0.09 (975)	0.09 (1271)	0.06 (1442)	0.06 (1314)	0.06 (1207)
ghost (318.1 Å) of Fe XVI (bl Mg VIII Fe XII) 335.33 Å						
(a)	0.47 (38)	0.80 (67)	0.36 (99)	0.45 (84)	0.66 (67)	0.29 (80)
(b)	1.45 (24)	0.73 (55)	1.30 (59)	0.66 (79)	0.64 (74)	0.92 (55)
ghost (318.67 Å) of Fe XVI (bl Mg VIII Fe XII) 335.33 Å						
(a)	2.96 (56)	1.98 (122)	2.53 (134)	2.15 (122)	1.82 (112)	1.61 (103)
(b)	4.34 (59)	3.17 (94)	2.63 (135)	3.08 (131)	3.00 (122)	2.87 (106)
ghost (408.61 Å) of Mg VIII (2) 436.8 Å						
(a)	0.07 (558)	0.08 (877)	0.11 (1212)	0.08 (1091)	0.06 (849)	0.05 (720)
(b)	0.12 (964)	0.10 (1053)	0.14 (1299)	0.16 (1399)	0.13 (1277)	0.10 (1173)
ghost (409.0 Å) of Mg VIII (2) 436.8 Å						
(a)	0.03 (594)	0.05 (944)	0.06 (1345)	0.06 (1177)	0.07 (902)	0.05 (756)
(b)	0.05 (1078)	0.08 (1156)	0.06 (1482)	0.07 (1619)	0.07 (1440)	0.05 (1289)
ghost (704.67 Å) of Mg IX (368.070 IIo) 736.0 Å						
(a)	0.13 (93)	0.19 (130)	0.23 (194)	0.15 (191)	0.18 (172)	0.10 (161)
(b)	0.20 (139)	0.07 (153)	0.22 (170)	0.24 (192)	0.06 (193)	0.18 (183)
ghost (744.16 Å) of Ne VIII 770.77 Å						
(a)	0.48 (366)	0.47 (528)	0.48 (747)	0.43 (625)	0.43 (503)	0.36 (447)
(b)	0.69 (337)	0.64 (426)	0.72 (412)	0.65 (497)	0.60 (456)	0.57 (398)

3.4.7 The physical characteristics of the off-limb (1997 May 4) and on-disc (1997 October 16) regions

Table 3.8 presents as an example the densities and temperatures derived from the 16th October (on-disc) and May 4 (off-limb) 1997 averaged spectra. All the other spectra examined, in October and June, have similar values. Note:

- that the densities and temperatures deduced from different ions and line ratios are close. In particular, the direct measurements from the temperature-sensitive Si XI 580.9 Å/ 303.3 Å(IIo) ratio are close to the other values which assume ionization equilibrium. However, the Si XI 580.9 Å/ 604.1 Å ratio instead gives higher temperatures, independent of the calibration used. Also, the density deduced from the Si IX ratios is similar to that obtained from the Si X ratio, thus suggesting that no corrections due to photoionization are therefore necessary for Si IX, at these densities.

- how a different calibration affects the physical parameters. The different sensitivity curve adopted has the effect of changing absolute values of densities, temperatures, and element abundances deduced from line ratios, although these changes can be within the errors when both lines fall in the same detector. In any case, it is important to consider how a different calibration could affect the physical parameters.

  Table 3.8 shows that the differences due to the use of the second standard NIS calibration (1999) are small, within the errors in most cases (the first NIS standard calibration – 1996-1998 – produced larger differences).

3.4.8 The NIS 1 internal calibration

The information from all of the observations mentioned above was used to constrain the NIS 1 sensitivity, i.e. find the wavelength dependence with the use of the diagnostic method. The resulting calibration is presented in figure 3.28, with other calibrations, for comparison.

The other curves represent:

- the first CDS standard calibration, which was based on the ground calibration (*Bromage et al.*, 1996 and *Lang et al.*, 1999). The data from *Lang et al.* (1999) are also displayed in the figure. It is evident that the ground calibration was obtained at only a few wavelengths. The two measurements around 360 Å suggested a constant sensitivity in this region. The wavelength dependence is that determined from theoretical calculations of various intensity ratios.

Table 3.8: *Table of some of the densities and temperatures deduced from the 16th October (on-disc) and May 4 (off-limb) 1997 averaged spectra. Temperatures were calculated at constant density* $N_e = 3.5 \times 10^8$ *and with the ionization equilibrium calculations of* Arnaud and Rothenflug *(1985). In some cases, the values deduced from the NIS second standard calibration (1999) are also shown.*

	on-disc			off-limb			
	ratio (counts)	ratio (calibrated)	value	ratio (counts)	ratio (calibrated)	value	
N_e(Fe XIV 353.831 / 334.172 Å)	1.45±0.35	0.85±0.20	$1.4 \times 10^{10} \pm 1.9 \times 10^{10}$	0.99±0.14	0.58±0.08	$5.0 \times 10^9 \pm 2.1 \times 10^9$	
(standard calibration)					0.75±0.11	$1.0 \times 10^{10} \pm 4.1 \times 10^9$	
N_e(Fe XIII 359.8 / 348.183 Å)	0.75±0.06	0.71±0.06	$9.4 \times 10^8 \pm 1.8 \times 10^8$	0.68±0.03	0.65±0.03	$7.9 \times 10^8 \pm 9.7 \times 10^7$	
(standard calibration)					0.57±0.03	$6.0 \times 10^8 \pm 7.3 \times 10^7$	
N_e(Fe XII 338.278/364.467 Å)	0.19±0.02	0.31±0.03	$1.4 \times 10^{10} \pm 4.7 \times 10^9$	0.14±0.01	0.23±0.01	$6.3 \times 10^9 \pm 1.2 \times 10^9$	
(standard calibration)					0.21±0.01	$4.7 \times 10^9 \pm 8.9 \times 10^8$	
N_e(Si X 356./347.4 Å)	0.76±0.02	0.73±0.01	$5.3 \times 10^8 \pm 3.1 \times 10^7$	0.65±0.01	0.62±0.01	$4.0 \times 10^8 \pm 2.2 \times 10^7$	
(standard calibration)					0.57±0.01	$3.3 \times 10^8 \pm 1.9 \times 10^7$	
N_e(Si IX 349.9/341.9 Å)	3.06±0.07	2.71±0.06	$5.0 \times 10^8 \pm 3.0 \times 10^7$	2.57±0.05	2.27±0.04	$3.3 \times 10^8 \pm 2.0 \times 10^7$	
(standard calibration)					2.29±0.04	$3.3 \times 10^8 \pm 2.0 \times 10^7$	
N_e(Si IX 349.9/345.1 Å)	1.09±0.02	1.03±0.01	$4.7 \times 10^8 \pm 2.8 \times 10^7$	1.00±0.01	0.95±0.01	$3.5 \times 10^8 \pm 2.1 \times 10^7$	
(standard calibration)					0.93±0.01	$3.3 \times 10^8 \pm 2.0 \times 10^7$	
N_e(Mg VIII 315.038 / 317.038 Å)	3.04±0.13	3.07±0.13	$1.2 \times 10^8 \pm 3.1 \times 10^7$	2.83±0.12	2.86±0.12	$8.9 \times 10^7 \pm 1.7 \times 10^7$	
N_e(Mg VIII 315.038 / 313.754 Å)	2.39±0.09	2.38±0.09	$1.9 \times 10^8 \pm 6.3 \times 10^7$	2.23±0.09	2.22±0.09	$1.3 \times 10^8 \pm 3.5 \times 10^7$	
N_e(Mg VII 319.027 / 367.67 Å)	0.12±0.02	0.36±0.06	$9.4 \times 10^8 \pm 3.1 \times 10^8$	0.10±0.01	0.28±0.04	$6.7 \times 10^8 \pm 1.4 \times 10^8$	
(standard calibration)		0.24±0.04	$5.3 \times 10^8 \pm 1.8 \times 10^8$				
N_e(O IV 625.853/608.397 Å)	0.07±0.01	0.06±0.00	$2.2 \times 10^{10} \pm 3.6 \times 10^9$				
(standard calibration)		0.07±0.01	$2.5 \times 10^{10} \pm 4.0 \times 10^9$				
N_e(Fe XIII 203.8 (2) / 202.0 Å)	0.37±0.06	0.37±0.06	$1.8 \times 10^8 \pm 1 \times 10^8$	0.29±0.08	0.30±0.08	$1.8 \times 10^8 \pm 1 \times 10^8$	
N_e(Fe X 175.3 (2) / 174.53	0.14±0.01	0.13±0.01	$1 \times 10^9 \pm 2 \times 10^8$	0.11±0.01	0.11±0.01	$6.7 \times 10^8 \pm 8 \times 10^7$	?
N_e(Mg VIII 436.7 (2) / 430.465	1.42±0.11	1.79±0.12	$9.4 \times 10^8 \pm 5 \times 10^8$	1.39±0.08	1.61±0.09	$3.3 \times 10^8 \pm 1.7 \times 10^8$	
(436.7 Ånot ghost-corrected)	1.42±0.11	1.48±0.11	$2.1 \times 10^8 \pm 1. \times 10^8$	1.39±0.08	1.45±0.08	$1.9 \times 10^8 \pm 6 \times 10^7$	
N_e(Mg VII 280.7 / 431.2 (2) Å)	0.09±0.03	0.19±0.07	$5.3 \times 10^8 \pm 2.5 \times 10^8$				
T_e(Si XII 520.7 Å/ Mg X 624.9 Å)	0.04±0.00	0.03±0.00	$1.2 \times 10^6 \pm 2.8 \times 10^3$	0.07±0.00	0.05±0.00	$1.2 \times 10^6 \pm 1.0 \times 10^4$	[a]
(standard calibration)					0.06±0.00	$1.2 \times 10^6 \pm 2.9 \times 10^3$	
T_e(Si XII 520.7 Å/ Si XI 580.91 Å)	0.55±0.05	0.45±0.04	$1.0 \times 10^6 \pm 1.1 \times 10^4$	0.84±0.03	0.69±0.03	$1.1 \times 10^6 \pm 7.3 \times 10^3$	
(standard calibration)					0.73±0.03	$1.1 \times 10^6 \pm 7.4 \times 10^3$	
T_e(Si XI 580.9 Å/ 303.3 Å) (IIo)	1.18±0.09	0.02±0.00	$3.5 \times 10^6 \pm 6.4 \times 10^5$	1.60±0.09	0.02±0.00	$1.6 \times 10^6 \pm 2.8 \times 10^5$	
T_e(Si XI 580.9 Å/ 604.1 Å)	4.92±0.57	3.94±0.46	$7.0 \times 10^6 \pm 1 \times 10^6$	7.34±0.87	5.89±0.70	$4.1 \times 10^6 \pm 5.9 \times 10^5$	
T_e(Fe XIV 334.2 Å/ Fe XIII 348.2 Å)	0.34±0.08	0.56±0.13	$1.5 \times 10^6 \pm 9.0 \times 10^4$	0.29±0.03	0.48±0.06	$1.5 \times 10^6 \pm 4.2 \times 10^4$	
(standard calibration)					0.35±0.04	$1.4 \times 10^6 \pm 3.6 \times 10^4$	
T_e(Fe XIII 348.183 Å/ Fe XII 364.467 Å)	0.27±0.02	0.31±0.02	$1.1 \times 10^6 \pm 1.8 \times 10^4$	0.23±0.01	0.27±0.01	$1.1 \times 10^6 \pm 1.0 \times 10^4$	
T_e (Mg X 624.9 Å/ Mg IX 368 Å)	0.59±0.00	0.16±0.00	$9.7 \times 10^5 \pm 2.2 \times 10^3$	0.62±0.01	0.17±0.00	$9.8 \times 10^5 \pm 2.3 \times 10^3$	
(standard calibration)					0.16±0.00	$9.6 \times 10^5 \pm 2.2 \times 10^3$	
T_e (Mg IX 368 Å/ Mg VII 367.7 Å)	7.44±0.22	7.23±0.22	$8.8 \times 10^5 \pm 4.1 \times 10^3$	12.90±0.51	12.53±0.49	$9.5 \times 10^5 \pm 4.4 \times 10^3$	
T_e (Mg IX 368.07 Å/ Mg VIII 315.04 Å)	7.22±0.13	2.39±0.04	$9.1 \times 10^5 \pm 4.2 \times 10^3$	12.10±0.24	4.01±0.08	$1.0 \times 10^6 \pm 4.7 \times 10^3$	
(standard calibration)					5.82±0.11	$1.1 \times 10^6 \pm 5.1 \times 10^3$	
T_e (Fe XII 364.47 Å/ Fe X 345.72 Å)	0.81±0.03	0.67±0.03	$1.1 \times 10^6 \pm 7.6 \times 10^3$	1.25±0.03	1.04±0.03	$1.2 \times 10^6 \pm 5.4 \times 10^3$	
T_e (Fe XII 364.47 Å/ Fe XI 352.66 Å)	0.69±0.03	0.60±0.02	$1.1 \times 10^6 \pm 1.0 \times 10^4$	0.90±0.02	0.78±0.02	$1.2 \times 10^6 \pm 8.3 \times 10^3$	
T_e(Fe XI 352.66 Å/ Fe X 345.72 Å)	1.18±0.02	1.11±0.02	$1.1 \times 10^6 \pm 7.5 \times 10^3$	1.39±0.02	1.32±0.02	$1.1 \times 10^6 \pm 7.9 \times 10^3$	
T_e(O V 629.732 Å/ O IV 608.397 Å)	17.06±0.16	14.81±0.14	$2.3 \times 10^5 \pm 5.3 \times 10^2$				

[a] assuming photospheric abundances

- The *Landi et al.* (1997a) calibration, increased by a factor of 2. *Landi et al.* (1997a) were not able to assess an absolute value of the sensitivity, but suggested that the NIS 1 sensitivities needed to be increased by a factor of between 2.5 and 5, relative to NIS 2.

- The second CDS standard calibration, introduced into the CDS software in December 1998. The absolute value at 368 Å, where the brightest NIS 1 line is, was derived from the *Brekke et al.* (1999) study (with a reported accuracy of 25%). However, the coarse resolution ($\simeq$ 5 Å) of the rocket flight spectrum, and the low signal-to-noise, did not allow a measurement of the wavelength dependence for NIS 1.

Superimposed on the off-limb calibration (thick solid line), some of the lines used to determine the wavelength dependence, are shown. The results from the on-disc observations, are not shown, since there is not much difference from the off-limb case (most of the NIS 1 lines are coronal), and the off-limb spectra have the advantage that they are not affected by scattered light blending with cool lines. The line identifications can be found in Table C.2.

For each ratio of two lines from the same ion, it was possible to determine the sensitivity ratio between the values at the wavelengths where the lines are, directly from the observed intensities (in phot-events) and the theoretical emissivity, *independent of element abundances, differential emission measure distribution, and ionization equilibrium.* These ratio values have been normalized and are shown in Figure 3.28. The following groups of lines were found suitable for calibration purposes, because they are well represented in CHIANTI-SERTS comparisons, are bright and do not appear to be blended in off-limb quiet sun observations:

- **Fe XVI** (335.41, 360. Å)

  Intensities from active region observations were used. In these cases, the 335.4 Å is all Fe XVI. Note that this measurement constrains the sensitivity ratio between those wavelengths. The *Landi et al.* (1997a) calibration also is also consistent with this line ratio.

- **Fe XII** (346.852, 352.106, 364.467 Å)

  These lines have already been described in Chapter 2. They are bright lines, free of blends in the off-limb spectra, and the agreement between CHIANTI and SERTS data is excellent. There is no reason why differences in the CDS observations should arise. These indicate an almost constant sensitivity at those wavelengths. The 352.106 Å line was used to normalize the ratio values of the lines shown in Figure 3.28.

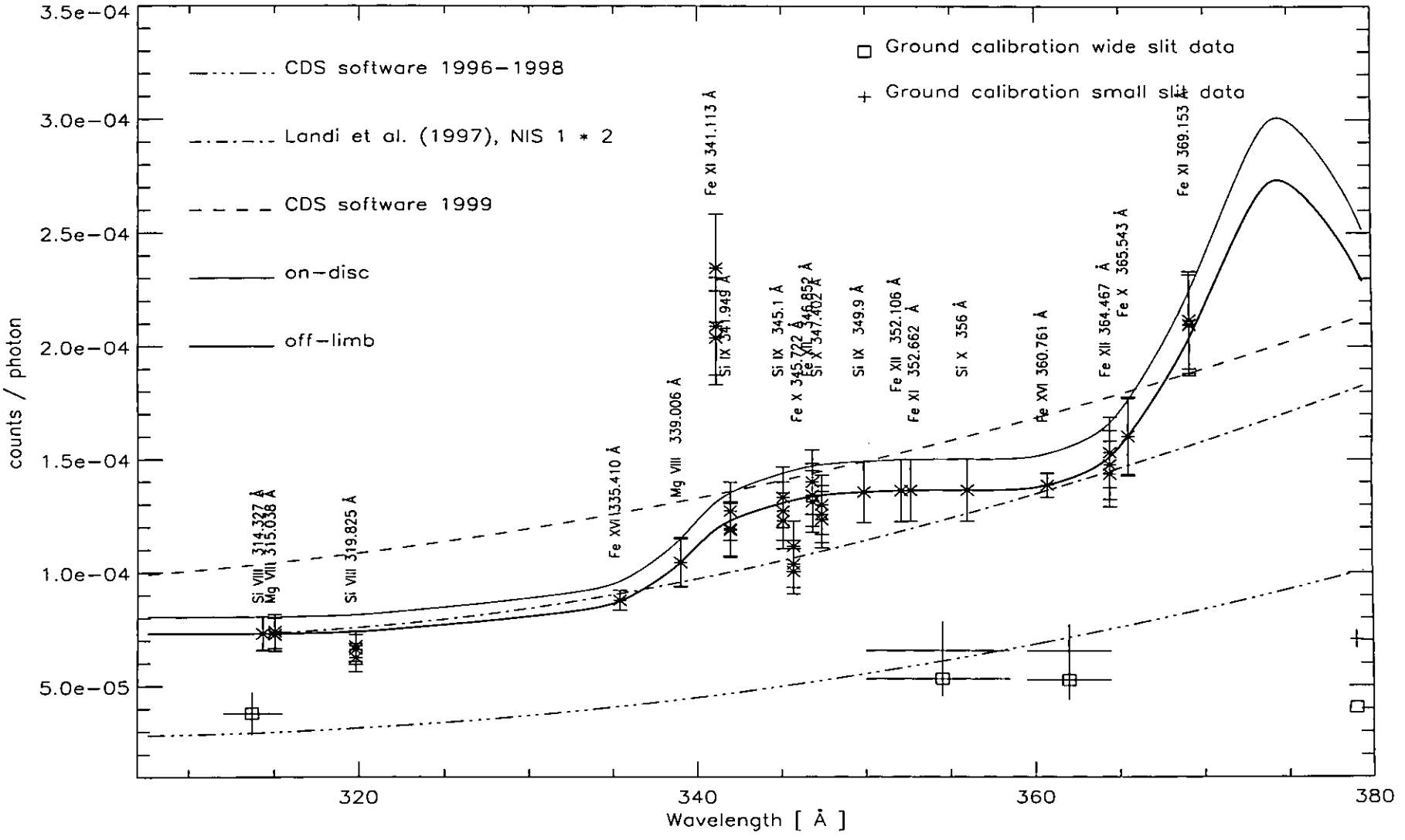

Figure 3.28: *The proposed CDS NIS 1 sensitivities (solid line), compared with the other calibrations.*

- **Fe XI** (341.113, 352.662, 356.519, 369.153 Å)

  The 369.153/352.662 is a branching ratio, well represented in the SERTS-89 observations. These lines are bright and well resolved, in particular in off-limb spectra, and require a large increase in the sensitivity toward the higher wavelengths. The Fe XI 341.113 Å is a bright well resolved line, that furthermore is well represented in the SERTS-89 case (also noted by *Young et al.*, 1998). However, in *all* the CDS spectra examined, this line is not well represented, and would require a much higher sensitivity than in the curve presented in Figure 3.28, where the 352.662 Å line was used as a reference line to normalize the other lines. The Fe XI 341.113 Å line therefore, must be blended in the CDS spectra. In the SERTS-89 spectrum, a very weak unidentified line is reported at 340.969 Å, with an intensity 0.17 times the intensity of the Fe XI line. Off-limb radial intensity profiles of the ratio of the 341.113 Å with the other Fe XI lines (not shown here), although changing, do not present large variations, and therefore the unidentified line that blends the 341.113 Å line must be a coronal line, and moreover not a high-temperature line (otherwise it would not contribute in the quiet sun on-disc or off-limb spectra). This therefore still leaves more than 30% of the observed line un-accounted for. This discrepancy would increase if a lower sensitivity at 341 Å is adopted. The 356.519 Å line is blended with an Fe XIV 356.641 Å line and is not directly usable.

- **Fe X** (345.722, 365.543 Å)

  These two bright lines form a branching ratio. The 365.543 is blended with a bright Ne V line in on-disc observations. In the off-limb observations, this line should be free of blending, and can be used in conjunction with the 345.722 Å to constrain the relative sensitivity between those wavelengths. This branching ratio would require a lower sensitivity at 345 Å than is presented here, and is therefore not in agreement with the results, unlike the SERTS-89 case. The region between 340 and 350 Å therefore has inconsistencies that will require more investigations.

- **Mg VIII** (315.038, 335.253, 339.006 Å)

  The Mg VIII (315.038, 339.006) lines always show a constant ratio (within few %), independently of the observed region and provide a good constraint on the relative sensitivity between those wavelengths. The 335.253 Å line is only usable as a check, because even when the Fe XVI contribution is absent, there is a non-negligible contribution from a previously unidentified Fe XII line, as explained below.

Also note:

- **Si IX and Si X**

Although the Si IX and Si X lines are density-sensitive, and were therefore not used as calibration lines, their normalised ratios are also plotted in Figure 3.28, to show that, within the errors, these ratios are all consistent with the curve of sensitivity that is presented here. As already shown, however, for the purposes of density diagnostics, a different sensitivity curve in the 340-360 Å region does not significantly affect the results. If Fe X is to be believed, then the sensitivity curve should be less constant, with effect of having slightly lower densities as derived from the Si IX and the Si X ratios. However, this would leave unexplained why the Fe XI and Fe XII would be wrong (being the Fe XII well represented in other spectra as SERTS).

- In most of the observations analysed the above lines provide similar ratios (only some are shown in Figure, and show the small scatter in the ratio values from different observations).

- The apparently unconstrained regions of the sensitivity curve are in fact constrained by lines of other ions, that are not shown in the figure. Among them are all the Fe XIII, Fe XIV, Fe XV lines that span almost the *whole* NIS 1 channel (from 308 to 373 Å), already shown in the active region spectrum. These confirm the calibration proposed here. Also, there are related lines in other channels which constrain the NIS sensitivity subject to the calibration of the other detectors. For example, the group of O III/N III lines $\sim$ 374 Å can be used in conjunction with the O III lines seen in GIS 4 and NIS 2. These also indicate much increased sensitivity at these wavelengths. The (uncertain) downturn at the end of the detector is constrained by the presence of the Ca IX-Na VII blend at 378 Å.

- The absolute values of the NIS 1 calibration are deduced from a relative calibration study that is described in Section 3.4.10.

- The absolute values almost coincide at 368 Å with the only reliable NIS 1 measurement cited in *Brekke et al.* (1999), producing *excellent agreement* with the rocket flight calibration.

In all the on-disc observations examined the sensitivity of all the NIS channel apparently increases by about 10%, as already indicated by the direct NIS 1 / GIS 2 comparison of the overlapping region (Section 3.4.6). These variations cannot be ascribed to variations in effective areas, nor to non-linear effects, for example, and remain unexplained. Departures from the optically thin limit can be ruled out, as are variations of the physical conditions for the coronal lines that are present in NIS 1, that are not substantially changing, as shown in Figure 3.25. The only effect that affects the NIS 1 channel as a whole is the scattered light (see e.g. Figure 3.38), which could therefore be related to this peculiar fact.

In fact, different selections of the background can easily account for a change in the line intensities up to factors of 15%. However, a 10% difference, even if real, is still well within all the other uncertainties in the observations and atomic physics (that are intrinsically difficult to estimate), that can be summed to at least 20-30%.

3.4.9 The NIS 2 internal calibration (first order)

Unlike the NIS 1 channel, there are not many lines emitted by the same ion that are seen in NIS 2. Moreover, some of these lines are complex blends between 'cool and hot' lines, and with second order lines, as already shown. The useful lines can be grouped into two classes:

1. The chromospheric and transition region (cool) lines that are only visible in on-disc quiet sun observations. Active region observations have to be avoided because of strong blending with second order lines.
2. Coronal lines observed in off-limb quiet sun observations. The active region observations produce second order lines that blend with some of the lines in the off-limb observations. The off-limb observations are required to eliminate the contribution from the cool lines to the coronal lines, as already shown in Section 3.4.6 (see e.g. Figure 3.27).

All the on-disc quiet sun NIS observations analysed have been used to constrain the sensitivity using the first group of lines, while all the off-limb quiet sun observations have been used in the other case. The information from such off-limb and on-disc observations is summarised in Figure 3.29, proposing a new calibration, scaled to match the *Brekke et al.* (1999) value at 584 Å. As in the NIS 1 case, the result is compared with the other calibrations in the last three years:

- the first CDS standard calibration, that was based on the ground calibration of *Bromage et al.* (1996). The most reliable measurements obtained there were from the wide slit He I (584.3, 537 Å) observations. Both these observations indicated the same sensitivity value of 0.00040. The measurement at 537 Å was adopted, and a linear variation along the detector was introduced to explain the O III (525.8/599.6 Å) ratio observed in-flight. The ground He I measurements were therefore not in agreement with the in-flight observations.
- The *Landi et al.* (1997a) calibration. The main features are an almost constant sensitivity along the central part of the channel, with an increase at the shorter wavelengths and a downturn at the end of the detector.

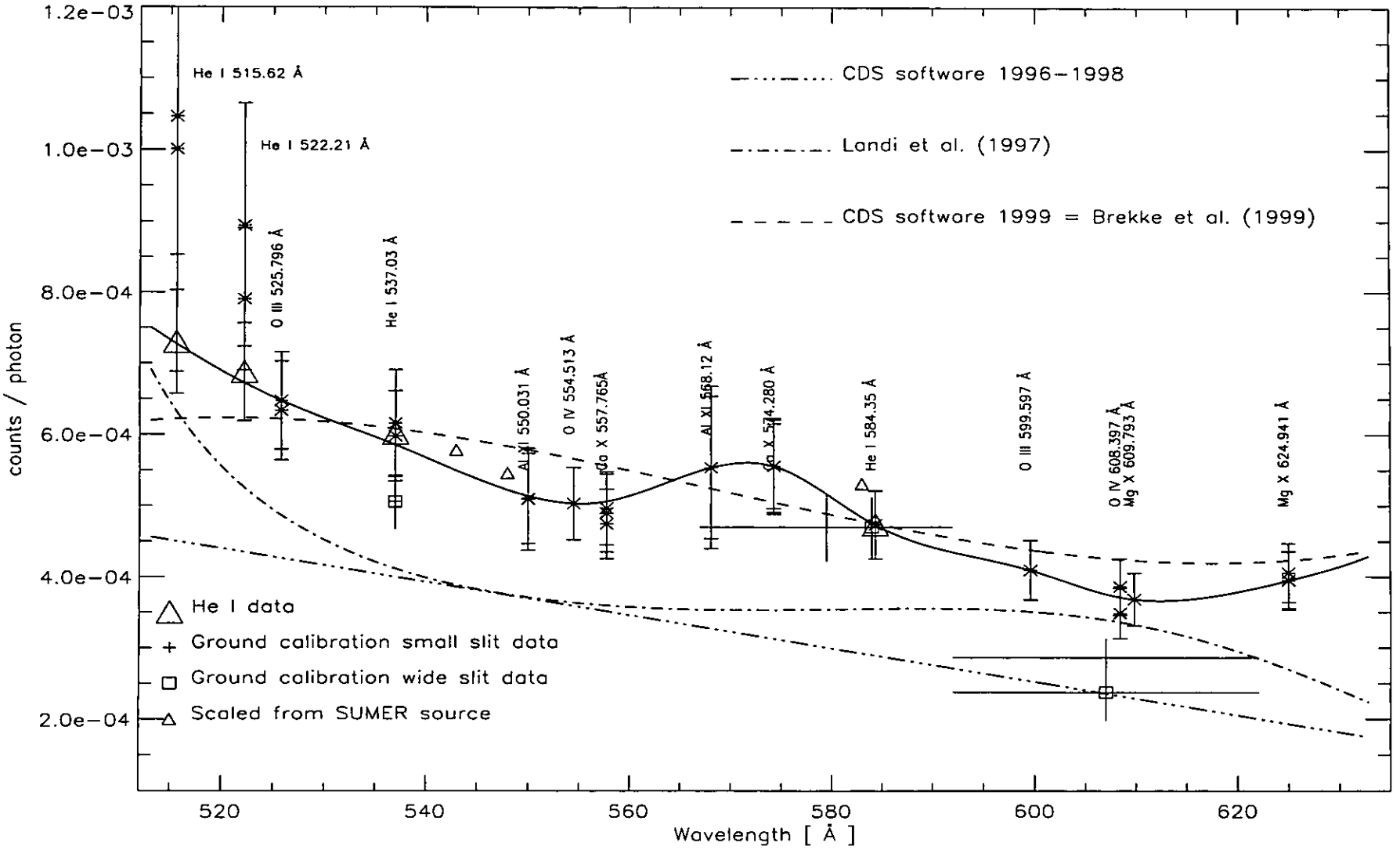

Figure 3.29: *The proposed CDS NIS 2 sensitivities (solid line), compared with the other calibrations.*

- The second CDS standard calibration, introduced into the CDS software in December 1998. This calibration is based on the *Brekke et al.* (1999) study. For the NIS 2 channel, in fact, the signal was sufficient to allow an estimate of the background intensity. The main features are an increased absolute sensitivity, by a factor of 1.6 compared to the previous ground calibration, a rise at the high wavelength and a downturn at wavelengths below 530 Å. The cited accuracy in terms of absolute values ranges from 15% at 584 Å, to 25% at either end of the spectrum. However, additional uncertainties (although ruled out in their paper) could be due to the fact that the rocket flight observed the sun as a star, and the CDS observations were not simultaneous.

- The revised ground calibration data of *Lang et al.* (1999) are displayed in the figure, with the same symbols as in their report. The main changes, compared to the previous ground calibration, are an increase in the absolute values of the wide slit He I data. In addition other measurements (done with wide and narrow slit). It should be noted that the measured values reported in *Lang et al.* (1999) are not in good agreement with the expected theoretical curve. The revised absolute value at 584 Å is instead in excellent agreement with the value derived by *Brekke et al.* (1999), suggesting that the NIS 2 sensitivity did not appreciably change over a long period of time (unlike the NIS 1 one). However, the other He I value at 537 Å (square box in the figure), nor the measurements around 610 Å(that indicate a very low sensitivity), are not in agreement with the value measured by *Lang et al.* (1999), as the Figure shows. While the measurement at 610 Å is not reliable (B. Bromage, 1999, priv. comm.), the He I measurement is, and the discrepancy cannot be easily explained, unless in-flight modifications of the NIS 2 sensitivity have taken place.

The transition region and chromospheric lines

The useful lines are:

O III (525.796, 599.597 Å) lines. Note that in active region spectra the 525.796 Å line is partly blended with Fe XVI 263 (second order). There is also an O III line at 597.817 Å which is weak and might be blended, although it is always in good agreement with the other two lines.

O IV lines. The O IV 608.397 was used in conjunction with any of the other O IV lines at 553-556 Å. The O IV line (three transitions) visible at 617.0 Å is very weak and partly blended with second order lines.

He I lines (515.62, 522.21, 537.03, 584.35 Å).

As noted by previous authors (e.g. *Andretta and Jones*, 1997, and *Macpherson and Jordan*, 1999), all the lines of the sequence present similar characteristics, independent of the type of solar region observed. In particular, the ratios of the line intensities versus the 584.35 Å intensity is very constant, as shown in Table 3.9, which reproduces the calibrated He I averaged intensities of *Vernazza and Reeves* (1978), together with the theoretical values in the optically thin approximation (using the Arcetri spectral code). This finding has been confirmed by the analysis of the on-disc NIS 2 spectra. This fact makes these lines suitable for an in-flight calibration. Unfortunately, there are no well calibrated recent He I line intensities, and the only set of well calibrated values are indeed those reported in *Vernazza and Reeves* (1978), which rely partly on previous rocket flights. However, assuming that the calibration is correct, then the CDS observations imply that the sensitivities at those wavelengths are those indicated by the large triangles in Figure 3.29(the values have been normalized at 584 Å). The values that the sensitivities should have if the He I emission is optically thin (a strong assumption for the He I lines, see the above-cited studies of *Andretta and Jones*, 1997, and *Macpherson and Jordan*, 1999, and references therein), are also shown in the Figure. It is interesting to note that:

- the 584 and 537 Å lines appear to be effectively optically thin.
- the sensitivity at 537 Å, derived from the *Vernazza and Reeves* (1978) calibrated values (and from the theoretical emissivities) are in excellent agreement with the *Brekke et al.* (1999) value, but not with the ground calibration value.
- The *Vernazza and Reeves* (1978) of the other two He I lines require an upturn of the sensitivity at the shorter wavelengths, and not an upturn, as suggested by *Brekke et al.* (1999). However, this upturn is not as steep as suggested by the *Landi et al.* (1997a) study.

Table 3.9: *The ratios of the calibrated He I intensities of* Vernazza and Reeves *(1978) for the various solar regions (QS: quiet sun; CH: coronal hole; AR: active region; cc: cell centres; net: network), with the theoretical ratios, calculated assuming optically thin emission. Note the small variations of these ratios, and how close they are with the predicted values. At the bottom, the calibrated intensity of the 584.35 Å is reported, to show the large variations of the observed intensities.*

ratio	QS avg	QS cc	QS net	CH avg	CH cc	CH net	AR	AR active	calculated
515.62/584.35 Å	0.028	0.028	0.031	0.024	0.022	0.032	0.027	0.027	0.021
522.21/584.35 Å	0.050	0.048	0.053	0.054	0.054	0.055	0.043	0.045	0.044
537.03/584.35 Å	0.130	0.128	0.132	0.136	0.132	0.142	0.113	0.115	0.133
I (584.35 Å)	544.98	426.22	827.71	250.12	221.93	300.94	5470.68	7233.50	

The coronal lines

NIS 2 observes the bright doublets: Ca X (557.765, 574.010 Å); Al XI (550.031, 568.12 Å) and Mg X (609.793, 624.941Å). In on-disc observations the Ca X 574.010 Å is blended with a C III 574.279 Å and the Mg X 609.793 is blended with a bright O IV 609.829 Å line. The Al XI 568.12 line is blended in active region observations with two second order lines (Fe XV and Al IX at 284.1 Å), and in on-disc observations with Ne V at 568.417 Å. In particular, the two Mg X lines have been used to determine the relative calibration between 610 Åand 625 Å, using off-limb observations.

Other lines

As in the NIS 1 case, other lines have been used to obtain a consistent calibration relative to the other CDS channels, and are not shown for simplicity in Figure 3.29. These are emitted from other ions that produce lines seen in the other CDS detectors. More details of the relative calibration are given in Section 3.4.10. Just as an example, the upturn at the longer wavelengths has the effect of reducing the calibrated intensity of one of the brightest lines in NIS 2, O V 629.732 Å, by almost a factor of 2. Only with this upturn it is possible to find a good agreement with the multiplet O V lines seen in GIS 4 $\simeq$ 760 Å. Also, when deducing emission measure (or DEM) the O V 629.732 Å line is out by a factor of 2 in intensity, compared to the other lines, when using the first standard CDS calibration.

Concluding comments on the NIS 1 and NIS 2 sensitivities

The only direct in-flight absolute calibration study is that of *Brekke et al.* (1999). In considering a detailed comparison with the diagnostic study presented here, it should be noted that the coarse resolution ($\simeq$ 5 Å) of the rocket flight spectrum limited the evaluation of the instrumental background, increasing the uncertainty. The spectra have been binned into six wavelength regions, and the background estimated from the (very) few regions free of line emission. With this in mind, the main differences (almost within the errors) between the in-flight calibration study of *Brekke et al.* (1999) and the NIS 2 relative calibration presented here are:

- the upturn in the calibration presented here at the shorter wavelengths. However, the downturn at wavelengths below 530 Å is regarded as uncertain by these authors, because of low signal.

- a decreased sensitivity at 610 Å, as derived from the O III and O IV lines. However, the region around 600 Å proved difficult to fit and was discarded in their work.
- The region between the He I 537 and 584 Å shows more variation in sensitivity in the calibration proposed here. However, one of the six wavelength bins (the central one) in the *Brekke et al.* (1999) study spanned the 545-575 Å range, and therefore the two calibrations are not in disagreement (the averaged sensitivity in the 545-575 Å range is similar).

Note that the upturn at the longer wavelengths was not expected from theoretical calculations of the sensitivity. In general, most of the ground calibration measurements, and the theoretical variation of the sensitivity are not in accordance with either direct in-flight (*Brekke et al.*, 1999) cross-calibrations, nor with the in-flight diagnostic study presented here. Therefore, there is no sensible reason why the even fewer ground measurements or theoretical curves for the NIS 1 channel (and the GIS ones for that matter) should be reliable, at least if accuracies of 20-30% are sought. Also, in terms of relative values between NIS 1 and NIS 2, the ground calibration data imply a much lower sensitivity than that one measured in flight, by both the present and the (*Brekke et al.*, 1999) study, by factors of more than 2. These differences could be due to the reflectivity of the optical parts (e.g. mirrors, gratings) having changed in-flight, or to the different illuminations, for example. The theoretical curves, based on the expected reflectivity of the optical parts were also not very accurate, probably, or in any case can not be directly applied to the in-flight data. Similarly, also the second order NIS sensitivities, and the GIS sensitivities presented here significantly differ from the pre-flight measurements, as Figure 3.30 shows.

More comments on the NIS 1 and 2 calibration can be found in Sections 3.4.11 and 3.4.12, where particular observations are presented.

3.4.10 The cross-calibration between all the NIS and GIS channels, first and second order

The whole process is an iterative one, only briefly outlined below. First, the internal calibration within each GIS channel was studied, following the same method explained in detail for the NIS 1 and NIS 2 case. However, only in the GIS 1 and GIS 2 spectra are there pairs of lines emitted by the same ion, which can be used for this purpose. The complete calibration of all the GIS spectra therefore relies on the cross-calibration with the NIS detectors. Also, the relative calibration between NIS 1 and NIS 2 depends on the GIS calibration. The procedure was to assume valid the internal NIS 1 and NIS 2 sensitivity curves shown above, and then cross-calibrate each GIS channel.

Cross-calibration between the NIS 1 and GIS 2

The cross-calibration in the overlapping region is straightforward, since both channels detect the same lines. The Si VIII 319.825 Å has been used to scale the relative sensitivities. This line has been chosen because it is the brightest line, is un-blended, not density-dependent, and is the only one in the overlapping region that is not significantly affected by the ghosting. In fact, it creates two weak ghosts in regions free of lines, and therefore it was possible to reconstruct this line. The values of the relative NIS 1/ GIS 2 sensitivity at 319.825 Å (as in Figure 3.23) have been deduced from the off-limb observations, where the contribution from the scattered light, that not only creates a background diffuse light, but is variable in time, is not present. The May, June, and October 1997 off-limb observations are all in accordance, suggesting that in that period the relative sensitivity between NIS 1 and GIS 2 had not appreciably changed. As already mentioned, the on-disc observations are not in close agreement with the off-limb ones, and present an apparent decrease of the GIS / NIS sensitivity of about 10%.

Other lines in the GIS 2 channel were used to derive the wavelength dependence. These include lines from Fe XIV, Fe XV, Fe XVI, Si X, Si VIII, Mg VII, using off-limb NIS/GIS and GIS active region observations.

Cross-calibration between NIS 1 and GIS 1

This is also relatively straightforward, since NIS 1 and GIS 1 observe in any on-disc or off-limb case many Fe X, XI, XII, and, in active region spectra, also bright Fe XIII and Fe XIV lines. Density-sensitivity is an issue for many of these lines, so the off-limb quiet sun spectra are again the best, because the density there is well established. Some of the useful bright lines are:

- Fe X: 345.722, 365.543 Å (NIS 1); 174.534, 177.242, 184.543, 190.0 Å (GIS 1).
- Fe XI: 352.662, 356.519, 369.153 Å (NIS 1); 180.4, 182.169, 188.2 (188.232+188.299) Å (GIS 1).
- Fe XII: 346.852, 352.106, 364.467 Å (NIS 1); 192.393, 193.521, 195.100 Å (GIS 1).
- Fe XIV: 334.172 Å (NIS 1); 211.320 Å (GIS 1).

Cross-calibration between NIS 1 and GIS 3

The calibration of the central part of GIS 3 was carried out using the bright Mg VIII and Mg VII lines visible in the 429-437 Å region with the Mg VIII and Mg VII lines seen in

NIS 1. The quiet sun off-limb observations are the most suitable, because the ghosting of the GIS lines can be checked (see below), and because blending with second order lines is negligible. The Mg VIII lines are more suitable than the Mg VII lines, because they vary much less with time.

GIS 3 also observes many Mg IX lines (439.176, 441.199, 443.973, 448.293 Å) that could be used in conjunction with the bright resonance 368.070 Å line observed in NIS 1. However, although excellent agreement among the GIS lines was found, no agreement with the 368.070 Å line could be found, confirming the SERTS-89 results described above.

Cross-calibration between the NIS 1 and NIS 2

The diagnostic method is almost unapplicable, since in NIS 1 and NIS 2 there are only a few cool lines emitted by the same ions. Only quiet sun on-disc observations, where the scattered light adds uncertainty in the measurements, can be used. Furthermore, these lines are weak and partly blended. The lines observed in NIS 1 are:

(1) a blend of Ne IV and Ne V at 357.8 Å. Some observations suggest that these lines are further blended.

(2) A weak and blended Ne V 359.382 Å line.

(3) a complex group of O III and N III transitions observed at 374 Å.

These lines were used as a cross-check of the relative NIS 1/ NIS 2 calibration in conjunction with the Ne IV (541.128, 542.072, 543.891 Å), Ne V (568.417, 569.824, 572.331), and O III (525.796, 599.597 Å) lines observed in NIS 2 (the N/O relative abundance can be checked using the N III and O III lines observed in GIS 4). Agreement with the results obtained from the other cross-calibrations was found in most cases.

On-disc cross-calibration between NIS 2, GIS 3, GIS 4

Since most of the NIS 2 lines are transition region lines, and the second order sensitivity is non-negligible, only the quiet sun on-disc observations could be used. Careful examination of any temporal changes had to be considered here, as already explained with the example in Figure 3.26 (above). The lines used for both the internal GIS 3 and GIS 4 calibration, and for the cross-calibration are (note that some of them are density-sensitive and were given lower importance in the iteration process) :

- O III: 702.8 (2), 703.8 (2) Å (GIS 4); 525.796, 597.817 (bl Ca VIII), 599.597 Å (NIS 2).

- O V: 758.676, 759.441, 760.4 (2), 761.127, 762.003 Å (GIS 4); 629.732 Å (NIS 2).
- Ne IV: 469.9 (4) Å (GIS 3); 541.128 (bl Fe XIV IIo 270.507), 542.072, 543.891 (bl Si X IIo 271.98) Å (NIS 2).
- Ne V: 416.194, 481.3, 482.982 Å (GIS 3); 568.4 (bl), 569.8 (2), 572.3 (3) Å (NIS 2). The lines observed in GIS are of limited use, for various reasons.
- Ne VI: 399.821 (bl), 401.136 (bl), 401.926, 435.648 Å (GIS 3); 558.594 (bl Ne VII), 562.803 (NIS 2).
- Ne VII: 465.22 Å (GIS 3); 559.948, 561.7 (2), 564.528 (bl) Å (NIS 2).
- S IV 661.4 (2), 748.392, 750.220, 753.759 (GIS 4).

Cross-calibration between NIS 1 and GIS 4 (first and second order)

The first order cross-calibration was not really possible, since only a few lines (with temperature and density effects) could be used: Mg IX 706.060, 749.551 Å (GIS 4) with the 368 Å (NIS 1), and the weak 782.338 Å at the very end of GIS 4, with the Mg VIII lines seen in NIS 1.

The cross-calibration of the second order GIS 4 sensitivity, however, is straightforward, since almost all the second order lines in GIS 4 are also observed in NIS 1. However, these lines are heavily blended with on-disc lines, and therefore only the off-limb quiet sun observations were usable.

Other cross-calibrations (first and second order)

Many other cross-calibrations and checks were possible, using many other lines.

The quiet sun off-limb observations were used to directly cross-calibrate the NIS 2 second order sensitivity (at the higher wavelengths), with the same lines, observed in first order in NIS 1 (and also to cross-calibrate with GIS 2). The rest of the NIS 2 second order sensitivity was directly cross-calibrated using the same lines seen in first order in GIS 2 (although strong ghosting limited part of the GIS 2). To do this, Off-limb quiet sun and active region spectra were used.

Part of the second order GIS 3 sensitivity was derived with a direct cross-calibration of the same lines seen in first order in GIS 1, using off-limb quiet sun spectra and active region spectra (these lines, in fact, are otherwise: (1) blended in the GIS 3 spectra with cool lines; (2) not visible, since they are all high-temperature lines (Fe XII, Fe XIII, Fe XIV)).

The rest of the GIS 3 second order could only be inferred from theoretical predictions of the lines intensities, with the use of *DEM* analyses of active regions and off-limb quiet sun regions.

Many other indirect cross-calibrations could be possible, using for example lines that have similar contribution functions, emitted by different elements, whenever it was possible to independently check the relative element abundance, and with the use of *DEM* analyses. Just as a simple example, the Mg/Si abundance can easily be checked using the two 315.038 (Mg VIII) and 316.205 (Si VIII) Å lines, observed in NIS 1 (in GIS 2 the Si VIII 316.205 has serious problems of ghosting and contaminations and cannot be used). These lines are close in wavelength and therefore their ratio of intensity does not depend on the calibration. Once the Mg/Si is known, then the Si VII line seen in GIS 2 $\sim$ 275.5 Å (others are blended, in some cases, with lines and ghosts) were used to cross-calibrate that spectral region with all the other regions (GIS 3, NIS 1) where all the Mg VII lines are seen, using *DEM* analyses to account for the (small) differences in the contribution functions the Si VII and Mg VII have.

Final results and comments

Figure 3.30 shows the CDS first and second order sensitivities that were derived from all the cross-calibrations from all the data analysed. These sensitivities have been applied to all the spectra presented in this thesis, unless explicitly stated otherwise.

Since it is virtually impossible to present all the observations, fits to the data, *DEMs*, cross-calibrations done, what has been done instead is to use all the spectra presented throughout this thesis to show the validity of this calibration. Examples in the form of Tables and synthetic spectra have already been given, while others (some more detailed) are given in the following Sections and in the Appendices. With this calibration, most of the lines are well represented within a 20% or so, at least for the lines emitted by the same ion (examples of lines emitted by different ions and that are not in agreement with theory have also been and will be given throughout the rest of this thesis). Considering all the uncertainties in either the atomic physics, the observations, the ghosting problem in the GIS spectra, this is already an achievement. However, this does not mean that this calibration can be considered to be correct within a 20% throughout all the channels. There are spectral regions where direct cross-calibrations were possible, and where suitable observations were analysed in order to derive direct sensitivity ratios, using bright lines. These regions are therefore well constrained. Other regions were also well constrained by having a large number of lines for a cross-calibration. Many other regions in the GIS spectra were so heavily affected by cross-ghosting that was not possible to use them

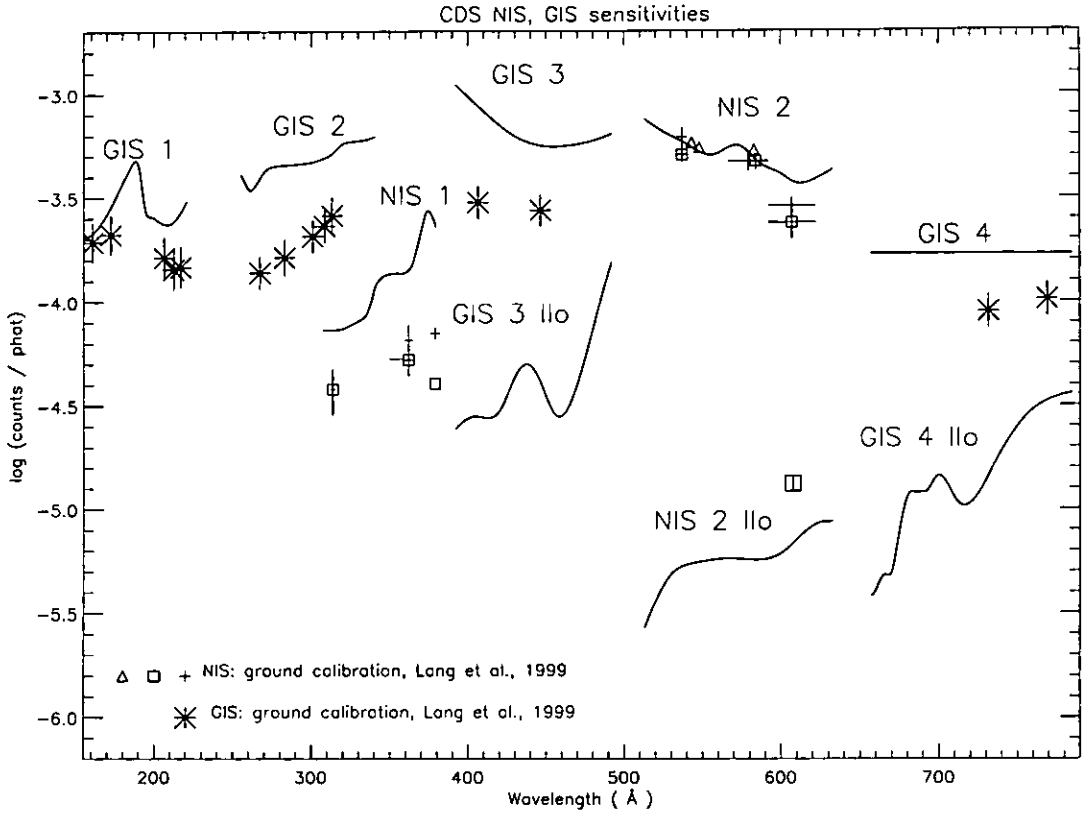

Figure 3.30: *The CDS NIS and GIS sensitivities (solid lines), first and second order, applied to the data presented in this thesis. All the pre-flight NIS and GIS measurements (*Lang *et al., 1999) are also displayed.*

to constrain the sensitivity. Wherever possible, a smooth sensitivity curve (within each channel) was sought.

The main features worth noting, comparing the calibration presented here with the pre-flight measurements (*Lang et al.*, 1999), keeping in mind that all the cross-calibration was based on fixing the absolute value at 584 Å to be in agreement, are:

- much higher sensitivities in NIS 1 and in all the GIS channels.
- A much lower second order NIS 2 sensitivity (the only pre-flight measurement of the NIS 2 sensitivity, at 608 Å, is shown in Figure).

It is also interesting to note:

- on average, the relative sensitivities between all the GIS channels (and the NIS 1) do not differ much between the pre-flight ones and this in-flight study.
- The variations with wavelength, within each GIS channel, can be regarded as consistent with the pre-flight GIS measurements, except for GIS 2 where a steeper wavelength dependence was measured on the ground.
- The same GIS wavelength variations follow the predicted sensitivities (see, e.g., Figure 36 in *Bromage et al.* (1996) and Figure 33 in *Lang et al.*, 1999), in most spectral regions. The predicted sensitivities were evaluated from the reflectivities of the telescope, the scan mirror, the grating, and the efficiencies of the detectors. They present a minimum sensitivity at 210 Å, followed by a rise with a sharp drop at 270 Å followed by a shallow increase until 380 Å, where the sensitivity decreases again, to reach a minimum in GIS 3 around 430 Å, and to then increase again at higher wavelengths. The GIS 4 spectral region was expected to have a constant sensitivity.
- The second order curves suggest that most of the sensitivity variations are due to the telescope and scan mirror reflectivities, rather than to the grating efficiency in second order. In fact, their wavelength variations are consistently similar to the correspondent first order variations (that have been derived independently).

3.4.11 The off-limb observation of May 4th 1997. The effect of different calibrations and ionization equilibrium calculations. Full list of identified lines

Since all the GIS off-limb spectra examined have shown similar characteristics (i.e. DEM, abundances, densities), only the results from the May 4th 1997 observation are presented here. These off-limb spectra are particularly simple to model, because they represent a simple structure. The plasma along the line of sight is almost isothermal, and has almost constant density. These spectra are therefore particularly suitable not only for calibration purposes (because variations in the line intensities due to temperature and/or density effects are minimised), but also as a check for the ionization state of the plasma, as described below.

The contribution functions have been calculated at constant density $N_e = 3.5\text{x}10^8$, as deduced from the observed lines (Table 3.8), except for two Fe XII transitions (338.278 and 335.339 Å) for which a constant density $N_e = 2\text{x}10^{10}$ was assumed (for reasons that are described below). Note that an error in the calibration does not significantly affect the derived density. The *Arnaud and Rothenflug* (1985) ionization equilibrium calculations have been used, with CHIANTI version 2.0 (plus recent Fe XIV calculations, *Storey et al.*, 1999, and Mg IX calculations, P. Young, priv. comm.). The photospheric abundances of *Grevesse and Anders* (1991) have been adopted, except for Na (+0.2), Al (+0.2), and Ca (+0.6) [numbers in parentheses are usual differences in dex from photospheric values].

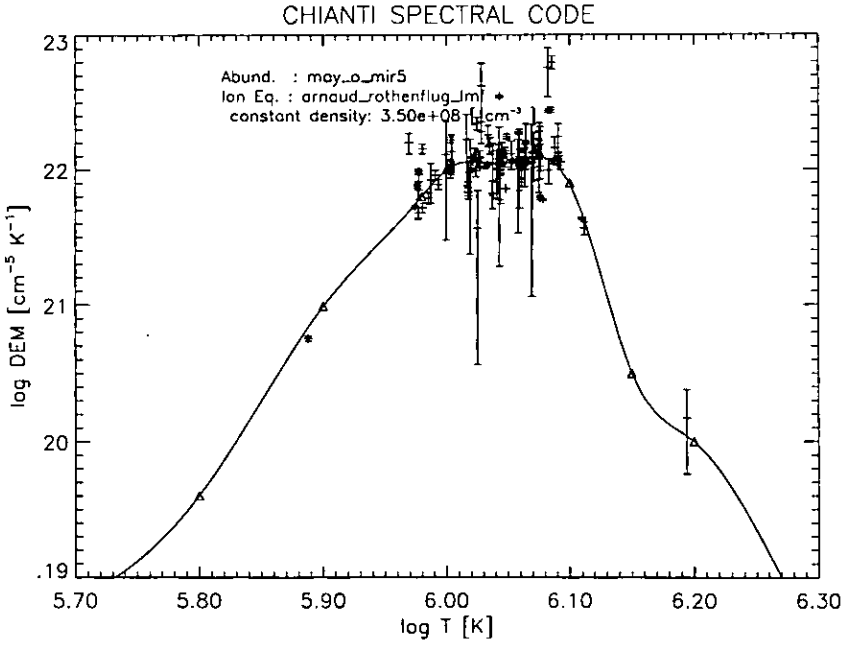

Figure 3.31: *The derived DEM for the off-limb quiet sun observation of May 4th 1997.*

Figure 3.31 shows the *DEM* that was found. The lack of (or weak) emission in cool (e.g. chromospheric and transition region) and hot (Fe XVI) lines constrains the *DEM* values away of a well-defined peak, around a million degree. However, The 'width' of the *DEM* shows that the plasma is not strictly isothermal. However, the peak temperature of the *DEM* distribution is in agreement with the temperatures derived from the line ratios (shown in Table 3.8).

Table 3.10: *Results of the analysis for the lines (first and second order) from the off-limb quiet sun observation of May 4th 1997. Some of the lines used for the calculation of the DEM of Figure 3.31, those used for cross-calibration between detectors (and orders), and a few other ones, are shown. The calculations were at constant density* $N_e = 3.5 \times 10^8$, *with the* Arnaud and Rothenflug *(1985) ionization equilibrium. Note the good agreement between lines of the same ion (confirming the adopted calibration), between lines of the same element (confirming the DEM), and between lines of different elements (confirming the adopted abundances). For some lines, the corresponding values obtained using the 'second standard CDS calibration (CDS software, 1999)' are shown. Note that: (1) no lines were observed at either higher and lower temperatures; the lines having log* $T_{eff} < 6$ *were weak, and suffered from intensity variations with time, and were not used for the cross-calibration. (2) considering the doublet lines and in general lines of the same ion, the 'second standard' calibration has larger relative deviations (up to 30%); (3) considering particular wavelength regions, the 'second standard' calibration produces deviations up to 50%, as is the case for the bright lines at the shortest wavelengths in NIS 1 (e.g. Mg VIII 315.0 Å and Si VIII 319.8 Å.*

Ion	λ_{th} (Å)	λ_{ob} (Å)	Transition	I_{ob}	I_{th}/I_{ob}	+/-	Det	log T_{eff}	log T_{max}	frac
O IV	555.263	555.1	2s2 2p $^2P_{3/2}$ - 2s 2p2 $^2P_{1/2}$	0.8	0.68	0.12	N 2	5.37	5.27	
Ne VI	562.803	562.9	2s2 2p $^2P_{3/2}$ - 2s 2p2 $^2D_{5/2}$	2.9	1.21	0.13	N 2	5.89	5.63	
Ne VII	561.728	561.7	2s2p $^3P_2$ - 2p2 $^3P_2$	4.6	1.04	0.11	N 2	5.97	5.72	0.83
Ne VII	561.378		2s2p $^3P_1$ - 2p2 $^3P_1$						5.72	0.17
Ne VII	465.22	465.2	2s2 $^1S_0$ - 2s2p $^1P_1$	142.2	0.76	0.08	G 3	5.98	5.72	
Mg VII	434.917	434.9	2s22p2 $^3P_2$ - 2s2p3 $^3D_3$	36.9	1.23	0.16	G 3	5.98	5.80	0.87
Mg VII	434.72		2s22p2 $^3P_2$ - 2s2p3 $^3D_2$						5.80	0.13
Mg VII	431.313	431.3	2s22p2 $^3P_1$ - 2s2p3 $^3D_2$	25.0	1.23	0.18	G 3	5.98	5.80	0.78
Mg VII	431.188		2s22p2 $^3P_1$ - 2s2p3 $^3D_1$						5.80	0.22
Mg VII	429.14	429.2	2s22p2 $^3P_0$ - 2s2p3 $^3D_1$	12.5	0.84	0.15	G 3	5.98	5.80	
Mg VII	367.674	367.7	2s22p2 $^3P_2$ - 2s2p3 $^3P_2$	84.7	0.61	0.07	N 1	5.98	5.81	0.77
Mg VII	367.683		2s22p2 $^3P_2$ - 2s2p3 $^3P_1$						5.81	0.23
Mg VII	363.772	363.8	2s22p2 $^3P_0$ - 2s2p3 $^3P_1$	13.7	0.73	0.12	N 1	5.98	5.81	
Mg VII	365.234	365.1	2s22p2 $^3P_1$ - 2s2p3 $^3P_2$	26.2	1.23	0.16	N 1	5.98	5.81	0.36
Mg VII	365.176		2s22p2 $^3P_1$ - 2s2p3 $^3P_0$						5.81	0.33
Mg VII	365.243		2s22p2 $^3P_1$ - 2s2p3 $^3P_1$						5.81	0.26
Mg VII	278.402	278.4	2s22p2 $^3P_2$ - 2s2p3 $^3S_1$	52.9	1.17	0.16	G 2	5.99	5.81	0.68
Si VII	278.443		2p4 $^3P_1$ - 2s.2p5 $^3P_2$						5.77	0.29
Mg VII	276.154	276.1	2s22p2 $^3P_0$ - 2s2p3 $^3S_1$	18.1	0.91	0.31	G 2	5.99	5.81	0.51
Si VII	275.667		2p4 $^3P_1$ - 2s.2p5 $^3P_1$						5.77	0.45
Si VII	275.353	275.3	2p4 $^3P_2$ - 2s.2p5 $^3P_2$	60.6	0.91	0.12	G 2	5.99	5.77	
Na VIII	411.166	411.1	2s2 $^1S_0$ - 2s.2p $^1P_1$	22.8	1.13	0.15	G 3	5.99	5.86	
Mg VIII	782.338	781.9	2p $^2P_{3/2}$ - 2s.2p2 $^4P_{3/2}$	6.7	0.77	0.59	G 4	6.00	5.90	
Mg VIII	430.465	430.5	2p $^2P_{1/2}$ - 2s.2p2 $^2D_{3/2}$	104.0	1.04	0.11	G 3	6.00	5.91	
Mg VIII	315.039	315.0	2p $^2P_{3/2}$ - 2s.2p2 $^2P_{3/2}$	264.8	1.05	0.11	N 1	6.00	5.91	
			(standard calibration)	185.8	1.50	0.15	N 1			
Mg VIII	315.039	630.0	2p $^2P_{3/2}$ - 2s.2p2 $^2P_{3/2}$	443.7	0.63	0.07	N 2	6.00	5.91	
Mg VIII	315.039	315.1	2p $^2P_{3/2}$ - 2s.2p2 $^2P_{3/2}$	290.8	0.96	0.10	G 2	6.00	5.91	
Mg VIII	313.754	313.7	2p $^2P_{1/2}$ - 2s.2p2 $^2P_{1/2}$	119.2	0.92	0.10	N 1	6.00	5.92	
Mg VIII	313.754	627.6	2p $^2P_{1/2}$ - 2s.2p2 $^2P_{1/2}$	100.5	1.09	0.16	N 2	6.00	5.92	
Mg VIII	339.006	339.0	2p $^2P_{3/2}$ - 2s.2p2 $^2S_{1/2}$	62.5	1.07	0.11	N 1	6.00	5.92	
			(standard calibration)	49.7	1.34	0.14	N 1			
Mg VIII	428.319	428.2	2s.2p2 $^2D_{5/2}$ - 2p3 $^2D_{5/2}$	4.3	0.78	0.27	G 3	6.00	5.92	0.55
Mg VIII	428.245		2s.2p2 $^2D_{3/2}$ - 2p3 $^2D_{3/2}$						5.92	0.35
Al VIII	387.957	775.4	2p2 $^3P_2$ - 2s.2p3 $^3D_3$	39.9	0.69	0.38	G 4	6.02	5.92	0.84
Al VIII	387.822		2p2 $^3P_2$ - 2s.2p3 $^3D_2$						5.92	0.14
Ne VIII	780.324	780.1	1s2 2s $^2S_{1/2}$ - 1s2 2p $^2P_{1/2}$	157.7	1.69	0.20	G 4	6.02	5.79	

Table 3.10: *(continued)*

Ion	λ_{th} (Å)	λ_{ob} (Å)	Transition	I_{ob}	I_{th}/I_{ob}	+/-	Det	log T_{eff}	log T_{max}	frac	
Ne VIII	770.409	770.8	1s2 2s $^2S_{1/2}$ - 1s2 2p $^2P_{3/2}$	294.1	1.81	0.20	G 4	6.02	5.79		
Al VIII	325.276	325.4	2p2 $^3P_1$ - 2s.2p3 $^3P_0$	13.5	1.42	0.28	N 1	6.02	5.92	0.37	
Al VIII	325.292		2p2 $^3P_1$ - 2s.2p3 $^3P_2$						5.92	0.33	
Al VIII	325.338		2p2 $^3P_1$ - 2s.2p3 $^3P_1$						5.92	0.29	
Si VIII	314.327	314.4	2s22p3 $^4S_{3/2}$ - 2s2p4 $^4P_{1/2}$	125.0	1.03	0.11	N 1	6.02	5.91		
Si VIII	314.327	628.8	2s22p3 $^4S_{3/2}$ - 2s2p4 $^4P_{1/2}$	107.7	1.20	0.91	N 2	6.02	5.91		
Si VIII	319.826	319.8	2s22p3 $^4S_{3/2}$ - 2s2p4 $^4P_{5/2}$	335.9	1.11	0.12	G 2	6.02	5.91		
Si VIII	319.826	319.9	2s22p3 $^4S_{3/2}$ - 2s2p4 $^4P_{5/2}$	323.0	1.15	0.12	N 1	6.02	5.91		
			(standard calibration)	220.3	1.69	0.17	N 1				
Ca X	574.01	574.1	3s $^2S_{1/2}$ - 3p $^2P_{1/2}$	20.9	0.94	0.10	N 2	6.02	5.82		
			(standard calibration)	23.0	0.85	0.09	N 2				
Ca X	557.765	557.8	3s $^2S_{1/2}$ - 3p $^2P_{3/2}$	39.6	1.00	0.10	N 2	6.02	5.82		
			(standard calibration)	36.1	1.10	0.11	N 2				
Fe IX	244.909	489.1	3p6 $^1S_0$ - 3p5.3d $^3P_1$	69.9	0.90	0.14	G 3	6.02	5.94		
Fe IX	241.739	483.3	3p6 $^1S_0$ - 3p5.3d $^3P_2$	140.8	1.18	0.16	G 3	6.02	5.94		
Al VIII	328.185	328.2	2p2 $^3P_2$ - 2s.2p3 $^3P_2$	34.3	0.97	0.16	N 1	6.02	5.92	0.69	
Al VIII	328.232		2p2 $^3P_2$ - 2s.2p3 $^3P_1$						5.92	0.23	
Mg IX	706.058	705.8	2s2 $^1S_0$ - 2s.2p $^3P_1$	45.8	0.52	0.08	G 4	6.02	5.98		
Na IX	694.147	694.2	1s2.2s $^2S_{1/2}$ - 1s2.2p $^2P_{1/2}$	6.0	3.13	2.84	G 4	6.03	5.92		
Mg IX	368.07	736.0	2s2 $^1S_0$ - 2s.2p $^1P_1$	1069.1	0.92	0.14	G 4	6.03	5.98		
Fe IX	171.073	171.1	3p6 $^1S_0$ - 3p5.3d $^1P_1$	3766.6	1.09	0.11	G 1	6.03	5.96		
Mg IX	368.07	368.1	2s2 $^1S_0$ - 2s.2p $^1P_1$	1060.8	0.94	0.09	N 1	6.03	5.98		
S VIII	198.553	198.7	2s2.2p5 $^2P_{3/2}$ - 2s.2p6 $^2S_{1/2}$	140.0	0.60	0.13	G 1	6.03	5.88	0.66	
Fe XI	198.545		3s2.3p4 $^1D_2$ -						6.11	0.32	
			3s2.3p3(2d*).3d $^3P_1$								
Mg IX	749.55	749.7	2s.2p $^1P_1$ - 2p2 $^1D_2$	9.0	0.27	0.13	G 4	6.03	5.99		
Si X	277.255	277.0	2p $^2P_{3/2}$ - 2s.2p2 $^2S_{1/2}$	213.5	1.07	0.12	G 2	6.03	6.13	0.38	
Si VIII	277.054		2s22p3 $^2D_{5/2}$ - 2s2p4 $^2D_{5/2}$						5.90	0.30	
Si VIII	276.838		2s22p3 $^2D_{3/2}$ - 2s2p4 $^2D_{3/2}$						5.90	0.13	
Mg VII	277		2s22p2 $^3P_1$ - 2s2p3 $^3S_1$						5.81	0.11	
Mg VIII	335.253	335.3	2p $^2P_{1/2}$ - 2s.2p2 $^2S_{1/2}$	73.1	1.05	0.11	N 1	6.03	5.92	0.65	
Fe XII	335.339		3s2.3p3 $^2D_{3/2}$ - 3s.3p4 $^2D_{3/2}$						6.16	0.33	[14]
O VI	184.117	184.0	1s2 2p $^2P_{3/2}$ - 1s2 3s $^2S_{1/2}$	72.4	0.62	0.13	G 1	6.03	5.51	0.67	
O VI	183.937		1s2 2p $^2P_{1/2}$ - 1s2 3s $^2S_{1/2}$						5.51	0.33	
O VI	173.079	173.1	1s2 2p $^2P_{3/2}$ - 1s2 3d $^2D_{5/2}$	116.2	0.74	0.13	G 1	6.04	5.51	0.60	
O VI	172.935		1s2 2p $^2P_{1/2}$ - 1s2 3d $^2D_{3/2}$						5.51	0.33	
S IX	221.241	442.5	2s2.2p4 $^3P_2$ - 2s.2p5 $^3P_1$	46.4	1.01	0.44	G 3	6.04	6.00		
Al IX	286.377	286.6	2s2.2p $^2P_{3/2}$ - 2s.2p2 $^2P_{1/2}$	15.5	1.39	0.36	G 2	6.04	6.03		
Al IX	282.422	282.6	2s2.2p $^2P_{1/2}$ - 2s.2p2 $^2P_{1/2}$	28.9	0.93	0.17	G 2	6.04	6.03		
Al IX	305.045	305.3	2s2.2p $^2P_{3/2}$ - 2s.2p2 $^2S_{1/2}$	14.3	1.00	0.26	G 2	6.04	6.03		
Si IX	349.873	349.9	2s22p2 $^3P_2$ - 2s2p3 $^3D_3$	226.6	1.00	0.10	N 1	6.04	6.03	0.84	
Si IX	349.794		2s22p2 $^3P_2$ - 2s2p3 $^3D_2$						6.03	0.16	
Si IX	349.873	699.8	2s22p2 $^3P_2$ - 2s2p3 $^3D_3$	267.1	0.85	0.17	G 4	6.04	6.03	0.84	
Si IX	349.794		2s22p2 $^3P_2$ - 2s2p3 $^3D_2$						6.03	0.16	
Si IX	341.949	342.0	2s22p2 $^3P_0$ - 2s2p3 $^3D_1$	99.4	1.03	0.10	N 1	6.04	6.03		
Si IX	341.949	684.4	2s22p2 $^3P_0$ - 2s2p3 $^3D_1$	103.8	0.98	0.82	G 4	6.04	6.03		
Si IX	296.117	592.6	2s22p2 $^3P_2$ - 2s2p3 $^3P_2$	949.9	0.32	0.03	N 2	6.04	6.03	0.72	[15]
Si IX	296.213		2s22p2 $^3P_2$ - 2s2p3 $^3P_1$						6.03	0.28	
Si IX	345.124	345.1	2s22p2 $^3P_1$ - 2s2p3 $^3D_2$	238.6	1.03	0.10	N 1	6.04	6.03	0.77	
Si IX	344.951		2s22p2 $^3P_1$ - 2s2p3 $^3D_1$						6.03	0.23	
Si IX	345.124	690.3	2s22p2 $^3P_1$ - 2s2p3 $^3D_2$	200.4	1.23	0.44	G 4	6.04	6.03	0.77	
Si IX	344.951		2s22p2 $^3P_1$ - 2s2p3 $^3D_1$						6.03	0.23	
Si IX	292.8	585.7	2s22p2 $^3P_1$ - 2s2p3 $^3P_0$	230.7	0.90	0.11	N 2	6.04	6.03	0.40	
Si IX	292.856		2s22p2 $^3P_1$ - 2s2p3 $^3P_1$						6.03	0.32	
Si IX	292.763		2s22p2 $^3P_1$ - 2s2p3 $^3P_2$						6.03	0.27	
Si IX	225.024	450.2	2s22p2 $^3P_1$ - 2s2p3 $^3S_1$	230.3	1.04	0.19	G 3	6.04	6.04	0.69	
S IX	225.22		2s2.2p4 $^3P_1$ - 2s.2p5 $^3P_1$						6.00	0.11	
Si IX	227	454.0	2s22p2 $^3P_2$ - 2s2p3 $^3S_1$	288.2	0.97	0.16	G 3	6.04	6.04		
Fe X	365.543	365.6	3s2.3p5 $^2P_{1/2}$ - 3s.3p6 $^2S_{1/2}$	74.2	0.93	0.10	N 1	6.04	6.04		
			(standard calibration)	66.0	1.04	0.11	N 1				
Fe X	345.723	345.7	3s2.3p5 $^2P_{3/2}$ - 3s.3p6 $^2S_{1/2}$	133.9	1.19	0.12	N 1	6.04	6.04		
			(standard calibration)	124.5	1.28	0.13	N 1				
Fe X	345.723	691.5	3s2.3p5 $^2P_{3/2}$ - 3s.3p6 $^2S_{1/2}$	141.0	1.13	0.50	G 4	6.04	6.04		
Fe X	225.161		3s2.3p5 $^2P_{3/2}$ - 3s2.3p4(1d).3d $^2D_{5/2}$						6.04	0.20	
Fe X	324.763	324.7	3s2.3p4(3p).3d $^4D_{7/2}$ -	13.3	0.84	0.19	N 1	6.05	6.04		
			3s.3p5(3p*).3d $^4F_{9/2}$								
Fe X	177.243	177.3	3s2.3p5 $^2P_{3/2}$ - 3s2.3p4(3p).3d $^2P_{3/2}$	2133.2	0.83	0.08	G 1	6.05	6.05		

[14] First identification

[15] Must be a blend with an unidentified line in first order

Table 3.10: *(continued)*

Ion	λ_{th} (Å)	λ_{ob} (Å)	Transition	I_{ob}	I_{th}/I_{ob}	+/-	Det	log T_{eff}	log T_{max}	frac	
Fe X	174.534	174.7	3s2.3p5 $^2P_{3/2}$ - 3s2.3p4(3p).3d $^2D_{5/2}$	3375.8	0.90	0.09	G 1	6.05	6.05		
Fe X	184.543	184.6	3s2.3p5 $^2P_{3/2}$ - 3s2.3p4(1d).3d $^2S_{1/2}$	759.0	0.88	0.09	G 1	6.05	6.05		
Fe XII	186.884	186.8	3s2.3p3 $^2D_{5/2}$ - 3s2.3p2(3p).3d $^2F_{7/2}$	261.9	0.81	0.09	G 1	6.05	6.16	0.49	
FE VIII	186.599								5.64	0.36	AC
Fe XII	186.851		3s2.3p3 $^2D_{3/2}$ - 3s2.3p2(3p).3d $^2F_{5/2}$						6.16	0.14	
Mg X	609.793	609.8	1s2.(1s).2s $^2S_{1/2}$ - 1s2.(1s).2p $^2P_{3/2}$	364.2	1.55	0.15	N 2	6.05	6.04		
			(standard calibration)	316.7	1.78	0.18	N 2				
Mg X	624.941	625.0	1s2.(1s).2s $^2S_{1/2}$ - 1s2.(1s).2p $^2P_{1/2}$	180.4	1.55	0.16	N 2	6.05	6.04		
			(standard calibration)	168.3	1.66	0.17	N 2				
Fe XI	202.706	202.7	3s2.3p4 $^1D_2$ - 3s2.3p3(2d*).3d $^1P_1$	180.6	0.86	0.22	G 1	6.05	6.11	0.75	
S VIII	202.61		2s2.2p5 $^2P_{1/2}$ - 2s.2p6 $^2S_{1/2}$						5.88	0.16	
Fe XI	358.621	358.6	3s2.3p4 $^3P_0$ - 3s.3p5 $^3P_1$	40.8	0.98	0.10	N 1	6.05	6.11	0.75	
Fe X	358.413		3s2.3p4(3p).3d $^4F_{9/2}$ - 3s.3p5(3p*).3d $^4F_{9/2}$						6.04	0.23	
S X	776.373	776.3	2s22p3 $^4S_{3/2}$ - 2s22p3 $^2P_{3/2}$	6.0	1.15	0.78	G 4	6.06	6.11		
Fe XI	182.169	182.3	3s2.3p4 $^3P_1$ - 3s2.3p3(4s*).3d $^3D_2$	459.1	0.61	0.07	G 1	6.06	6.11	0.85	
Fe X	182.31		3s2.3p5 $^2P_{1/2}$ - 3s2.3p4(3p).3d $^2P_{3/2}$						6.05	0.15	
Fe XI	341.113	341.1	3s2.3p4 $^3P_2$ - 3s.3p5 $^3P_1$	75.4	0.63	0.06	N 1	6.06	6.11		
Fe XI	352.662	705.2	3s2.3p4 $^3P_2$ - 3s.3p5 $^3P_2$	176.2	1.11	0.39	G 4	6.06	6.11		
Fe XI	369.153	369.2	3s2.3p4 $^3P_1$ - 3s.3p5 $^3P_2$	54.7	1.07	0.11	N 1	6.06	6.11		
			(standard calibration)	59.2	0.99	0.10	N 1				
Fe XI	369.153	738.1	3s2.3p4 $^3P_1$ - 3s.3p5 $^3P_2$	62.9	0.93	0.56	G 4	6.06	6.11		
Fe XI	352.662	352.7	3s2.3p4 $^3P_2$ - 3s.3p5 $^3P_2$	177.1	1.10	0.11	N 1	6.06	6.11		
			(standard calibration)	156.8	1.24	0.12	N 1				
Fe XI	180.408	180.5	3s2.3p4 $^3P_2$ - 3s2.3p3(4s*).3d $^3D_3$	2182.8	0.98	0.10	G 1	6.06	6.11		
Al X	332.789	332.8	2s2 $^1S_0$ - 2s.2p $^1P_1$	104.1	1.14	0.13	N 1	6.06	6.09		
			(standard calibration)	70.4	1.68	0.19	N 1				
Fe XI	188.232	188.3	3s2.3p4 $^3P_2$ - 3s2.3p3(2d*).3d $^3P_2$	1406.5	0.85	0.09	G 1	6.06	6.11	0.72	
Fe XI	188.299		3s2.3p4 $^3P_2$ - 3s2.3p3(2d*).3d $^1P_1$						6.11	0.26	
S X	259.496	519.2	2s22p3 $^4S_{3/2}$ - 2s2p4 $^4P_{3/2}$	129.2	1.19	0.21	N 2	6.06	6.13		
Si X	356.012	711.8	2p $^2P_{3/2}$ - 2s.2p2 $^2D_{5/2}$	127.6	1.05	0.38	G 4	6.06	6.13	0.76	
Si X	356.05		2p $^2P_{3/2}$ - 2s.2p2 $^2D_{3/2}$						6.13	0.24	
Si X	356.012	356.0	2p $^2P_{3/2}$ - 2s.2p2 $^2D_{5/2}$	129.9	1.03	0.10	N 1	6.06	6.13	0.76	
Si X	356.05		2p $^2P_{3/2}$ - 2s.2p2 $^2D_{3/2}$						6.13	0.24	
Si X	258.372	258.5	2p $^2P_{3/2}$ - 2s.2p2 $^2P_{3/2}$	321.0	0.86	0.09	G 2	6.06	6.13		
Si X	261.063	261.2	2p $^2P_{3/2}$ - 2s.2p2 $^2P_{1/2}$	133.3	1.06	0.13	G 2	6.06	6.13		
Si X	258.372	516.8	2p $^2P_{3/2}$ - 2s.2p2 $^2P_{3/2}$	353.8	0.78	0.09	N 2	6.06	6.13		
Si X	347.403	347.4	2p $^2P_{1/2}$ - 2s.2p2 $^2D_{3/2}$	208.4	1.06	0.11	N 1	6.06	6.13		
Si X	347.403	694.7	2p $^2P_{1/2}$ - 2s.2p2 $^2D_{3/2}$	293.1	0.76	0.29	G 4	6.06	6.13		
Si X	271.983	272.0	2p $^2P_{1/2}$ - 2s.2p2 $^2S_{1/2}$	105.4	1.03	0.12	G 2	6.07	6.13		
Si IX	227.361		2s22p2 $^1D_2$ - 2s2p3 $^1P_1$						6.03	0.31	
Al IX	284.042	284.5	2s2.2p $^2P_{3/2}$ - 2s.2p2 $^2P_{3/2}$	79.7	1.11	0.14	G 2	6.07	6.03	0.76	
Fe XV	284.16		3s2 $^1S_0$ - 3s3p $^1P_1$						6.29	0.24	
Fe XII	227.406	454.9	3s2.3p3 $^2P_{1/2}$ - 3s2.3p2(3p).3d $^2P_{1/2}$	20.7	1.07	0.97	G 3	6.07	6.16	0.62	
Fe XII	346.852	346.9	3s2.3p3 $^4S_{3/2}$ - 3s.3p4 $^4P_{1/2}$	51.7	0.90	0.09	N 1	6.07	6.16		
			(standard calibration)	48.1	0.97	0.10	N 1				
Fe XII	352.106	352.1	3s2.3p3 $^4S_{3/2}$ - 3s.3p4 $^4P_{3/2}$	102.4	0.92	0.09	N 1	6.07	6.16		
			(standard calibration)	91.3	1.04	0.10	N 1				
Fe XII	364.467	364.5	3s2.3p3 $^4S_{3/2}$ - 3s.3p4 $^4P_{5/2}$	138.3	0.95	0.10	N 1	6.07	6.16		
			(standard calibration)	117.7	1.11	0.11	N 1				
Fe XII	352.106	704.2	3s2.3p3 $^4S_{3/2}$ - 3s.3p4 $^4P_{3/2}$	101.5	0.92	0.37	G 4	6.07	6.16		
Fe XII	364.467	728.5	3s2.3p3 $^4S_{3/2}$ - 3s.3p4 $^4P_{5/2}$	123.7	1.05	0.47	G 4	6.07	6.16		
Fe XII	193.521	193.6	3s2.3p3 $^4S_{3/2}$ - 3s2.3p2(3p).3d $^4P_{3/2}$	828.5	0.84	0.09	G 1	6.07	6.16		
Fe XII	338.278	338.3	3s2.3p3 $^2D_{5/2}$ - 3s.3p4 $^2D_{5/2}$	32.1	0.89	0.10	N 1	6.07	6.16		
Fe XII	195.118	195.2	3s2.3p3 $^4S_{3/2}$ - 3s2.3p2(3p).3d $^4P_{5/2}$	1103.8	0.99	0.10	G 1	6.08	6.16		
Fe XIII	321.4	321.6	3s2 3p2 $^3P_2$ - 3s 3p3 $^3P_1$	14.0	1.17	0.26	G 2	6.08	6.20	0.66	
Fe X	321.732		3s2.3p4(3p).3d $^4D_{5/2}$ - 3s.3p5(3p*).3d $^4F_{7/2}$						6.04	0.23	
Fe XIII	240.696	481.4	3s2 3p2 $^3P_0$ - 3s 3p3 $^3S_1$	29.1	0.81	0.30	G 3	6.08	6.20	0.84	
Al VII	240.777		2s22p3 $^2D_{5/2}$ - 2s2p4 $^2P_{3/2}$						5.78	0.14	
Al XI	568.12	568.2	1s2.(1s).2s $^2S_{1/2}$ - 1s2.(1s).2p $^2P_{1/2}$	6.4	2.02	0.22	N 2	6.08	6.16		
			(standard calibration)	6.7	1.92	0.20	N 2				
Al XI	550.031	550.1	1s2.(1s).2s $^2S_{1/2}$ - 1s2.(1s).2p $^2P_{3/2}$	12.5	2.08	0.21	N 2	6.08	6.16		
			(standard calibration)	11.1	2.34	0.24	N 2				
Si XI	580.907	580.9	2s2 $^1S_0$ - 2s.2p $^3P_1$	12.5	0.44	0.05	N 2	6.08	6.19		
S XI	281.401	281.5	2s22p2 $^3P_0$ - 2s2p3 $^3D_1$	17.8	1.21	0.28	G 2	6.08	6.24		
Si XI	303.324	606.7	2s2 $^1S_0$ - 2s.2p $^1P_1$	560.5	0.42	0.05	N 2	6.08	6.20		
Si XI	604.147	604.3	2s.2p $^1P_1$ - 2p2 $^1D_2$	2.1	0.19	0.03	N 2	6.09	6.20		
Fe XIII	359.842	359.7	3s2 3p2 $^3P_1$ - 3s 3p3 $^3D_1$	24.5	0.99	0.11	N 1	6.09	6.20	0.55	

Table 3.10: *(continued)*

Ion	λ_{th} (Å)	λ_{ob} (Å)	Transition	I_{ob}	I_{th}/I_{ob}	+/-	Det	log T_{eff}	log T_{max}	frac
Fe XIII	359.642		3s2 3p2 $^3P_1$ - 3s 3p3 $^3D_2$						6.20	0.43
Fe XIII	320.809	320.8	3s2 3p2 $^3P_2$ - 3s 3p3 $^3P_2$	13.2	0.77	0.18	G 2	6.09	6.20	
Fe XIII	348.183	348.2	3s2 3p2 $^3P_0$ - 3s 3p3 $^3D_1$	55.0	0.92	0.11	N 1	6.09	6.20	
Fe XIII	202.044	202.1	3s2 3p2 $^3P_0$ - 3s2 3p 3d $^3P_1$	493.9	0.87	0.13	G 1	6.09	6.21	
Fe XIV	274.2	274.1	3s2 3p $^2P_{1/2}$ - 3s 3p2 $^2S_{1/2}$	37.5	0.89	0.14	G 2	6.09	6.25	0.81
Si VII	274.174		2p4 $^3P_1$ - 2s.2p5 $^3P_0$						5.77	0.19
Si XII	520.665	520.8	1s2.2s $^2S_{1/2}$ - 1s2.2p $^2P_{1/2}$	8.6	1.09	0.11	N 2	6.11	6.26	
Fe XIV	334.172	334.2	3s2 3p $^2P_{1/2}$ - 3s 3p2 $^2D_{3/2}$	18.2	1.14	0.17	N 1	6.11	6.24	
			(standard calibration)	12.3	1.68	0.25	N 1			

Table 3.10 presents a selection of lines, with some of those used for the calculation of the *DEM* of Figure 3.31, and those useful for cross-calibration between detectors (and between first and second order). Note:

- the good agreement (in most cases within 10%) between lines of the same ion, also including the lines seen in second order, thus confirming the validity of the adopted NIS/GIS calibration.
- The good agreement between lines of the same element, thus confirming the validity of the *DEM*.
- The good agreement between lines of different elements, thus confirming the validity of the adopted abundances.
- The problems with the Li-like ions Ne VIII, Mg X, Al XI, Na IX (and also O VI, although only partially). See below for a discussion of it.
- The 1999 standard CDS calibration fails to represent the doublet lines well nor in general pairs of lines of the same ion, with deviations from expected intensities of up to 30%. Note that density- or temperature- dependent effects of this size can be ruled out as a cause. So, unless all the theoretical intensities of all the ions are wrong, or basic assumptions (such as the fact that the lines are optically thin) fail, the 1999 standard CDS calibration appear to be at fault (the first standard CDS calibration was even less accurate).
- Considering particular wavelength regions, the 1999 CDS standard calibration produces intensity deviations of up to 50-60%, as is the case for all the bright lines at the shortest wavelengths in NIS 1 (e.g. Mg VIII 315.0 Åand Si VIII 319.8 Å which appear weaker than expected). These deviations are independent of the ionization equilibrium calculations, since only particular spectral regions are affected while other lines of the same ions, observed in the different CDS channels, are well represented.

- Many lines exhibit the same deviations as were found in the SERTS-89 (and other) spectra. For example, with the adopted calibration, the Fe XII 338.278 Å transition is not well represented. To increase the theoretical intensity a much higher density is required, as already noted in the SERTS spectra. Assuming a density $N_e = 2\text{x}10^{10}$, this line becomes well represented. But the Fe XII transition predicted by CHIANTI at 335.339 Å is also density dependent as is the 338.278 Å line, and there is no reason why the 335.339 Å should not show the same observed characteristics as the 338.278 Å line. In fact, assuming a higher density for the 335.339 Å line increases the contribution of this line by up to a third, a non-negligible effect never reported before. This *first identification* of the line explains the problem with the 335.4 Å blend. In fact, in active region spectra the Fe XVI dominates, while in spectra such as those examined in this Section, any Fe XVI contribution is obviously ruled out, because the other un-blended Fe XVI line of the doublet is absent, and the Mg VIII 335.253 is not sufficient to explain the observed intensity.

- The complete list of identified lines of these spectra is given in Table C.2.

A comparison of different ionization equilibrium calculations

In these quiet sun equatorial regions the plasma is expected to be in ionization equilibrium, and since the thermal distribution is almost isothermal, and many lines from different sequences and ions are observed, this type of observations allow a direct check of the ionization equilibrium calculations, something that has not previously been done in detail. In fact, very few such attempts have been made, only comparing a few ions. For example, *Brickhouse et al.* (1995) presented a comparison between the results obtained from using only the Fe lines with the *Arnaud and Rothenflug* (1985) and *Arnaud and Raymond* (1992) calculations, but with no definite conclusions.

Table 3.11: *A selection of lines from the off-limb quiet sun observation of May 4th 1997, showing the comparisons of the results when using different ionization equilibrium calculations. For each observed line, the first line gives the results as calculated with* Arnaud and Rothenflug *(1985). All of them have been calculated at the same constant density* $N_e = 3.5\text{x}10^8$ *and with the same DEM shown in Figure 3.31. Note the large differences for the different ionization equilibrium calculations.*

Ion	λ_{th} (Å)	λ_{ob} (Å)	Transition	I_{ob}	I_{th}/I_{ob}	+/-	Det	log T_{eff}	log T_{max}	frac
Ne VII	465.22	465.2	2s2 $^1S_0$ - 2s2p $^1P_1$	142.2	0.76	0.08	G 3	5.98	5.72	
			(*Mazzotta et al.*, 1998)		1.21	0.13		5.98	5.71	
Mg VII	367.674	367.7	2s22p2 $^3P_2$ - 2s2p3 $^3P_2$	84.7	0.61	0.07	N 1	5.98	5.81	0.77
			(*Mazzotta et al.*, 1998)		0.48	0.05		5.98	5.81	
Mg VII	367.683		2s22p2 $^3P_2$ - 2s2p3 $^3P_1$						5.81	0.23
Ca IX	466.239	466.3	3s2 $^1S_0$ - 3s.3p $^1P_1$	39.8	0.45	0.06	G 3	5.98	5.78	
			(*Mazzotta et al.*, 1998)		2.02	0.26		6.00	5.80	
Si VII	275.353	275.3	2p4 $^3P_2$ - 2s.2p5 $^3P_2$	60.6	0.91	0.12	G 2	5.99	5.77	
			(*Mazzotta et al.*, 1998)		1.25	0.17		6.00	5.77	
Na VIII	411.166	411.1	2s2 $^1S_0$ - 2s.2p $^1P_1$	22.8	1.13	0.15	G 3	5.99	5.86	
			(*Mazzotta et al.*, 1998)		1.57	0.21		6.00	5.86	
Mg VIII	315.039	315.0	2p $^2P_{3/2}$ - 2s.2p2 $^2P_{3/2}$	264.8	1.05	0.11	N 1	6.00	5.91	

Table 3.11: *(continued)*

Ion	λ_{th} (Å)	λ_{ob} (Å)	Transition	I_{ob}	I_{th}/I_{ob}	+/-	Det	log T_{eff}	log T_{max}	frac
			(*Mazzotta et al.*, 1998)		0.97	0.10		6.00	5.91	
Ne VIII	770.409	770.8	1s2 2s $^2S_{1/2}$ - 1s2 2p $^2P_{3/2}$	294.1	1.81	0.20	G 4	6.02	5.79	
			(*Mazzotta et al.*, 1998)		1.86	0.21		6.02	5.80	
Si VIII	319.826	319.9	2s22p3 $^4S_{3/2}$ - 2s2p4 $^4P_{5/2}$	323.0	1.15	0.12	N 1	6.02	5.91	
			(*Mazzotta et al.*, 1998)		1.66	0.17		6.03	5.93	
Ca X	557.765	557.8	3s $^2S_{1/2}$ - 3p $^2P_{3/2}$	39.6	1.00	0.10	N 2	6.02	5.82	
			(*Mazzotta et al.*, 1998)		3.24	0.33		6.03	5.86	
Fe IX	171.073	171.1	3p6 $^1S_0$ - 3p5.3d $^1P_1$	3766.6	1.09	0.11	G 1	6.03	5.96	
			(*Mazzotta et al.*, 1998)		0.93	0.09		6.01	5.85	
			(*Arnaud and Raymond*, 1992)		0.94	0.10		6.01	5.85	
Mg IX	368.07	736.0	2s2 $^1S_0$ - 2s.2p $^1P_1$	1069.1	0.92	0.14	G 4	6.03	5.98	
			(*Mazzotta et al.*, 1998)		1.32	0.13		6.03	5.98	
O VI	173.079	173.1	1s2 2p $^2P_{3/2}$ - 1s2 3d $^2D_{5/2}$	116.2	0.74	0.13	G 1	6.04	5.51	0.60
			(*Mazzotta et al.*, 1998)		0.74	0.12		6.04	5.51	
O VI	172.935		1s2 2p $^2P_{1/2}$ - 1s2 3d $^2D_{3/2}$						5.51	0.33
Al IX	282.422	282.6	2s2.2p $^2P_{1/2}$ - 2s.2p2 $^2P_{1/2}$	28.9	0.93	0.17	G 2	6.04	6.03	
			(*Mazzotta et al.*, 1998)		0.72	0.13		6.04	6.04	
Si IX	341.949	342.0	2s22p2 $^3P_0$ - 2s2p3 $^3D_1$	99.4	1.03	0.10	N 1	6.04	6.03	
			(*Mazzotta et al.*, 1998)		0.90	0.09		6.05	6.06	
Fe X	345.723	345.7	3s2.3p5 $^2P_{3/2}$ - 3s.3p6 $^2S_{1/2}$	133.9	1.19	0.12	N 1	6.04	6.04	
			(*Mazzotta et al.*, 1998)		1.17	0.12		6.03	5.98	
			(*Arnaud and Raymond*, 1992)		1.16	0.12		6.03	5.98	
Mg X	609.793	609.8	1s2.(1s).2s $^2S_{1/2}$ - 1s2.(1s).2p $^2P_{3/2}$	364.2	1.55	0.15	N 2	6.05	6.04	
			(*Mazzotta et al.*, 1998)		1.47	0.15		6.05	6.05	
Fe XI	352.662	352.7	3s2.3p4 $^3P_2$ - 3s.3p5 $^3P_2$	177.1	1.10	0.11	N 1	6.06	6.11	
			(*Arnaud and Raymond*, 1992)		1.35	0.14		6.05	6.06	
			(*Mazzotta et al.*, 1998)		1.36	0.14		6.05	6.06	
Al X	332.789	332.8	2s2 $^1S_0$ - 2s.2p $^1P_1$	104.1	1.14	0.13	N 1	6.06	6.09	
			(*Mazzotta et al.*, 1998)		1.34	0.15		6.06	6.10	
Si X	271.983	272.0	2p $^2P_{1/2}$ - 2s.2p2 $^2S_{1/2}$	105.4	1.03	0.12	G 2	6.07	6.13	
			(*Mazzotta et al.*, 1998)		0.75	0.09		6.07	6.14	
Al IX	284.042	284.5	2s2.2p $^2P_{3/2}$ - 2s.2p2 $^2P_{3/2}$	79.7	1.11	0.14	G 2	6.07	6.03	0.76
			(*Mazzotta et al.*, 1998)		1.04	0.13		6.08	6.04	0.63
Fe XV	284.16		3s2 $^1S_0$ - 3s3p $^1P_1$						6.29	0.24
			(*Mazzotta et al.*, 1998)						6.32	0.37
Fe XII	364.467	364.5	3s2.3p3 $^4S_{3/2}$ - 3s.3p4 $^4P_{5/2}$	138.3	0.95	0.10	N 1	6.07	6.16	
			(*Arnaud and Raymond*, 1992)		1.71	0.18		6.07	6.13	
			(*Mazzotta et al.*, 1998)		1.70	0.17		6.07	6.14	
Al XI	550.031	550.1	1s2.(1s).2s $^2S_{1/2}$ - 1s2.(1s).2p $^2P_{3/2}$	12.5	2.08	0.21	N 2	6.08	6.16	
			(*Mazzotta et al.*, 1998)		1.88	0.19		6.08	6.16	
Si XI	580.907	580.9	2s2 $^1S_0$ - 2s.2p $^3P_1$	12.5	0.44	0.05	N 2	6.08	6.19	
			(*Mazzotta et al.*, 1998)		.48	0.05		6.09	6.20	
Fe XIII	348.183	348.2	3s2 3p2 $^3P_0$ - 3s 3p3 $^3D_1$	55.0	0.92	0.11	N 1	6.09	6.20	
			(*Arnaud and Raymond*, 1992)		1.86	0.22		6.08	6.20	
			(*Mazzotta et al.*, 1998)		1.82	0.21		6.08	6.20	
Si XII	520.665	520.8	1s2.2s $^2S_{1/2}$ - 1s2.2p $^2P_{1/2}$	8.6	1.09	0.11	N 2	6.11	6.26	
			(*Mazzotta et al.*, 1998)		0.85	0.09		6.11	6.28	
Fe XIV	334.172	334.2	3s2 3p $^2P_{1/2}$ - 3s 3p2 $^2D_{3/2}$	18.2	1.14	0.17	N 1	6.11	6.24	
			(*Arnaud and Raymond*, 1992)		2.01	0.30		6.10	6.26	
			(*Mazzotta et al.*, 1998)		1.93	0.29		6.10	6.26	

Table 3.11 presents a further selection of lines, representative of some of the principal ions observed, together with a comparison of the results that are obtained with different ionization equilibrium calculations (*Arnaud and Rothenflug*, 1985 and *Mazzotta et al.*, 1998 for all the ions, and *Arnaud and Raymond*, 1992 for the Fe ions). All the theoretical intensities have been calculated at the same constant density $N_e = 3.5 \times 10^8$ and with the *DEM* shown in Figure 3.31. The following conclusions can be drawn:

- the *Arnaud and Raymond* (1992) calculations for Fe are in disagreement with those

derived from the *Arnaud and Rothenflug* (1985), both using Fe and other elements. In particular, all the higher Fe ionization states (Fe XI, Fe XII, Fe XIII, Fe XIV) present increasing disagreements up to almost a factor of 2.

- The recent calculations of *Mazzotta et al.* (1998) present a completely different picture. The intensities of all the Fe ions are in general agreement with those of *Arnaud and Raymond* (1992), while most of the ions of the other elements are changed by large factors, when compared to *Arnaud and Rothenflug* (1985). This comparison shows how much the ionization equilibrium affects the calculations. Unfortunately, even these recent calculations do not produce consistent results. The intensities of all the 'hotter' Fe ions are increased by large factors, cancelling the disagreement between these lines and the Li-like ions Mg X, Al XI. However, other ions such as Si X (or Mg VIII) have decreased theoretical intensities, making it impossible to find a different DEM that could well represent the brightest lines from the observed ions. It should be noted that the *Mazzotta et al.* (1998) calculations as a consequence imply different element abundances. For example, for Ca IX and Ca X, the differences are to increase the theoretical intensities by large factors, thus cancelling the need to increase the Ca abundance from its photospheric value, needed if *Arnaud and Rothenflug* (1985) is used. For the Na and Al ions, the differences are not so large and not consistent for each element, and the element abundances deduced from the *Arnaud and Rothenflug* (1985) are probably correct.

In conclusion, the old *Arnaud and Rothenflug* (1985) ionization equilibrium calculations better represent the majority of the ions, and should not be used in conjunction with the *Arnaud and Raymond* (1992) calculations. The recent *Mazzotta et al.* (1998) results indicate that some element abundances deduced by the use of *Arnaud and Rothenflug* (1985) are probably wrong (Ca in particular), and that some of the disagreement between the Li-like ions and all the others may also be due to incorrect ionization equilibrium calculations (if indeed there is equilibrium at all). However, the *Mazzotta et al.* (1998) calculations do not produce a coherent picture and are not used in the rest of this thesis. Note that these conclusions are the same independently on the adopted calibration, since the differences between the calibration presented in this thesis and the CDS standard one are smaller.

The line identifications and the theoretical spectra

Table C.2 presents a list of the principal lines identified in the spectra, with comments. Only those lines that are a complex combination of first and second order lines, and the

few unidentified ones are not displayed in the Table. Figures 3.32,3.34, 3.35,3.36 show the calculated synthetic spectra, that consider both first and second order lines, with the observed spectra displayed for comparison. The agreement is excellent, confirming that overall, the instrument calibration and the various assumptions are reasonable. The evident disagreements are in all cases due to either ghosting problems in the GIS or in the case of lines of Li-like ions. Figure 3.33 shows the NIS 1 synthetic spectrum, in physical units, and visually confirms the much reduced NIS 1 sensitivity at the shorter wavelengths. These types of figures were created for all the observations analysed, all the detectors and for the first and second order, and used as a general check.

The GIS ghosts

Figures C.7,C.8,C.9,C.10 show the off-limb GIS spectra (May 4th 1997) with the blue- and red-shifted and the likely ghosting areas, while Table C.2.1 presents the corrections for ghosting that have been applied. Many lines are complex combinations of contaminations and ghosting and have not been corrected. The GIS 2 detector is the worst case, although strong ghosting is also present in GIS 1 and GIS 4.

These off-limb spectra are particularly useful to check the ghosting (or not) of some lines. As an example, the ghosting of the lines in the 430-440 Å region into the 400-410 Å region can be almost completely ruled out, because no bright ghosts are observed. In any on-disc spectra, the 400-410 Å region has bright transition region lines, that could have masked the presence of ghosts. On the other hand, ghosting of the lines in the 400-410 Å region toward the 430-440 Å region can not be ruled out completely (and furthermore is impossible to observationally check, because the lines in the 430-440 Å region are always visible when those in the 400-410 Å region are. More details on which lines have ghosting or are contaminated can be found in the Table, which also lists the 'pure ghosts' identified (see the comparison observed-versus-synthetic spectra for a direct visual identification of the brightest ghosts).

3.4.12 The on-disc observation of October 16th 1997. Full list of identified lines

A *DEM* analysis was performed on the on-disc spectra of 1997 October 16. A constant pressure $P_e = 4\text{x}10^{14}$ (cm^{-3} K) was used for the calculation of the contribution functions. Figure 3.37 shows the resulting *DEM*, that has a peak at 1.1 x10^6 K. The photospheric abundances of *Grevesse and Anders* (1991) were used, except for Ne (+0.2), Al (+0.3), Ca (+0.6) [numbers in parentheses are usual differences in dex from photospheric values].

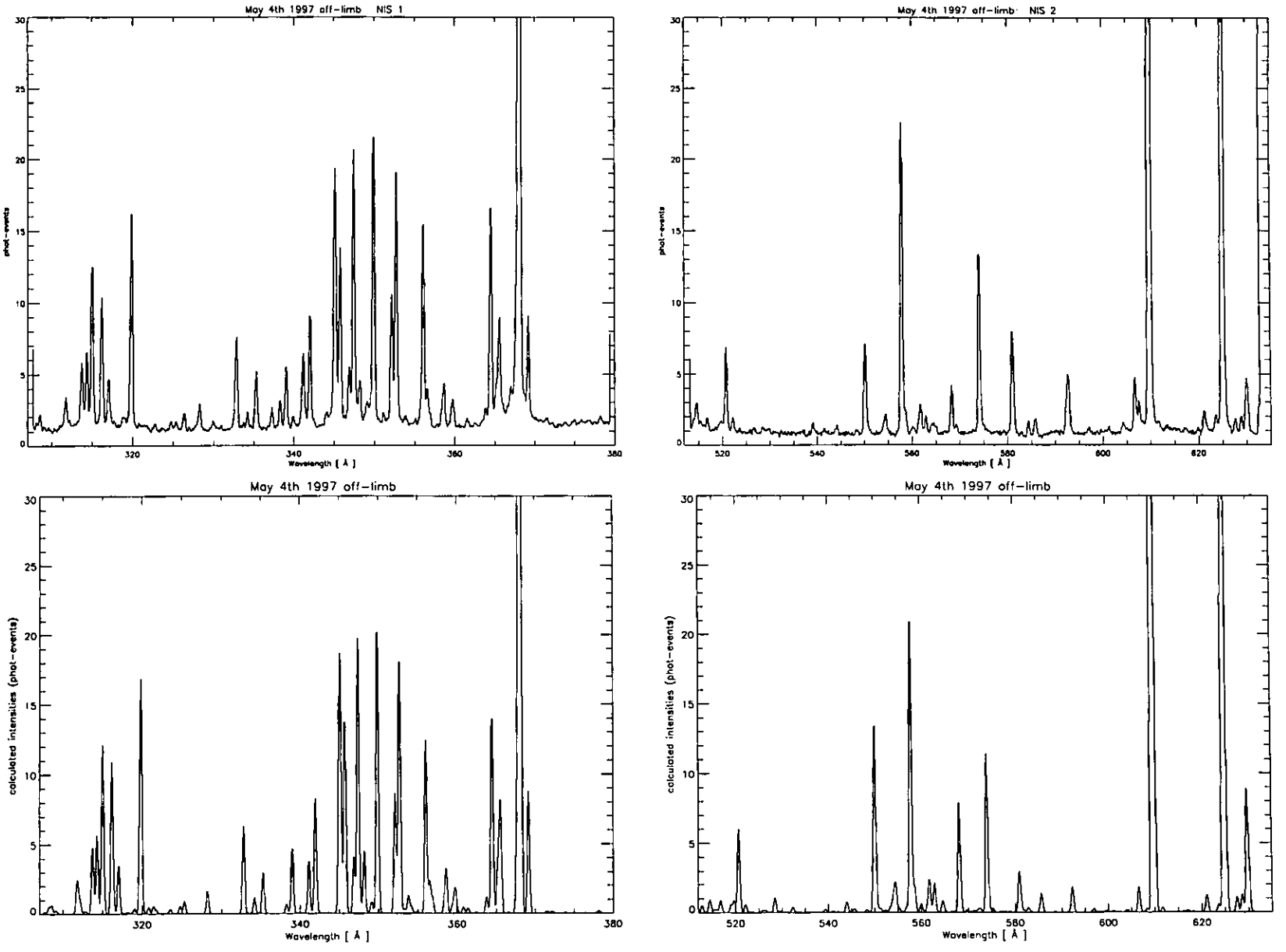

Figure 3.32: *Top: the NIS 1 and NIS 2 spectra of the off-limb quiet sun observation of May 4th 1997. Bottom: the corresponding synthetic spectra.*

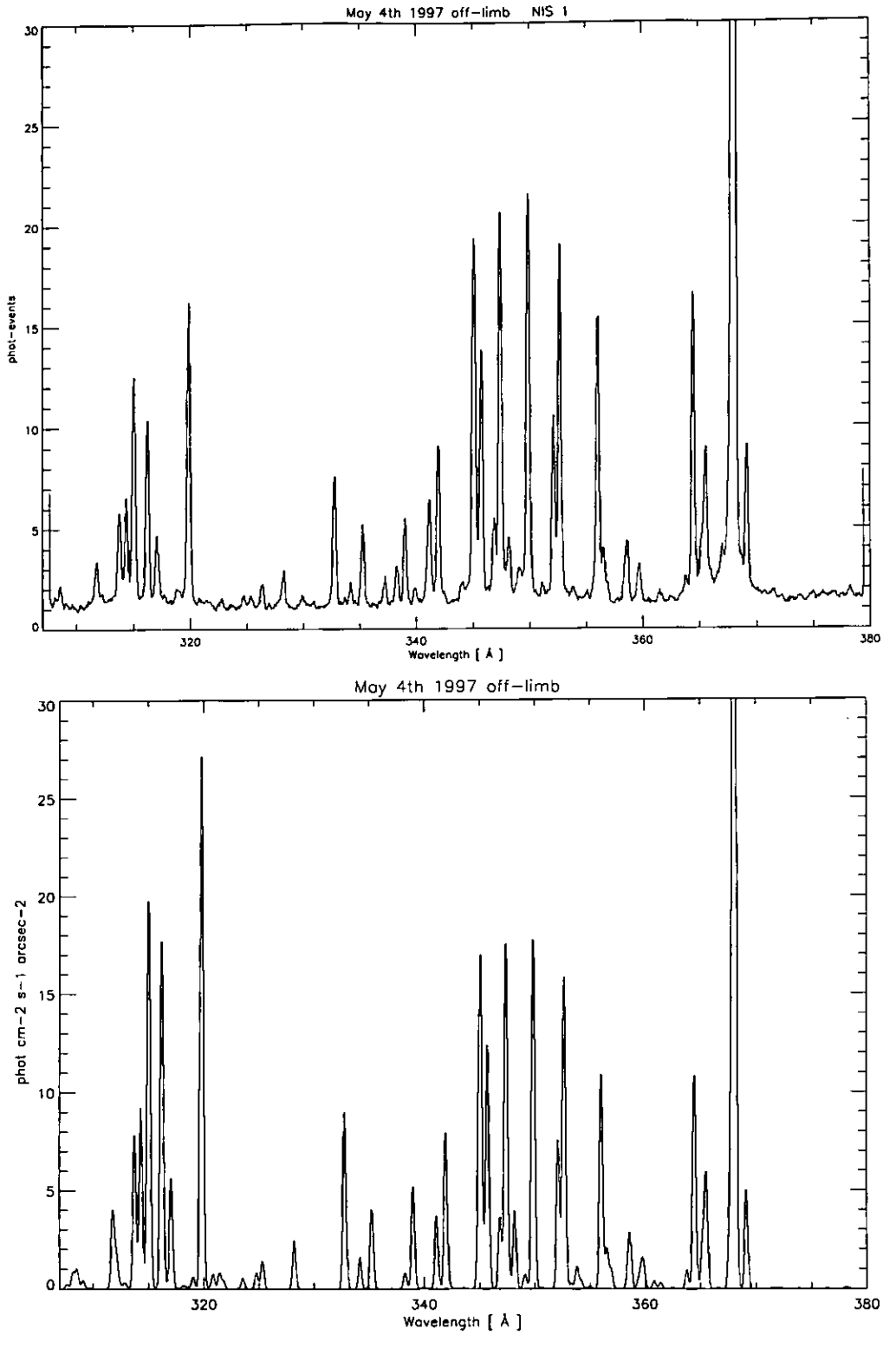

Figure 3.33: *Top: the NIS 1 spectrum of the off-limb quiet sun observation of May 4th 1997. Bottom: the corresponding synthetic spectrum, in physical units. Note how how the lines at shorter wavelengths are much depressed in the observed spectrum, indicating a much lower NIS 1 sensitivity at those wavelengths. Also, note that the central region of the spectrum is well represented, indicating how the instrument sensitivity is fairly constant there. Similar examples for all the other channels, first and second order have been produced for all the observations analysed, and used as a general check.*

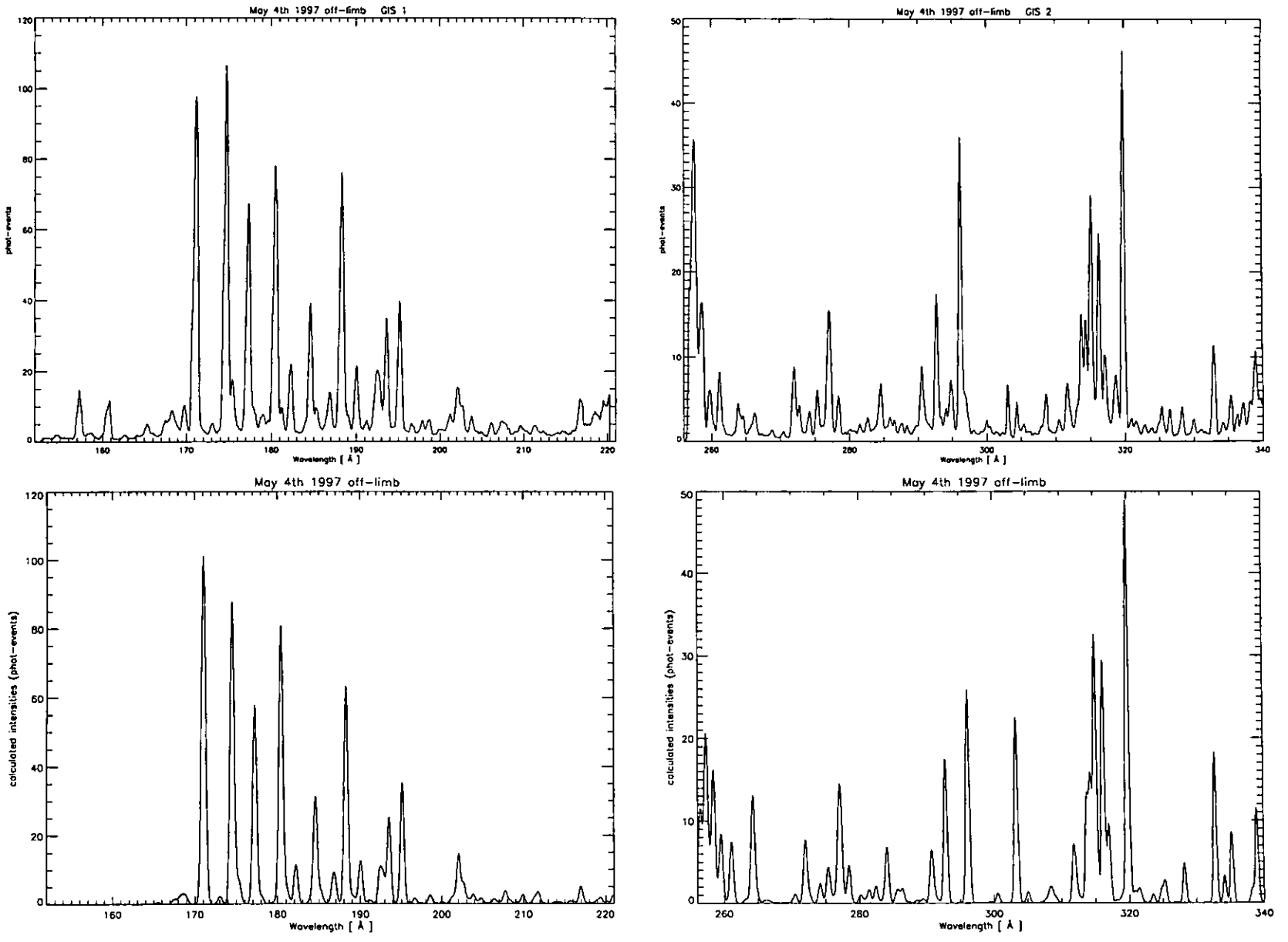

Figure 3.34: *Top: the GIS 1 and GIS 2 spectra of the off-limb quiet sun observation of May 4th 1997. Bottom: the corresponding synthetic spectra.*

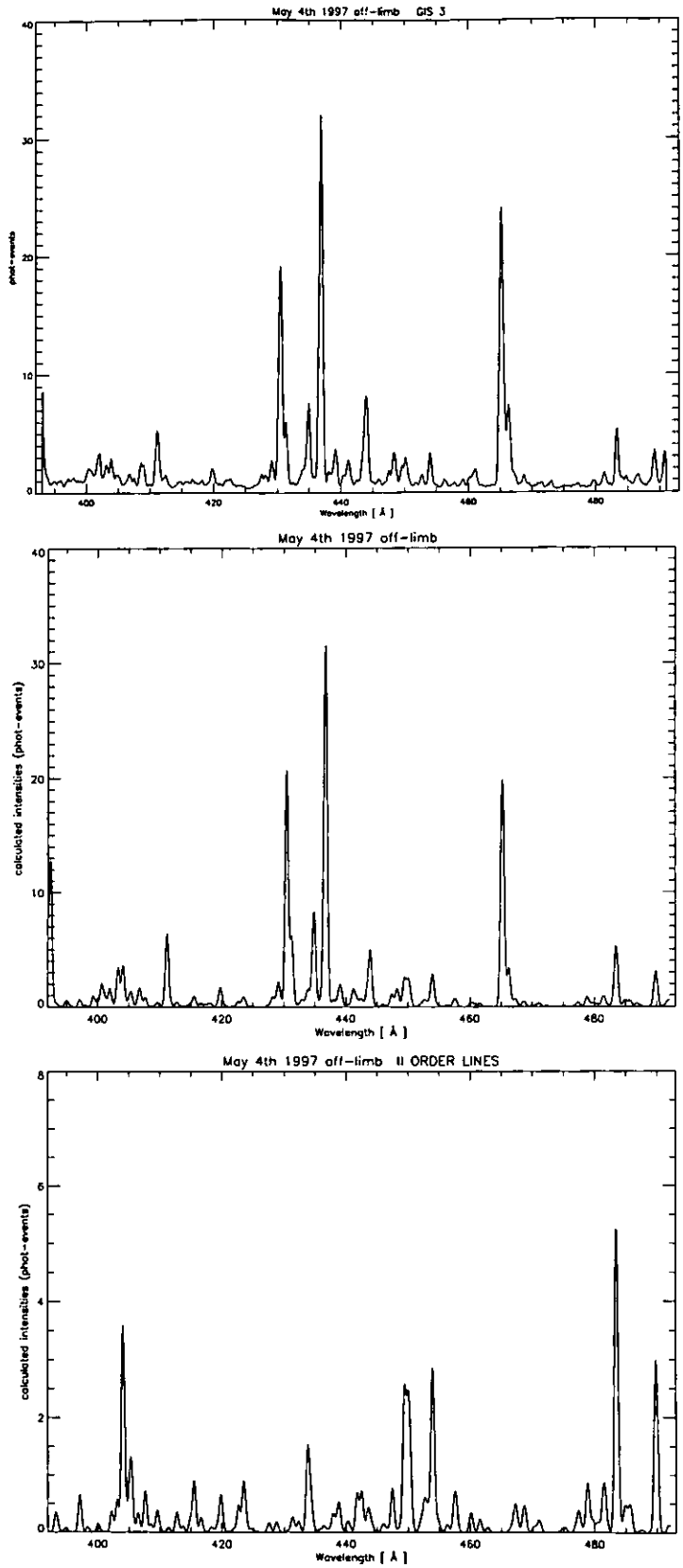

Figure 3.35: *Top: the GIS 3 spectrum of the off-limb quiet sun observation of May 4th 1997. Middle: the corresponding synthetic spectrum, on the same scale. Bottom: the synthetic spectrum with only the second order lines (note the different scale). Many second order lines are blended with first order ones, here, but there are still many that are not, in particular at middle and higher wavelengths. These lines were used to constrain the second order sensitivity.*

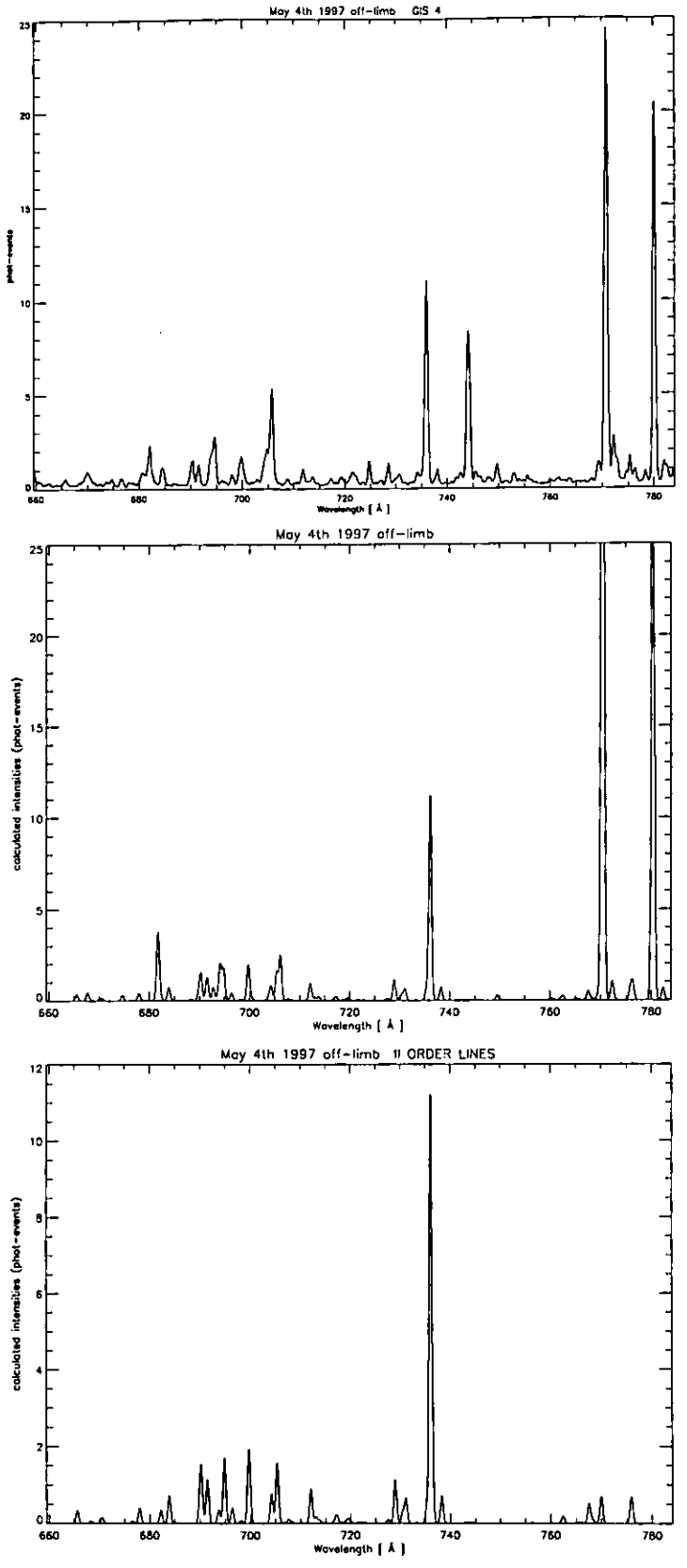

Figure 3.36: *Top: the GIS 4 spectrum of the off-limb quiet sun observation of May 4th 1997. Middle: the corresponding synthetic spectrum, on the same scale. Bottom: the synthetic spectrum with only the second order lines (different scale) Note the fact that most of the lines that are seen in GIS 4 are second order lines, and moreover not blended with the cool lines. These types of observations were used to constrain the GIS 4 second order sensitivity in the central and higher wavelength region.*

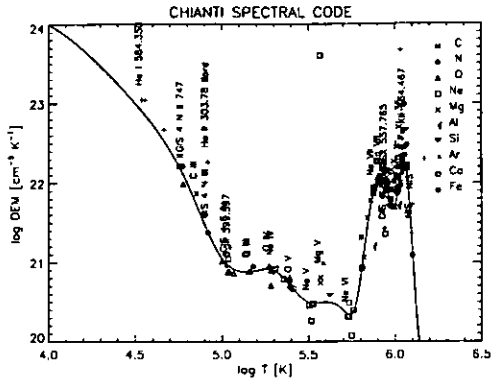

Figure 3.37: *The derived DEM for the on-disc quiet sun observation of 1997 October 16.*

Table C.4 lists the identified lines in the spectra. As in the off-limb case, synthetic spectra were calculated. They are displayed together with the observed spectra, for a direct comparison, in Figures 3.38, 3.39, 3.40.

The GIS ghosts

Figures C.17,C.18,C.19,C.20 show the on-disc GIS spectra (October 16th, 1997) with the blue- and red-shifted and the likely ghosting areas, while Table C.3.1 presents the corrections for ghosting that have been applied.

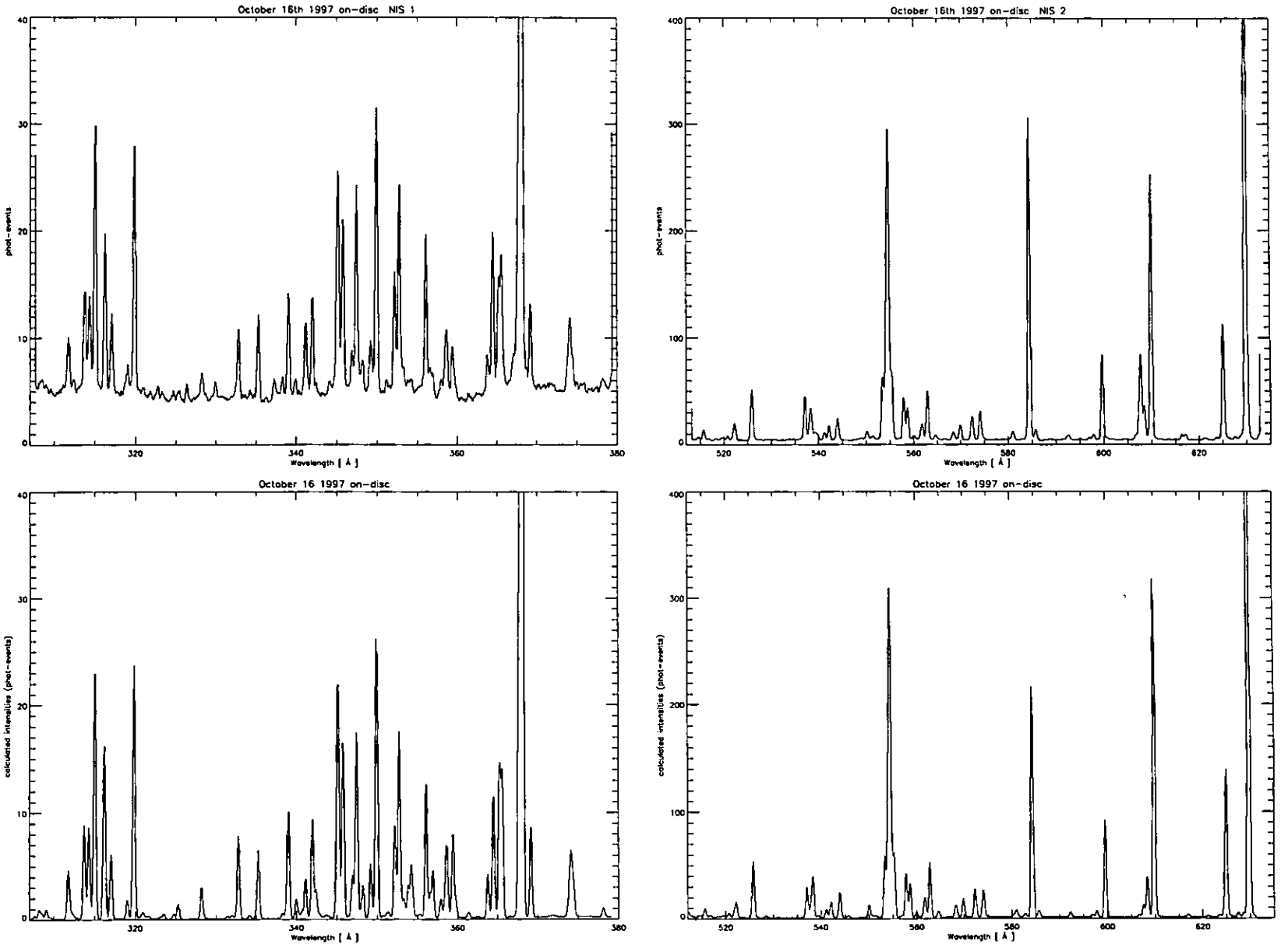

Figure 3.38: *Top: the NIS 1 and NIS 2 spectra of the on-disc quiet sun observation of October 16th 1997. Bottom: the corresponding synthetic spectra.*

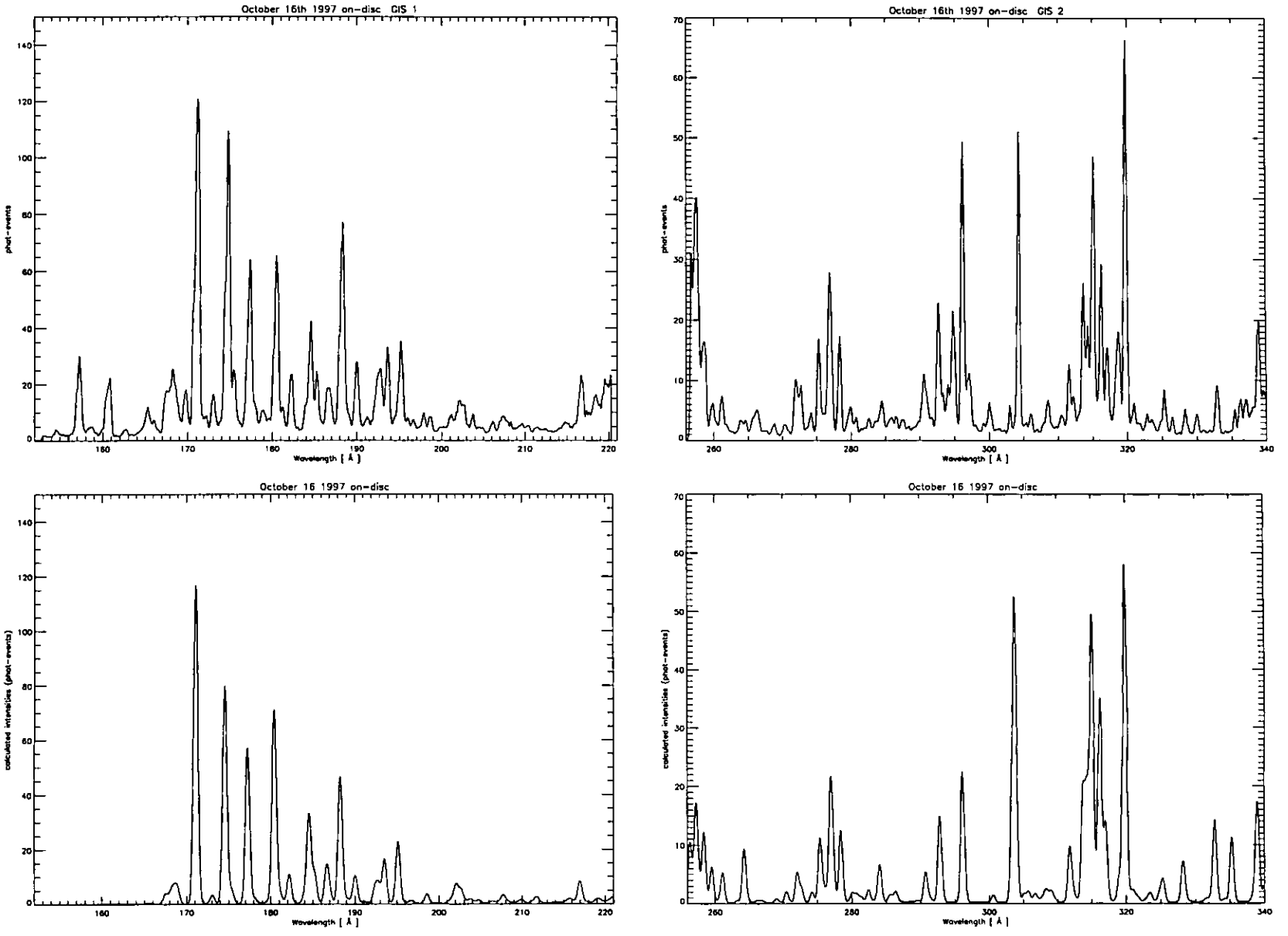

Figure 3.39: *Top: the GIS 1 and GIS 2 spectra of the on-disc quiet sun observation of October 16th 1997. Bottom: the corresponding synthetic spectra.*

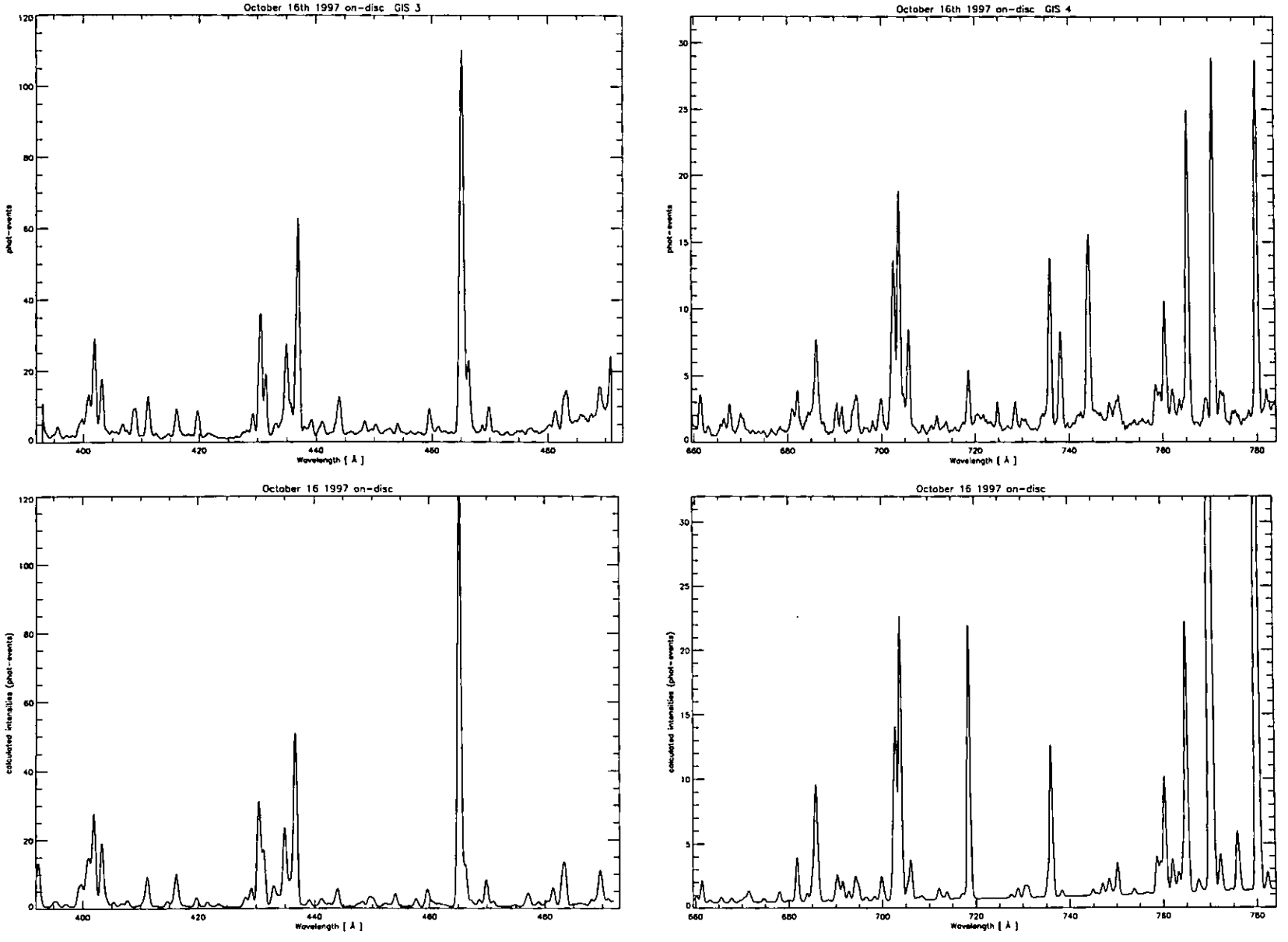

Figure 3.40: *Top: the GIS 3 and GIS 4 spectra of the on-disc quiet sun observation of October 16th 1997. Bottom: the corresponding synthetic spectra.*

Chapter 4

Observations and data analysis

A large number of CDS observations were planned and executed. Most of them were made during three periods (totalling more than two months) in which the author was, together with B. Bromage, at the SOHO operation centre at Goddard Space Flight Center (GSFC), Greenbelt, MD, USA. Most of the observations were acquired during August-September 1996 and September-October 1997. In many cases, the CDS observations have been supported by observations with the other SOHO instruments, and by ground based observatories. All the raw data are now in publicly available databases on the WWW.

The first Section (4.1) of this Chapter describes some of the CDS studies that were developed to study coronal holes with CDS, to give an idea of the type of problems CDS observations of coronal holes have posed. The following Sections briefly describe some of the observations that have been taken during the period 1996-1998, excluding the calibration studies, already described in Chapter 3. The CDS instrument has successfully produced a wealth of data of all different types, incomparable to anything obtained in the past. For example, the data collected for this thesis, listed in Table B.1, amounts to several G-bytes. This has posed new problems in, for example, the storage and analysis of such large datasets. Note that most of the data obtained have been partly analysed or at least examined. The results presented in this thesis are from a selected subset of these data.

Section(4.5) presents the methods and the software that were developed by the author to tackle some of the problems encountered in the data analysis.

4.1 Some of the CDS studies used or developed

Most of the CDS studies already available (and used by most people) used the smallest slits (2″x2″ or 2″x240″). A preliminary analysis of many observations was performed, and

showed that the small slits, contrary to expectation, were *not* producing any significant increase in spectral resolution compared to the larger 4″ slits. The only advantage is the spatial resolution, but at the expense of losing half the signal. This fact, together with short exposure times, made almost all the CDS studies already present in the CDS database unsuitable for coronal hole observations, simply because of the low signal.

Many CDS studies were therefore designed and developed by the author and B. Bromage. The design of a study has to take into account and balance exposure times, telemetry, number and width of the extraction windows, use of different slits, movements of the mirror and solar rotation, just to mention a few, and is quite complex. It is not possible to describe in detail the pros and cons of each type of study. However, Table 4.1 lists a few of the CDS studies used by the author, just to give an idea of the various possibilities offered by CDS. Table 4.2 lists the principal lines observed by some of the most commonly used studies, which can be grouped into these types:

- **Large field of view**

  The largest area of the Sun that can be observed with a single NIS observation, is (4′x4′). One example is the CDS study LIMB which, with only a limited number of extraction windows, including lines emitted from the chromosphere to the corona, provides temperature and density information. The exposure time is kept low in order to have the total area observed say within an hour, to approximate a snapshot of the Sun. LIMB uses a 4″x240″ slit and a 30s exposure to build with 60 movements of the scan mirror a 4′x4′ raster. Only 15 lines are extracted, including chromospheric transition region and coronal lines, and the density diagnostic Si IX lines. The total duration of this study is 37 minutes. The restrictions of this study are a) the narrow spectral windows (20 pixels), which in some cases make it difficult to estimate the background, and b) the short exposure time.

  Another similar study is UCLAN_N4, more suitable for coronal hole observation than LIMB, because of the longer exposure time, larger windows and more diagnostic lines (at the expense of a longer duration).

  During the planning, a series of such observations were pointed so that the regions overlapped. This enabled a 'mosaic' of data to be formed, as explained in Section 4.5, giving an overall view over large portions of the Sun, with some density and temperature diagnostic lines included. The CDS daily synoptic study, SYNOP, is also made up of a series of 4′x4′ rasters, this time covering a N-S strip of the Sun centred on the meridian.

- **Medium field of view**

Table 4.1: *Some of the CDS studies developed or used (those already present in the database are marked with a *). Each line represents one or more 'study variation', depending on the exposure time, and telemetry rate, for example. (NR) indicates normal rate, while (HR) high-rate. Note that the indicated area covered by each NIS raster is not equivalent to the usable one, due to the slant of the spectra. All NIS studies also extracted 4 background windows. For the studies with data extraction windows, their number and the width in pixels of each window is given.*

study name	Sp	slit	exposure time (s)	area covered	duration	type of extraction	compression	comments
UCLAN_N2	NIS	4″x240″	160 (NR) - 80(HR)	120″x150″	2h30m (NR) - 1h09m (HR)	all lines	none	
UCLAN_N2	NIS	4″x240″	120 (NR) - 60(HR)	120″x150″	1h19m (NR) - 45m (HR)	all lines	sum (2 lines)	
UCLAN_N3	NIS	4″x240″	120 (NR) - 60(HR)	120″x180″	1h13m (NR) - 39m (HR)	12 windows (90 pix)	none	
UCLAN_N3	NIS	4″x240″	90 (NR) - 45(HR)	120″x180″	54m (NR) - 33m (HR)	12 windows (90 pix)	sum (2 lines)	
CHBOPT2	NIS	4″x240″	50 (NR)	60″x240″	1h (NR)	16 windows (35 pix)	none	complex raster
UCLAN_N4	NIS	4″x240″	60 (NR) - 30(HR)	240″x240″	1h10m (NR) - 39m (HR)	8 windows (45 pix)	none	
LIMB	NIS	4″x240″	30 (NR)	240″x240″	37m (NR)	8 windows (20 pix)	none	*
WIDE3LA1	NIS	90″x240″	25 (NR)	234″x240″	1m53s (NR)	He I, O V, Mg IX	none	* for movies
MOVIE	NIS	90″x240″	50 (NR)	90″x240″	1h (NR)	He I, O V, Mg IX	none	* 60 xeach position
NISAT	NIS	2″x240″	50 (NR)	20″x240″	1h (NR)	all lines	none	*
NISAT_S5	NIS	4″x240″	150 (NR) - 150(HR)	40″x240″	1h06m (NR) - 48m (HR)	all lines	none	
ARC_CALN	NIS	4″x240″	45 (NR)	32″x70″	13m (NR)	all lines	none	
DEM_GIS	GIS	4″x4″	20 (NR)	24″x24″	13m (NR)	all lines	none	*
NSGSCAN1	GIS	4″x4″	400 (NR)	4″x60″	1h40m(NR)	all lines	none	
EWGSCAN2	GIS	4″x4″	400 (NR)	120″x4″	3h20m (NR)	all lines	none	
G2AL/v2	GIS	4″x4″	400 (NR)	80″x4″	2h14m (NR)	all lines	none	
NSGSCAN2	GIS	4″x4″	400 (NR)	4″x120″	3h20m (NR)	all lines	none	
HRBNDWE	GIS	4″x4″	5 (HR)	60″x4″	2h48m (HR)	all lines	none	100 xeach position
MICRO_2	GIS	4″x4″	50 (HR)	20″x20″	22m (HR)	all lines	none	

Table 4.2: *Principal Selected Lines in the CDS/NIS Wavelength Bands. The lines observed by the different CDS studies are marked with a star. Wavelengths are taken from the CHIANTI database. When only one decimal place is indicated, the lines are blends of at least two transitions. The temperature of maximum ionization fraction is also indicated.*

Ion	Wavelength [Å]	log T_e [K]	NIS	LIMB	CHBOPT2
Fe XI	341.113	6.1	1		*
Si IX	341.9	6.0	1	*	*
Si IX	345.1	6.0	1		*
Fe X	345.722	6.0	1		*
Fe XII	346.852	6.1	1		
Si X	347.402	6.1	1		
Fe XIII	348.183	6.2	1		
Mg VI (bl Fe XI)	349.2	5.7	1	*	*
Si IX	349.9	6.0	1	*	*
Fe XII	352.106	6.1	1		*
Fe XI	352.662	6.1	1		*
Mg V	353.091	5.5	1		*
Si X	356.0	6.1	1		
Fe XI	356.519	6.1	1		
Ne IV (bl Fe XI)	358.7	5.3	1		
Ne V	359.4	5.5	1		
Fe XVI	360.761	6.4	1		
Mg VII	363.772	5.8	1		*
Fe XII	364.467	6.1	1		*
Mg VII	367.7	5.8	1	*	*
Mg IX	368.070	6.0	1	*	*
Fe XI	369.153	6.1	1		*
O III (bl N III)	374.0	5.1	1		
N III (bl O III)	374.4	5.1	1		
Si XII	520.665	6.3	2	*	*
O III	525.796	5.1	2		
C III (bl O II)	538.3	5.0	2		
Ne IV	541.128	5.3	2		*
Ne IV	542.072	5.3	2		*
Ne IV	543.891	5.3	2		*
Al XI	550.031	6.2	2		
O IV	553.329	5.3	2		
O IV	554.513	5.3	2		
O IV	555.263	5.3	2		
Ca X	557.765	5.8	2		*
Ne VI (bl Ne VII)	558.594	5.6	2		*
Ne VII	561.728	5.7	2		*
Ne VI	562.803	5.6	2		*
Ne V	569.8	5.5	2		
Ne V	572.3	5.5	2		
Ca X (bl O III)	574.0	5.8	2		
Ar VII	585.754	5.5	2		
O III	599.597	5.1	2		*
Si XI (II order)	303.324	6.2	2	*	*
He II (II order)	303.78	4.9	2	*	*
O IV	608.397	5.3	2	*	*
Mg X	624.941	6.0	2	*	*
O IV	625.853	5.3	2	*	*
O V	629.732	5.4	2	*	*

A smaller area is rastered, but more lines are obtained. The purpose of these observations was to study coronal holes in more detail, with a higher signal-to-noise and with lines suitable for *DEM* and element abundance analysis.

An example is the CHBOPT2 study, which is composed of a series of 3 adjacent rasters (slit 4″x240″) of 20″x240″ covering a total area of 1′x4′. The CHBOPT2 was optimized to account for the lower sensitivity of the NIS 1 detector, compared with the NIS 2 one. For each 20″x240″ raster, a series of NIS 2 windows with a 50s exposure time is extracted. Then, three 20″x240″ rasters are repeated on the same region extracting only NIS 1 windows, with the aim of increasing the S/N to a level similar to that of NIS2 by averaging the exposures. Each 20″x240″ raster lasts about 5 minutes, and the total duration of the study is about an hour. The drawback of this study is the lack of co-temporality between the observed intensity of NIS 1 and NIS 2 lines. A temporal variability of lower transition region line intensities over 5 minute time scales cannot be ruled out, as brightenings in the network. However, spatial averages over large areas would smooth out such variations.

Another study that was developed is UCLAN_N3, where a large portion of the NIS spectrum is extracted, to make use of all the diagnostic capabilities of CDS. With a relatively large area (2′x3′) covered, it typically observes the whole of a network cell.

- **Full rasters**

  In this case, the full NIS spectral range is recorded, at the expense of an even smaller area. The full raster studies provide enough spectral information to perform a more complete *DEM* analysis.

  Examples are the spectral atlas NISAT_S5 study, covering a small 40″x240″ area, and UCLAN_N2. NISAT_S5 was designed by the author to raster a small (40″x240″) area with the 4″x240″ slit and a long (150 s) exposure time. One drawback is that most of the time is spent telemetering the data (longer exposures are not possible because of the cosmic ray problem).

  A much better study is UCLAN_N2, a raster of 120″x150″, that after the correction for the slant becomes 2′x2′. In this case, the telemetry time is close to the exposure time and no time is 'wasted'.

4.2 The observations during August-September 1996

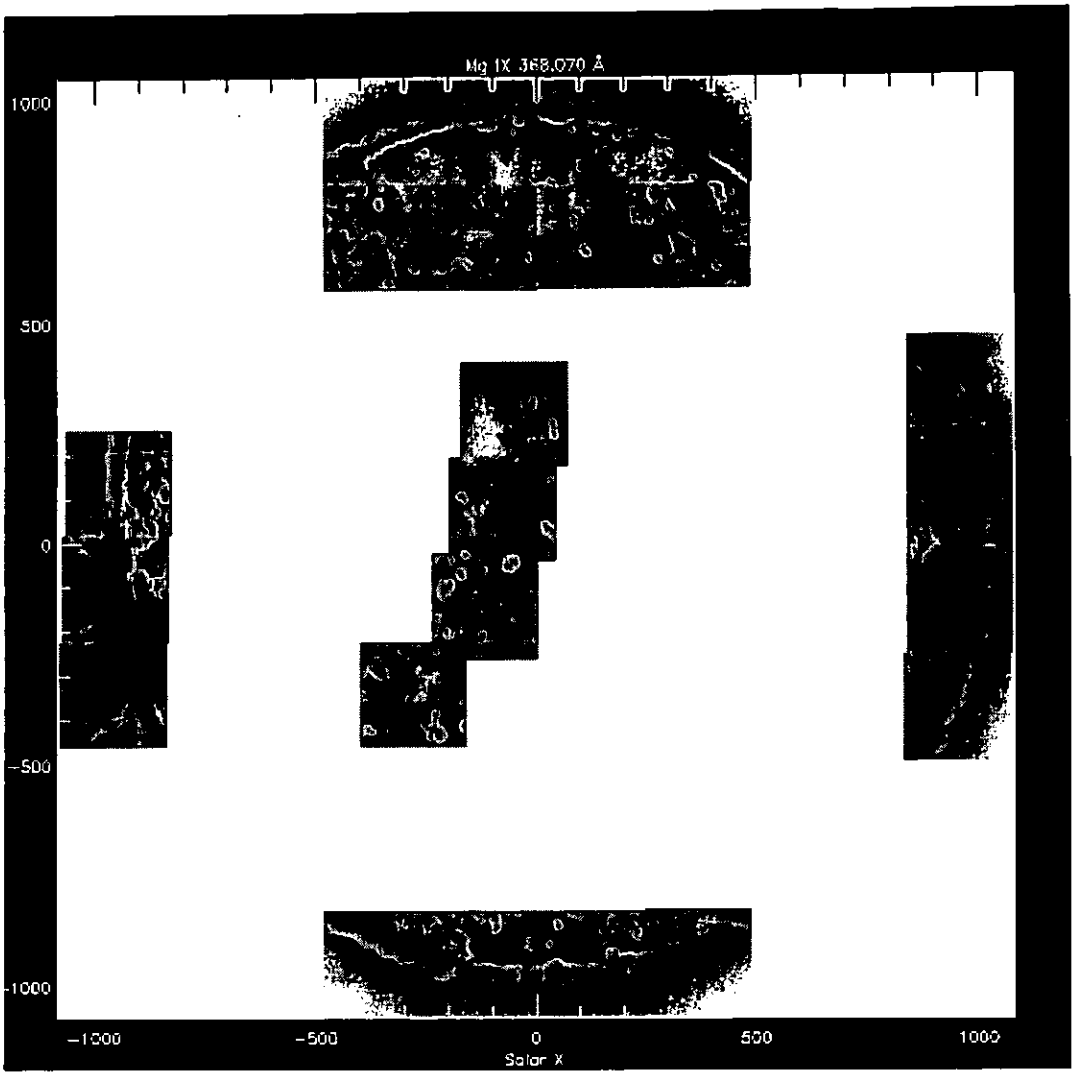

Figure 4.1: *A mosaic of Mg IX 368 Å monochromatic images (negative image) created from a series of CDS observations, centred around August 25th 1996. Note the extended North polar hole, the active region on the limb, and the Elephant's Trunk coronal hole in the centre.*

During 1996 the Sun was still around minimum activity, had extended polar coronal holes (see e.g. Figure 4.1), few active regions, and symmetric equatorial streamers. A SOHO campaign, called Whole Sun Month (WSM), was organised by S. Gibson and D. Biesecker to study the solar minimum corona between 1 and 3 $R_\odot$ for a whole solar rotation using all the SOHO instruments. One of the main goals was to then gather all this information in order to determine the large-scale physical properties (such as densities, temperatures) of the relatively simple azimuthally symmetric streamers, and the extended coronal holes.

August 1996 was chosen as the observation month, after a last minute change of plans. Since the first series of CDS observations for this thesis was planned in the same month,

and since most of the scientific objectives were in common with the WSM campaign, some effort was spent by B. Bromage and the author (at GSFC for the whole month of August) in coordinating the two sets of observations. The CDS studies for the WSM campaign were developed by A. Fludra. Section 4.2.1 describes the observations that were carried out, which mainly concentrated on the two polar regions and the two east and west limbs. Figure 4.1 shows a mosaic including such observations.

The northern polar coronal hole was large and tilted towards the Earth during this month, making it appear much larger than the south pole. In the second half of August a large 'dark' area appeared on the solar disc, and was identified by the author (with a quick-look spectral analysis) as a large equatorial coronal hole, and named 'Elephant's Trunk' (or 'tusk'), because of its appearance. Figure 4.1 (central part) shows a CDS Mg IX image of the Elephant's Trunk on August 26th 1996.

A series of CDS observations of the Elephant's Trunk was carried out during the last week of August 1996, following the passage of the hole across the disc. These observations are outlined in Section 4.2.2.

4.2.1 The Whole Sun Month (WSM) campaign

Equatorial regions above the east/west limb

A series of four LIMB studies was used in order to cover a 4′x16′ area. Figure 4.2 shows a mosaic image made in the Mg IX 368 Å line at the West limb on 1996 August 26. Observations like this were made regularly every few days from 12th August to 8th September 1996. Observations on the East limb were performed on August 13, 20, 27, 30, and September 3, 6. Observations on the West limb were made on August 12, 15, 19, 22, 26, 29, and September 2, 8.

Typically, these NIS observations were supported by GIS observations, a small slit scan across the limb in the E-W direction (G2AL study), and a long slit scan (GWEST and GEAST studies), to observe the corona at larger distances from the Sun, as shown in Figure 4.2.

Since the long slit GIS observations were un-calibrated, and in general to check the GIS calibration, various sets of observations were planned and executed by the author (although not analysed yet). These include slit 2″x2″- 4″x4″checks (using the TEST5_2 and MICRO studies) and 4″x4″- 2″x240″checks (using the GISAT_S and RWPM_1 studies).

A few observations with the large 90″x240″ slit were also carried out in support. Movies have been created, that show the highly dynamic nature of all the solar structures observed,

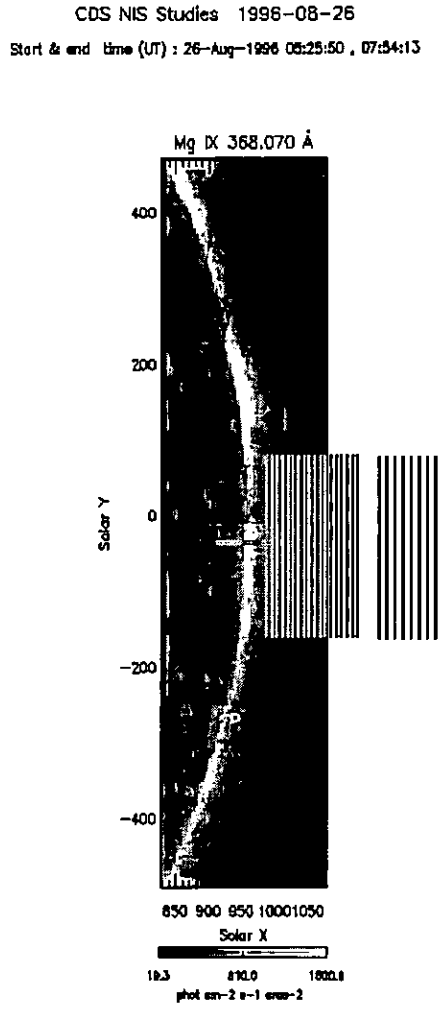

Figure 4.2: *A mosaic of four Mg IX 368 Å images taken by CDS at the Sun's west limb on August 26, 1996, showing also the position of the GIS studies, small and long slits.*

as seen off-limb.

Polar coronal holes

The observations over the polar coronal holes were a combination of observations planned by the author and those planned for the WSM.

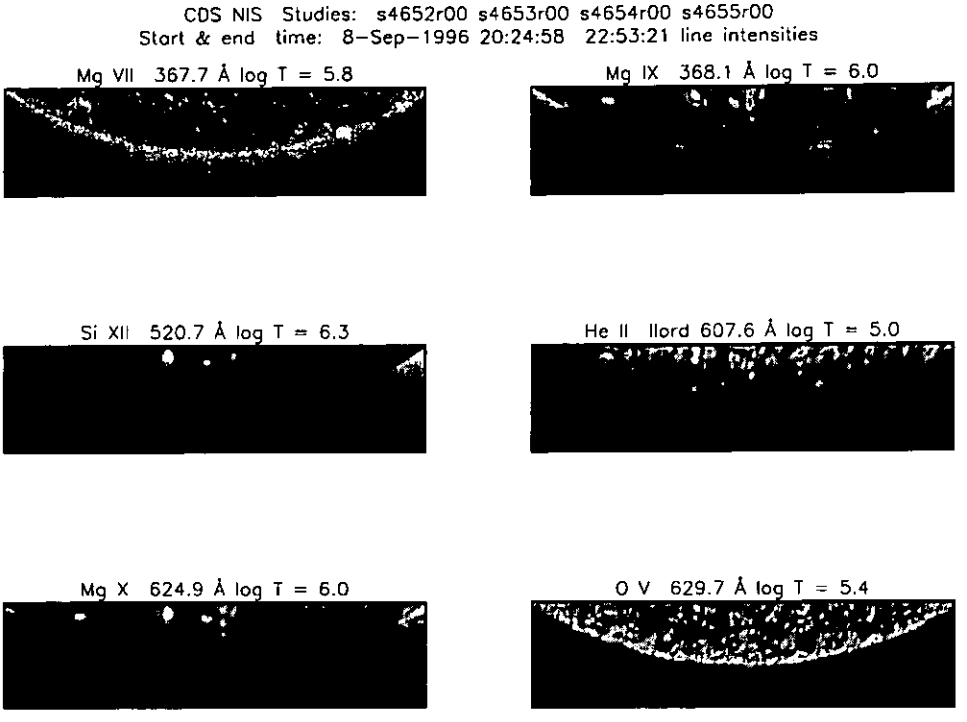

Figure 4.3: *A mosaic of four LIMB studies taken on September 8, 1996, in the south coronal hole. The total area in each panel is about 16′x4′.*

In this case, a series of four LIMB studies was used to cover a 16′x4′ area, as a mapping to study the structure and evolution of the coronal holes, and as 'context' observations for more detailed studies. Figure 4.3 shows mosaics created from the September 8 1996 observations. The upper transition region (Mg VII) and lower corona (Mg IX) lines show the presence of polar plumes. Observations of this type were made on August 10, 16, 17, 24, 25, 31, and September 7 to observe the north coronal hole. Observations of the south coronal hole were made on August 11, 18, and September 1, 8. In some cases, these observations were supported by GIS scans across the limb.

4.2.2 The Elephant's trunk

Figure 4.4 shows a magnetogram (SOHO/MDI) and an EUV image (SOHO/EIT) of the Sun taken on 26th August 1996. The Elephant's Trunk appeared as a predominantly

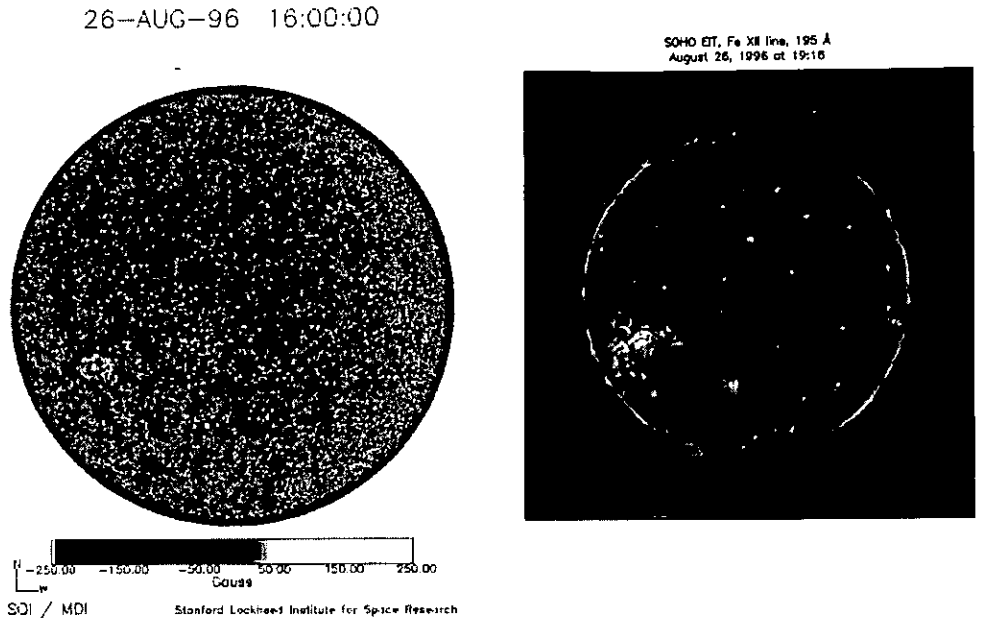

Figure 4.4: *The Elephant's Trunk as seen on the 26th August 1996. Left: a magnetogram from SOHO/MDI (courtesy of C. DeForest). Right: a SOHO/EIT image.*

unipolar region, that extended from the north coronal hole to a region of strong magnetic field associated with an active region just south of the equator. This field had the same polarity as the north polar hole. A neutral line appears to run along the prominence channel parallel to the coronal hole to the East. This equatorial coronal hole resembled the famous 'Italy boot-shaped' (CH 1) coronal hole observed by Skylab in 1973 and described in Chapter 1.

The Elephant's Trunk provided a rare and important opportunity to study coronal holes because:

- it crossed the Sun centre, making it possible to perform spectroscopic observations with a largely radial line of sight. Thus it was possible to observe the coronal hole, without contamination from foreground quiet sun material.
- The Sun was at solar minimum. Therefore, any contamination from foreground quiet sun material was further minimised.

A series of CDS observations of the Elephant's Trunk was carried out on the 25th, 26th, 27th, and 29th of August 1996.

A series of NIS observations (LIMB studies) were made on the 25th, 26th and 29th of August 1996 in order to create composite monochromatic images and to give an overall picture of the coronal hole. Figure 4.5 shows the CDS mosaics in Mg IX, created from

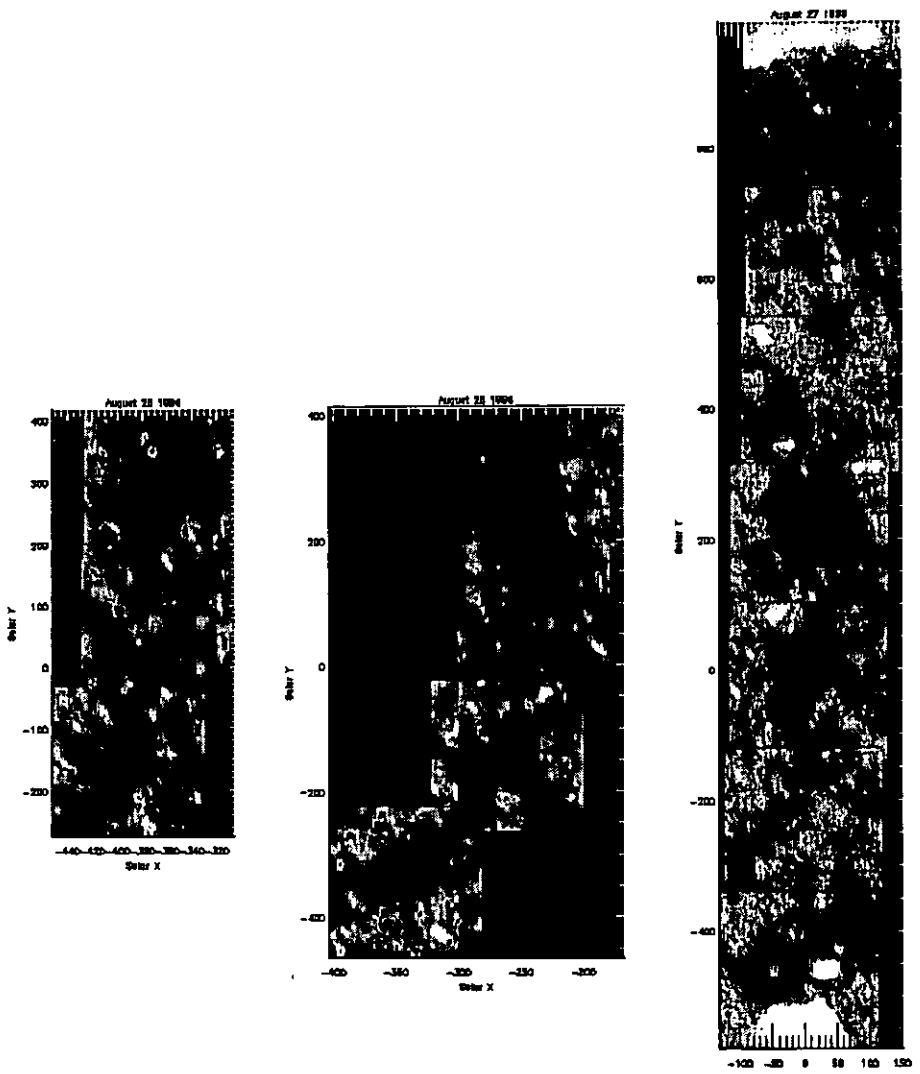

Figure 4.5: *The Elephant's Trunk as seen on the 25th 26th and 27th August 1996 in the coronal line Mg IX 368 Å by CDS, showing changes over the time-scale of one day.*

observations taken on the 25th, 26th and from a SYNOP sequence of 27th August. Small changes in the boundaries and inside the hole were visible on all time-scales, making it difficult to perform accurately pointed observations. The overall structure of the Elephant's Trunk, however, persisted for a long time. In fact, the hole largely decayed over a time scale of the order of two solar rotations, with parts remaining for much longer.

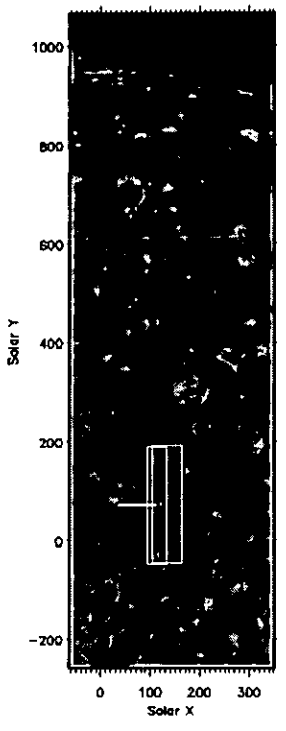

Figure 4.6: *EIT 195 Å - 27th August 1996 12:15 UT with the regions rastered by CDS. The CHBOPT2 is the rectangular region on the right, while the narrower NISAT_S5, partly overlapping, is on the left. A GIS E-W scan across the hole is also shown.*

A region near the solar equator was observed on the 25th, 26th and 27th, as it rotated across the meridian, using CHBOPT2 and NISAT_S5. Figure 4.6 shows the position of the rasters for the 27th. On the same days, some E-W GIS scans across the hole were obtained with the 4″x4″slit, to observe both the east and west boundaries. Specific simultaneous observations with other instruments on board SOHO were also organised on the 27th, the day of the meridian passage. EIT and MDI observed the hole with high time and spatial resolution. SUMER produced reference spectra.

On the 29th, a GIS scan inside the hole, in the N-S direction was obtained, together with a NISAT_S5 raster.

4.3 The observations during September-October 1997

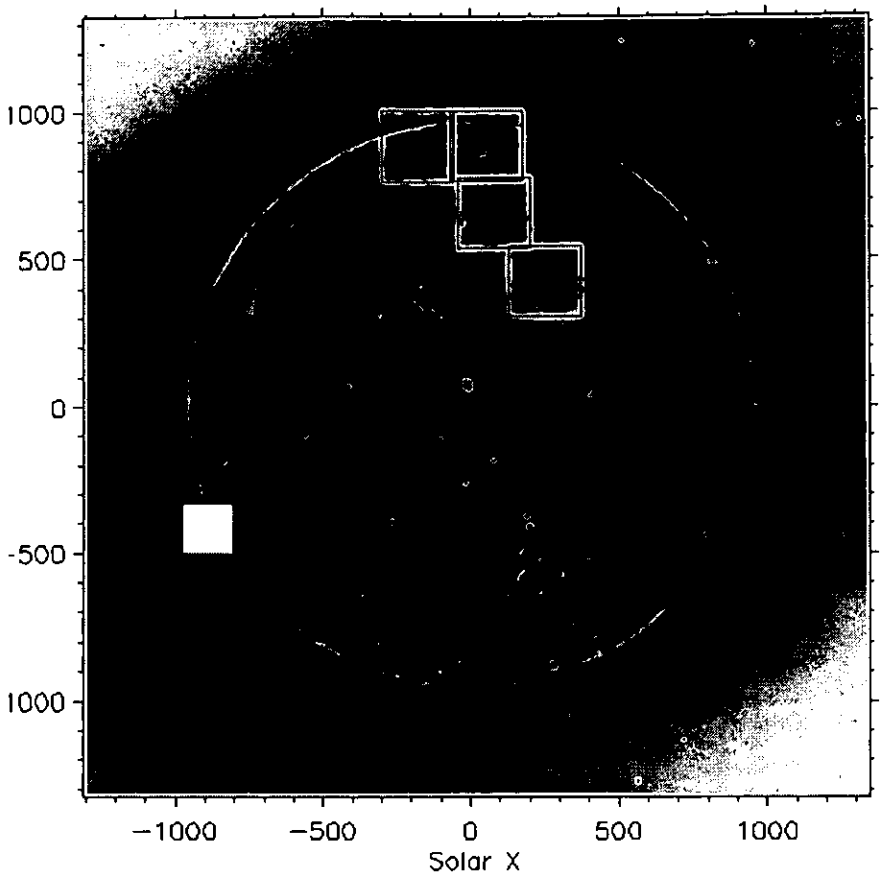

Figure 4.7: *EIT 195 Å - 7th October 1997, with the regions rastered by CDS. Negative image created with the IDL routine IMAGE_TOOL.*

During this period the Sun was in the rise phase of cycle 23. In the corona (see Figures 4.7, 4.8, and 4.9), many new active regions were forming at high-latitudes, and both polar holes were much reduced in area, with a bright polar crown region, emitting also high-temperature lines. The Sun was tilted in such a way that the north polar hole was more visible than the southern hole, which disappeared at times. A coronal hole Campaign (# 1990) was organised by B. Bromage and the author, with supporting ground observations and observations by the other SOHO instruments, in particular SUMER, EIT, and MDI. Mostly, the observations were of the north polar region, with meridian studies and with studies that followed the same region day by day. In particular, an extension of the polar hole, and a region in the N-W were studied in more detail. As in August 1996, mapping of the coronal holes was performed with large field-of-view NIS rasters (as shown in Figure 4.7), while more detailed observations were made using smaller field-of-view GIS and NIS observations. Figure 4.8 shows as an example the sequence of areas observed on the 2nd October 1997 with the WIDE3LA1, UCLAN_N3, DEM_GIS, NSGSCAN1 studies,

to observe the boundary of the north coronal hole, at the meridian (special SUMER support was also organised).

There were some periods of high-telemetry, when special sequences were run. Many full-wavelength spectra were taken (NISAT_S5, UCLAN_N2 studies) over the boundary of the north coronal hole. In particular, on the 14th of October, UCLAN_N2 was repeated 6 times on the same area. Also, various high-rate GIS E-W scans (HRBNDWE study) were run over coronal hole regions, including plumes. On the 17th of October one of these scans was done above the north limb.

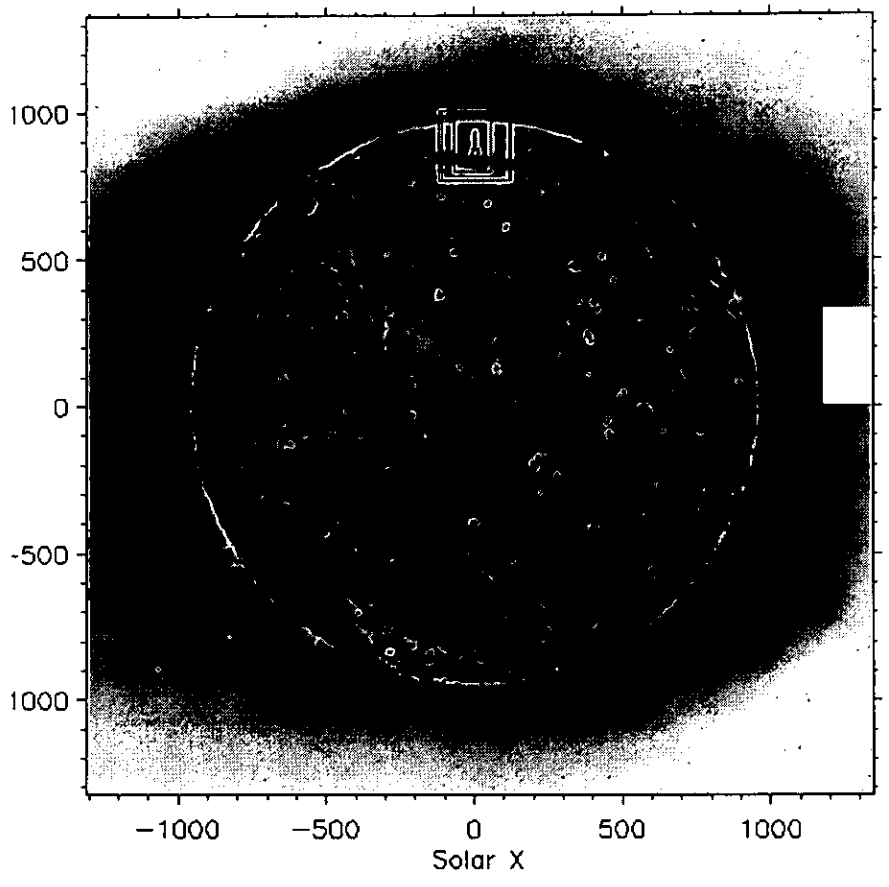

Figure 4.8: *EIT 195 Å – 2nd October 1997, with the regions rastered by CDS. Negative image created with the IDL routine IMAGE_TOOL.*

During the last week of September, some observations were performed in off-limb regions, in support of EISCAT IPS observations, together with LASCO observations.

In order to study the relationship between the observed features at radio and EUV wavelengths (see *Gopalswamy et al.*, 1998), specific CDS simultaneous observations with the Nobeyama Radio telescope were planned, in collaboration with Dr. Gopalswamy. Mainly, the NIS WIDE3LA1 study, which is composed of three scan positions with the wide slit, was used to build movies in the brightest He I, O V, Mg IX lines seen by CDS. Simulta-

neous observations on October 10–11th, 14–15th were executed and analysed.

4.4 Off-limb observations of polar holes (February - April and October 1997)

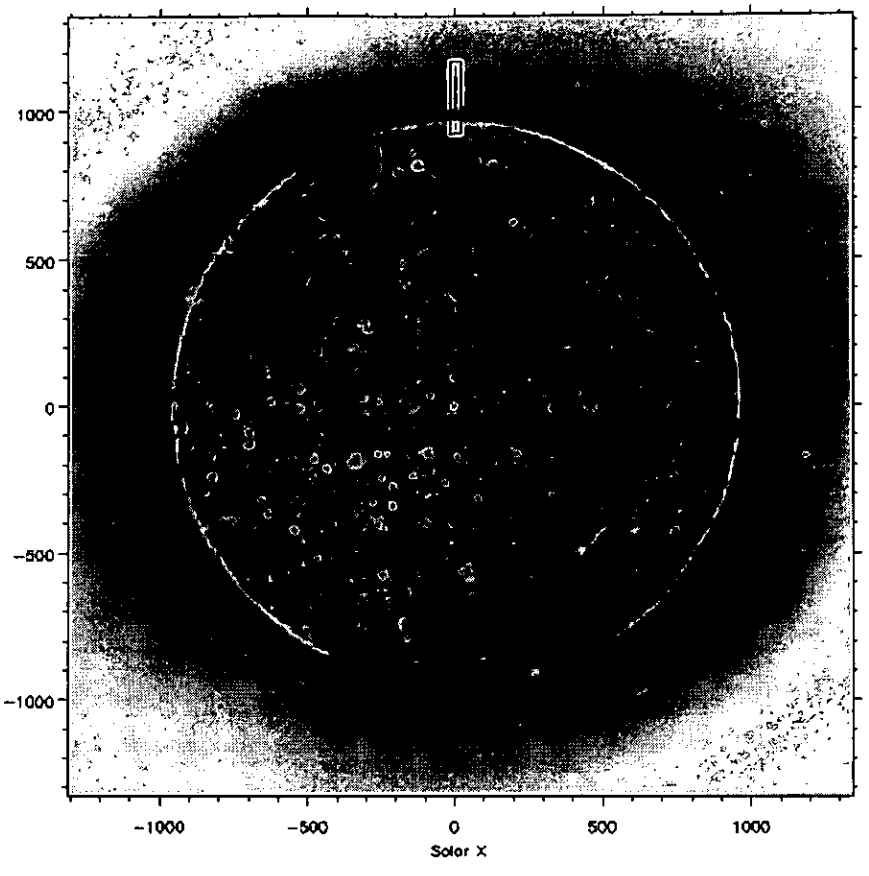

Figure 4.9: *EIT 195 Å - 12th October 1997 17:26 UT, with the off-limb NISAT_S5 raster positions. The NIS observations started at 8:55 UT and ended at 13:43 UT. Negative image created with the IDL routine IMAGE_TOOL.*

To take advantage of high-telemetry, on the 12th of October 1997, a series of 6 NISAT_S5 studies were taken off-limb in an inter-plume region (see Figure 4.9). This sequence of rasters represents the longest off-limb full-spectrum NIS observation taken by CDS, as far as the author is aware. The solar corona at that time was such that any effects of plasma from extended hot loops overlying the coronal holes were very limited, as can be seen in the EIT picture in Figure 4.9, and therefore most of the observed emission comes from the inter-plume region.

A few GIS N-S scans over the north or south polar limbs were performed. In addition, a particular set of observations was developed to study plume and inter-plume regions off-limb, and named *'off-limb cross'*. The main idea was to perform one N-S scan just

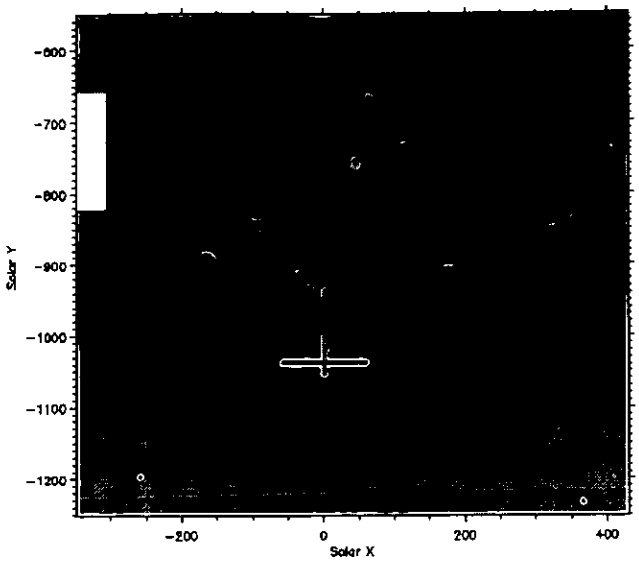

Figure 4.10: *EIT 195 Å - 27th March 1997 12:49 UT, with the GIS 'off-limb cross' rasters. Negative image created with the IDL routine IMAGE_TOOL.*

off-limb and one E-W scan at larger distances, to form a cross (see Figure 4.10) centred at the meridian. Since the error in the CDS pointing (10″) is of the order of the plume dimensions (20″), such a combination of two rasters was designed to check the pointing. The N-S raster was pointed to have a few exposures inside the limb, and therefore to be able to check its Solar Y position. From the E-W scan it is possible to distinguish between plume and inter-plume areas, since the plumes (if there are any) are aligned along the N-S direction around the meridian. The Solar Y (i.e. the distance from the limb) of this raster could easily be checked with the help of the N-S raster, because the intensities of the lines have an exponential fall-off with distance making it easy to find the intersection of the two rasters.

The exposure times, distances and length (120″) of the rasters were adjusted to be able to observe on average at least one plume and inter-plume region as far as possible from the limb, with good signal-to-noise and with a total duration (about 7h) not too long, so that effects of the solar rotation (which are minimal on the meridian at the poles) would be negligible.

Observations such as that shown in Figure 4.10 were repeated on the 13th February, 10th March (this had missing data and wrong pointing), 29th March (again with large data dropouts), 1st April 1997, and the 23rd October, all in 1997.

4.5 The software developed for the data analysis

This Section gives a short description of the procedures developed for the analysis of the CDS data and of the software that was written in IDL by the author. Basic software was available to read the data, perform the standard corrections (such as flat-fielding), and the line fitting (which became available only in 1997), as described in Chapter 3. The high versatility of the CDS instrument, in terms of type of observations, meant that each CDS study (or sequence of studies) required the development of appropriate analysis software. A set of programs was written with the flexibility to automate and simplify the data analysis of as many CDS studies as possible. IDL routines were also written for other purposes, some of which (e.g. CDS calibration or *DEM* analysis) have already been described. About 200 IDL routines containing a total of more than 100 000 lines of code were written. Some of the software has been released for public use (the *DEM* package, *Del Zanna et al.*, 1997), and some has been distributed as part of international collaborations. Only a short description of some of the software used in this thesis is given here, to give an idea of the type of problems encountered and how they have been solved.

The data analysis of a single observation.

Each single CDS observation is stored as a FITS file. Routines were written to perform the *first step standard analysis* on the raw data, applying one-by-one all the corrections that have been described in Chapter 3, with various options, plots and checks. Depending on which instrument was used, on the type of raster (e.g. one-dimensional or bi-dimensional for the GIS), and on the type of data extraction, an appropriate routine had to be written. In the NIS case, contiguous windows (if any) are merged. Then, the background is estimated and line intensities found, by summing the pixel values and/or applying the multiple line fitting described in Chapter 3. The results are then saved in IDL 'save files'. Routines were written to display the results in various ways, and to perform subsequent analyses on the data.

The data analysis of a series of FITS files

In many cases a 'single' observation consisted of a series of FITS files, that had to be processed one by one, and then combined. The complexity of the data processing followed the complexity of the type of CDS study. Among the most complex and time consuming for the data analysis, were the CHBOPT2 and the HRBNDWE studies.

The mosaics of the data

Mosaics of the monochromatic images were formed from the single observations, interactively adjusting the relative position of each one to obtain the best composite image.

Specific features (such as the solar limb in chromospheric lines) that do not change in time, were usually used for this purpose. The IDL save files of the single observations were read and then the combined data were saved in a new IDL save file. Other routines were written to perform subsequent analyses on the merged data. These include displays of the images and ratios of any two of them, examination of the results, selection of areas to average, production of line fitting, and storage of the results in various forms.

The selection of areas to average

In most cases, even long exposures were not enough to achieve sufficient signal, in particular in coronal holes, and averaging of spectra was needed to improve the signal-to-noise in the weak lines, especially the density-diagnostic ones. For the off-limb observations, software was developed to interactively select areas to spatially average spectra along concentric arcs at fixed heights above the limb, to provide a one-dimensional, radial dependence of the spectra (after the gaussian fitting of the line intensities). It is also possible to select a range of position angles, in order to select regions of different latitudes. The software also allows selection of an intersection of these concentric areas and other areas selected by other criteria (e.g. to include only an inter-plume region or to exclude an active region). For the on-disc case, software was written to select areas, add them, 'intersect' and overplot them, in order to produce a single spectrum, or a sequence of spectra along one spatial direction.

In summary, specific customised analysis software needed to be written to deal with the various analyses, depending on which type of region was selected (e.g. a single region or a sequence of regions), which instrument was used (i.e. NIS or GIS), and which type of observation was made (e.g. full- or windowed-spectrum for NIS).

Chapter 5

Results for coronal holes, quiet sun and plumes

This Chapter presents a selection of 'typical' results from the analyses of coronal hole and quiet sun regions, and of coronal hole plumes, using the data described in Chapter 4. First, off-limb densities and temperatures derived from 1996 to 1998 quiet sun and coronal hole observations, are presented in Section 5.1, to show the main differences between these regions, and how they have not significantly changed over that period. Secondly, results from some of the near Sun centre observations done in 1996 are presented in Section 5.2. They include densities, temperatures and abundances for the Elephant's Trunk coronal hole, a nearby quiet sun region and a low-latitude plume. These observations are then compared and summarised in Section 5.2.4.

Part of the analyses done have already been published (see below for details), and the results are only outlined here. Some of the data presented in these published papers have been re-analysed for this thesis using the most up-to-date instrument calibration (Chapter 3), improved atomic physics, and different ionization equilibrium. The results of these re-analyses, presented here, do not affect the main findings, but have some differences from those already published. It is important to make clear which are the main reasons for these differences.

- A new instrument calibration (Chapter 3) has been adopted.

  While results based on lines close in wavelength and seen in the same detector (as the densities based on the Si IX and Si X line ratios, for example) are not much dependent on the calibration, others, such as those derived from the use of the Mg and Ne lines seen in NIS 1 and NIS 2, can be different by a factor of 2, depending on which calibration is adopted. Since the Mg/Ne abundance is the only one that can be used to constrain the relative abundances of all the other high- and low-FIP ions (if only NIS observations are used), a different calibration affects results in terms of

FIP effect. Also, with the calibration adopted here, many bright coronal lines (Mg X, Al XI, Si XII) seen in NIS 2 are not in good agreement with those observed in NIS 1, as already seen.

- A different ionization equilibrium. Here, the *Arnaud and Rothenflug* (1985) ionization equilibrium for all the ions has been adopted, together with the calculations of *Landini and Monsignori Fossi* (1991) for the minor elements. In some of the previous publications the *Arnaud and Raymond* (1992) calculations for Fe were used. Chapter 3 already illustrated some of the differences that are found when other ionization equilibrium calculations are adopted, with variations of a factor of almost 2 for some ions, and how the *Arnaud and Rothenflug* (1985) calculations give more consistent results between most of the ions. Different choices of ionization equilibrium affect both the DEM distribution (although slightly), and the relative element abundances that are found with the use of any differential emission measure (or line emission measure) method.

  The *Arnaud and Rothenflug* (1985) ionization equilibrium has been assumed here in deriving all isothermal temperatures from line ratios.

- More recent atomic data, in the form of CHIANTI v.2 (*Landi et al.*, 1999b) have been used. The main differences between CHIANTI v.2 and the previous versions, that concern the results presented here, are new calculations for Ne IV, Ne VII, and Fe X, together with the inclusion of many new ions. The differences in the emissivities are considerable for some lines. Then, CHIANTI v.2 contains a correction for an error in the earlier O IV database, that affected the 608.4 and 609 Å lines, such that densities derived using the 608.4 Å line were overestimated by about a factor of 2.

  In addition to the CHIANTI upgrade, recent Fe XIV calculations (*Storey et al.*, 1999) and Mg IX calculations (P. Young, 1999, priv. comm.) have been used here, although the differences for Mg IX are small and the Fe XIV lines are weak or absent from the spectra used. For those ions that are not present in the CHIANTI database, the Arcetri spectral code (AC, see, e.g. *Landi and Landini*, 1998a) was used. The continuum emission has been calculated with the method described in *Landi et al.* (1999b).

5.1 General characteristics of off-limb densities and temperatures for the quiet sun and polar coronal holes from 1996 to 1998

August 1996 was a good choice for the Whole Sun Month (WSM) international campaign. During this month, there was little variation in longitude of the equatorial streamer structure (in particular around the 20th), as shown for example by coronagraph images, and this simple structure became the best test the Sun could offer for comparisons of different instruments' data and modelling. Two workshops were organised to coordinate the effort, and the author actively participated in these. The main outcome of the WSM campaign has been a series of refereed journal papers, collected into a special issue of the Journal of Geophysical Research – Space Physics in May 1999. As well as leading one paper, the author contributed directly to two papers doing a large part of the data analysis and providing software (*Fludra et al.*, 1999a; *Gibson et al.*, 1999). Preliminary results were given by *Fludra et al.* (1997a), and *Fludra et al.* (1997b). The observations that were analysed in collaboration with A. Fludra, together with the main results, are presented in this Section.

Off-limb observations of the equatorial regions

From the large data set presented in Chapter 4, NIS data taken on six days were selected for analysis of the equatorial regions above the east/west limb. Three pairs of dates approximately half a solar rotation period apart were chosen: 12 and 27 August, 15 and 30 August, and 19 August and 3 September. This allowed direct comparison of the same location viewed both on the East and West limb to check the time variability in the coronal streamer structure. In addition, the dates of 12 and 19 August (and 27 August and 3 September) are seven days apart, thus sampling different areas separated by 90 degrees in longitude. All of the monochromatic images obtained for the above dates showed quiet Sun areas, almost free from any active region emission. In two cases where active region loops were present, these areas were excluded from analysis, and only the quiet part of the solar corona was analysed.

As an example, some results for the off-limb observation of on 1996 August 19 are presented here. The data have been averaged along concentric arcs of constant radius and spanning a range of position angles, to produce (after a multi-gaussian fit to the spectra) an averaged radial dependence of the line intensities. From these, physical parameters such as electron density and temperature have been derived as a function of the radial distance above the limb. Spatial averaging along concentric arcs increased the signal-to-noise, allowing

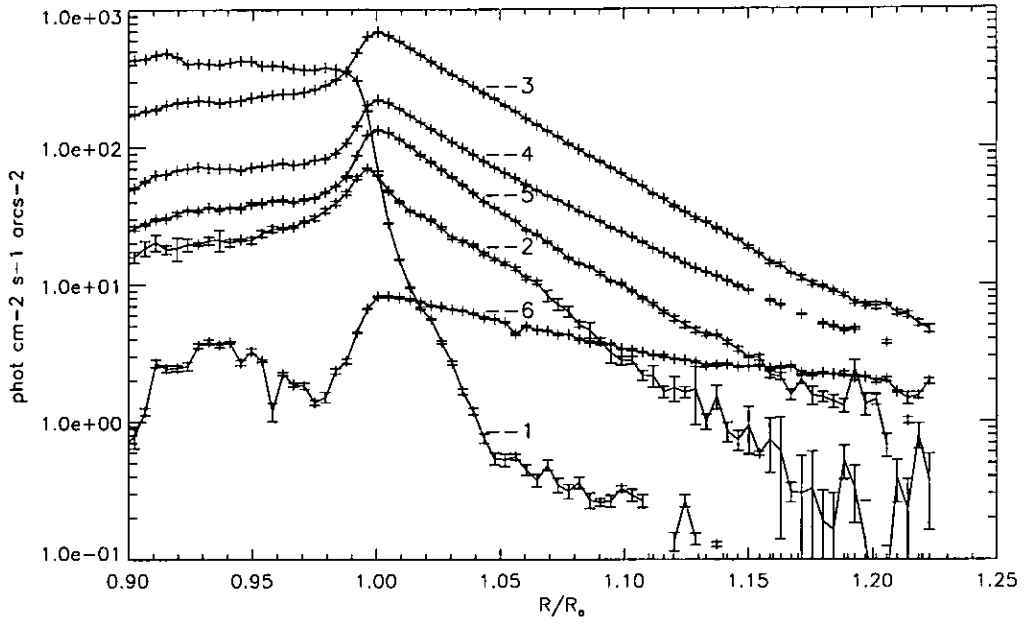

Figure 5.1: *The off-limb intensities of selected lines – 19th August 1996, plotted on a log scale. 1: He I 584.3 Å; 2: Mg VII 367.7 Å; 3: Mg IX 368.1 Å; 4: Mg X 624.9 Å; 5: Si IX 349.9 Å; 6: Si XII 520.7 Å. Note the different slopes of intensities versus radial distance above the limb.*

measurement of the coronal line intensities up to 1.2 $R_\odot$. These are shown in Figure 5.1. Note: (1) the rapid drop of the He I intensity, showing there is little off-limb stray light; (2) how the line intensities have near-exponential decreases, with different slopes for different lines.

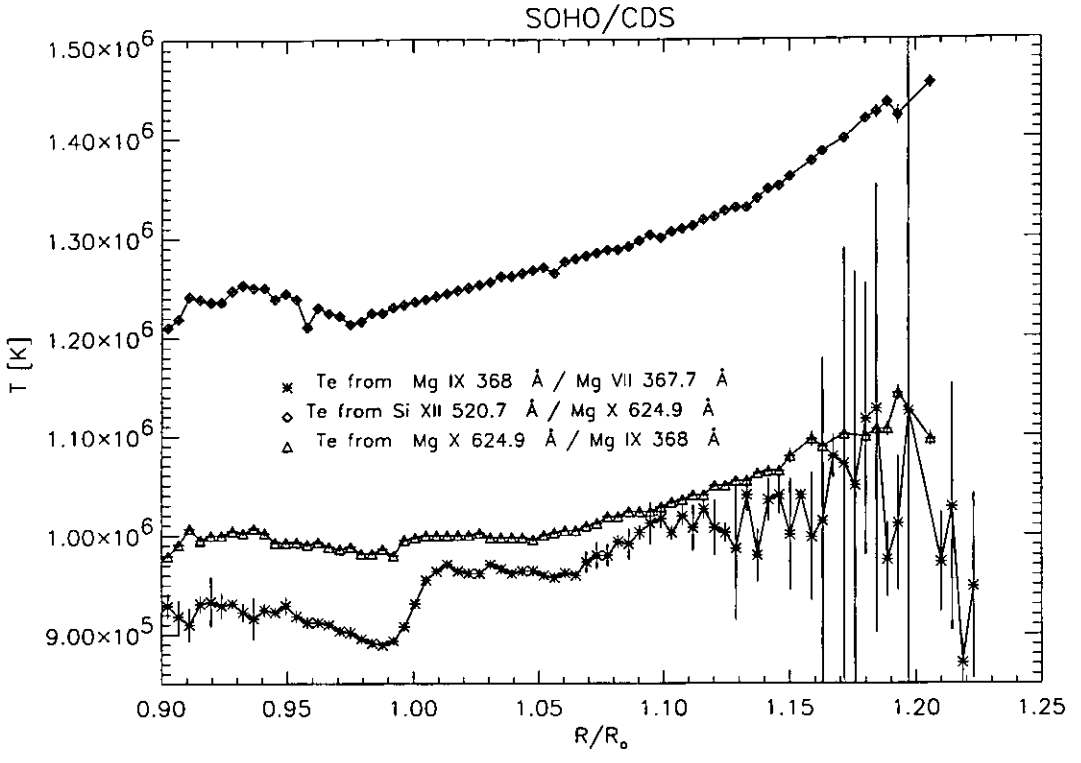

Figure 5.2: *The off-limb isothermal temperatures as derived from different line ratios. – 19th August 1996. The temperature from the Si XII / Mg X ratio was derived assuming photospheric abundances.*

Figure 5.2 shows the isothermal temperatures as derived from various line ratios. The fact that the various ratios yield different temperatures shows that the plasma was not strictly isothermal at those radial distances. Each temperature increases by about 10% from the limb to 1.2 $R_\odot$.

Figure 5.3 shows how the two Si IX lines used for density estimates, have different radial profiles, and how the derived density (that is an average along the line of sight) decreases from 5 x10^8 on the disc and at the limb, to 1 x10^8 (cm^{-3}) at 1.2 $R_\odot$.

Further results are presented in *Fludra et al.* (1999a) and *Gibson et al.* (1999). Electron densities were derived from the observed Si IX 349.9/341.9 Å ratio, while isothermal temperatures from Si XII/Mg X and Si XII/Mg IX ratios were calculated up to 0.2 $R_\odot$ above the limb. The results showed little time variability over a period of 20 days. Densities in the streamer region decreased exponentially with height, while temperatures showed an

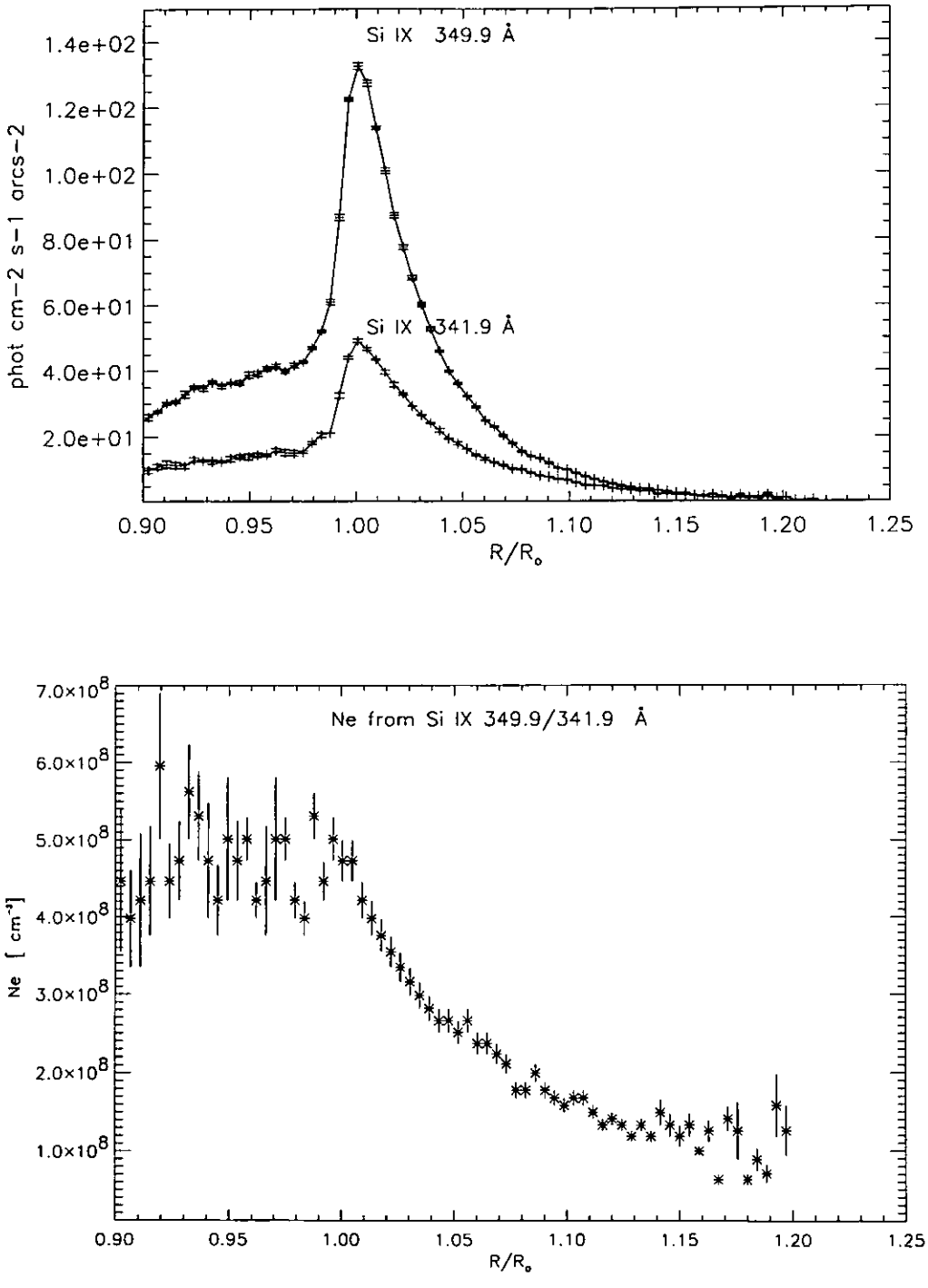

Figure 5.3: *The off-limb intensities of the two Si IX lines (above) and the derived densities (below) – 19th August 1996.*

increase up to 1.2 $R_\odot$ after which they maintained level values. A comparison with Yohkoh SXT data (*Fludra et al.* 1999a) showed a good agreement in terms of temperatures, for the streamer region of August 19. This direct comparison of nearly-simultaneous observations of a simple structure indicates that the results from direct EUV line intensities and broad-band filter ratio techniques can sometimes be in good agreement.

The streamer data were used by *Gibson et al.* (1999) for a comparison with results from white-light data. The densities determined from CDS and those determined from the *van de Hulst* (1950) inversion technique were very similar. This allowed the radial dependence of the electron density (averaged along the line of sight) over the 1–4 $R_\odot$ range to be simultaneously determined for the first time. Remembering that the white light intensity is proportional to an integral of N_e along the line of sight , while EUV line intensities depend on ${N_e}^2$, this result is quite remarkable.

Polar coronal holes

The North polar coronal hole observations of 1996 August 24, 31, and September 7, and South polar coronal hole observations of August 18 were analysed for the *Fludra et al.* (1999a) paper. The same spatial averaging along concentric arcs of constant radius described above was applied to the data.

Some preliminary results were given by *Fludra et al.* (1997a) and *Fludra et al.* (1997b), while a more complete analysis is presented in *Fludra et al.* (1999a). Densities and temperatures of the polar coronal hole regions were obtained using the same diagnostics described above. The main results are that densities and temperatures were lower in coronal holes, and that the derived values presented little variability over that period. Densities were decreasing with height, having lower values (by about a factor of 2) compared to the equatorial regions.

A similar analysis of off-limb NIS spectra was repeated on further sets of coronal hole observations, planned and executed in 1997 and 1998 by A. Fludra. Some of the results obtained are described in *Fludra et al.* (1999b), and are not repeated here. One remarkable result is that densities and temperatures showed similar values to those of August 1996.

5.2 Results from near-disc-centre observations, 1996 August

Coronal hole CDS observations of the 1996 August 26 and 27, which benefited from a near-radial line of sight, are presented here. In addition, results from a full raster observation on August 25, of a quiet sun region near the disc centre, westward of the coronal hole, are also presented and used as a quiet sun reference observation for that period.

5.2.1 The results from the Elephant's Trunk observations of the 26th August 1996

The following results are derived from composite series of four LIMB studies of the 26th (11:21-13:49 UT) and the CHBOPT2 study of the same day (Solar X=-62, Solar Y=72, 15:00-15:57 UT).

Figure 5.4 shows monochromatic images of the Elephant's Trunk on the 26th, when it was close to the meridian. A few characteristic features are of note. It is well-known that emission from both coronal lines and from He I (and He II) lines (in the network) is depressed in coronal holes. Figure 5.4 confirms this picture and also reveals that the cell centres in this coronal hole were somewhat elongated and enlarged, as seen at both chromospheric (He II) and transition region (O V) levels. At higher temperatures, the network pattern tends to disappear, and the emission has a more diffuse character. Emission from the hottest ion observed (Si XII) is completely absent in the coronal hole.

The scattered light

Figure 5.5 displays the 'background' level corresponding to the same observation, at the same wavelengths shown in Figure 5.4. Most of this scattered light (discussed in Chapter 3) is spatially-dependent, being more intense in the network regions (defined below).

The definition of cell-centre and network areas

The intensity of the O V 629.7 Å line has been used to distinguish between cell-centre and network areas (see, e.g., *Reeves*, 1976 for the technique, and *Gallagher et al.*, 1998, for a recent re-examination of the quiet sun cell and network structures) in order to produce consistently-defined average spectra of the regions examined, and to look for possible broad correlations of the supergranular structure with variations of the deduced parameters (temperature, density, and abundances).

This transition region line was chosen because its intensities in the network are not diminished inside coronal hole areas, unlike the chromospheric He lines, and because is one of

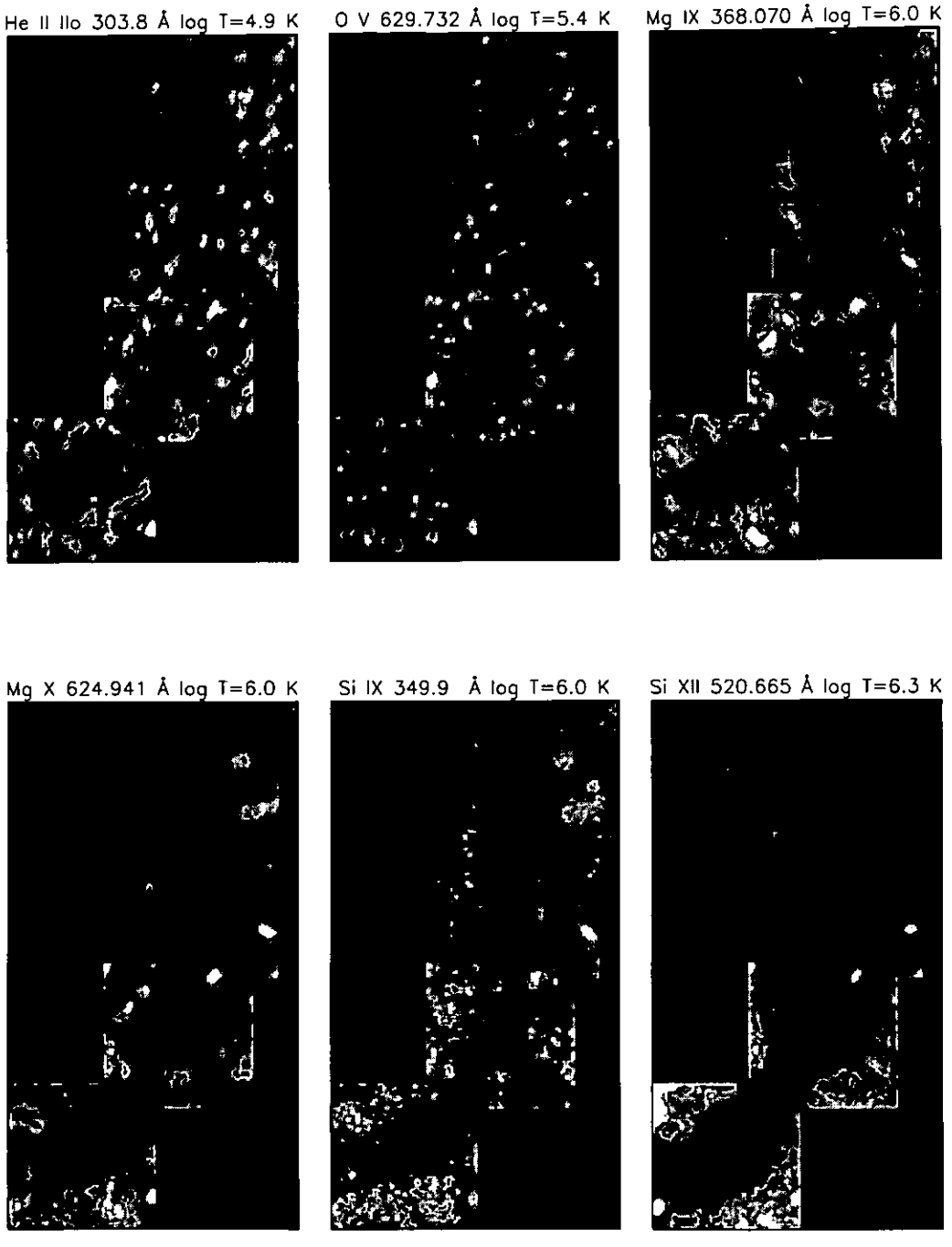

Figure 5.4: *The Elephant's Trunk in the solar corona imaged in EUV emission lines observed by CDS/SOHO on August 26, 1996.*

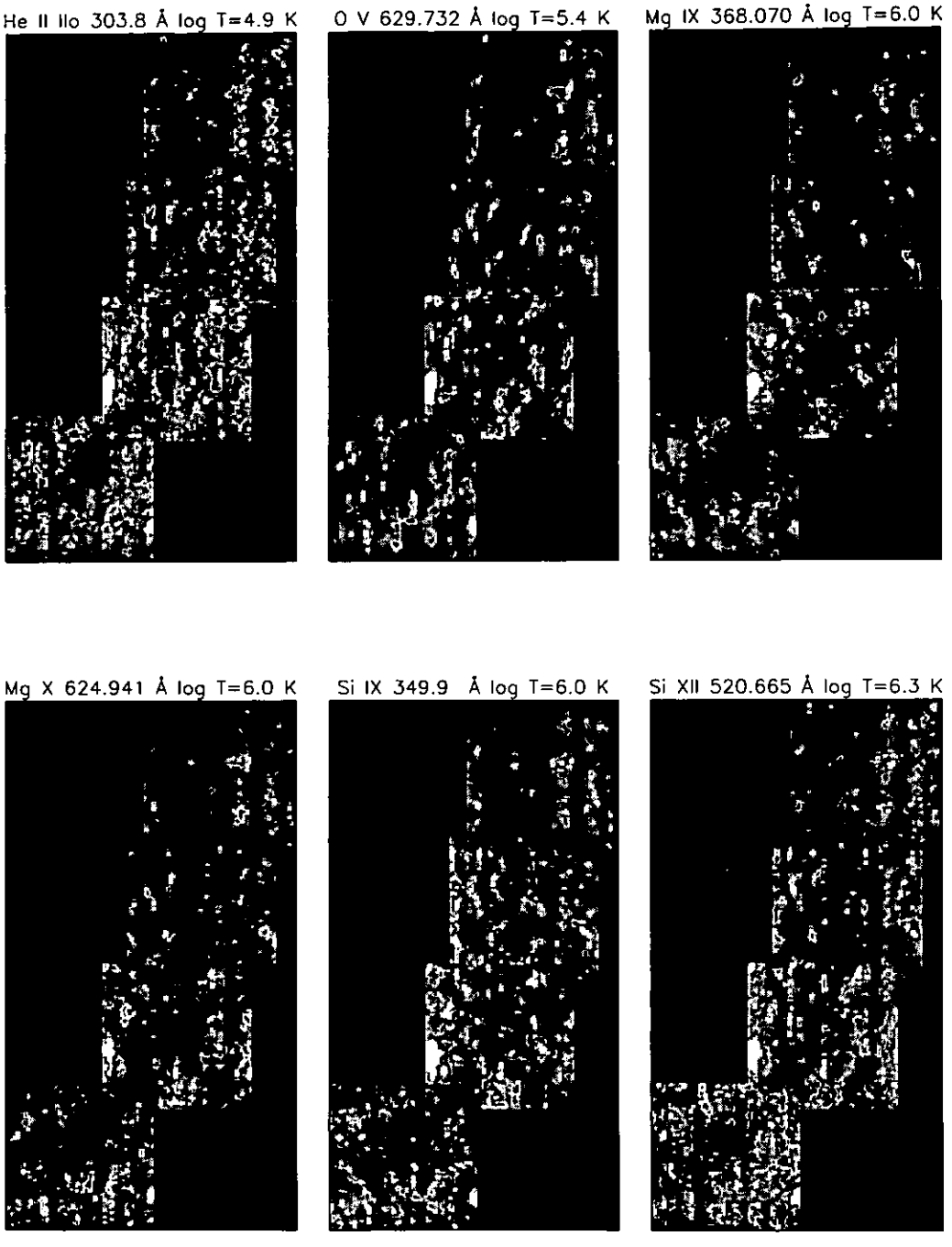

Figure 5.5: *The background level at the wavelengths corresponding to the lines indicated, in the same region shown in Figure 5.4.*

the brightest lines in the NIS spectra. The intensity distribution in O V has been fitted by a double Gaussian profile. Cell-centre (network) areas were defined as those regions having intensities less than (above) the value at the crossover of the two Gaussian profiles. This criterion has been applied to all the coronal hole and quiet sun observations analyzed. Figure 5.6 shows a histogram of the intensity over the whole of the mosaic area, and a visual representation of the cell-centre regions selected with the adopted criterion. It should be said that different choices of definitions of cell-centre and network regions lead to slightly different results.

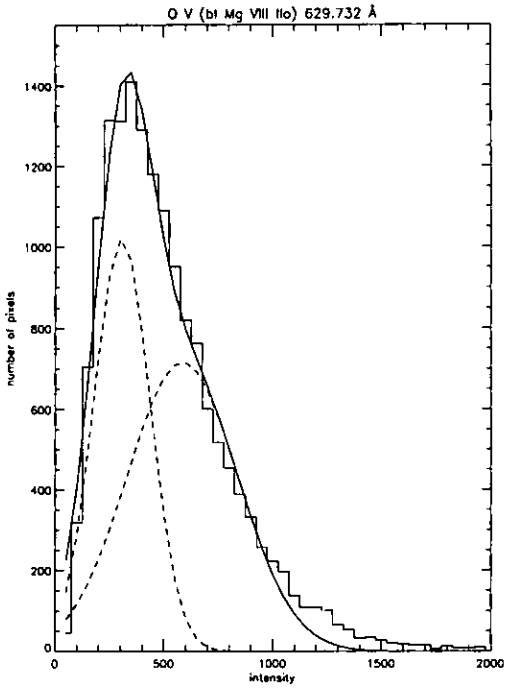

Figure 5.6: *The histogram of the O V 630 Å intensities from the August 26 1996, observation, showing the two-component gaussian fit used to define cell centre and network regions. The high-intensity tail represents localised brightenings in the network.*

The definition of coronal hole boundaries

It is difficult to unambiguously define coronal hole boundaries using EUV on-disc observations. Using intensities of coronal lines can be highly misleading, since the emission measure at any particular temperature along the line of sight can be expected to vary, and also abundance variations can affect the integrated intensity along the line of sight. An isothermal temperature map, on the other hand, shows much more clearly the boundaries of coronal holes. In the case of the Elephant's Trunk, the isothermal temperature map (Figure 5.7) clearly shows the extension of the polar hole down to the equator, and its continuity all the way from the north pole to the associated active region, as also shown

by magnetograms.

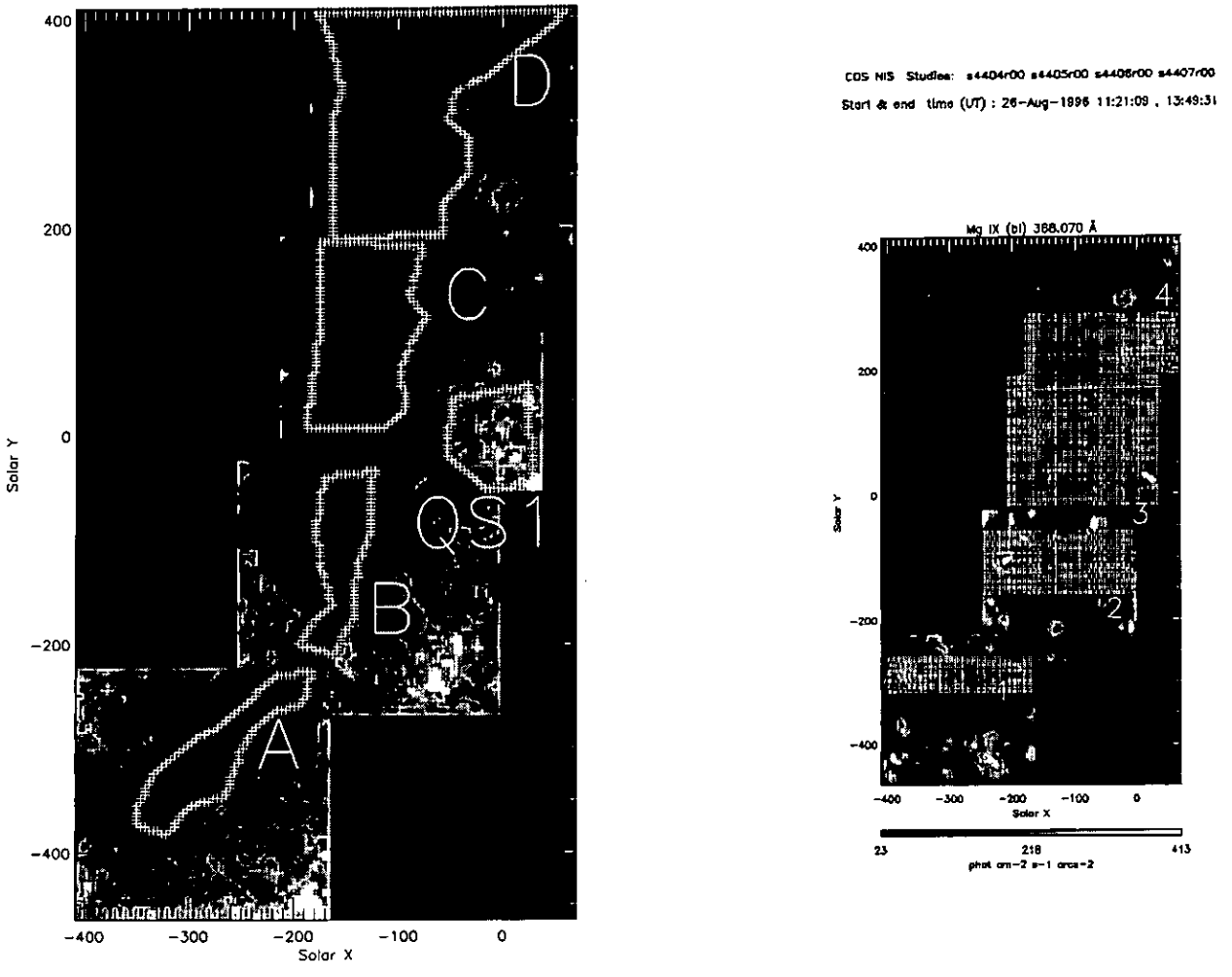

Figure 5.7: Left: an isothermal temperature map (Mg X 625 Å/ Mg IX 368 Å ratio) with the selected coronal hole areas, on August 26, 1996. Right: the Mg IX 368 Å image with the regions selected to get averaged E-W profiles.

Figure 5.7 shows the isothermal temperature map of the hole based on the [Mg X 624.9 Å/ Mg IX 368.0 Å] ratio. This image indicates a steep change in temperature at the boundaries of the hole. In this work, coronal hole areas were defined as regions with an isothermal temperature $T \leq 9.3\text{x}10^5$ K ($\log T \leq 5.97$). Other temperature ratios (e.g. Si XII/Si XI, Fe XII/Fe X) represent the coronal hole in a similar way. This Mg ratio was chosen because even inside the coronal hole both lines still have detectable intensities.

Since the coronal hole extended mainly along the N-S direction, regions near the equator were selected (see also Figure 5.7), and spectra were averaged along the N-S direction in order to increase the signal to noise and to produce intensity profiles across the hole (i.e. in the E-W direction). Figure 5.8 shows the two E-W intensity profiles (corresponding to the

regions 2 and 3 in Figure 5.7) for the cell-centre areas in five different lines, together with the corresponding isothermal temperatures. The profile of the isothermal temperature shows that a log T value of 5.97 is a reasonable limit to use in defining the 'coldest' regions inside the hole (see also the temperatures derived from GIS lines, Figure 5.20). Similar temperature changes across the hole were found when looking at the other latitudes. The temperature on the eastern boundary of the hole was found in many places to be higher than on the west.

Using the Mg X/Mg IX intensity ratio to define coronal hole regions would bias any difference between coronal hole and quiet sun regions toward a temperature effect. However, this choice is in quite good agreement with the shape of the hole as seen in He I 10830 Å and YOHKOH images, that are usually used to trace the coronal hole boundaries.

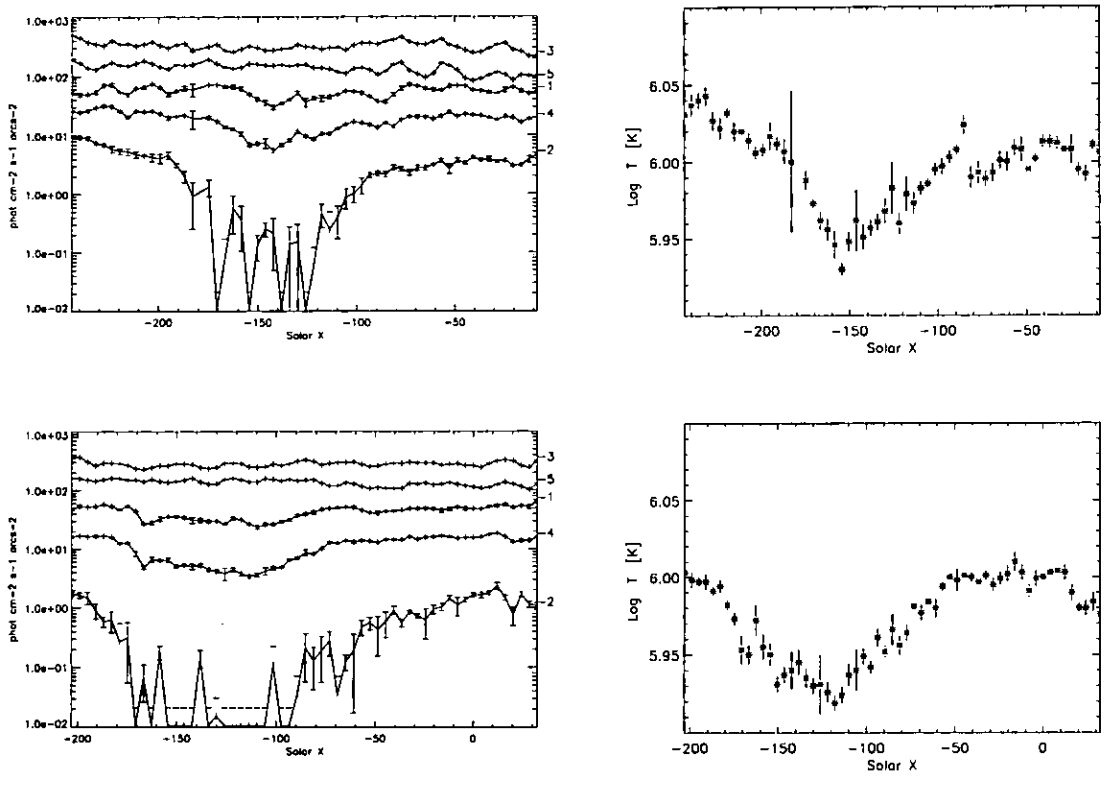

Figure 5.8: *Left: Intensity profiles across the coronal hole as deduced from cell-centre-averaged spectra of the regions 2 (above) and 3 (below) in Figure 5.7. (1) Mg IX 368. Å; (2) Si XII 520.7 Å; (3) He I 584.3 Å; (4) Mg X 625 Å; (5) O V 629.7 Å. Right: Profiles of the isothermal temperature derived from the Mg X 625 Å/ Mg IX 368 Å ratio. Note the decrease in the temperature.*

Figure 5.8 also shows that the cell-centre intensity in the He lines is almost unaltered. Similar studies over the network regions are also interesting, and show the well-known depression of the He lines inside coronal holes. There is also a tendency for transition

Table 5.1: *Electron Densities and Temperatures Deduced From the August 26, 1996, LIMB and CHBOPT2 Observations, for the Cell Centres and Network of the Selected Coronal Hole and Quiet Sun Areas. CC, cell centre; Net, network; CH, coronal hole; QS 1, quiet sun. Densities, deduced from the Si IX [349.9 Å/ 341.9 Å] and O IV [625.9 Å/ 608.4 Å] ratios are in cm^{-3}. Temperatures, deduced from the [Mg X 624.9 Å/ Mg IX 368.0 Å] ratio are in K. Intensities of a selection of lines are also shown, expressed as a proportion of the corresponding intensities seen in the quiet sun full raster observation of August 25, 1996.*

REGION	N_e (Si IX)	N_e (O IV)	T_e	He II	O V	Mg IX	Si XI
Mosaic CH A CC	2.8±.3 10^8	0.7±.1 10^{10}	8.95±.03 10^5	0.86	0.94	0.43	0.43
Mosaic CH B CC	1.7±.3 10^8	1.1±.4 10^{10}	9.06±.05 10^5	1.07	1.02	0.61	0.57
Mosaic CH C CC	2.2±.6 10^8	0.6±.1 10^{10}	8.8±.02 10^5	1.07	1.07	0.44	0.44
CHBOPT2 CH CC	1.6±.3 10^8	0.7±.1 10^{10}	8.57±.04 10^5	1.04	1.06	0.41	0.22
Mosaic CH D CC	2.0±0.5 10^8	0.6±.1 10^{10}	8.59±.03 10^5	0.87	1.0	0.40	0.37
Mosaic QS 1 CC	3.8±.5 10^8	1.2±.3 10^{10}	1.05±.02 10^6	1.0	0.85	0.58	0.96
Mosaic CH A Net	2.1±.5 10^8	0.5±.1 10^{10}	8.91±.05 10^5	0.69	0.91	0.43	0.47
Mosaic CH B Net	2.0±.7 10^8	0.7±.1 10^{10}	9.16±.05 10^5	0.80	0.94	0.63	0.57
Mosaic CH C Net	2.2±.3 10^8	0.5±.1 10^{10}	8.87±.04 10^5	0.86	1.06	0.49	0.49
CHBOPT2 CH Net	1.7±.5 10^8	0.5±.1 10^{10}	8.63±.04 10^5	0.72	0.93	0.38	0.19
Mosaic CH D Net	2.7±1. 10^8	0.5±.1 10^{10}	8.53±.03 10^5	0.66	0.94	0.38	0.39
Mosaic QS 1 Net	4.5±1. 10^8	0.5±.1 10^{10}	1.03±.04 10^6	0.94	0.84	0.74	0.94

region lines (O V) to have an increased intensity in both cell-centres and network (see also the results in Table 5.1). Also note the expansion of the coronal hole with height, as shown by the fact that higher-temperature lines show broader intensity depressions at the hole.

Figure 5.7 also indicates the four coronal hole regions (A, B, C, and D) that were selected to produce averaged spectra from the LIMB observations of the 26th of August. A region of quiet sun (QS 1; Figure 5.7) near Sun centre was chosen for comparison. This region does not necessarily represent the typical quiet sun, but on the other hand the notion of the so-called quiet sun has been radically changed by SOHO results. (Different averaged line intensities have been found from different quiet sun regions, and these differences can be quite large in particular for transition region lines in the network areas, because of the occurrence of repeated brightenings). All the quiet sun and coronal hole regions selected here were subdivided into cell-centre and network regions to enable separate measurement of the line intensities for each region to be made. The results are shown in Table 5.1.

Figure 5.9 shows the averaged spectra for the cell-centres of the coronal hole C region. Note how the line profiles are well defined even in this case, where intensities are very low, both in coronal lines (because of sampling inside a coronal hole), and in the other lines (because of sampling in the darker cell-centres).

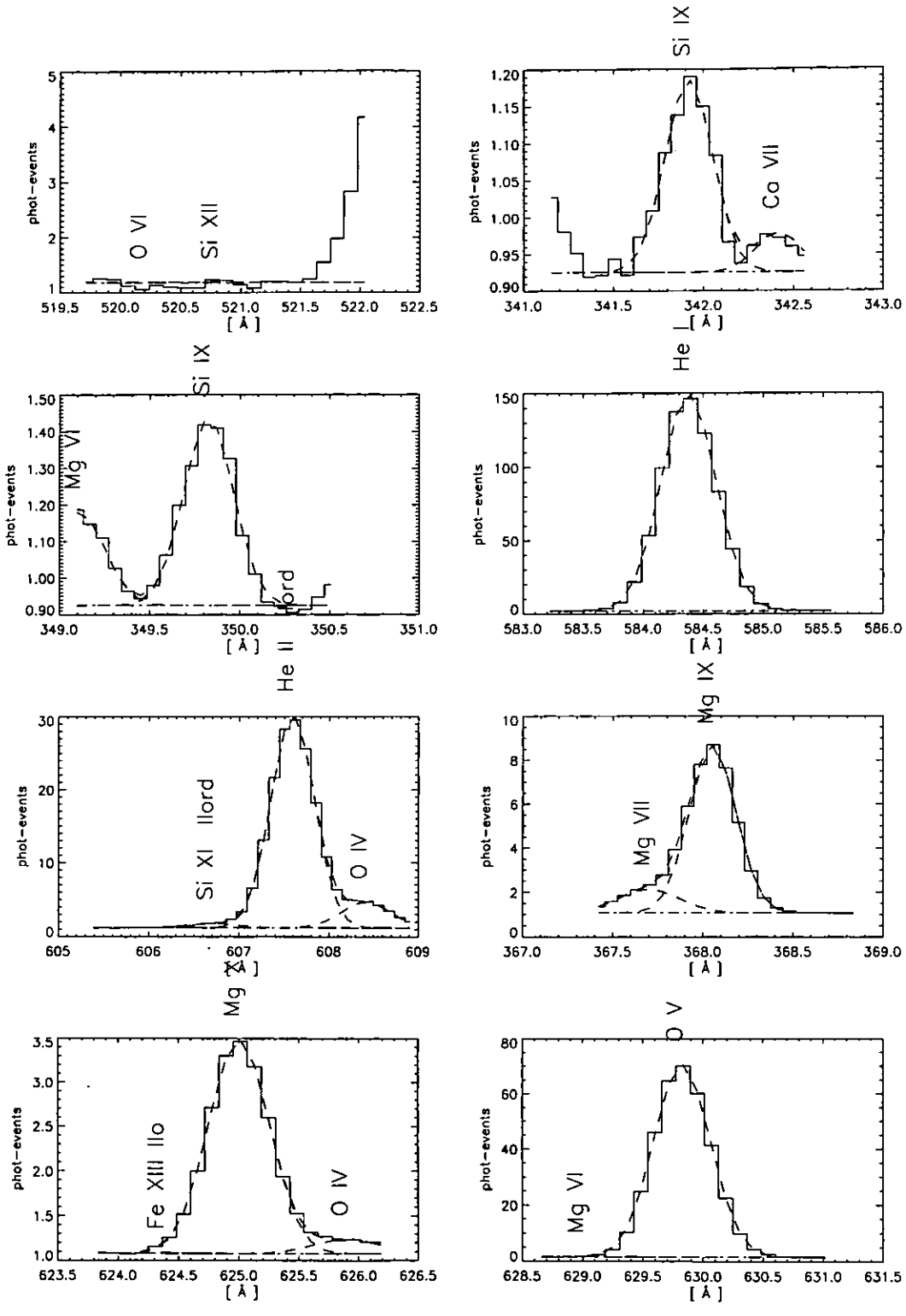

Figure 5.9: *The averaged spectra for the cell-centres of the coronal hole C region. – August 26, 1996.*

Table 5.1 also shows the results from the CHBOPT2 observation of August 26, which partly overlaps region C of the composite image.

Averaged coronal densities in the QS 1 region are about a factor of 2 higher than the coronal hole values . Coronal densities are not significantly different for network and cell-centre data, as one would expect, but at transition region heights the O IV ratio shows lower densities in the coronal hole areas, with a tendency to higher densities in the cell centres. While the quiet sun area QS 1 shows a temperature $T \simeq 1\text{x}10^6$ K, the coronal hole regions had temperatures $T \simeq 8.5 - 9\text{x}10^5$ K. Table 5.1 also shows the intensities of a few lines expressed relative to those in the quiet sun (full raster) observation of August 25 (see next section). The coronal lines Si XI 303.3 Å (second order) and Mg IX 368.0 Å are weaker by more than 50% inside the coronal hole. The transition region line O V 629.732 Å is slightly enhanced in the cell-centre regions inside the coronal hole, while the He II 303.8 Å (second order) line displays the well-known characteristic of decreased intensity in the coronal hole network, by 20-30%.

5.2.2 Results from the quiet sun reference observation - 1996, Aug 25

Before describing the results of the full diagnostic analysis performed on the coronal hole observations of Aug 27, results from the reference (full raster) quiet sun observation are now presented. This region was fairly homogeneous and very quiet. The NISAT observation on the Quiet Sun on 1996, Aug 25 was analyzed and cell-centre and network regions were selected following the same criterion previously described. Averaged spectra were then obtained, and line intensities derived.

The derived densities and temperatures are presented along with corresponding results for the Elephant's Trunk, in Table 5.4, below, for a more direct comparison. Averaged coronal densities are lower than in the region QS 1, while the isothermal temperature is about the same, around a million degrees. The [Mg VI 349.17 Å/ Ne VI 562.8 Å] ratio values shown in Table 5.4 indicate some differences in the elemental abundances between the cell centres and the network. This is confirmed by the Mg VII / Ne VII ratios.

DEM analyses were performed on the averaged cell-centre and network spectra, assuming a constant electron pressure of $4\text{x}10^{14}$ cm^{-3} K. The photospheric abundances of *Grevesse and Anders* (1991) in order to obtain a satisfactory fit were used initially, but some of the element abundances had to be modified (see Table 5.4 for the values adopted). Figure 5.10 shows the DEM distribution of the cell-centre quiet sun averaged spectrum.

Table 5.2: *A selection of lines of different ions, used for the DEM of the quiet sun averaged cell-centre region – 1996 August 27.*

Ion	λ_{th} (Å)	λ_{ob} (Å)	Transition	I_{ob}	I_{th}/I_{ob}	+/-	Det	log T_{eff}	log T_{max}	frac
C III	538.31	538.2	2s2p $^3P_2$ - 2s3s $^3S_1$	10.1	0.86	0.33	N 2	4.87	4.96	0.35
O II	538.32		2s22p3 $^2D_{3/2}$ - 2s2p4 $^2P_{3/2}$						4.87	0.33
C III	538.147		2s2p $^3P_1$ - 2s3s $^3S_1$						4.96	0.21
O III	599.597	599.6	2s22p2 $^1D_2$ - 2s2p3 $^1D_2$	24.9	1.17	0.19	N 2	5.05	5.06	
O IV	554.513	554.5	2s2 2p $^2P_{3/2}$ - 2s 2p2 $^2P_{3/2}$	82.4	0.98	0.12	N 2	5.26	5.27	
O IV	553.329	553.4	2s2 2p $^2P_{1/2}$ - 2s 2p2 $^2P_{3/2}$	14.3	1.12	0.24	N 2	5.26	5.27	
O IV	608.397	608.4	2s2 2p $^2P_{1/2}$ - 2s 2p2 $^2S_{1/2}$	13.6	0.90	0.40	N 2	5.26	5.27	
Ne IV	541.128	541.1	2s2 2p3 $^4S_{3/2}$ - 2s 2p4 $^4P_{1/2}$	1.9	1.03	0.93	N 2	5.29	5.27	
Ne IV	543.892	543.9	2s2 2p3 $^4S_{3/2}$ - 2s 2p4 $^4P_{5/2}$	5.7	1.04	0.52	N 2	5.29	5.27	
O V	629.73	629.8	2s2 $^1S_0$ - 2s.2p $^1P_1$	183.7	0.92	0.11	N 2	5.40	5.39	
Ne V	569.824	569.8	2s22p2 $^3P_1$ - 2s2p3 $^3D_2$	3.7	1.21	0.51	N 2	5.50	5.47	0.76
Ne V	569.753		2s22p2 $^3P_1$ - 2s2p3 $^3D_1$						5.47	0.24
Ne V	572.331	572.3	2s22p2 $^3P_2$ - 2s2p3 $^3D_3$	5.7	1.22	0.38	N 2	5.50	5.47	0.85
Ne V	572.098		2s22p2 $^3P_2$ - 2s2p3 $^3D_2$						5.47	0.14
Mg V	353.092	353.1	2p4 $^3P_2$ - 2s.2p5 $^3P_2$	3.9	0.56	0.40	N 1	5.54	5.47	
Ne VI	562.803	562.8	2s2 2p $^2P_{3/2}$ - 2s 2p2 $^2D_{5/2}$	10.3	1.12	0.25	N 2	5.68	5.63	
Ne VI	558.594	558.6	2s2 2p $^2P_{1/2}$ - 2s 2p2 $^2D_{3/2}$	7.3	0.94	0.28	N 2	5.70	5.63	0.88
Ne VII	558.609		2s2p $^3P_1$ - 2p2 $^3P_2$						5.72	0.12
Mg VI	349.168	349.1	2s2.2p3 $^2D_{5/2}$ - 2s.2p4 $^2D_{5/2}$	7.7	0.80	0.72	N 1	5.83	5.65	0.46
Mg VI	349.137		2s2.2p3 $^2D_{3/2}$ - 2s.2p4 $^2D_{3/2}$						5.65	0.38
Ne VII	561.728	561.7	2s2p $^3P_2$ - 2p2 $^3P_2$	3.2	0.92	0.49	N 2	5.85	5.72	0.83
Ne VII	561.378		2s2p $^3P_1$ - 2p2 $^3P_1$						5.72	0.17
Mg VII	367.674	367.7	2s22p2 $^3P_2$ - 2s2p3 $^3P_2$	19.3	0.83	0.46	N 1	5.92	5.81	0.77
Mg VII	367.683		2s22p2 $^3P_2$ - 2s2p3 $^3P_1$						5.81	0.23
Mg VII	365.234	365.2	2s22p2 $^3P_1$ - 2s2p3 $^3P_2$	10.3	0.96	0.87	N 1	5.93	5.81	0.37
Mg VII	365.176		2s22p2 $^3P_1$ - 2s2p3 $^3P_0$						5.81	0.34
Mg VII	365.243		2s22p2 $^3P_1$ - 2s2p3 $^3P_1$						5.81	0.27
Fe X	365.543	365.5	3s2.3p5 $^2P_{1/2}$ - 3s.3p6 $^2S_{1/2}$	13.3	1.18	0.76	N 1	5.95	6.04	0.70
Ne V	365.603		2s22p2 $^1D_2$ - 2s2p3 $^1P_1$						5.49	0.28
Mg X	609.793	609.8	1s2.(1s).2s $^2S_{1/2}$ - 1s2.(1s).2p $^2P_{3/2}$	85.7	1.34	0.19	N 2	5.97	6.04	0.80
O IV	609.829		2s2 2p $^2P_{3/2}$ - 2s 2p2 $^2S_{1/2}$						5.27	0.20
Mg VIII	339.006	339.0	2p $^2P_{3/2}$ - 2s.2p2 $^2S_{1/2}$	11.9	1.16	1.05	N 1	5.98	5.92	
Ca X	557.765	557.8	3s $^2S_{1/2}$ - 3p $^2P_{3/2}$	7.8	0.70	0.19	N 2	5.99	5.82	
Si VIII	319.826	319.8	2s22p3 $^4S_{3/2}$ - 2s2p4 $^4P_{5/2}$	53.0	1.34	0.83	N 1	6.00	5.91	
Mg IX	368.07	368.0	2s2 $^1S_0$ - 2s.2p $^1P_1$	176.2	0.97	0.13	N 1	6.02	5.98	
Si IX	349.873	349.8	2s22p2 $^3P_2$ - 2s2p3 $^3D_3$	33.6	1.13	0.59	N 1	6.04	6.02	0.84
Si IX	349.794		2s22p2 $^3P_2$ - 2s2p3 $^3D_2$						6.03	0.16
Fe X	345.723	345.7	3s2.3p5 $^2P_{3/2}$ - 3s.3p6 $^2S_{1/2}$	23.1	1.14	0.92	N 1	6.04	6.04	
Si IX	341.949	341.9	2s22p2 $^3P_0$ - 2s2p3 $^3D_1$	16.7	1.01	0.92	N 1	6.04	6.04	
Mg X	624.941	625.0	1s2.(1s).2s $^2S_{1/2}$ - 1s2.(1s).2p $^2P_{1/2}$	30.4	1.55	0.33	N 2	6.05	6.04	
Fe XI	352.662	352.6	3s2.3p4 $^3P_2$ - 3s.3p5 $^3P_2$	31.4	1.03	0.63	N 1	6.07	6.11	
Fe XI	369.153	369.1	3s2.3p4 $^3P_1$ - 3s.3p5 $^3P_2$	8.6	1.13	0.83	N 1	6.07	6.11	
Al X	332.789	332.8	2s2 $^1S_0$ - 2s.2p $^1P_1$	22.0	0.88	0.79	N 1	6.07	6.10	
Si X	356.012	356.0	2p $^2P_{3/2}$ - 2s.2p2 $^2D_{5/2}$	21.5	1.05	0.95	N 1	6.07	6.12	0.76
Si X	356.05		2p $^2P_{3/2}$ - 2s.2p2 $^2D_{3/2}$						6.14	0.24
Si X	347.403	347.4	2p $^2P_{1/2}$ - 2s.2p2 $^2D_{3/2}$	37.3	1.04	0.62	N 1	6.08	6.14	
Fe XII	352.106	352.1	3s2.3p3 $^4S_{3/2}$ - 3s.3p4 $^4P_{3/2}$	22.1	0.78	0.61	N 1	6.09	6.16	
Fe XII	346.852	346.8	3s2.3p3 $^4S_{3/2}$ - 3s.3p4 $^4P_{1/2}$	11.5	0.75	0.68	N 1	6.09	6.16	
Fe XII	364.467	364.4	3s2.3p3 $^4S_{3/2}$ - 3s.3p4 $^4P_{5/2}$	31.3	0.78	0.27	N 1	6.10	6.16	
Fe XIII	348.183	348.1	3s2 3p2 $^3P_0$ - 3s 3p3 $^3D_1$	10.5	1.19	1.08	N 1	6.13	6.21	
Fe XVI	360.761	360.6	3s $^2S_{1/2}$ - 3p $^2P_{1/2}$	2.5	0.79	0.71	N 1	6.34	6.34	

The lines used in the *DEM* analysis were formed over a wide range of temperatures and were from many different ions. Table 5.2 shows a selection of the lines used for the *DEM* analysis. Almost all the intense lines in both NIS 1 and NIS 2 detectors are well fitted, within a 20% accuracy, which is a remarkable result, considering the uncertainties in the

calculations of the line intensities, in the atomic physics calculations and in the calibration.

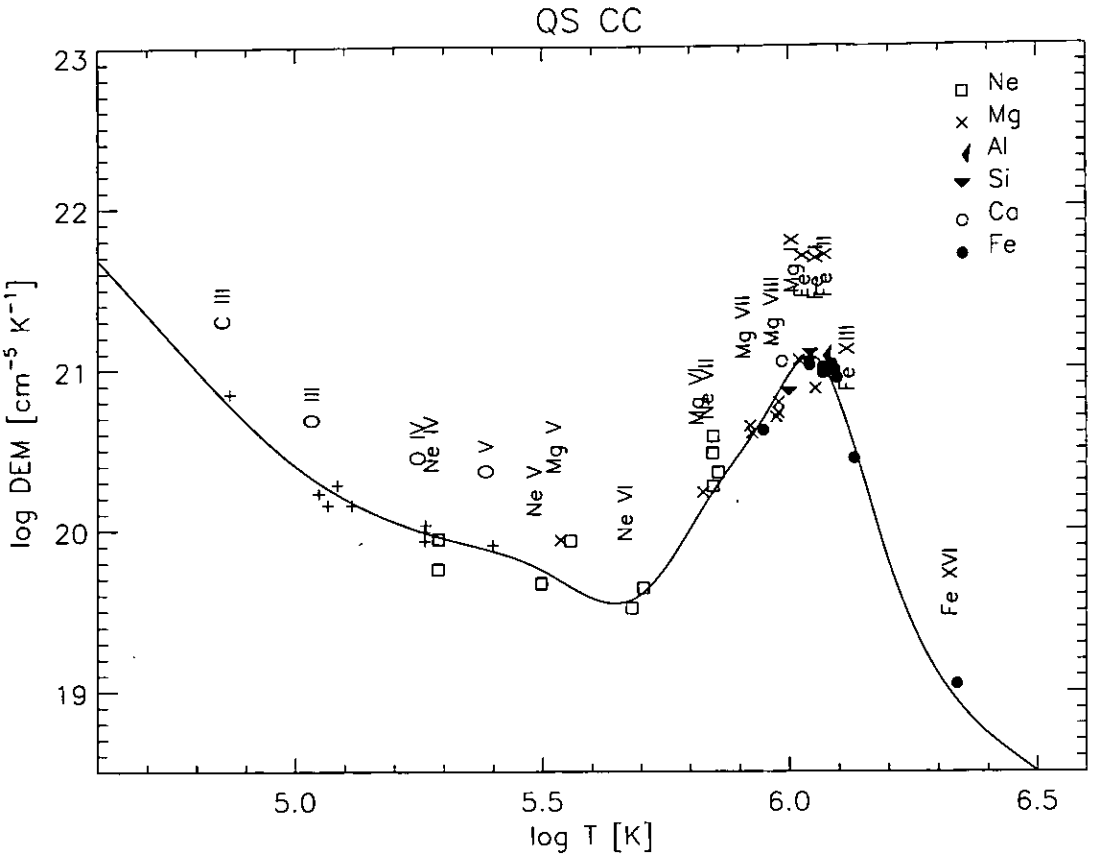

Figure 5.10: *The DEM distribution of the full raster quiet sun cell-centres region on August 25, 1996.*

This quiet sun DEM distribution is similar to those derived by previous authors (e.g., *Raymond and Doyle, 1981b; Brosius et al., 1996; Mason et al.,* 1997, *Doschek*, 1997). The DEM curve between $\log T = 5.0$ and $\log T = 5.4$ is constrained by O III, O IV, and O V lines. The DEM values between $\log T = 5.3$ and $\log T = 5.8$ are also well constrained by bright NIS 2 lines of Ne IV, Ne V, Ne VI, and Ne VII. The DEM distribution here is therefore independent of relative O/Ne element abundances. The relative O/Ne abundance was in fact constrained by O IV and Ne IV lines: The Ne abundance was increased by a factor 1.6 (0.2 dex), relative to O. The abundances of the low-FIP elements were then scaled with the Ne value.

The temperature of the coronal peak of the DEM distribution is in agreement with the isothermal temperature deduced from the [Mg X 624.9 Å/ Mg IX 368.0 Å] ratio (Table 5.4). This shows that the Sun at that time was very quiet, with a much lower emission at temperatures above a million degrees, compared to previous analyses (e.g., *Raymond and Doyle*, 1981b).

For consistency, the same set of lines was used for the DEM analyses of the quiet sun network and the coronal hole regions, described below, The DEM distribution of the quiet sun network is shown in Figure 5.11. The shape and position of the coronal peaks in the cell-centre and network quiet sun DEM distributions are similar, whereas the network DEM shows much higher emission measures in the whole of the transition region, as expected. The two *DEM* distributions are directly compared in Figure 5.21, below.

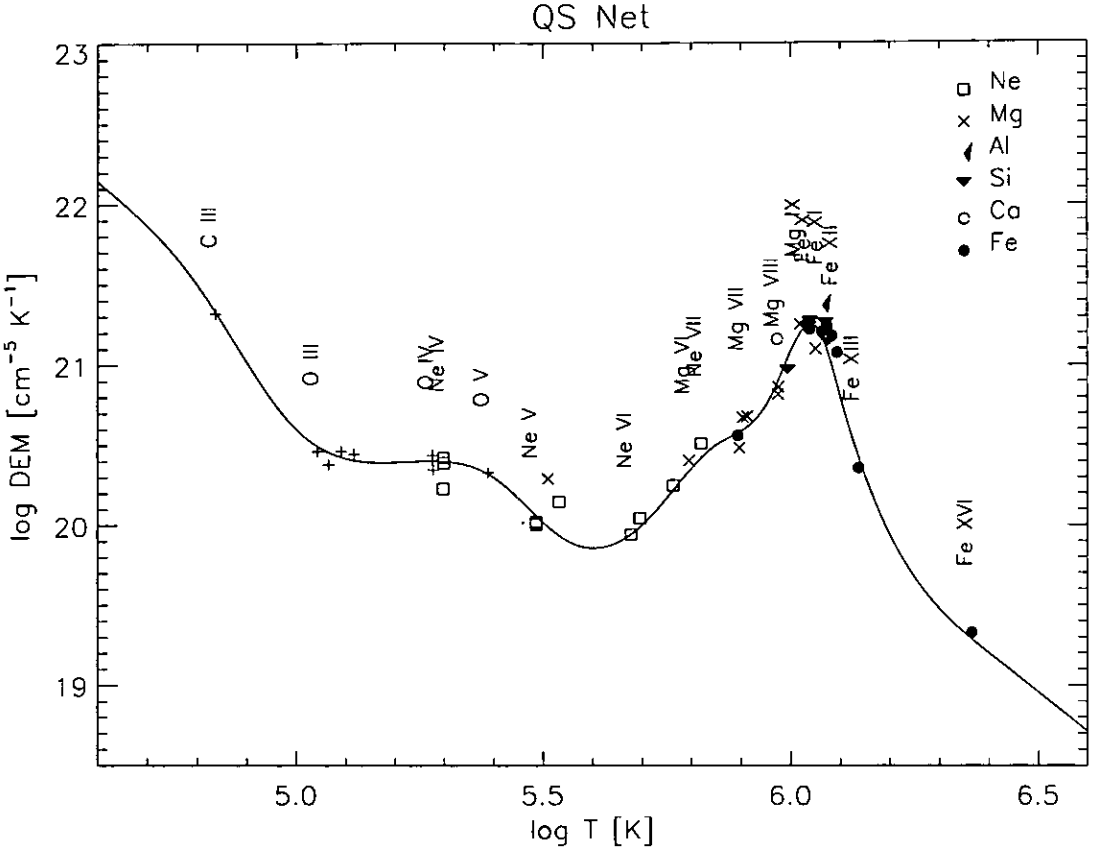

Figure 5.11: *The DEM distribution of the full raster quiet sun network region on August 25, 1996.*

5.2.3 Coronal hole and plume densities, temperatures and abundances - 1996 August 27

Results based on the analysis of the CHBOPT2, the NISAT_S5 and one of the G2AL/v2 studies of the 27th August are presented here (see Figure 4.6 for the pointing of these CDS observations). The GIS E-W raster (fits file s4431r00) was the first one to be run, starting at 06:32 UT, at Solar Y = 81″, very close to the disc centre. This study used the 4″x4″slit and 400s exposures. Then, after a second GIS E-W scan, the full NIS spectrum (NISAT_S5 study, Solar X=107″, Solar Y=71″, 11:01-12:08 UT) was performed, and then the CHBOPT2 observation followed (Solar X=142″, Solar Y=71″, 12:13-13:10 UT). The

CHBOPT2 and NISAT_S5 rasters of the 27th therefore pointed at the same region in the N-S direction, but were shifted E-W, so as to have an overlap between the two.

Figure 5.12 shows monochromatic images in a few selected lines from the CHBOPT2 observation. The full spectrum (NISAT_S5) observation has been used to perform a *DEM* analysis of the Elephant's Trunk (see below).

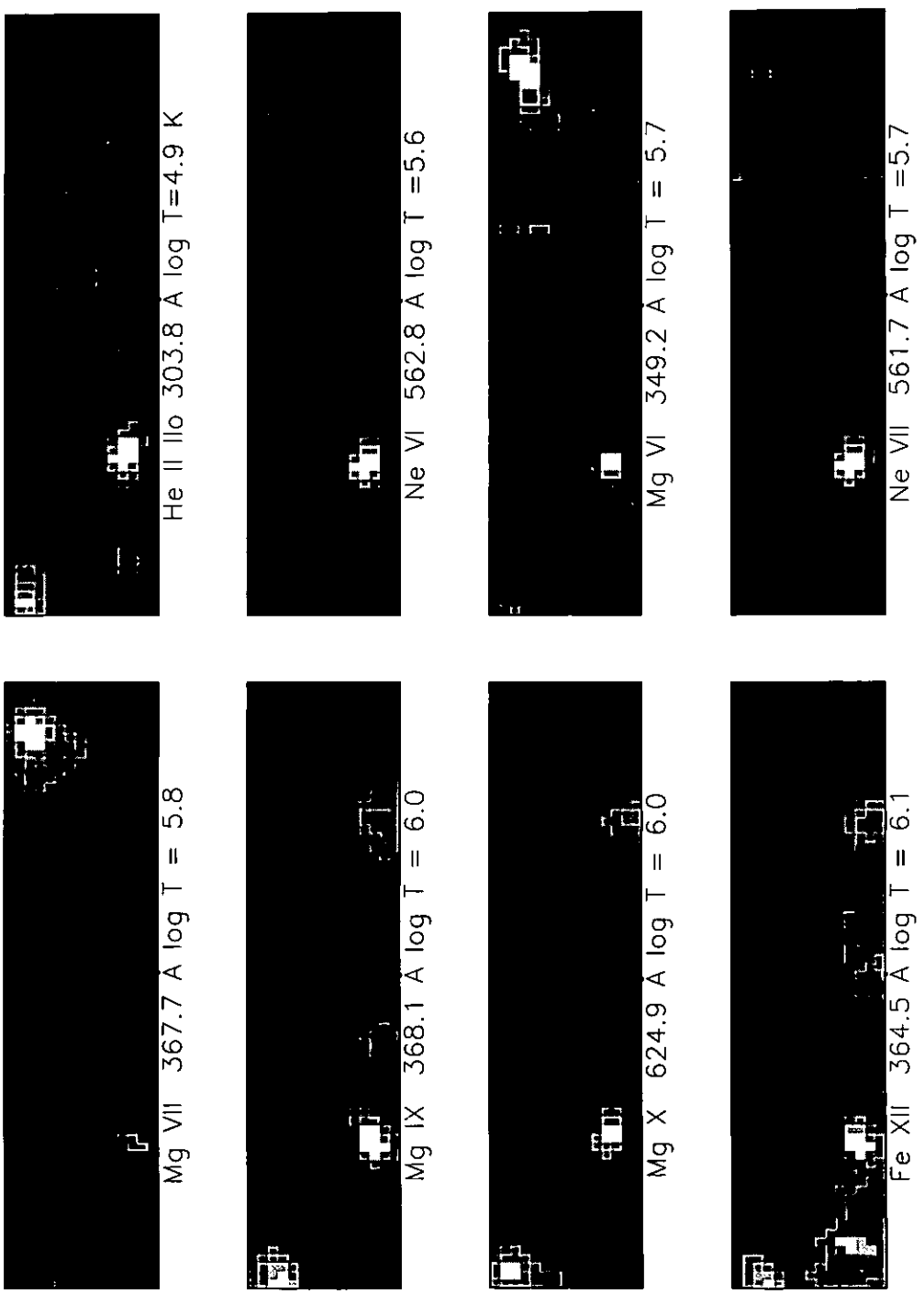

Figure 5.12: Monochromatic images of the CHBOPT2 observation on August 27, 1996.

Examination of Figure 5.12 shows that the network signature is evident in the transition region lines and tends to disappear when lines that form at higher temperatures are examined. The coronal hole boundary is clearly visible in the Fe XII image.

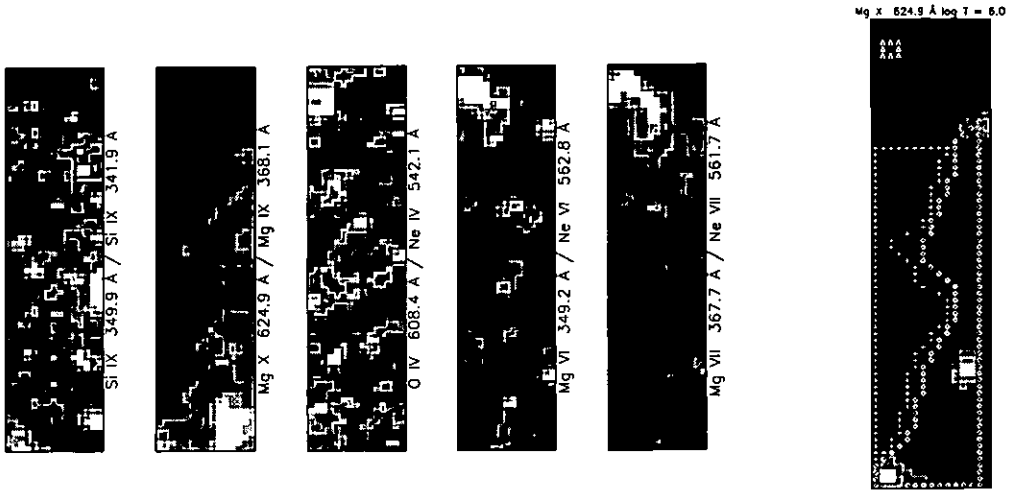

Figure 5.13: *Left: ratio images of the CHBOPT2 observation on August 27, 1996, showing density ratios (Si IX); temperature ratio (Mg X / Mg IX); and abundance ratios. Right: selected regions from which average spectra were extracted (see Figure 5.14). Triangles refer to the plume region, crosses refer to the coronal hole region, and diamonds refer to the west boundary region.*

Figure 5.13 shows density, temperature, and abundance maps of the same region. Small-scale inhomogeneities are present in all the ratio images, but some large-scale patterns are recognizable. At coronal levels (Si IX), a decrease in density toward the 'deepest' region of the coronal hole is evident. The Mg X / Mg IX image shows a clear temperature decrease in the coronal hole region, corresponding to the darker area in the Fe XII image. The whole eastward region (left in the images) in the raster could therefore be interpreted as a coronal hole region, with the upper part showing lower temperatures than the rest of the coronal hole.

In the low coronal line Mg IX 368.0 Å (Figure 5.12), a diffuse emission is present in the upper part of the image, also visible in the EIT 195 Å image (Figure 4.6) but not in the higher temperature lines Mg X 624.9 Å and Fe XII 364.5 Å observed by CDS. In the same region, the abundance maps indicate a strong enhancement in the Mg/Ne relative abundance, compared to the remainder of the coronal hole, and a bright feature can be seen in the same position in the Mg VI and Mg VII images (Figure 5.12). The Mg/Ne enhancement is typical of plumes observed in Skylab data, suggesting that this feature is a small plume, directed almost toward the observer (see later).

At the base (higher Solar Y) of the plume a (small) increase in the O IV/Ne IV ratio suggests that some of the Mg/Ne enhancement is due to a low Ne abundance relative to O. The variations of the [Mg VI 349.17 Å/ Ne VI 562.8 Å] ratio in the rest of the coronal hole area suggests a possible enhancement of Mg/Ne in cell-centre regions over those in the network (cf. He II intensities in Figure 5.12, which show the supergranular structure).

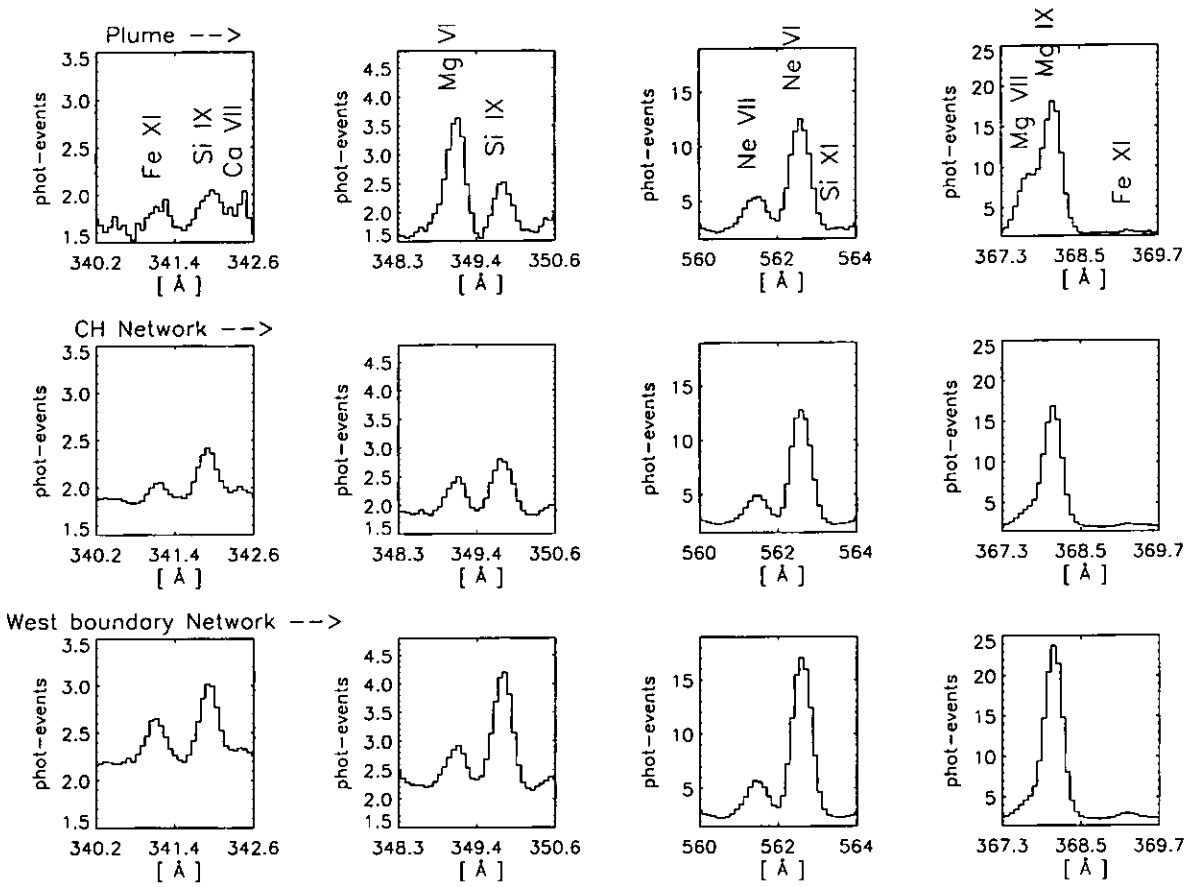

Figure 5.14: *Averaged spectra of the selected regions (see Figure 5.13) of the CHBOPT2 observation on August 27, 1996: (top) plume, (middle) coronal hole network, and (bottom) west boundary (quiet sun) network. Note the same intensity scale and the enhancements in the Mg VI and Mg VII lines in the plume.*

Figure 5.13 (right hand image) also shows some selected regions of the CHBOPT2 study: a small area centred on the base of the plume; a coronal hole region; and a nearby quiet sun region on the western boundary of the hole. Figure 5.14 shows averaged line profiles in a few selected lines, for these three regions.

The enhancements in the Mg VI and Mg VII lines in the plume region are particularly evident, as compared, for example, with Ne VI and Mg IX. The most striking differences between the plume and the coronal hole are seen in the Mg IX / Mg VII blend at 368 Å. This indicates a different plasma temperature distribution at the base of the plume, with large emission measures at Mg VII temperatures, compared with the nearby regions.

The fact that Ne VI and Ne VII emissions in the plume are very similar to those in the coronal hole then suggests a variation of the Mg/Ne abundance. This is studied below with a *DEM* analysis.

Coronal hole regions excluding the plume have also been selected and then subdivided into coronal hole cell centre and network in the usual way. Since the plume was partly visible in the NISAT_S5 field of view, it was possible to perform a *DEM* analysis based on all the NIS lines seen at the base of the plume. This is also presented below. Results based on the line intensities of the CHBOPT2 observation are presented in *Del Zanna and Bromage* (1999a). Table 5.4 shows the results for the plume and the coronal hole regions, as derived from the NISAT_S5 observation (together with the results of the quiet sun observation). The plume had an isothermal temperature $T \simeq 8\text{x}10^5$ K, lower than the values found in the average coronal hole regions ($T = 8.3 - 9\text{x}10^5$ K). The plume also had a higher value (1.04) for the [Mg VI 349.17 Å/ Ne VI 562.8 Å] ratio, as compared with the coronal hole values ($\simeq$ 0.4) and quiet sun values (0.54–0.75).

This 'plume' feature shows all the characteristics of polar plumes seen on-disc with CDS, as shown in Chapter 6 of this thesis. These characteristics include: lower temperature than the ambient coronal hole region; visibility only in lines emitted in a restricted range of temperatures; and enhanced Mg/Ne relative abundance. All this evidence supports the hypothesis that this feature is indeed a low-latitude plume. **This is the first identification of a low-latitude coronal hole plume** based on spectroscopic analysis. The results support the conclusions of previous authors (who based their conclusions on morphological characteristics) that plumes exist in low-latitude coronal holes as well as in polar holes (e.g., *Wang and Sheeley*, 1995a).

The spectra and *DEM* of the Elephant's Trunk coronal hole

NISAT_S5 spectra were spatially averaged over the coronal hole regions, and subdivided into cell-centre areas and network in the usual manner. A *DEM* analysis was then performed using all the measured NIS line intensities. (Figures D.1 and D.2 show as an example the full NIS averaged spectra for the network region). Note that even with long exposures (150s), the wider 4″slit, and spatial averaging, the signal is still quite low. All the high-temperature lines are either very weak or absent.

For the *DEM* analyses on the network and cell-centre averaged spectra, a constant electron pressure of $2\text{x}10^{14}$ cm^{-3} K has been assumed. Table 5.4 (below) shows the abundances that were obtained from these *DEM* analysis. The resulting *DEM* distributions are shown in Figures 5.15 and 5.16, and Table 5.3 lists some of the lines used for the *DEM*

and abundance analysis for the network region. Note from Table 5.3 how all lines are well represented, except for Mg V (only one is shown in Table). This confirms the problem with the Mg V already noted in this thesis, and also present in the SERTS-89 spectra.

Note from Table 5.4 that the Ne abundance was slightly increased, compared to the photospheric value, but that on the other hand all the low-FIP elements had abundances slightly lower than photospheric (except Ca). Note from Figure 5.15 the very low emission measure values at high temperatures. The same figure shows the DEM_L values of the same lines. These confirm the very low emission measures at the highest temperatures, and the validity of the adopted relative abundances (because of the small scatter of points).

Table 5.3: *A selection of lines of different ions, used for the DEM analysis of the coronal hole averaged network region – 27th August 1996.*

Ion	λ_{th} (Å)	λ_{ob} (Å)	Transition	I_{ob}	I_{th}/I_{ob}	+/-	Det	log T_{eff}	log T_{max}	frac
O II	538.32	538.3	2s22p3 $^2D_{3/2}$ - 2s2p4 $^2P_{3/2}$	18.7	1.11	0.16	N 2	4.83	4.87	0.39
C III	538.31		2s2p $^3P_2$ - 2s3s $^3S_1$						4.96	0.32
C III	538.147		2s2p $^3P_1$ - 2s3s $^3S_1$						4.96	0.19
O III	599.597	599.7	2s22p2 $^1D_2$ - 2s2p3 $^1D_2$	55.5	1.03	0.11	N 2	5.03	5.06	
N III	374.434	374.5	2s2 2p $^2P_{3/2}$ - 2s2 3d $^2D_{5/2}$	5.0	0.95	0.76	N 1	5.08	5.09	0.34
O III	374.435		2s22p2 $^3P_2$ - 2s22p3s $^3P_1$						5.11	0.34
O III	374.33		2s22p2 $^3P_1$ - 2s22p3s $^3P_0$						5.11	0.28
O IV	554.513	554.6	2s2 2p $^2P_{3/2}$ - 2s 2p2 $^2P_{3/2}$	171.7	0.94	0.10	N 2	5.28	5.27	
Ne IV	543.892	544.0	2s2 2p3 $^4S_{3/2}$ - 2s 2p4 $^4P_{5/2}$	10.0	0.95	0.16	N 2	5.30	5.27	
O V	629.73	629.9	2s2 $^1S_0$ - 2s.2p $^1P_1$	391.5	0.98	0.10	N 2	5.39	5.39	
Ne V	572.331	572.4	2s22p2 $^3P_2$ - 2s2p3 $^3D_3$	9.8	1.17	0.15	N 2	5.49	5.47	0.86
Ne V	572.098		2s22p2 $^3P_2$ - 2s2p3 $^3D_2$						5.47	0.14
Mg V	353.092	353.1	2p4 $^3P_2$ - 2s.2p5 $^3P_2$	5.2	0.47	0.34	N 1	5.54	5.47	
Ne VI	562.803	562.9	2s2 2p $^2P_{3/2}$ - 2s 2p2 $^2D_{5/2}$	18.3	1.09	0.13	N 2	5.71	5.63	
Ne VI	558.594	558.7	2s2 2p $^2P_{1/2}$ - 2s 2p2 $^2D_{3/2}$	12.1	1.00	0.13	N 2	5.73	5.63	0.85
Ne VII	558.609		2s2p $^3P_1$ - 2p2 $^3P_2$						5.72	0.15
Mg VI	349.168	349.1	2s2.2p3 $^2D_{5/2}$ - 2s.2p4 $^2D_{5/2}$	6.6	1.10	0.98	N 1	5.81	5.65	0.51
Mg VI	349.137		2s2.2p3 $^2D_{3/2}$ - 2s.2p4 $^2D_{3/2}$						5.65	0.41
Ne VII	561.728	561.8	2s2p $^3P_2$ - 2p2 $^3P_2$	5.1	1.01	0.18	N 2	5.83	5.72	
Mg VII	367.674	367.7	2s22p2 $^3P_2$ - 2s2p3 $^3P_2$	18.2	1.14	0.52	N 1	5.88	5.81	0.76
Mg VII	367.683		2s22p2 $^3P_2$ - 2s2p3 $^3P_1$						5.81	0.23
Mg VII	365.234	365.2	2s22p2 $^3P_1$ - 2s2p3 $^3P_2$	12.5	1.00	0.57	N 1	5.88	5.81	0.37
Mg VII	365.176		2s22p2 $^3P_1$ - 2s2p3 $^3P_0$						5.81	0.35
Mg VII	365.243		2s22p2 $^3P_1$ - 2s2p3 $^3P_1$						5.81	0.27
Ca X	557.765	557.9	3s $^2S_{1/2}$ - 3p $^2P_{3/2}$	4.7	0.95	0.18	N 2	5.90	5.82	
Mg VIII	339.006	339.0	2p $^2P_{3/2}$ - 2s.2p2 $^2S_{1/2}$	10.1	1.05	0.75	N 1	5.92	5.92	
Mg IX	368.07	368.1	2s2 $^1S_0$ - 2s.2p $^1P_1$	76.6	0.92	0.14	N 1	5.96	5.98	
Si IX	349.873	349.9	2s22p2 $^3P_2$ - 2s2p3 $^3D_3$	8.2	1.25	0.93	N 1	5.98	6.02	0.81
Si IX	349.794		2s22p2 $^3P_2$ - 2s2p3 $^3D_2$						6.03	0.19
Fe X	345.723	345.7	3s2.3p5 $^2P_{3/2}$ - 3s.3p6 $^2S_{1/2}$	8.4	0.93	0.83	N 1	5.99	6.04	
Si IX	341.949	342.0	2s22p2 $^3P_0$ - 2s2p3 $^3D_1$	6.4	0.99	0.90	N 1	5.99	6.04	
Mg X	624.941	625.0	1s2.(1s).2s $^2S_{1/2}$ - 1s2.(1s).2p $^2P_{1/2}$	7.3	1.52	0.25	N 2	6.02	6.04	
Fe XI	369.153	369.3	3s2.3p4 $^3P_1$ - 3s.3p5 $^3P_2$	2.0	1.06	0.96	N 1	6.05	6.11	
Al X	332.789	332.8	2s2 $^1S_0$ - 2s.2p $^1P_1$	8.5	0.75	0.68	N 1	6.05	6.09	
Fe XI	352.662	352.7	3s2.3p4 $^3P_2$ - 3s.3p5 $^3P_2$	7.2	0.96	0.87	N 1	6.05	6.11	
Fe XII	364.467	364.5	3s2.3p3 $^4S_{3/2}$ - 3s.3p4 $^4P_{5/2}$	6.9	0.67	0.60	N 1	6.11	6.16	
Fe XII	346.852	347.0	3s2.3p3 $^4S_{3/2}$ - 3s.3p4 $^4P_{1/2}$	2.4	0.69	0.62	N 1	6.11	6.16	
Fe XIII	348.183	348.1	3s2 3p2 $^3P_0$ - 3s 3p3 $^3D_1$	2.8	1.10	1.00	N 1	6.16	6.20	
Fe XVI	360.761	360.6	3s $^2S_{1/2}$ - 3p $^2P_{1/2}$	1.7	0.76	0.69	N 1	6.38	6.34	

The cell-centre *DEM* distribution (Figure 5.16) also shows very low emission measures.

The coronal hole emission measures are directly compared in Figure 5.21, and discussed below.

The DEM of the low-latitude plume

A spatially averaged NISAT_S5 spectrum of a small region at the base of the plume was obtained and used for a *DEM* analysis. The results are shown in Figure 5.17 and in Table 5.4, where the adopted relative abundances can be found. The same set of spectral lines was used. A constant electron pressure of $2x10^{14}$ cm^{-3} K was assumed for the calculation of the contribution functions. As in the previous cases, the relative O/Ne abundance is constrained by O IV and Ne IV lines. This time, the O/Ne abundance has photospheric values. Mg VI/Ne VI and Mg VII/Ne VII lines were used to constrain the Mg/Ne abundance, and consequently also all the other low-FIP elements. A small FIP bias effect was found.

This plume showed an almost isothermal distribution at coronal heights, with a peak in the DEM at $T \simeq 7.7 \cdot 10^5$ K, close to the isothermal temperatures deduced from line ratios. The largest emission measures are thus at upper transition region temperatures (Mg VII, Ca X, Mg VIII), which explains why plumes are most clearly seen in lines emitted at those temperatures. A direct comparison with the other *DEM* distributions is presented in Figure 5.21, and discussed below.

The GIS E-W scan across the hole: abundance variations

Figure 5.18 shows the intensities of twenty lines from the GIS E-W scan across the hole. The intensities of the lower transition region lines (upper row) delineate the network and cell centre areas, and these tend to be less evident in the lines emitted at higher temperatures (lower rows). The low intensities inside the coronal hole are particularly evident for the hottest lines. While the eastward (left) part of this scan was in quiet sun, the westward (right hand end) is still partly in the coronal hole.

The thermal distribution inside the hole is different from that of the quiet sun, with intensities of the hottest lines being more depressed than those of the cooler ones (Fe XII/Fe X; Fe X/Fe IX), indicating much lower emission measures of the hotter lines inside the hole. The ratios of lines emitted by ions of different elements, but that have similar contribution functions, give an indication of possible abundance variations, as already discussed. GIS can detect many more lines useful for element abundance studies than can NIS.. Some examples are shown here in Figure 5.19. While some of the elements show constant relative abundance, (e.g. Mg and Si), others show large variations that follow

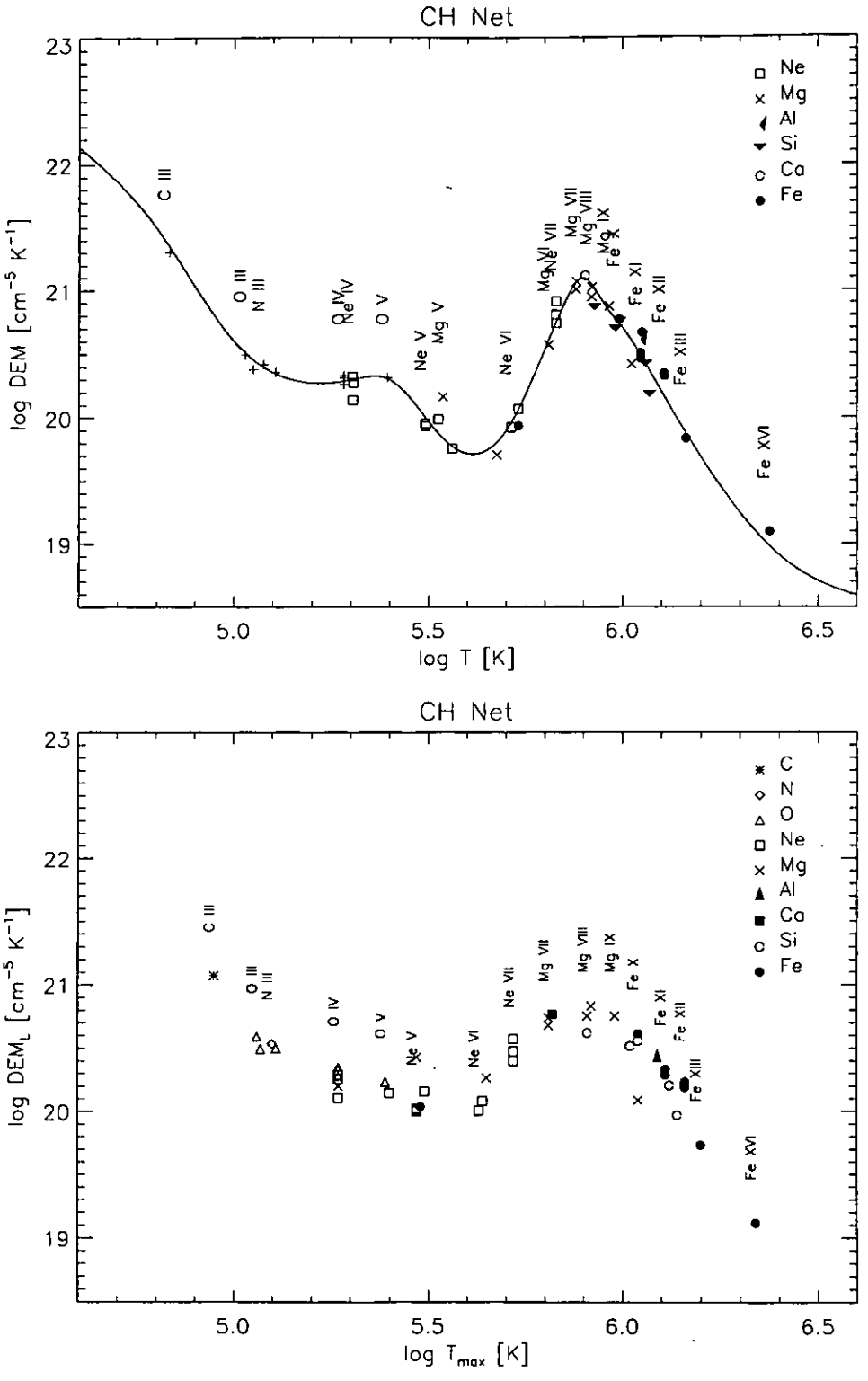

Figure 5.15: *The DEM distribution for the coronal hole network (CH Net) on August 27, 1996 (above), and the corresponding DEM_L values, plotted at the temperature T_{max}.*

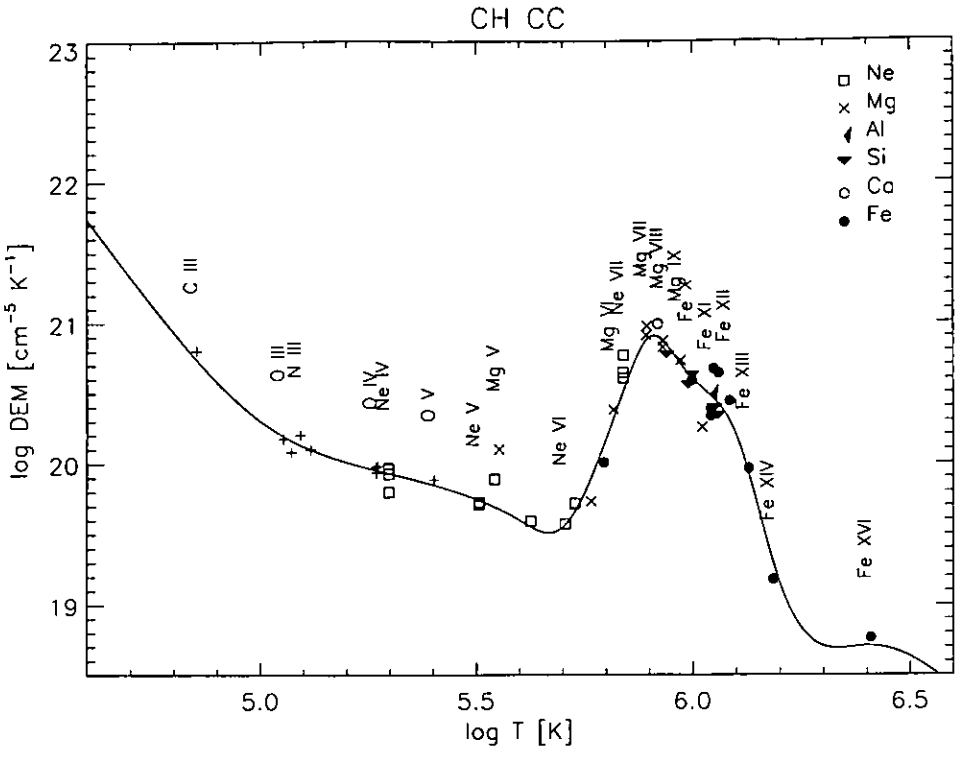

Figure 5.16: *The DEM distribution of the coronal hole cell-centre (CH CC) on August 27, 1996.*

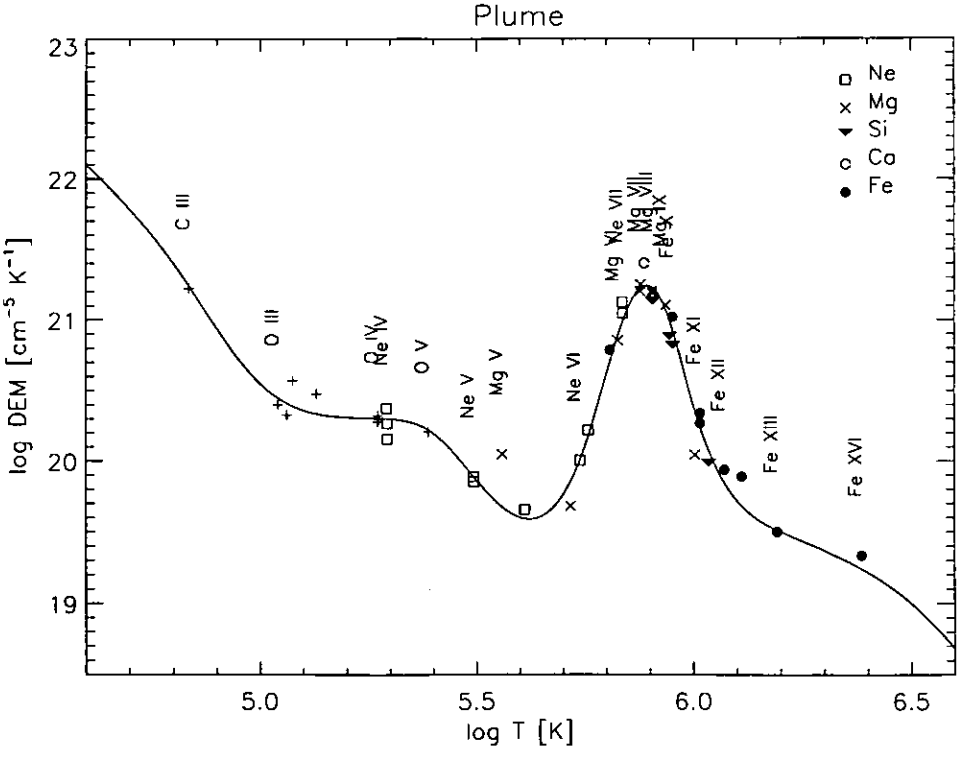

Figure 5.17: *The DEM distribution of the low-latitude plume in the Elephant's Trunk – August 27, 1996.*

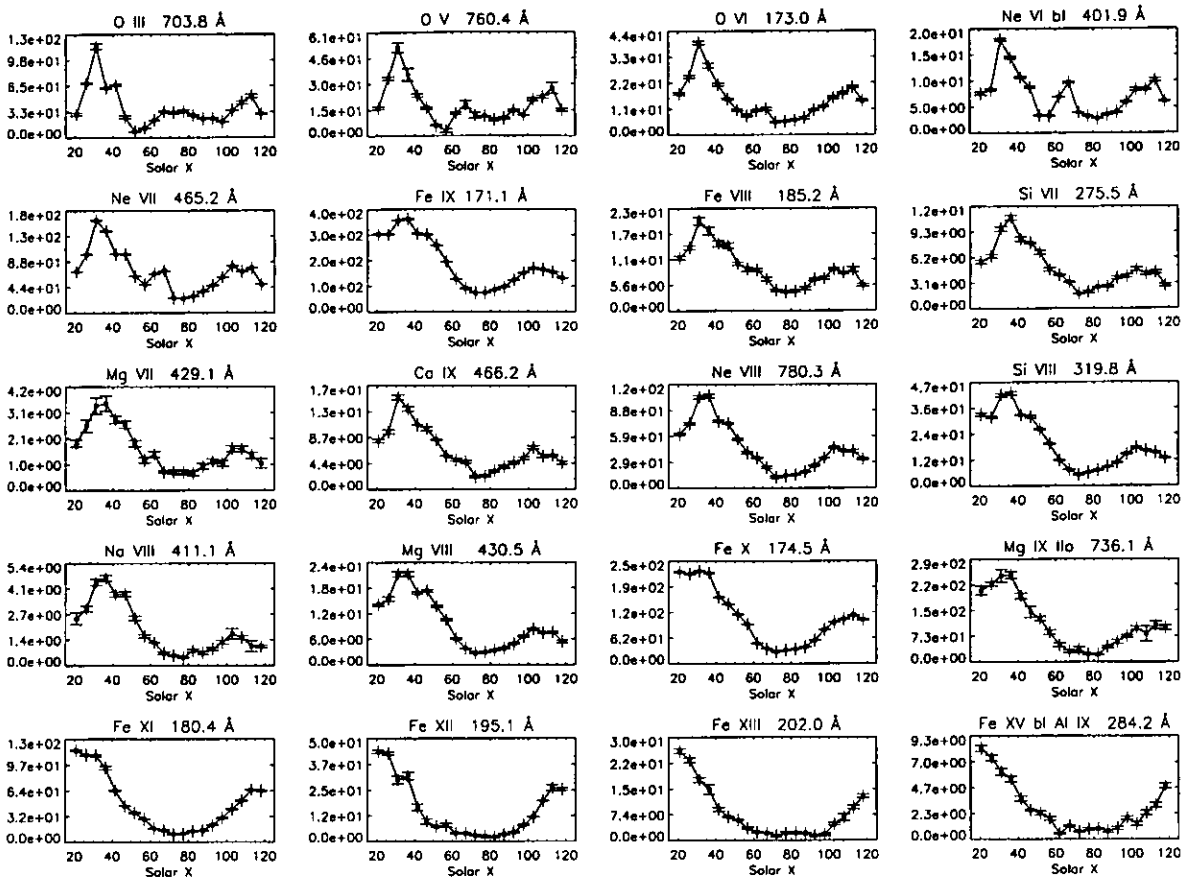

Figure 5.18: *Intensities of twenty lines from the GIS E-W scan across the hole - 1996 August 27.*

the cell centre network pattern. Note for example the Mg VI / Ne VI ratio variations. An inspection of other such combinations suggests that the Mg/Ne variations are principally due to a decreased Ne abundance in the cell centres, which appears to occur relative to both low-FIP elements (Mg, Fe, Ca) and high-FIP ones (O). This has been confirmed by other GIS analyses. However, a more complete analysis is still required, taking into account possible density and *DEM* variations.

An example of coronal hole GIS spectra

Figures D.3, D.4, D.5, D.6 show the GIS spectra of a network region (Solar X =67″, see Figure 5.19) in the coronal hole. Note that, even with a long exposure (400s) and the use of the wide slit (4″x4″), the signal in most of the lines is very weak. A *DEM* analysis was performed, which confirmed the relative abundances derived from the NIS spectra, in particular concerning the Mg/Ne relative abundance ratio, using the bright group of Ne VI and Mg VI lines seen in GIS 3 $\simeq$ 401 Å. The relative Mg/Ne abundance ratio for the coronal hole network has a lower value (0.19) than the photospheric one (0.3). This *DEM*

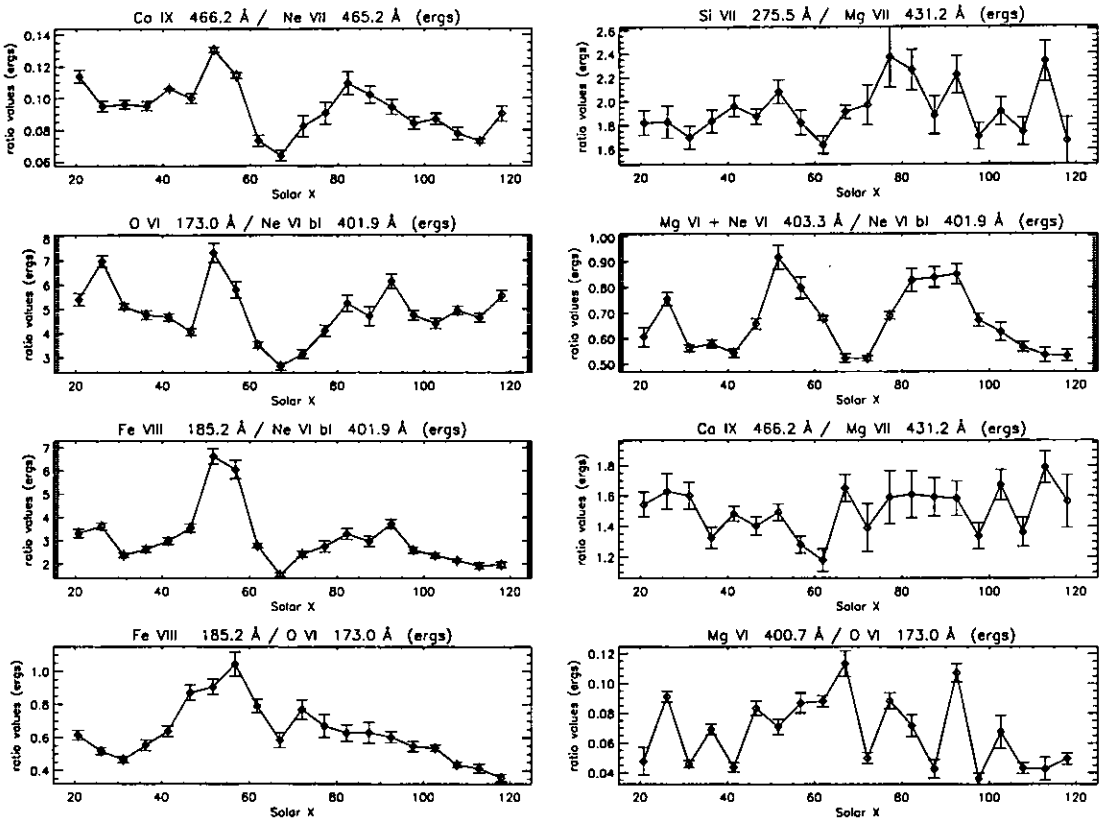

Figure 5.19: *Intensity ratios of selected lines of the GIS E-W scan across the hole - 1996 August 27.*

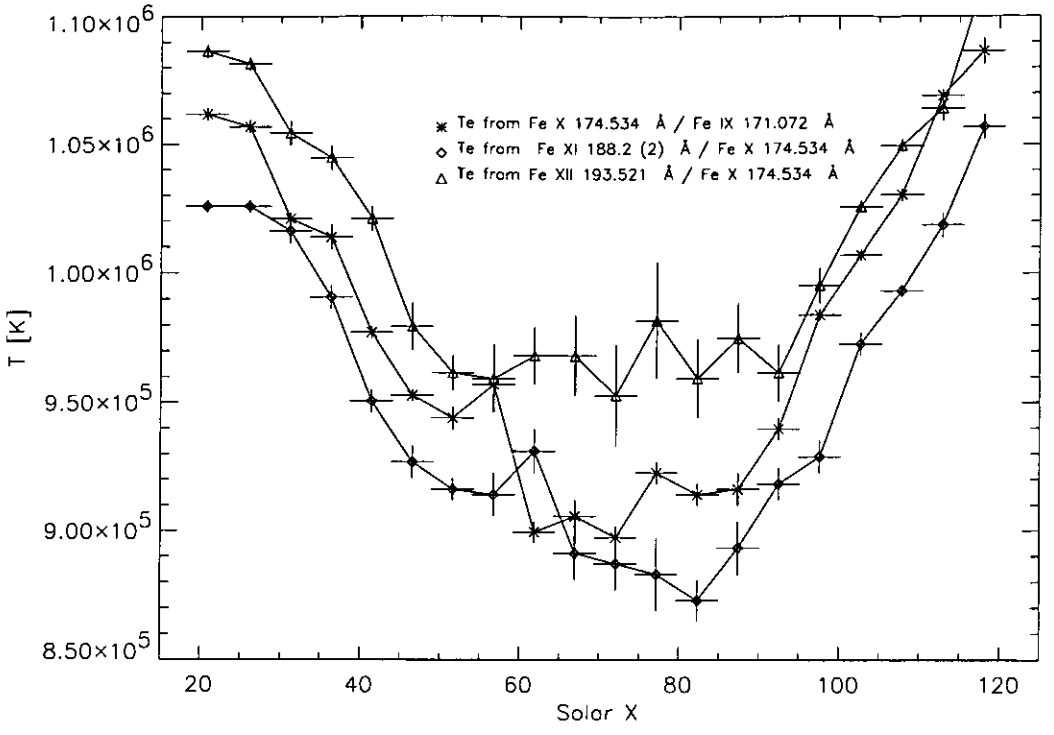

Figure 5.20: *Temperatures across the hole, derived from GIS lines – 1996 August 27.*

analysis also confirmed the mismatch between observations and theory regarding the Ne VIII and C IV lines of the Li-like isoelectronic sequence. These spectra show many lines from low-temperature ions, such as Fe VIII, some of which have been indicated.

5.2.4 Intercomparison and summary of the near-disc-centre results

This section summarises densities, temperatures and abundances derived from various observed structures. The main results are given in Table 5.4 and Figure 5.21. The latter reproduces on one plot the *DEM* distributions already presented separately in the previous section.

- As one would expect, the *DEM* values in the lower transition region are similar for the coronal hole and quiet sun network regions, and the plume. Indeed, coronal holes and plumes are indistinguishable from the quiet sun regions in the lower transition region lines. Similarly, the transition region emission measures for the coronal hole cell centres are similar to those of the quiet sun region cell centres.
- The network regions had much larger *DEM* values than to the cell-centre regions. This is not a new result: it confirms the conclusion of the results from Skylab data, for example.

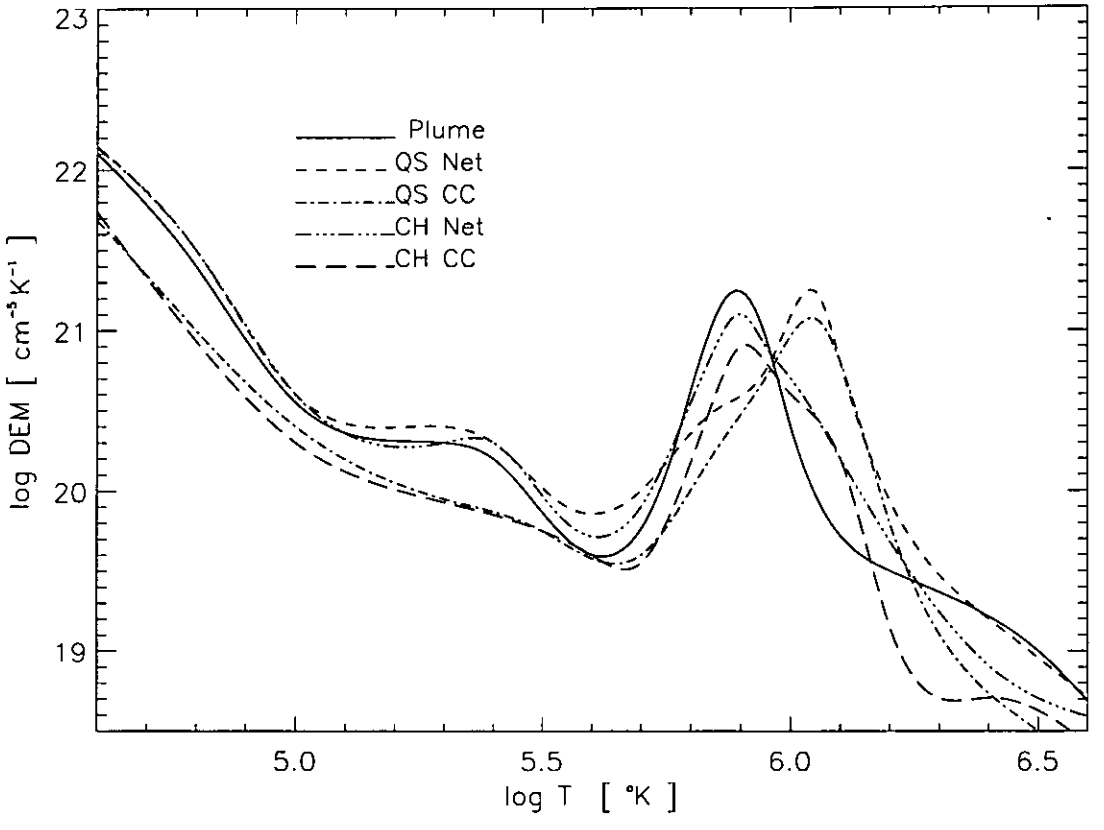

Figure 5.21: *The DEM distribution of the low-latitude plume (solid line), compared to the coronal hole and quiet sun distributions. Note the different peak temperatures and widths at coronal temperatures, and the larger values in the network, at transition region temperatures.*

- The peaks of the emission measure distributions are at increasing temperatures for the plume ($T \simeq 7.7 \cdot 10^5$), coronal hole ($T \simeq 8 \cdot 10^5$) and quiet sun ($T \simeq 1.1 \cdot 10^6$) areas examined. The plume has the highest emission measures at the peak of the DEM, at upper transition region temperatures (Mg VII, Ca X), which explains why plumes are most visible in lines emitted at those temperatures.

- The plume had an almost isothermal distribution at coronal heights, while the DEM distributions of the coronal hole and the quiet sun are increasingly less isothermal. This explains why different line ratios produce increasingly different isothermal temperatures. (Note for example the values derived from the Mg VII-VIII-IX ratios).

- The very low emission measures at temperatures above 10^6 K indicate that in August 1996, during solar minimum, the Sun was very quiet in such areas, with little high-temperature emission.

- The peak of the *DEM* derived from the Skylab coronal hole data (Figure 2.12, Chapter 2) is at a higher temperature than that for of the Elephant's Trunk. However, it was not possible from the Skylab data to derive with accuracy the *DEM* values at higher temperatures, something that has been possible with CDS.

- The different regions show different element abundances. The abundances derived from the Skylab cell-centre data are not too different from those derived for the Elephant's Trunk. For Skylab, the Ne abundance was increased by a factor of 0.2 dex compared to O, whilst here it is increased by 0.1 dex. The relative Mg/Ne abundance was difficult to assess from the Skylab data, due to the paucity of unblended lines. Here, the Ne/O relative abundance shows small variations, as does also the Mg/Ne relative one, although the average is the photospheric value. The low-FIP elements such as Mg are always in agreement among themselves, confirming the presence of a (small) FIP bias effect in these observations. Furthermore, evidence has been found in all the observations analysed, of a variation of the Ne abundance that follows the network pattern.

  The relative Mg/Ne abundance for the plume had a value of about 0.5, higher (by a factor of 1.6) than the photospheric one. This plume therefore showed a small FIP effect. Note that when compared to the ambient coronal hole regions, the Mg/Ne relative abundance in the plume is 2.5 higher.

- The density inside the coronal hole region, both at coronal (Si IX) and transition region (O IV) heights is about a factor of 2 lower than in the quiet sun.

- There are indications that the transition region densities are higher in the cell-centre areas. This is confirmed by other observations, presented in later Sections.

Table 5.4: *Table of parameters deduced from the 1996 August 27 coronal hole observations, divided into plume, network and cell centres, together with the parameters deduced from the quiet sun observation of August the 25th, 1996. The densities are in cm^{-3}, and the isothermal temperatures are in K. A few of the intensity ratios are also shown. The abundances , deduced from the DEM analysis, are logarithmic differences relative to the photospheric values (*Grevesse and Anders, *1991), i.e. they are quoted in 'dex' in the standard way.*

	Plume	coronal hole Network	quiet sun Network	coronal hole Cell-Centre	quiet sun Cell-Centre
N_e (O IV 625.8/608.4 Å)	0.8±0.6 10^{10}	0.5±0.1 10^{10}	0.8±0.2 10^{10}	0.4±0.1 10^{10}	1.4±0.2 10^{10}
N_e (Mg VII 319.027/367.67 Å)	1.1±1 10^{9}	1.±0.2 10^{9}	1.8±1 10^{9}	1.3±0.3 10^{9}	1.4±0.6 10^{9}
N_e(Mg VIII 315.038 / 317.038 Å)	1.3±1 10^{8}	1.3±0.5 10^{8}	0.8±0.4 10^{8}	1.0±0.2 10^{8}	1.2±0.7 10^{8}
N_e (Si IX 349.9/341.9 Å)	2.±1. 10^{8}	1.4±0.2 10^{8}	3.0±0.2 10^{8}	1.4±0.2 10^{8}	2.7±0.3 10^{8}
N_e (Si IX 349.9/345.1 Å)	1.8±1. 10^{8}	1.3±0.3 10^{8}	3.0±0.2 10^{8}	1.2±0.2 10^{8}	3.5±0.4 10^{8}
N_e (Si X 356./347.4 Å)	7±7. 10^{8}	2.8±1 10^{8}	5.0±0.3 10^{8}	2.8±1 10^{8}	3.2±0.4 10^{8}
T_e (Mg X 624.9 Å/ Mg IX 368 Å)	7.9±0.1 10^{5}	8.7±0.1 10^{5}	9.8±0.1 10^{5}	8.5±0.1 10^{5}	9.8±0.1 10^{5}
T_e (Mg IX 368.07 Å/ Mg VIII 315.04 Å)	8.3±0.1 10^{5}	9.±0.1 10^{5}	1.0±0.1 10^{6}	8.8±0.1 10^{5}	9.1±0.1 10^{5}
T_e (Mg IX 368.07 Å/ Mg VII 367.7 Å)	8.0±0.1 10^{5}	8.3±0.1 10^{5}	9.2±0.1 10^{5}	8.3±0.1 10^{5}	9.1±0.1 10^{5}
T_e(Fe XII 364.47 Å/ Fe X 345.72 Å)	1.0±0.1 10^{6}	1.0±0.1 10^{6}	1.2±0.1 10^{6}	1.1±0.1 10^{6}	1.2±0.1 10^{6}
T_e(Fe XI 352.66 Å/ Fe X 345.72 Å)	9.±0.1 10^{5}	1.0±0.1 10^{6}	1.1±0.1 10^{6}	9.9±0.1 10^{5}	1.1±0.1 10^{6}
T_{max} (DEM)	7.7 10^{5}	7.9 10^{5}	1.1 10^{6}	8.1 10^{5}	1.1 10^{6}
I (O IV 608.40 Å/ Ne IV 542.07 Å)	4.9±1.2	4.3±0.1	4.2±0.1	3.9±0.1	4.0±0.2
I (Mg VI 349.17 Å/ Ne VI 562.8 Å)	1.04±0.29	0.39±0.03	0.54±0.03	0.42±0.03	0.75±0.08
I(Mg VII 367.67 Å/ Ne VII 561.73 Å)	9.10±2.39	3.56±0.16	3.75±0.34	3.93±0.14	6.21±0.31
Ab(Ne)	0	+0.1	+0.1	+0.1	+0.2
Ab(Mg)	+0.2	-0.1	+0.1	-0.1	+0.2
Ab(Si)	+0.2	-0.1	+0.1	-0.1	+0.2
Ab(Fe)	+0.2	-0.1	+0.1	-0.1	+0.2
Ab(Ca)	+0.5	+0.3	+0.4	+0.3	+0.6

Chapter 6

Results for polar coronal holes and polar plumes

This Chapter is organized as follows. First, Section 6.1 presents examples of on-disc observations of polar holes, to show the similarities between the Elephant's Trunk equatorial coronal hole and the polar holes. Examples of off-limb coronal hole observations can then be found in Section 6.2, where plume and inter-plume regions are treated separatedly, in order to establish the contribution of plume material in the determination of the coronal hole plasma parameters. Examples of how off-limb coronal hole observations can be affected by background diffuse emission, are also given in Section 6.2. Section 6.3 then presents results from two on-disc observations of polar plumes, and shows the similarities with the Elephant's Trunk low-latitude plume presented in Chapter 5, with a CDS-EIT comparison.

As for the results presented in Chapter 5, the *Arnaud and Rothenflug* (1985) ionization equilibrium for all the ions has been adopted, together with the calculations of *Landini and Monsignori Fossi* (1991) for the minor elements. CHIANTI v.2 (*Landi et al.*, 1999b), together with the recent Fe XIV calculations (*Storey et al.*, 1999) and Mg IX calculations (P. Young, 1999, priv. comm.) have been used. For those ions that are not present in the CHIANTI database, the Arcetri spectral code (AC, see, e.g. *Landi and Landini*, 1998a) was used. The continuum emission has been calculated by the method described in *Landi et al.* (1999b).

6.1 On-disc observations of polar holes

All the polar coronal hole observations analysed by the author have shown the same type of characteristics as the equatorial hole (Elephant's trunk), although some spatial and temporal variations of all the parameters have been observed. An example of an

observation containing various structures is given here.

The October 10th 1997 observations of a polar coronal hole region, with a plume, quiet sun, and a bright point

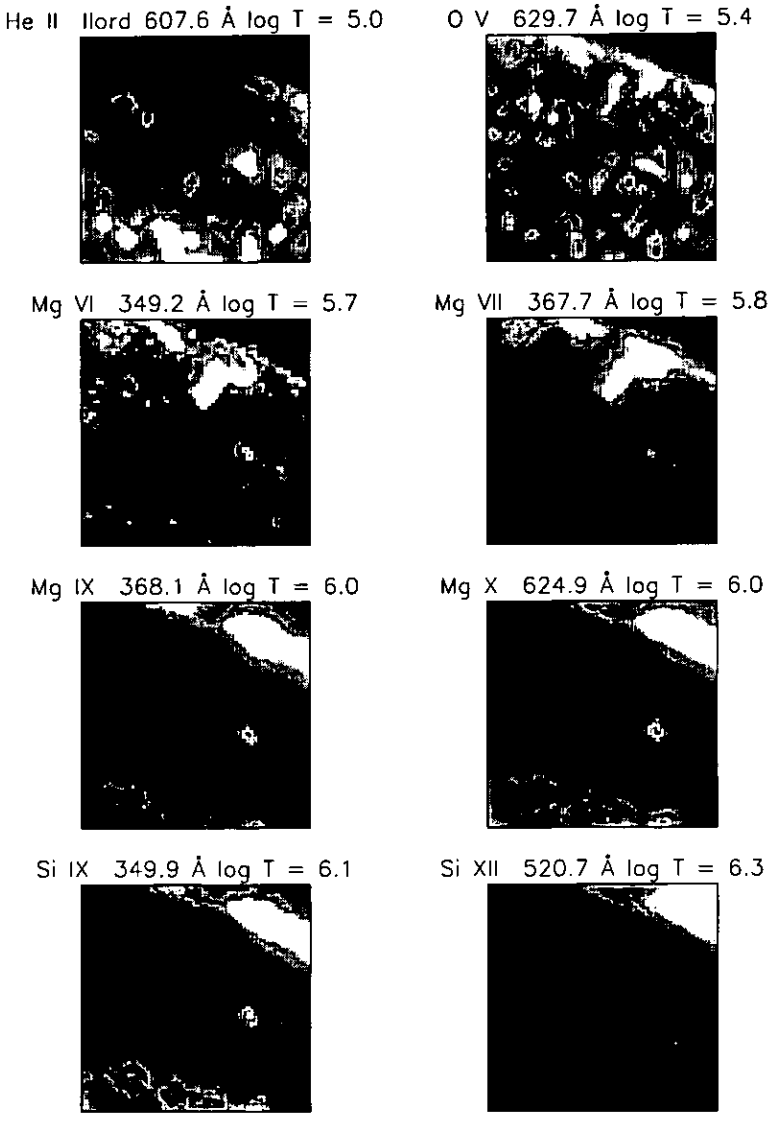

Figure 6.1: *Monochromatic images – 10th October 1997.*

On 1997 October 10, a NW region of the solar corona was rastered three times with NIS (in 2 hours). The spectra have been averaged, to increase the signal-to-noise (temporal variations were small). Figure 6.1 shows some monochromatic images. This area contains a quiet sun region in the lower part, a bright polar plume (visible in Mg VI-IX lines) and a bright point (visible in all lines). This observation is typical of those made in 1997. The main difference compared to the 1996 observations, was an increased diffuse emission in all the higher-temperature (above a million degrees) lines, even apparent in coronal hole

regions.

Intensity ratio images were formed and are shown in Figure 6.2. They show temperatures and densities (at both coronal and transition region heights).

Densities and temperatures have been derived from spatially-averaged spectra of various areas (Figure 6.3). The results are presented in Table 6.1. The coronal hole and quiet sun temperatures and densities are similar to the values deduced from the August 1996 observations. Note from Figure 6.2 and Table 6.1:

- a decrease in the density inside the coronal hole region, both at coronal (Si IX) and transition region (O IV) heights. At coronal heights, densities decrease from $N_e \simeq 4\text{x}10^8$ cm^{-3} to $N_e \simeq 2\text{x}10^8$ cm^{-3}, in the coronal holes, i.e. a factor of two lower.

- In the lower transition region (O IV), the averaged coronal hole density is $N_e \simeq 1\text{x}10^{10}$ cm^{-3} in the network, with consistently higher values (by a factor of 2) in the cell-centre areas. In the quiet sun areas, the densities in the network and cell-centre regions are both a factor of 2 higher than in the coronal hole region.

- Isothermal temperature maps show coronal holes having lower temperatures than quiet sun areas. Values in the quiet sun are $T \simeq$ 9-11 x10^5 K, while values in the coronal hole region are in the range $T \simeq$ 8.4-8.9 x10^5 K.

- The bright point shows a higher coronal density $N_e \simeq 6\text{x}10^8$ cm^{-3} (with even higher values from Fe XIII) and similar temperatures to the quiet sun.

- The plume is not visible in Si IX and the data yield average densities similar to the coronal hole, but marked lower temperature. At upper transition region heights, the Mg VII intensity is very high, and it is possible to deduce a plume density $N_e = 1.1 \pm 0.2\text{x}10^9$ cm^{-3} with small uncertainties.

- The plume had even lower temperatures than the ambient coronal hole regions, with $T \simeq 7.9$ x10^5 K.

Figure 6.4 shows a coronal 'pressure' image, created by multiplying the densities obtained from the intensity ratio image of Si IX, with the temperatures obtained from the Mg X/Mg IX intensity ratio. The difference between coronal hole regions and the quiet sun is obviously highlighted. Similarly, pressure maps in the transition region, show the large differences in pressure between the various regions.

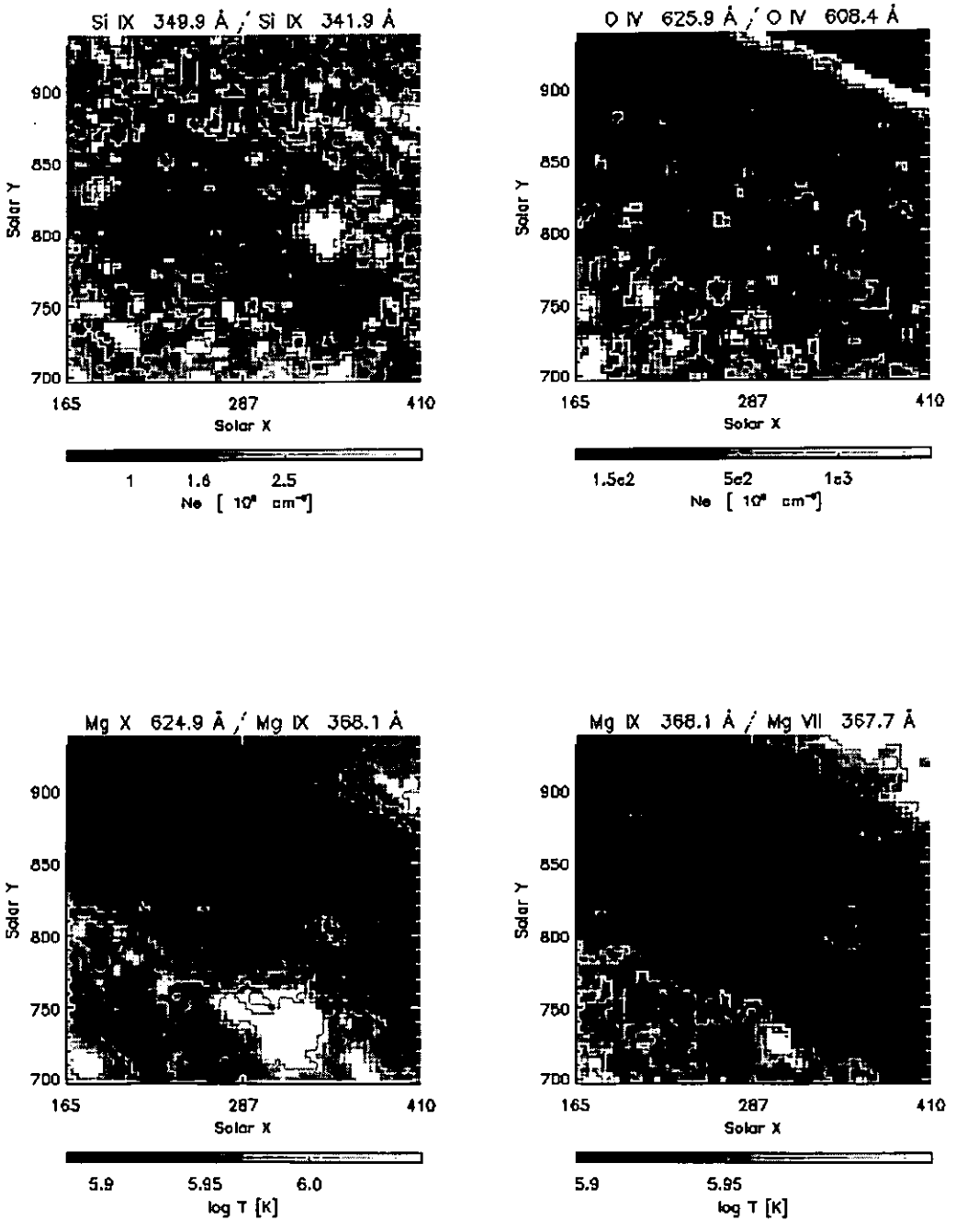

Figure 6.2: *Intensity ratio images – October 10th 1997.*

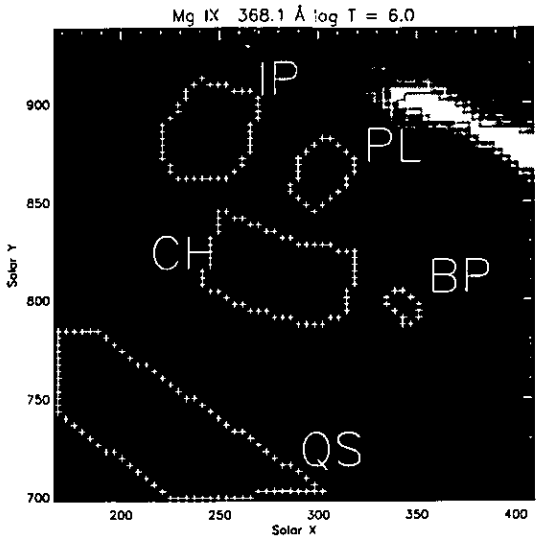

Figure 6.3: *Selected areas: plume (PL); inter-plume (IP); coronal hole (CH); quiet sun (QS); bright point (BP). – October 10th 1997.*

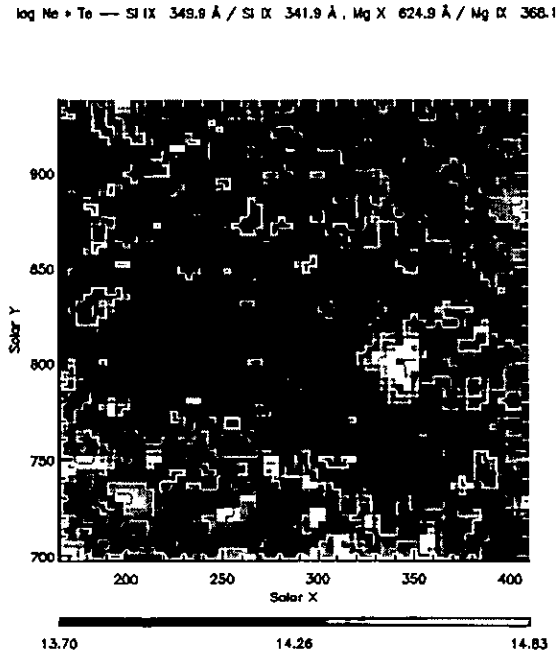

Figure 6.4: *A pressure image – October 10th 1997.*

Table 6.1: *Table of parameters deduced from the 10th October 1997 averaged spectra of the selected regions. The coronal hole (CH) and quiet sun (QS) regions have been subdivided into network (Net) and cell centres (CC).*

	plume	inter-plume	CH Net	CH CC	QS Net	QS CC	BP
N_e (O IV 625.8/554.5 Å)	0.6±0.1 10^{10}	0.7±0.1 10^{10}	0.7±0.2 10^{10}	1.2±0.5 10^{10}	1.5±0.2 10^{10}	2.7±0.2 10^{10}	1.6±0.3 10^{10}
N_e (O IV 625.8/608.4 Å)	0.7±0.1 10^{10}	0.8±0.1 10^{10}	0.7±0.1 10^{10}	1.5±0.5 10^{10}	1.6±0.1 10^{10}	2.5±0.3 10^{10}	1.9±0.4 10^{10}
N_e (Mg VII 319.0 / 367.7 Å)	1.1±0.2 10^{9}	7±3 10^{8}	9±6 10^{8}	3.3±1 10^{8}	1.0±0.3 10^{9}	8±3 10^{8}	9±5 10^{8}
N_e (Si IX 349.9/341.9 Å)	2.±0.8 10^{8}	1.9±0.6 10^{8}	1.9±0.7 10^{8}	2.3±1 10^{8}	4.±0.6 10^{8}	3.6±0.5 10^{8}	6±3 10^{8}
N_e (Fe XIII 320.8 / 348.183 Å)	6±6 10^{8}	2±2 10^{9}	4±3 10^{8}	8.4±5 10^{8}	6.7±0.8 10^{8}	5.3±1 10^{8}	2.1±0.8 10^{9}
T_e (Mg X 624.9 Å/ Mg IX 368 Å)	8.1±0.1 10^{5}	8.6±0.1 10^{5}	8.8±0.1 10^{5}	8.9±0.1 10^{5}	1.1±0.1 10^{6}	1.1±0.1 10^{6}	9.8±0.1 10^{5}
T_e (Mg IX 368 Å/ Mg VII 367.7 Å)	7.7±0.1 10^{5}	8.1±0.1 10^{5}	8.4±0.1 10^{5}	8.4±0.1 10^{5}	9.0±0.1 10^{5}	9.1±0.1 10^{5}	8.6±0.1 10^{5}

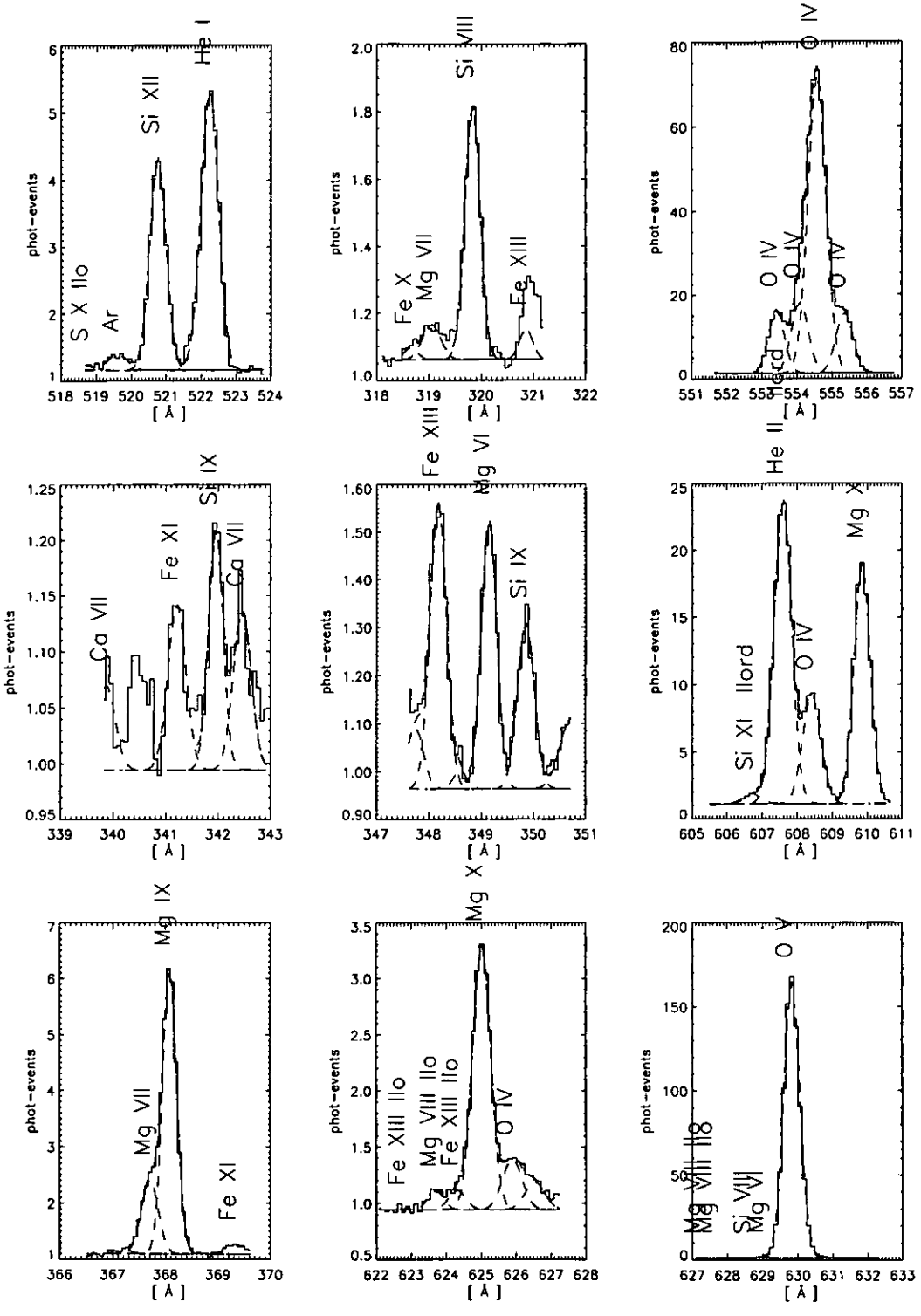

Figure 6.5: *Averaged spectra of the network coronal hole region – October 10th 1997. Note how high-temperature lines such as Fe XIII and Si XII are now bright, compared to the 1996 observations of the Elephant's Trunk (see, e.g., Figure 5.9).*

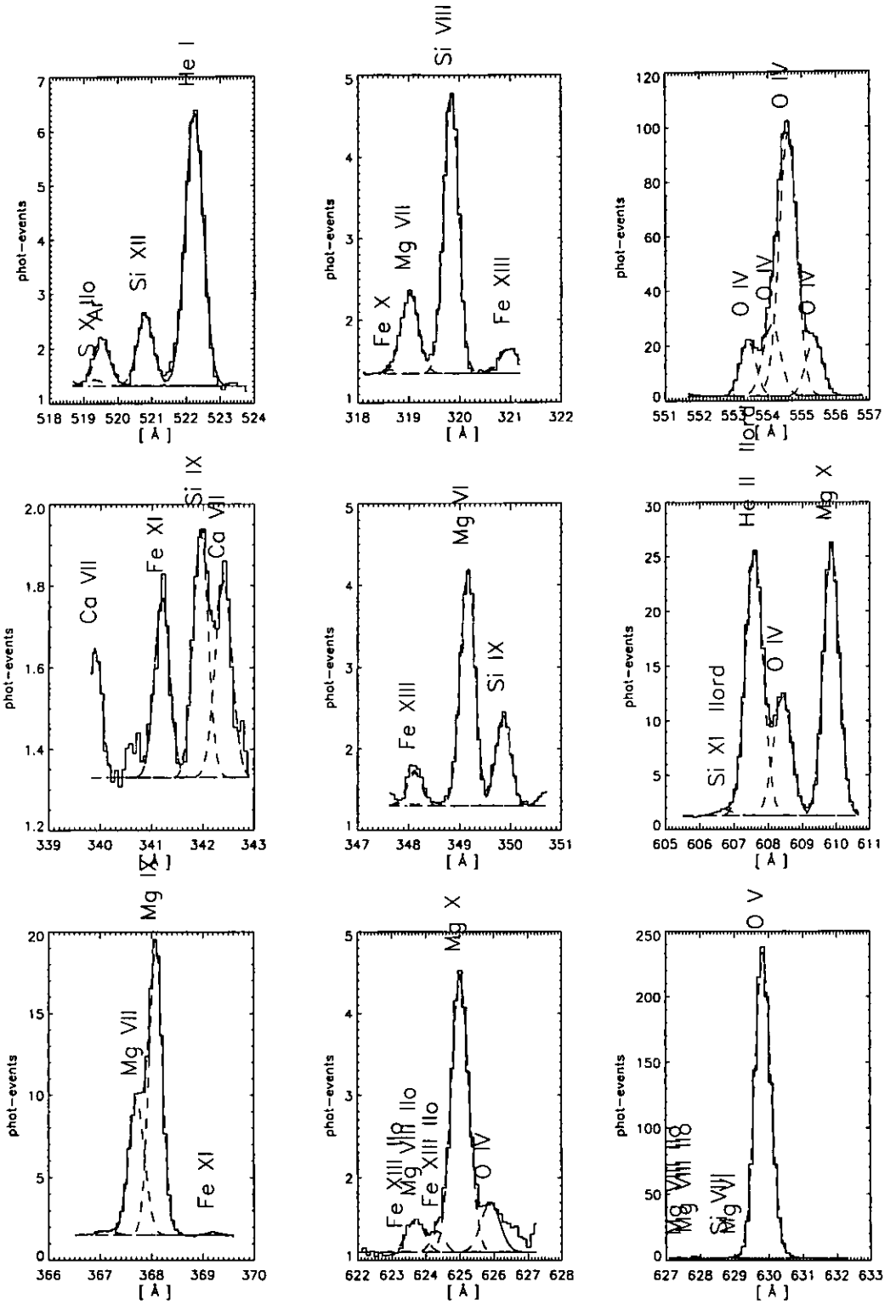

Figure 6.6: *Averaged spectra of the plume region – October 10th 1997. Note the similarities with the Elephant's Trunk plume, in the bright transition region lines emitted by Mg VI, Mg VII and Ca VII.*

Observations of the quiet sun – coronal hole boundary

During 1996 and 1997, many observations of quiet sun – coronal hole boundaries were performed, mainly near the meridian on some equatorward extensions of one of the polar holes. In general terms, all observations produced the same type of result for this boundary that has already been described for the Elephant's Trunk. The boundary is evident in the He lines and in the coronal lines, and in terms of physical parameters is not sharp, but shows a slow decrease of electron density and temperature toward the coronal hole regions, where the pressure is lower. Small-scale inhomogeneities in all the derived parameters have been observed.

The relative element abundances appear to vary slightly, with values similar to the photospheric ones. There is a tendency to have a small FIP effect related to the supergranular pattern, with a difference between the coronal hole and the quiet sun regions, although as already shown some of these differences can be explained in terms of differential emission measure variations. DEM analyses on the polar regions have been done, but they have the drawback of suffering from some projection effects and the derived element abundances may not be correct. The near-disc-centre observations are to be preferred for DEM and abundance analysis. In fact, in the polar observations, if regions in the network are selected from the intensity of a transition region line, then the corresponding area at coronal heights might have some mixing of plasma that instead originated from nearby cell-centre regions, close to the line of sight. However, the observed abundance variations have been seen in all the NIS rasters analysed, independent of the angle of the line of sight to the radial direction.

Figure 6.7 shows as an example a series of monochromatic images of a coronal hole boundary observed on 1997 October 14. Six repetitions of the NIS full wavelength raster UCLAN_N2 have been analysed and averaged, to increase the signal-to-noise. The boundary is evident in the He and coronal lines.

Figure 6.8 shows some intensity ratio images, illustrating the decrease in density and temperature, and possible element abundance variations, in the region of the coronal hole boundary.

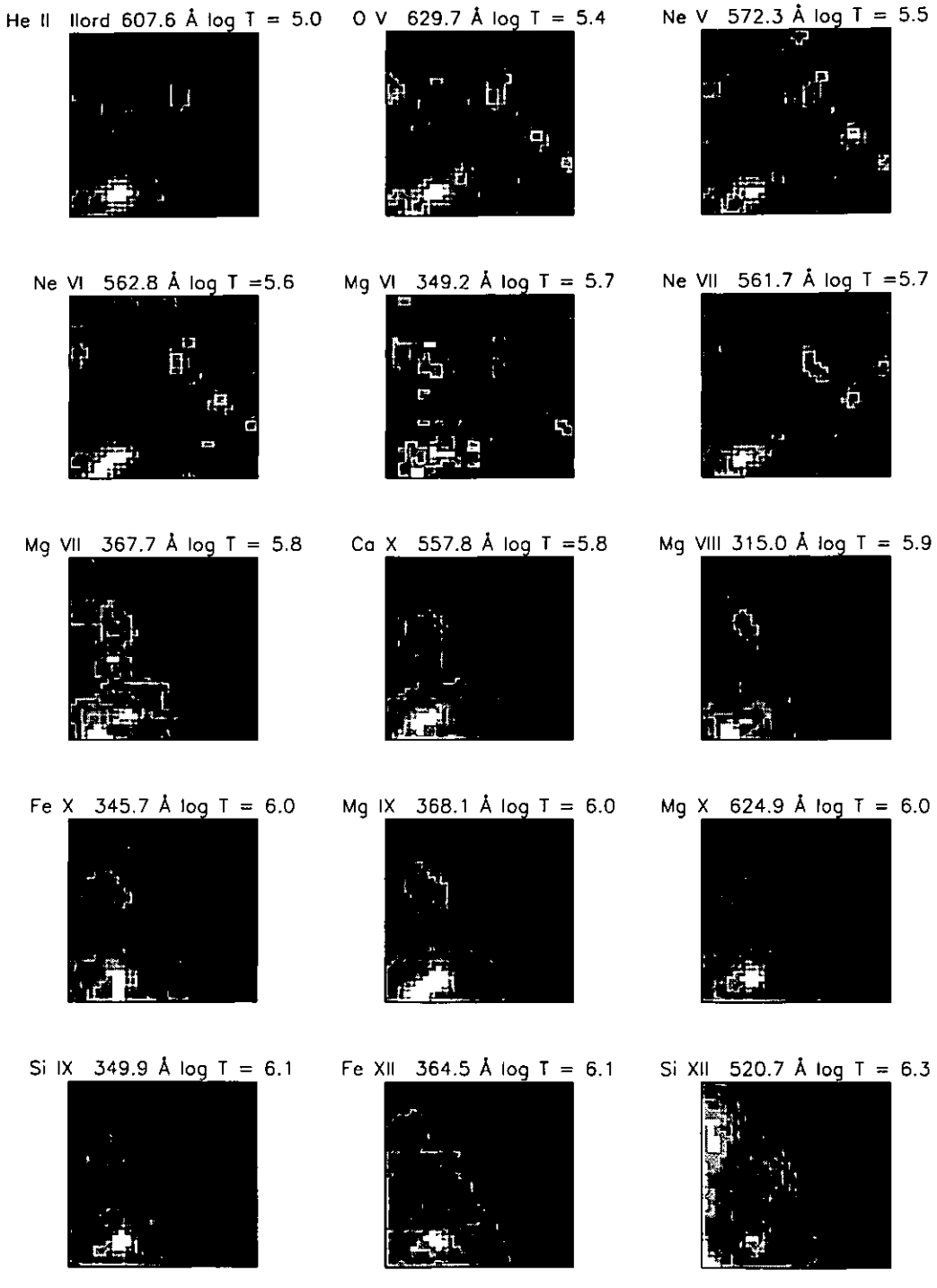

Figure 6.7: – *Monochromatic images of a boundary – 14th October 1997.*

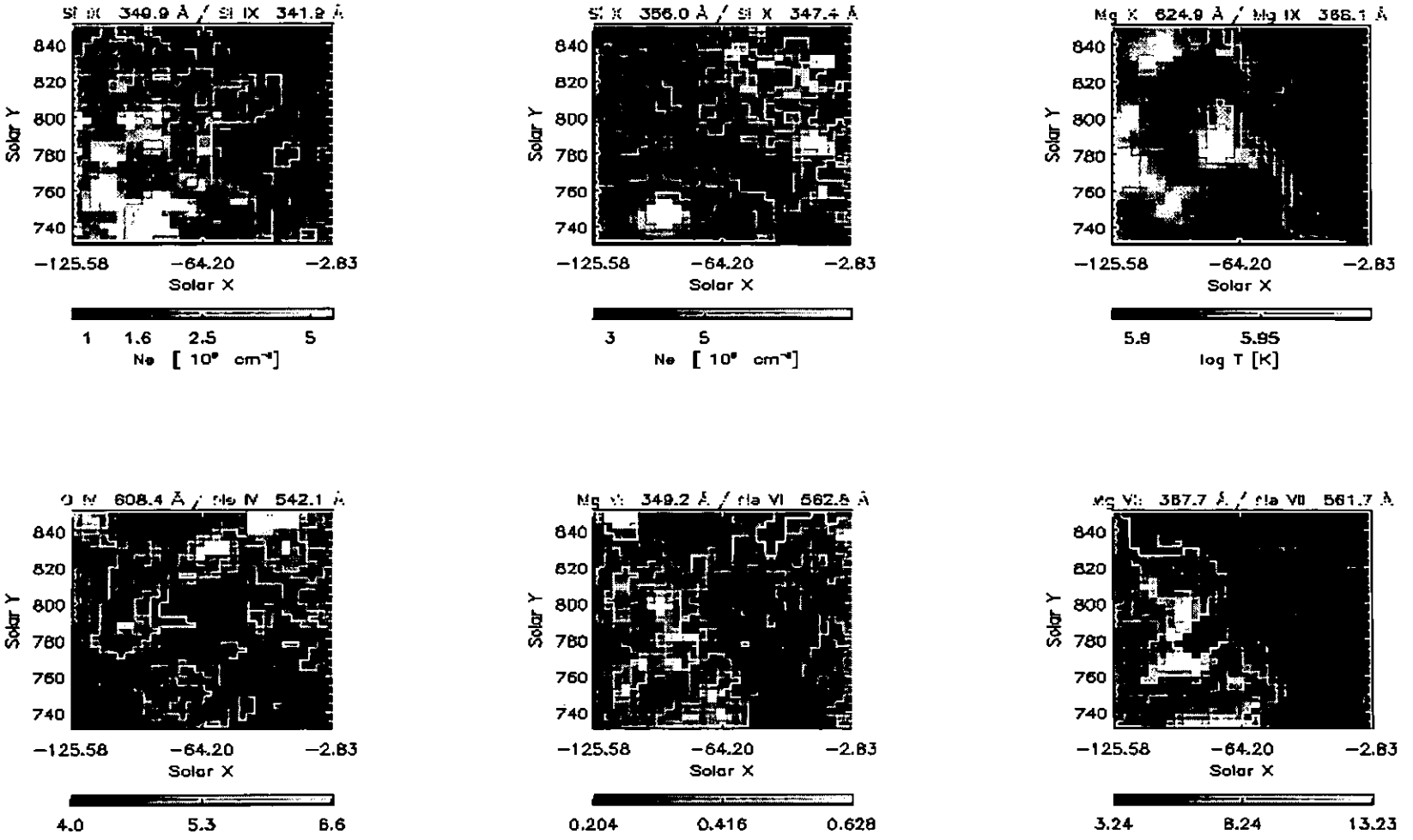

Figure 6.8: - *Ratio images of a boundary - 14th October 1997.*

6.2 Off-limb observations of polar holes and plumes

The off-limb coronal hole observations of the 12th of September 1997

On 1997 October 12 between 16:01 and 18:28 UT, CDS observed the north polar hole with the CORO24W study, as part of a synoptic program devised by A. Fludra. The CORO24W study extracts only a limited number of lines. Figure 6.9 displays a mosaic of monochromatic images of the observed region. These show the presence of two plumes, one on each side of the meridian, most visible in the upper transition region lines (excluding the Ne lines).

Prior to these studies, six repetitions of the NISAT_S5 study, starting at 08:55 UT, were performed (see Figure 4.9). This observation represents the longest off-limb inter-plume observation by CDS, since it lasted for almost 7 hours. An analysis of the single observations showed very little variations in time. The six observations were therefore subsequently averaged, to increase the signal-to-noise. Furthermore, an inter-plume area of 24″in Solar X (centred at Solar X = -7) was selected for the average, to produce radial profiles. This averaging along Solar Y, using increasing spatial areas with radial distance, was also applied to the spectra before fitting and deriving the line intensities. Figure 6.11 (top four rows) shows intensity profiles of some selected lines. With all the averaging performed, the signal was of acceptable strength for most lines. Two areas in the CORO24W study were selected for comparisons (these are shown in Figure 6.10): 1) the brightest plume region; and 2) an inter-plume region eastward of the eastern plume. Figure 6.11 also shows the radial profiles of the intensities of some lines in the plume region. Note how the chromospheric and transition region intensities rapidly fall off-limb, showing how little stray light was present, and how lines that are formed at different temperatures have different profiles.

Figures 6.12 and 6.13 (upper plots) present densities and isothermal temperatures as derived from some of the line ratios where the signal was acceptable. These results extend out to R= 1.2 $R_\odot$ those presented by *Fludra et al.* (1999a) and (1999b), that in the coronal hole regions extended out to 1.1 $R_\odot$, and moreover distinguish between plume and inter-plume regions. Note that:

- very low values of $N_e \simeq 5\text{x}10^7$ cm^{-3} are reached at 1.2 $R_\odot$; and
- the densities derived from Si IX are slightly higher (at lower heights) than those derived from Mg VIII. This difference could be the signature of the photoionization processes that have been neglected in calculating the densities (see discussion in Chapter 2). However, Si X densities in the same region are even higher.

The differences in the derived densities could be real, and not due to having neglected photoionization in the level population calculations. In fact, the plasma that emits these ions is not co-spatial. Indeed, evidence from deriving temperatures from line ratios suggest that the plasma is not isothermal, as Figure 6.13 shows. While temperatures from the Mg X / Mg IX ratio show increasing values between $T \simeq 8\text{x}10^5$ K and $T \simeq 9\text{x}10^5$ K, other ratios show different values, except for the Mg IX / Mg VII ratio near the base of the plume. Using ratios of higher-temperature ions, such as Si XII / Si XI and Fe XIII /Fe XII, the temperature appears to rapidly increase just off-limb, and then decrease. This is due to some diffuse background emission at temperatures above a million degrees, which is present along the line of sight , as shown with a *DEM* analysis below.

A rectangular area across the plumes was selected between 1.04 and 1.06 $R_\odot$, and spectra were averaged along the Solar Y direction. Figure 6.14 shows some of the intensity profiles across the plumes, together with densities and temperatures. The higher-temperature lines (e.g. Fe XIII, Fe XVI) show the presence of diffuse hot plasma in the background, in particular in the western side of the observations. The transition region lines (Mg VII, Ca X in particular) show the profiles of the two plumes. Note how these profiles are different in all the lines examined, and how complex the emission is. Densities derived from Si IX show slightly higher values in the plume regions, while temperatures derived from Mg IX/Mg VII indicate lower values ($T \simeq 8.5\text{x}10^5$ K) in the region of the brightest plume. The temperature as derived from Mg X/Mg IX agrees only in this plume region, indicating isothermal plasma. In Figure 6.13 (bottom) it can be seen that the plume is only strictly isothermal between 1.02 and 1.06 $R_\odot$. Temperatures derived from Fe XII/Fe X are higher, again because most of the Fe XII emission is not from the plume, but from the background and foreground regions.

A more complete analysis in which the plume and background emission are separated is deferred for future work, but a *DEM* analysis on an off-limb inter-plume region is presented here, because it helps to assess the contamination from hot plasma in the coronal hole region. This region is indicated in Figure 6.10. It is far from the region where there is obvious contamination from hot plasma (see again Figure 6.14).

A constant density $N_e = 1\text{x}10^8$ cm^{-3} was assumed, with the *Arnaud and Rothenflug* (1985) ionization equilibrium, photospheric abundances, and CHIANTI v.2 data. Figure 6.15 shows the result. The peak of the DEM is at $T = 9.5\text{x}10^5$ K, a value close to that derived from the Mg IX/Mg VII ratio (Figure 6.13, middle and Figure 6.14, bottom). However, the plasma distribution along the line of sight is evidently not isothermal, due to the high-temperature plasma in the background that produces significant emission measures above a million degrees.

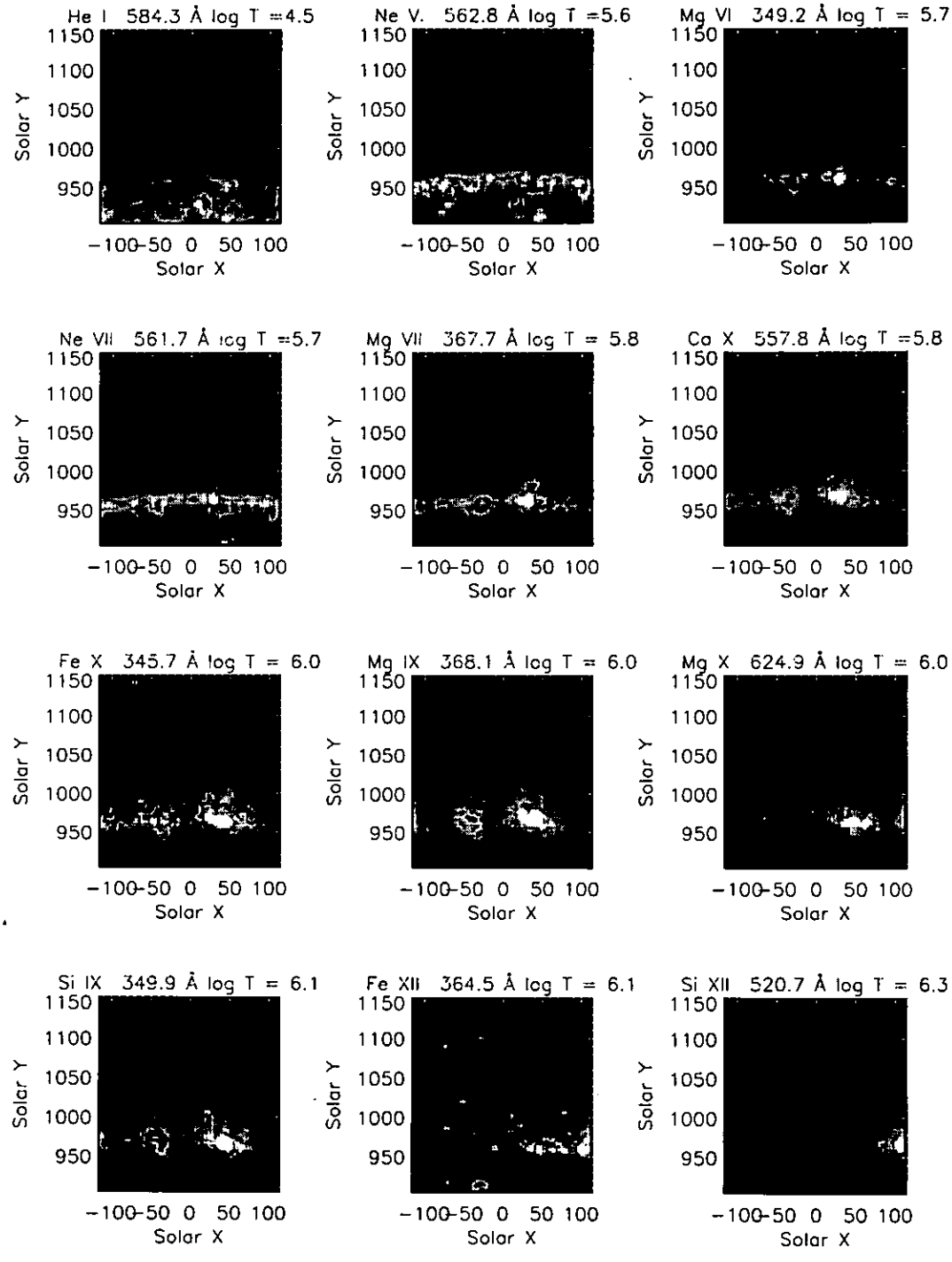

Figure 6.9: *Some off-limb monochromatic images from the CORO24W study – 12th October 1997.*

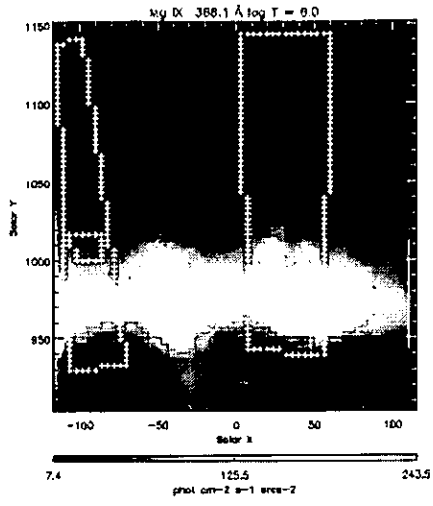

Figure 6.10: *Some selected areas - 12th October 1997. Left: a long, narrow inter-plume area for off-limb radial profiles, and a small area within it for a DEM analysis. Right: a plume area. The full-wavelengths NISAT spectra were centred on the meridian, in the inter-plume region in the middle of the figure (see also Figure 4.9).*

In conclusion, the observations of 1997 October 12 illustrate the difficulties in dealing with off-limb coronal hole observations. Even with long exposures, the signal in coronal holes is low, and errors in the derivation of the parameters can be substantial. Contamination from background emission may be present (in this case in the form of diffuse background emission from hot plasma), even in regions that at first sight seem unaffected. This contamination probably affects all temperature estimates based on lines that are emitted at $T > 10^6$ K. The plasma distribution along the line of sight is not isothermal in most of the regions, except near the base of the plumes.

The off-limb observations of 1998 February 9

Other observations of plume and inter-plume regions off-limb were analysed, and showed a variety of results (that are not presented here), but which confirm that in general plumes are quasi-isothermal structures, having temperatures slightly lower than the surrounding coronal hole region. For example, a *DEM* analysis of an off-limb observation of the 9th February 1998 was performed over a plume region just 40″off-limb and a nearby inter-plume region, at the same height from the limb. The plume showed an almost isothermal *DEM* distribution, with a peak temperature $T = 8.1\text{x}10^5$ K, while the adjacent region had a *DEM* with a peak at $T = 8.5\text{x}10^5$ K. In this observation the amount of quiet sun

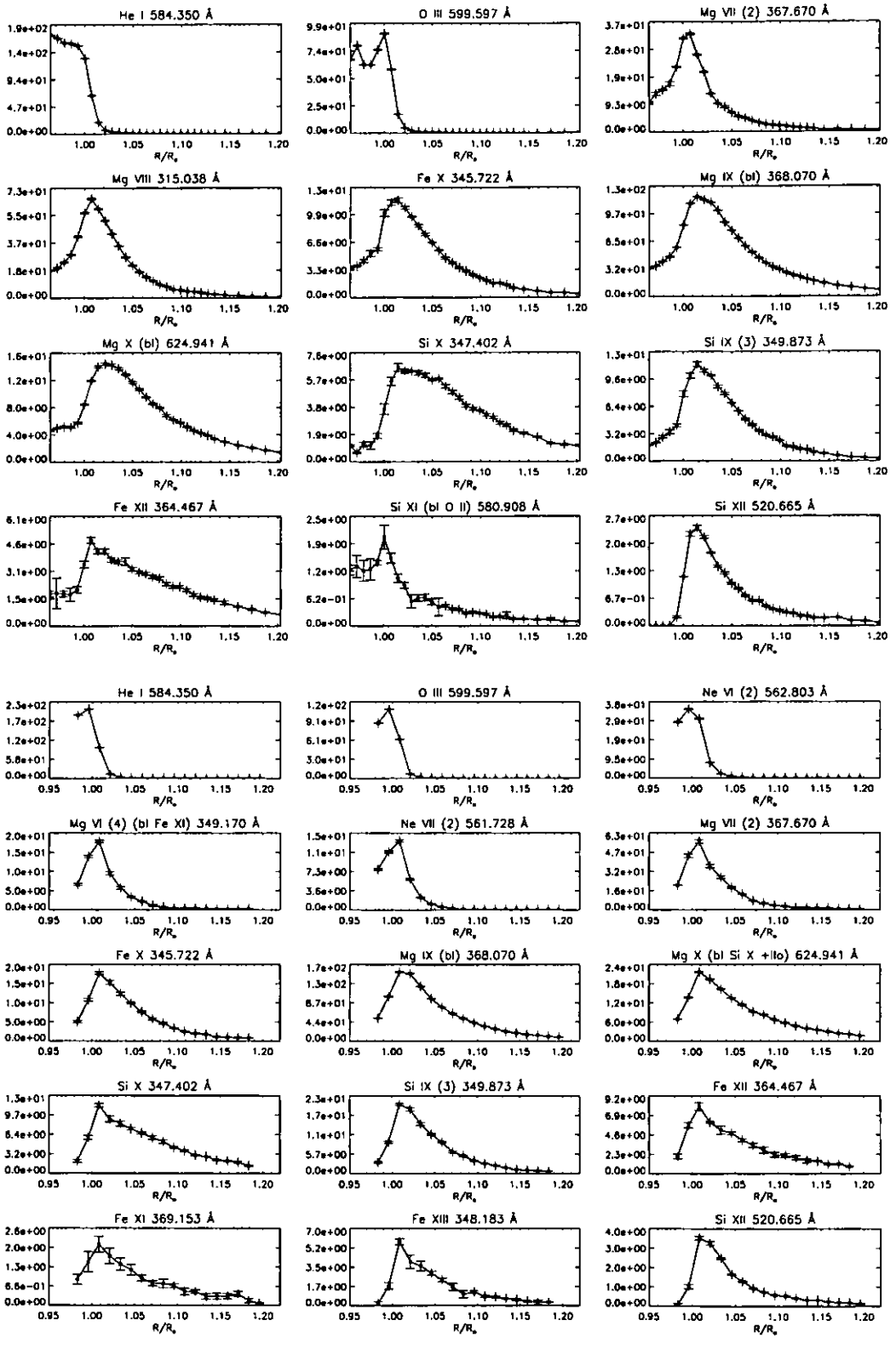

Figure 6.11: *The off-limb inter-plume (from NISAT_S5, upper 4 rows) and plume intensities (from CORO24W, below) - 12th October 1997.*

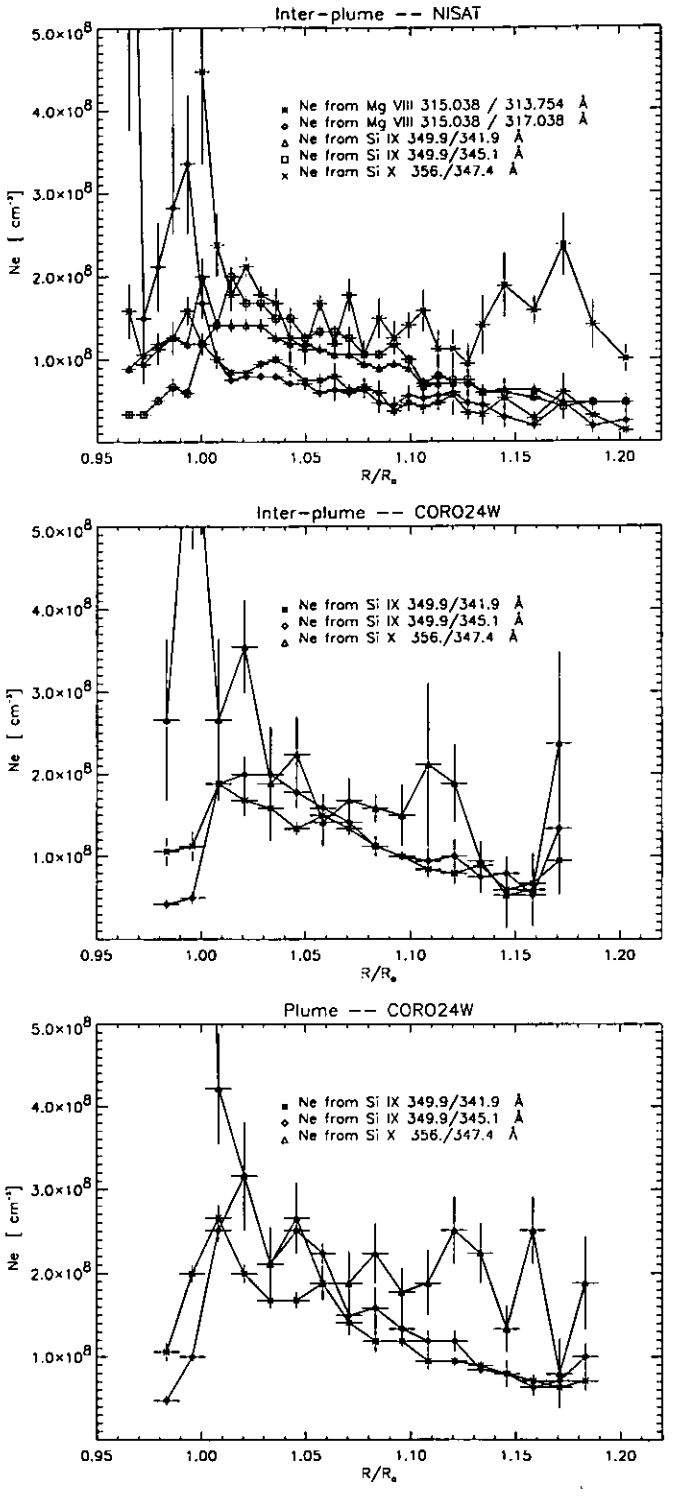

Figure 6.12: *The off-limb inter-plume (from NISAT_S5, top, and from CORO24W, middle) and plume (from CORO24W, bottom) densities - 12th October 1997.*

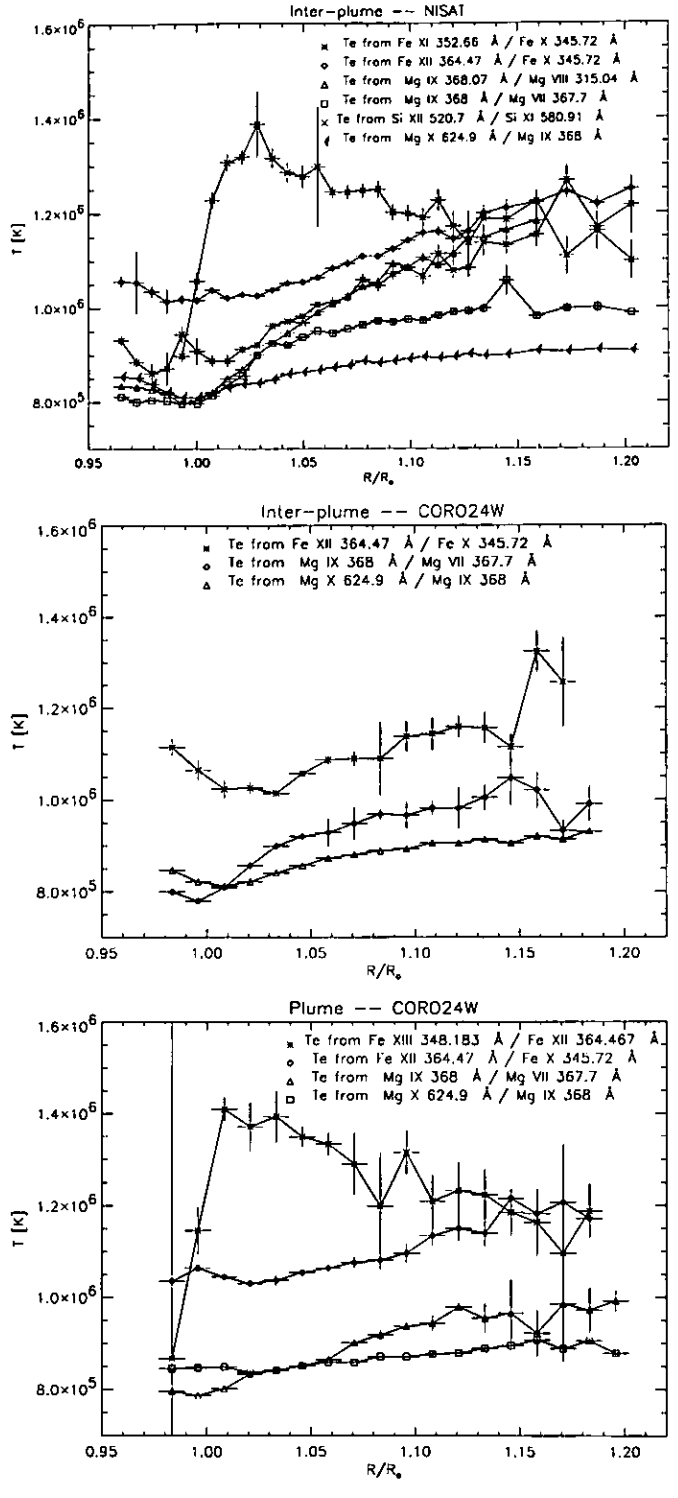

Figure 6.13: *The off-limb inter-plume (from NISAT_S5, top, and from CORO24W, middle) and plume (from CORO24W, bottom) temperatures, derived from various line ratios, assuming ionization equilibrium – 12th October 1997.*

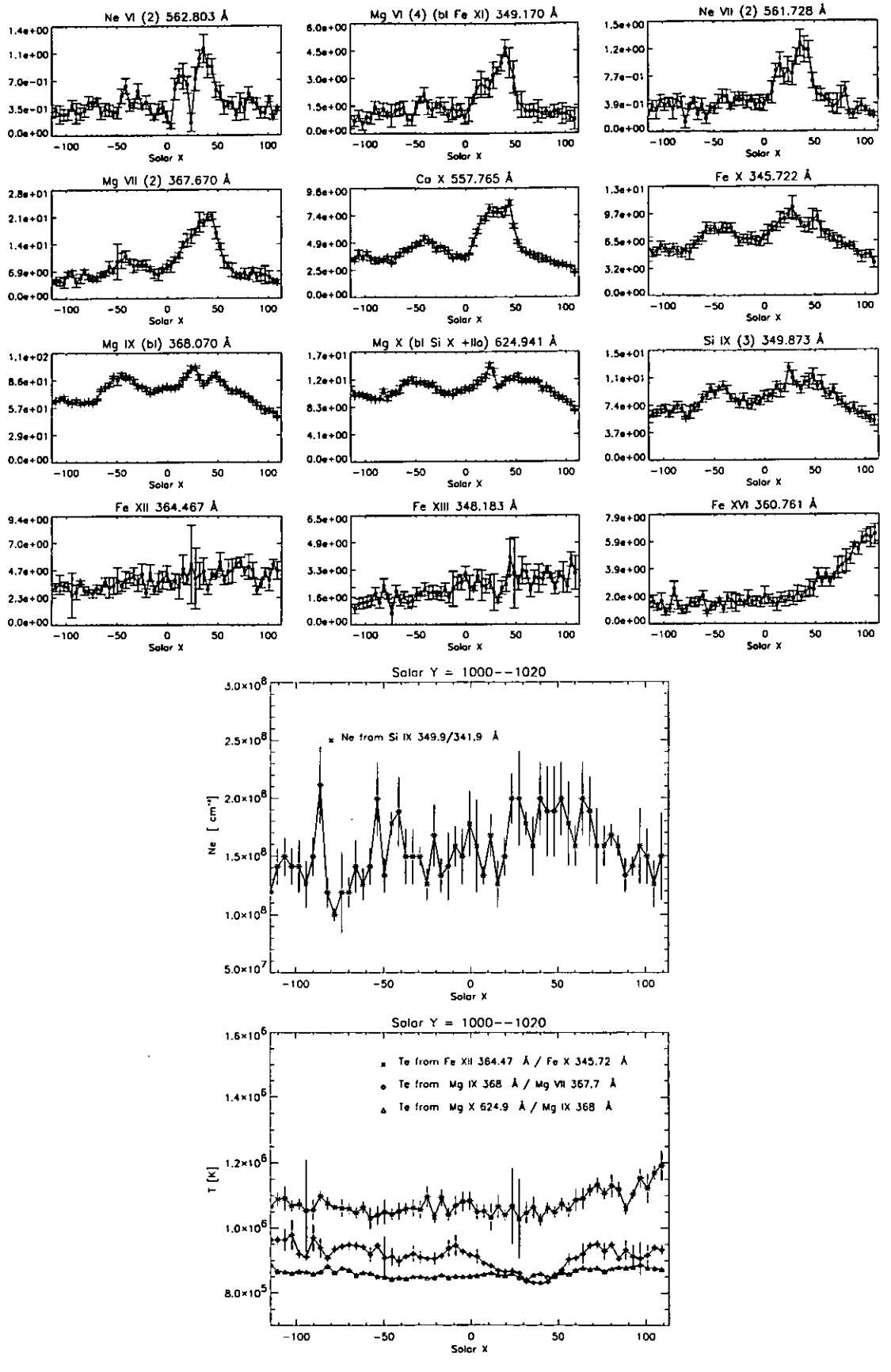

Figure 6.14: *Some intensity profiles across the plumes, at 1.05 $R_\odot$ (above), with averaged densities and temperatures (below) - 12th October 1997.*

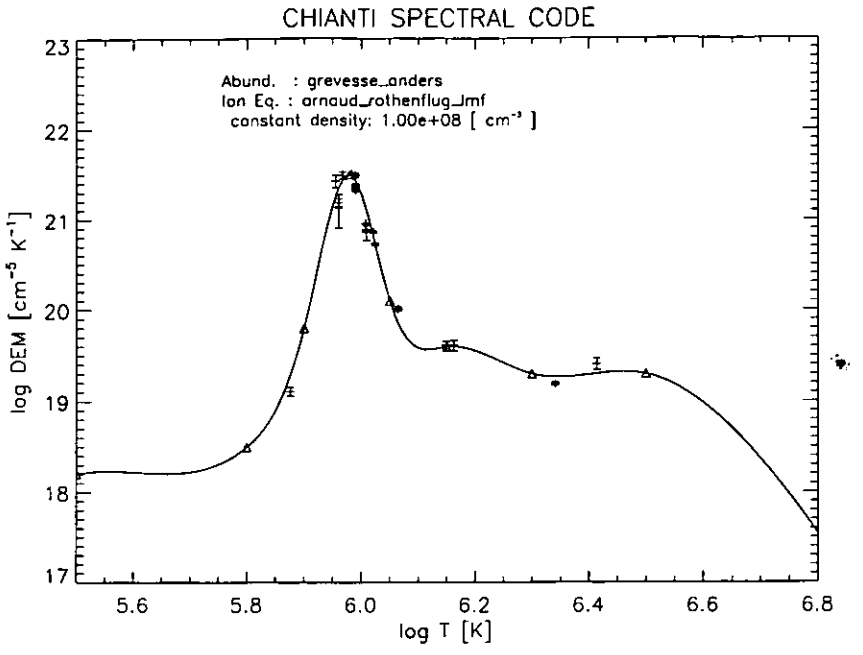

Figure 6.15: *The off-limb inter-plume DEM – 12th October 1997. Note the high-temperature tail, that is constrained up to log $T \sim 6.5$ by the presence of high-temperature lines.*

material along the line of sight was low.

The GIS cross

Here some results from the off-limb GIS cross study of the 27th March 1997 are presented. The observations were performed over the south pole. The N-S scan observed a bright plume that was visible on the meridian (see Figure 4.10), from just inside the limb out to 1.1 $R_\odot$, while the off-limb E-W scan created a series of spectra across the plume, (Solar X = -60 : + 60), at a distance $\simeq$ 1.08 $R_\odot$. The plume lasted for the whole period of the GIS observation (almost 7 hours). The N-S scan was performed on the meridian (Solar X = 0), along the eastern edge of the plume.

Figure 6.16 shows the intensity profiles of some lines in the N-S off-limb observation, with averaged densities and temperatures derived from different line ratios. Note that the Fe X densities are in agreement with those derived from Mg VIII, off-limb, and that this plume had relatively high densities at the limb, and values $N_e \simeq 1\text{x}10^8$ cm^{-3} at 1.1 $R_\odot$. The temperatures derived from Fe ions are all consistent, showing this plume to be isothermal, and having slightly increasing temperatures ranging from $T \simeq 9\text{x}10^5$ K near the limb, to $T \simeq 1.05\text{x}10^6$ K at 1.1 $R_\odot$. This plume was therefore not only a very bright plume, but also a 'hot' one. A direct measurement of the electron temperature was attempted, using

the Mg IX 368/706 Å ratio, but the values have a large scatter, due to the low signal and the fact that the Mg IX 368 Å was strongly ghosting. No conclusive results could be obtained.

Figure 6.17 shows the intensity profiles of some lines in the E-W observation, with densities and temperatures as derived from different line ratios. Note how the plume is still visible at that distance, in all the lines (except at high-temperature), and is centred around Solar X = 20″, about 40″wide. The densities derived from Mg VIII do not show appreciable variation across the plume, while those derived from Fe X show an increase. Interestingly, the temperatures derived from the Fe ions only show a very small decrease in the temperature, where the plume was, showing that at that distance the plume was isothermal with the inter-plume region (with $T \simeq 1.03\text{x}10^6$ K).

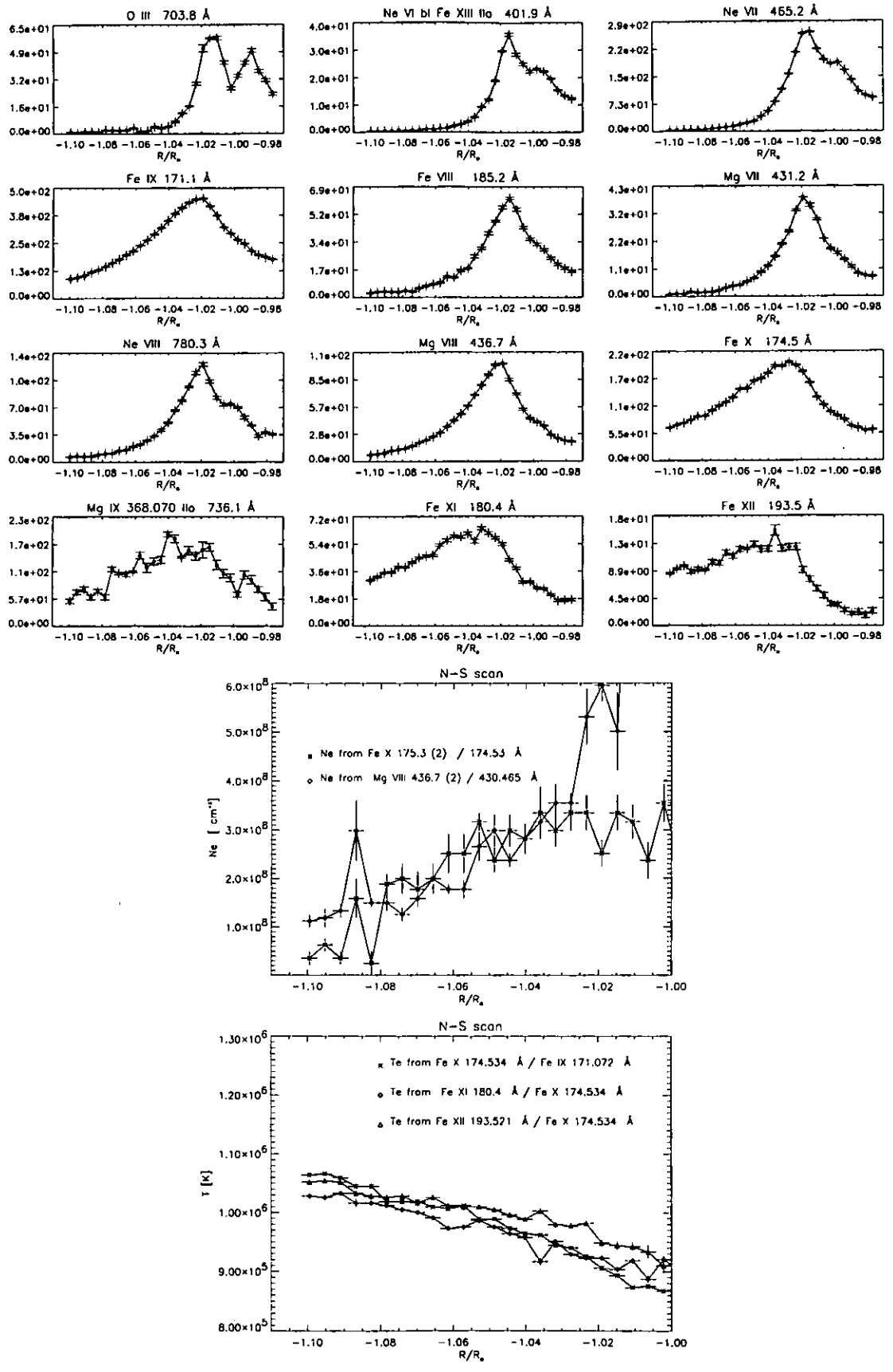

Figure 6.16: *The GIS N-S off-limb scan along a plume - 27th March 1997. Some intensity profiles (above), averaged densities and temperatures derived from different line ratios (below).*

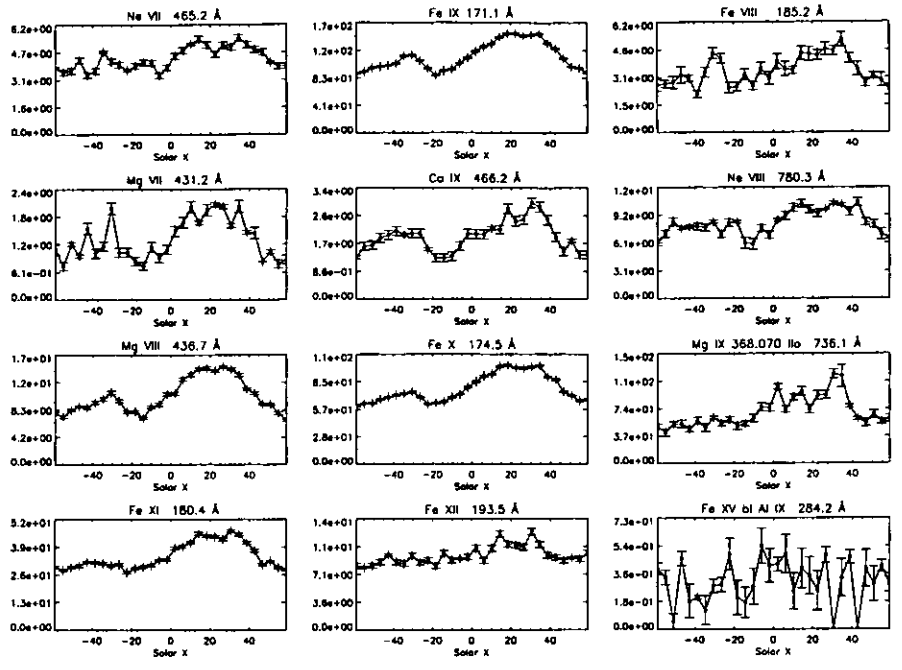

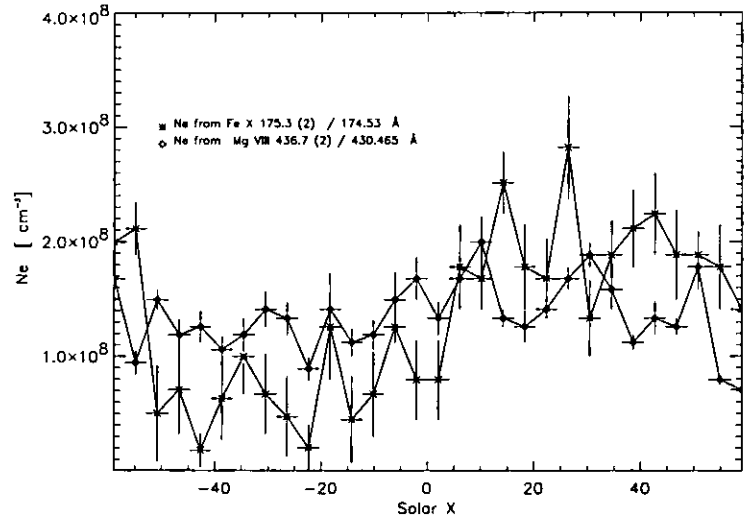

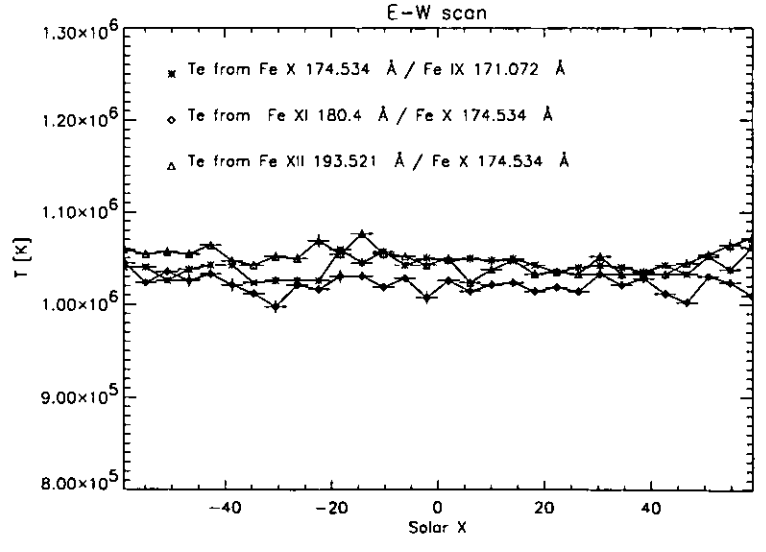

Figure 6.17: *The GIS E-W off-limb scan across a plume, at $R \simeq 1.08\ R_{\odot}$ - 27th March 1997. Some intensity profiles (above), averaged densities and temperatures derived from different line ratios (below).*

6.3 Polar plumes observed on-disc

Observations of two polar plumes seen on the disc are presented here and compared to nearby coronal hole regions and to the observations of the low-latitude plume described in Chapter 5. The two polar plumes were seen on the 23rd August 1996 and on the 11th of October 1997. These plumes were stable structures lasting for several days in the north polar coronal hole. A Joint Operation Programme (JOP # 42) was organised by C. Deforest to observe the first plume. During this programme, all SOHO instruments carried simultaneous observations. The CDS observations have been planned, executed and analysed by the author. The analysis of a time sequence of CDS large-field-of-view observations of this plume has shown that this feature was stable during the whole observing period (few hours). The second plume, is the one already mentioned and observed on October 10 1997.

The two plumes discussed here are considered to be typical faint plumes as observed by CDS during the minimum of the solar cycle. They were found to have the same main characteristics as the equatorial plume (i.e. lower temperature, increased Mg/Ne and O/Ne intensities, visibility in only a few lines emitted over a limited temperature range) thus confirming the identification of the low-latitude feature as a plume. However, an analysis of CDS observations of many plumes has revealed that some do show different characteristics, for example some plumes had compact EUV enhancements at their base, and were very hot and dense (see *Bromage et al.*, 1997b, and *Young*, 1999).

Plumes seen on the disc were chosen, because in this case it is possible to distinguish them from the coronal hole regions and see their base. In coronal hole off-limb observations, it is in fact more difficult to exclude the possibility that there might be some plume material (from plumes rooted on the far side of the Sun) contaminating the 'true' coronal hole regions, thus affecting measurements of densities and temperatures. In addition, there might be more than one plume along the line of sight.

The principal aims of the rest of this Chapter are: to describe how plumes can be recognised from their appearance in CDS spectra; to apply spectroscopic diagnostic techniques to CDS observations in order to characterise plumes in terms of densities, temperatures and element abundances; to point to the complexity of the interpretation of such data, in particular when element abundances are deduced; and to clarify some observational points, in particular showing how plumes appear in EIT images. No attempt is made to study the evolution of plumes, where imaging instruments such as EIT are more appropriate.

In the EUV, plumes are known to be visible only in emission lines that form over a narrow range of temperatures (e.g., *Widing and Feldman*, 1992), with emission almost

absent from ions that form at temperatures above a million degree. It has been therefore quite surprising to see plumes with the SOHO EIT 195 Å filter, where the emission is generally assumed to be due to Fe XII, which has an ionization equilibrium temperature $T_e \simeq 1.6 \cdot 10^6$. Nevertheless, *DeForest et al.* (1997) use EIT 195 Å and 171 Å images to estimate plume temperatures. In order to check the validity of this broad-band filter ratio estimate, a comparison between EIT and CDS observations of one polar plume is presented in Section 6.3.3 below.

6.3.1 Results for a polar plume observed on 1996 August 23

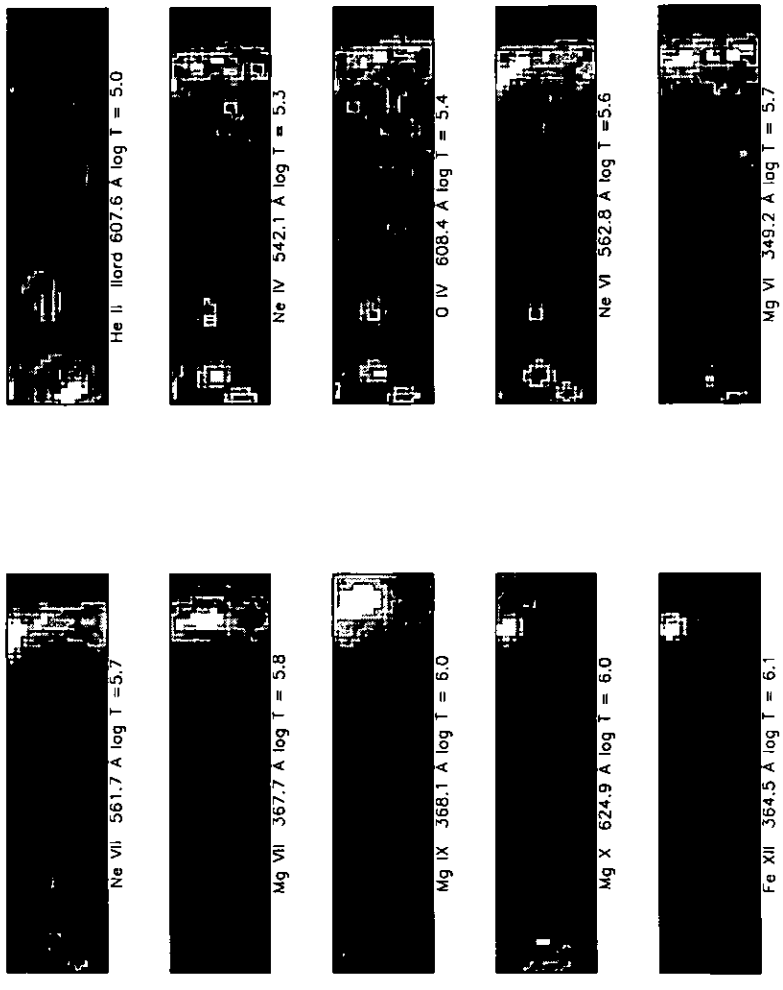

Figure 6.18: *Monochromatic images of the NIS observation – 23rd August 1996. The plume is seen best in Mg VII and Mg IX, with its base near the centre of the raster and the 'plume' extending up to the limb (and above).*

Fig. 6.18 shows monochromatic images of the region rastered by the NIS on 1996 August

23. This plume presents the typical characteristics of plumes as observed by CDS. The peak of the emission in the plume is in the upper transition region lines Mg VII, and Mg IX. The plume is not visible in the high-FIP Ne lines, nor in the high-temperature (e.g. Fe XII) lines. The cooler lines (He II,Ne IV) show the cell centre - network pattern.

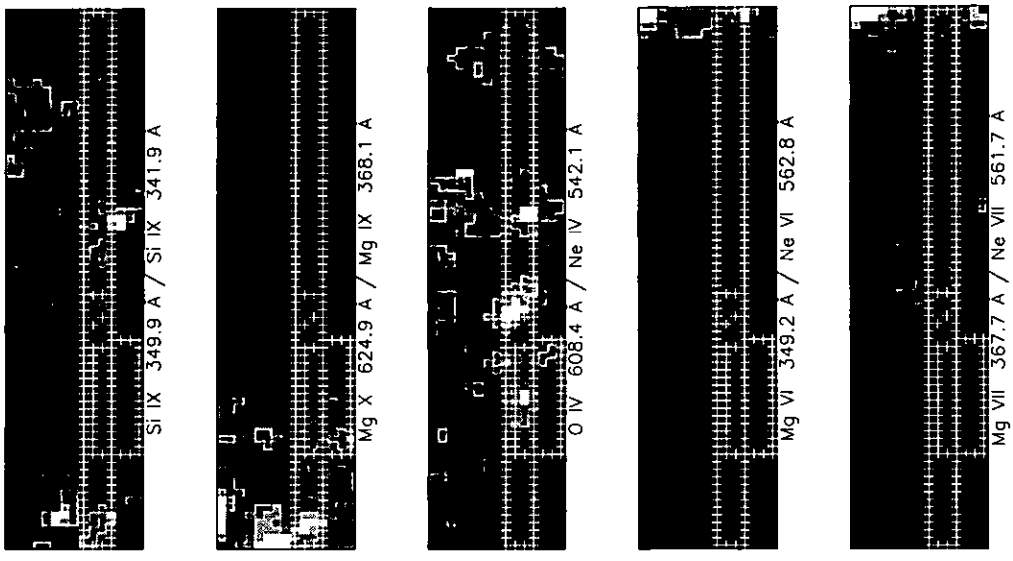

Figure 6.19: *Ratio images of the NIS observation – 23rd August 1996, showing density ratios (Si IX); temperature ratio (Mg X / Mg IX); and O/Ne, Mg/Ne line ratios, indicating relative abundances. Selected areas are over-plotted. The plume area is a small region (within the long thin area) indicated by four '+' characters.*

Since the plume was aligned at an angle to the line of sight, the peak of the emission appears at different spatial locations, when lines emitted at different temperatures are examined. Strictly speaking, only the emission of lines of similar temperatures comes from the same region along the line of sight.

Intensity ratios of lines can give some indications of variations of density, temperature and abundances across the plume. Figure 6.19 shows some intensity ratio images, which indicate that the plume area has lower temperature, and at the base has increased Mg/Ne and O/Ne intensities (with values similar to those of the low-latitude plume, discussed in Chapter 5.

In order to increase the S/N, averaged spectra of three regions, shown in Figure 6.19, have been extracted: a profile along the plume, in the N-S direction; a region at the base of the plume; and a coronal hole region to the SW of the plume.

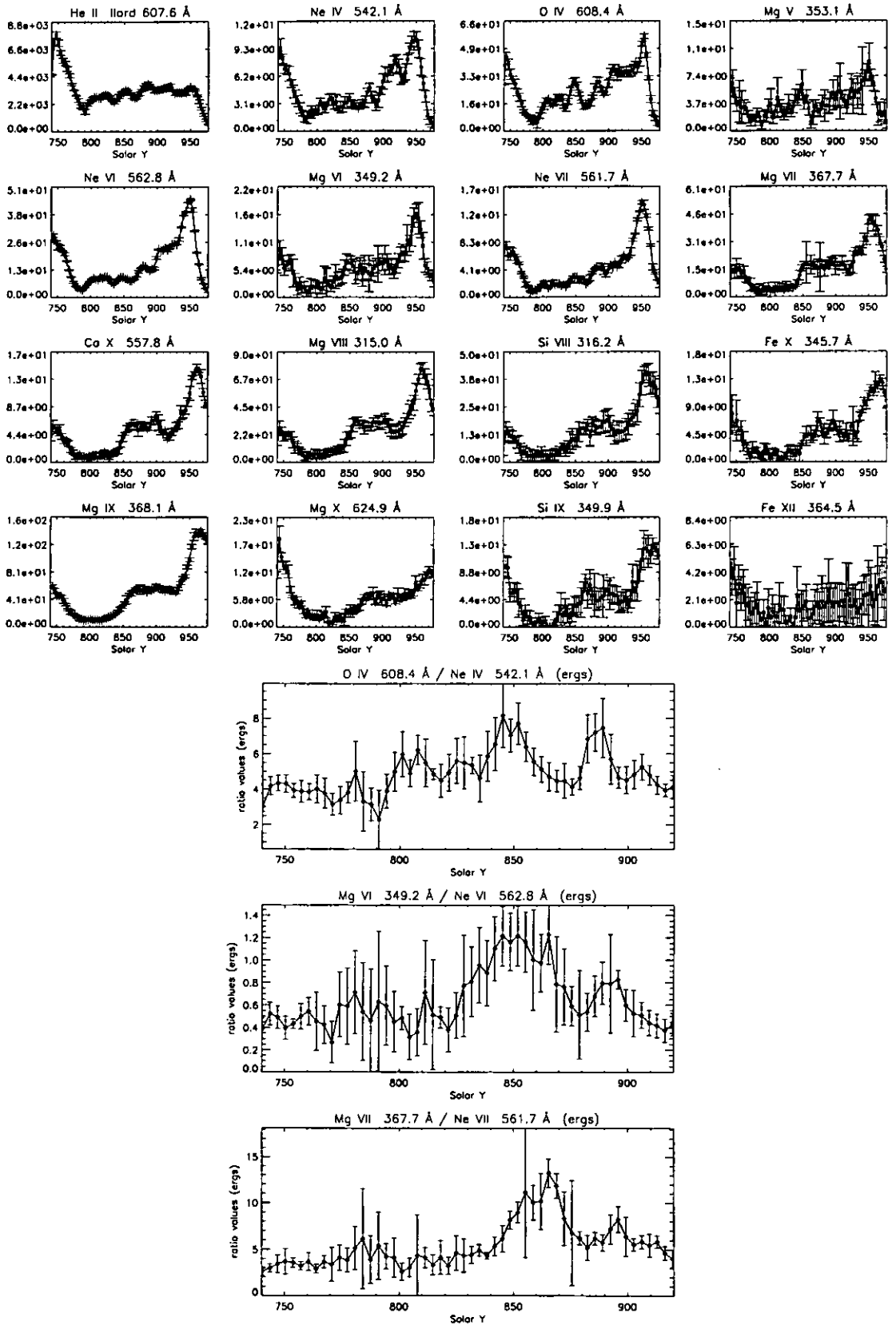

Figure 6.20: *Intensities of a selection of NIS lines along the N-S direction, with corresponding intensity ratios - 23rd August 1996.*

Figure 6.20 shows the profiles of the intensities and the ratio of intensities of some selected lines from the N-S scan, from which it appears clear that the base of the plume (situated around Solar Y=850) is close to a network junction (where SOHO/MDI magnetograms show a concentration of unipolar flux). Note that lines emitted at higher temperatures have a peak emission shifted toward the North, due to the tilt effect, so it is difficult to locate the base of the plume precisely relative to the network revealed in cooler lines.

The O/Ne and Mg/Ne ratios clearly show the presence of the plume base at Solar Y=850, and also indicate a possible second plume in the line of sight at Solar Y=890. These ratios also indicate that it is probably the Ne abundance that is varying. Indeed, a preliminary *DEM* analysis of this plume region has confirmed that the Ne/O abundance has a value lower than photospheric, by a 0.2 dex.

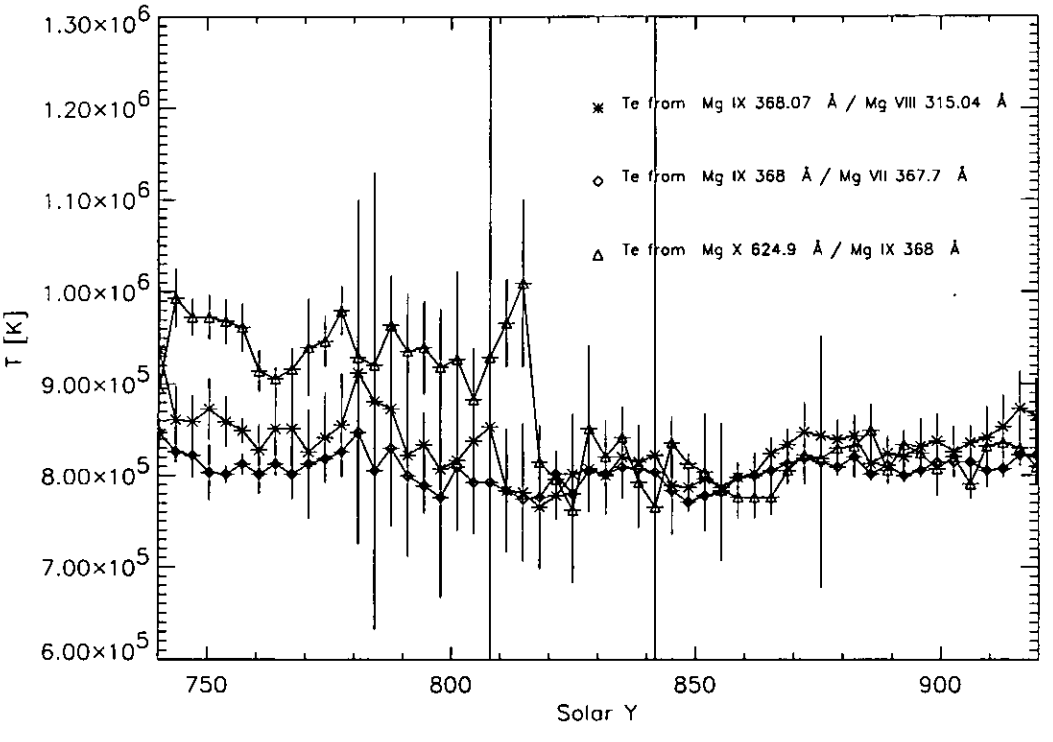

Figure 6.21: *Isothermal temperatures along the N-S scan - 23rd August 1996. Note that the plume lies along this scan, above about 825 "(solar Y). This is the region where the temperature profiles become coincident, indicating isothermal plasma.*

Figure 6.21 shows isothermal temperatures derived from different ratios. Note that the three different line ratios produce different temperatures in the coronal hole region, while in the plume region they are in close agreement, another strong indication of plumes being quasi-isothermal.

Table 6.2 shows the values of the parameters deduced from the averaged spectra of the

Table 6.2: Table of parameters deduced from the 23rd August 1996 averaged spectra of the selected regions.

	plume base	Coronal hole
N_e (O IV 625.8/608.4 Å)	7.5±4 10^9	7.1±1 10^9
N_e (Mg VIII 315.0/317.0 Å)	1.2±0.8 10^8	0.6±0.4 10^8
N_e (Mg VIII 315.0/313.7 Å)	0.8±0.5 10^8	0.7±0.4 10^8
N_e (Si IX 349.9/341.9 Å)	1.3±0.8 10^8	0.5±0.5 10^8
N_e (Si IX 349.9/345.1 Å)	0.9±0.8 10^8	0.2±0.2 10^8
T_e (Mg X 624.9 Å/ Mg IX 368 Å)	8.1±0.2 10^5	8.9±0.2 10^5
T_e (Mg IX 368 Å/ Mg VIII 315.0 Å)	8.0±0.1 10^5	8.2±0.3 10^5
T_e (Mg IX 368 Å/ Mg VII 367.7 Å)	7.8±0.1 10^5	7.9±0.8 10^5
I([O IV 608.4 Å/ Ne IV 542.1 Å])	7.4±0.9	4.5±0.2
I([Mg VI 349.17 Å/ Ne VI 562.8 Å])	1.1±0.1	0.4±0.1
I([Mg VII 367.67 Å/ Ne VII 561.7 Å])	7.1±1	4.1±3

plume base and the nearby coronal hole region. Although the results have relatively large errors, the indication is that the density in the plume area was $N_e \simeq 1\text{x}10^8$ cm^{-3}, about a factor of two higher than the nearby coronal hole region, which had a very low density. The temperature ratios indicate a more isothermal distribution inside the plume ($T \simeq 8\text{x}10^5$ K), with lower temperatures than in the coronal hole area.

6.3.2 Results for a polar plume observed on 1997 October 11

The second plume was also a long-lasting structure that was visible during the second week of October 1997 in the north polar hole. Fig. 6.22 displays a sequence of EIT 171 Å images, showing the stability of this plume over a period of a few days. A series of CDS observations of this plume were performed, of which only those of the 11th of October 1997 are presented here. On this day, CDS was in high-telemetry mode, i.e. the information was telemetered to the ground at double the normal rate.

The NIS observations presented here used the UCLAN_N3 study. The UCLAN_N3 covered a large area (2'x3', see Fig. 6.23) in about 40m (with a 60s exposure time, high-telemetry) starting at 15:00:37 UT.

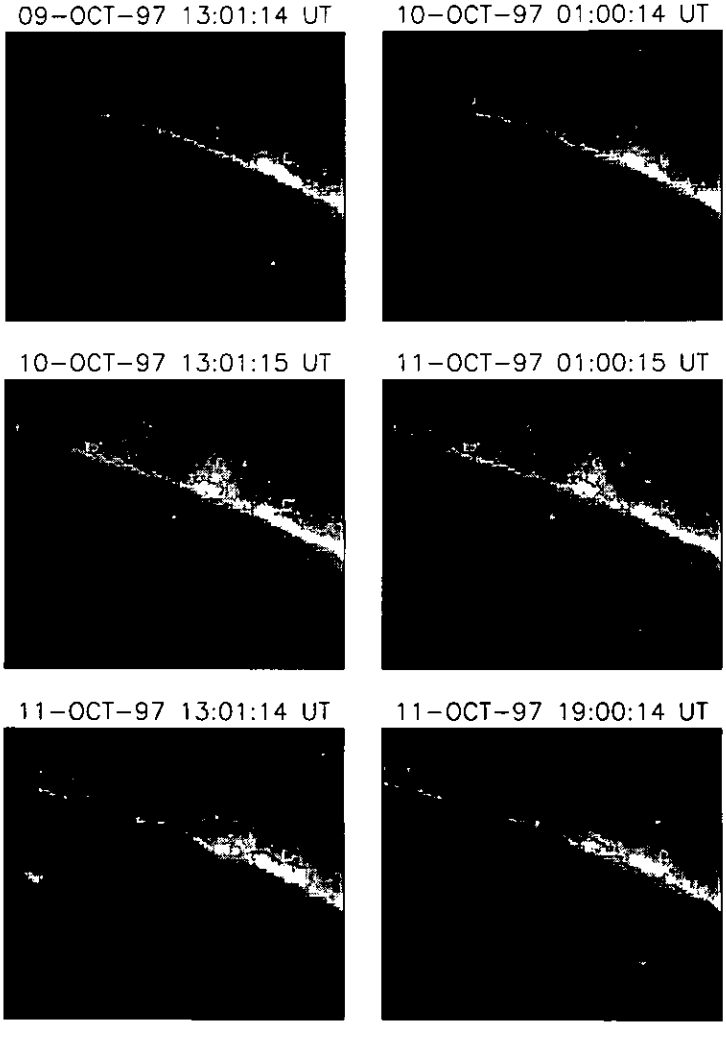

Figure 6.22: *Sequence of SOHO EIT 171 Å images of the north polar coronal hole, showing the persistence of a polar plume.*

Figure 6.23 shows monochromatic images of the region rastered by the NIS. This plume

shows the same characteristics as the plume of the 23rd of August 1996, i.e. maximum visibility in the upper transition region lines Mg VI, Mg VII, Ca X, Mg VIII, Mg IX, and it is not visible in the high-FIP Ne lines, nor in the high-temperature lines. The intensities of the He II, and Ne V lines show the presence of a network boundary close to the base of the plume. This plume is also tilted, compared to the line of sight, and the comparison between lines that are formed at very different temperatures should be made with caution, as in the previous case.

The ratio images in Figure 6.24 show a marked decrease of the temperature and increase of Mg/Ne and O/Ne intensity ratios at the base of the plume, again indicating a decrease in the Ne abundance.

A GIS scan across the plume, starting at 16:16:40 UT was performed after the NIS observation. This GIS observation used the high-telemetry *study* HRBNDWE, where the 4″x 4″slit is rastered from west to east in order to cover a 4″x 60″region with 15 spatial positions. For each of these positions, GIS recorded 100 exposures of 5s each, in a time span of 11m. It took about 2h50m to scan the whole 4″x 60″area. The GIS observed the plume region about one hour after NIS observed it. In order to increase the S/N, the data analysis on the GIS spectra was performed on the average of the 100 exposures, one for each spatial location (although a preliminary study of the high time variability was performed).

The intensities of the NIS lines have been extracted from NIS spatially-averaged spectra over the region rastered by the GIS. The NIS and GIS observations were not simultaneous, and an instrument repointing took place between the two observations. The analysis of the NIS and GIS observations has shown a need to adjust the position of the GIS rasters by 10″, relative to the position of the NIS observations. With this small adjustment, most of the lines have similar profiles across the plume, as shown in Figure 6.25 (and in particular this is true for the few lines that are visible in both GIS and NIS). Only the low-temperature lines present some differences, as expected. Nevertheless, in both GIS and NIS lines it is evident that the base of the plume is near a network region (i.e. a region where the low-transition region lines are enhanced).

Figure 6.25 shows how the intensities of several GIS and NIS lines vary across the plume. The upper transition region lines increase by a factor of about 4 in the plume area, while the high-temperature lines do not show any increase in intensity.

Figure 6.26 shows isothermal temperatures and densities across the plume. There are indications of a density increase inside the plume area, but they are within the errors. What is more obvious is a more isothermal temperature and a sharp decrease in the value

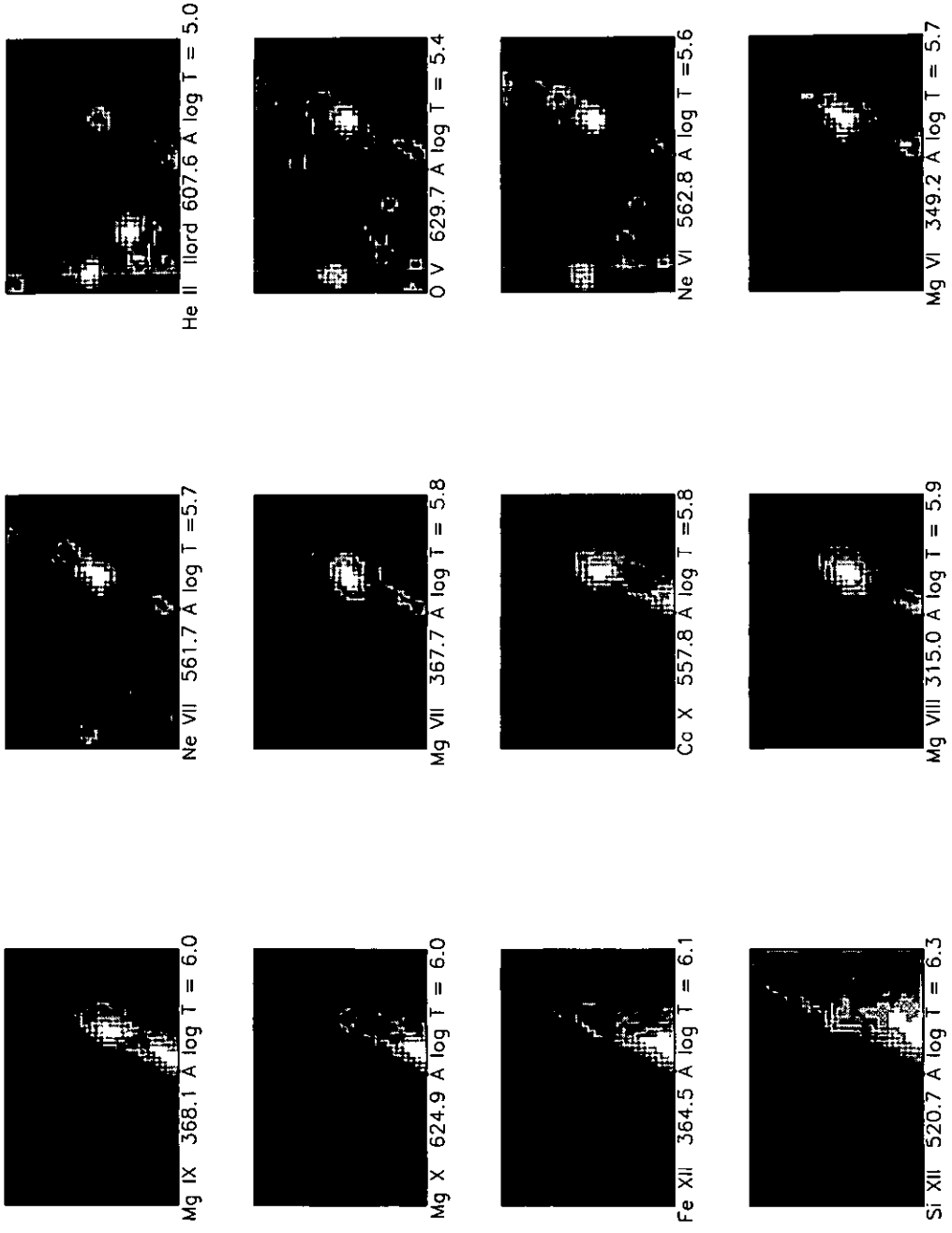

Figure 6.23: *Monochromatic images of the NIS observation - 11th October 1997.*

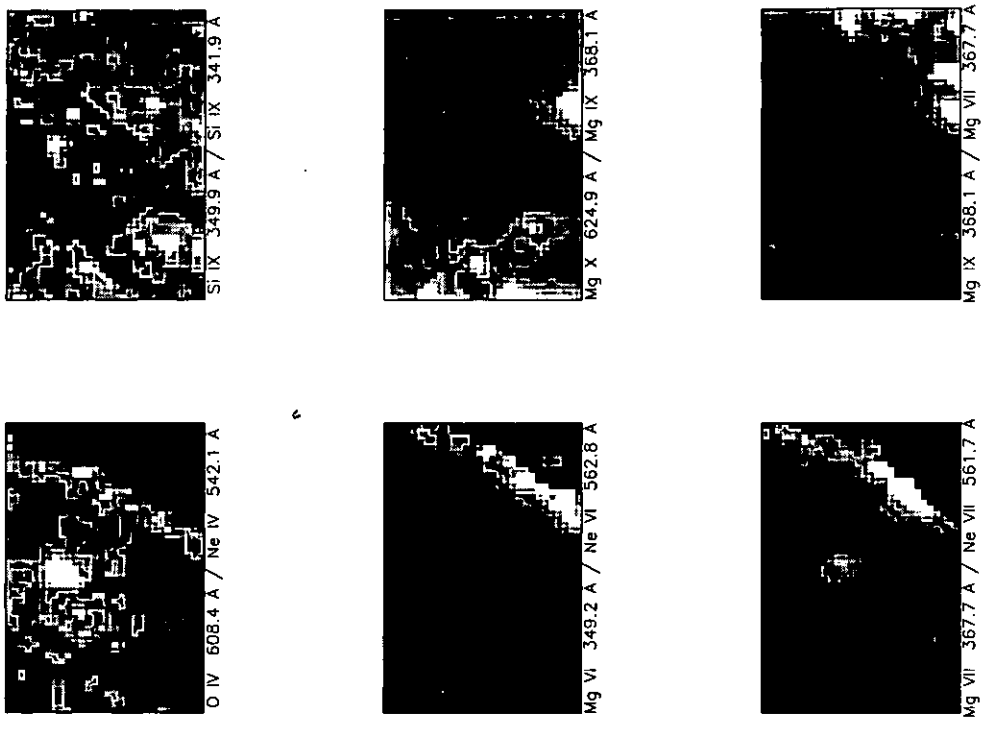

Figure 6.24: *Ratio images of the NIS observation - 11th October 1997. A density ratio (Si IX), a temperature ratio (Mg X / Mg IX) and abundance ratios (O/Ne and Mg/Ne) are shown. Note the high O IV/Ne IV and Mg/Ne intensity ratios at the base of the plume.*

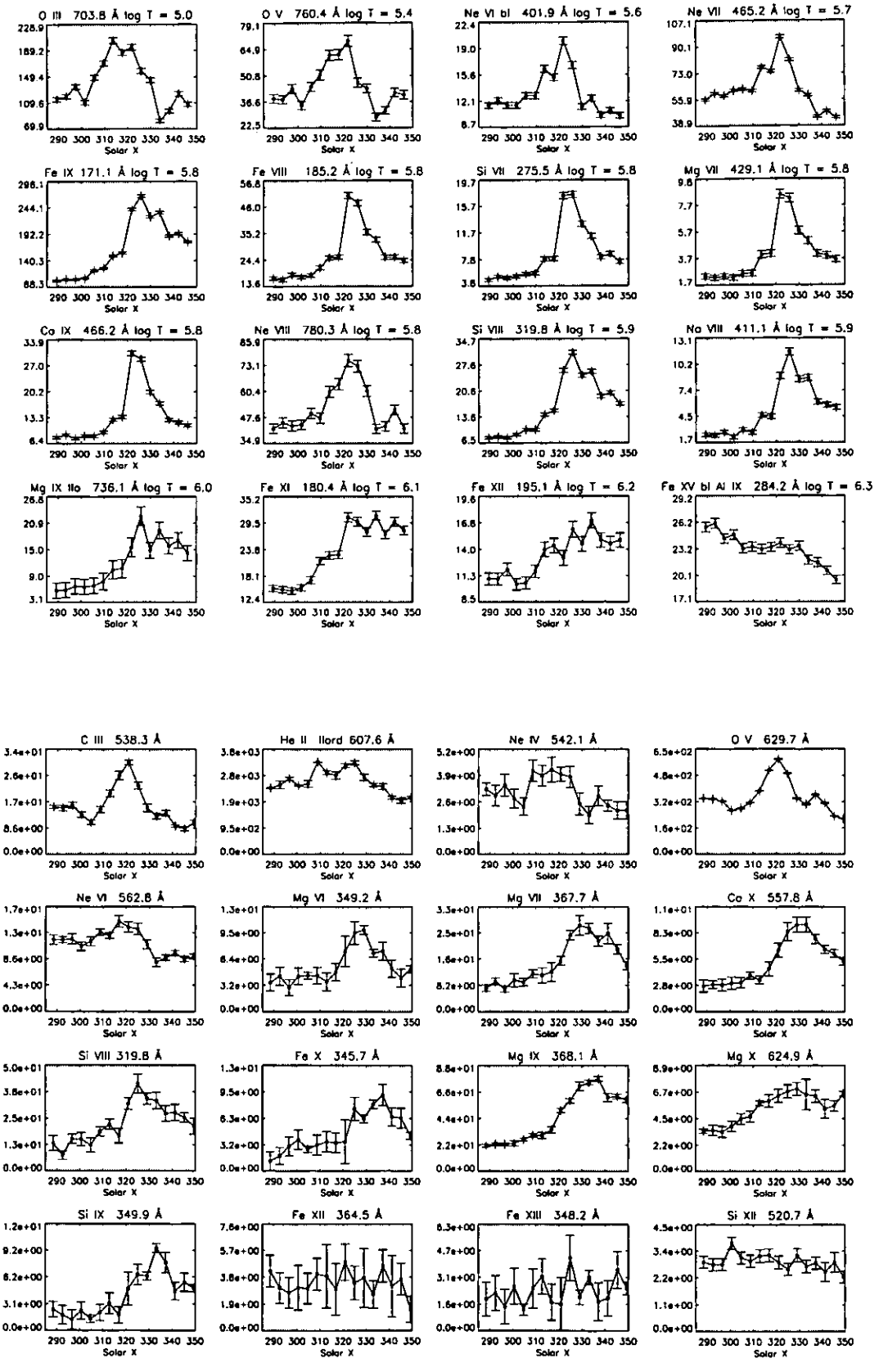

Figure 6.25: *Intensities of a selection of lines from the GIS E-W scan across the plume (top) with corresponding intensities in NIS lines. - 11th October 1997.*

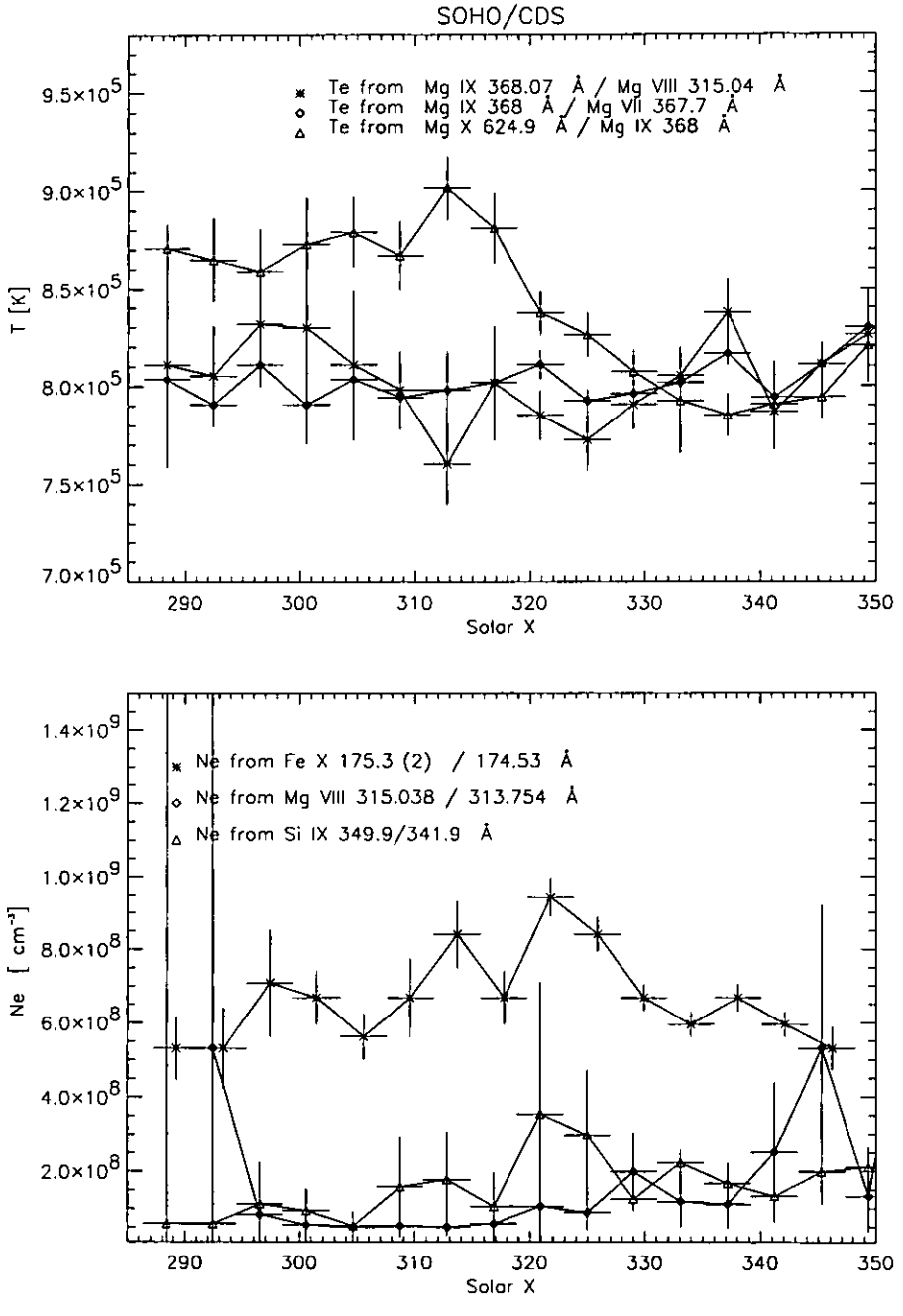

Figure 6.26: *Isothermal temperatures and densities across the plume - 11th October 1997.*

derived from Mg X / Mg IX, (as already seen for other plumes).

Figure 6.27 shows some intensity ratios derived from the GIS and NIS observations. All the low-FIP to high-FIP intensity ratios undoubtedly show a large increase in the plume, and therefore a probable FIP effect, while the O/Ne ratios also show variations, as was observed for the plume of the 23rd of August 1996 and the equatorial plume.

Other ratios examined (e.g. Mg/Si) indicate that the relative abundances between the low-FIP elements remain almost unchanged.

Two spatial positions have been selected as representative of the coronal hole and plume areas, at $SolarX = 289$ and 326, respectively. For these areas, the intensities of the GIS and NIS lines have been considered jointly, in order to characterise the plasma. This might not be valid, because of the lack of co-temporality between the GIS and NIS observations, but is justified by the stability of the plume and the similarity between the observations of common lines. Considering NIS and GIS line intensities at the same time has great advantages. The cross-calibration studies performed on the 1st and the 16th of October (outlined in Chapter 3) produced confidence in the stability of the CDS detectors, and on the reliability of using GIS and NIS together. Only a 30% correction factor was applied to all the calibrated GIS lines, for the plume region, possibly indicating that the field of view was slightly different between the two observations. The source region in each case is only 4″x4″, while the width of the plume is typically 20″, so although it is clear that both NIS and GIS observations are within the plume, the lower signal may indicate that this source is nearer the edge.

Figure 6.28 shows a comparison between the GIS spectra of the coronal hole and plume areas. There are large differences in the intensity of upper transition region lines (e.g. Mg VI, Mg VII, Mg VIII), together with a small decrease of the high-temperature lines (e.g. Fe XV) in the plume data, and a variation of the Mg/Ne and Ca/Ne ratios, as already discussed. In particular the region around 402 Å shows how different the spectra are. Other parts of the GIS spectra are shown in Figs. 6.31 and 6.32 (see Section 6.3.3, where the GIS-EIT comparison is presented), and also stress the different temperature structure between the coronal hole and the plume area examined. Lower temperature lines (such as Fe VIII) increase their intensity inside the plume. The complete GIS spectra are also shown in Figures E.1, E.2, E.3, E.4.

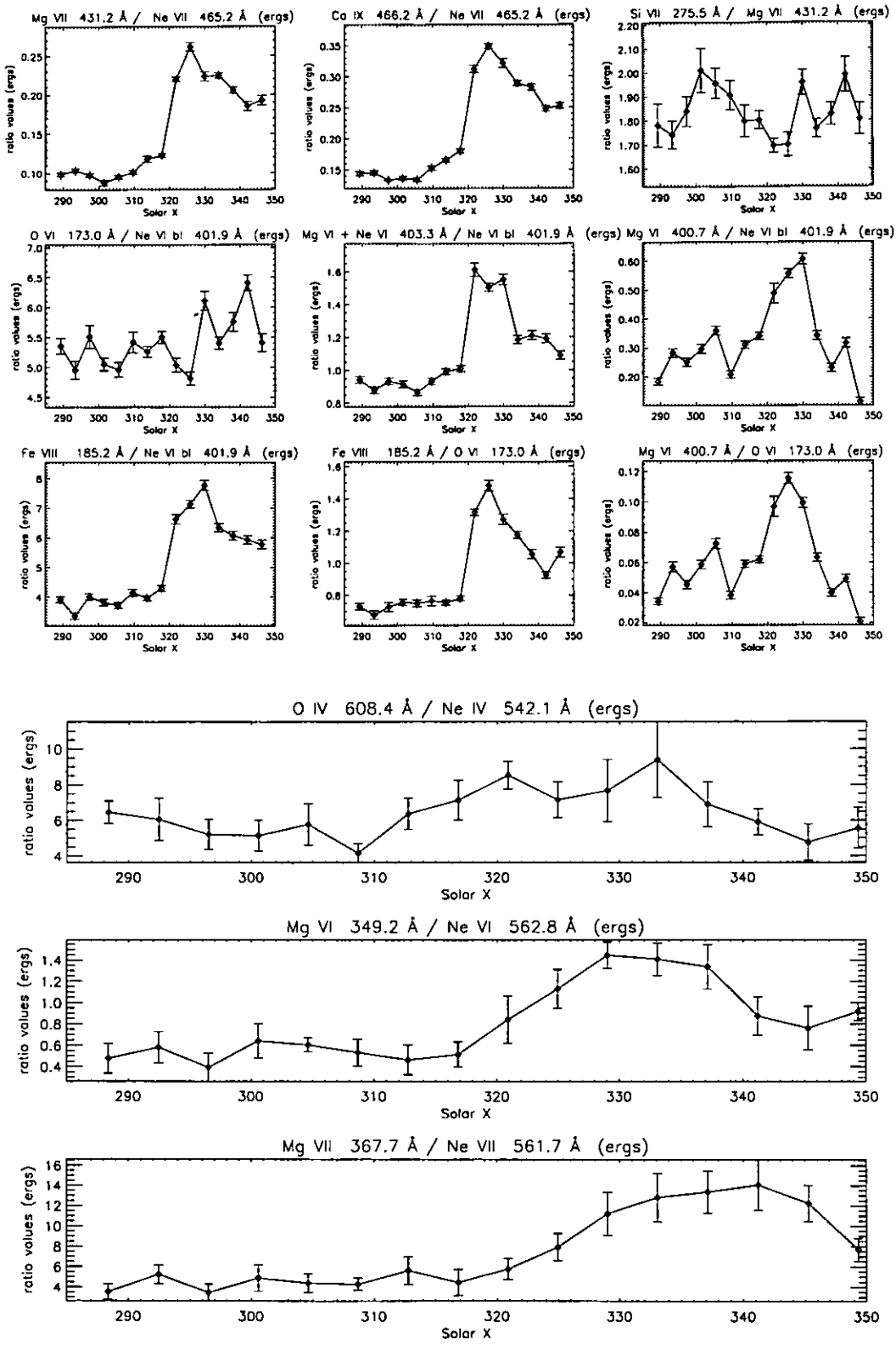

Figure 6.27: *Intensity ratios of selected lines of the GIS E-W scan across the plume (top) with corresponding ratios of NIS lines - 11th October 1997.*

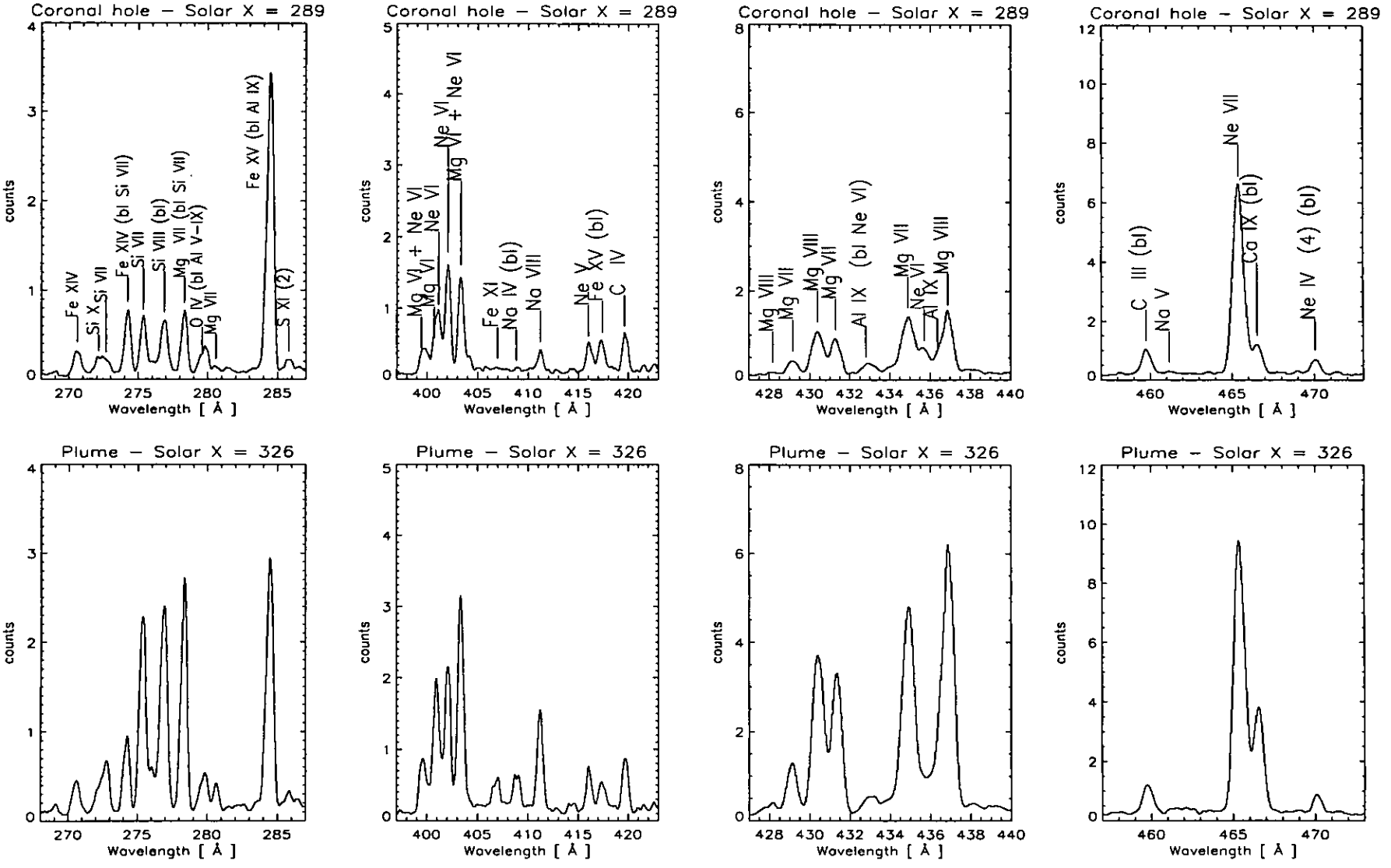

Figure 6.28: *GIS spectra in selected wavelength regions, for the coronal hole (above) and plume (below) areas – 11th October 1997.*

Table 6.3: *Table of parameters deduced from the 1997 October 11 CDS spectrum of the base of a plume. The densities are in cm^{-3}, while temperatures are in K. Some intensity ratios, indicative of elemental abundance differences, are also shown. The element abundances, deduced from the DEM analysis, are shown at the bottom as logarithmic differences relative to the photospheric values (*Grevesse and Anders, *1991), i.e. they are quoted in dex in the standard way. The elements are ordered by their FIP value, indicated in parentheses.*

N_e (O IV 625.8/608.4 Å)	5±3 10^9
N_e (Mg VII 319.0 / 367.7 Å)	3.8±2 10^9
N_e (Si IX 349.9/341.9 Å)	3.±2 10^8
N_e (Si IX 349.9/345.1 Å)	1.2±0.7 10^8
N_e (Mg VIII 315.0/317.0 Å)	0.8±0.7 10^8
N_e (Mg VIII 315.0/313.7 Å)	0.9±0.7 10^8
N_e (Fe X 175.3 (2) / 174.53Å)	8.5±0.6 10^8
N_e (436.7 (2) / 430.465 Å)	2.2±0.7 10^8
N_e (Fe XIII 203.8 (2) / 202.0 Å)	1.8±0.5 10^8
T_e (Mg X 624.9 Å/ Mg IX 368 Å)	8.3±0.1 10^9
T_e (Mg IX 368 Å/ Mg VIII 315.0 Å)	7.7±0.2 10^9
T_e (Mg IX 368 Å/ Mg VII 367.7 Å)	7.9±0.1 10^9
T_{max} (DEM)	7 10^5
I (O IV 608.40 Å/ Ne IV 542.07 Å)	7.2±0.9
I (Mg VI 349.17 Å/ Ne VI 562.8 Å)	1.1±0.2
I(Mg VII 367.67 Å/ Ne VII 561.73 Å)	7.9±1.3
A_b (Ne) (21.56 eV)	-0.15
A_b (N) (14.53 eV)	0.
A_b (O) (13.61 eV)	0.
A_b (C) (11.26 eV)	0.1
A_b (S) (10.36 eV)	+0.3
A_b (Si) (8.15 eV)	0.
A_b (Fe) (7.87 eV)	+0.2
A_b (Mg) (7.64 eV)	+0.1
A_b (Ca) (6.11 eV)	+0.4
A_b (Na) (5.14 eV)	+0.2

The DEM of the plume area

The NIS and GIS line intensities were then used to deduce plasma parameters, shown in Table 6.3. A *DEM* analysis of the combined intensities was performed, in order to better describe the thermal structure of the plume and to determine element abundances. A constant pressure of 2 x10^{14} cm^{-3} K was adopted, together with the usual assumptions, described at the beginning of this Chapter.

The results are shown in Figure 6.29 and in Table E.1. The DEM peaks at upper transition region temperatures (Mg VII, Ca X), $T \simeq 7$x10^5 with a quasi-isothermal distribution at these heights.

In the GIS 4 instrument, a comparison of on-disc and off-limb observations clearly shows the presence of a continuum emission. This emission is mainly hydrogen Lyman continuum. This is obvious from any on-disc GIS observation. On the other hand, off-limb observations show both the absence of this recombination continuum and very little stray

light ('background'). The wavelength dependence of this continuum can be used as a temperature diagnostic. In particular, the continuum emission in the GIS 4 wavelength range is particularly sensitive to the DEM values at $T \simeq 3 - 6\text{x}10^4$ K, and can therefore be used to constrain the DEM values at those temperatures.

For this observation, as an exercise, the continuum has been evaluated at three different wavelengths, and compared to the theoretical emissivity, in the DEM analysis, together with the emission lines. The continuum emissivities have been calculated (see *Landi et al.*, 1999b for a description of the method) with photospheric abundances and a constant density $N_e = 1\text{x}10^{16}$ cm^{-3} (a different choice of these parameters, however, does not significantly alter the result). The continuum points are displayed in Figure 6.29.

There is good agreement between the DEM values required to explain the observed continuum emission and those required to explain the emission of the 'cooler' lines. It is also interesting to note that the He lines are well represented, with the photospheric abundances. This is not new, as it was pointed out by *Jordan* (1975), and recently confirmed by quiet sun SUMER and CDS observations by *Macpherson and Jordan* (1999). However, it should be noted that these lines are probably not optically thin, nor is all the observed continuum emission true continuum emission. If an absolute (and accurate) measurement of the continuum emission is achieved (considering all the possible instrumental effects), then, since this emission is $\sim N_H^2$, it is possible to directly relate the element abundances to the proton density.

Also note that even assuming that the NIS and GIS intensities could not be used for a DEM analysis, due to lack of co-temporality, if one considers only GIS lines and only NIS lines and derive from them a DEM, obtains the same shaped curve. This DEM should not be considered a typical plume DEM because some effects due to the tilt of the plume may still be present. However, this study was made to investigate the validity of the (few) NIS lines that were used for abundance analysis, by adding the information from the GIS spectra. Table E.1 shows that there is good agreement between most of the lines, at least when lines close in temperature are considered. It is well known that the Fe VIII lines require more atomic physics research. Here it is shown how important they are. In fact, they are among the brightest low-FIP lines that are emitted in the lower corona, and could therefore be used in conjunction with the high-FIP O VI or Ne VI lines for further studies of the FIP effect. It should be noted that in this case too, the lines from the Li-like ions are underestimated or overestimated by large factors, which casts serious doubts on their reliability for use as diagnostic lines.

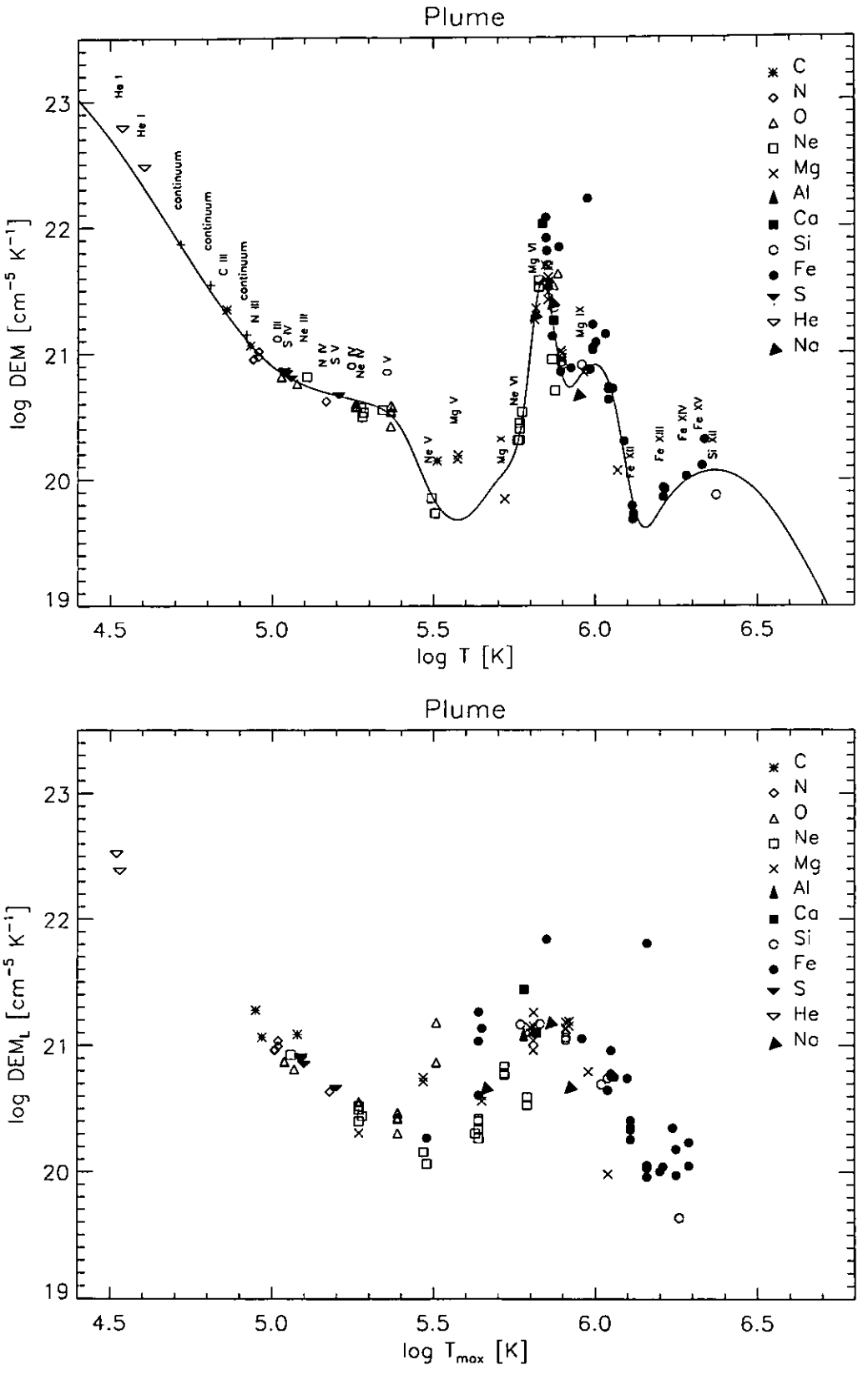

Figure 6.29: *Top: the DEM distribution of the plume area, with the observed points. Bottom: the DEM_L values of the same points. These have been produced using intensities from both GIS and NIS.*

6.3.3 Comparison of GIS spectra with EIT (1997 October 11 data)

The EIT instrument (*Delaboudiniere et al.*, 1995) observes the Sun with four EUV filters, centred around 171, 195, 284, 303 Å. The first two are the principal ones, since the filter at 284 Å has a lower sensitivity, and the filter at 303 Å observes both the chromospheric line He II 303.8 Å and the coronal line Si XI 303.3 Å. The first two filters are referred in the literature as *the Fe IX/X and the Fe XII*, because it is thought that these are the ions that contribute most to the emission. Ratios of images from these two filters have been used by *DeForest et al.* (1997) to estimate that plumes are about 30% cooler than the surrounding coronal hole regions.

In order to confirm this estimate, a comparison between the GIS scan and the EIT 171 Å and 195 Å filters was performed, using EIT images taken almost simultaneously with the GIS spectra on October 11 1997. This was possible because GIS spectrally resolves the emission lines observed by the EIT filters.

Average intensity profiles in the two EIT filters, over the region observed by GIS, were extracted, as shown in Fig. 6.30, where also the ratio of the 195 Å to the 171 Å filter is presented. No intensity calibration factors were applied here, since they are small. This ratio shows a decrease of about 20% from the coronal hole region to the plume region. The observed GIS spectra were then 'filtered' applying the EIT pre-flight filter responses to the CDS spectra (see Fig. 6.31 and Fig. 6.32 for examples on how these filters act on the incident radiation), calculating then the total filtered intensity for each spatial position. The results are shown in Fig. 6.30, with the absolute values arbitrarily scaled. The agreement is quite good, giving confidence in the wavelength-dependence of the pre-flight filter responses.

The GIS intensity ratios of Fe XII 195.1 Å/Fe IX 171.07 Å are also plotted in Fig. 6.30, showing that the *real* intensity ratio is much lower (by a factor of about 0.2) than the value deduced from the EIT filter ratio. Nevertheless, this ratio does decrease (mainly because of the increased Fe IX 171.07 Å intensity) from the coronal hole to the plume, by about 15%, although the spatial position of the minimum is not the same as in the filter ratio curve. This minimum coincides with the peak of the intensity in the line profile.

To see in more detail how the observed EIT intensity changes, depending on the type of solar structure observed, GIS spectra of the two previously selected regions, chosen as representative of coronal hole and plume areas, are plotted in Figs. 6.31 and 6.32, with the same spectra multiplied by the EIT filter response. A quiet sun GIS observation has been added for comparison. The three spectra presented here show how lines, which form at different temperatures, can contribute to the emission seen by EIT.

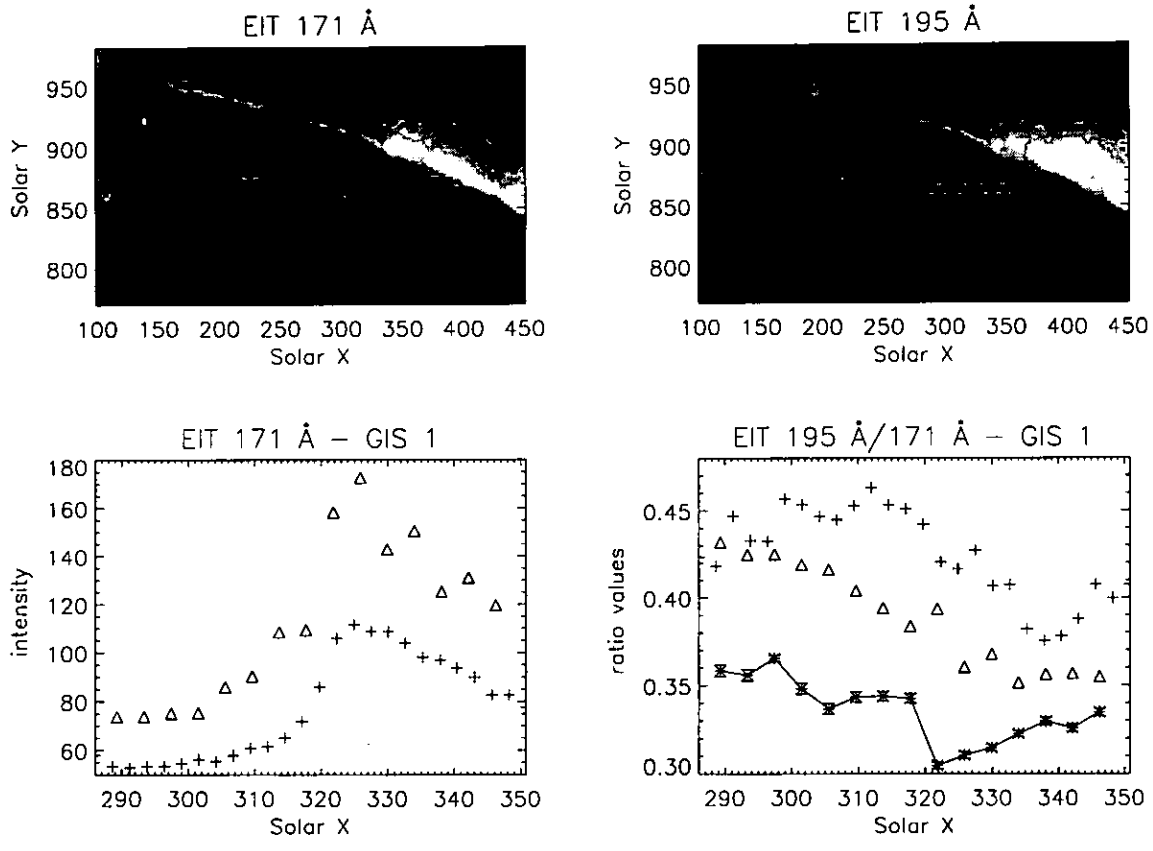

Figure 6.30: *Top: EIT images of the 11th of October 97 (19:00:14 UT - 171 Å; 19:12:30 UT - 195 Å), with a selected area across the plume overlaid. Bottom left: intensity profiles of the selected area in EIT 171 Å (crosses) with superimposed the observed CDS intensity filtered using the EIT filter response (triangles; intensity in arbitrary units). Bottom right: EIT 195 Å/171 Å intensity ratio (crosses) with the corresponding CDS intensity ratio filtered (triangles) and the intensity ratio of Fe XII 195.1 Å/Fe IX 171.07 Å obtained from CDS (asterisks), shifted by 0.25 for ease of comparison. Note the minimum in the line intensity ratio occurs close to the apparent base of the plume.*

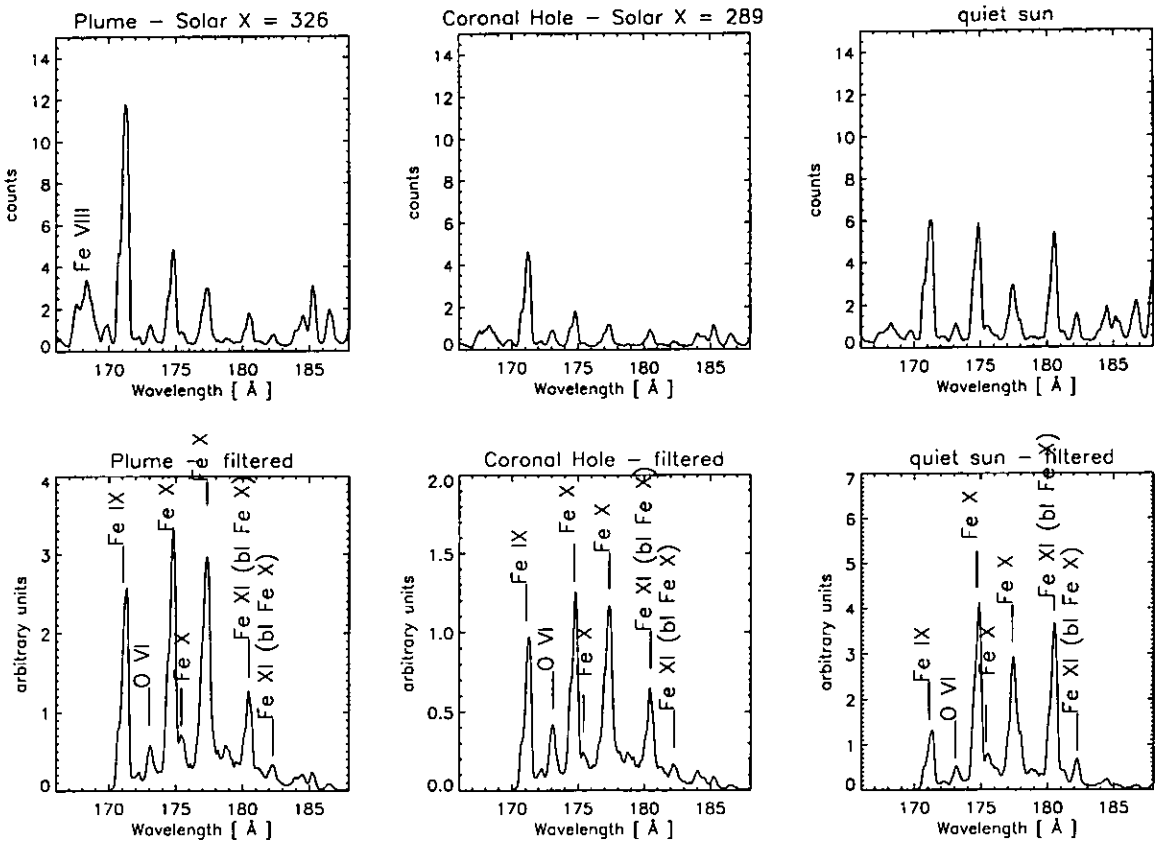

Figure 6.31: *Top: GIS 1 spectra of plume, coronal hole and quiet sun (on the same scale). Bottom: same as above, but multiplied by the EIT 171 Å filter response (scales adjusted separately).*

Considering first the EIT 171 Å filter, Fig. 6.31 shows that in the coronal hole and plume regions the main intensity is from Fe X lines, with some contribution from Fe IX and Fe XI lines, while in the quiet sun spectrum Fe IX 171 Å becomes small. However, the band-pass of the filter includes only emission produced by a restricted temperature range, almost isothermal. In the EIT 195 Å filter, the situation is not quite the same, as Fig.6.32 shows. While in the quiet sun spectrum the main contribution is from Fe XII lines, mixed with some Fe XI and Fe XIII emission, in the coronal hole and plume spectra the cooler lines (Fe VIII, Fe X, Fe XI) become increasingly significant, when compared to the Fe XII lines, as one would expect.

This shows that it is incorrect to assume that the observed emission in the EIT 195 Å filter is always predominantly Fe XII, and explains why plumes are still quite bright in the EIT 195 Å images. In fact, as shown, the emission in the plumes is mainly from low-temperature lines that are visible through the EIT filter. Furthermore, since the lines observed in the EIT 195 Å filter are formed over a wide range of temperatures, it is strictly inappropriate to use this filter for temperature diagnostics. Although not shown

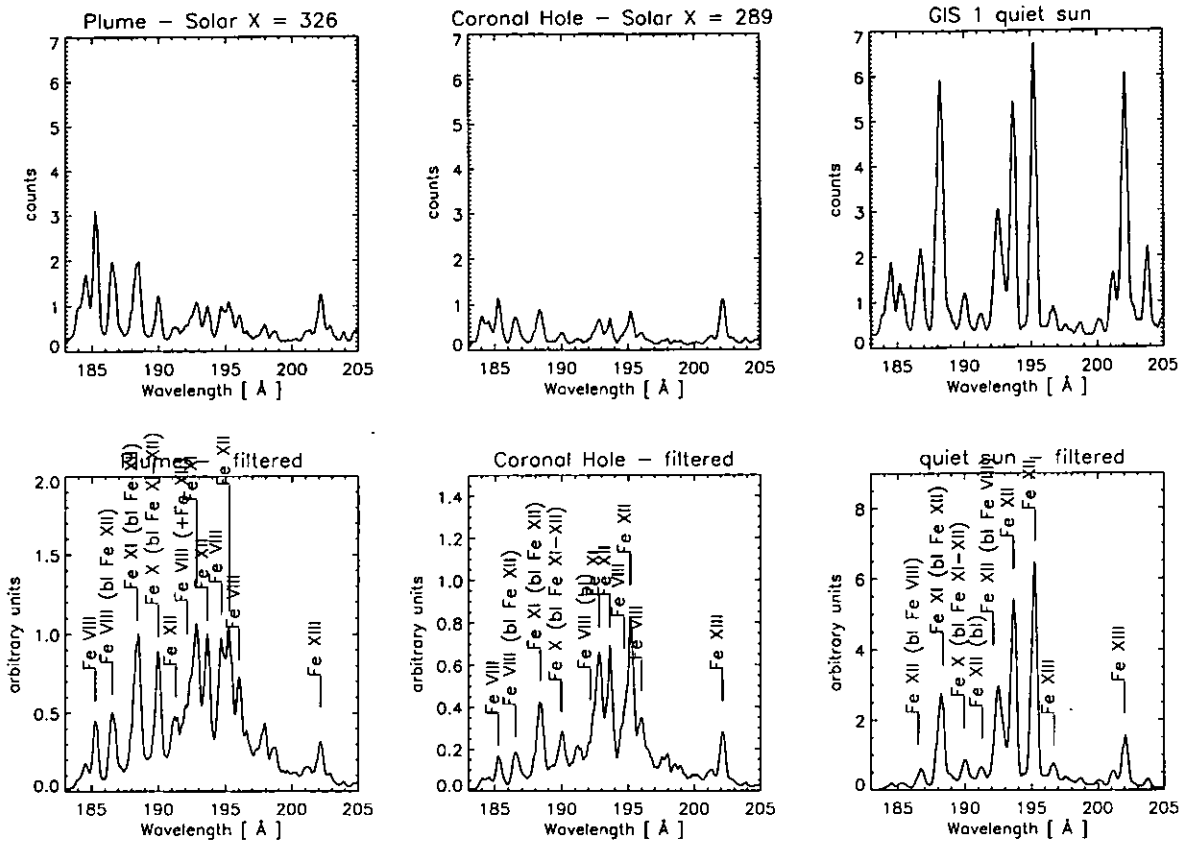

Figure 6.32: *Top: GIS 1 spectra of plume, coronal hole and quiet sun (on the same scale). Bottom: same as above, but multiplied by the EIT 195 Å filter response (scales adjusted separately).*

here, a similar result applies to the EIT 284 Å filter, where the emission is a mix of Fe XV and much cooler lines (Si VII, Mg VII) that are close to this line, as Fig. 6.28 shows.

Finally, it should be stressed that the results shown here are independent of the relative EIT/GIS intensity calibration (which was not a concern here), but only depend on the adopted EIT filter transmission curve, and on the assumption that the plasma characteristics did not change significantly between the GIS and the EIT observation. The latter assumption is reasonable, since all the lines seen in the two filters are coronal and so are not subject to rapid fluctuations. GIS *ghosting*, which becomes non-negligible in the quiet sun observation, does not change the main characteristics of the spectra in this case.

Chapter 7

Conclusions and further work

7.1 Summary of results and conclusions

The main findings and results of this thesis work are now summarised. During the research work leading to this thesis, many new results have been obtained. Some of these have already been published or are in press (*Mason et al.*, 1997; *Del Zanna and Bromage*, 1997; *Bromage et al.*, 1997; *Landi et al.*, 1997b; *Bromage et al.*, 1997b; *Fludra et al.*, 1997a; *DeForest et al.*, 1997a; *Fludra et al.*1997b; *Gopalswamy et al.*, 1998; *Del Zanna and Bromage*, 1999a; *Fludra et al.*, 1999a; *Gibson et al.*, 1999; *Bromage et al.*, 1999; *Landi et al.*, 1999a; *Del Zanna and Bromage*, 1999b; *Fludra et al.*, 1999b, *Del Zanna and Bromage*, 1999c), some have been presented in detail in the previous Chapters and the Appendices, whilst others are in the process of being studied in more detail.

The CDS instrument has allowed spectroscopic diagnostic techniques to be used to describe the temperature distribution, densities and elemental abundances of the plasma in the lower solar corona. This instrument has provided the opportunity of observing (for the first time with sufficient spectral and spatial resolution) a large number of emission lines from a wide range of ions of different elements, in order to achieve these analyses.

The level of accuracy and completeness of the CHIANTI atomic database, has allowed an in-flight calibration of the CDS detectors to be made. The work for this thesis has included a contribution to the testing of the various versions of this database, and to the development of software for its use (Chapter 2). CHIANTI has enabled the identification of many hundreds of lines observed in all the different CDS spectra examined here.

7.1.1 Spectroscopic diagnostic methods and the CDS

- Various diagnostic methods for emission measure, differential emission measure , and element abundance determinations have been inter-compared in a consistent way. A

critical discussion and re-evaluation of previous studies has been presented.

- A diagnostic method based on the differential emission measure (DEM) analysis has been developed to allow: a) the thermal structure of the emitting plasma to be studied; b) the relative element abundances to be estimated from non-flaring solar plasmas, for the first time; and c) the detailed assessment of line blends, for the first time.

- A detailed DEM re-analysis of a Skylab coronal hole spectrum has been presented and compared to previous studies, to show how more recent atomic data and different assumptions change the results and how blending limits the applicability of the diagnostic method.

- The diagnostic method has been applied for the first time to the entire high-resolution SERTS-89 spectrum to give a complete picture of all the ions observed, point ions out which require further study to assess the identification of all the lines and the blendings in order to to help in identifying the lines that CDS also observes, and which can be used for calibration purposes.

- Detailed CDS observations of the solar corona, and in particular of coronal holes have been planned. Software has been developed (in IDL) to analyse the large body of CDS spectral observations obtained by the author and Dr. Barbara Bromage and collaborators. These data sets are still only partly analysed.

- An extensive presentation and comparison of CDS NIS and GIS spectra of many different types of solar regions and structures have been given for the first time.

- For the first time, a complete in-flight cross-calibration between all the CDS detectors has been presented. In particular, the first full in-flight calibration of the GIS detectors has been given, including an assessment of the second order sensitivities for which no pre-flight estimates were available. Also for the first time the in-flight NIS 2 second order sensitivities are presented.

  The difficulties in calibrating an EUV spectroscope have been described in detail. The GIS and NIS sensitivities have been fully assessed, and temporal variations over a period of six months in 1997 studied in detail, showing that during this period of time the relative calibrations between all the CDS detectors did not appreciably change. A comparison with the pre-flight calibration data and with other studies has been given, showing the effects of different calibrations on the results.

- An in-flight assessment of various peculiar GIS characteristics has been made. This included a study of line profiles, the wavelength calibration, and, most important, a

study of the ghosting. Examples of the various effects that ghosting has on the GIS spectra have been presented in detail, to provide suggestions on which part of the detectors are usable with some accuracy.

- The usefulness of many CDS spectral lines employed in density, temperature, and abundance diagnostics has been assessed in detail (for coronal hole and quiet sun observations), in terms both of blending and impact on deduced parameters.

- Considering all the spectra presented here, several newly-observed lines have been identified for the first time, while in several other cases new identifications of previously observed lines or previously unreported blends have been pointed out.

- The first comprehensive compilation of line lists and identifications for the whole CDS NIS and GIS wavelength region, including second order lines and GIS 'virtual' lines (ghosts) has been presented. However, a complete CDS spectral line list of identifications is virtually impossible, due to the moderate CDS resolution, the overlapping of first and second order lines, and the GIS ghosts and other peculiar characteristics. The complexity of the observed structures seen along the line of sight , together with the moderate spatial resolution, inevitably means that contributions to most CDS lines are highly variable from case to case. In addition, for GIS, different instrument settings yield different ghosting patterns. Some examples of how these differences affect a line identification have been presented here.

- Many cases of disagreement between theory and CDS observations have been highlighted. These occur either for all the lines in some ions (e.g. Mg V), or for single lines of other ions (e.g. Mg IX). These differences cannot be explained by instrument calibration problems, and could be due to inaccurate ionization equilibrium calculations or atomic physics. In fact, in various cases, the re-analyses of previous spectra (e.g. Skylab and SERTS-89) presented here, has shown analogous problems, indicating that solutions have to be sought in improvements to the theory, rather than in experimental calibrations or measurement errors.

- It has been shown with the use of the *DEM* analysis, that in most of the spectra examined (and presented throughout this thesis) the lines of Li-like ions have large discrepancies (by factors of 2 or more) compared with all the other lines. Some of these discrepancies were already pointed out by other authors.

- A comparison of the results of three different published ionization equilibrium calculations (presented in Chapter 3) has pointed out that large variations (by factors of 2-3) in the calculated intensities of the lines can simply be due to the use of a different ionization equilibrium. Some of the peculiar observed intensities (e.g. the

Ca IX and Ca X lines) can easily be explained in terms of an inaccurate ionization equilibrium calculation, rather than due to a variation of the element abundance. Some of the reported discrepancies for the Li-like ions can also be partly explained in terms of ionization equilibrium. The *Arnaud and Rothenflug* (1985) calculations were found to produce more consistent results for most of the ions.

- A detailed CDS - EIT comparison is presented for the first time, showing how important it is to compare observations from EUV filter images with detailed spectra of the same bandpass, in order to assess the possibility of using filter images for diagnostic purposes.

7.1.2 Solar physics results and conclusions

During 1996 the Sun was at minimum activity, and coronal conditions were at their most favourable for the study of coronal holes. Most of the CDS observations taken for this investigation were made in coronal hole regions. Considering that in the EUV only one previous set of coronal hole spectra for line intensities had ever been measured (by Skylab) before the advent of SOHO, the latter (and CDS) can be regarded as a coronal hole 'discovery mission'. Thus, many new exciting results have been produced. Some of the unanswered questions described in Chapter 1 are now finding answers from the SOHO observations. The solar physics results from the present work are now summarised.

- In all the observations analysed, temporal and spatial variations of all the measurable quantities were common.

- Average line-of-sight *coronal electron densities* in coronal holes and the quiet sun have been presented, in both on-disc and off-limb observations. Reliable measurements based on a number of unblended density-sensitive coronal lines, have been presented for coronal hole regions for the first time. Coronal holes are found to have densities about a factor of two lower than the quiet sun areas.

- Average line-of-sight (isothermal) *electron temperatures* in the same coronal holes and quiet sun regions were deduced using lines emitted by different stages of ionization of the same element, thereby eliminating uncertainties due to element abundance variations. This was the first time that this had been done for coronal hole plasmas.

- A large *equatorial coronal hole*, the Elephant's Trunk, was identified and a series of CDS observations carried out during the last week of August 1996.

- The on-disc CDS observations of both the Elephant's Trunk and polar coronal holes during 1996, 1997 and 1998, have shown average coronal electron densities $N_e \simeq 1 - 2\text{x}10^8$ (cm^{-3}). This is about a factor of two lower than in the quiet sun areas.

- *Transition region electron densities* also appear to be lower, by a factor of two, in coronal hole areas, with quiet sun values $N_e \simeq 1\text{x}10^{10}$ (cm^{-3}). This is also a new result, only suggested by some Skylab observations, and recently confirmed by SOHO SUMER observations (*Doschek et al.*, 1998a).

  Moreover, in the transition region, the cell-centres show consistently higher densities (by a factor of 2) compared to those at the network boundaries. This observation confirms the (only) earlier suggestion (*Dupree et al.*, 1976) of increased densities at the cell-centres, an observation that was based on Skylab HCO C III data.

- On-disc coronal hole observations (including the Elephant's Trunk) have shown, on average, isothermal coronal temperatures $T \simeq 8 - 9\text{x}10^5$ K, about 10% lower than the quiet sun, although the precise values obtained depend on the region examined.

- For the first time, a complete *DEM* analysis of a near-disc-centre observation of a coronal hole has been performed, including high-temperature emission lines, something that was not possible with the Skylab HCO instrument, due to the low sensitivity at the lower wavelengths where these lines are observed. The Elephant's Trunk and a nearby quiet sun region showed different thermal distributions, with peaks of the *DEM* at $T \simeq 8\text{x}10^5$ K and $T \simeq 1.1\text{x}10^6$ K, respectively.

- Some results from on-disc coronal hole observations performed during the rising phase of the solar cycle in 1997, have shown that coronal hole observations are significantly affected by the presence of foreground over-lying quiet sun plasma, in particular if lines that are emitted above a million degrees are used for coronal hole diagnostics.

- Analogously, off-limb coronal hole observations have shown that the presence of diffuse background emission from non-coronal-hole regions can affect coronal hole measurements.

- The variation of averaged densities and temperatures *with distance from the Sun* has been obtained from off-limb observations. This was performed for both coronal hole regions (distinguishing between plume and inter-plume regions), and equatorial quiet sun regions, up to a radial distance of 1.2 $\text{R}_\odot$.

  Observations (in 1996, 1997, and early 1998) of equatorial quiet sun regions have shown similar general characteristics from year to year, with densities decreasing

from $4 - 5\text{x}10^8$ in the lower corona, to $\simeq 1\text{x}10^8$ cm^{-3} at 1.2 $R_\odot$. Densities in inter-plume coronal hole regions showed a decrease from $1 - 2\text{x}10^8$ in the lower corona, to $\simeq 5\text{x}10^7$ cm^{-3} at 1.2 $R_\odot$.

Temperatures were more difficult to establish, because the plasma has rarely been exactly isothermal, so that referring to 'a temperature' is not correct, and only a *DEM* analysis is appropriate to describe the temperature distribution of the plasma along the line of sight . However, measurements of line ratios, together with *DEM* analyses for off-limb quiet sun and coronal hole regions have all confirmed the Elephant's Trunk measurement, that coronal holes are much 'cooler' than the quiet sun. Temperatures in quiet sun areas are about $T \simeq 1.0 - 1.1\text{x}10^6$ K and then tend to increase with distance, up to 1.2 $R_\odot$, where they appear to reach a constant level.

In coronal holes, the temperatures have a much shallower gradient (as already known from Skylab observations), increasing slightly from $T \simeq 8\text{x}10^5$ K, to $T \simeq 0.9 - 1\text{x}10^6$ K. It should be noted that these isothermal temperatures vary depending on which structure is observed, and by the amount of foreground and background line of sight. However, these variations with height are consistent with the recent results of *David et al.* (1998), up to 1.2 $R_\odot$, the limit of the observations presented here. In fact, *David et al.* (1998) also derive from CDS and SUMER observations that the temperature gradient (from O VI ratios) in coronal holes is only slightly increasing up to about 1.15 $R_\odot$, after which they measure a decrease in the electron temperature.

- An examination of intensity ratios of lines of different elements but which have similar contribution functions, over a range of solar structures, has shown that in some cases the results are the same, while in others large variations are found. These variations appear to be correlated with the supergranular pattern, both in coronal hole and quiet sun regions, something that has never been reported before. Some of these variations could be due to different temperature gradients in the cell-centres and the network regions.

Coronal hole plumes

- For the first time, spectroscopic analyses of on-disc EUV observations of *coronal hole plumes* have been performed. This allowed a spectroscopic characterisation of plumes to be obtained for the first time. As for many other coronal structures, plumes have also shown a wide range of characteristics. Here, only typical faint plumes as observed by CDS during the minimum of the solar cycle are considered. Their main characteristics are lowered temperature and an enhanced Mg/Ne intensity ratio.

- For the first time, a low-latitude plume in a coronal hole (Elephant's Trunk) has been

identified from its spectroscopic characteristics, rather than from its morphology.

- These plumes show lower temperatures (derived from line ratios) than the ambient coronal hole regions. No emission in high-temperature lines, formed above 1.2x10^5 K, was observed. *DEM* analyses have shown that plumes have an almost isothermal plasma distribution at coronal heights, with a peak in the differential emission measure at $T \simeq 7 - 8$x10^5 K, very similar to the temperatures deduced from line ratios. The surrounding coronal hole regions are less isothermal, at least at low heights. Off-limb observations suggest that plumes have even shallower radial temperature gradients than the coronal hole, and that these temperature differences tend to disappear with distance, as all the coronal hole plasma becomes almost isothermal.

  In terms of densities, measurements at lower-corona heights ($T \simeq 8 - 9$x10^5 K; e.g., Mg VIII, Si IX) have rarely shown significative differences between plume and interplume regions ($N_e \simeq 2$x10^8 cm^{-3}). However, due to low signal, the uncertainties are large and do not exclude the possibility of slightly higher density in plumes. A more detailed analysis is required, for example taking into account all the possible effects that a different temperature distribution can have on the evaluation of the densities from line ratios. At lower temperatures ($T \sim 7$x10^5 K), where plumes have their maximum emission measures and visibility, the density (Mg VII) is $N_e \simeq 1 - 4$x10^9 (cm^{-3}), higher than in the coronal hole regions, but similar to quiet sun values. At even lower temperatures ($T \sim 2$x10^5 K), in the lower transition region (O IV), plumes are not visible. Indeed, they appear to have the same densities as in the nearby coronal hole network regions ($N_e \simeq 5$x10^9 cm^{-3}). However, as well as exhibit enhanced Mg/Ne intensity ratios, plumes also show an enhancement in the O IV/Ne IV intensity ratios (reported here for the first time).

  The large FIP effect in plumes (reported by *Widing and Feldman*, 1992, in terms of Mg/Ne relative abundance), could be checked. For the first time, the relative abundances of many other elements have also been estimated. The observed large increases of the Mg/Ne intensity ratios at the base of the plumes, compared to the nearby coronal hole regions, can largely be explained by the plumes having a slightly *lower Ne abundance* (compared to oxygen), together with a much steeper temperature gradient in the upper transition region, thus confirming the *Phillips* (1997a) suggestion that the previously reported high-FIP in plumes could be due to a temperature effect. However, after taking into account the *DEM* distribution of the plume, a small FIP effect does appear to be present, although other high-FIP elements (such as S) have also shown increased abundances, compared to the photospheric values. This small FIP effect suggests that plumes may not be the source of the fast solar wind.

For the first time, it has been shown that the continuum observed in GIS 4 can be used to constrain the *absolute abundances of the elements* (relative to hydrogen). The measurements are consistent with coronal holes having absolute abundances which are photospheric.

7.2 Further work

CDS has produced a wealth of data that still requires a more detailed analysis. Now that clearer understanding of the instrument behaviour, calibration and line identification has been achieved, it is possible to extend the spectral analysis of the solar corona in much greater detail. It is very important to continue to perform comparisons of results obtained from different instruments in co-spatial and co-temporal observations, in order to remove remaining uncertainties due to instrument calibration or the diagnostic method adopted.

A more detailed study should be undertaken of the CDS absolute calibration, as a function of time throughout the mission. All CDS analyses, that were based on the preliminary calibrations (that were available until the end of 1998), will have to be revisited.

A more detailed analysis of the GIS spectra is still required, now that the various instrumental problems, including the ghosting problem, are better understood.

Atomic physics studies

Although atomic databases such as CHIANTI have proved to be extremely valuable in the EUV spectral region, there are still many unidentified lines, and many others that require more research. The recent case of Fe XIV has shown how more refined atomic physics calculations can bring theory into agreement with observations.

The coronal hole observations have shown the presence of many low-temperature lines that were not previously reported in quiet sun or active region solar spectra, including Fe VIII, Ca IV, and Ca VIII spectral lines. In particular, a detailed atomic physics study of Fe VIII is needed, since many instruments such as SOHO/EIT and TRACE (Transition Region Coronal Explorer) observe the solar corona with EUV filters in wavelength regions where Fe VIII line intensities are not negligible.

More work should also be undertaken on the validity of the ionization equilibrium and its relation to the problem of the Li-like ions. One possible method of comparing different ionization equilibria has been suggested here. Another possibility is to study the observed emission at high spatial and temporal resolutions. A preliminary analysis of the high-cadence (5s) GIS studies performed has suggested the presence of large temporal variations.

However, observations with new instruments with much higher sensitivities is required to further study non-equilibrium effects on such short time-scales.

Short-time-scale events

Many wide-slit CDS observations have been performed and analysed by the author in order to create 'movies' of various solar regions, with a time resolution of the order of a minute (but with no spectral resolution). Some of these movies were created in an attempt to correlate Bright Points in coronal holes, observed with the Nobeyama radio-heliograph at 17 GHz (*Gopalswamy et al.*, 1998), with the chromospheric and transition region brightenings observed with CDS. No direct correlation was found. However, most of the brightenings observed with CDS were very brief events, lasting for only one or two exposures. Therefore, a more detailed analysis will require new instruments that will be able to measure intensities on time-scales much less than a minute.

Also worth noting is that in most cases these brightenings were almost simultaneous, in the transition region and in the lower corona. In order to understand the relation between the transition region and the corona, more detailed studies are needed, with improved spectroscopic capabilities. These need to be able to provide measurements of line widths and line shifts, and to have diagnostic capabilities, in order to give co-temporal information on density variations.

The future SOLAR-B mission, due to launch in 2004, should be able to address these issues.

Coronal holes, the transition region and the plumes

The off-limb and on-disc coronal hole observations presented here have shown that the Elephant's Trunk was an ideal subject for coronal hole studies, because of the near-disc centre, and solar minimum conditions. Hence, a full study is needed of all the remaining observations of this feature that are not yet fully analysed.

A more extended analysis of the transition region characteristics is required, to confirm the abundances, temperature, and density variations presented here. The fact that the transition region densities in the network seem lower than in the cell-centres, together with the fact that the emission measures there are much higher, indicates that the cell-centres have higher plasma pressures, as one would anyway expect, since the magnetic pressure there is lower. It also indicates that the filling factors in the transition region are highly variable (although much higher spatial resolution than CDS has is required in order to estimate the volume from which the observed emission originates).

Other information should be added, in order to constrain the various physical models of the transition region, and relate the transition region to the outer solar atmosphere. One possibility is to use the DEM distributions presented in this thesis to test models of the transition region such as the study presented by *Dowdy et al.* (1987), which compared the DEM curves derived from Skylab data, with model calculations.

Another possibility is to use the FIP effect. In fact, the processes that take place in the chromosphere/transition region may create a fractionation of the elements that follows the structure of the cell-centre regions. Once this fractionation has taken place, the abundance characteristics of a structure should not change much with height (although gravitational settling might play a role), and should therefore not only be visible at transition-region and coronal heights (with spectroscopic instruments), but should also exhibit a signature in in-situ observations of the solar wind. For example, the near-photospheric element abundances found here in the coronal hole network could represent the signature of the fast solar wind originating from the chromospheric network and propagating through coronal funnels (see the model of *Marsch and Tu*, 1997, and references therein), which from in-situ measurements does not show a significant FIP effect. Recent SUMER observations (e.g., *Hassler et al.*, 1999) have also confirmed that the fast solar wind appears to be originating at the junctions of the chromospheric network.

Coronal hole plumes deserve much more detailed investigation. This is not only for the reasons outlined in the introduction, but also because CDS observations have shown that, among the complex zoo of coronal large scale structures, they are probably the simplest ones to model. This is because: (1) their geometry is relatively well defined, which for example helps theoretical modelling, and estimates of the filling factors (a preliminary analysis indicates that plumes have filling factors close to 1.); (2) they are long lasting quasi-stationary structures; and (3) they are almost isothermal. Studies of their peculiar element abundances should surely also shed some light on the wider coronal abundance problems, and address the question of why coronal abundances appear to be different from the photospheric ones.

Bibliography

Ahmad, I. A. and Withbroe, G. L., 1977, *EUV analysis of polar plumes*, Sol. Phys., 53, 397.

Ahmad, I. A. and Webb, D. F., 1978, *X-ray analysis of a polar plume*, Sol. Phys., 58, 323.

Almleaky, Y. M., Brown, J.C., Sweet, P.A., 1989, *Density diagnostics and inhomogeneous plasmas. I - Isothermal plasmas*, Astron. Astrophys., 224, 328.

Andretta, V., Jones, H. P., 1997, *On the Role of the Solar Corona and Transition Region in the Excitation of the Spectrum of Neutral Helium*, Astrophys. J., 489, 375.

Arnaud, M. and Rothenflug, R., 1985, *An updated evaluation of recombination and ionization rates*, Astron. Astrophys. Suppl. Ser., 60, 425.

Arnaud, M. and Raymond, J., 1992, *Iron ionization and recombination rates and ionization equilibrium*, Astrophys. J., 398, 394.

Athay, R. G., 1976, *The solar chromosphere and corona: quiet Sun*, Reidel.

Athay, R. G., 1982, *Responses of transition region models to magnetic field geometry and downflow velocities*, Astrophys. J., 263, 982.

Athay, R. G. and Dere, K. P., 1991, *Chromospheric and transition region diagnostics using emission-line intensities*, Astrophys. J., 379, 776.

Bartoe J. D. F., Brueckner, G. E., Purcell, J. D., and Tousey, R., 1977, *Appl. Optics*, 16, 879.

Behring, W. E., Cohen, L., and Feldman, U. , 1972, *The solar spectrum: wavelengths and identifications from 60 to 385 Å*, Astrophys. J., 175, 493.

Behring, W. E., Cohen, L., Feldman, U., Doschek, G.A., 1976, *The solar spectrum - Wavelengths and identifications from 160 to 770 Å*, Astrophys. J., 203, 521.

Bocchialini, K. and Vial, J.C., 1996, *High-Chromosphere and Low-Transition-Region Network: a Different Organization in an Equatorial Coronal Hole?*, Solar Physics, 168, 37.

Breeveld, E. R., Culhane, J. L., Norman, K., Parkinson, J. H. and Gabriel, A. H., 1988, *CHASE observations of the solar corona*, Astrophys. J. Letters, 27, 155.

Breeveld, A. A., Edgar, M. L., Smith, A., Lappington, J. S., Thomas, P.D., 1992, Rev.Sci.Instr., 63, 1.

Breeveld A. A., 1996, *Ultraviolet Detectors for Solar Observations on the SOHO Spacecraft*, University of London Ph.D. Thesis.

Brekke, P., 1993, *Observed redshifts in O V and downflows in the solar transition region*, Astrophys. J., 408, 735.

Brekke P., Thompson W. T., Woods T. N., Eparvier F. G., 1998, *The EUV solar irradiance spectrum observed with the Coronal Diagnostic Spectrometer (CDS) on SOHO*, Astrophys. J., to be submitted.

Brickhouse, N. S., Raymond, J. C. and Smith, B. W., 1995, *New model of iron spectra in the extreme ultraviolet and application to SERTS and EUV observations: A solar active region and capella*, Astrophys. J. Suppl. Ser., 97, 551.

Bromage, B. J. I., Breeveld, A. A., Kent, B. J., Pike, C. D. and Harrison, R. A., 1996, *UCLan Report CFA/96/09.*

Bromage, B. J. I., Del Zanna, G., DeForest, C., Thompson, B., and Clegg, J. R., 1997, *An equatorial coronal hole at solar minimum*, Proc. of the Fifth SOHO Workshop, ESA SP-404, 319.

Bromage B. J. I., Del Zanna G., Fludra A., DeForest C. E., and Thompson B., 1997, *The Structure and Evolution of Solar Coronal Holes Observed by SOHO During August and September 1996*, ESA-SP 415, 307.

Bromage B. J. I., Clegg J. R., Del Zanna G., and Thompson B., 1999, *Tales of an Elephant's Trunk*, ASP Conf. Ser. 158, 370.

Brosius, J. W., Davila, J. M., Thomas, R. J., Monsignori-Fossi, B. C., 1996, *Measuring active and quiet-sun coronal plasma properties with extreme-ultraviolet spectra from SERTS*, Astrophys. J. Suppl. Ser., 106, 143.

Brosius, J. W., Davila, J. M. and Thomas, R. J., 1998a, *Calibration of the SERTS-95 Spectrograph from Iron Line Intensity Ratios*, Astrophys. J. Letters, 497, L113.

Brosius, J. W., Davila, J. M. and Thomas, R. J., 1998b, *Solar active regions and quiet-sun extreme-ultraviolet spectra form SERTS-95*, Astrophys. J. Suppl. Ser., 119, 255.

Brueckner, G. E. and Bartoe, J. -D. F., 1983, *Observations of high-energy jets in the corona above the quiet sun, the heating of the corona, and the acceleration of the solar wind*, Astrophys. J., 272, 329.

Bruner, E. C. , Jr. and MCWhirter, R. W. P., 1979, *The observation and interpretation of the profile of C IV lambda-1548 emitted from a quiet region of the sun*, Astrophys. J., 231, 557.

Chae, J., Yun, H. S. and Poland, A. I., 1997, *Effects of Non-LTE Radiative Loss and Partial Ionization on the Structure of the Transition Region*, Astrophys. J., 480, 817.

Cook, J. W. and Nicolas, K. R., 1979, *Solar C III line intensity ratios observed from Skylab*, Astrophys. J., 229, 1163.

Cook, J. W., Keenan, F. P., Dufton, P. L., Kingston, A. E., Pradhan, A. K., Zhang, H. L., Doyle, J. G. and Hayes, M. A., 1995, *The O IV and S IV intercombination lines in solar and stellar ultraviolet spectra*, Astrophys. J., 444, 936.

Craig, I. J. D. and Brown, J. C., 1976, *Fundamental limitations of X-ray spectra as diagnostics of plasma temperature structure*, Astron. Astrophys., 49, 239.

David, C., Gabriel, A. H., and F. Bely-Dubau, 1997, *Measurement of above-limb coronal intensities*, Proc. of the Fifth SOHO WORKSHOP, ESA SP-404, 313.

David, C., Gabriel, A. H., Bely-Dubau, F., Fludra, A., Lemaire, P., and Wilhelm, K., 1998, *Measurement of the electron temperature gradient in a solar coronal hole*, Astron. Astrophys., 336, L90–L94.

Deforest, C. E., Bromage B.J.I., Del Zanna, G., Hassler, D. M., and Thompson, B. J., 1997, *Coordinated Observation of a Low-Latitude Coronal Hole*, Spring Meeting of the American Geophysical Union May 27-30, 1997, Baltimore, Maryland.

Deforest, C. E., Hoeksema, J. T., Gurman, J. B., Thompson, B. J., Plunkett, S. P., Howard, R., Harrison, R. C. and Hassler, D. M., 1997, *Polar Plume Anatomy: Results of a Coordinated Observation*, Sol. Phys., 175, 393.

Deforest, and C. E., Gurman, J. B., 1998, *Observation of Quasi-periodic Compressive Waves in Solar Polar Plumes*, Astrophys. J. Letters, 501, L217.

Del Zanna G., Landini M., Landi E. and Monsignori Fossi B.C., 1996, *Comparison of temperature and density diagnostics in the coronae of α Centauri and the sun*, ASP Conf. Ser. 109: Ninth Cambridge Workshop on Cool Stars, Stellar Systems, and the Sun, 9, 259.

Del Zanna, G., Bromage, B. J. I., Dere, K. P., Pike, C. D., 1997, SOHO-CDS software note No. 50.

Del Zanna, G., and Bromage, B. J. I., 1997, *Spectroscopic diagnostics applied to the August 1996 equatorial coronal hole*, Proc. of the Fifth SOHO workshop, ESA SP-404, 319.

Del Zanna, G. and Bromage, B.J.I., 1999a, *The Elephant's Trunk: Spectroscopic diagnostics applied to SOHO/CDS observations of the August 1996 equatorial coronal hole*, J. Geophys. Res., 104, 9753.

Del Zanna G., and Bromage, B.J.I., 1999b, *Characterisation of solar coronal holes and plumes using spectroscopic diagnostic techniques applied to SOHO/CDS observations*, Space Sci. Rev., in press.

Del Zanna, G., and Bromage, B. J. I., 1999c, *Transition region densities and abundances as derived from SOHO/CDS observations*, Proc. of the 8th SOHO workshop, Paris.

Del Zanna, L., Hood, A. W., and Longbottom, A. W., 1997, *An MHD model for solar coronal plumes*, Astron. Astrophys., 318, 963.

Delaboudiniere, J. -P., Artzner, G. E., Brunaud, J., Gabriel, A. H., Hochedez, J. F., Millier, F., Song, X. Y., Au, B., Dere, K. P., Howard, R. A., Kreplin, R., Michels, D. J., Moses, J. D., Defise, J. M., Jamar, C., Rochus, P., Chauvineau, J. P., Marioge, J. P., Catura, R. C., Lemen, J. R., Shing, L., Stern, R. A., Gurman, J. B., Neupert, W. M., Maucherat, A., Clette, F., Cugnon, P., and Van Dessel, E. L., 1995, *EIT: Extreme-Ultraviolet Imaging Telescope for the SOHO Mission*, Sol. Phys., 162, 291.

Dere, K. P., 1978, *Spectral lines observed in solar flares between 171 and 630 angstroms*, Astrophys. J., 221, 1062.

Dere, K. P., 1978b, *Errors in Differential Emission Measure Solutions*, Astron. Astrophys., 70, 439.

Dere, K. P., 1982, *Extreme ultraviolet spectra of solar active regions and their analysis*, Sol. Phys., 77, 93.

Dere, K. P., Bartoe, J.-D. F., and Brueckner, G. E., 1982, *Solar transition zone pressures from EUV observations of O IV and N IV*, Astrophys. J., 259, 366.

Dere, K. P., Bartoe, J.-D., Brueckner, G. E., Cook,J. W . and Socker,D. G., 1987, *Subresolution structures in the solar transition zone*, Sol. Phys., 114, 223.

Dere, K. P., Bartoe, J.-D., Brueckner, G.E. and Recely, F., 1989, *Transition zone flows observed in a coronal hole on the solar disk*, Astrophys. J., 345, L95.

Dere, K. P. and Mason, H. E., 1993, *Nonthermal velocities in the solar transition zone observed with the high-resolution telescope and spectrograph*, Sol. Phys., 144, 217.

Dere, K. P., Landi, E., Mason, H. E., Monsignori Fossi, B. C. and Young, P. R., 1997, *CHIANTI: an Atomic Database for Emission Lines*, Astron. Astrophys. Suppl. Ser., 125, 149.

Doschek, G. A. Feldman, U., Bhatia, A. K., Mason, H. E., 1978, *Densities in the quiet sun and polar coronal holes from EUV line ratios involving O III 1666.15 Å*, Astrophys. J., 226, 1129.

Doschek, G. A., Mariska, J. T. and Feldman, 1981, *Mass motions in optically thin solar transition zone lines*, Mon. Not. R. Astron. Soc., 195, 107.

Doschek, G. A., 1984, *The effects of a multidensity plasma on ultraviolet spectroscopic electron density diagnostics*, Astrophys. J., 279, 446.

Doschek, G. A., 1997, *Emission measures and electron densities for the solar transition region*, Astrophys. J., 476, 903.

Doschek, G. A., Warren, H. P., Laming, J. M., Mariska, J. T., Wilhelm, K., Lemaire, P., Schuehle, U., Moran, T. G., 1997b, *Electron densities in the solar polar coronal holes from density sensitive line ratios of Si VIII and Si X*, Astrophys. J. Letters, 482, L109.

Doschek, G. A., Feldman, U., Laming, J. M., Warren, H. P., Schuehle, U. and Wilhelm, K., 1998a, *The Electron Pressure in the Solar Lower Transition Region Determined from O V and Si III Density-sensitive Line Ratios*, Astrophys. J., 507, 991.

Doschek, G. A., Laming, J. M., Feldman, U., Wilhelm, K., Lemaire, P., Schuehle, U. and Hassler, D. M., 1998b, *The Si/Ne Abundance Ratio in Polar Coronal Hole and Quiet-Sun Coronal Regions*, Astrophys. J., 504, 573.

Dowdy, J. F. , Jr., Moore, R. L., and Emslie, A. G., 1987, *On the inability of magnetically constricted transition regions to account for the 10^5 to 10^6 K plasma in the quiet solar atmosphere*, Sol. Phys., 112, 255.

Dupree, A. K., 1972, *Analysis of the extreme-ultraviolet quiet solar spectrum*, Astrophys. J., 178, 527.

Dupree, A. K., Foukal, P. V. and Jordan, C., 1976, *Plasma diagnostic techniques in the ultraviolet - The C III density-sensitive lines in the sun*, Astrophys. J., 209, 621.

Dwivedi, B. N. and Raju, P. K., 1980, *Density dependence of solar emission lines of boron-like ions*, Sol. Phys., 68, 111.

Dwivedi, B. N. and Mohan, A., 1995a, *On the electron density in a coronal hole*, Sol. Phys., 156, 197.

Dwivedi, B. N. and Mohan, A., 1995b, *Theoretical Ne VI/Mg VI line diagnostics for SUMER*, Sol. Phys., 157, 135.

Dwivedi, B. N. and Mohan, A., 1995c, *Line diagnostics for Ne V and Mg V solar ions*, Sol. Phys., 158, 237.

Dwivedi, B. , Mohan, A. and Thomas, R., 1998, *Spectral Diagnostics of an Active Region Observed by the Solar EUV Rocket Telescope and Spectrograph (SERTS)*, Sol. Phys., 180, 157.

Esser, R., Brickhouse, N. S., Habbal, S. R., Altrock, R. C. and Hudson, H. C., 1995, *Using Fe X 6374 and Fe XIV 5303 Spectral Line Intensities to Study the Effect of the Line of Sight on Coronal Hole Temperature Inferences.*, J. Geophys. Res., 100, 19829.

Falconer, D. A., Davila, J. M. and Thomas, R. J., 1997, *Relative Elemental Abundances of the Quiet Solar Corona as Determined by SERTS*, ApJ, 482, 1050.

Feldman, U., Doschek, G. A., Mariska, J. T., 1979, *On the structure of the solar transition zone and lower corona*, Astrophys. J., 229, 369.

Feldman, U., 1987, *Atlas of extreme ultraviolet spectroheliograms from 170 to 625 Å, Volume 1 and 2*, Washington DC, Naval Research Laboratory, E.O. Hulburt Center, USA, edited by Feldman, Uri.

Feldman, U. and Widing, K. G., 1990, *Photospheric abundances of oxygen, neon, and argon derived from the XUV spectrum of an impulsive flare*, Astrophys. J., 363, 292.

Feldman, U., 1992a, *Elemental abundances in the upper solar atmosphere*, Phys. Scripta, 46, 202.

Feldman, U., Mandelbaum, P., Seely, J. F., Doschek, G.A., Gursky, H., 1992b, *The potential for plasma diagnostics from stellar extreme-ultraviolet observations*, Astrophys. J. Suppl. Ser., 81, 387.

Feldman, U. and Widing, K. G., 1993, *Elemental abundances in the upper solar atmosphere of quiet and coronal hole regions ($T_e \simeq 4.3 \times 10^5$ K)*, Astrophys. J., 413, 381.

Feldman, U. and Laming, J. M., 1994, *On the absence of a relationship between the properties of the $T_e \geq 10^6$ K and the properties of the $T_e \leq 10^5$ solar plasmas*, Astrophys. J., 434, 370.

Feldman, U., Schuhle, U., Widing, K. G. and Laming, J. M., 1998, *Coronal Composition above the Solar Equator and the North Pole as Determined from Spectra Acquired by the SUMER Instrument on SOHO*, Astrophys. J., 505, 999.

Firth, J. G., Freeman, F. F., Gabriel, A. H., Jones, B. B., Jordan, C., Negus, C. R., Shenton, D. B., Turner, R. F., 1974, *Observations of the solar spectrum in the region 150 Åto 870 Åemitted from the disk and above the limb*, Mon. Not. R. Astron. Soc., 166, 543.

Fisher, R. and Guhathakurta, M. , 1995, *Physical Properties of Polar Coronal Rays and Holes as Observed with the SPARTAN 201-01 Coronagraph*, Astrophys. J. Letters, 447, L139.

Fludra, A., Schmelz, J.T., 1995, *Absolute abundances of flaring coronal plasma derived from SMM spectral observations*, Astrophys. J., 447, 936.

Fludra, A., Del Zanna,G., Bromage B.J.I., Thomas,R.J., 1997a, *EUV line intensities above the limb measured by CDS*, Proc. of the Fifth SOHO workshop, ESA SP-404, 385.

Fludra, A., Del Zanna, G., Bromage B. J. I., 1997b, *Observations of the Quiet Sun Corona and Coronal Holes with the Coronal Diagnostic Spectrometer on SOHO*, AAS/Solar Physics Division Meeting, 29, 0109, June 27 -July 1, 1997 MSU-Bozeman.

Fludra, A., Del Zanna, G., Alexander,D., Bromage B. J. I., 1999a, *Electron density and temperature of the lower solar corona*, J. Geophys. Res., 104, 9709.

Fludra, A., Del Zanna, G., Bromage B. J. I., 1999b,

, Space Sci. Rev., in press, EUV observations above polar coronal holes.

Foster, V. J., Keenan, F. P., Reid, R. H. G., Doyle, J. G., Zhang, H. L., Pradhan, A. K. and Widing, K. G., 1997, *Mg VIII diagnostic line ratios in skylab solar observations*, Sol. Phys., 170, 217.

Gabriel, A. H., 1976, *A magnetic model of the solar transition region*, Royal Society of London Philosophical Transactions Series, 281, 339.

Gallagher, P. T., Phillips, K. J. H., Harra-Murnion, L. K., and Keenan, F. P., 1998, *Properties of the quiet Sun EUV network*, Astron. Astrophys., 335, 733.

Galvin, A. B., Ipavich, F. M., Gloeckler, G., Hovestadt, D., Klecker, B. and Scholer, M., 1984, *Solar wind ionization temperatures inferred from the charge state composition of diffuse particle events*, J. Geophys. Res., 89, 2655.

Geiss, J., Gloeckler, G. and Von Steiger, R., 1995, *Origin of the Solar Wind From Composition Data*, Space Sci. Rev., 72, 49.

Gibson, S.E., Fludra, A., Bagenal, F., Biesecker, D., Del Zanna, G., Bromage, B. J. I., 1999, *Solar minimum streamer densities and temperatures using Whole Sun Month coordinated data-sets*, J. Geophys. Res., 104, 9691.

Golub, L., Nystrom, G., Herant, M., Kalata, K. and Lovas, I., 1990, *Sub-arcsecond observations of the solar X-ray corona*, Nature, 344, 842.

Golub, L. and Pasachoff, J. M., 1997, *The Solar Corona*, Cambridge University Press.

Gopalswamy, N. , Schmahl, E. J. and Kundu, M. R., 1992, *Observations of stationary radio sources: Coronal polar plumes ?*, Proc. of the First SOHO Workshop, ESA SEE N93-31343, 113.

Gopalswamy, N., Deforest, C., Bromage, B., Del Zanna, G. and Shibasaki, K., 1998, *Multiwavelength Observations of a Low-Latitude Coronal Hole*, ASP Conf. Ser. 140, Synoptic Solar Physics, E33.

Grevesse, N. and Anders, E., 1989, in *Cosmic abundances of Matter* ed. C.J. Waddington (New York: AIP), 1.

Grevesse, N., and Anders, E., 1991, *Solar element abundances*, in Solar Interior and Atmosphere, ed. A. N. Cox, W. C. Livingston, & M. S. Matthews, (Tucson: Univ. Arizona Press), 1227.

Grevesse, N., and Sauval, A. J., 1998, *Standard Solar Composition*, Space Sci. Rev., 85, 174.

Grevesse, N. and Sauval, A. J., 1999, *The solar abundance of iron and the photospheric model*, Astron. Astrophys., 347, 354.

Guhathakurta, M., Rottman, G. J., Fisher, R. R., Orral, R. Q. and R. C. Altrock, 1992, *Coronal density and temperature structure from coordinated observations associated with the toal solar eclipse of 1988 March 18*, Astrophys. J., 388, 633.

Guhathakurta, M., Fisher, R. R. and Altrock, R. C., 1993, *Large-scale coronal temperature and density distributions, 1984-1992*, Astrophys. J. Letters, 414, L145.

Guhathakurta, M. and Holzer, T. E., 1994, *Density structure inside a polar coronal hole*, Astrophys. J., 426, 782.

Guhathakurta, M. and Fisher, R., 1995, *Physical Properties of the Polar Corona as Observed with the SPARTAN 201 Coronagraph, 8 - 10 September, 1995*, American Astronomical Society Meeting, 187, 12207.

Guhathakurta, M. , Fisher, R. and Strong, K. , 1996, *Temperature Structure of the High-Latitude Corona*, Astrophys. J. Letters, 471, L69.

Guhathakurta, M. and Fisher, R. , 1998, *Solar Wind Consequences of a Coronal Hole Density Profile: Spartan 201-03 Coronagraph and Ulysses Observations from 1.15 R sub sun to 4 AU*, Astrophys. J. Letters, 499, L215.

Habbal, S. R., Esser, and M. B. Arndt, 1993, *How reliable are coronal hole temperatures deduced from observations ?*, Astrophys. J., 413, 435.

Habbal, S. R., Esser, R., Guhathakurta, M. and Fisher, R. R., 1995, *Flow Properties of the Solar Wind Derived from a Two-Fluid Model with Constraints from White Light and in situ Interplanetary Observations*, Geophys. Res. Lett., 22, 1465.

Hansen, E., Schaffner, S. (eds.): 1977, Proceedings of the November 7-10, 1977 OSO-8 Workshop, Univ. of Colorado.

Hara, H., Tsuneta, S., Acton, L.W., Bruner, M.E., Lemen, J.R. and Ogawara, Y., 1994, *Temperatures of coronal holes observed with the YOHKOH SXT*, Publ. Astr. Soc. Japan, 46, 493.

Hara, H., 1997, *A high-temperature component in coronal holes as confirmed by a partial-eclipse observation*, Publ. Astr. Soc. Japan, 49, 413.

Harrison, R.A. and Thompson, A.M. (eds.), 1992, *Intensity integral inversion techniques: a study in preparation for the SOHO mission*, RAL-91-092, Rutherford Appleton Laboratory.

Harrison, R.A., and 38 co-authors, 1995, *The Coronal Diagnostic Spectrometer for the Solar and Heliospheric Observatory*, Sol. Phys., 162, 233.

Hassler, D. M., Rottman, G. J. and Orrall, F. Q., 1991, *Systematic radial flows in the chromosphere, transition region, and corona of the quiet sun*, Astrophys. J., 372, 710.

Hassler, D. M. and Moran, T. G., 1994, *Broadening of Fe X (637.4Å) profiles above the limb in a coronal hole*, Space Sci. Rev., 70, 373.

Hassler, D. M., Wilhelm, K., Lemaire, P. and Schuehle, U, 1997, *Observations of Polar Plumes with the Sumer Instrument on Soho*, Sol. Phys., 175, 375.

Hassler, D. M., Dammasch, I. E., Lemaire, P., Brekke, P., Curdt, W., Mason, H. E., Vial, J. -C., and Wilhelm, K. , 1999, *Solar Wind Outflow and the Chromospheric Magnetic Network*, Science, 283, 810.

Haugan, S. V. H., 1997, CDS software note No. 47

Haugan, S. V. H., 1999, *Anomalous Line Shifts From Local Intensity Gradients on the Soho/cds nis Detector*, Sol. Phys., 185, 275.

Hubeny, V. and Judge, P. G., 1995, *Solution to the Bivariate Integral Inversion Problem: The Determination of Emission Measures Differential in Temperature and Density*, Astrophys. J. Letters, 448, L61.

Huber, M. C. E., Foukal, P. V., Noyes, R. W., Reeves, E. M., Schmahl, E. J., Timothy, J. G., Vernazza, J. E. and Withbroe, G. L., 1974, *Extreme-ultraviolet observations of coronal holes - Initial results from Skylab*, Astrophys. J., 194, L115–L118.

Insley, J. E., Moore, V. and Harrison, R. A., 1995, *The differential rotation of the corona as indicated by coronal holes*, Sol. Phys., 160, 1.

Insley,J.E., Moore,V., Harrison,R.A., 1997, *First observations of coronal hole structure and evolution using SOHO-CDS*, Sol. Phys., 175, 437.

Ipavich, F. M., Galvin, A. B., Gloeckler, G., Dovestadt, D. and Klecker, B., 1986, *Solar wind Fe and CNO measurements in high-speed flows*, J. Geophys. Res., 91, 4133.

Jakimiec, J., Sylwester, J., Lemen J.R., Mewe, R., Bentley R. B., Fludra, A., Schrijver, J., and Sylwester, B, 1984, *Differential emission measure analysis of hot-flare plasma from Solar-Maximum Mission X-ray data*, Adv. Space Res., 4, 203.

Jordan, C., 1970, *Ionization equilibria for high ions of Fe and Ni*, Mon. Not. R. Astron. Soc., 148, 17.

Jordan, C. & Wilson, R. 1971. In: *Physics of the Solar Corona*, (ed. C. J. Macris), p. 199, Reidel, Dordrecht.

Jordan, C., 1975, *The intensities of helium lines in the solar EUV spectrum*, Mon. Not. R. Astron. Soc., 170, 429.

Jordan, C. and Ayres, T. R. and Brown, A. and Linsky, J. L. and Simon, T., 1987, *The chromospheres and coronae of five G-K main-sequence stars*, Mon. Not. R. Astron. Soc., 225, 903.

Judge, P. G., Woods, T. N., Brekke, P. and Rottman, G. J., 1995, *On the Failure of Standard Emission Measure Analysis for Solar Extreme-Ultraviolet and Ultraviolet Irradiance Spectra*, Astrophys. J. Letters, 455, L85.

Jupen, C., Isler, R. C. and Trabert, E., 1993, *Solar identifications of fex-fexivl based on comparison with beam-foil tokamak and laser-produced plasma spectra*, Mon. Not. R. Astron. Soc., 264, 627.

Kahler, S. W. and Moses, D., 1990, *Discrete changes in solar coronal hole boundaries*, Astrophys. J., 362, 728.

Kastner, S. O., Rothe, E. D. and Neupert, W. M., 1974, *Limb-brightening observations from the OSO-7 satellite. I - Electron density and temperature of the non-equatorial corona from EUV lines of Fe XIV and other Fe ions*, Astron. Astrophys., 37, 339.

Kastner, S. O., Rothe, E. D. and Neupert, W. M., 1976, *Limb-brightening observations from the OSO-7 satellite. II - Comparison of Abel-inverted intensities of Fe XIV and Fe XIII EUV emission lines with predictions*, Astron. Astrophys., 53, 203.

Keenan, F. P., Warren, G. A., Doyle, J. G., Berrington, K. A. and Kingston, A. E., 1994, *Theoretical emission line strengths for O V compared to EUV solar observations*, Sol. Phys., 150, 61.

Keenan, F. P., Brekke, P., Byrne, P. B. and Greer, C. J., 1995, *The O V 1371.29 Å / 1218.35 Å emission line ratio in solar and stellar spectra*, Mon. Not. R. Astron. Soc., 276, 915.

Keenan, F. P., 1996, *Spectroscopic Diagnostics Applicable to the UV and EUV Spectra of Astrophysical Sources*, Space Sci. Rev., 75, 537.

Ko, Y. -K., Fisk, L. A., Geiss, J., Gloeckler, G., and Guhathakurta, M. , 1997, *An empirical study of the electron temperature and heavy ion velocities in the south polar coronal hole*, Sol. Phys., 171, 345.

Kohl, J. L., Weiser, H., Withbroe, G. L., Noyes, R. W., Parkinson, W. H., Reeves, E. M., Munro, R. H. and Macqueen, R. M., 1980, *Measurements of coronal kinetic temperatures from 1.5 to 3 solar radii*, Astrophys. J. Letters, 241, L117.

Kohl, J. L., Gardner, L. D., Strachan, L. and Hassler, D. M., 1994, *Ultraviolet spectroscopy of the extended solar corona during the SPARTAN 201 mission*, Space Sci. Rev., 70, 253.

Kohl, J. L., Noci, G., Antonucci, E., Tondello, G., Huber, M. C. E., Gardner, L. D., Nicolosi, P., Fineschi, S.,Raymond, J. C., Romoli, M., Spadaro, D., Siegmund, O. H. W., Benna, C., Ciaravella, A., Cranmer, S.R., Giordano, S., Karovska, M., Martin, R. Michels, J., Modigliani, A.,Naletto, G.,Panasyuk, A., Pernechele, C., Poletto, G., Smith, P. L., and Strachan, L., 1997, *Measurements of H I and O VI velocity distributions in the extended solar corona with UVCS/SOHO and UVCS/Spartan 201*, Adv. Space Res., 20, 3.

Krieger, A.S., Timothy, A.F., and Roelof, E.C., 1973, Sol. Phys., 29, 505.

Laming, J.M., Drake, J.J., Widing, K.G., 1995, *Stellar coronal abundances. 3: The solar first ionization potential effect determined from full-disk observation*, Astrophys. J., 443, 416.

Laming, J. M., Feldman, U., Schuehle, U., Lemaire, P., Curdt, W. and Wilhelm, K., 1997a, *Electron Density Diagnostics for the Solar Upper Atmosphere from Spectra Obtained by SUMER/SOHO*, Astrophys. J., 485, 911.

Laming, J. M., Feldman, U., Drake, J. J., Schuhle, U., Curdt, W., Wilhelm, K. and Lemaire, P., 1997b, *The Off-Limb Behaviour of the Solar Transition Region FIP Effect*, American Astronomical Society Meeting, 191, 7301.

Lamy, P., Llebaria, A., Koutchmy, S., Reynet, P., Molodensky, M., Howard, R., Schwenn, R., Simnett, G., 1997, *Characterisation of Polar Plumes from LASCO-C2 Images*, Proc. of the Fifth SOHO Workshop, ESA SP-404, 487.

Landi, E., Landini, M., Pike, C. D., Mason, H. E., 1997a, *SOHO CDS-NIS in-flight intensity calibration using a plasma diagnostic method*, Sol. Phys., 175, 553.

Landi, E., Del Zanna, G., Landini, M., Bromage, B.J.I., Breeveld, E.R., and Pike, C.D., 1997b, *GIS calibration study with a plasma diagnostic method*, Proc. of the Fifth SOHO workshop, ESA SP-404, 501.

Landi, E. and Landini, M., 1998a, *The Arcetri Spectral Code for thin plasmas*, Astron. Astrophys. Suppl. Ser., 133, 411.

Landi, E., Del Zanna, G., Breeveld, E. R., Landini, M., Bromage, B. J. I., and Pike, C. D., 1999a, *Relative intensity calibration of CDS-GIS detectors on SOHO using a plasma diagnostic technique*, Astron. Astrophys. Suppl. Ser., 135, 171.

Landi, E., Landini, M., Dere, K.P., Young, P.R.. and Mason, H. E., 1999, *CHIANTI - an atomic database for emission lines III – Continuum radiation and extension of the ion database*, Astron. Astrophys., 135, 339.

Landini, M. and Monsignori Fossi, B. C., 1991, *Ion equilibrium for minor components in a thin plasma*, Astron. Astrophys. Suppl. Ser., 91, 183.

Lang J., B.J. Kent, A.A. Breeveld, E.R. Breeveld, B.J.I. Bromage, J. Hollandt, J. Payne, C.D. Pike and W.T. Thompson, 1999, RAL Technical Report RAL-TR-1999-036.

Loucif, M. L. , 1994, *Giant macrospicules as possible sources of the fast solar wind*, Astron. Astrophys., 281, 95.

Macpherson, K.P., and Jordan, C., 1999, *The anomalous intensities of helium lines in the quiet solar transition region*, Mon. Not. R. Astron. Soc., in press.

Macqueen, R. M., Eddy, J. A., Gosling, J. T., Hildner, E., Munro, R. H., Newkirk, G. A. , Jr., Poland, A. I. and Ross, C. L., 1974, *The outer solar corona as observed from skylab: preliminary results*, Astrophys. J. Letters, 187, L85.

Malinovsky, L. and Heroux, M., 1973, *An analysis of the solar extreme-ultraviolet between 50 and 300 A*, Astrophys. J., 181, 1009.

Mariska, J.T., 1978, *Analysis of extreme-ultraviolet observations of a polar coronal hole*, Astrophys. J., 225, 252.

Mariska, J. T., 1980, *Relative chemical abundances in different solar regions*, Astrophys. J., 235, 268.

Mariska, J. T., 1992, *The solar Transition Region*, Cambridge Astrophysics Series no. 23, Cambridge University Press.

Marsch, E., 1991, in *Physics of the inner Heliosphere*, R. Schwenn and E. Marsch (Eds.), Vol. II, 45.

Marsch, E., Tu, C. Y., 1997, *Solar wind and chromospheric network*, Sol. Phys., 176, 87.

Martin, W. C., and Wiese, W.L., 1996, in *Atomic, Molecular, & Optical Physics Handbook*, ed. by G.W.F. Drake (AIP, Woodbury, NY, 1996) Chapter 10, pp. 135-153.

Masai, K., 1994, *Density dependence of line intensities and application to plasma diagnostic*, J. Quant. Spectrosc. Radiat. Transfer, 51, 211.

Mason, H.E., 1992, in Proc. of the First SOHO Workshop, Annapolis, 25-28 August 1992, ESA SP-348, 297.

Mason, H.E. and Monsignori Fossi, B.C., 1994, *Spectroscopic diagnostics in the VUV for solar and stellar plasmas*, The Astron. Astrophys. Rev., 6, 123.

Mason, H.E., 1995, *The application of atomic physics to the study of solar abundances and their variations*, Adv. Space Res., 15, 53.

Mason H.E., Young P.R., Pike C.D., Harrison R.A., Fludra A., Bromage B.J.I., Del Zanna G., 1997, *Application of Spectroscopic Diagnostics to Early Observations with the SOHO Coronal Diagnostic Spectrometer*, Sol. Phys., 170, 143.

Mazzotta, P., Mazzitelli, G. and Colafrancesco, 1998, *Ionization balance for optically thin plasmas: Rate coefficients for all atoms and ions of the elements H to Ni*, Astron. Astrophys. Suppl. Ser., 133, 403.

Meyer, J.-P., 1985, *Solar-stellar outer atmospheres and energetic particles, and galactic cosmic rays*, Astrophys. J. Suppl. Ser., 57, 173.

Meyer, J.-P., 1993, *Elemental abundances in active region, flares and interplanetary medium*, Adv. Space Res., 13(9), 377.

Meyer, J. P., 1996, *Abundance anomalies in the solar outer atmosphere.* The sun and beyond /edited by J. Tran Thanh Van, L. M. Celnikier, Hua Chon Trung, S. Vauclair, Proceedings of the Second Recontres du Vietnam, October 22-28, 1995. Cedex, France: Editions Frontieres, p. 27.

Monsignori Fossi B.C. and Landini M., 1991, *Models for inner corona parameters*, Adv. Space Res., 11, 281.

Munro, R. H., Withbroe, G. L., 1972, *Properties of a coronal 'Hole' derived from extreme-ultraviolet observations*, Astrophys. J., 176, 511.

Munro, R. H., and B. V. Jackson, 1977, *Physical properties of a polar coronal hole from 2 to 5 Rsun*, Astrophys. J., 213, 874.

Neupert, W. M., and Pizzo, V., 1974, J. Geophys. Res., 79, 3701.

Neupert, W. M. and Kastner, S. O., 1983, *A spectroscopic method for calibration of solar extreme ultraviolet instrumentation*, Astron. Astrophys., 128, 181.

Newton, E. K., Emslie, A. G. and Mariska, J. T., 1995, *The Velocity Differential Emission Measure: Diagnostic of Bulk Plasma Motion in Solar Flares*, Astrophys. J., 447, 915.

Noci, G., Kohl, J. L., Antonucci, E., Tondello, G., Huber, M. C. E., Fineschi, S., Gardner, L. D., Naletto, G., Nicolosi, P., Raymond, J. C., Romoli, M., Spadaro, D., Siegmund, O. H. W., Benna, C., Ciaravella, A., Giordano, S., Michels, J., Modigliani, A., Panasyuk, A., Pernechele, C., Poletto, G., Smith, P. L., and Strachan, L. , 1997, *First results from UVCS/SOHO*, Adv. Space Res., 20, 2219.

Nolte, J. T, Krieger, A. S., Timothy, A. F., Gold, A. F., Roleof, E. C., Vaiana, G. S., Lazarus, A. J., Sullivan, J. D. and McIntosh, P. S., 1976, *Coronal holes as sources of solar wind*, Sol. Phys., 46, 303.

Noyes, R. W.: 1971, in Physics of the Solar Corona, ed. C. J. Macris, D. Reidel Publ. Co., Dordrecht-Holland, p 192

Orrall, F. Q., 1981, A Monograph from the Skylab Solar Workshop I, Solar Active Regions, Colorado Univ. Press.

Penn, M. J. and Kuhn, J. R., 1994, *Ground-based detection of an infrared (Si X) coronal emission line and improved wavelengths for the infrared (Fe XIII) emission lines*, Astrophys. J., 434, 807.

Peter, H. , 1998, *Element fractionation in the solar chromosphere driven by ionization-diffusion processes*, Astron. Astrophys., 335, 691.

Phillips, K. J. H., 1992, *Guide to the sun*, Cambridge University Press.

Phillips, K. J. H., Pike, C. D., Lang, J., Watanabe, T. and Takahashi, M., 1994, *Iron K beta line emission in solar flares observed by Yohkoh and the solar abundance of iron*, Astrophys. J., 435, 888.

Phillips, K. J. H. Pike, C. D. Lang, J., Zarro, D. M., Fludra, A. Watanabe, T. and Takahashi, M., 1995, *Evidence for the equality of the solar photospheric and coronal abundance of iron*, Adv. Space Res., 15, 33.

Phillips, K. J. H., 1997, *Abundances in the solar corona*, Adv. Space Res., 20, 79.

Phillips, K. J. H., Greer, C. J., Bhatia, A. K., Coffey, I. H., Barnsley, R. and Keenan, F. P., 1997b, *Fe XVII X-ray lines in solar coronal and laboratory plasmas*, Astron. Astrophys., 324, 381.

Pinfield, D. J., Mathioudakis, M., Keenan, F. P., Phillips, K. JK. H., and Curdt, W., 1999, Astron. Astrophys., in press.

Pottasch, S.R., 1963, *The lower solar corona: interpretation of the ultraviolet spectrum*, Astrophys. J., 137, 945.

Pottasch, S.R., 1964, *On the interpretation of the solar ultraviolet emission line spectrum*, Space Sci. Rev., 3, 816.

Raymond, J. C. and Doyle, J. G., 1981a, *The energy balance in coronal holes and average quiet-sun regions*, Astrophys. J., 245, 1141.

Raymond, J. C. and Doyle, J. G., 1981b, *The energy balance in coronal holes and average quiet-sun region*, Astrophys. J., 247, 686.

Raymond, J. C., Kohl, J. L., Noci, G., Antonucci, E., Tondello, G., Huber, M. C. E., Gardner, L. D., Nicolosi, P., Fineschi, S., Romoli, M., Spadaro, D., Siegmund, O. H. W., Benna, C., Ciaravella, A., Cranmer, S., Giordano, S., Karovska, M., Martin, R., Michels, J., Modigliani, A., Naletto, G., Panasyuk, A., Pernechele, C., Poletto, G., Smith, P. L., Suleiman, R. M. and Strachan, L., 1997, *Composition of Coronal Streamers from the SOHO Ultraviolet Coronagraph Spectrometer*, Sol. Phys., 175, 645.

Reames, D. V., 1995, *Coronal abundances determined from energetic particles*, Advances in Space Research, 15, 41.

Reeves, E. M. and Parkinson, W. H., 1970, *An Atlas of Extreme-Ultraviolet Spectroheliograms from OSO-IV*, Astrophys. J. Suppl. Ser., 21, 1.

Reeves, E. M., Timothy, J. G., and Huber, M. C. E., 1974, *The photoelectric spectroheliometer on ATM*, Proc. SPIE, 44, 159.

Reeves, E. M., 1976, *The EUV chromospheric network in the quiet sun*, Sol. Phys., 46, 53.

Saba, J. L. R., 1995, *Spectroscopic measurements of element abundances in the solar corona: Variations on the FIP theme*, Advances in Space Research, 15, 13.

Saito, K., 1965, *Polar Rays of the Solar Corona, II.*, Publ. Astr. Soc. Japan, 17, 1.

Schmelz, J. T., 1993, *Elemental abundances of flaring solar plasma: enhanced neon and sulfur*, Astrophys. J., 408, 373.

Schmelz, J. T., Saba, J. L. R., Ghosh, D. and Strong, K. T., 1996, *Anomalous Coronal Neon Abundances in Quiescent Solar Active Regions*, Astrophys. J., 473, 519.

Sheeley, N.R. Jr., 1996, *Elemental abundance variations in the solar atmosphere*, Astrophys. J., 469, 423.

Spitzer, L., 1965, Physics of fully ionized gases, nterscience Tracts on Physics and Astronomy, New York: Interscience Publication.

Storey, P. J., Mason, H. E., Young, P. R., 1999, submitted to Astron. Astrophys..

Sturrock, P.A.: 1980, A Monograph from the Skyab Solar Workshop II, Solar Flares, Colorado Univ. Press

Summers,H.P., Brooks, D.H., Hammond, T.J., Lanzafame, A.C. and Lang, J., 1996, RAL Technical Report RAL-TR-96-017.

Thomas, R. J. and Neupert, W. M., 1994, *Extreme ultraviolet spectrum of a solar active region from SERTS*, Astrophys. J. Suppl. Ser., 91, 461.

Thompson, W.T., 1997, CDS software note No. 49

Timothy, A. F., Krieger, A. S. and Vaiana, G. S., 1975, *The Structure and Evolution of Coronal Holes*, Sol. Phys., 42, 135.

Tsuneta, S., Acton, L., Bruner, M., Lemen, J., Brown, W., Caravalho, R., Catura, R., Freeland, S., Jurcevich, B. and Owens, J., 1991, *The soft X-ray Telescope for the Solar-A mission*, Sol. Phys., 136, 37-67.

Tsuneta S. and Lemen, J.R, 1993, in Physics of Solar and Stellar Corona: G.S. Vaiana memorial symposium, eds J.F. Linsky, S. Serio, 113.

van de Hulst, H. C., 1950, Bull. Astron. Inst. Netherlands, 11, 135.

Veck, N. J. and Parkinson, J. H., 1981, *Solar abundances from X-ray flare observations*, Mon. Not. R. Astron. Soc., 197, 41.

Velli, M., Habbal, S. R. and Esser, R., 1994, *Coronal plumes and final scale structure in high speed solar wind streams*, Space Science Reviews, 70, 391.

Vernazza, J.E., Mason, H.E., 1978, *Density sensitivity of the solar EUV emission from boron-like ions*, Astrophys. J., 226, 720.

Vernazza, J. E. and Reeves, E. M., 1978, *Extreme ultraviolet composite spectra of representative solar features*, Astrophys. J. Suppl. Ser., 37, 485.

Walker, A. B. C. , Jr., Lindblom, J. F., Barbee, T. W. , Jr. and Hoover, R. B., 1988, *Soft X-ray images of the solar corona with a normal-incidence Cassegrain multilayer telescope*, Science, 241, 1781.

Walker, A. B. C. , Barbee, T. W. , Jr., and Hoover, R. B., 1993, in UV and X-Ray Spectroscopy of Astrophysical and Laboratory Plasmas, eds. E.H. Silver, S.M. Kahn, Camb. Univ. Press, p 193.

Wang, Y. -M. and Sheeley, N. R. , Jr., 1993, *Understanding the rotation of coronal holes*, Astrophys. J., 414, 916.

Wang, Y. -M., 1994, *Polar plumes and the solar wind*, Astrophys. J. Letters, 435, L153–L156.

Wang, Y. -M. and Sheeley, N. R. , Jr., 1995a, *Identification of low-latitude coronal plumes in extreme-ultraviolet spectroheliograms*, Astrophys. J., 446, L51-L53.

Wang, Y. -M. and Sheeley, N. R. , Jr., 1995b, *Coronal plumes and their relationship to network activity*, Astrophys. J., 452, 457.

Wang, Y. -M., Sheeley, N. R. , Jr., Dere, K. P., Duffin, R. T., Howard, R. A., Michels, D. J., Moses, J. D., Harvey, J. W., Branston, D. D., Delaboudiniere, J. -P., Artzner, G. E., Hochedez, J. F., Defise, J. M., Catura, R. C., Lemen, J. R., Gurman, J. B., Neupert, W. M., Newmark, J., Thompson, B. and Maucherat, A. , 1997, *Association of Extreme-Ultraviolet Imaging Telescope (EIT) Polar Plumes with Mixed-Polarity Magnetic Network*, Astrophys. J. Letters, 484, L75.

Wang, Y. M., 1998, *Network Activity and the Evaporative Formation of Polar Plumes*, Astrophys. J. Letters, 501, L145-+.

Warren, H. P., Mariska, J. T. and Lean, J., 1998, *A new reference spectrum for the EUV irradiance of the quiet Sun, 1, Emission measure formulation*, J. Geophys. Res., 103, 12077.

Warren, H. P. and Hassler, D. M., 1999, *The density structure of a solar polar coronal hole*, J. Geophys. Res., 104, 9781.

Widing, K. G., Feldman, U. and Bhatia, A. K., 1986, *The extreme-ultraviolet spectrum (300-630 Å) of an erupting prominence observed from Skylab*, Astrophys. J., 308, 982.

Widing, K. G. and Feldman, U., 1989, *Abundance variations in the outer solar atmosphere observed in Skylab spectroheliograms*, Astrophys. J., 344, 1046.

Widing, K. G. and Feldman, U., 1992, *Element abundances and plasma properties in a coronal polar plume*, Astrophys. J., 392, 715.

Widing, K. G. and Feldman, U., 1993, *Nonphotospheric Abundances in a Solar Active Region*, Astrophys. J., 416, 392.

Wilhelm, K. , Marsch, E. , Dwivedi, B. N., Hassler, D. M., Lemaire, P. , Gabriel, A. H. and Huber, M. C. E., 1998, *The Solar Corona above Polar Coronal Holes as Seen by SUMER on SOHO*, Astrophys. J., 500, 1023.

Withbroe, G. L. and Noyes, R. W., 1977, *Mass and energy flow in the solar chromosphere and corona*, *Ann. Rev. Astr. Ap.*, 15, 363.

Withbroe, G. L., 1978, *The thermal phase of a large solar flare*, Astrophys. J., 225, 641.

Withbroe, G. L., Kohl, J. L. and Weiser, H., 1986, *Analysis of coronal H I Lyman-alpha measurements in a polar region of the sun observed in 1979*, Astrophys. J., 307, 381.

Withbroe G.L., 1988, *The temperature structure, mass and energy flow in the corona and inner solar wind*, Astrophys. J., 325, 442.

Woo,R., 1996, *Detection of low-latitude plumes by Ulysses radio ranging measurements*, Astrophys. J. Letters, 464, L95-L98.

Young,P.R. and Mason H.E., 1997, *The Mg/Ne abundance ratio in a recently emerged flux region observed by CDS*, Sol. Phys., 175, 523.

Young, P.R., Landi, E. and Thomas R.J., 1998, *CHIANTI: an atomic database for emission lines II. Comparison with the SERTS-89 active region spectrum*, Astron. Astrophys., 329, 291.

Young, P.R., 1998t, *PhD thesis*, DAMTP, Cambridge University.

Young, P.R., Klimchuk, J.A., Mason, H.E., 1999, *Temperature and density in a polar plume - measurements from CDS/SOHO*, submitted to Astron. Astrophys.

Zirker, J.: 1977, A Monograph from the Skylab Solar Workshop I, Solar Wind, Colorado Univ. Press.

Appendix A

The results for SERTS-89

Table A.1: *Results of the analysis of the active region SERTS-89 spectrum. Second order lines are indicated with a (IIo), while those with question marks have either problems of blending, calibration or atomic physics (e.g. ionization equilibrium).*

Ion	λ_{th} (Å)	λ_{ob} (Å)	Transition	I_{ob}	I_{th}/I_{ob}	+/-	log T_{eff}	log T_{max}	frac	
C III	386.202	386.150	2s2 $^1S_0$ - 2s3p $^1P_1$	9.3	0.83	0.26	4.80	4.97		[1]
N III	374.198	374.160	2s2 2p $^2P_{1/2}$ - 2s2 3d $^2D_{3/2}$	4.9	0.95	0.61	4.99	5.08	0.60	
O III	374.164		2s22p2 $^3P_1$ - 2s22p3s $^3P_1$					5.11	0.40	
Ne III	379.307	379.306	2s2 2p4 $^1D_2$ - 2s 2p5 $^1P_1$	7.6	0.56	0.17	5.05	5.10		
O III	374.075	374.051	2s22p2 $^3P_2$ - 2s22p3s $^3P_2$	14.4	0.98	0.32	5.08	5.11	0.69	
O III	374.005		2s22p2 $^3P_0$ - 2s22p3s $^3P_1$					5.11	0.18	
O III	374.164		2s22p2 $^3P_1$ - 2s22p3s $^3P_1$					5.11	0.13	
Ne IV	421.609	421.592	2s2 2p3 $^2P_{3/2}$ - 2s 2p4 $^2S_{1/2}$	4.3	0.69	0.24	5.34	5.29	0.66	
Ne IV	421.597		2s2 2p3 $^2P_{1/2}$ - 2s 2p4 $^2S_{1/2}$					5.29	0.34	
Ne IV	388.216	388.228	2s2 2p3 $^2P_{3/2}$ - 2s 2p4 $^2P_{3/2}$	1.4	1.12	0.65	5.35	5.30	0.82	
Ne IV	388.206		2s2 2p3 $^2P_{1/2}$ - 2s 2p4 $^2P_{3/2}$					5.30	0.18	
Ne V	357.954		2s22p2 $^3P_0$ - 2s2p3 $^3S_1$					5.49	0.44	
Ne V	416.194	416.208	2s22p2 $^1D_2$ - 2s2p3 $^1D_2$	24.2	1.04	0.18	5.56	5.48		
Ne V	359.382	359.378	2s22p2 $^3P_2$ - 2s2p3 $^3S_1$	26.3	0.57	0.11	5.57	5.49		
Mg V	352.201	352.213	2p4 $^3P_1$ - 2s.2p5 $^3P_0$	4.3	0.39	0.29	5.58	5.46		?
Mg V	355.329	355.339	2p4 $^3P_1$ - 2s.2p5 $^3P_2$	11.3	0.18	0.10	5.58	5.46		?
Mg V	276.582	276.600	2p4 $^1D_2$ - 2s.2p5 $^1P_1$	22.4	0.15	0.08	5.59	5.47		?
Mg V	353.092	353.084	2p4 $^3P_2$ - 2s.2p5 $^3P_2$	10.4	0.65	0.25	5.71	5.46		?
Ne VI	433.176	433.161	2s2 2p $^2P_{1/2}$ - 2s 2p2 $^2S_{1/2}$	7.5	1.90	0.78	5.71	5.64		?
Ne VI	435.648	435.632	2s2 2p $^2P_{3/2}$ - 2s 2p2 $^2S_{1/2}$	9.8	2.42	0.62	5.71	5.64		?
Ne VI	399.821	399.837	2s2 2p $^2P_{1/2}$ - 2s 2p2 $^2P_{3/2}$	14.9	1.11	0.24	5.72	5.64		
Ne VI	401.926	401.936	2s2 2p $^2P_{3/2}$ - 2s 2p2 $^2P_{3/2}$	84.6	1.00	0.15	5.72	5.64		
Mg V	354.225	354.162	2p4 $^3P_0$ - 2s.2p5 $^3P_1$	9.0	0.19	0.10	5.74	5.46		?
Mg V	351.088	351.117	2p4 $^3P_2$ - 2s.2p5 $^3P_1$	13.1	0.18	0.06	5.76	5.46	0.89	?
Cr XIII	351.150		3s.3p $^3P_0$ - 3p2 $^3P_1$					6.19	0.10	
Mg VI	403.307	403.296	2s2.2p3 $^4S_{3/2}$ - 2s.2p4 $^4P_{5/2}$	45.6	1.09	0.17	5.76	5.65	0.62	
Ne VI	403.255		2s2 2p $^2P_{3/2}$ - 2s 2p2 $^2P_{1/2}$					5.64	0.38	
Ne VI	401.136	401.139	2s2 2p $^2P_{1/2}$ - 2s 2p2 $^2P_{1/2}$	29.9	1.16	0.19	5.78	5.64		
Mg VI	399.281	399.275	2s2.2p3 $^4S_{3/2}$ - 2s.2p4 $^4P_{1/2}$	9.3	1.12	0.24	5.79	5.65		
Mg VI	270.390	270.401	2s2.2p3 $^2D_{5/2}$ - 2s.2p4 $^2P_{3/2}$	59.1	0.26	0.08	5.79	5.66	0.88	
Mg VI	270.400		2s2.2p3 $^2D_{3/2}$ - 2s.2p4 $^2P_{3/2}$					5.66	0.12	
Mg VI	400.662	400.668	2s2.2p3 $^4S_{3/2}$ - 2s.2p4 $^4P_{3/2}$	16.2	1.40	0.26	5.81	5.65		
Na VII	353.296	353.290	2p $^2P_{3/2}$ - 2s.2p2 $^2P_{3/2}$	10.1	0.99	0.32	5.83	5.78	0.88	
Mg V	353.300		2p4 $^3P_1$ - 2s.2p5 $^3P_1$					5.46	0.12	
C IV	312.420	312.429	1s2 2s $^2S_{1/2}$ - 1s2 3p $^2P_{3/2}$	14.2	0.29	0.15	5.83	5.09	0.67	?
C IV	312.451		1s2 2s $^2S_{1/2}$ - 1s2 3p $^2P_{1/2}$					5.09	0.33	
Mg VI	293.110	293.140	2s2.2p3 $^2P_{3/2}$ - 2s.2p4 $^2P_{3/2}$	14.0	0.20	0.12	5.83	5.66		?
C IV	384.031	384.032	1s2 2p $^2P_{1/2}$ - 1s2 3d $^2D_{3/2}$	8.6	0.27	0.11	5.84	5.09		?
Al VIII	248.453	248.460	2p2 $^3P_1$ - 2s.2p3 $^3S_1$	59.7	0.34	0.20	5.85	5.93	0.48	?

[1] Previously identified as Ti XI

Table A.1: *(continued)*

Ion	λ_{th} (Å)	λ_{ob} (Å)	Transition	I_{ob}	I_{th}/I_{ob}	+/-	log T_{eff}	log T_{max}	frac	
O V	248.461		2s.2p $^1P_1$ - 2s.3s $^1S_0$					5.42	0.45	
Mg VI	314.647	314.592	2s2.2p3 $^2P_{3/2}$ - 2s.2p4 $^2S_{1/2}$	15.8	0.20	0.08	5.87	5.65	0.59	?
Mg VI	314.540		2s2.2p3 $^2P_{1/2}$ - 2s.2p4 $^2S_{1/2}$					5.65	0.33	
Mg VII	434.917	434.917	2s22p2 $^3P_2$ - 2s2p3 $^3D_3$	27.9	1.67	0.29	5.88	5.80		?
Si VII	275.353	275.377	2p4 $^3P_2$ - 2s.2p5 $^3P_2$	105.0	0.55	0.16	5.89	5.77		
Mg VI	349.163	349.162	2s2.2p3 $^2D_{5/2}$ - 2s.2p4 $^2D_{5/2}$	55.2	0.64	0.12	5.89	5.65	0.42	
Mg VI	349.124		2s2.2p3 $^2D_{3/2}$ - 2s.2p4 $^2D_{3/2}$					5.65	0.32	
Fe XI	349.046		3s2.3p4 $^3P_1$ - 3s.3p5 $^3P_0$					6.11	0.21	
Mg VII	434.720	434.691	2s22p2 $^3P_2$ - 2s2p3 $^3D_2$	2.3	2.85	1.64	5.89	5.80		?
Mg VII	431.313	431.288	2s22p2 $^3P_1$ - 2s2p3 $^3D_2$	17.6	1.96	0.43	5.89	5.80	0.78	?
Mg VII	431.188		2s22p2 $^3P_1$ - 2s2p3 $^3D_1$					5.80	0.22	
Mg VII	431.188	431.141	2s22p2 $^3P_1$ - 2s2p3 $^3D_1$	9.2	0.81	0.28	5.89	5.80		
Mg VII	429.140	429.132	2s22p2 $^3P_0$ - 2s2p3 $^3D_1$	10.9	1.07	0.27	5.89	5.80		
Mg VII	367.674	367.675	2s22p2 $^3P_2$ - 2s2p3 $^3P_2$	46.2	1.24	0.20	5.89	5.81	0.77	
Mg VII	367.683		2s22p2 $^3P_2$ - 2s2p3 $^3P_1$					5.81	0.23	
Si VII	275.667	275.617	2p4 $^3P_1$ - 2s.2p5 $^3P_1$	17.6	0.50	0.39	5.89	5.77		
Mg VII	278.402	278.407	2s22p2 $^3P_2$ - 2s2p3 $^3S_1$	114.0	0.56	0.13	5.89	5.81	0.71	
Si VII	278.443		2p4 $^3P_1$ - 2s.2p5 $^3P_2$					5.77	0.29	
Mg VII	276.154	276.148	2s22p2 $^3P_0$ - 2s2p3 $^3S_1$	21.9	0.41	0.18	5.90	5.81		
Mg VII	365.234	365.210	2s22p2 $^3P_1$ - 2s2p3 $^3P_2$	23.2	1.54	0.32	5.90	5.81	0.36	
Mg VII	365.176		2s22p2 $^3P_1$ - 2s2p3 $^3P_0$					5.81	0.33	
Mg VII	365.243		2s22p2 $^3P_1$ - 2s2p3 $^3P_1$					5.81	0.26	
Fe X	358.413	358.455	3s2.3p4(3p).3d $^4F_{9/2}$ - 3s.3p5(3p*).3d $^4F_{9/2}$	15.2	1.27	0.33	5.91	6.04	0.53	
Ne V	358.484		2s22p2 $^3P_1$ - 2s2p3 $^3S_1$					5.49	0.47	
C IV	419.713	419.718	1s2 2p $^2P_{3/2}$ - 1s2 3s $^2S_{1/2}$	12.4	0.32	0.07	5.93	5.08	0.67	?
Fe XIII	419.819		3s2 3p2 $^1S_0$ - 3s 3p3 $^3P_1$					6.20	0.18	
Ca X	419.754		3p $^2P_{3/2}$ - 3d $^2D_{5/2}$					5.82	0.15	
Mg VII	280.737	280.749	2s22p2 $^1D_2$ - 2s2p3 $^1P_1$	9.4	1.74	1.40	5.95	5.80		
Al VII	353.769	353.741	2s22p3 $^4S_{3/2}$ - 2s2p4 $^4P_{3/2}$	9.9	0.99	0.53	5.96	5.78		
Si VIII	277.054	277.045	2s22p3 $^2D_{5/2}$ - 2s2p4 $^2D_{5/2}$	85.1	0.93	0.27	5.96	5.90	0.62	
Mg VII	277.000		2s22p2 $^3P_1$ - 2s2p3 $^3S_1$					5.81	0.34	
Mg VIII	313.754	313.736	2p $^2P_{1/2}$ - 2s.2p2 $^2P_{1/2}$	80.3	0.83	0.15	5.96	5.91		
Mg VIII	436.735	436.726	2p $^2P_{3/2}$ - 2s.2p2 $^2D_{5/2}$	67.5	1.72	0.27	5.97	5.91		?
Mg VIII	430.465	430.445	2p $^2P_{1/2}$ - 2s.2p2 $^2D_{3/2}$	40.3	1.57	0.25	5.97	5.91		?
Mg VIII	315.039	315.024	2p $^2P_{3/2}$ - 2s.2p2 $^2P_{3/2}$	253.0	0.73	0.11	5.97	5.91		
Mg VIII	339.006	339.000	2p $^2P_{3/2}$ - 2s.2p2 $^2S_{1/2}$	53.8	0.78	0.15	5.97	5.92		
Na VIII	411.166	411.164	2s2 $^1S_0$ - 2s.2p $^1P_1$	26.0	1.17	0.20	5.98	5.86		
Mg VIII	317.039	317.008	2p $^2P_{3/2}$ - 2s.2p2 $^2P_{1/2}$	57.5	0.82	0.21	5.98	5.91		
Al VIII	285.469	285.449	2p2 $^1D_2$ - 2s.2p3 $^1D_2$	27.8	0.19	0.09	5.98	5.91		?
Mg VI	268.991	269.038	2s2.2p3 $^2D_{3/2}$ - 2s.2p4 $^2P_{1/2}$	37.1	0.24	0.12	5.99	5.66	0.82	?
Mn XV	269.107		3p $^2P_{1/2}$ - 3d $^2D_{3/2}$					6.32	0.18	
Si VIII	314.327	314.345	2s22p3 $^4S_{3/2}$ - 2s2p4 $^4P_{1/2}$	54.1	1.15	0.25	5.99	5.91		
Si VIII	319.826	319.839	2s22p3 $^4S_{3/2}$ - 2s2p4 $^4P_{5/2}$	113.0	1.59	0.25	5.99	5.91		
Si VIII	316.205	316.220	2s22p3 $^4S_{3/2}$ - 2s2p4 $^4P_{3/2}$	88.7	1.33	0.24	5.99	5.91		
Fe IX	244.909	244.916	3p6 $^1S_0$ - 3p5.3d $^3P_1$	162.0	0.21	0.06	6.00	5.94		?
Fe IX	241.739	241.747	3p6 $^1S_0$ - 3p5.3d $^3P_2$	195.0	0.37	0.14	6.00	5.95		?
Fe X	365.543	365.565	3s2.3p5 $^2P_{1/2}$ - 3s.3p6 $^2S_{1/2}$	43.0	1.06	0.18	6.00	6.04	0.67	
Ne V	365.603		2s22p2 $^1D_2$ - 2s2p3 $^1P_1$					5.49	0.31	
Fe IX	171.073	171.061	3p6 $^1S_0$ - 3p5.3d $^1P_1$	1510.0	1.29	0.42	6.01	5.96		(IIo)
Mg VII	319.027	319.023	2s22p2 $^1D_2$ - 2s2p3 $^1D_2$	76.4	0.45	0.08	6.02	5.80	0.85	
Ni XV	319.063		3s2.3p2 $^3P_2$ - 3s.3p3 $^3D_3$					6.36	0.15	
Fe IX	217.101	217.102	3p6 $^1S_0$ - 3p5.3d $^3D_1$	70.5	0.35	0.17	6.02	5.94	0.87	?
Fe XI	217.112		3s2.3p4 $^1S_0$ - 3s2.3p3(2d*).3d $^3P_1$					6.11	0.13	
Al IX	384.971	385.023	2s2.2p $^2P_{1/2}$ - 2s.2p2 $^2D_{3/2}$	7.0	2.15	0.65	6.05	6.03		?
Mg IX	441.199	441.221	2s.2p 3P0.0 - 2p2 3P1.0	7.7	0.59	0.22	6.07	5.98		?
Al IX	392.403	392.414	2s2.2p $^2P_{3/2}$ - 2s.2p2 $^2D_{5/2}$	15.3	1.63	0.33	6.07	6.03		
Fe X	345.723	345.735	3s2.3p5 $^2P_{3/2}$ - 3s.3p6 $^2S_{1/2}$	75.8	0.96	0.16	6.07	6.04		
Mg IX	439.176	439.173	2s.2p 3P1.0 - 2p2 3P2.0	9.4	0.61	0.17	6.07	5.98		
Mg IX	443.973	443.956	2s.2p 3P2.0 - 2p2 3P2.0	19.6	0.83	0.16	6.07	5.98		
Mg IX	448.293	448.279	2s.2p $^3P_2$ - 2p2 $^3P_1$	4.7	1.12	0.38	6.07	5.98		

Table A.1: *(continued)*

Ion	λ_{th} (Å)	λ_{ob} (Å)	Transition	I_{ob}	I_{th}/I_{ob}	+/-	log T_{eff}	log T_{max}	frac	
Mg IX	443.403	443.371	2s.2p 3P1.0 - 2p2 3P1.0	5.6	0.59	0.21	6.07	5.98		
Al IX	282.422	282.431	2s2.2p $^2P_{1/2}$ - 2s.2p2 $^2P_{1/2}$	28.4	0.49	0.23	6.07	6.03		
Fe X	257.239	257.257	3s2.3p5 $^2P_{3/2}$ - 3s2.3p4(3p).3d $^4D_{7/2}$	132.0	0.71	0.20	6.07	6.04	0.71	
Fe X	257.285		3s2.3p5 $^2P_{3/2}$ - 3s2.3p4(3p).3d $^4D_{5/2}$					6.04	0.29	
Si VIII	276.838	276.850	2s22p3 $^2D_{3/2}$ - 2s2p4 $^2D_{3/2}$	65.6	0.85	0.24	6.08	5.90	0.64	
Si VII	276.839		2p4 $^3P_0$ - 2s.2p5 $^3P_1$					5.77	0.21	
Fe XVII	276.797		2p5.3p $^3D_1$ - 2p5.3d $^1D_2$					6.59	0.12	
Fe X	174.534	174.517	3s2.3p5 $^2P_{3/2}$ - 3s2.3p4(3p).3d $^2D_{5/2}$	764.0	1.80	0.86	6.08	6.05		? (IIo)
Mg VIII	311.796	311.778	2p $^2P_{1/2}$ - 2s.2p2 $^2P_{3/2}$	79.1	0.55	0.11	6.08	5.91	0.81	?
Ni XV	311.755		3s2.3p2 $^3P_1$ - 3s.3p3 $^3D_2$					6.36	0.17	
Si IX	258.080	258.095	2s22p2 $^1D_2$ - 2s2p3 $^1D_2$	49.7	0.31	0.12	6.08	6.03		?
Si IX	349.873	349.872	2s22p2 $^3P_2$ - 2s2p3 $^3D_3$	140.0	1.03	0.16	6.09	6.03	0.88	
Si IX	349.794		2s22p2 $^3P_2$ - 2s2p3 $^3D_2$					6.03	0.11	
Si IX	345.124	345.130	2s22p2 $^3P_1$ - 2s2p3 $^3D_2$	70.9	1.20	0.21	6.09	6.03		
Si IX	296.117	296.128	2s22p2 $^3P_2$ - 2s2p3 $^3P_2$	146.0	1.15	0.27	6.09	6.03	0.77	
Si IX	296.213		2s22p2 $^3P_2$ - 2s2p3 $^3P_1$					6.03	0.23	
Si IX	292.800	292.801	2s22p2 $^3P_1$ - 2s2p3 $^3P_0$	70.6	1.43	0.36	6.09	6.03	0.36	
Si IX	292.763		2s22p2 $^3P_1$ - 2s2p3 $^3P_2$					6.03	0.34	
Si IX	292.856		2s22p2 $^3P_1$ - 2s2p3 $^3P_1$					6.03	0.30	
Si IX	344.951	344.958	2s22p2 $^3P_1$ - 2s2p3 $^3D_1$	17.3	1.26	0.33	6.09	6.03		
Si IX	341.949	341.974	2s22p2 $^3P_0$ - 2s2p3 $^3D_1$	29.4	1.29	0.25	6.09	6.03		
Si IX	296.213	296.228	2s22p2 $^3P_2$ - 2s2p3 $^3P_1$	34.0	1.13	0.87	6.09	6.03		
Mg IX	368.070	368.063	2s2 $^1S_0$ - 2s.2p $^1P_1$	1070.0	0.48	0.07	6.09	5.98		
Si VIII	216.915	216.936	2s22p3 $^2D_{5/2}$ - 2s2p4 $^2P_{3/2}$	30.6	2.30	1.78	6.10	5.91	0.75	? (IIo)
Fe XIV	216.928		3s.3p2 4P2.5 - 3s.3p(3P).3d 4D3.5					6.24	0.25	
Si IX	290.690	290.693	2s22p2 $^3P_0$ - 2s2p3 $^3P_1$	33.2	1.08	0.50	6.11	6.03		
Fe XI	341.113	341.114	3s2.3p4 $^3P_2$ - 3s.3p5 $^3P_1$	37.3	0.82	0.15	6.13	6.10		
Fe XI	356.519	356.530	3s2.3p4 $^3P_1$ - 3s.3p5 $^3P_1$	15.0	1.03	0.35	6.13	6.10		
Fe XI	369.153	369.163	3s2.3p4 $^3P_1$ - 3s.3p5 $^3P_2$	37.9	0.91	0.15	6.14	6.10		
Fe XI	352.662	352.672	3s2.3p4 $^3P_2$ - 3s.3p5 $^3P_2$	130.0	0.88	0.14	6.14	6.11		
Fe XI	406.811	406.791	3s2.3p4 $^1D_2$ - 3s.3p5 $^3P_2$	2.9	1.06	0.42	6.14	6.11		
Fe XI	188.232	188.209	3s2.3p4 $^3P_2$ - 3s2.3p3(2d*).3d $^3P_2$	1140.0	0.49	0.12	6.14	6.11		? (IIo)
Fe XI	308.548	308.575	3s2.3p4 $^1D_2$ - 3s.3p5 $^1P_1$	84.4	0.25	0.05	6.20	6.10	0.61	?
Fe XIII	308.686		3s2 3p2 $^1S_0$ - 3s 3p3 $^3S_1$					6.20	0.25	
Ni XIII	308.551		3s2.3p4 $^3P_0$ - 3s.3p5 $^3P_1$					6.29	0.11	
Fe XII	352.106	352.106	3s2.3p3 $^4S_{3/2}$ - 3s.3p4 $^4P_{3/2}$	144.0	0.85	0.13	6.20	6.16		
Fe XII	338.278	338.273	3s2.3p3 $^2D_{5/2}$ - 3s.3p4 $^2D_{5/2}$	76.6	0.35	0.06	6.20	6.16		?
Fe XII	219.437	219.428	3s2.3p3 $^2D_{5/2}$ - 3s2.3p2(3p).3d $^2P_{3/2}$	136.0	0.63	0.29	6.21	6.16		? (IIo)
Fe XII	196.648	196.618	3s2.3p3 $^2D_{5/2}$ - 3s2.3p2(1d).3d $^2D_{5/2}$	279.0	0.42	0.21	6.21	6.16		? (IIo)
Fe XII	346.852	346.857	3s2.3p3 $^4S_{3/2}$ - 3s.3p4 $^4P_{1/2}$	66.9	0.91	0.15	6.21	6.16		
C IV	384.173	384.165	1s2 2p $^2P_{3/2}$ - 1s2 3d $^2D_{5/2}$	9.5	0.51	0.14	6.21	5.09	0.69	?
Fe XX	384.220		2s2.2p3 $^4S_{3/2}$ - 2s2.2p3 $^2P_{1/2}$					6.86	0.18	
Fe XII	193.521	193.511	3s2.3p3 $^4S_{3/2}$ - 3s2.3p2(3p).3d $^4P_{3/2}$	1280.0	0.73	0.15	6.21	6.16		(IIo)
Fe XII	195.118	195.115	3s2.3p3 $^4S_{3/2}$ - 3s2.3p2(3p).3d $^4P_{5/2}$	1220.0	1.28	0.25	6.21	6.16		(IIo)
Fe XII	192.393	192.373	3s2.3p3 $^4S_{3/2}$ - 3s2.3p2(3p).3d $^4P_{1/2}$	2370.0	0.14	0.02	6.21	6.16		? (IIo)
S XII	291.367	291.359	2s.2p2 $^2D_{3/2}$ - 2p3 $^2D_{3/2}$	10.3	0.26	0.16	6.21	6.32	0.55	?[2]
Mg VI	291.363		2s2.2p3 $^2P_{1/2}$ - 2s.2p4 $^2P_{1/2}$					5.66	0.45	?
Fe XII	364.467	364.468	3s2.3p3 $^4S_{3/2}$ - 3s.3p4 $^4P_{5/2}$	233.0	0.78	0.12	6.21	6.16		
Fe XII	186.884	186.883	3s2.3p3 $^2D_{5/2}$ - 3s2.3p2(3p).3d $^2F_{7/2}$	1330.0	0.33	0.09	6.22	6.16	0.63	? (IIo)
Fe XII	186.851		3s2.3p3 $^2D_{3/2}$ - 3s2.3p2(3p).3d $^2F_{5/2}$					6.16	0.32	(IIo)
Cr XIII	328.267	328.259	3s2 $^1S_0$ - 3s.3p $^1P_1$	91.0	0.52	0.09	6.22	6.19	0.57	[3]
Al VIII	328.185		2p2 $^3P_2$ - 2s.2p3 $^3P_2$					5.92	0.33	
Si X	356.012	356.027	2p $^2P_{3/2}$ - 2s.2p2 $^2D_{5/2}$	218.0	1.00	0.15	6.22	6.13	0.88	
Si X	356.050		2p $^2P_{3/2}$ - 2s.2p2 $^2D_{3/2}$					6.13	0.12	
Si X	253.788	253.808	2p $^2P_{1/2}$ - 2s.2p2 $^2P_{3/2}$	207.0	0.36	0.10	6.22	6.13		?
Si X	258.372	258.368	2p $^2P_{3/2}$ - 2s.2p2 $^2P_{3/2}$	377.0	1.03	0.19	6.22	6.13		
Fe XII	382.866	382.854	3s2.3p3 $^2P_{3/2}$ - 3s.3p4 $^2D_{5/2}$	7.1	0.68	0.21	6.22	6.16		
Fe XIV	358.681	358.667	3s.3p2 2D2.5 - 3p3 2D2.5	72.6	0.84	0.14	6.22	6.25	0.37	
Fe XI	358.621		3s2.3p4 $^3P_0$ - 3s.3p5 $^3P_1$					6.10	0.32	

[2] Previously identified as only Mg VI

[3] Previously identified as only Cr XIII

Table A.1: *(continued)*

Ion	λ_{th} (Å)	λ_{ob} (Å)	Transition	I_{ob}	I_{th}/I_{ob}	+/-	log T_{eff}	log T_{max}	frac	
Si XI	358.652		2s.2p $^3P_1$ - 2p2 $^3P_2$					6.20	0.18	
Ne IV	358.686		2s2 2p3 $^2D_{5/2}$ - 2s 2p4 $^2P_{3/2}$					5.30	0.12	
Si X	261.063	261.049	2p $^2P_{3/2}$ - 2s.2p2 $^2P_{1/2}$	140.0	0.97	0.21	6.22	6.13		
Si X	347.403	347.406	2p $^2P_{1/2}$ - 2s.2p2 $^2D_{3/2}$	210.0	0.87	0.22	6.22	6.13		
Si X	271.983	271.992	2p $^2P_{1/2}$ - 2s.2p2 $^2S_{1/2}$	131.0	0.80	0.17	6.22	6.13		
Si X	277.255	277.268	2p $^2P_{3/2}$ - 2s.2p2 $^2S_{1/2}$	114.0	0.75	0.18	6.22	6.13		
Fe XII	291.053	291.007	3s2.3p3 $^2D_{5/2}$ - 3s.3p4 $^2P_{3/2}$	109.0	0.40	0.08	6.23	6.16	0.80	?
Fe XIV	291.050		3s.3p2 4P1.5 - 3p3 2D1.5					6.24	0.20	
Al X	332.789	332.782	2s2 $^1S_0$ - 2s.2p $^1P_1$	159.0	0.82	0.13	6.24	6.09		
S X	264.230	264.221	2s22p3 $^4S_{3/2}$ - 2s2p4 $^4P_{5/2}$	96.3	1.29	0.45	6.25	6.13		
S X	259.496	259.495	2s22p3 $^4S_{3/2}$ - 2s2p4 $^4P_{3/2}$	123.0	0.68	0.25	6.25	6.13		
S X	257.146	257.144	2s22p3 $^4S_{3/2}$ - 2s2p4 $^4P_{1/2}$	28.8	1.52	0.95	6.25	6.13		
Fe XIII	240.696	240.723	3s2 3p2 $^3P_0$ - 3s 3p3 $^3S_1$	148.0	0.84	0.36	6.27	6.20		
Fe XIV	363.750	363.753	3s.3p2 2D2.5 - 3p3 2D1.5	11.2	4.49	1.28	6.27	6.24	0.78	?
Mg VII	363.772		2s22p2 $^3P_0$ - 2s2p3 $^3P_1$					5.81	0.22	
Fe XIII	311.552	311.555	3s2 3p2 $^3P_1$ - 3s 3p3 $^3P_2$	40.8	0.47	0.13	6.27	6.20		?
Fe XIII	318.128	318.120	3s2 3p2 $^1D_2$ - 3s 3p3 $^1D_2$	96.0	0.28	0.05	6.27	6.20		?
Fe XIII	312.109	312.174	3s2 3p2 $^3P_1$ - 3s 3p3 $^3P_1$	85.9	1.02	0.18	6.27	6.20		
Fe XIII	359.642	359.644	3s2 3p2 $^3P_1$ - 3s 3p3 $^3D_2$	147.0	0.72	0.11	6.27	6.20		
Fe XIII	413.032	412.997	3s2 3p2 $^1D_2$ - 3s 3p3 $^3D_3$	6.9	0.82	0.23	6.27	6.20		
Fe XIII	368.171	368.163	3s2 3p2 $^3P_2$ - 3s 3p3 $^3D_3$	128.0	0.76	0.16	6.27	6.20		
Fe XIII	320.809	320.800	3s2 3p2 $^3P_2$ - 3s 3p3 $^3P_2$	172.0	0.79	0.13	6.28	6.20		
Fe XIII	312.872	312.868	3s2 3p2 $^3P_1$ - 3s 3p3 $^3P_0$	47.6	0.89	0.27	6.28	6.20		
Fe XIII	201.128	201.121	3s2 3p2 $^3P_1$ - 3s2 3p 3d $^3D_1$	394.0	0.87	0.32	6.28	6.21		(Ilo)
Fe XIII	348.183	348.182	3s2 3p2 $^3P_0$ - 3s 3p3 $^3D_1$	128.0	1.12	0.17	6.28	6.20		
Fe XIII	321.400	321.463	3s2 3p2 $^3P_2$ - 3s 3p3 $^3P_1$	32.9	1.32	0.32	6.28	6.20		
Fe XIII	246.211	246.195	3s2 3p2 $^3P_1$ - 3s 3p3 $^3S_1$	160.0	1.81	0.57	6.28	6.20		?
Fe XIII	251.956	251.943	3s2 3p2 $^3P_2$ - 3s 3p3 $^3S_1$	364.0	1.49	0.27	6.28	6.20		
Fe XIII	213.771	213.774	3s2 3p2 $^3P_2$ - 3s2 3p 3d $^3P_2$	58.3	3.02	1.48	6.28	6.21		? (Ilo)
Fe XIII	209.621	209.615	3s2 3p2 $^3P_1$ - 3s2 3p 3d $^3P_2$	93.7	1.90	1.05	6.28	6.21		? (Ilo)
Fe XIII	221.827	221.830	3s2 3p2 $^1D_2$ - 3s2 3p 3d $^1D_2$	152.0	1.75	0.57	6.28	6.21		? (Ilo)
Fe XIII	204.263	204.251	3s2 3p2 $^3P_1$ - 3s2 3p 3d $^1D_2$	141.0	1.04	0.32	6.28	6.21		(Ilo)[4]
Fe XIII	203.828	203.824	3s2 3p2 $^3P_2$ - 3s2 3p 3d $^3D_3$	1060.0	1.25	0.22	6.28	6.21	0.75	(Ilo)
Fe XIII	203.797		3s2 3p2 $^3P_2$ - 3s2 3p 3d $^3D_2$					6.21	0.25	
Fe XIII	359.842	359.830	3s2 3p2 $^3P_1$ - 3s 3p3 $^3D_1$	22.4	1.70	0.37	6.28	6.20		
Fe XIII	204.945	204.952	3s2 3p2 $^3P_2$ - 3s2 3p 3d $^3D_1$	348.0	0.28	0.08	6.28	6.21		? (Ilo)
Fe XIII	202.044	202.043	3s2 3p2 $^3P_0$ - 3s2 3p 3d $^3P_1$	646.0	2.00	0.39	6.28	6.21		(Ilo)
Si XI	361.412	361.406	2s.2p $^3P_0$ - 2p2 $^3P_1$	23.7	0.54	0.11	6.29	6.20	0.78	?
Fe X	361.406		3s2.3p4(3p).3d $^4F_{7/2}$ - 3s.3p5(3p*).3d $^4F_{7/2}$					6.04	0.22	
Fe XIV	429.544	429.540	3s2.3p 2P0.5 - 3s.3p2 4P1.5	3.1	1.41	0.48	6.30	6.24	0.74	[5]
Fe XII	429.520		3s2.3p3 $^2D_{3/2}$ - 3s.3p4 $^4P_{5/2}$					6.16	0.26	
Fe XV	321.802	321.782	3s3p $^3P_2$ - 3p2 $^3P_1$	35.4	0.68	0.17	6.32	6.29	0.59	[6]
Ni XIII	321.882		3s2.3p4 $^3P_1$ - 3s.3p5 $^3P_2$					6.29	0.18	
Fe X	321.732		3s2.3p4(3p).3d $^4D_{5/2}$ - 3s.3p5(3p*).3d $^4F_{7/2}$					6.04	0.16	
Fe XIV	299.413	299.427	3s.3p2 4P2.5 - 3p3 2D1.5	35.3	0.85	0.36	6.33	6.24		[7]
Fe XIV	447.331	447.343	3s2 3p $^2P_{3/2}$ - 3s 3p2 $^4P_{5/2}$	34.3	1.74	0.28	6.33	6.24		?
Fe XIV	444.257	444.241	3s2 3p $^2P_{1/2}$ - 3s 3p2 $^4P_{1/2}$	11.9	2.73	0.68	6.33	6.24		?
Si XI	365.433	365.419	2s.2p $^3P_2$ - 2p2 $^3P_2$	39.8	0.76	0.14	6.33	6.20		
Si XI	371.503	371.499	2s.2p $^3P_2$ - 2p2 $^3P_1$	14.5	0.76	0.21	6.34	6.20		
Fe XIV	219.136	219.117	3s2 3p $^2P_{3/2}$ - 3s2 3d $^2D_{5/2}$	412.0	1.26	0.23	6.34	6.24		
Fe XIV	274.200	274.209	3s2 3p $^2P_{1/2}$ - 3s 3p2 $^2S_{1/2}$	1030.0	1.01	0.16	6.34	6.25		
Fe XIV	356.641	356.649	3s2 3p $^2P_{3/2}$ - 3s 3p2 $^2D_{3/2}$	18.0	1.33	0.45	6.34	6.24		
Fe XIV	334.172	334.171	3s2 3p $^2P_{1/2}$ - 3s 3p2 $^2D_{3/2}$	642.0	1.12	0.17	6.34	6.24		
Fe XIV	264.780	264.783	3s2 3p $^2P_{3/2}$ - 3s 3p2 $^2P_{3/2}$	1040.0	0.92	0.14	6.34	6.25		
Fe XIV	252.191	252.201	3s2 3p $^2P_{1/2}$ - 3s 3p2 $^2P_{3/2}$	190.0	1.23	0.40	6.34	6.25		

[4] Previously identified as Fe XII
[5] Previously identified as only Fe XIV
[6] Previously identified as only Fe XV
[7] Previously unidentified

Table A.1: *(continued)*

Ion	λ_{th} (Å)	λ_{ob} (Å)	Transition	I_{ob}	I_{th}/I_{ob}	+/-	log T_{eff}	log T_{max}	frac		
Fe XIV	289.148	289.171	3s2 3p $^2P_{3/2}$ - 3s 3p2 $^2S_{1/2}$	74.3	1.05	0.34	6.34	6.25			
Fe XIV	270.507	270.522	3s2 3p $^2P_{3/2}$ - 3s 3p2 $^2P_{1/2}$	489.0	1.09	0.18	6.34	6.25			
Fe XIV	220.088	220.072	3s2 3p $^2P_{3/2}$ - 3s2 3d $^2D_{3/2}$	253.0	1.57	0.34	6.34	6.25		?	(Ho)
Fe XIV	211.320	211.315	3s2 3p $^2P_{1/2}$ - 3s2 3d $^2D_{3/2}$	1020.0	1.83	0.31	6.34	6.25		?	(Ho)
Si XI	303.324	303.324	2s2 $^1S_0$ - 2s.2p $^1P_1$	2930.0	0.65	0.10	6.34	6.20			
S XI	285.822	285.830	2s22p2 $^3P_1$ - 2s2p3 $^3D_2$	68.4	1.19	0.31	6.34	6.24			
Fe XIV	257.381	257.395	3s2 3p $^2P_{1/2}$ - 3s 3p2 $^2P_{1/2}$	187.0	2.05	0.44	6.34	6.25		?	
S XI	281.401	281.440	2s22p2 $^3P_0$ - 2s2p3 $^3D_1$	36.3	1.81	0.82	6.35	6.24		?	
S XI	246.895	246.887	2s22p2 $^3P_2$ - 2s2p3 $^3P_2$	104.0	0.64	0.28	6.35	6.24			
S XI	239.816	239.834	2s22p2 $^3P_0$ - 2s2p3 $^3P_1$	130.0	0.25	0.11	6.35	6.24		?	
S XI	285.587	285.578	2s22p2 $^3P_1$ - 2s2p3 $^3D_1$	53.4	0.61	0.21	6.35	6.24			
S XI	247.159	247.159	2s22p2 $^3P_2$ - 2s2p3 $^3P_1$	85.0	0.44	0.22	6.36	6.24		?	
Ni XVI	239.550	239.488	3s2 3p $^2P_{1/2}$ - 3s 3p2 $^2S_{1/2}$	174.0	0.72	0.37	6.37	6.39	0.82		
Fe XI	239.422		3s2.3p4 $^3P_2$ - 3s2.3p3(2d*).3d $^3D_3$					6.10	0.17		
Fe XV	393.980	393.969	3s2 $^1S_0$ - 3s3p $^3P_2$	16.1	0.83	0.17	6.38	6.29			
Fe XV	417.258	417.245	3s2 $^1S_0$ - 3s3p $^3P_1$	339.0	0.87	0.13	6.38	6.29			
Fe XV	372.787	372.758	3s3d $^3D_3$ - 3p3d $^3F_4$	16.2	0.15	0.04	6.38	6.29		?	
Fe XV	284.160	284.158	3s2 $^1S_0$ - 3s3p $^1P_1$	7560.0	1.28	0.19	6.38	6.29			
Fe XV	327.011	327.030	3s3p $^3P_2$ - 3p2 $^1D_2$	87.5	1.12	0.20	6.38	6.29			
S XII	299.518	299.534	2s2.2p $^2P_{3/2}$ - 2s.2p2 $^2D_{5/2}$	47.2	1.34	0.54	6.39	6.31			
S XII	288.434	288.401	2s2.2p $^2P_{1/2}$ - 2s.2p2 $^2D_{3/2}$	135.0	1.89	0.35	6.39	6.32		?	
Fe XV	292.372	292.392	3s3p $^3P_1$ - 3p2 $^3P_2$	55.8	0.51	0.19	6.39	6.29		?	
Ni XV	298.151	298.118	3s2.3p2 $^3P_0$ - 3s.3p3 $^3D_1$	41.3	0.90	0.36	6.39	6.36			
Fe XV	312.539	312.554	3s3p $^3P_1$ - 3p2 $^1D_2$	66.2	1.15	0.27	6.39	6.29	0.76		
Co XVII	312.543		3s $^2S_{1/2}$ - 3p $^2P_{3/2}$					6.43	0.23		
Cr XIV	412.052	412.039	3s $^2S_{1/2}$ - 3p $^2P_{1/2}$	30.4	0.73	0.12	6.40	6.24			
Cr XIV	389.864	389.854	3s $^2S_{1/2}$ - 3p $^2P_{3/2}$	77.3	0.58	0.09	6.40	6.24		?	
Fe XV	243.790	243.780	3s3p $^1P_1$ - 3s3d $^1D_2$	545.0	1.38	0.27	6.40	6.29	0.75		
Ar XIV	243.740		2p $^2P_{1/2}$ - 2s.2p2 $^2D_{3/2}$					6.49	0.25		
Ni XVI	288.166	288.163	3s2 3p $^2P_{1/2}$ - 3s 3p2 $^2D_{3/2}$	59.1	1.23	0.35	6.41	6.39		[8]	
S XIII	256.684	256.683	2s2 $^1S_0$ - 2s.2p $^1P_1$	527.0	2.35	0.39	6.41	6.38		?	
Fe XVI	265.014	265.018	3p $^2P_{3/2}$ - 3d $^2D_{3/2}$	84.0	0.64	0.20	6.42	6.34			
Mn XV	361.011	360.963	3s $^2S_{1/2}$ - 3p $^2P_{3/2}$	78.7	0.46	0.08	6.42	6.32			
Ni XVII	366.797	366.800	3s2 $^1S_0$ - 3s.3p $^3P_1$	21.0	0.26	0.05	6.42	6.41			
Mn XV	384.764	384.745	3s $^2S_{1/2}$ - 3p $^2P_{1/2}$	26.9	0.65	0.11	6.42	6.32			
Fe XVI	360.761	360.754	3s $^2S_{1/2}$ - 3p $^2P_{1/2}$	4320.0	0.84	0.16	6.42	6.34			
Fe XVI	335.410	335.401	3s $^2S_{1/2}$ - 3p $^2P_{3/2}$	10400.0	0.71	0.13	6.42	6.34			
Ni XVII	249.177	249.178	3s2 $^1S_0$ - 3s.3p $^1P_1$	534.0	0.97	0.18	6.42	6.41			
Ar XIII	236.272	236.335	2s2.2p2 $^3P_0$ - 2s.2p3 $^3D_1$	248.0	1.09	0.48	6.42	6.41		[9]	
Fe XVI	251.074	251.067	3p $^2P_{1/2}$ - 3d $^2D_{3/2}$	445.0	0.72	0.14	6.42	6.34			
Fe XVI	262.984	262.978	3p $^2P_{3/2}$ - 3d $^2D_{5/2}$	654.0	0.83	0.13	6.42	6.34			
Fe XIV	353.831	353.833	3s2 3p $^2P_{3/2}$ - 3s 3p2 $^2D_{5/2}$	291.0	1.36	0.21	6.42	6.24	0.69	[10]	
Ar XVI	353.920		1s2.2s $^2S_{1/2}$ - 1s2.2p $^2P_{3/2}$					6.61	0.28		
Co XVII	339.495	339.540	3s $^2S_{1/2}$ - 3p $^2P_{1/2}$	9.3	0.89	0.46	6.45	6.43			
Ni XVIII	320.565	320.558	3s $^2S_{1/2}$ - 3p $^2P_{1/2}$	152.0	1.09	0.18	6.45	6.45			
S XIV	417.660	417.640	1s2.2s $^2S_{1/2}$ - 1s2.2p $^2P_{3/2}$	184.0	3.95	0.60	6.45	6.44		?	
S XIV	445.700	445.660	1s2.2s $^2S_{1/2}$ - 1s2.2p $^2P_{1/2}$	65.5	5.23	0.81	6.46	6.44		?	
Ni XVIII	291.984	291.988	3s $^2S_{1/2}$ - 3p $^2P_{3/2}$	357.0	0.97	0.15	6.46	6.45			
Fe XVII	367.261	367.287	2p5.3s $^3P_2$ - 2p5.3p $^3D_2$	7.5	1.18	0.63	6.47	6.59			
Fe XVII	358.243	358.247	2p5.3s $^1P_1$ - 2p5.3p $^3P_1$	7.0	1.00	0.45	6.50	6.59			
Fe XVII	409.690	409.705	2p5.3s $^3P_2$ - 2p5.3p $^3S_1$	6.7	2.04	0.64	6.50	6.58		?	
Fe XVII	350.496	350.477	2p5.3s $^3P_2$ - 2p5.3p $^3D_3$	21.1	1.08	0.27	6.50	6.59			
Ar XV	221.151	221.138	2s2 $^1S_0$ - 2s.2p $^1P_1$	64.7	4.81	2.35	6.50	6.54		?	(Ho)
Fe XVII	347.850	347.814	2p5.3s $^3P_1$ - 2p5.3p $^1D_2$	14.4	1.04	0.29	6.51	6.60			
Fe XVII	254.868	254.892	2p5.3s $^3P_1$ - 2p5.3p $^1S_0$	53.7	0.99	0.49	6.51	6.60			
Ar XVI	389.135	389.075	1s2.2s $^2S_{1/2}$ - 1s2.2p $^2P_{1/2}$	12.8	4.64	0.92	6.59	6.61	0.88	?	
Fe XVII	389.081		2p5.3s $^1P_1$ - 2p5.3p $^3D_2$					6.59	0.12		
K XVI	206.253	206.267	2s2 $^1S_0$ - 2s.2p $^1P_1$	123.0	0.03	0.01	6.59	6.61		?	(Ho)

[8] Previously identified as Zn XX

[9] Previously identified as Ni XVIII

[10] Possible belnd with Ar XVI

Table A.1: *(continued)*

Ion	λ_{th} (Å)	λ_{ob} (Å)	Transition	I_{ob}	I_{th}/I_{ob}	+/-	log T_{eff}	log T_{max}	frac	
Ar XVI	353.920	353.963	1s2.2s $^2S_{1/2}$ - 1s2.2p $^2P_{3/2}$	7.7	14.50	7.12	6.60	6.61		?
Ca XVIII	344.760	344.772	1s2.2s $^2S_{1/2}$ - 1s2.2p $^2P_{1/2}$	13.6	0.96	0.35	6.73	6.75		
Ca XVIII	302.190	302.167	1s2.2s $^2S_{1/2}$ - 1s2.2p $^2P_{3/2}$	25.3	1.14	0.46	6.73	6.75		

Appendix B

The CDS observations (1996-1998)

Table B.1: *The observations 1996-1998. The columns indicate: the fits file name; the date of the start of the observation; the starting time (UT); the spectrometer used; the pointing, in Solar X and Y (arc sec from Sun centre); the CDS study name; and a comment. In case of multiple exposures, within the same CDS study, only the description for the first file is displayed.*

file	date	time	sp	pointing	study	note
s4053r00–r11	1996/08/07	12:41	NIS	(398, -802)	CHBOPT1/v1	Test for CH study
s4054r00	1996/08/07	14:05	GIS	(397, -699)	CHMAP_A/v2	Test for CH study
s4055r00	1996/08/07	14:08	GIS	(396, -742)	CHMAP_A/v2	Test for CH study
s4056r00	1996/08/07	14:10	GIS	(401, -782)	CHMAP_A/v2	Test for CH study
s4057r00	1996/08/07	14:13	GIS	(399, -823)	CHMAP_A/v2	Test for CH study
s4058r00	1996/08/07	14:16	GIS	(400, -862)	CHMAP_A/v2	Test for CH study
s4059r00	1996/08/07	14:19	GIS	(400, -901)	CHMAP_A/v2	Test for CH study
s4060r00	1996/08/07	14:22	GIS	(400, -689)	CHMAP_B/v3	Test for CH study
s4084r00	1996/08/08	21:58	GIS	(-1, 784)	CHBNDGI/v1	Test for CH study
s4097r00	1996/08/09	20:37	NIS	(61, 812)	BOUND_Y/v4	Test for CH study
s4098r00	1996/08/09	20:50	GIS	(62, 813)	NSGSCAN1/v1	Test for CH study
s4099r00–r11	1996/08/09	22:31	NIS	(62, 812)	CHBOPT2/v1	Test for CH study
s4101r00	1996/08/10	06:33	NIS	(-121, 939)	LIMB/v16	coronal hole study
s4102r00	1996/08/10	07:10	NIS	(-360, 939)	LIMB/v16	coronal hole study
s4103r00	1996/08/10	07:48	NIS	(-535, 750)	BOUND_X/v14	coronal hole boundary study
s4103r01	1996/08/10	08:24	NIS	(-534, 751)	BOUND_X/v14	coronal hole boundary study
s4103r02	1996/08/10	09:01	NIS	(-535, 750)	BOUND_X/v14	coronal hole boundary study
s4103r03	1996/08/10	09:37	NIS	(-535, 750)	BOUND_X/v14	coronal hole boundary study
s4104r00	1996/08/10	10:14	NIS	(-572, 747)	MOVIE_V1/v2	NIS Movie
s4105r00	1996/08/10	11:10	NIS	(-502, 749)	MOVIE_V1/v2	NIS Movie
s4106r00	1996/08/10	12:07	NIS	(-119, 711)	LIMB/v16	coronal hole study
s4107r00	1996/08/10	12:44	NIS	(-359, 711)	LIMB/v16	coronal hole study
s4108r00	1996/08/10	13:21	NIS	(-593, 711)	LIMB/v16	coronal hole study
s4109r00	1996/08/10	14:00	NIS	(394, 907)	LIMB/v16	coronal hole study
s4110r00	1996/08/10	14:37	NIS	(152, 918)	LIMB/v16	coronal hole study
s4111r00	1996/08/10	15:15	NIS	(623, 674)	LIMB/v16	coronal hole study
s4112r00	1996/08/10	15:52	NIS	(384, 681)	LIMB/v16	coronal hole study
s4113r00	1996/08/10	16:29	NIS	(116, 706)	LIMB/v16	coronal hole study
s4114r00	1996/08/10	18:36	NIS	(436, 803)	MOVIE_V1/v2	NI movie
s4117r00	1996/08/11	06:31	NIS	(359, -899)	LIMB/v16	S polar coronal hole mapping (NIS)
s4118r00	1996/08/11	07:08	NIS	(116, -902)	LIMB/v16	S polar coronal hole mapping (NIS)
s4119r00	1996/08/11	07:45	NIS	(-122, -902)	LIMB/v16	S polar coronal hole mapping (NIS)
s4120r00	1996/08/11	08:22	NIS	(-358, -902)	LIMB/v16	S polar coronal hole mapping (NIS)
s4121r00	1996/08/11	09:26	GIS	(201, -919)	CHMAP_A/v2	Sampled map of ch boundary (S)
s4122r00	1996/08/11	09:29	GIS	(289, -898)	CHMAP_A/v2	Sampled map of ch boundary (S)
s4123r00	1996/08/11	09:32	GIS	(361, -880)	CHMAP_A/v2	Sampled map of ch boundary (S)
s4124r00	1996/08/11	09:35	GIS	(359, -848)	CHMAP_A/v2	Sampled map of ch boundary (S)
s4125r00	1996/08/11	09:38	GIS	(361, -820)	CHMAP_A/v2	Sampled map of ch boundary (S)
s4126r00	1996/08/11	09:40	GIS	(359, -790)	CHMAP_A/v2	Sampled map of ch boundary (S)

Table B.1: *(continued)*

file	date	time	sp	pointing	study	note
s4127r00	1996/08/11	09:43	GIS	(422, -749)	CHMAP_B/v3	Sampled map of ch boundary (S)
s4128r00	1996/08/11	09:57	GIS	(294, -732)	CHMAP_B/v3	Sampled map of ch boundary (S)
s4129r00	1996/08/11	10:11	GIS	(206, -768)	CHMAP_B/v3	Sampled map of ch boundary (S)
s4130r00	1996/08/11	10:25	GIS	(92, -779)	CHMAP_B/v3	Sampled map of ch boundary (S)
s4131r00	1996/08/11	10:39	GIS	(1, -825)	CHMAP_B/v3	Sampled map of ch boundary (S)
s4132r00	1996/08/11	10:54	GIS	(-159, -768)	CHMAP_B/v3	Sampled map of ch boundary (S)
s4133r00	1996/08/11	11:08	GIS	(-272, -729)	CHMAP_B/v3	Sampled map of ch boundary (S)
s4134r00	1996/08/11	11:22	GIS	(-396, -727)	CHMAP_B/v3	Sampled map of ch boundary (S)
s4135r00	1996/08/11	11:36	GIS	(-481, -718)	CHMAP_B/v3	Sampled map of ch boundary (S)
s4136r00	1996/08/11	11:51	GIS	(-379, -860)	CHMAP_A/v2	Sampled map of ch boundary (S)
s4137r00	1996/08/11	11:54	GIS	(-330, -831)	CHMAP_A/v2	Sampled map of ch boundary (S)
s4138r00	1996/08/11	11:57	GIS	(-472, -801)	CHMAP_A/v2	Sampled map of ch boundary (S)
s4139r00	1996/08/11	12:00	GIS	(-468, -771)	CHMAP_A/v2	Sampled map of ch boundary (S)
s4140r00	1996/08/11	12:02	GIS	(-468, -740)	CHMAP_A/v2	Sampled map of ch boundary (S)
s4141r00	1996/08/11	12:05	GIS	(-501, -711)	CHMAP_A/v2	Sampled map of ch boundary (S)
s4142r00	1996/08/11	12:12	NIS	(461, -680)	NISAT_S/v2	spectral atlas
s4143r00–r11	1996/08/11	13:16	GIS	(76, -803)	HTBNDWE/v2	Test for CH study
s4145r00–r11	1996/08/11	16:15	NIS	(-420, 729)	CHBOPT2/v1	CH boundary studies (N)
s4146r00	1996/08/11	17:13	GIS	(-398, 779)	NSGSCAN1/v1	CH boundary studies (N)
s4147r00	1996/08/11	18:54	GIS	(-401, 739)	DEM_GIS/v1	CH boundary studies (N)
s4148r00	1996/08/11	20:14	NIS	(0, 729)	MOVIE_V1/v2	NIS Movie
s4149r00	1996/08/11	21:14	GIS	(0, 749)	NSGSCAN1/v1	CH boundary studies (N)
s4150r00	1996/08/11	22:55	GIS	(0, 707)	DEM_GIS/v1	CH boundary studies (N)
s4152r00	1996/08/12	06:32	GIS	(955, 0)	G2AL/v1	W limb detection
s4153r00	1996/08/12	07:06	GIS	(991, -1)	NSGSCAN1/v1	Looking off-limb W
s4154r00	1996/08/12	08:47	GIS	(1126, -1)	NSGSCAN1/v1	Looking off-limb W
s4155r00	1996/08/12	10:28	GIS	(1261, -1)	NSGSCAN1/v1	Looking off-limb W
s4156r00	1996/08/12	12:10	NIS	(954, 360)	LIMB/v16	Looking at W limb
s4157r00	1996/08/12	12:47	NIS	(954, 118)	LIMB/v16	Looking at W limb
s4158r00	1996/08/12	13:24	NIS	(953, -123)	LIMB/v16	Looking at W limb
s4159r00	1996/08/12	14:01	NIS	(952, -363)	LIMB/v16	Looking at W limb
s4160r00	1996/08/12	14:31	NIS	(179, -852)	LIMB/v16	Looking at W limb
s4161r00	1996/08/12	15:11	NIS	(421, 758)	LIMB/v16	Looking at W limb
s4162r00	1996/08/12	15:48	NIS	(180, 758)	LIMB/v16	Looking at W limb
s4163r00	1996/08/12	16:25	NIS	(0, 517)	LIMB/v16	CH boundary studies (N+S)
s4165r00–r11	1996/08/12	17:25	NIS	(49, 719)	CHBOPT2/v1	CH boundary studies (N)
s4166r00–r11	1996/08/12	18:22	NIS	(-12, 717)	CHBOPT2/v1	CH boundary studies (N)
s4167r00	1996/08/12	19:21	GIS	(0, 749)	NSGSCAN1/v1	CH boundary studies (N)
s4168r00	1996/08/12	21:01	GIS	(0, 809)	NSGSCAN1/v1	CH boundary studies (N)
s4169r00	1996/08/12	22:42	GIS	(0, 707)	DEM_GIS/v1	CH boundary studies (N)
s4171r00	1996/08/13	06:32	GIS	(-955, -2)	G2AL/v1	East limb detection
s4172r00	1996/08/13	07:32	GIS	(-1058, -1)	GEAST/v1	JOP44 E Limb
s4172r01	1996/08/13	08:03	GIS	(-1199, -1)	GEAST/v1	JOP44 E Limb
s4174r00	1996/08/13	09:48	NIS	(-957, 114)	LIMB/v16	JOP44 E Limb
s4175r00	1996/08/13	10:25	NIS	(-955, -126)	LIMB/v16	JOP44 E Limb
s4176r00	1996/08/13	11:02	NIS	(-953, -364)	LIMB/v16	JOP44 E Limb
s4177r00	1996/08/13	12:06	GIS	(-252, 725)	SPECT_1/v1	GI spectral atlas
s4178r00	1996/08/13	15:44	GIS	(-253, 763)	NSGSCAN1/v1	CH boundary studies (N)
s4179r00–r11	1996/08/13	17:25	NIS	(-234, 741)	CHBOPT2/v1	CH boundary studies (N)
s4180r00	1996/08/13	18:30	NIS	(0, 719)	MOVIE_V1/v2	NIS Movie
s4181r00	1996/08/13	19:31	GIS	(0, 749)	NSGSCAN1/v1	CH boundary studies (N)
s4182r00	1996/08/13	21:12	GIS	(0, 808)	NSGSCAN1/v1	CH boundary studies (N)
s4183r00	1996/08/13	22:52	GIS	(0, 707)	DEM_GIS/v1	CH boundary studies (N)
s4192r00	1996/08/14	19:46	GIS	(0, 721)	HTBNDSS1/v2	CH boundary studies (N) - test
s4192r01	1996/08/14	19:57	GIS	(0, 719)	HTBNDSS1/v2	CH boundary studies (N) - test
s4193r00–r11	1996/08/14	20:09	NIS	(0, 720)	CHBOPT2/v1	CH boundary studies (N)
s4194r00	1996/08/14	21:32	GIS	(0, 780)	NSGSCAN1/v1	CH boundary studies (N)
s4195r00	1996/08/14	22:55	GIS	(0, 740)	DEM_GIS/v1	CH boundary studies (N)
s4197r00	1996/08/15	06:32	GIS	(955, 0)	G2AL/v1	West limb detection
s4198r00	1996/08/15	07:31	GIS	(1009, -42)	BROAD/v1	Line broadening
s4199r00	1996/08/15	10:22	NIS	(954, 360)	LIMB/v16	JOP44 W Limb
s4200r00	1996/08/15	10:59	NIS	(954, 118)	LIMB/v16	JOP44 W Limb

Table B.1: *(continued)*

file	date	time	sp	pointing	study	note
s4201r00	1996/08/15	11:36	NIS	(953, -123)	LIMB/v16	JOP44 W Limb
s4202r00	1996/08/15	12:14	NIS	(952, -363)	LIMB/v16	JOP44 W Limb
s4206r00-r11	1996/08/15	14:40	NIS	(16, 716)	CHBOPT2/v1	CH boundary studies (N)
s4207r00-r11	1996/08/15	15:37	NIS	(-41, 718)	CHBOPT2/v1	CH boundary studies (N)
s4208r00	1996/08/15	17:00	GIS	(1, 761)	NSGSCAN1/v1	CH boundary studies (N)
s4209r00	1996/08/15	18:41	GIS	(0, 728)	DEM_GIS/v1	CH boundary studies (N)
s4211r00	1996/08/16	02:34	GIS	(-451, 883)	CHBNDGI/v1	CH boundary studies (NE limb)
s4212r00-r11	1996/08/16	09:17	NIS	(-449, 809)	CHBOPT2/v1	CH boundary studies (NE limb)
s4213r00-r11	1996/08/16	10:15	NIS	(-510, 809)	CHBOPT2/v1	CH boundary studies (NE limb)
s4214r00-r11	1996/08/16	11:12	NIS	(-571, 807)	CHBOPT2/v1	CH boundary studies (NE limb)
s4215r00	1996/08/16	12:11	NIS	(360, 817)	LIMB/v16	CH boundary studies (N)
s4216r00	1996/08/16	12:49	NIS	(119, 819)	LIMB/v16	CH boundary studies (N)
s4217r00	1996/08/16	13:26	NIS	(-122, 818)	LIMB/v16	CH boundary studies (N)
s4218r00	1996/08/16	14:03	NIS	(-360, 817)	LIMB/v16	CH boundary studies (N)
s4219r00	1996/08/16	14:42	GIS	(42, 769)	NSGSCAN1/v1	CH boundary studies (N)
s4220r00-r11	1996/08/16	16:23	NIS	(41, 798)	CHBOPT2/v1	CH boundary studies (N)
s4227r00	1996/08/16	20:21	GIS	(0, 799)	NSGSCAN1/v1	CH boundary studies (N)
s4228r00	1996/08/16	22:02	GIS	(0, 757)	DEM_GIS/v1	CH boundary studies (N)
s4231r00	1996/08/17	06:33	NIS	(360, 939)	LIMB/v16	JOP 44 / North CH
s4232r00	1996/08/17	07:10	NIS	(119, 939)	LIMB/v16	JOP 44 / North CH
s4233r00	1996/08/17	07:48	NIS	(-122, 939)	LIMB/v16	JOP 44 / North CH
s4234r00	1996/08/17	08:25	NIS	(-362, 938)	LIMB/v16	JOP 44 / North CH
s4235r00	1996/08/17	09:03	NIS	(549, 778)	MOVIE_V1/v2	JOP44/CH Bound (NW)
s4236r00	1996/08/17	10:00	NIS	(621, 697)	LIMB/v16	JOP 44 / North CH Boundary
s4237r00	1996/08/17	10:37	NIS	(357, 697)	LIMB/v16	JOP 44 / North CH Boundary
s4238r00	1996/08/17	11:15	NIS	(117, 697)	LIMB/v16	JOP 44 / North CH Boundary
s4239r00	1996/08/17	12:19	GIS	(0, -2)	SPECT_1/v1	GIS ATLAS
s4240r00	1996/08/17	15:33	NIS	(-120, 941)	LIMB/v16	JOP 44/ NE Coronal Hole
s4241r00	1996/08/17	16:11	NIS	(-362, 938)	LIMB/v16	JOP 44/ NE Coronal Hole
s4242r00	1996/08/17	16:48	NIS	(-119, 711)	LIMB/v16	JOP 44/ NE Coronal Hole
s4243r00	1996/08/17	17:25	NIS	(-362, 710)	LIMB/v16	JOP 44/ NE Coronal Hole
s4244r00	1996/08/17	18:02	NIS	(-600, 709)	LIMB/v16	JOP 44/ NE Coronal Hole
s4245r00-r11	1996/08/17	18:40	NIS	(19, 758)	CHBOPT2/v2	Coronal Hole Studies (N)
s4246r00	1996/08/17	20:03	GIS	(-1, 749)	DEM_GIS/v1	DEM - GIS
s4247r00	1996/08/17	21:04	GIS	(0, 788)	NSGSCAN1/v1	N-S CH scan
s4248r00	1996/08/17	23:11	GIS	(0, -2)	GIMCP_1B/v2	GIS MCP 1
s4249r00	1996/08/17	23:40	GIS	(0, -2)	GIMCP_2/v1	GIS MCP 2
s4251r00	1996/08/18	06:31	NIS	(359, -899)	LIMB/v16	JOP 44 South CH hole
s4252r00	1996/08/18	07:08	NIS	(115, -903)	LIMB/v16	JOP 44 South CH hole
s4253r00	1996/08/18	07:45	NIS	(-121, -901)	LIMB/v16	JOP 44 South CH hole
s4254r00	1996/08/18	08:22	NIS	(-361, -904)	LIMB/v16	JOP 44 South CH hole
s4255r00	1996/08/18	09:36	GIS	(1,-1020)	NSGSCAN1/v1	CH Scan below south limb JOP 44
s4256r00	1996/08/18	11:17	GIS	(1, -960)	NSGSCAN1/v1	CH Scan below south limb JOP 44
s4257r00-r11	1996/08/18	13:03	NIS	(250, 748)	CHBOPT2/v2	North Coronal Boundary Study
s4258r00	1996/08/18	14:02	GIS	(226, 772)	NSGSCAN1/v1	North Coronal Boundary Study
s4259r00	1996/08/18	15:42	GIS	(232, 733)	DEM_GIS/v1	North Coronal Boundary Study
s4260r00	1996/08/18	16:47	NIS	(356, -902)	LIMB/v16	JOP 44 South CH hole
s4261r00	1996/08/18	17:24	NIS	(117, -901)	LIMB/v16	JOP 44 South CH hole
s4262r00	1996/08/18	18:01	NIS	(-123, -903)	LIMB/v16	JOP 44 South CH hole
s4263r00	1996/08/18	18:38	NIS	(-362, -901)	LIMB/v16	JOP 44 South CH hole
s4264r00	1996/08/18	19:17	NIS	(1, 2)	NISAT_S/v2	NIS Atlas
s4265r00-r11	1996/08/18	20:22	NIS	(-46, 830)	CHBOPT2/v2	Base of Polar Plume
s4266r00	1996/08/18	21:20	GIS	(-74, 840)	NSGSCAN1/v1	Base of Polar Plume
s4267r00	1996/08/18	23:00	GIS	(-68, 843)	DEM_GIS/v1	Base of Polar Plume
s4269r00	1996/08/19	07:18	GIS	(967, 0)	G2AL/v1	JOP 44 West Limb
s4270r00	1996/08/19	08:17	GIS	(1070, 0)	GWEST/v1	JOP 44 West Limb
s4270r01	1996/08/19	08:48	GIS	(1212, 0)	GWEST/v1	JOP 44 West Limb
s4271r00	1996/08/19	09:56	NIS	(965, 356)	LIMB/v16	JOP 44 West Limb
s4272r00	1996/08/19	10:33	NIS	(965, 117)	LIMB/v16	JOP 44 West Limb
s4273r00	1996/08/19	11:11	NIS	(964, -122)	LIMB/v16	JOP 44 West Limb
s4274r00	1996/08/19	11:48	NIS	(964, -359)	LIMB/v16	JOP 44 West Limb
s4275r00	1996/08/19	12:51	GIS	(1017, 0)	BROAD/v1	West Limb JOP 44 support

Table B.1: *(continued)*

file	date	time	sp	pointing	study	note
s4284r00-r11	1996/08/19	18:31	NIS	(17, 730)	CHBOPT2/v2	Meridian CH Boundary
s4285r00	1996/08/19	19:54	GIS	(-1, 720)	NSGSCAN1/v1	Meridian CH Boundary
s4286r00	1996/08/19	21:35	GIS	(0, 679)	DEM_GIS/v1	Meridian CH Boundary
s4287r00	1996/08/19	22:37	NIS	(0, 712)	MOVIE_V1/v2	Meridian CH Boundary
s4290r00	1996/08/20	13:02	GIS	(-966, -3)	G2AL/v1	JOP 44 East Limb
s4291r00	1996/08/20	14:02	GIS	(-1070, 0)	GEAST/v1	JOP 44 East Limb
s4291r01	1996/08/20	14:33	GIS	(-1215, -3)	GEAST/v1	JOP 44 East Limb
s4292r00	1996/08/20	15:40	NIS	(-965, 356)	LIMB/v16	JOP 44 East Limb
s4293r00	1996/08/20	16:18	NIS	(-966, 116)	LIMB/v16	JOP 44 East Limb
s4294r00	1996/08/20	16:55	NIS	(-965, -122)	LIMB/v16	JOP 44 East Limb
s4295r00	1996/08/20	17:32	NIS	(-964, -360)	LIMB/v16	JOP 44 East Limb
s4296r00-r11	1996/08/20	19:42	NIS	(306, 511)	CHBOPT2/v2	Meridian CH Boundary
s4297r00-r11	1996/08/20	20:39	NIS	(23, 797)	CHBOPT2/v2	Meridian CH Boundary
s4298r00-r11	1996/08/20	21:37	NIS	(29, 799)	CHBOPT2/v2	Meridian CH Boundary
s4299r00	1996/08/20	22:34	NIS	(-10, 799)	MOVIE_V1/v2	Meridian CH Boundary
s4312r00	1996/08/21	23:30	GIS	(478, -960)	G2AL/v1	JOP44 West Limb
s4313r00	1996/08/22	00:29	GIS	(1018, -427)	GWEST/v1	JOP44 W Limb
s4313r01	1996/08/22	01:00	GIS	(1201, 0)	GWEST/v1	JOP44 W Limb
s4314r00	1996/08/22	02:08	NIS	(953, 357)	LIMB/v16	JOP44 West Limb
s4315r00	1996/08/22	02:46	NIS	(955, 78)	LIMB/v16	JOP44 West Limb
s4316r00	1996/08/22	03:23	NIS	(953, -123)	LIMB/v16	JOP44 West Limb
s4317r00	1996/08/22	04:00	NIS	(951, -362)	LIMB/v16	JOP44 West Limb
s4322r00-r11	1996/08/22	13:25	NIS	(9, 779)	CHBOPT2/v2	Meridian CH Boundary
s4323r00-r11	1996/08/22	14:23	NIS	(-51, 777)	CHBOPT2/v2	Meridian CH Boundary
s4324r00-r11	1996/08/22	15:20	NIS	(-112, 778)	CHBOPT2/v2	Meridian CH Boundary
s4325r00	1996/08/22	16:43	GIS	(-68, 728)	CHBNDGI/v1	Meridian CH Boundary
s4341r00	1996/08/23	19:02	NIS	(-50, 867)	LIMB/v16	JOP 48 /Plumes
s4342r00	1996/08/23	19:38	NIS	(-49, 866)	LIMB/v16	JOP 48 /Plumes
s4343r00-r11	1996/08/23	20:15	NIS	(-47, 869)	CHBOPT2/v2	JOP 48 /Plumes
s4344r00	1996/08/23	21:13	NIS	(-45, 867)	LIMB/v16	JOP 48 /Plumes
s4345r00	1996/08/23	21:49	NIS	(-43, 869)	LIMB/v16	JOP 48 /Plumes
s4346r00-r11	1996/08/23	22:26	NIS	(-41, 865)	CHBOPT2/v2	JOP 48 /Plumes
s4347r00	1996/08/23	23:23	NIS	(-40, 868)	LIMB/v16	JOP 48 /Plumes
s4348r00	1996/08/24	00:00	NIS	(-38, 866)	LIMB/v16	JOP 48 /Plumes
s4349r00-r11	1996/08/24	00:37	NIS	(-35, 869)	CHBOPT2/v2	JOP 48 /Plumes
s4350r00	1996/08/24	02:00	GIS	(-38, 856)	NSGSCAN1/v1	JOP 48 /Plumes
s4358r00	1996/08/24	16:02	NIS	(368, 932)	LIMB/v16	JOP44/CH Bound (NW)
s4359r00	1996/08/24	16:39	NIS	(126, 930)	LIMB/v16	JOP44/CH Bound (NW)
s4360r00	1996/08/24	17:16	NIS	(-115, 931)	LIMB/v16	JOP44/CH Bound (NW)
s4361r00	1996/08/24	17:54	NIS	(-358, 932)	LIMB/v16	JOP44/CH Bound (NW)
s4362r00	1996/08/24	18:32	NIS	(369, 932)	LIMB/v16	JOP44/CH Bound (NW)
s4363r00	1996/08/24	19:09	NIS	(127, 931)	LIMB/v16	JOP44/CH Bound (NW)
s4364r00	1996/08/24	19:46	NIS	(367, 689)	LIMB/v16	JOP44/CH Bound (NW)
s4365r00	1996/08/24	20:23	NIS	(122, 689)	LIMB/v16	JOP44/CH Bound (NW)
s4367r00	1996/08/25	03:28	NIS	(367, 931)	LIMB/v16	JOP44/CH Bound (NE)
s4368r00	1996/08/25	04:06	NIS	(126, 930)	LIMB/v16	JOP44/CH Bound (NE)
s4369r00	1996/08/25	04:43	NIS	(-116, 930)	LIMB/v16	JOP44/CH Bound (NE)
s4370r00	1996/08/25	05:20	NIS	(-356, 930)	LIMB/v16	JOP44/CH Bound (NE)
s4371r00	1996/08/25	05:57	NIS	(-113, 931)	LIMB/v16	JOP44/CH Bound (NE)
s4372r00	1996/08/25	06:35	NIS	(-358, 932)	LIMB/v16	JOP44/CH Bound (NE)
s4373r00	1996/08/25	07:12	NIS	(-107, 697)	LIMB/v16	JOP44/CH Bound (NE)
s4374r00	1996/08/25	07:49	NIS	(-355, 688)	LIMB/v16	JOP44/CH Bound (NE)
s4375r00	1996/08/25	08:33	NIS	(366, -947)	LIMB/v16	JOP44/CH BOUND (SW)
s4376r00	1996/08/25	09:10	NIS	(120, -950)	LIMB/v16	JOP44/CH BOUND (SW)
s4377r00	1996/08/25	09:47	NIS	(-114, -950)	LIMB/v16	JOP44/CH BOUND (SW)
s4378r00	1996/08/25	10:24	NIS	(-356, -948)	LIMB/v16	JOP44/CH BOUND (SW)
s4381r00	1996/08/25	12:56	NIS	(-288, 295)	LIMB/v16	Activity Boundary
s4382r00	1996/08/25	13:33	NIS	(-279, 77)	LIMB/v16	Activity Boundary
s4383r00	1996/08/25	14:10	NIS	(-320, -143)	LIMB/v16	Activity Boundary
s4384r00	1996/08/25	15:13	GIS	(-279, 80)	G2AL/v1	Activity Boundary
s4385r00	1996/08/25	15:47	GIS	(-340, 79)	G2AL/v1	Activity Boundary
s4386r00-r11	1996/08/25	16:22	NIS	(-258, 77)	CHBOPT2/v2	Activity Boundary

Table B.1: *(continued)*

file	date	time	sp	pointing	study	note
s4387r00	1996/08/25	17:42	NIS	(366, -947)	LIMB/v16	JOP44/CH BOUND (SW)
s4388r00	1996/08/25	18:19	NIS	(121, -949)	LIMB/v16	JOP44/CH BOUND (SW)
s4389r00	1996/08/25	18:56	NIS	(-114, -950)	LIMB/v16	JOP44/CH BOUND (SW)
s4390r00	1996/08/25	19:33	NIS	(-356, -948)	LIMB/v16	JOP44/CH BOUND (SW)
s4392r00	1996/08/26	02:47	GIS	(954, -1)	G2AL/v1	JOP 44/West Limb
s4393r00	1996/08/26	03:47	GIS	(1058, -2)	GWEST/v1	JOP 44/West Limb
s4393r01	1996/08/26	04:18	GIS	(1201, 0)	GWEST/v1	JOP 44/West Limb
s4394r00	1996/08/26	05:25	NIS	(953, 357)	LIMB/v16	JOP 44/West Limb
s4397r00	1996/08/26	07:17	NIS	(952, -363)	LIMB/v16	JOP 44/West Limb
s4404r00	1996/08/26	11:21	NIS	(-64, 299)	LIMB/v16	Equatorial Coronal Hole
s4405r00	1996/08/26	11:58	NIS	(-72, 79)	LIMB/v16	Equatorial Coronal Hole
s4406r00	1996/08/26	12:35	NIS	(-104, -132)	LIMB/v16	Equatorial Coronal Hole
s4407r00	1996/08/26	13:12	NIS	(-268, -325)	LIMB/v16	Equatorial Coronal Hole
s4408r00	1996/08/26	13:51	GIS	(-64, 79)	G2AL/v1	Equatorial Coronal Hole
s4409r00	1996/08/26	14:25	GIS	(-126, 81)	G2AL/v1	Equatorial Coronal Hole
s4410r00–r11	1996/08/26	15:00	NIS	(-42, 79)	CHBOPT2/v2	Equatorial Coronal Hole
s4411r00	1996/08/26	16:10	NIS	(-71, 80)	BOUND_X/v14	Equatorial Coronal Hole
s4412r00	1996/08/26	16:46	NIS	(-63, 81)	BOUND_X/v14	Equatorial Coronal Hole
s4413r00	1996/08/26	17:23	NIS	(-60, 78)	BOUND_X/v14	Equatorial Coronal Hole
s4414r00	1996/08/26	18:00	NIS	(-54, 84)	BOUND_X/v14	Equatorial Coronal Hole
s4415r00	1996/08/26	18:36	NIS	(-46, 76)	MOVIE_V1/v2	Equatorial Coronal Hole
s4416r00	1996/08/26	19:33	NIS	(-48, 83)	BOUND_Y/v4	Equatorial Coronal Hole
s4417r00	1996/08/26	19:45	NIS	(-45, 80)	BOUND_Y/v4	Equatorial Coronal Hole
s4418r00	1996/08/26	19:57	NIS	(-44, 82)	BOUND_Y/v4	Equatorial Coronal Hole
s4419r00	1996/08/26	20:09	NIS	(-43, 79)	BOUND_Y/v4	Equatorial Coronal Hole
s4420r00	1996/08/26	20:21	NIS	(-40, 82)	BOUND_Y/v4	Equatorial Coronal Hole
s4422r00	1996/08/26	20:45	NIS	(-36, 82)	BOUND_Y/v4	Equatorial Coronal Hole
s4431r00	1996/08/27	06:32	GIS	(59, 81)	G2AL/v2	Equatorial Coronal Hole
s4432r00	1996/08/27	08:46	GIS	(128, 78)	G2AL/v2	Equatorial Coronal Hole
s4433r00	1996/08/27	11:01	NIS	(107, 78)	NISAT_S5/v2	Equatorial Coronal Hole
s4434r00–r11	1996/08/27	12:12	NIS	(163, 78)	CHBOPT2/v2	Equatorial Coronal Hole
s4435r00	1996/08/27	13:22	GIS	(958, 2)	G2AL/v1	JOP 44/East Limb
s4436r00	1996/08/27	14:25	GIS	(-1057, -1)	GEAST/v1	JOP 44/East Limb
s4436r01	1996/08/27	14:56	GIS	(-1204, -3)	GEAST/v1	JOP 44/East Limb
s4437r00	1996/08/27	16:04	NIS	(-954, 358)	LIMB/v16	JOP 44/East Limb
s4438r00	1996/08/27	16:41	NIS	(-956, 115)	LIMB/v16	JOP 44/East Limb
s4439r00	1996/08/27	17:18	NIS	(-958, -125)	LIMB/v16	JOP 44/East Limb
s4440r00	1996/08/27	17:55	NIS	(-952, -363)	LIMB/v16	JOP 44/East Limb
s4448r00–r11	1996/08/28	08:09	NIS	(350, 85)	CHBOPT2/v2	Equatorial Coronal Hole
s4452r00	1996/08/28	11:57	NIS	(361, 87)	LIMB/v16	Equatorial Coronal Hole
s4453r00	1996/08/28	12:34	NIS	(316, -130)	LIMB/v16	Equatorial Coronal Hole
s4456r00	1996/08/29	06:44	NIS	(491, 27)	LIMB/v16	Equatorial Coronal Hole
s4457r00	1996/08/29	07:21	NIS	(457, 265)	LIMB/v16	Equatorial Coronal Hole
s4465r00	1996/08/29	10:26	NIS	(519, 22)	LIMB/v16	Equatorial Coronal Hole
s4466r00	1996/08/29	11:03	NIS	(486, 264)	LIMB/v16	Equatorial Coronal Hole
s4467r00	1996/08/29	11:40	NIS	(490, 261)	COHO22/v8	Equatorial Coronal Hole
s4467r01	1996/08/29	12:09	NIS	(490, 261)	COHO22/v8	Equatorial Coronal Hole
s4468r00	1996/08/29	12:37	NIS	(495, 266)	LIMB/v16	Equatorial Coronal Hole
s4469r00–r11	1996/08/29	13:14	NIS	(560, 99)	CHBOPT2/v2	Equatorial Coronal Hole
s4471r00	1996/08/29	15:31	NIS	(535, 281)	NISAT_S5/v2	Equatorial Coronal Hole
s4472r00	1996/08/29	17:08	GIS	(543, 281)	NSGSCAN1/v1	Equatorial Coronal Hole
s4473r00	1996/08/29	18:46	GIS	(954, -1)	G2AL/v1	JOP 44/West Limb
s4474r00	1996/08/29	19:45	GIS	(1058, -2)	GWEST/v1	JOP 44/West Limb
s4474r01	1996/08/29	20:16	GIS	(1201, 0)	GWEST/v1	JOP 44/West Limb
s4475r00	1996/08/29	21:24	NIS	(953, 357)	LIMB/v16	JOP 44/West Limb
s4476r00	1996/08/29	22:01	NIS	(953, 118)	LIMB/v16	JOP 44/West Limb
s4477r00	1996/08/29	22:39	NIS	(954, -122)	LIMB/v16	JOP 44/West Limb
s4478r00	1996/08/29	23:16	NIS	(951, -363)	LIMB/v16	JOP 44/West Limb
s4480r00	1996/08/30	06:42	NIS	(606, 290)	LIMB/v16	Equatorial Coronal Hole
s4481r00–r11	1996/08/30	07:19	NIS	(641, 292)	CHBOPT2/v2	Equatorial Coronal Hole
s4488r00	1996/08/30	13:26	GIS	(955, -2)	G2AL/v1	JOP 44/East Limb
s4490r00	1996/08/30	16:41	NIS	(-953, 116)	LIMB/v16	JOP 44/East Limb

Table B.1: *(continued)*

file	date	time	sp	pointing	study	note
s4491r00	1996/08/30	17:18	NIS	(-958, -125)	LIMB/v16	JOP 44/East Limb
s4492r00	1996/08/30	17:56	NIS	(-952, -363)	LIMB/v16	JOP 44/East Limb
s4493r00	1996/08/30	19:02	NIS	(303, 885)	LIMB/v16	JOP 44/East Limb
s4493r01	1996/08/30	19:38	NIS	(303, 885)	LIMB/v16	JOP 44/East Limb
s4494r00-r11	1996/08/30	20:15	NIS	(330, 882)	CHBOPT2/v2	JOP 48 /Plumes
s4495r00	1996/08/30	21:38	GIS	(308, 883)	NSGSCAN1/v1	JOP 48 /Plumes
s4496r00	1996/08/30	23:20	NIS	(708, 290)	LIMB/v16	Equatorial Coronal Hole
s4497r00-r11	1996/08/31	00:00	NIS	(745, 292)	CHBOPT2/v2	Equatorial Coronal Hole
s4498r00	1996/08/31	00:58	NIS	(321, 882)	LIMB/v16	JOP 48 /Plumes
s4498r01	1996/08/31	01:35	NIS	(321, 882)	LIMB/v16	JOP 48 /Plumes
s4499r00-r11	1996/08/31	02:12	NIS	(336, 882)	CHBOPT2/v2	JOP 48 /Plumes
s4512r00	1996/08/31	15:02	NIS	(362, 957)	LIMB/v16	JOP44/CH Bound
s4513r00	1996/08/31	15:39	NIS	(120, 957)	LIMB/v16	JOP44/CH Bound
s4514r00	1996/08/31	16:16	NIS	(-123, 956)	LIMB/v16	JOP44/CH Bound
s4515r00	1996/08/31	16:53	NIS	(-366, 952)	LIMB/v16	JOP44/CH Bound
s4516r00	1996/08/31	17:32	NIS	(602, 700)	LIMB/v16	JOP44/CH Bound
s4517r00	1996/08/31	18:18	NIS	(599, 720)	LIMB/v16	JOP44/CH Bound
s4518r00	1996/08/31	18:55	NIS	(358, 719)	LIMB/v16	JOP44/CH Bound
s4519r00	1996/08/31	19:33	NIS	(119, 715)	LIMB/v16	JOP44/CH Bound
s4520r00	1996/08/31	20:10	NIS	(-121, 715)	LIMB/v16	JOP44/CH Bound
s4521r00	1996/08/31	20:47	NIS	(-361, 718)	LIMB/v16	JOP44/CH Bound
s4522r00	1996/08/31	21:24	NIS	(-601, 718)	LIMB/v16	JOP44/CH Bound
s4523r00	1996/08/31	22:28	GIS	(1, 999)	G2AL/v2	JOP44/CH Bound
s4529r00	1996/09/01	10:31	NIS	(358, -940)	LIMB/v16	JOP44/CH Bound
s4530r00	1996/09/01	11:09	NIS	(113, -943)	LIMB/v16	JOP44/CH Bound
s4531r00	1996/09/01	11:46	NIS	(-121, -943)	LIMB/v16	JOP44/CH Bound
s4532r00	1996/09/01	12:23	NIS	(-361, -942)	LIMB/v16	JOP44/CH Bound
s4533r00	1996/09/01	13:01	GIS	(1, -969)	G2AL/v2	JOP44/CH Bound (NW)
s4534r00	1996/09/01	15:15	GIS	(0,-1002)	G2AL/v2	JOP44/CH Bound (NW)
s4535r00	1996/09/01	17:29	GIS	(-1,-1033)	G2AL/v2	JOP44/CH Bound (NW)
s4536r00	1996/09/01	19:44	NIS	(0,-1000)	NISAT_S5/v2	JOP44/CH BOUND
s4538r00	1996/09/02	04:00	GIS	(955, -2)	G2AL/v1	JOP 44 West Limb
s4539r00	1996/09/02	04:59	GIS	(1058, -2)	GWEST/v1	JOP 44 West Limb
s4539r01	1996/09/02	05:30	GIS	(1201, 0)	GWEST/v1	JOP 44 West Limb
s4540r00	1996/09/02	06:38	NIS	(953, 357)	LIMB/v16	JOP 44 West Limb
s4541r00	1996/09/02	07:15	NIS	(952, 117)	LIMB/v16	JOP 44 West Limb
s4542r00	1996/09/02	07:52	NIS	(954, -122)	LIMB/v16	JOP 44 West Limb
s4543r00	1996/09/02	08:29	NIS	(950, -363)	LIMB/v16	JOP 44 West Limb
s4544r00-r11	1996/09/02	09:08	NIS	(115, 810)	CHBOPT2/v2	Coronal hole observations
s4545r00	1996/09/02	10:31	GIS	(101, 832)	NSGSCAN1/v1	Coronal hole observations
s4546r00	1996/09/02	12:12	GIS	(104, 795)	DEM_GIS/v1	Coronal hole observations
s4547r00	1996/09/02	13:14	NIS	(110, 810)	MOVIE_V1/v2	Coronal hole observations
s4565r00	1996/09/03	18:27	GIS	(-956, -3)	G2AL/v1	JOP 44 East Limb
s4566r00	1996/09/03	19:27	GIS	(-1057, -1)	GEAST/v1	JOP 44 East Limb
s4566r01	1996/09/03	19:58	GIS	(-1204, -3)	GEAST/v1	JOP 44 East Limb
s4567r00	1996/09/03	21:06	NIS	(-953, 357)	LIMB/v16	JOP 44 East Limb
s4568r00	1996/09/03	21:43	NIS	(-955, 115)	LIMB/v16	JOP 44 East Limb
s4569r00	1996/09/03	22:20	NIS	(-956, -124)	LIMB/v16	JOP 44 East Limb
s4570r00	1996/09/03	22:57	NIS	(-953, -363)	LIMB/v16	JOP 44 East Limb
s4576r00	1996/09/05	07:26	NIS	(279, 941)	LIMB/v16	JOP 44 West Limb
s4577r00	1996/09/05	08:03	NIS	(518, 859)	LIMB/v16	JOP 44 West Limb
s4578r00	1996/09/05	08:40	NIS	(729, 701)	LIMB/v16	JOP 44 West Limb
s4579r00	1996/09/05	09:18	NIS	(909, 458)	LIMB/v16	JOP 44 West Limb
s4604r00	1996/09/06	17:26	NIS	(-61, 821)	NISAT_S/v2	NIS Spectral Atlas (Coronal hole)
s4605r00	1996/09/06	18:27	GIS	(-956, -3)	G2AL/v1	JOP 44 East Limb
s4606r00	1996/09/06	19:26	GIS	(-1060, -4)	GEAST/v1	JOP 44 East Limb
s4606r01	1996/09/06	19:57	GIS	(-1204, -3)	GEAST/v1	JOP 44 East Limb
s4607r00	1996/09/06	21:05	NIS	(-952, 356)	LIMB/v16	JOP 44 East Limb
s4608r00	1996/09/06	21:42	NIS	(-956, 115)	LIMB/v16	JOP 44 East Limb
s4609r00	1996/09/06	22:20	NIS	(-957, -126)	LIMB/v16	JOP 44 East Limb
s4610r00	1996/09/06	22:57	NIS	(-952, -363)	LIMB/v16	JOP 44 East Limb
s4615r00	1996/09/07	10:46	NIS	(-122, 938)	LIMB/v16	JOP44/CH Bound (NE)

Table B.1: *(continued)*

file	date	time	sp	pointing	study	note
s4616r00	1996/09/07	11:23	NIS	(-365, 935)	LIMB/v16	JOP44/CH Bound (NE)
s4617r00	1996/09/07	12:00	NIS	(-359, 694)	LIMB/v16	JOP44/CH Bound (NE)
s4618r00	1996/09/07	12:37	NIS	(-119, 699)	LIMB/v16	JOP44/CH Bound (NE)
s4619r00	1996/09/07	13:15	NIS	(-602, 698)	LIMB/v16	JOP44/CH Bound (NE)
s4631r00	1996/09/07	19:03	NIS	(121, 939)	LIMB/v16	JOP44/CH Bound (NE)
s4632r00	1996/09/07	19:40	NIS	(362, 938)	LIMB/v16	JOP44/CH Bound (NE)
s4633r00	1996/09/07	20:18	NIS	(-119, 745)	LIMB/v16	JOP44/CH Bound (NE)
s4634r00	1996/09/07	20:55	NIS	(120, 746)	LIMB/v16	JOP44/CH Bound (NE)
s4635r00	1996/09/07	21:33	NIS	(362, 747)	LIMB/v16	JOP44/CH Bound (NE)
s4636r00	1996/09/07	22:10	NIS	(91, 715)	COHO22/v8	Coronal hole observations
s4637r00	1996/09/07	22:38	NIS	(95, 715)	COHO22/v8	Coronal hole observations
s4638r00	1996/09/07	23:07	NIS	(95, 715)	COHO22/v8	Coronal hole observations
s4639r00	1996/09/07	23:36	NIS	(102, 716)	COHO22/v8	Coronal hole observations
s4643r00	1996/09/08	08:12	NIS	(954, 356)	LIMB/v16	JOP 44 West Limb
s4644r00	1996/09/08	08:50	NIS	(953, 118)	LIMB/v16	JOP 44 West Limb
s4645r00	1996/09/08	09:27	NIS	(955, -123)	LIMB/v16	JOP 44 West Limb
s4646r00	1996/09/08	10:04	NIS	(950, -363)	LIMB/v16	JOP 44 West Limb
s4652r00	1996/09/08	20:24	NIS	(358, -940)	LIMB/v16	JOP44/CH Bound (SW)
s4653r00	1996/09/08	21:02	NIS	(115, -941)	LIMB/v16	JOP44/CH Bound (SW)
s4654r00	1996/09/08	21:39	NIS	(-121, -943)	LIMB/v16	JOP44/CH Bound (SW)
s4655r00	1996/09/08	22:16	NIS	(-360, -940)	LIMB/v16	JOP44/CH Bound (SW)
s4926r00	1996/09/24	16:06	GIS	(307, 220)	GIBOUND/v1	Equatorial Coronal Hole (GIS)
s4926r03	1996/09/24	18:14	GIS	(308, 219)	GIBOUND/v1	Equatorial Coronal Hole (GIS)
s4926r04	1996/09/24	18:57	GIS	(309, 220)	GIBOUND/v1	Equatorial Coronal Hole (GIS)
s4927r00	1996/09/24	19:40	NIS	(335, 219)	CHSTR_X/v19	Equatorial Coronal Hole (NIS)
s6936r00	1997/02/09	13:14	NIS	(-79, -823)	CHSTR_X/v19	Coronal Hole Boundary
s6936r01	1997/02/09	14:47	NIS	(-79, -823)	CHSTR_X/v19	Coronal Hole Boundary
s6936r02	1997/02/09	16:21	NIS	(-79, -823)	CHSTR_X/v19	Coronal Hole Boundary
s6936r03	1997/02/09	17:54	NIS	(-78, -822)	CHSTR_X/v19	Coronal Hole Boundary
s6936r04	1997/02/09	19:27	NIS	(-79, -823)	CHSTR_X/v19	Coronal Hole Boundary
s6937r00	1997/02/09	21:01	NIS	(-77, -824)	MOVIE_V1/v2	Coronal Hole Boundary
s6938r00	1997/02/09	22:23	GIS	(-77, -822)	EWSCAN/v2	Coronal Hole Boundary
s6966r00	1997/02/12	14:01	NIS	(-6, -843)	CHSTR_X/v19	Coronal Hole Boundary
s6966r01	1997/02/12	15:35	NIS	(-6, -843)	CHSTR_X/v19	Coronal Hole Boundary
s6966r02	1997/02/12	17:08	NIS	(-6, -843)	CHSTR_X/v19	Coronal Hole Boundary
s6966r03	1997/02/12	18:42	NIS	(-6, -843)	CHSTR_X/v19	Coronal Hole Boundary
s6967r00	1997/02/12	20:40	GIS	(41, -780)	NSGSCAN1/v1	Coronal Hole Boundary
s6968r00	1997/02/12	22:41	GIS	(39, -784)	NSGSCAN1/v1	Coronal Hole Boundary
s6968r01	1997/02/13	00:21	GIS	(39, -717)	NSGSCAN1/v1	Coronal Hole Boundary
s6970r00	1997/02/13	07:41	GIS	(-2,-1033)	G2AL/v2	Coronal Hole Boundary
s6971r00	1997/02/13	09:55	GIS	(1,-1003)	NSGSCAN1/v1	Coronal Hole Boundary
s6972r00	1997/02/13	11:38	NIS	(-176, 98)	CHSTR_X/v19	Coronal Hole Boundary
s6972r01	1997/02/13	13:11	NIS	(-177, 99)	CHSTR_X/v19	Coronal Hole Boundary
s6972r02	1997/02/13	14:45	NIS	(-177, 99)	CHSTR_X/v19	Coronal Hole Boundary
s6973r00	1997/02/13	16:45	GIS	(57, -768)	GIBOUND/v1	Coronal Hole Boundary
s6973r01	1997/02/13	17:29	GIS	(57, -768)	GIBOUND/v1	Coronal Hole Boundary
s6973r02	1997/02/13	18:13	GIS	(57, -768)	GIBOUND/v1	Coronal Hole Boundary
s6973r03	1997/02/13	18:58	GIS	(57, -768)	GIBOUND/v1	Coronal Hole Boundary
s6973r04	1997/02/13	19:42	GIS	(57, -768)	GIBOUND/v1	Coronal Hole Boundary
s6974r00	1997/02/13	20:26	NIS	(58, -768)	LIMB/v19	Coronal Hole Boundary
s6974r01	1997/02/13	21:05	NIS	(58, -768)	LIMB/v19	Coronal Hole Boundary
s6974r02	1997/02/13	21:43	NIS	(58, -768)	LIMB/v19	Coronal Hole Boundary
s6974r03	1997/02/13	22:21	NIS	(58, -768)	LIMB/v19	Coronal Hole Boundary
s6975r00	1997/02/13	22:59	NIS	(43, -843)	NISAT_S/v2	NIS Atlas
s6980r00	1997/02/15	10:02	GIS	(251, 138)	NSGSCAN1/v1	Coronal Hole Studies (UCLAN)
s6981r00	1997/02/15	11:44	NIS	(287, 139)	VIEWF/v2	Coronal Hole Studies (UCLAN)
s6982r00	1997/02/15	11:45	GIS	(287, 138)	G2AL/v2	Coronal Hole Studies (UCLAN)
s6983r00	1997/02/15	14:00	NIS	(236, 140)	VIEWF/v2	Coronal Hole Studies (UCLAN)
s6984r00	1997/02/15	14:01	GIS	(237, 141)	G2AL/v1	Coronal Hole Studies (UCLAN)
s6984r01	1997/02/15	14:35	GIS	(237, 141)	G2AL/v1	Coronal Hole Studies (UCLAN)
s6985r00	1997/02/15	15:10	NIS	(278, 140)	VIEWF/v2	Coronal Hole Studies (UCLAN)
s6986r00	1997/02/15	15:12	GIS	(278, 141)	NSGSCAN1/v1	Coronal Hole Studies (UCLAN)

Table B.1: *(continued)*

file	date	time	sp	pointing	study	note
s6987r00	1997/02/15	16:53	NIS	(278, 140)	MOVIE_V1/v3	Coronal Hole Studies (UCLAN)
s6988r00	1997/02/15	17:25	NIS	(261, 178)	CHSTR_X/v19	Coronal Hole Studies (UCLAN)
s6988r01	1997/02/15	18:58	NIS	(260, 179)	CHSTR_X/v19	Coronal Hole Studies (UCLAN)
s7248r00	1997/03/10	07:21	GIS	(-1, -992)	EWGSCAN2/v1	Plumes - South Limb
s7249r00	1997/03/10	10:42	GIS	(-1,-1021)	NSGSCAN2/v1	Plumes - South Limb
s7444r00	1997/03/27	06:52	GIS	(0,-1041)	EWGSCAN2/v1	Plume study
s7445r00	1997/03/27	10:13	GIS	(0, -999)	NSGSCAN2/v1	Plume study
s7446r00	1997/03/27	13:35	NIS	(0, -999)	LIMB/v19	Plume study
s7494r00	1997/04/01	16:47	GIS	(0,-1041)	EWGSCAN2/v1	Plume study
s7495r00	1997/04/01	20:08	GIS	(1, -997)	NSGSCAN2/v1	Plume study
s9215r00-11	1997/09/20	22:44	GIS	(411, 893)	HTBNDWE/v2	Coronal Hole Campaign
s9227r01	1997/09/22	23:10	NIS	(576, -670)	UCLAN_N4/v37	Coronal Hole Campaign
s9230r00	1997/09/23	10:11	NIS	(-149, 611)	UCLAN_N4/v37	Coronal Hole Campaign
s9230r01	1997/09/23	11:20	NIS	(-376, 608)	UCLAN_N4/v37	Coronal Hole Campaign
s9230r02	1997/09/23	12:29	NIS	(-260, 411)	UCLAN_N4/v37	Coronal Hole Campaign
s9233r00	1997/09/23	21:57	NIS	(-158, 554)	UCLAN_N3/v25	Coronal Hole Campaign
s9239r00	1997/09/24	11:27	GIS	(-8, 668)	GIBOUND/v1	Coronal Hole Campaign
s9243r00	1997/09/24	22:01	NIS	(-19, 605)	UCLAN_N2/v24	Coronal Hole Campaign
s9258r00	1997/09/25	20:41	NIS	(219, 618)	NISAT_S5/v2	Coronal Hole Campaign
s9258r01	1997/09/25	21:29	NIS	(176, 615)	NISAT_S5/v2	Coronal Hole Campaign
s9258r02	1997/09/25	22:17	NIS	(138, 614)	NISAT_S5/v2	Coronal Hole Campaign
s9258r03	1997/09/25	23:05	NIS	(98, 615)	NISAT_S5/v2	Coronal Hole Campaign
s9265r00	1997/09/26	19:16	NIS	(-182, 895)	UCLAN_N3/v25	Coronal Hole Campaign
s9265r01	1997/09/26	20:33	NIS	(-303, 896)	UCLAN_N3/v25	Coronal Hole Campaign
s9265r02	1997/09/26	21:50	NIS	(-420, 896)	UCLAN_N3/v25	Coronal Hole Campaign
s9265r03	1997/09/26	23:07	NIS	(-176, 719)	UCLAN_N3/v25	Coronal Hole Campaign
s9266r00	1997/09/27	00:20	NIS	(0, 875)	SYNOP_F/v1	Synoptic Meridian Images
s9266r01	1997/09/27	01:03	NIS	(-1, 655)	SYNOP_F/v1	Synoptic Meridian Images
s9266r02	1997/09/27	01:46	NIS	(0, 435)	SYNOP_F/v1	Synoptic Meridian Images
s9271r00	1997/09/27	17:03	NIS	(553, -810)	LIMB/v19	Coronal Hole Campaign
s9272r00-29	1997/09/27	17:41	GIS	(553, -811)	HTBNDWE/v2	Coronal Hole Campaign
s9273r00	1997/09/27	23:50	NIS	(497, -806)	LIMB/v19	Coronal Hole Campaign
s9279r00	1997/09/28	17:03	NIS	(553, -809)	LIMB/v19	Coronal Hole Campaign
s9280r00-14	1997/09/28	17:41	GIS	(553, -810)	HTBNDWE/v2	Coronal Hole Campaign
s9281r00	1997/09/28	20:45	NIS	(554, -807)	LIMB/v19	Coronal Hole Campaign
s9287r00	1997/09/29	17:32	NIS	(553, -810)	LIMB/v19	Coronal Hole Campaign
s9288r00-29	1997/09/29	18:10	GIS	(552, -811)	HTBNDWE/v2	Coronal Hole Campaign
s9289r00	1997/09/30	00:20	NIS	(496, -806)	LIMB/v19	Coronal Hole Campaign
s9319r00	1997/10/02	19:33	NIS	(0, 883)	WIDE3LA1/v3	Coronal Hole Campaign
s9320r00	1997/10/02	19:35	NIS	(-14, 884)	UCLAN_N3/v25	Coronal Hole Campaign
s9321r00	1997/10/02	21:17	GIS	(0, 860)	DEM_GIS/v1	Coronal Hole Campaign
s9322r00	1997/10/02	22:18	GIS	(0, 898)	NSGSCAN1/v1	Coronal Hole Campaign
s9323r00	1997/10/03	00:00	NIS	(0, 883)	WIDE3LA1/v3	Coronal Hole Campaign
s9332r00	1997/10/03	18:53	NIS	(-615, 847)	UCLAN_N4/v37	Coronal Hole Campaign
s9332r01	1997/10/03	20:02	NIS	(-615, 616)	UCLAN_N4/v37	Coronal Hole Campaign
s9333r00	1997/10/03	21:12	GIS	(-618, 777)	NSGSCAN1/v1	Coronal Hole Campaign
s9334r00	1997/10/03	22:53	NIS	(-618, 778)	MOVIE/v1	Coronal Hole Campaign
s9336r00	1997/10/04	15:17	NIS	(124, 239)	UCLAN_N3/v25	Coronal Hole Campaign
s9337r00	1997/10/04	16:30	NIS	(136, 238)	UCLAN_N3/v25	Coronal Hole Campaign
s9338r00	1997/10/04	17:48	GIS	(150, 238)	DEM_GIS/v1	Coronal Hole Campaign
s9339r00	1997/10/04	18:50	NIS	(153, 243)	LIMB/v19	Coronal Hole Campaign
s9351r00	1997/10/05	16:18	NIS	(429, 880)	UCLAN_N4/v37	Coronal Hole Campaign
s9351r01	1997/10/05	17:27	NIS	(189, 883)	UCLAN_N4/v37	Coronal Hole Campaign
s9351r02	1997/10/05	18:36	NIS	(-48, 879)	UCLAN_N4/v37	Coronal Hole Campaign
s9351r03	1997/10/05	19:46	NIS	(-282, 881)	UCLAN_N4/v37	Coronal Hole Campaign
s9351r04	1997/10/05	20:56	NIS	(-518, 882)	UCLAN_N4/v37	Coronal Hole Campaign
s9352r00	1997/10/05	22:19	NIS	(-84, 831)	UCLAN_N2/v24	Coronal Hole Campaign
s9355r00-14	1997/10/06	18:49	GIS	(2, 782)	HTBNDWE/v2	Coronal Hole Campaign
s9356r00	1997/10/06	21:52	NIS	(2, 782)	UCLAN_N3/v25	Coronal Hole Campaign
s9364r00	1997/10/07	13:06	NIS	(66, 655)	LIMB/v19	Coronal Hole Campaign
s9364r01	1997/10/07	13:44	NIS	(48, 881)	LIMB/v19	Coronal Hole Campaign
s9364r02	1997/10/07	14:22	NIS	(-182, 881)	LIMB/v19	Coronal Hole Campaign

Table B.1: *(continued)*

file	date	time	sp	pointing	study	note
s9365r00	1997/10/07	15:00	NIS	(248, 420)	LIMB/v19	Coronal Hole Campaign
s9374r00	1997/10/07	23:06	NIS	(-357, 945)	LIMB/v19	Coronal Hole Campaign
s9376r00	1997/10/08	06:30	NIS	(48, 754)	UCLAN_N2/v24	Coronal Hole Campaign
s9377r00	1997/10/08	08:50	NIS	(89, 756)	WIDE3LA1/v3	Coronal Hole Campaign
s9378r00	1997/10/08	08:53	GIS	(89, 756)	NSGSCAN1/v1	Coronal Hole Campaign
s9379r00	1997/10/08	10:34	NIS	(97, 757)	WIDE3LA1/v3	Coronal Hole Campaign
s9390r00	1997/10/09	07:41	GIS	(246, 965)	G2NS/v1	Coronal Hole Campaign
s9391r00	1997/10/09	09:06	NIS	(247, 960)	UCLAN_N2/v24	Coronal Hole Campaign
s9392r00	1997/10/09	11:35	NIS	(222, 811)	LIMB/v19	Coronal Hole Campaign
s9393r00	1997/10/09	12:12	NIS	(222, 811)	LIMB/v19	Coronal Hole Campaign
s9394r00	1997/10/09	12:49	NIS	(222, 811)	LIMB/v19	Coronal Hole Campaign
s9403r00	1997/10/10	09:47	NIS	(129, 864)	UCLAN_N4/v37	Coronal Hole Campaign
s9404r00	1997/10/10	10:56	NIS	(198, 866)	MOVIE_V1/v2	Coronal Hole Campaign
s9405r00	1997/10/10	11:53	NIS	(132, 863)	UCLAN_N4/v37	Coronal Hole Campaign
s9406r00	1997/10/10	13:10	NIS	(-54, 778)	NISAT_S/v2	NIS Spectral Atlas
s9408r00	1997/10/10	18:26	NIS	(287, 818)	UCLAN_N4/v40	Coronal Hole Campaign
s9408r01	1997/10/10	19:05	NIS	(288, 818)	UCLAN_N4/v40	Coronal Hole Campaign
s9408r02	1997/10/10	19:44	NIS	(290, 814)	UCLAN_N4/v40	Coronal Hole Campaign
s9409r00-14	1997/10/10	20:46	GIS	(355, 777)	HRBNDWE/v1	Coronal Hole Campaign
s9410r00-49	1997/10/10	23:34	NIS	(287, 819)	WIDE3LA1/v3	Movie - collaboration with Nobeyama
s9416r00	1997/10/11	15:00	NIS	(347, 859)	UCLAN_N3	Coronal Hole Campaign
s9417r00-14	1997/10/11	16:05	GIS	(351, 854)	HRBNDWE/v1	Coronal Hole Campaign
s9418r00	1997/10/11	18:54	NIS	(353, 856)	WIDE3LA1/v3	Coronal Hole Campaign
s9423r00	1997/10/12	08:55	NIS	(-1, 1044)	NISAT_S5/v2	Coronal Hole Campaign
s9423r01	1997/10/12	09:43	NIS	(-1, 1044)	NISAT_S5/v2	Coronal Hole Campaign
s9423r02	1997/10/12	10:31	NIS	(-1, 1044)	NISAT_S5/v2	Coronal Hole Campaign
s9423r03	1997/10/12	11:19	NIS	(-1, 1044)	NISAT_S5/v2	Coronal Hole Campaign
s9423r04	1997/10/12	12:07	NIS	(-1, 1044)	NISAT_S5/v2	Coronal Hole Campaign
s9423r05	1997/10/12	12:55	NIS	(-1, 1044)	NISAT_S5/v2	Coronal Hole Campaign
s9424r00	1997/10/12	16:01	NIS	(55, 1025)	CORO24W/v22	Coronal Hole Monitoring (North)
s9424r01	1997/10/12	17:15	NIS	(-55, 1025)	CORO24W/v22	Coronal Hole Monitoring (North)
s9425r00	1997/10/12	19:07	NIS	(0, 855)	UCLAN_N2	Coronal Hole Campaign
s9425r01	1997/10/12	20:16	NIS	(0, 855)	UCLAN_N2	Coronal Hole Campaign
s9426r00-14	1997/10/12	21:25	GIS	(3, 895)	HRBNDWE/v1	Coronal Hole Study
s9430r00	1997/10/13	17:51	NIS	(387, 683)	UCLAN_N4/v40	Coronal Hole Campaign
s9430r01	1997/10/13	18:30	NIS	(389, 897)	UCLAN_N4/v40	Coronal Hole Campaign
s9430r02	1997/10/13	19:09	NIS	(157, 895)	UCLAN_N4/v40	Coronal Hole Campaign
s9430r03	1997/10/13	19:48	NIS	(-79, 892)	UCLAN_N4/v40	Coronal Hole Campaign
s9430r04	1997/10/13	20:28	NIS	(-318, 892)	UCLAN_N4/v40	Coronal Hole Campaign
s9430r05	1997/10/13	21:07	NIS	(-283, 710)	UCLAN_N4/v40	Coronal Hole Campaign
s9431r00-14	1997/10/13	21:47	GIS	(343, 885)	HRBNDWE/v1	Coronal Hole Study
s9435r00	1997/10/14	16:30	NIS	(-63, 791)	UCLAN_N2	Coronal Hole Campaign
s9435r01	1997/10/14	17:39	NIS	(-63, 791)	UCLAN_N2	Coronal Hole Campaign
s9436r00	1997/10/14	18:47	NIS	(-60, 795)	UCLAN_N2	Coronal Hole Campaign
s9436r01	1997/10/14	19:56	NIS	(-60, 795)	UCLAN_N2	Coronal Hole Campaign
s9437r00	1997/10/14	21:04	NIS	(-56, 791)	UCLAN_N2	Coronal Hole Campaign
s9437r01	1997/10/14	22:13	NIS	(-56, 791)	UCLAN_N2	Coronal Hole Campaign
s9438r00	1997/10/14	23:21	NIS	(0, 794)	WIDE3LA1/v3	Coronal Hole Campaign
s9438r49	1997/10/15	00:44	NIS	(0, 794)	WIDE3LA1/v3	Coronal Hole Campaign
s9443r00	1997/10/15	13:01	NIS	(59, 812)	WIDE3LA1/v3	Coronal Hole Campaign
s9444r00-14	1997/10/15	13:29	GIS	(18, 826)	HRBNDWE/v1	Coronal Hole Campaign
s9445r00	1997/10/15	16:18	NIS	(7, 825)	UCLAN_N2	Coronal Hole Campaign
s9446r00	1997/10/15	18:44	NIS	(382, 903)	UCLAN_N4/v40	Coronal Hole Campaign
s9446r01	1997/10/15	19:23	NIS	(174, 904)	UCLAN_N4/v40	Coronal Hole Campaign
s9446r02	1997/10/15	20:03	NIS	(-55, 903)	UCLAN_N4/v40	Coronal Hole Campaign
s9446r03	1997/10/15	20:42	NIS	(102, 761)	UCLAN_N4/v40	Coronal Hole Campaign
s9447r00-14	1997/10/15	21:21	GIS	(173, 813)	HRBNDWE/v1	Coronal Hole Campaign
s9449r00	1997/10/16	07:10	NIS	(119, 896)	NISAT_S/v2	NIS Spectral Atlas
s9468r00	1997/10/16	22:27	NIS	(-7, 887)	UCLAN_N3/v27	Coronal Hole Campaign
s9469r00	1997/10/16	23:33	GIS	(11, 879)	G2NS/v1	Coronal Hole Campaign
s9477r00-14	1997/10/17	22:00	GIS	(19, 1032)	HRBNDWE/v1	Coronal Hole Campaign
s9478r00	1997/10/18	00:48	NIS	(2, 1012)	UCLAN_N3/v27	Coronal Hole Campaign

Table B.1: *(continued)*

file	date	time	sp	pointing	study	note
s9491r00	1997/10/19	18:37	GIS	(980, 5)	G2AL4/v3	Limb Monitoring (low rate)
s9491r01	1997/10/19	20:21	GIS	(980, 6)	G2AL4/v3	Limb Monitoring (low rate)
s9491r02	1997/10/19	22:06	GIS	(980, 5)	G2AL4/v3	Limb Monitoring (low rate)
s9494r00	1997/10/20	10:36	GIS	(-1, 968)	G2NS3/v1	N. Limb Monitoring (low rate)
s9507r00-59	1997/10/23	04:53	NIS	(45, 474)	WIDE3LA1/v3	Movie (NCH boundary, low rate)
s9508r00	1997/10/23	10:40	GIS	(46, 437)	G2NS	GIS North-South scan
s9509r00	1997/10/23	12:05	GIS	(56, 507)	NSGSCAN1	GIS North-South scan
s9510r00	1997/10/23	12:33	GIS	(0, 1036)	EWGSCAN2/v1	Low Rate Campaign (Off-limb cross)
s9511r00	1997/10/23	15:55	GIS	(0, 991)	NSGSCAN2/v1	Low Rate Campaign (Off-limb cross)
s9514r10-59	1997/10/24	16:53	NIS	(299, 544)	WIDE3LA1/v3	Movie (NCH boundary, low rate)
s9515r00	1997/10/24	21:55	GIS	(308, 549)	G2NS	GIS North-South scan
s9516r00	1997/10/24	23:20	GIS	(319, 538)	NSGSCAN1	GIS North-South scan

Appendix C

The calibration of the CDS instrument

C.1 The observations for the CDS calibration

Table C.1: *The observations designed by the author for the CDS instrument calibration. The columns indicate: the fits file name; the date of the start of the observation; the starting time (UT); the spectrometer used; the pointing, in Solar X and Y (arc sec from Sun centre); the CDS study name; and a comment. At the end, standard CDS observations used for calibration purposes are listed.*

file	date	time	sp	pointing	study	note
s7172r00	1997/03/05	09:54	GIS	(0, -5)	ARC_CALG/v1	GIS/NIS Calibration
s7173r00	1997/03/05	10:31	NIS	(0, -1)	ARC_CALN/v3	GIS/NIS Calibration
s7174r00	1997/03/05	10:46	GIS	(-1, -6)	ARC_CALG/v1	GIS/NIS Calibration
s7175r00	1997/03/05	11:22	NIS	(0, -1)	ARC_CALN/v3	GIS/NIS Calibration
s7176r00	1997/03/05	11:38	GIS	(0, -5)	ARC_CALG/v1	GIS/NIS Calibration
s7177r00	1997/03/05	12:14	NIS	(0, -1)	ARC_CALN/v3	GIS/NIS Calibration
s7772r00	1997/05/04	18:41	GIS	(970, 0)	DEM_GIS/v2	GIS/NIS Calibration
s7773r00	1997/05/04	18:55	NIS	(970, 0)	ARC_CALN/v3	GIS/NIS Calibration
s7774r00	1997/05/04	19:10	GIS	(970, 0)	DEM_GIS/v2	GIS/NIS Calibration
s7775r00	1997/05/04	19:24	NIS	(970, 0)	ARC_CALN/v3	GIS/NIS Calibration
s7776r00	1997/05/04	19:40	GIS	(970, 0)	DEM_GIS/v2	GIS/NIS Calibration
s7777r00	1997/05/04	19:53	NIS	(970, 0)	ARC_CALN/v3	GIS/NIS Calibration
s7778r00	1997/05/04	20:09	GIS	(970, 0)	DEM_GIS/v2	GIS/NIS Calibration
s7779r00	1997/05/04	20:23	NIS	(970, 0)	ARC_CALN/v3	GIS/NIS Calibration
s7780r00	1997/05/04	20:38	GIS	(970, 0)	DEM_GIS/v2	GIS/NIS Calibration
s7781r00	1997/05/04	20:52	NIS	(970, 0)	ARC_CALN/v3	GIS/NIS Calibration
s7782r00	1997/05/04	21:07	GIS	(970, 0)	DEM_GIS/v2	GIS/NIS Calibration
s7783r00	1997/05/04	21:21	NIS	(961, 0)	ARC_CALN/v3	GIS/NIS Calibration
s7784r00	1997/05/04	21:37	GIS	(961, -1)	DEM_GIS/v2	GIS/NIS Calibration
s7785r00	1997/05/04	21:50	NIS	(961, -1)	ARC_CALN/v3	GIS/NIS Calibration
s7786r00	1997/05/04	22:06	GIS	(961, -1)	DEM_GIS/v2	GIS/NIS Calibration
s7787r00	1997/05/04	22:20	NIS	(961, -1)	ARC_CALN/v3	GIS/NIS Calibration
s7788r00	1997/05/04	22:35	GIS	(961, -1)	DEM_GIS/v2	GIS/NIS Calibration
s7789r00	1997/05/04	22:49	NIS	(961, -1)	ARC_CALN/v3	GIS/NIS Calibration
s7790r00	1997/05/04	23:04	GIS	(961, -1)	DEM_GIS/v2	GIS/NIS Calibration
s7791r00	1997/05/04	23:18	NIS	(961, -1)	ARC_CALN/v3	GIS/NIS Calibration
s7792r00	1997/05/04	23:33	GIS	(961, -1)	DEM_GIS/v2	GIS/NIS Calibration
s7850r00	1997/05/09	15:23	NIS	(65, 50)	UCLAN_N1/v1	GIS/NIS on-disc calibration
s7850r01	1997/05/09	15:51	NIS	(65, 50)	UCLAN_N1/v1	GIS/NIS on-disc calibration
s7850r02	1997/05/09	16:22	NIS	(65, 50)	UCLAN_N1/v1	GIS/NIS on-disc calibration
s7850r03	1997/05/09	16:53	NIS	(65, 50)	UCLAN_N1/v1	GIS/NIS on-disc calibration
s7850r04	1997/05/09	17:24	NIS	(65, 50)	UCLAN_N1/v1	GIS/NIS on-disc calibration
s7851r00	1997/05/09	17:56	GIS	(65, 46)	ARC_CALG/v1	GIS/NIS on-disc calibration

Table C.1: *(continued)*

file	date	time	sp	pointing	study	note
s7852r00	1997/05/09	18:33	NIS	(65, 50)	UCLAN_N1/v1	GIS/NIS on-disc calibration
s7852r01	1997/05/09	19:02	NIS	(65, 50)	UCLAN_N1/v1	GIS/NIS on-disc calibration
s7852r02	1997/05/09	19:33	NIS	(65, 50)	UCLAN_N1/v1	GIS/NIS on-disc calibration
s7852r03	1997/05/09	20:04	NIS	(65, 50)	UCLAN_N1/v1	GIS/NIS on-disc calibration
s7852r04	1997/05/09	20:35	NIS	(65, 50)	UCLAN_N1/v1	GIS/NIS on-disc calibration
s8198r00	1997/06/17	07:48	GIS	(899, -329)	DEM_GIS/v2	GIS/NIS Calibration
s8199r00	1997/06/17	08:02	NIS	(899, -329)	ARC_CALN/v3	GIS/NIS Calibration
s8200r00	1997/06/17	08:17	GIS	(899, -329)	DEM_GIS/v2	GIS/NIS Calibration
s8202r00	1997/06/17	08:46	GIS	(899, -329)	DEM_GIS/v2	GIS/NIS Calibration
s8203r00	1997/06/17	09:00	NIS	(899, -329)	ARC_CALN/v3	GIS/NIS Calibration
s8204r00	1997/06/17	09:15	GIS	(899, -329)	DEM_GIS/v2	GIS/NIS Calibration
s8205r00	1997/06/17	09:29	NIS	(899, -329)	ARC_CALN/v3	GIS/NIS Calibration
s8206r00	1997/06/17	09:44	GIS	(899, -329)	DEM_GIS/v2	GIS/NIS Calibration
s8207r00	1997/06/17	09:58	NIS	(899, -329)	ARC_CALN/v3	GIS/NIS Calibration
s8229r00	1997/06/20	07:08	GIS	(959, -1)	DEM_GIS/v2	UCLAN GIS/NIS Calibration
s8230r00	1997/06/20	07:22	NIS	(959, -1)	ARC_CALN/v3	UCLAN GIS/NIS Calibration
s8231r00	1997/06/20	07:37	GIS	(959, -1)	DEM_GIS/v2	UCLAN GIS/NIS Calibration
s8232r00	1997/06/20	07:51	NIS	(959, -1)	ARC_CALN/v3	UCLAN GIS/NIS Calibration
s8233r00	1997/06/20	08:06	GIS	(959, -1)	DEM_GIS/v2	UCLAN GIS/NIS Calibration
s8234r00	1997/06/20	08:20	NIS	(959, -1)	ARC_CALN/v3	UCLAN GIS/NIS Calibration
s8235r00	1997/06/20	08:35	GIS	(959, -1)	DEM_GIS/v2	UCLAN GIS/NIS Calibration
s8236r00	1997/06/20	08:49	NIS	(959, -1)	ARC_CALN/v3	UCLAN GIS/NIS Calibration
s8237r00	1997/06/20	09:04	GIS	(959, 0)	DEM_GIS/v2	UCLAN GIS/NIS Calibration
s8238r00	1997/06/20	09:18	NIS	(959, -1)	ARC_CALN/v3	UCLAN GIS/NIS Calibration
s9234r00	1997/09/23	23:40	GIS	(0, 961)	DEM_GIS/v2	Test alignment slits
s9235r00	1997/09/23	23:54	NIS	(0, 961)	ARC_CALN/v3	Test alignment slits
s9298r00	1997/10/01	13:50	GIS	(967, -2)	DEM_GIS/v2	GIS/NIS calibration
s9299r00	1997/10/01	14:04	NIS	(967, -2)	ARC_CALN/v3	GIS/NIS calibration
s9300r00	1997/10/01	14:19	GIS	(967, -2)	DEM_GIS/v2	GIS/NIS calibration
s9301r00	1997/10/01	14:33	NIS	(967, -2)	ARC_CALN/v3	GIS/NIS calibration
s9302r00	1997/10/01	14:48	GIS	(967, -2)	DEM_GIS/v2	GIS/NIS calibration
s9303r00	1997/10/01	15:02	NIS	(967, -2)	ARC_CALN/v3	GIS/NIS calibration
s9304r00	1997/10/01	15:17	GIS	(967, -2)	DEM_GIS/v2	GIS/NIS calibration
s9305r00	1997/10/01	15:31	NIS	(967, -2)	ARC_CALN/v3	GIS/NIS calibration
s9306r00	1997/10/01	15:48	GIS	(967, -2)	DEM_GIS/v2	GIS/NIS calibration
s9307r00	1997/10/01	16:01	NIS	(967, -2)	ARC_CALN/v3	GIS/NIS calibration
s9371r00	1997/10/07	19:56	NIS	(0, 0)	UCLAN_N1/v1	GIS/NIS Intercalibration
s9371r01	1997/10/07	20:25	NIS	(0, 0)	UCLAN_N1/v1	GIS/NIS Intercalibration
s9372r00	1997/10/07	20:57	GIS	(0, -3)	ARC_CALG/v1	GIS/NIS Intercalibration
s9373r00	1997/10/07	21:34	NIS	(0, 0)	UCLAN_N1/v1	GIS/NIS Intercalibration
s9373r01	1997/10/07	22:02	NIS	(0, 0)	UCLAN_N1/v1	GIS/NIS Intercalibration
s9373r02	1997/10/07	22:33	NIS	(0, 0)	UCLAN_N1/v1	GIS/NIS Intercalibration
s9380r00	1997/10/08	11:12	GIS	(1021, -15)	GISAT_S/v1	GIS long slit test
s9381r00	1997/10/08	11:46	GIS	(1024, -14)	RWPM_1/v2	GIS long slit test
s9382r00	1997/10/08	12:33	GIS	(1023, -14)	GISAT_S/v1	GIS long slit test
s9383r00	1997/10/08	13:07	GIS	(1025, -14)	RWPM_1/v2	GIS long slit test
s9450r00	1997/10/16	07:51	GIS	(119, 896)	TEST5_2/v1	GIS Slit 1-2 Test
s9451r00	1997/10/16	08:52	GIS	(120, 893)	MICRO/v1	GIS Slit 1-2 Test
s9452r00	1997/10/16	09:23	GIS	(119, 896)	TEST5_2/v1	GIS Slit 1-2 Test
s9453r00	1997/10/16	10:24	GIS	(120, 897)	MICRO/v1	GIS Slit 1-2 Test
s9454r00	1997/10/16	11:22	GIS	(956, 9)	DEM_GIS/v2	GIS/NIS Calibration
s9455r00	1997/10/16	11:36	NIS	(968, -2)	ARC_CALN/v3	GIS/NIS Calibration
s9456r00	1997/10/16	11:45	GIS	(968, -2)	DEM_GIS/v2	GIS/NIS Calibration
s9457r00	1997/10/16	11:59	NIS	(968, -2)	ARC_CALN/v3	GIS/NIS Calibration
s9458r00	1997/10/16	12:07	GIS	(968, -1)	DEM_GIS/v2	GIS/NIS Calibration
s9459r00	1997/10/16	12:21	NIS	(968, -1)	ARC_CALN/v3	GIS/NIS Calibration
s9460r00	1997/10/16	12:30	GIS	(968, -1)	DEM_GIS/v2	GIS/NIS Calibration
s9461r00	1997/10/16	12:44	NIS	(968, -1)	ARC_CALN/v3	GIS/NIS Calibration
s9462r00	1997/10/16	12:52	GIS	(968, -1)	DEM_GIS/v2	GIS/NIS Calibration
s9463r00	1997/10/16	13:06	NIS	(968, -1)	ARC_CALN/v3	GIS/NIS Calibration
s8257r00	1997/06/22	21:53	NIS	(0, 0)	NISAT_S/v2	NIS Calibration - QS
s9253r00	1997/09/25	18:01	NIS	(-55, 157)	NISAT_S/v2	NIS Calibration - AR

Table C.1: *(continued)*

file	date	time	sp	pointing	study	note
s9487r00	1997/10/19	06:41	NIS	(-1, 3)	NISAT_S/v2	NIS Calibration - QS

C.2 The spectra and line identifications for the off-limb observation – May 4th 1997

Table C.2: *Line identifications for the off-limb quiet sun observation of May 4th 1997.*

Ion	λ_{th} (Å)	λ_{ob} (Å)	Transition	I_{ob}	I_{th}/I_{ob}	+/-	Det	log T_{eff}	log T_{max}	frac	
Fe XI	308.548	308.5	3s2.3p4 $^1D_2$ - 3s.3p5 $^1P_1$	26.7	0.54	0.08	N 1	6.06	6.10		
Mg VIII	311.796	311.8	2p $^2P_{1/2}$ - 2s.2p2 $^2P_{3/2}$	58.7	0.92	0.11	N 1	6.00	5.91		
Fe XIII	312.109	312.3	3s2 3p2 $^3P_1$ - 3s 3p3 $^3P_1$	17.7	1.48	0.30	N 1	6.08	6.20		
Fe XIII	312.872	313.0	3s2 3p2 $^3P_1$ - 3s 3p3 $^3P_0$	12.7	0.35	0.08	N 1	6.09	6.20	0.82	
P X	312.981		2s22p2 $^3P_1$ - 2s2p3 $^3D_2$						6.16	0.18	
Mg VIII	313.754	313.7	2p $^2P_{1/2}$ - 2s.2p2 $^2P_{1/2}$	119.2	0.92	0.10	N 1	6.00	5.92		
Si VIII	314.327	314.4	2s22p3 $^4S_{3/2}$ - 2s2p4 $^4P_{1/2}$	125.0	1.03	0.11	N 1	6.02	5.91		
Mg VIII	315.039	315.0	2p $^2P_{3/2}$ - 2s.2p2 $^2P_{3/2}$	264.8	1.05	0.11	N 1	6.00	5.91		
Si VIII	316.205	316.2	2s22p3 $^4S_{3/2}$ - 2s2p4 $^4P_{3/2}$	213.4	1.15	0.12	N 1	6.02	5.91		
Mg VIII	317.039	317.1	2p $^2P_{3/2}$ - 2s.2p2 $^2P_{1/2}$	92.6	0.84	0.09	N 1	6.00	5.92		
Mg VII	319.027	318.9	2s22p2 $^1D_2$ - 2s2p3 $^1D_2$	23.8	0.36	0.06	N 1	5.97	5.80		
Si VIII	319.826	319.9	2s22p3 $^4S_{3/2}$ - 2s2p4 $^4P_{5/2}$	323.0	1.15	0.12	N 1	6.02	5.91		
Fe XIII	320.809	320.8	3s2 3p2 $^3P_2$ - 3s 3p3 $^3P_2$	11.4	0.89	0.22	N 1	6.09	6.20		
Fe XIII	321.4	321.4	3s2 3p2 $^3P_2$ - 3s 3p3 $^3P_1$	9.1	1.20	0.46	N 1	6.09	6.20		
Fe X	321.732	321.8	3s2.3p4(3p).3d $^4D_{5/2}$ - 3s.3p5(3p*).3d $^4F_{7/2}$	7.4	0.74	0.31	N 1	6.05	6.04	0.69	
Fe X	321.804		3s2.3p4(3p).3d $^4D_{7/2}$ - 3s.3p5(3p*).3d $^4F_{7/2}$						6.04	0.29	
Fe X	324.763	324.7	3s2.3p4(3p).3d $^4D_{7/2}$ - 3s.3p5(3p*).3d $^4F_{9/2}$	13.3	0.84	0.19	N 1	6.05	6.04		
Al VIII	325.276	325.4	2p2 $^3P_1$ - 2s.2p3 $^3P_0$	13.5	1.42	0.28	N 1	6.02	5.92	0.37	
Al VIII	325.292		2p2 $^3P_1$ - 2s.2p3 $^3P_2$						5.92	0.33	
Al VIII	325.338		2p2 $^3P_1$ - 2s.2p3 $^3P_1$						5.92	0.29	
S X	326.327	326.4	2s22p3 $^2D_{3/2}$ - 2s2p4 $^4P_{1/2}$	25.1	0.00	0.00	N 1	6.06	6.13		
Al VIII	328.185	328.2	2p2 $^3P_2$ - 2s.2p3 $^3P_2$	34.3	0.97	0.16	N 1	6.02	5.92	0.69	
Al VIII	328.232		2p2 $^3P_2$ - 2s.2p3 $^3P_1$						5.92	0.23	
Al X	332.789	332.8	2s2 $^1S_0$ - 2s.2p $^1P_1$	104.1	1.14	0.13	N 1	6.06	6.09		
Fe XIV	334.172	334.2	3s2 3p $^2P_{1/2}$ - 3s 3p2 $^2D_{3/2}$	18.2	1.14	0.17	N 1	6.11	6.24		
Mg VIII	335.253	335.3	2p $^2P_{1/2}$ - 2s.2p2 $^2S_{1/2}$	73.1	1.05	0.11	N 1	6.03	5.92	0.65	
Fe XII	335.339		3s2.3p3 $^2D_{3/2}$ - 3s.3p4 $^2D_{3/2}$						6.16	0.33	[1]
Fe XII	338.278	338.3	3s2.3p3 $^2D_{5/2}$ - 3s.3p4 $^2D_{5/2}$	32.1	0.89	0.10	N 1	6.07	6.16		
Mg VIII	339.006	339.0	2p $^2P_{3/2}$ - 2s.2p2 $^2S_{1/2}$	62.5	1.07	0.11	N 1	6.00	5.92		
Fe XI	341.113	341.1	3s2.3p4 $^3P_2$ - 3s.3p5 $^3P_1$	75.4	0.63	0.06	N 1	6.06	6.11		
Si IX	341.949	342.0	2s22p2 $^3P_0$ - 2s2p3 $^3D_1$	99.4	1.03	0.10	N 1	6.04	6.03		
Si IX	345.124	345.1	2s22p2 $^3P_1$ - 2s2p3 $^3D_2$	238.6	1.03	0.10	N 1	6.04	6.03	0.77	
Si IX	344.951		2s22p2 $^3P_1$ - 2s2p3 $^3D_1$						6.03	0.23	
Fe X	345.723	345.7	3s2.3p5 $^2P_{3/2}$ - 3s.3p6 $^2S_{1/2}$	133.9	1.19	0.12	N 1	6.04	6.04		
Fe XII	346.852	346.9	3s2.3p3 $^4S_{3/2}$ - 3s.3p4 $^4P_{1/2}$	51.7	0.90	0.09	N 1	6.07	6.16		
Si X	347.403	347.4	2p $^2P_{1/2}$ - 2s.2p2 $^2D_{3/2}$	208.4	1.06	0.11	N 1	6.06	6.13		
Fe XIII	348.183	348.2	3s2 3p2 $^3P_0$ - 3s 3p3 $^3D_1$	55.0	0.92	0.11	N 1	6.09	6.20		
Fe XI	349.046	349.2	3s2.3p4 $^3P_1$ - 3s.3p5 $^3P_0$	24.9	0.39	0.04	N 1	5.99	6.10	0.38	
Mg VI	349.163		2s2.2p3 $^2D_{5/2}$ - 2s.2p4 $^2D_{5/2}$						5.65	0.32	
Mg VI	349.124		2s2.2p3 $^2D_{3/2}$ - 2s.2p4 $^2D_{3/2}$						5.65	0.24	
Si IX	349.873	349.9	2s22p2 $^3P_2$ - 2s2p3 $^3D_3$	226.6	1.00	0.10	N 1	6.04	6.03	0.84	
Si IX	349.794		2s22p2 $^3P_2$ - 2s2p3 $^3D_2$						6.03	0.16	
Fe XII	352.106	352.1	3s2.3p3 $^4S_{3/2}$ - 3s.3p4 $^4P_{3/2}$	102.4	0.92	0.09	N 1	6.07	6.16		
Fe XI	352.662	352.7	3s2.3p4 $^3P_2$ - 3s.3p5 $^3P_2$	177.1	1.10	0.11	N 1	6.06	6.11		
Na VII	353.296	353.4	2p $^2P_{3/2}$ - 2s.2p2 $^2P_{3/2}$	3.7	0.86	0.14	N 1	5.96	5.78		
Al VII	353.769	353.8	2s22p3 $^4S_{3/2}$ - 2s2p4 $^4P_{3/2}$	10.6	1.35	0.18	N 1	6.05	5.78	0.54	
Fe XIV	353.831		3s2 3p $^2P_{3/2}$ - 3s 3p2 $^2D_{5/2}$						6.24	0.45	
Si X	356.012	356.0	2p $^2P_{3/2}$ - 2s.2p2 $^2D_{5/2}$	129.9	1.03	0.10	N 1	6.06	6.13	0.76	
Si X	356.05		2p $^2P_{3/2}$ - 2s.2p2 $^2D_{3/2}$						6.13	0.24	
Fe XI	356.519	356.5	3s2.3p4 $^3P_1$ - 3s.3p5 $^3P_1$	27.9	0.88	0.09	N 1	6.06	6.11		
Al VII	356.888	356.9	2s22p3 $^4S_{3/2}$ - 2s2p4 $^4P_{5/2}$	8.4	1.38	0.19	N 1	5.99	5.78		
Fe XI	358.621	358.6	3s2.3p4 $^3P_0$ - 3s.3p5 $^3P_1$	40.8	0.98	0.10	N 1	6.05	6.11	0.75	
Fe X	358.413		3s2.3p4(3p).3d $^4F_{9/2}$ - 3s.3p5(3p*).3d $^4F_{9/2}$						6.04	0.23	
Fe XIII	359.842	359.7	3s2 3p2 $^3P_1$ - 3s 3p3 $^3D_1$	24.5	0.99	0.11	N 1	6.09	6.20	0.55	
Fe XIII	359.642		3s2 3p2 $^3P_1$ - 3s 3p3 $^3D_2$						6.20	0.43	
Fe XVI	360.761	360.6	3s $^2S_{1/2}$ - 3p $^2P_{1/2}$	1.2	0.74	0.46	N 1	6.19	6.34	0.83	
Fe X	360.454		3s2.3p4(1d).3d $^2P_{3/2}$ - 3s.3p5(3p*).3d $^4F_{3/2}$						6.04	0.17	
Fe X	361.406	361.5	3s2.3p4(3p).3d $^4F_{7/2}$ - 3s.3p5(3p*).3d $^4F_{7/2}$	6.3	0.58	0.09	N 1	6.05	6.04	0.79	
Si XI	361.412		2s.2p $^3P_0$ - 2p2 $^3P_1$						6.20	0.21	
Mg VII	363.772	363.8	2s22p2 $^3P_0$ - 2s2p3 $^3P_1$	13.7	0.73	0.12	N 1	5.98	5.81		
Fe X	364.189	364.2	3s2.3p4(1d).3d $^2P_{3/2}$ - 3s.3p5(3p*).3d $^4F_{5/2}$	2.6	0.02	0.02	N 1	6.04	6.04		
Fe XII	364.467	364.5	3s2.3p3 $^4S_{3/2}$ - 3s.3p4 $^4P_{5/2}$	138.3	0.95	0.10	N 1	6.07	6.16		

[1] First identification

Table C.2: *(continued)*

Ion	λ_{th} (Å)	λ_{ob} (Å)	Transition	I_{ob}	I_{th}/I_{ob}	+/-	Det	log T_{eff}	log T_{max}	frac	
Mg VII	365.234	365.1	$2s22p2\ ^3P_1$ - $2s2p3\ ^3P_2$	26.2	1.23	0.16	N 1	5.98	5.81	0.36	
Mg VII	365.176		$2s22p2\ ^3P_1$ - $2s2p3\ ^3P_0$						5.81	0.33	
Mg VII	365.243		$2s22p2\ ^3P_1$ - $2s2p3\ ^3P_1$						5.81	0.26	
Fe X	365.543	365.6	$3s2.3p5\ ^2P_{1/2}$ - $3s.3p6\ ^2S_{1/2}$	74.2	0.93	0.10	N 1	6.04	6.04		
Mg VII	367.674	367.7	$2s22p2\ ^3P_2$ - $2s2p3\ ^3P_2$	84.7	0.61	0.07	N 1	5.98	5.81	0.77	
Mg VII	367.683		$2s22p2\ ^3P_2$ - $2s2p3\ ^3P_1$						5.81	0.23	
Mg IX	368.07	368.1	$2s2\ ^1S_0$ - $2s.2p\ ^1P_1$	1060.8	0.94	0.09	N 1	6.03	5.98		
Fe XI	369.153	369.2	$3s2.3p4\ ^3P_1$ - $3s.3p5\ ^3P_2$	54.7	1.07	0.11	N 1	6.06	6.11		
Ca IX	378.081	378.2	$3s.3p\ ^3P_2$ - $3s.3d\ ^3D_3$	3.8	0.31	0.06	N 1	5.97	5.78	0.50	
Na VII	378.216		$2p\ ^2P_{1/2}$ - $2s.2p2\ ^2S_{1/2}$						5.78	0.46	
Si X	258.372	516.8	$2p\ ^2P_{3/2}$ - $2s.2p2\ ^2P_{3/2}$	353.8	0.78	0.09	N 2	6.06	6.13		
Si XII	520.665	520.8	$1s2.2s\ ^2S_{1/2}$ - $1s2.2p\ ^2P_{1/2}$	8.6	1.09	0.11	N 2	6.11	6.26		
Si X	261.063	522.2	$2p\ ^2P_{3/2}$ - $2s.2p2\ ^2P_{1/2}$	318.7	0.44	0.05	N 2	6.06	6.13		[2]
Si X	271.983	544.1	$2p\ ^2P_{1/2}$ - $2s.2p2\ ^2S_{1/2}$	161.8	0.67	0.08	N 2	6.07	6.13		
Al XI	550.031	550.1	$1s2.(1s).2s\ ^2S_{1/2}$ - $1s2.(1s).2p\ ^2P_{3/2}$	12.5	2.08	0.21	N 2	6.08	6.16		
Si X	277.255	554.5	$2p\ ^2P_{3/2}$ - $2s.2p2\ ^2S_{1/2}$	213.4	0.41	0.05	N 2	6.06	6.13		[3]
Mg VII	278.402	556.9	$2s22p2\ ^3P_2$ - $2s2p3\ ^3S_1$	84.1	0.72	0.11	N 2	5.98	5.81	0.69	
Si VII	278.443		$2p4\ ^3P_1$ - $2s.2p5\ ^3P_2$						5.77	0.29	
Ca X	557.765	557.8	$3s\ ^2S_{1/2}$ - $3p\ ^2P_{3/2}$	39.6	1.00	0.10	N 2	6.02	5.82		
Ne VI	558.594	558.7	$2s2\ 2p\ ^2P_{1/2}$ - $2s\ 2p2\ ^2D_{3/2}$	3.6	0.87	0.09	N 2	5.93	5.63	0.57	
Ne VII	558.609		$2s2p\ ^3P_1$ - $2p2\ ^3P_2$						5.72	0.43	
Ne VII	559.948	560.2	$2s2p\ ^3P_0$ - $2p2\ ^3P_1$	1.5	0.75	0.09	N 2	5.98	5.72		
Ne VII	561.728	561.7	$2s2p\ ^3P_2$ - $2p2\ ^3P_2$	4.6	1.04	0.11	N 2	5.97	5.72	0.83	
Ne VII	561.378		$2s2p\ ^3P_1$ - $2p2\ ^3P_1$						5.72	0.17	
Ne VI	562.803	562.9	$2s2\ 2p\ ^2P_{3/2}$ - $2s\ 2p2\ ^2D_{5/2}$	2.9	1.21	0.13	N 2	5.89	5.63		
Ne VII	564.528	564.5	$2s2p\ ^3P_2$ - $2p2\ ^3P_1$	1.7	0.75	0.09	N 2	5.97	5.72		
Al XI	568.12	568.2	$1s2.(1s).2s\ ^2S_{1/2}$ - $1s2.(1s).2p\ ^2P_{1/2}$	6.4	2.02	0.22	N 2	6.08	6.16		[4]
Ca X	574.01	574.1	$3s\ ^2S_{1/2}$ - $3p\ ^2P_{1/2}$	20.9	0.94	0.10	N 2	6.02	5.82		[5]
Si XI	580.907	580.9	$2s2\ ^1S_0$ - $2s.2p\ ^3P_1$	12.5	0.44	0.05	N 2	6.08	6.19		[6]
Si IX	290.69	581.4	$2s22p2\ ^3P_0$ - $2s2p3\ ^3P_1$	128.1	0.56	0.14	N 2	6.04	6.03		
Ca VIII	582.846	582.8		0.8	0.79	0.16	N 2	5.92	5.73		[7] AC
He I	584.334	584.3	$1s2\text{-}1s2p\ ^1S$ - ^1P	2.1			N 2				[8] AC
Si IX	292.8	585.7	$2s22p2\ ^3P_1$ - $2s2p3\ ^3P_0$	230.7	0.90	0.11	N 2	6.04	6.03	0.40	[9]
Si IX	292.856		$2s22p2\ ^3P_1$ - $2s2p3\ ^3P_1$						6.03	0.32	
Si IX	292.763		$2s22p2\ ^3P_1$ - $2s2p3\ ^3P_2$						6.03	0.27	
Si IX	296.117	592.6	$2s22p2\ ^3P_2$ - $2s2p3\ ^3P_2$	949.9	0.32	0.03	N 2	6.04	6.03	0.72	[10]
Si IX	296.213		$2s22p2\ ^3P_2$ - $2s2p3\ ^3P_1$						6.03	0.28	
Si XI	604.147	604.3	$2s.2p\ ^1P_1$ - $2p2\ ^1D_2$	2.1	0.19	0.03	N 2	6.09	6.20		
Si XI	303.324	606.7	$2s2\ ^1S_0$ - $2s.2p\ ^1P_1$	560.5	0.42	0.05	N 2	6.08	6.20		
He II	303.78	607.6	$1s\ ^2S_{1/2}$ - $2p\ ^2P_{3/2}$	282.8			N 2				[11]
He II	303.786		$1s\ ^2S_{1/2}$ - $2p\ ^2P_{1/2}$								
Mg X	609.793	609.8	$1s2.(1s).2s\ ^2S_{1/2}$ - $1s2.(1s).2p\ ^2P_{3/2}$	364.2	1.55	0.15	N 2	6.05	6.04		
Si X	621.079	621.2	$2p\ ^2P_{1/2}$ - $2s.2p2\ ^4P_{1/2}$	4.1	0.73	0.09	N 2	6.06	6.12		
Mg VIII	311.796	623.6	$2p\ ^2P_{1/2}$ - $2s.2p2\ ^2P_{3/2}$	112.2	0.48	0.40	N 2	6.00	5.91		
Mg X	624.941	625.0	$1s2.(1s).2s\ ^2S_{1/2}$ - $1s2.(1s).2p\ ^2P_{1/2}$	180.4	1.55	0.16	N 2	6.05	6.04		
Mg VIII	313.754	627.6	$2p\ ^2P_{1/2}$ - $2s.2p2\ ^2P_{1/2}$	100.5	1.09	0.16	N 2	6.00	5.92		
Si VIII	314.327	628.8	$2s22p3\ ^4S_{3/2}$ - $2s2p4\ ^4P_{1/2}$	107.7	1.20	0.91	N 2	6.02	5.91		
Mg VIII	315.039	630.0	$2p\ ^2P_{3/2}$ - $2s.2p2\ ^2P_{3/2}$	443.7	0.63	0.07	N 2	6.00	5.91		[12]
		154.6	ghost of 174.5 Å				G 1				
		157.2	ghost of 177.2 Å				G 1				
		158.5	ghost of 178.0 Å				G 1				
		160.6	ghost of 180.4 Å				G 1				
		162.7	ghost of 182.1 Å				G 1				
		165.3	ghost of 184.5 Å				G 1				
		166.1	ghost of 185.2 Å				G 1				
Fe VIII	167.486	167.5		193.4	0.35	0.06	G 1	5.99	5.65		AC

[2] bl He I 522.21 Å (stray light ?)
[3] bl O IV 554.513 Å
[4] Can be blended with Fe XV (bl Al IX) 284.1 Å, but not here
[5] Usually blended in on-disc observations with C III 574.28 Å
[6] Usually blended in on-disc observations with O II
[7] AC: Arcetri code
[8] (stray light ?)
[9] Usually Ar VII 585.75 Å in on-disc observations
[10] Must be a blend with an unidentified line in first order
[11] (stray light ?)
[12] Usually O V 629.732 Å in on-disc observations. Here still contributes about 40% of the observed line

Table C.2: *(continued)*

Ion	λ_{th} (Å)	λ_{ob} (Å)	Transition	I_{ob}	I_{th}/I_{ob}	+/-	Det	log T_{eff}	log T_{max}	frac	
Fe VIII	168.545	168.3		336.7	0.49	0.06	G 1	5.99	5.65	0.50	AC
Fe VIII	168.17								5.65	0.40	
Fe VIII	168.93	168.9		73.5	1.24	0.35	G 1	5.99	5.65		AC
Fe IX	171.073	171.1	3p6 $^1S_0$ - 3p5.3d $^1P_1$	3766.6	1.09	0.11	G 1	6.03	5.96		
O VI	173.079	173.1	1s2 2p $^2P_{3/2}$ - 1s2 3d $^2D_{5/2}$	116.2	0.74	0.13	G 1	6.04	5.51	0.60	
O VI	172.935		1s2 2p $^2P_{1/2}$ - 1s2 3d $^2D_{3/2}$						5.51	0.33	
Fe X	174.534	174.7	3s2.3p5 $^2P_{3/2}$ - 3s2.3p4(3p).3d $^2D_{5/2}$	3375.8	0.90	0.09	G 1	6.05	6.05		
Fe X	175.266	175.5	3s2.3p5 $^2P_{1/2}$ - 3s2.3p4(3p).3d $^2D_{3/2}$	358.7	0.65	0.08	G 1	6.04	6.04	0.71	
Fe X	175.443		3s2.3p5 $^2P_{3/2}$ - 3s2.3p4(3p).3d $^2P_{1/2}$						6.04	0.29	
Fe X	177.243	177.3	3s2.3p5 $^2P_{3/2}$ - 3s2.3p4(3p).3d $^2P_{3/2}$	2133.2	0.83	0.08	G 1	6.05	6.05		
Fe XI	178.06	178.0	3s2.3p4 $^3P_2$ - 3s2.3p3(4s*).3d $^3D_2$	152.4	0.43	0.06	G 1	6.06	6.11		
Fe XI	180.408	180.5	3s2.3p4 $^3P_2$ - 3s2.3p3(4s*).3d $^3D_3$	2182.8	0.98	0.10	G 1	6.06	6.11		
Fe XI	181.137	181.3	3s2.3p4 $^3P_0$ - 3s2.3p3(4s*).3d $^3D_1$	136.2	0.68	0.10	G 1	6.06	6.11		
Fe XI	182.169	182.3	3s2.3p4 $^3P_1$ - 3s2.3p3(4s*).3d $^3D_2$	459.1	0.61	0.07	G 1	6.06	6.11	0.85	
Fe X	182.31		3s2.3p5 $^2P_{1/2}$ - 3s2.3p4(3p).3d $^2P_{3/2}$						6.05	0.15	
O VI	184.117	184.0	1s2 2p $^2P_{3/2}$ - 1s2 3s $^2S_{1/2}$	72.4	0.62	0.13	G 1	6.03	5.51	0.67	
O VI	183.937	.	1s2 2p $^2P_{1/2}$ - 1s2 3s $^2S_{1/2}$						5.51	0.33	
Fe X	184.543	184.6	3s2.3p5 $^2P_{3/2}$ - 3s2.3p4(1d).3d $^2S_{1/2}$	759.0	0.88	0.09	G 1	6.05	6.05		
Fe VIII	185.213	185.3		189.7	0.38	0.05	G 1	5.99	5.64		AC
Fe XII	186.884	186.8	3s2.3p3 $^2D_{5/2}$ - 3s2.3p2(3p).3d $^2F_{7/2}$	261.9	0.81	0.09	G 1	6.05	6.16	0.49	
Fe VIII	186.599								5.64	0.36	AC
Fe XII	186.851		3s2.3p3 $^2D_{3/2}$ - 3s2.3p2(3p).3d $^2F_{5/2}$						6.16	0.14	
Fe XI	188.232	188.3	3s2.3p4 $^3P_2$ - 3s2.3p3(2d*).3d $^3P_2$	1406.5	0.85	0.09	G 1	6.06	6.11	0.72	
Fe XI	188.299		3s2.3p4 $^3P_2$ - 3s2.3p3(2d*).3d $^1P_1$						6.11	0.26	
Fe XI	189.129	189.1	3s2.3p4 $^3P_1$ - 3s2.3p3(2d*).3d $^3P_1$	71.4	0.48	0.08	G 1	6.06	6.11		
Fe X	190.043	190.0	3s2.3p5 $^2P_{1/2}$ - 3s2.3p4(1d).3d $^2S_{1/2}$	368.8	0.64	0.07	G 1	6.05	6.05		
S XI	191.266	191.1	2s22p2 $^3P_2$ - 2s2p3 $^3S_1$	69.7	0.40	0.08	G 1	6.08	6.24	0.61	
Fe XI	190.888		3s2.3p4 $^1D_2$ - 3s2.3p3(4s*).3d $^3D_2$						6.11	0.16	
Fe XII	191.053		3s2.3p3 $^2P_{3/2}$ - 3s2.3p2(3p).3d $^2D_{5/2}$						6.16	0.16	
S XI	191.266	191.3	2s22p2 $^3P_2$ - 2s2p3 $^3S_1$	17.8	0.96	0.55	G 1	6.08	6.24		
Fe XII	192.393	192.4	3s2.3p3 $^4S_{3/2}$ - 3s2.3p2(3p).3d $^4P_{1/2}$	270.2	0.86	0.12	G 1	6.08	6.16		
Fe XI	192.83	192.8	3s2.3p4 $^3P_1$ - 3s2.3p3(2d*).3d $^3P_2$	336.4	0.59	0.07	G 1	6.06	6.11		
Fe XII	193.521	193.6	3s2.3p3 $^4S_{3/2}$ - 3s2.3p2(3p).3d $^4P_{3/2}$	828.5	0.84	0.09	G 1	6.07	6.16		
Fe XII	194.609	194.5	3s2.3p3 $^4S_{3/2}$ - 3s2.3p2(3p).3d $^2P_{1/2}$	79.3	0.14	0.04	G 1	6.06	6.16	0.81	
Fe VIII	194.661		3p6.(1s).3d $^2D_{5/2}$ - 3p6.(1s).4p $^2P_{3/2}$						5.67	0.18	AC
Fe XII	195.118	195.2	3s2.3p3 $^4S_{3/2}$ - 3s2.3p2(3p).3d $^4P_{5/2}$	1103.8	0.99	0.10	G 1	6.08	6.16		
Fe VIII	195.972	195.9	3p6.(1s).3d $^2D_{3/2}$ - 3p6.(1s).4p $^2P_{1/2}$	24.4	0.25	0.13	G 1	6.01	5.64	0.77	AC
S X	196.108		2s22p3 $^2P_{1/2}$ - 2s2p4 $^2P_{3/2}$						6.12	0.23	
Fe XII	196.648	196.6	3s2.3p3 $^2D_{5/2}$ - 3s2.3p2(1d).3d $^2D_{5/2}$	104.8	0.51	0.10	G 1	6.08	6.16		
S VIII	198.553	198.7	2s2.2p5 $^2P_{3/2}$ - 2s.2p6 $^2S_{1/2}$	140.0	0.60	0.13	G 1	6.03	5.88	0.66	
Fe XI	198.545		3s2.3p4 $^1D_2$ - 3s2.3p3(2d*).3d $^3P_1$						6.11	0.32	
Fe XIII	200.022	200.1	3s2 3p2 $^3P_1$ - 3s2 3p 3d $^3D_2$	54.7	0.33	0.14	G 1	6.09	6.20		
Fe XIII	201.128	201.2	3s2 3p2 $^3P_1$ - 3s2 3p 3d $^3D_1$	198.7	0.23	0.05	G 1	6.09	6.21		
Fe XIII	202.044	202.1	3s2 3p2 $^3P_0$ - 3s2 3p 3d $^3P_1$	493.9	0.87	0.13	G 1	6.09	6.21		
Fe XI	202.706	202.7	3s2.3p4 $^1D_2$ - 3s2.3p3(2d*).3d $^1P_1$	180.6	0.86	0.22	G 1	6.05	6.11	0.75	
S VIII	202.61		2s2.2p5 $^2P_{1/2}$ - 2s.2p6 $^2S_{1/2}$						5.88	0.16	
Fe XIII	203.828	203.8	3s2 3p2 $^3P_2$ - 3s2 3p 3d $^3D_3$	145.9	0.60	0.16	G 1	6.09	6.20	0.73	
Fe XIII	203.797		3s2 3p2 $^3P_2$ - 3s2 3p 3d $^3D_2$						6.20	0.26	
Fe XII	206.371	206.1	3s2.3p3 $^2D_{3/2}$ - 3s2.3p2(1s).3d $^2D_{3/2}$	94.1	0.46	0.12	G 1	6.08	6.16		
Fe XI	207.777	207.5	3s2.3p4 $^3P_1$ - 3s2.3p3(2p*).3d $^3D_2$	120.6	1.12	0.31	G 1	6.06	6.11	0.79	
Fe X	207.447		3s2.3p5 $^2P_{3/2}$ - 3s2.3p4(1d).3d $^2F_{5/2}$						6.04	0.20	
Fe XIII	209.919	209.7	3s2 3p2 $^3P_2$ - 3s2 3p 3d $^3P_1$	77.4	1.12	0.49	G 1	6.09	6.21	0.85	
Fe XIII	209.621		3s2 3p2 $^3P_1$ - 3s2 3p 3d $^3P_2$						6.20	0.15	
Fe XIV	211.32	211.3	3s2 3p $^2P_{1/2}$ - 3s2 3d $^2D_{3/2}$	84.3	0.59	0.19	G 1	6.11	6.25		
Si VIII	216.915	216.8	2s22p3 $^2D_{5/2}$ - 2s2p4 $^2P_{3/2}$	255.2	0.54	0.09	G 1	6.03	5.90	0.54	
Fe IX	217.101		3p6 $^1S_0$ - 3p5.3d $^3D_1$						5.94	0.23	
Si X	258.372	258.5	2p $^2P_{3/2}$ - 2s.2p2 $^2P_{3/2}$	321.0	0.86	0.09	G 2	6.06	6.13		
S X	259.496	259.8	2s22p3 $^4S_{3/2}$ - 2s2p4 $^4P_{3/2}$	106.2	1.48	0.19	G 2	6.06	6.13		
Si X	261.063	261.2	2p $^2P_{3/2}$ - 2s.2p2 $^2P_{1/2}$	133.3	1.06	0.13	G 2	6.06	6.13		
Fe XIV	264.78	264.6	3s2 3p $^2P_{3/2}$ - 3s 3p2 $^2P_{3/2}$	27.0	0.69	0.16	G 2	6.11	6.25		
		266.3	ghost of 290.7 Å(bl)				G 2				
		268.8	ghost of 292.8 Å				G 2				
Fe XIV	270.507	270.4	3s2 3p $^2P_{3/2}$ - 3s 3p2 $^2P_{1/2}$	6.8	2.38	1.10	G 2	6.08	6.25	0.78	?
Mg VI	270.39		2s2.2p3 $^2D_{5/2}$ - 2s.2p4 $^2P_{3/2}$						5.66	0.19	
Si X	271.983	272.0	2p $^2P_{1/2}$ - 2s.2p2 $^2S_{1/2}$	105.4	1.03	0.12	G 2	6.07	6.13		
Si VII	272.638	272.7	2p4 $^3P_2$ - 2s.2p5 $^3P_1$	42.1	0.31	0.05	G 2	5.99	5.77		[13]
Fe XIV	274.2	274.1	3s2 3p $^2P_{1/2}$ - 3s 3p2 $^2S_{1/2}$	37.5	0.89	0.14	G 2	6.09	6.25	0.81	
Si VII	274.174		2p4 $^3P_1$ - 2s.2p5 $^3P_0$						5.77	0.19	

[13] bl ghost of 296.1 Å

Table C.2: *(continued)*

Ion	λ_{th} (Å)	λ_{ob} (Å)	Transition	I_{ob}	I_{th}/I_{ob}	+/-	Det	log T_{eff}	log T_{max}	frac	
Si VII	275.353	275.3	2p4 $^3P_2$ - 2s.2p5 $^3P_2$	60.6	0.91	0.12	G 2	5.99	5.77		
Mg VII	276.154	276.1	2s22p2 $^3P_0$ - 2s2p3 $^3S_1$	18.1	0.91	0.31	G 2	5.99	5.81	0.51	
Si VII	275.667		2p4 $^3P_1$ - 2s.2p5 $^3P_1$						5.77	0.45	
Si X	277.255	277.0	2p $^2P_{3/2}$ - 2s.2p2 $^2S_{1/2}$	213.5	1.07	0.12	G 2	6.03	6.13	0.38	
Si VIII	277.054		2s22p3 $^2D_{5/2}$ - 2s2p4 $^2D_{5/2}$						5.90	0.30	
Si VIII	276.838		2s22p3 $^2D_{3/2}$ - 2s2p4 $^2D_{3/2}$						5.90	0.13	
Mg VII	277		2s22p2 $^3P_1$ - 2s2p3 $^3S_1$						5.81	0.11	
Mg VII	278.402	278.4	2s22p2 $^3P_2$ - 2s2p3 $^3S_1$	52.9	1.17	0.16	G 2	5.99	5.81	0.68	
Si VII	278.443		2p4 $^3P_1$ - 2s.2p5 $^3P_2$						5.77	0.29	
Al IX	280.151	280.1	2s2.2p $^2P_{1/2}$ - 2s.2p2 $^2P_{3/2}$	10.9	1.19	0.41	G 2	6.04	6.03		
Mg VII	280.737	280.7	2s22p2 $^1D_2$ - 2s2p3 $^1P_1$	6.8	0.61	0.29	G 2	5.98	5.80		
S XI	281.401	281.5	2s22p2 $^3P_0$ - 2s2p3 $^3D_1$	17.8	1.21	0.28	G 2	6.08	6.24		
Al IX	282.422	282.6	2s2.2p $^2P_{1/2}$ - 2s.2p2 $^2P_{1/2}$	28.9	0.93	0.17	G 2	6.04	6.03		
Fe XII	283.449	283.6	3s2.3p3 $^2D_{3/2}$ - 3s.3p4 $^2P_{1/2}$	15.5	0.21	0.06	G 2	6.07	6.16		bl ?
Al IX	284.042	284.5	2s2.2p $^2P_{3/2}$ - 2s.2p2 $^2P_{3/2}$	79.7	1.11	0.14	G 2	6.07	6.03	0.76	
Fe XV	284.16		3s2 $^1S_0$ - 3s3p $^1P_1$						6.29	0.24	
S XI	285.587	285.8	2s22p2 $^3P_1$ - 2s2p3 $^3D_1$	33.8	0.64	0.12	G 2	6.08	6.24	0.48	
S XI	285.822		2s22p2 $^3P_1$ - 2s2p3 $^3D_2$						6.24	0.40	
Al VIII	285.469		2p2 $^1D_2$ - 2s.2p3 $^1D_2$						5.91	0.11	
Al IX	286.377	286.6	2s2.2p $^2P_{3/2}$ - 2s.2p2 $^2P_{1/2}$	15.5	1.39	0.36	G 2	6.04	6.03		
Fe XII	287.263	287.5	3s2.3p3 $^2D_{3/2}$ - 3s.3p4 $^2P_{3/2}$	20.4	0.09	0.02	G 2	6.07	6.16		bl ?
S XII	288.434	288.4	2s2.2p $^2P_{1/2}$ - 2s.2p2 $^2D_{3/2}$	9.6	0.42	0.16	G 2	6.11	6.32	0.57	
Fe XIII	288.565		3s2 3p2 $^1S_0$ - 3s 3p3 $^1P_1$						6.20	0.43	
S XII	288.434	288.7	2s2.2p $^2P_{1/2}$ - 2s.2p2 $^2D_{3/2}$	4.7	0.86	0.78	G 2	6.11	6.32	0.57	
Fe XIII	288.565		3s2 3p2 $^1S_0$ - 3s 3p3 $^1P_1$						6.20	0.43	
P IX	289.531	289.7	2s22p3 $^4S_{3/2}$ - 2s2p4 $^4P_{5/2}$	17.5	0.29	0.08	G 2	6.05	6.05	.	[14]
Si IX	290.69	290.5	2s22p2 $^3P_0$ - 2s2p3 $^3P_1$	78.8	0.91	0.12	G 2	6.04	6.03		[15]
Si IX	292.8	292.7	2s22p2 $^3P_1$ - 2s2p3 $^3P_0$	182.2	1.15	0.13	G 2	6.04	6.03	0.40	[16]
Si IX	292.856		2s22p2 $^3P_1$ - 2s2p3 $^3P_1$						6.03	0.32	
Si IX	292.763		2s22p2 $^3P_1$ - 2s2p3 $^3P_2$						6.03	0.27	
		293.3	ghost of 313.7 Å ?				G 2				
		294.	ghost of 314.3 Å ?				G 2				
		294.8	ghost of 315. Å				G 2				
Si IX	296.117	296.2	2s22p2 $^3P_2$ - 2s2p3 $^3P_2$	337.2	0.90	0.09	G 2	6.04	6.03	0.72	[17]
Si IX	296.213		2s22p2 $^3P_2$ - 2s2p3 $^3P_1$						6.03	0.28	
		296.9	ghost of 317. Å (bl ?)				G 2				
		299.9	ghost of 319.8 Å				G 2				
Al IX	305.045	305.3	2s2.2p $^2P_{3/2}$ - 2s.2p2 $^2S_{1/2}$	14.3	1.00	0.26	G 2	6.04	6.03		
Si VIII	308.195	307.9	2s22p3 $^2P_{3/2}$ - 2s2p4 $^2D_{5/2}$	11.9	1.29	0.42	G 2	6.02	5.90	0.76	
Si VIII	307.652		2s22p3 $^2P_{1/2}$ - 2s2p4 $^2D_{3/2}$						5.90	0.23	
Fe XI	308.548	308.5	3s2.3p4 $^1D_2$ - 3s.3p5 $^1P_1$	40.5	0.36	0.05	G 2	6.06	6.10		[18]
		310.4	ghost of 328.3 Å ?				G 2				
Mg VIII	311.796	311.6	2p $^2P_{1/2}$ - 2s.2p2 $^2P_{3/2}$	55.9	0.99	0.13	G 2	6.01	5.91		[19]
Fe XIII	312.109	312.1	3s2 3p2 $^3P_1$ - 3s 3p3 $^3P_1$	16.2	1.44	0.38	G 2	6.09	6.20		[20]
Mg VIII	313.754	313.7	2p $^2P_{1/2}$ - 2s.2p2 $^2P_{1/2}$	112.1	0.98	0.12	G 2	6.00	5.92		[21]
Si VIII	314.327	314.3	2s22p3 $^4S_{3/2}$ - 2s2p4 $^4P_{1/2}$	124.1	1.04	0.12	G 2	6.02	5.91		[22]
Mg VIII	315.039	315.1	2p $^2P_{3/2}$ - 2s.2p2 $^2P_{3/2}$	290.8	0.96	0.10	G 2	6.00	5.91		[23]
Si VIII	316.205	316.3	2s22p3 $^4S_{3/2}$ - 2s2p4 $^4P_{3/2}$	171.6	1.43	0.16	G 2	6.02	5.91		[24]
Mg VIII	317.039	317.1	2p $^2P_{3/2}$ - 2s.2p2 $^2P_{1/2}$	116.8	0.67	0.08	G 2	6.00	5.92		[25]
		318.6	ghost of 335.4 Å (bl Mg VII 319.)				G 2				
Si VIII	319.826	319.8	2s22p3 $^4S_{3/2}$ - 2s2p4 $^4P_{5/2}$	335.9	1.11	0.12	G 2	6.02	5.91		[26]
Fe XIII	320.809	320.8	3s2 3p2 $^3P_2$ - 3s 3p3 $^3P_2$	13.2	0.77	0.18	G 2	6.09	6.20		[27]
Fe XIII	321.4	321.6	3s2 3p2 $^3P_2$ - 3s 3p3 $^3P_1$	14.0	1.17	0.26	G 2	6.08	6.20	0.66	

[14] bl with a ghost ?
[15] Ghosting to 266.7 Å + ghost of 311.7 Å
[16] Ghosting to 268.8 Å + ghost of 313. Å
[17] Ghosting to 272.6 Å + ghost of 316.2 Å
[18] Ghosting and ghosted ?
[19] Ghosting to 290.6 Å + ghost ?
[20] Ghosting 291.4 Å + ghost of 329.7 Å
[21] Ghosting to 293.3 Å
[22] Ghosting to 294. Å
[23] Ghosting to 294.8 Å
[24] Ghosting to 296.2 Å + ghost of 332.8 Å
[25] Ghosting to 296.9 Å + ghost of 334.1 Å
[26] Ghosting to 336.1, 299.9 Å
[27] Could be contaminated by the unidentified line at 337.2 Å

Table C.2: *(continued)*

Ion	λ_{th} (Å)	λ_{ob} (Å)	Transition	I_{ob}	I_{th}/I_{ob}	+/-	Det	log T_{eff}	log T_{max}	frac	
Fe X	321.732		3s2.3p4(3p).3d $^4D_{5/2}$ - 3s.3p5(3p*).3d $^4F_{7/2}$						6.04	0.23	
Al X	332.789	332.9	2s2 $^1S_0$ - 2s.2p $^1P_1$	63.7	1.85	0.30	G 2	6.06	6.09		[28]
Fe XIV	334.172	334.2	3s2 3p $^2P_{1/2}$ - 3s 3p2 $^2D_{3/2}$	9.9	2.09	0.79	G 2	6.11	6.24		[29]
Mg VIII	335.253	335.3	2p $^2P_{1/2}$ - 2s.2p2 $^2S_{1/2}$	91.8	0.83	0.11	G 2	6.03	5.92	0.65	[30]
Fe XII	335.339		3s2.3p3 $^2D_{3/2}$ - 3s.3p4 $^2D_{3/2}$						6.16	0.33	
		336.1	ghost of 319.8 Å				G 2				
Fe XII	338.278	338.1	3s2.3p3 $^2D_{5/2}$ - 3s.3p4 $^2D_{5/2}$	22.5	1.27	0.34	G 2	6.07	6.16		
Mg VIII	339.006	339.0	2p $^2P_{3/2}$ - 2s.2p2 $^2S_{1/2}$	61.7	1.11	0.18	G 2	6.00	5.92		
Ne VI	401.926	401.9	2s2 2p $^2P_{3/2}$ - 2s 2p2 $^2P_{3/2}$	11.8	0.44	0.07	G 3	5.89	5.64		[31]
Mg VI	403.307	403.1	2s2.2p3 $^4S_{3/2}$ - 2s.2p4 $^4P_{5/2}$	8.5	1.25	0.25	G 3	5.94	5.65	0.89	[32]
Ne VI	403.255		2s2 2p $^2P_{3/2}$ - 2s 2p2 $^2P_{1/2}$						5.64	0.11	
Fe XIII	202.044	403.9	3s2 3p2 $^3P_0$ - 3s2 3p 3d $^3P_1$	264.5	1.63	0.33	G 3	6.09	6.21		
Fe XI	202.448	404.7	3s2.3p4 $^3P_2$ - 3s2.3p3(2p*).3d $^3D_2$	123.8	0.39	0.15	G 3	6.06	6.11		
Fe XI	406.811	406.8	3s2.3p4 $^1D_2$ - 3s.3p5 $^3P_2$	3.6	1.55	0.54	G 3	6.06	6.11		
Fe XIII	203.828	407.5	3s2 3p2 $^3P_2$ - 3s2 3p 3d $^3D_3$	79.0	1.11	0.44	G 3	6.09	6.20	0.73	
Fe XIII	203.797		3s2 3p2 $^3P_2$ - 3s2 3p 3d $^3D_2$						6.20	0.26	
		408.5	ghost of 436.5 Å ?				G 3				[33]
		409.	ghost of 436.7 Å				G 3				
Na VIII	411.166	411.1	2s2 $^1S_0$ - 2s.2p $^1P_1$	22.8	1.13	0.15	G 3	5.99	5.86		
Fe XV	417.258	417.3	3s2 $^1S_0$ - 3s3p $^3P_1$	1.1	0.61	0.55	G 3	6.15	6.29		
Ca X	419.754	419.7	3p $^2P_{3/2}$ - 3d $^2D_{5/2}$	8.5	0.59	0.13	G 3	6.02	5.82	0.60	
C IV	419.713		1s2 2p $^2P_{3/2}$ - 1s2 3s $^2S_{1/2}$						5.08	0.25	
C IV	419.525		1s2 2p $^2P_{1/2}$ - 1s2 3s $^2S_{1/2}$						5.08	0.12	
Fe XIV	211.32	422.7	3s2 3p $^2P_{1/2}$ - 3s2 3d $^2D_{3/2}$	75.0	0.66	0.27	G 3	6.11	6.25		
Fe XIII	213.771	427.5	3s2 3p2 $^3P_2$ - 3s2 3p 3d $^3P_2$	98.1	0.13	0.04	G 3	6.09	6.20		bl ?
Mg VIII	428.319	428.2	2s.2p2 $^2D_{5/2}$ - 2p3 $^2D_{5/2}$	4.3	0.78	0.27	G 3	6.00	5.92	0.55	
Mg VIII	428.245		2s.2p2 $^2D_{3/2}$ - 2p3 $^2D_{3/2}$						5.92	0.35	
Mg VII	429.14	429.2	2s22p2 $^3P_0$ - 2s2p3 $^3D_1$	12.5	0.84	0.15	G 3	5.98	5.80		
Mg VIII	430.465	430.5	2p $^2P_{1/2}$ - 2s.2p2 $^2D_{3/2}$	104.0	1.04	0.11	G 3	6.00	5.91		[34]
Mg VII	431.313	431.3	2s22p2 $^3P_1$ - 2s2p3 $^3D_2$	25.0	1.23	0.18	G 3	5.98	5.80	0.78	[35]
Mg VII	431.188		2s22p2 $^3P_1$ - 2s2p3 $^3D_1$						5.80	0.22	
Mg VII	434.917	434.9	2s22p2 $^3P_2$ - 2s2p3 $^3D_3$	36.9	1.23	0.16	G 3	5.98	5.80	0.87	[36]
Mg VII	434.72		2s22p2 $^3P_2$ - 2s2p3 $^3D_2$						5.80	0.13	
Mg VIII	436.735	436.9	2p $^2P_{3/2}$ - 2s.2p2 $^2D_{5/2}$	191.4	0.91	0.10	G 3	6.00	5.91	0.89	[37]
Mg VIII	436.672		2p $^2P_{3/2}$ - 2s.2p2 $^2D_{3/2}$						5.91	0.11	[38]
Fe IX	218.937	438.0	3p6 $^1S_0$ - 3p5.3d $^1D_2$	41.8	0.44	0.19	G 3	6.02	5.94		
Fe XIV	219.136	438.4	3s2 3p $^2P_{3/2}$ - 3s2 3d $^2D_{5/2}$	68.9	0.13	0.05	G 3	6.09	6.24	0.58	bl ?
Fe XI	219.198		3s2.3p4 $^1D_2$ - 3s2.3p3(2p*).3d $^3D_2$						6.11	0.41	
Mg IX	439.175	439.1	2s.2p $^3P_1$ - 2p2 $^3P_2$	19.3	0.46	0.07	G 3	6.03	5.98		
Fe XIV	220.088	440.4	3s2 3p $^2P_{3/2}$ - 3s2 3d $^2D_{3/2}$	58.7	0.24	0.10	G 3	6.10	6.25	0.70	bl ?
Fe XI	220.249		3s2.3p4 $^3P_2$ - 3s2.3p3(2d*).3d $^3G_3$						6.10	0.23	
Mg IX	441.198	441.2	2s.2p $^3P_0$ - 2p2 $^3P_1$	14.5	0.53	0.09	G 3	6.02	5.98		
S IX	221.241	442.5	2s2.2p4 $^3P_2$ - 2s.2p5 $^3P_1$	46.4	1.01	0.44	G 3	6.04	6.00		
Mg IX	443.402	443.3	2s.2p $^3P_1$ - 2p2 $^3P_1$	9.2	0.59	0.16	G 3	6.03	5.98		
Mg IX	443.972	444.0	2s.2p $^3P_2$ - 2p2 $^3P_2$	48.5	0.54	0.07	G 3	6.03	5.98		
Si IX	223.742	447.4	2s22p2 $^3P_0$ - 2s2p3 $^3S_1$	109.3	0.57	0.15	G 3	6.05	6.04	0.90	[39]
Fe XIII	223.777		3s2 3p2 $^1D_2$ - 3s2 3p 3d $^3P_1$						6.21	0.10	
Mg IX	448.293	448.4	2s.2p $^3P_2$ - 2p2 $^3P_1$	18.3	0.47	0.07	G 3	6.03	5.98		
S IX	224.725	449.5	2s2.2p4 $^3P_2$ - 2s.2p5 $^3P_2$	123.3	1.68	0.43	G 3	6.04	6.00		?
Si IX	225.024	450.2	2s22p2 $^3P_1$ - 2s2p3 $^3S_1$	230.3	1.04	0.19	G 3	6.04	6.04	0.69	
Fe X	225.161		3s2.3p5 $^2P_{3/2}$ - 3s2.3p4(1d).3d $^2D_{5/2}$						6.04	0.20	
S IX	225.22		2s2.2p4 $^3P_1$ - 2s.2p5 $^3P_1$						6.00	0.11	
Fe X	226.02	451.7	3s2.3p5 $^2P_{3/2}$ - 3s2.3p4(3p).3d $^4P_{3/2}$	37.7	0.45	0.31	G 3	6.04	6.04		bl ?
Fe X	226.32	452.7	3s2.3p5 $^2P_{3/2}$ - 3s2.3p4(3p).3d $^4P_{5/2}$	109.4	0.48	0.13	G 3	6.05	6.04		bl ?

[28] Ghosting to 316.2 Å

[29] Ghosting to 317. Å

[30] Ghosting to 318.6 Å

[31] Only partly blended with the ghost of 430.5 Å

[32] Not blended with the ghost of 431.2 Å

[33] There might still a small contribution from unidentified lines. In the SERTS-89 spectrum, a weak line at 408.393 Å was observed.

[34] Could be ghosting to 401.9 Å

[35] Could in principle be ghosting to 403.3 Å, but is not.

[36] Could in principle be ghosting to 406.8 Å, but is not.

[37] Could be ghosting to 408.5-409 Å.

[38] Could be ghosting to 408.5-409 Å.

[39] Blended with a Fe XIV 447.331 Å in first order.

Table C.2: *(continued)*

Ion	λ_{th} (Å)	λ_{ob} (Å)	Transition	I_{ob}	I_{th}/I_{ob}	+/-	Det	log T_{eff}	log T_{max}	frac	
Si IX	227	454.0	2s22p2 $^3P_2$ - 2s2p3 $^3S_1$	288.2	0.97	0.16	G 3	6.04	6.04		
Fe XII	227.406	454.9	3s2.3p3 $^2P_{1/2}$ - 3s2.3p2(3p).3d $^2P_{1/2}$	20.7	1.07	0.97	G 3	6.07	6.16	0.62	
Si IX	227.361		2s22p2 $^1D_2$ - 2s2p3 $^1P_1$						6.03	0.31	
Fe XIII	228.159	456.3	3s2 3p2 $^1D_2$ - 3s2 3p 3d $^3P_2$	70.0	0.21	0.09	G 3	6.08	6.20	0.70	bl ?
S X	228.164		2s22p3 $^2D_{3/2}$ - 2s2p4 $^2D_{3/2}$						6.11	0.23	
Ne VII	465.22	465.2	2s2 $^1S_0$ - 2s2p $^1P_1$	142.2	0.76	0.08	G 3	5.98	5.72		
Ca IX	466.239	466.3	3s2 $^1S_0$ - 3s.3p $^1P_1$	39.8	0.45	0.06	G 3	5.98	5.78		
Fe X	233.644	467.2	3s2.3p5 $^2P_{3/2}$ - 3s2.3p4(1d).3d $^2P_{3/2}$	102.1	0.47	0.14	G 3	6.04	6.04	0.77	[40]
Fe X	233.482		3s2.3p5 $^2P_{3/2}$ - 3s2.3p4(3p).3d $^4F_{3/2}$						6.04	0.23	
Fe X	234.353	468.7	3s2.3p5 $^2P_{3/2}$ - 3s2.3p4(3p).3d $^4F_{5/2}$	81.5	0.49	0.15	G 3	6.04	6.04	0.64	bl ?
Si VIII	234.241		2s22p3 $^2P_{3/2}$ - 2s2p4 $^2P_{1/2}$						5.90	0.12	
Fe X	234.326		3s2.3p5 $^2P_{1/2}$ - 3s2.3p4(3p).3d $^4P_{3/2}$						6.04	0.12	
Fe XI	235.088	469.5	3s2.3p4 $^3P_2$ - 3s2.3p3(2d*).3d $^3F_2$	14.3	0.34	0.31	G 3	6.06	6.10		[41]
Si VIII	235.549	471.5	2s22p3 $^2P_{3/2}$ - 2s2p4 $^2P_{3/2}$	18.3	0.83	0.69	G 3	6.02	5.90		
Fe XIII	240.696	481.0	3s2 3p2 $^3P_0$ - 3s 3p3 $^3S_1$	14.3	1.51	1.29	G 3	6.09	6.20		[42]
Fe XIII	240.696	481.4	3s2 3p2 $^3P_0$ - 3s 3p3 $^3S_1$	29.1	0.81	0.30	G 3	6.08	6.20	0.84	[43]
Al VII	240.777		2s22p3 $^2D_{5/2}$ - 2s2p4 $^2P_{3/2}$						5.78	0.14	
Fe IX	241.739	483.3	3p6 $^1S_0$ - 3p5.3d $^3P_2$	140.8	1.18	0.16	G 3	6.02	5.94		
Fe IX	244.909	489.1	3p6 $^1S_0$ - 3p5.3d $^3P_1$	69.9	0.90	0.14	G 3	6.02	5.94		[44]
Al X	332.789	665.7	2s2 $^1S_0$ - 2s.2p $^1P_1$	121.3	0.97	0.88	G 4	6.06	6.09		
Fe XII	338.278	676.6	3s2.3p3 $^2D_{5/2}$ - 3s.3p4 $^2D_{5/2}$	71.2	0.40	0.36	G 4	6.07	6.16		
Na IX	681.721	681.5	1s2.2s $^2S_{1/2}$ - 1s2.2p $^2P_{3/2}$	3.3	11	2	G 4	6.03	5.92		?
Fe XI	341.113	682.1	3s2.3p4 $^3P_2$ - 3s.3p5 $^3P_1$	287.9	0.16	0.07	G 4	6.06	6.11		bl ?
Si IX	341.949	684.4	2s22p2 $^3P_0$ - 2s2p3 $^3D_1$	103.8	0.98	0.82	G 4	6.04	6.03		
Si IX	345.124	690.3	2s22p2 $^3P_1$ - 2s2p3 $^3D_2$	200.4	1.23	0.44	G 4	6.04	6.03	0.77	
Si IX	344.951		2s22p2 $^3P_1$ - 2s2p3 $^3D_1$						6.03	0.23	
Fe X	345.723	691.5	3s2.3p5 $^2P_{3/2}$ - 3s.3p6 $^2S_{1/2}$	141.0	1.13	0.50	G 4	6.04	6.04		
Fe XII	346.852	693.8	3s2.3p3 $^4S_{3/2}$ - 3s.3p4 $^4P_{1/2}$	194.6	0.24	0.15	G 4	6.07	6.16		bl ?
Na IX	694.147	694.2	1s2.2s $^2S_{1/2}$ - 1s2.2p $^2P_{1/2}$	6.0	3.13	2.84	G 4	6.03	5.92		?
Si X	347.403	694.7	2p $^2P_{1/2}$ - 2s.2p2 $^2D_{3/2}$	293.1	0.76	0.29	G 4	6.06	6.13		
Fe XIII	348.183	696.2	3s2 3p2 $^3P_0$ - 3s 3p3 $^3D_1$	26.1	1.95	1.76	G 4	6.09	6.20		?
Fe XI	349.046	698.0	3s2.3p4 $^3P_1$ - 3s.3p5 $^3P_0$	61.8	0.15	0.08	G 4	5.99	6.10	0.39	bl ?
Mg VI	349.163		2s2.2p3 $^2D_{5/2}$ - 2s.2p4 $^2D_{5/2}$						5.65	0.33	
Mg VI	349.124		2s2.2p3 $^2D_{3/2}$ - 2s.2p4 $^2D_{3/2}$						5.65	0.25	
Si IX	349.873	699.8	2s22p2 $^3P_2$ - 2s2p3 $^3D_3$	267.1	0.85	0.17	G 4	6.04	6.03	0.84	
Si IX	349.794		2s22p2 $^3P_2$ - 2s2p3 $^3D_2$						6.03	0.16	
Fe XII	352.106	704.2	3s2.3p3 $^4S_{3/2}$ - 3s.3p4 $^4P_{3/2}$	101.5	0.92	0.37	G 4	6.07	6.16		
		704.7	ghost of Mg IX IIo 368.07 Å ?				G 4				
Fe XI	352.662	705.2	3s2.3p4 $^3P_2$ - 3s.3p5 $^3P_2$	176.2	1.11	0.39	G 4	6.06	6.11		
Mg IX	706.058	705.8	2s2 $^1S_0$ - 2s.2p $^3P_1$	45.8	0.52	0.08	G 4	6.02	5.98		
Si X	356.012	711.8	2p $^2P_{3/2}$ - 2s.2p2 $^2D_{5/2}$	127.6	1.05	0.38	G 4	6.06	6.13	0.76	
Si X	356.05		2p $^2P_{3/2}$ - 2s.2p2 $^2D_{3/2}$						6.13	0.24	
Fe XI	356.519	712.9	3s2.3p4 $^3P_1$ - 3s.3p5 $^3P_1$	27.4	0.87	0.79	G 4	6.06	6.11		
Fe XI	358.621	717.3	3s2.3p4 $^3P_0$ - 3s.3p5 $^3P_1$	48.9	0.64	0.58	G 4	6.06	6.11		
Fe XIII	359.642	719.2	3s2 3p2 $^3P_1$ - 3s 3p3 $^3D_2$	58.4	0.19	0.15	G 4	6.08	6.20		
Fe XIII	359.842	719.7	3s2 3p2 $^3P_1$ - 3s 3p3 $^3D_1$	16.4	0.81	0.73	G 4	6.09	6.20		
Fe XVI	360.761	721.6	3s $^2S_{1/2}$ - 3p $^2P_{1/2}$	89.9	0.01	0.01	G 4	6.18	6.34	0.77	bl ?
Fe X	360.839		3s2.3p4(3p).3d $^4F_{3/2}$ - 3s.3p5(3p*).3d $^4F_{3/2}$						6.04	0.23	
Fe XII	364.467	728.5	3s2.3p3 $^4S_{3/2}$ - 3s.3p4 $^4P_{5/2}$	123.7	1.05	0.47	G 4	6.07	6.16		
Mg VII	365.234	729.9	2s22p2 $^3P_1$ - 2s2p3 $^3P_2$	31.6	0.97	0.88	G 4	5.98	5.81	0.37	
Mg VII	365.176		2s22p2 $^3P_1$ - 2s2p3 $^3P_0$						5.81	0.35	
Mg VII	365.243		2s22p2 $^3P_1$ - 2s2p3 $^3P_1$						5.81	0.28	
Fe X	365.543	730.7	3s2.3p5 $^2P_{1/2}$ - 3s.3p6 $^2S_{1/2}$	56.8	1.21	1.09	G 4	6.04	6.04		
Mg VII	367.674	735.4	2s22p2 $^3P_2$ - 2s2p3 $^3P_2$	94.9	0.54	0.48	G 4	5.98	5.81	0.77	
Mg VII	367.683		2s22p2 $^3P_2$ - 2s2p3 $^3P_1$						5.81	0.23	
Mg IX	368.07	736.0	2s2 $^1S_0$ - 2s.2p $^1P_1$	1069.1	0.92	0.14	G 4	6.03	5.98		[45]
Fe XI	369.153	738.1	3s2.3p4 $^3P_1$ - 3s.3p5 $^3P_2$	62.9	0.93	0.56	G 4	6.06	6.11		[46]
		742.6	ghost of 769.3 Å				G 4				
		744.1	ghost of Ne VIII 770.4 Å				G 4				
		745.5	ghost of 772.26 Å				G 4				
Mg IX	749.55	749.7	2s.2p $^1P_1$ - 2p2 $^1D_2$	9.0	0.27	0.13	G 4	6.03	5.99		

[40] Blended with first order Fe XIV 467.395 Å line.

[41] Blended ? + a Ne IV 469.9 Å in on-disc observations.

[42] + a Ne V 480.4 Å in on-disc observations.

[43] + a Ne V 481.3 Å in on-disc observations.

[44] + Ne III 489 Å in on-disc observations.

[45] Ghosting to 704.7 Å ?

[46] It appears not to be ghosting. On-disc, it is blended with a ghost of N IV 765.1 Å.

Table C.2: *(continued)*

Ion	λ_{th} (Å)	λ_{ob} (Å)	Transition	I_{ob}	I_{th}/I_{ob}	+/-	Det	log T_{eff}	log T_{max}	frac	
Ca IX	378.081	755.6	3s.3p $^3P_2$ - 3s.3d $^3D_3$	17.1	0.07	0.06	G 4	5.97	5.78	0.52	
Al IX	384.971	769.3	2s2.2p $^2P_{1/2}$ - 2s.2p2 $^2D_{3/2}$	75.8	0.37	0.15	G 4	6.04	6.03		[47]
Ne VIII	770.409	770.8	1s2 2s $^2S_{1/2}$ - 1s2 2p $^2P_{3/2}$	294.1	1.81	0.20	G 4	6.02	5.79		[48]
Mg VIII	772.26	772.1	2p $^2P_{3/2}$ - 2s.2p2 $^4P_{5/2}$	21.7	0.38	0.13	G 4	6.00	5.90		[49]
Al VIII	387.957	775.4	2p2 $^3P_2$ - 2s.2p3 $^3D_3$	39.9	0.69	0.38	G 4	6.02	5.92	0.84	[50]
Al VIII	387.822		2p2 $^3P_2$ - 2s.2p3 $^3D_2$						5.92	0.14	
S X	776.373	776.3	2s22p3 $^4S_{3/2}$ - 2s22p3 $^2P_{3/2}$	6.0	1.15	0.78	G 4	6.06	6.11		
Ne VIII	780.324	780.1	1s2 2s $^2S_{1/2}$ - 1s2 2p $^2P_{1/2}$	157.7	1.69	0.20	G 4	6.02	5.79		
Mg VIII	782.338	781.9	2p $^2P_{3/2}$ - 2s.2p2 $^4P_{3/2}$	6.7	0.77	0.59	G 4	6.00	5.90		

[47] Blended with a Mg VIII 769.343 Å. Ghosting to 742.6.
[48] Ghosting to 744.1 Å.
[49] Blended ? (ghosting to 745.5 Å)
[50] This identification with second order Al VIII is uncertain.

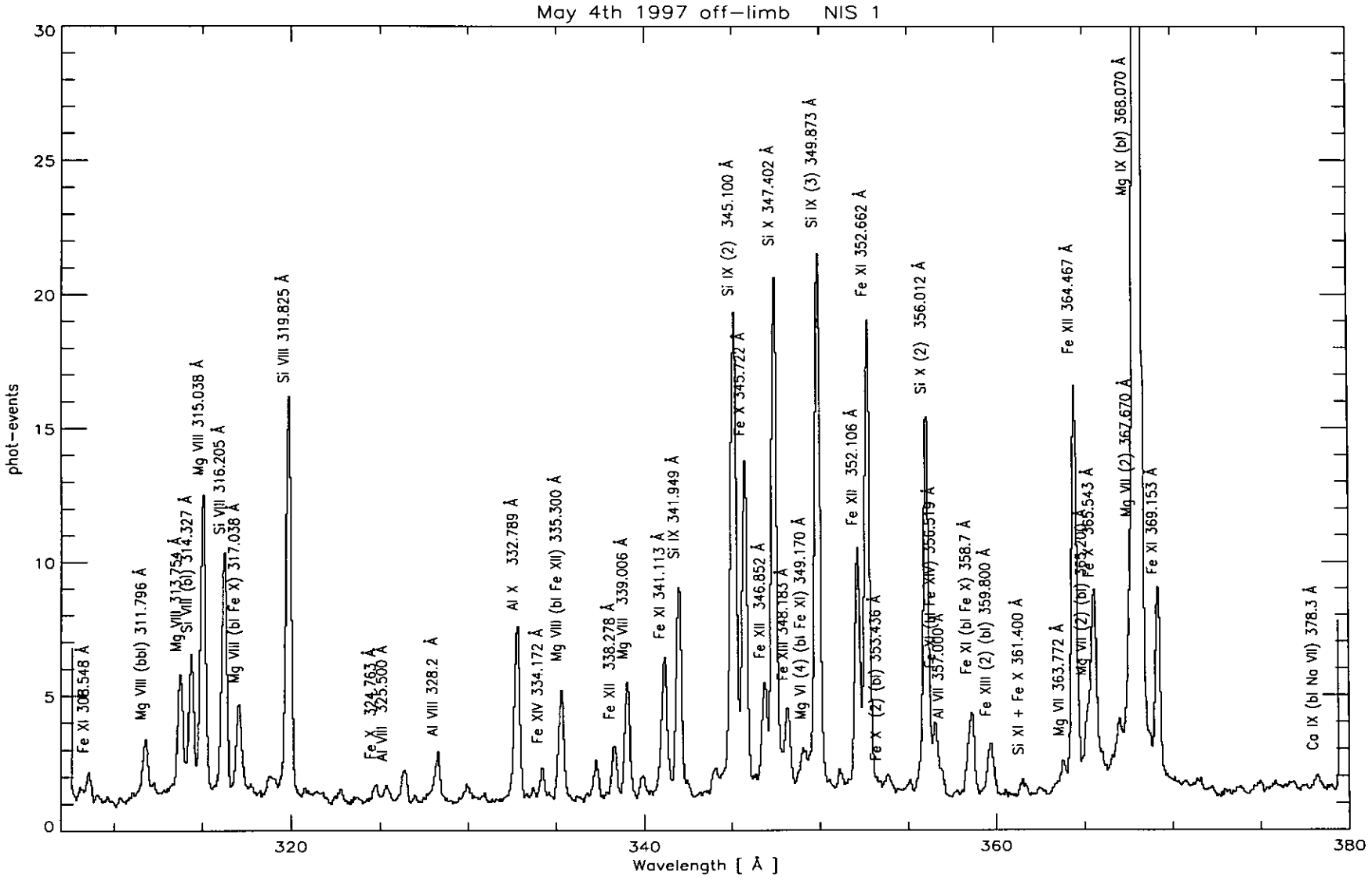

Figure C.1: *The NIS 1 averaged spectra of an area of the off-limb quiet sun observation of May 4th 1997.*

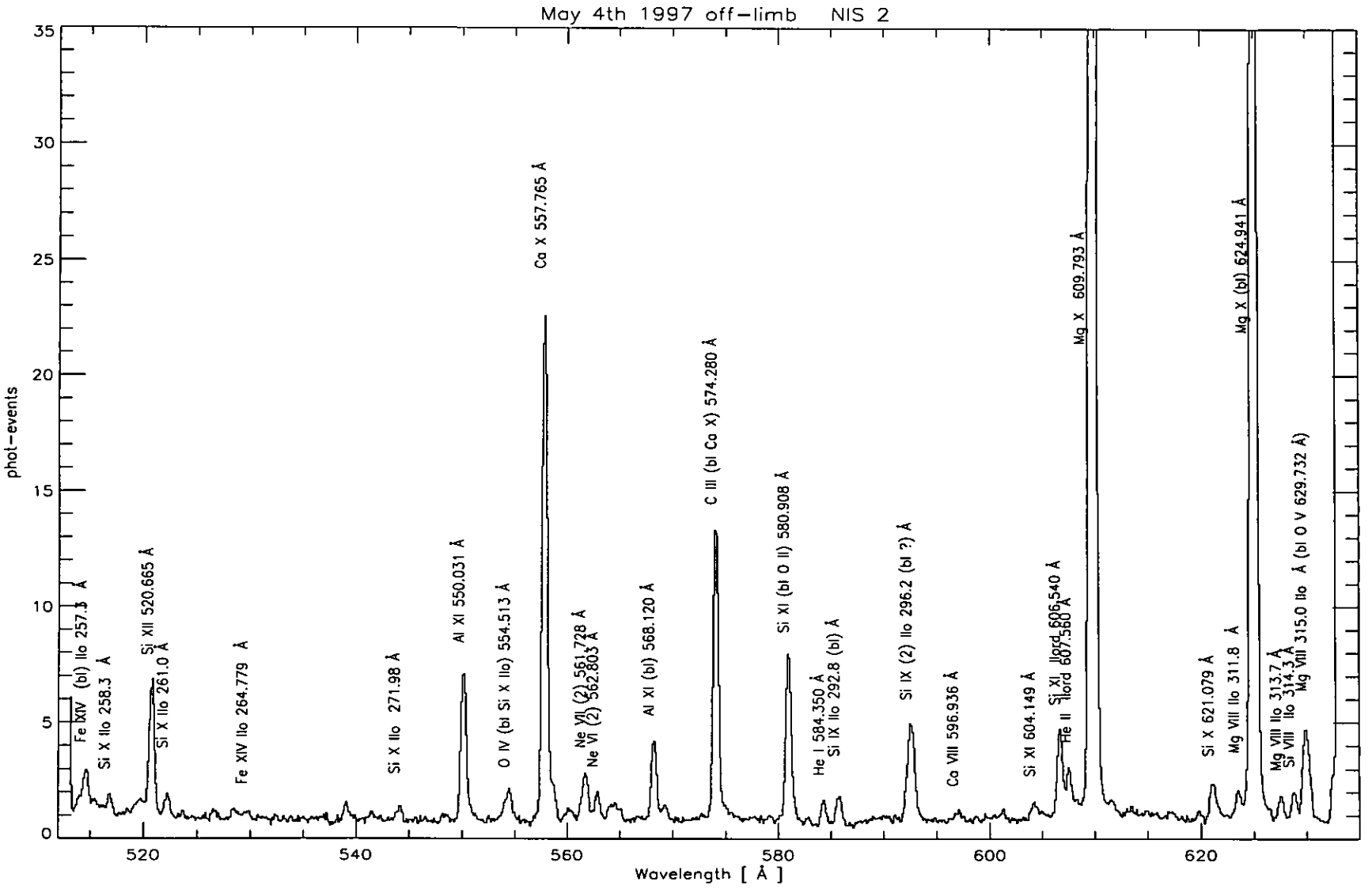

Figure C.2: *The NIS 2 averaged spectra of an area of the off-limb quiet sun observation of May 4th 1997.*

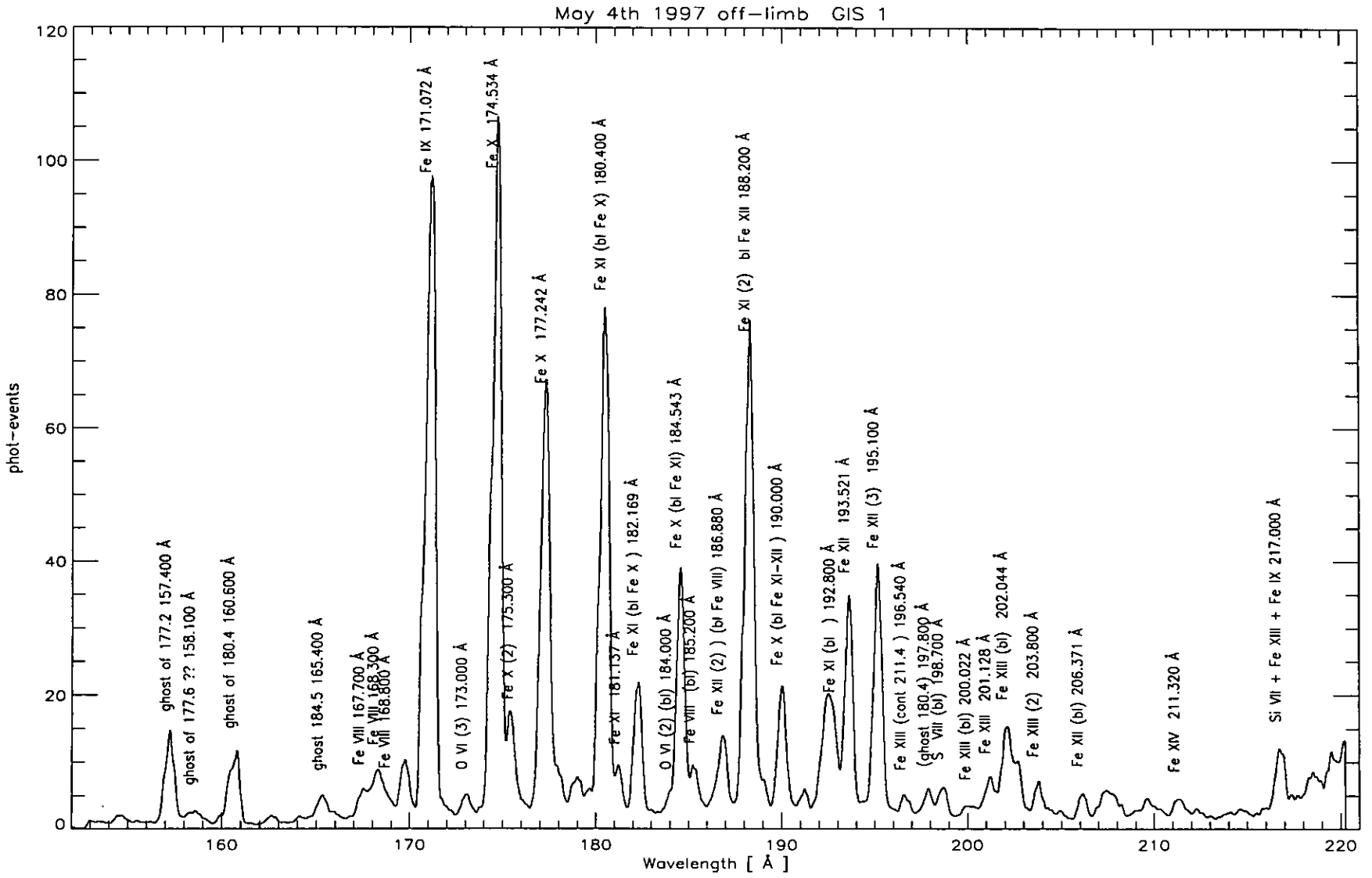

Figure C.3: *The GIS 1 averaged spectra of an area of the off-limb quiet sun observation of May 4th 1997.*

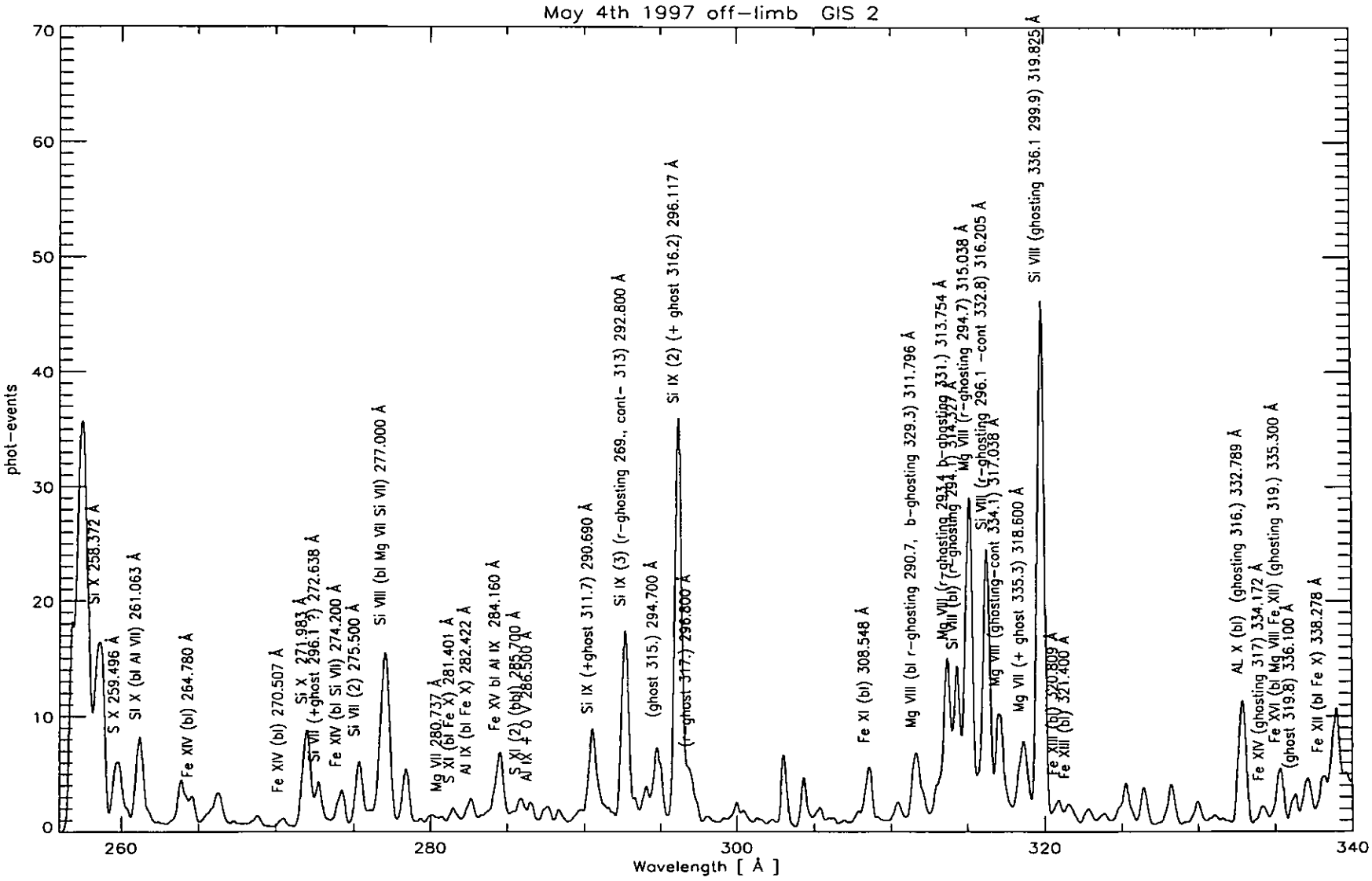

Figure C.4: *The GIS 2 averaged spectra of an area of the off-limb quiet sun observation of May 4th 1997.*

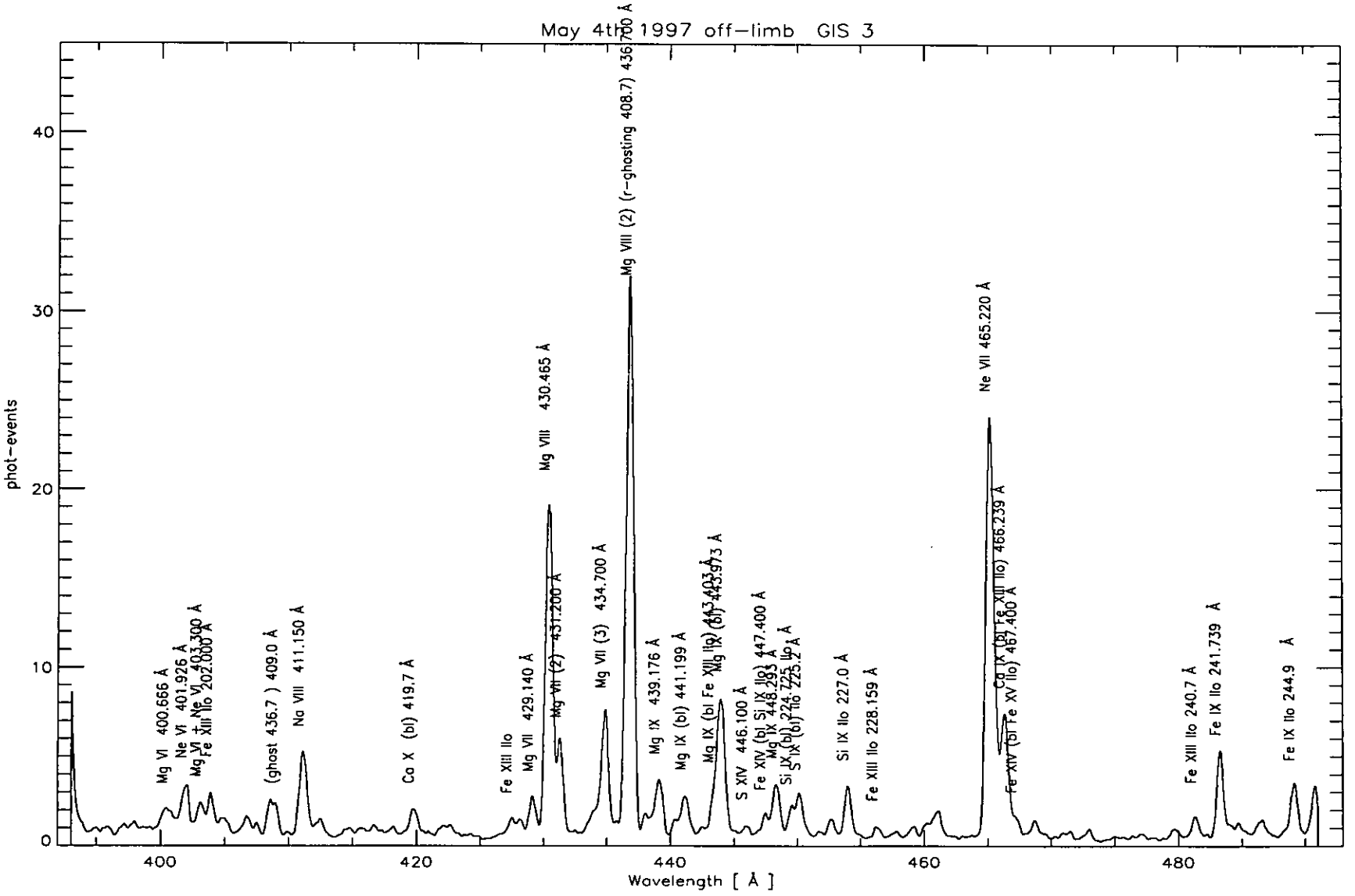

Figure C.5: *The GIS 3 averaged spectra of an area of the off-limb quiet sun observation of May 4th 1997.*

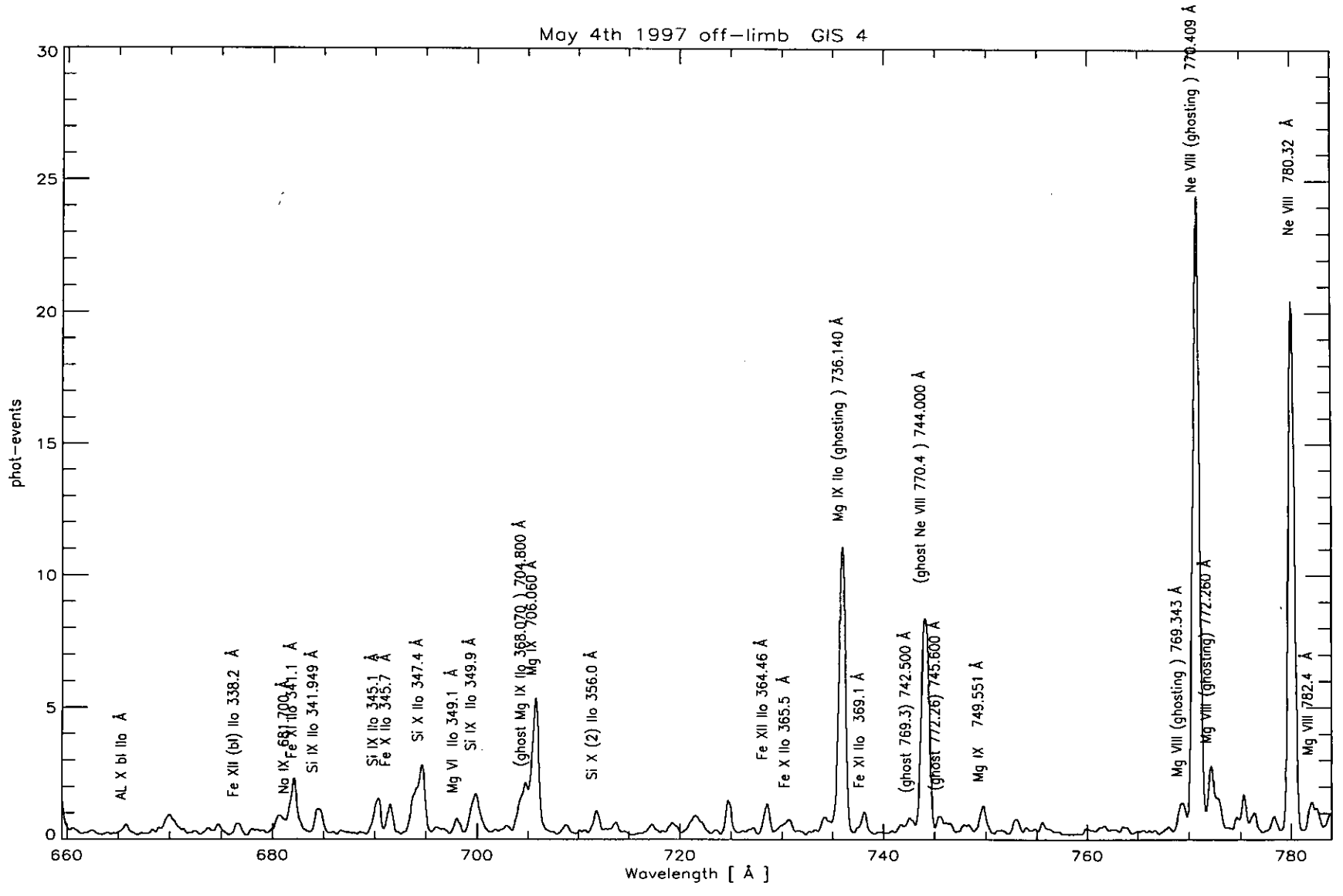

Figure C.6: *The GIS 4 averaged spectra of an area of the off-limb quiet sun observation of May 4th 1997.*

Table C.3: *Some of the ghosting reconstruction applied to the GIS off-limb spectra of May 4th, 1997. The averaged positions of the ghost and parent (i.e. ghosting) lines are indicated in columns (1) and (3). The ratio of the intensity of the ghost with that one of the ghosting line (in counts) is presented in column (2), while the intensity of the ghosting line (in counts), is shown in column (4). Note that the correction for ghosting is important for many lines, and that some lines have been corrected twice, for both the red- and blue-shifted ghosts.*

λ_{ob} (Å) (ghost)	ratio (counts)	λ_{ob} (Å) (parent)	I (counts) (parent)
154.629	0.01	174.677	1779.27
157.232	0.24	177.3	1026.74
160.628	0.17	180.491	1217.41
197.405	0.01	180.491	1426.13
197.896	0.04	180.491	1436.96
162.658	0.05	182.263	322.152
165.299	0.15	184.582	530.512
166.079	0.20	185.327	130.323
331.218	0.04	313.688	173.599
294.015	0.25	314.333	162.36
294.769	0.25	315.101	375.66
332.5	0.03	315.101	470.292
296.932	0.68	317.064	120.914
300.102	0.05	319.782	557.139
336.238	0.05	319.782	585.483
268.764	0.05	292.659	233.177
318.21	0.28	335.304	58.688
318.647	1.47	335.304	74.836
408.53	0.06	436.892	448.4
409.032	0.04	436.892	473.787
704.691	0.12	735.988	117.175
742.642	0.51	769.316	12.79
744.117	0.42	770.761	267.646
745.499	0.25	772.135	22.549

C.2.1 The GIS ghosts for the off-limb observation – May 4th 1997

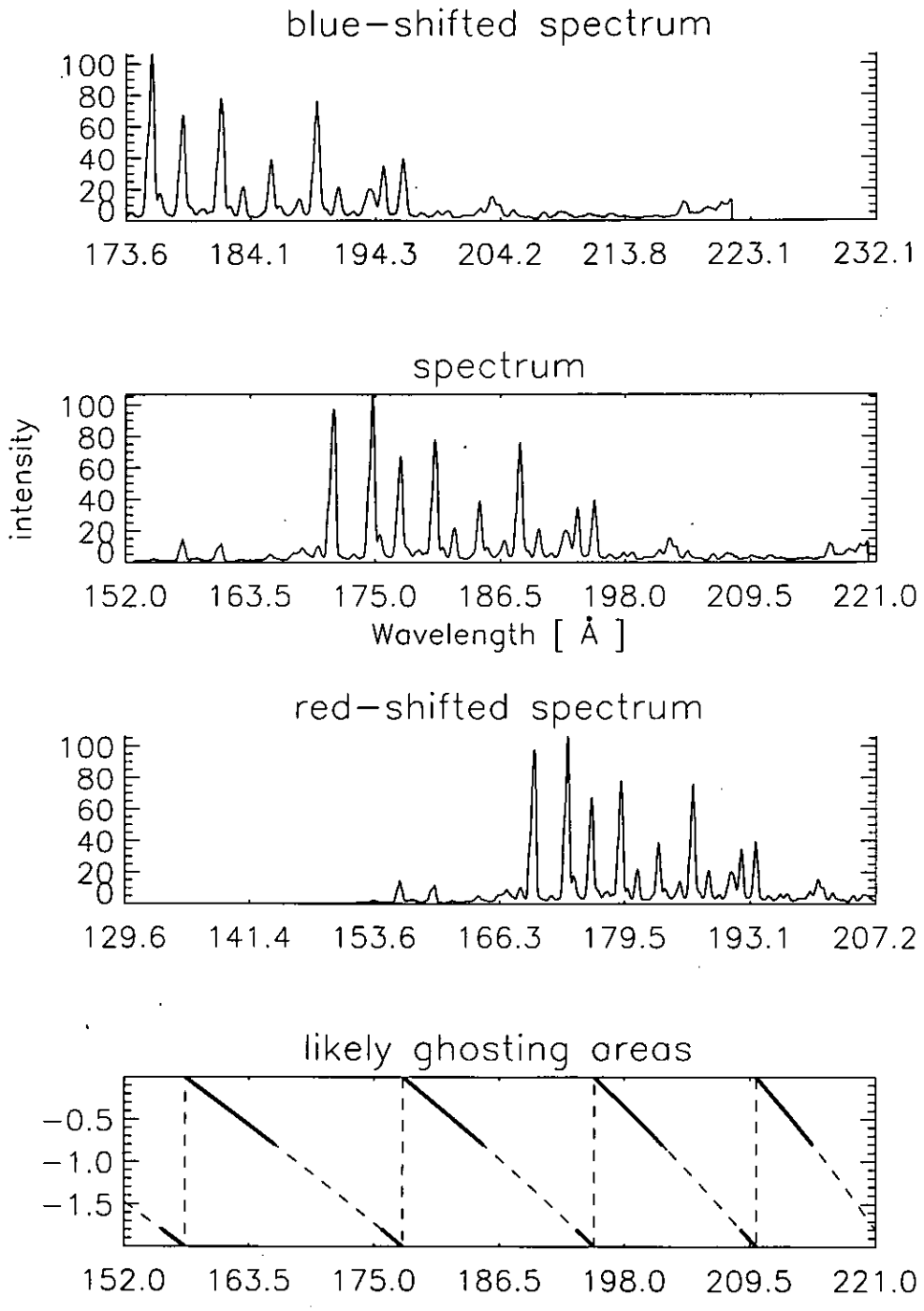

Figure C.7: *The GIS 1 spectrum of May 4th 1997, off-limb (middle), with the blue- and red-shifted and the likely ghosting areas.*

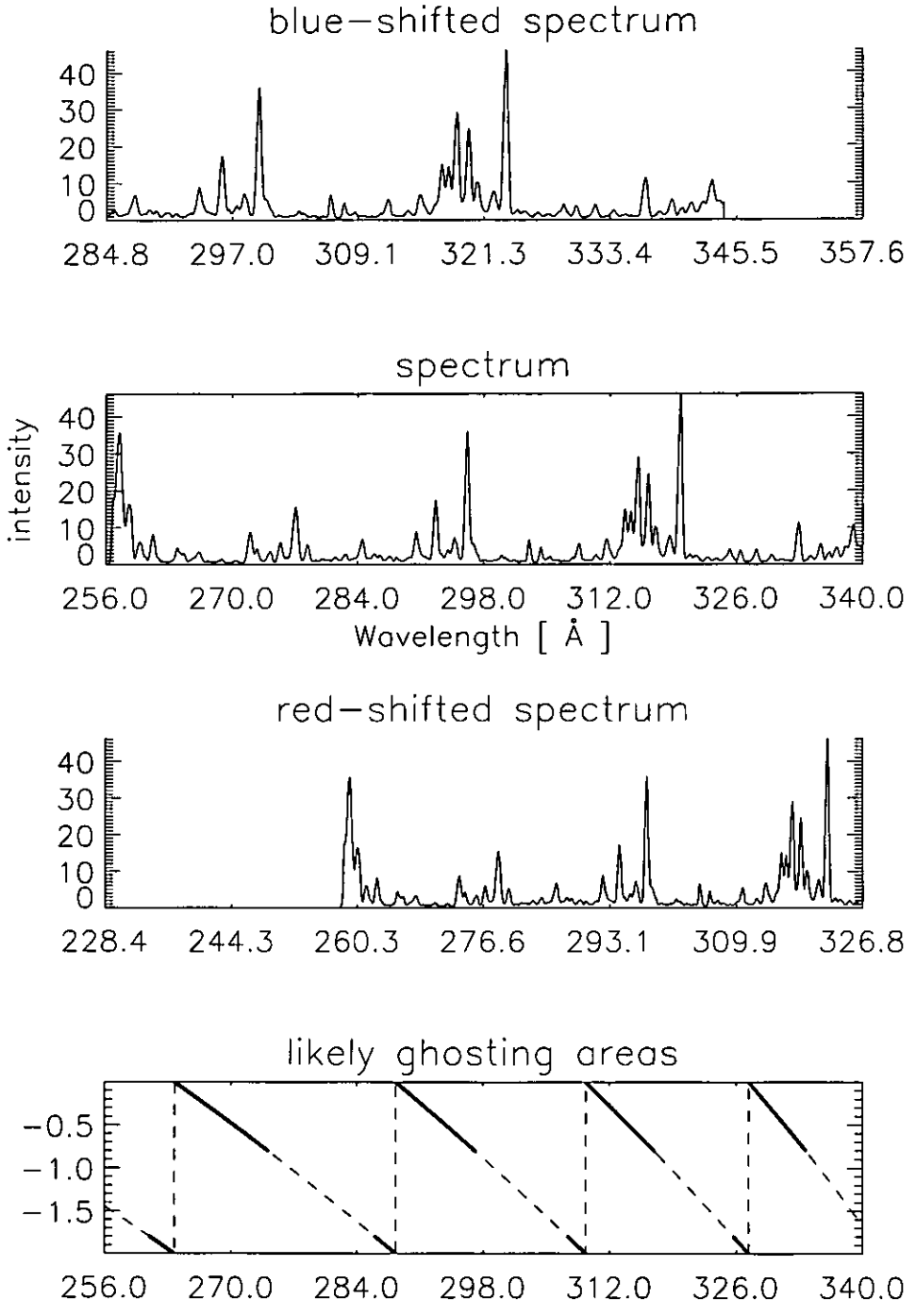

Figure C.8: *The GIS 2 spectrum of May 4th 1997, off-limb (middle), with the blue- and red-shifted and the likely ghosting areas.*

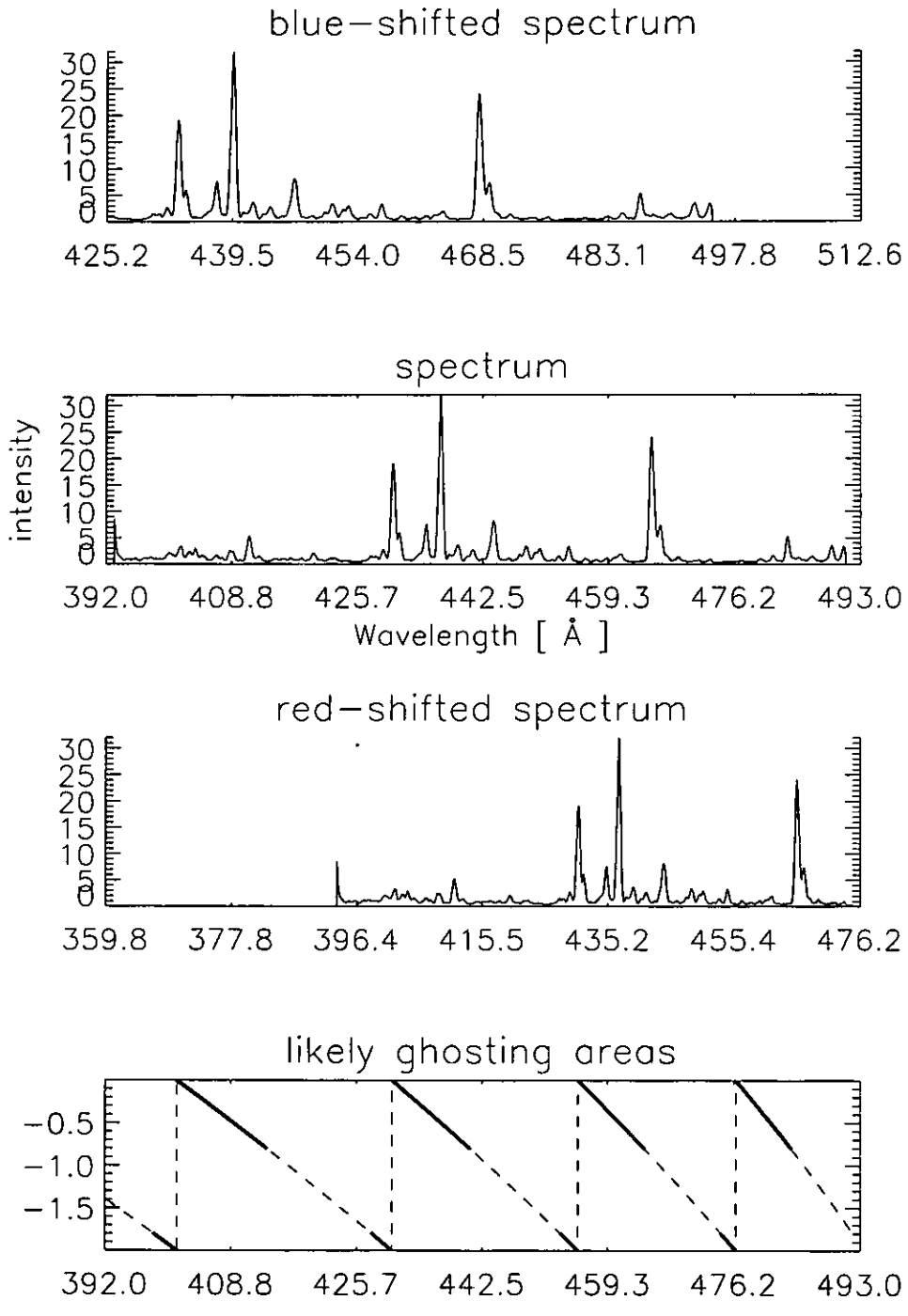

Figure C.9: *The GIS 3 spectrum of May 4th 1997, off-limb (middle), with the blue- and red-shifted and the likely ghosting areas.*

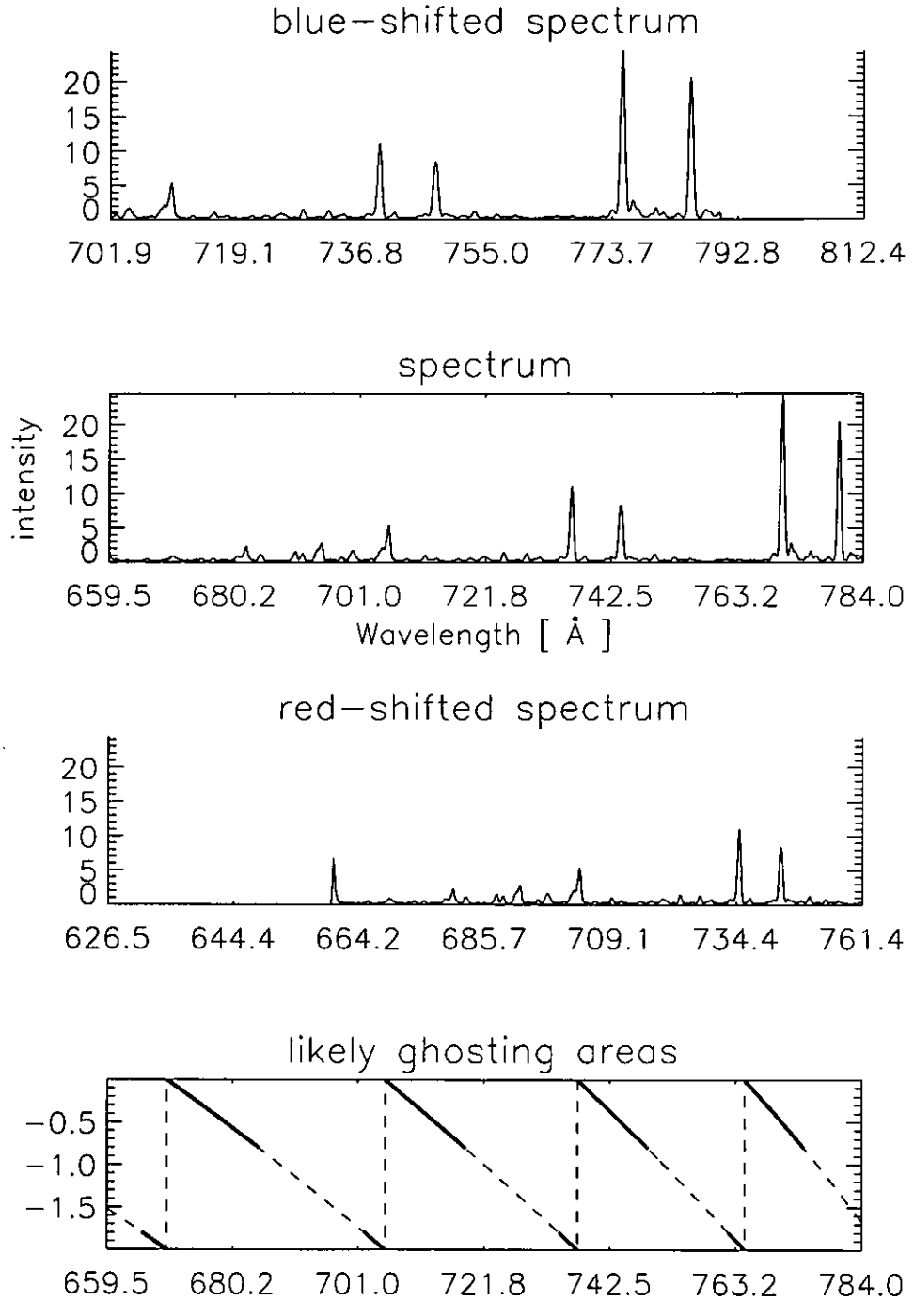

Figure C.10: *The GIS 4 spectrum of May 4th 1997, off-limb (middle), with the blue- and red-shifted and the likely ghosting areas.*

C.3 The spectra and line identifications for the on-disc observation – October 16th, 1997

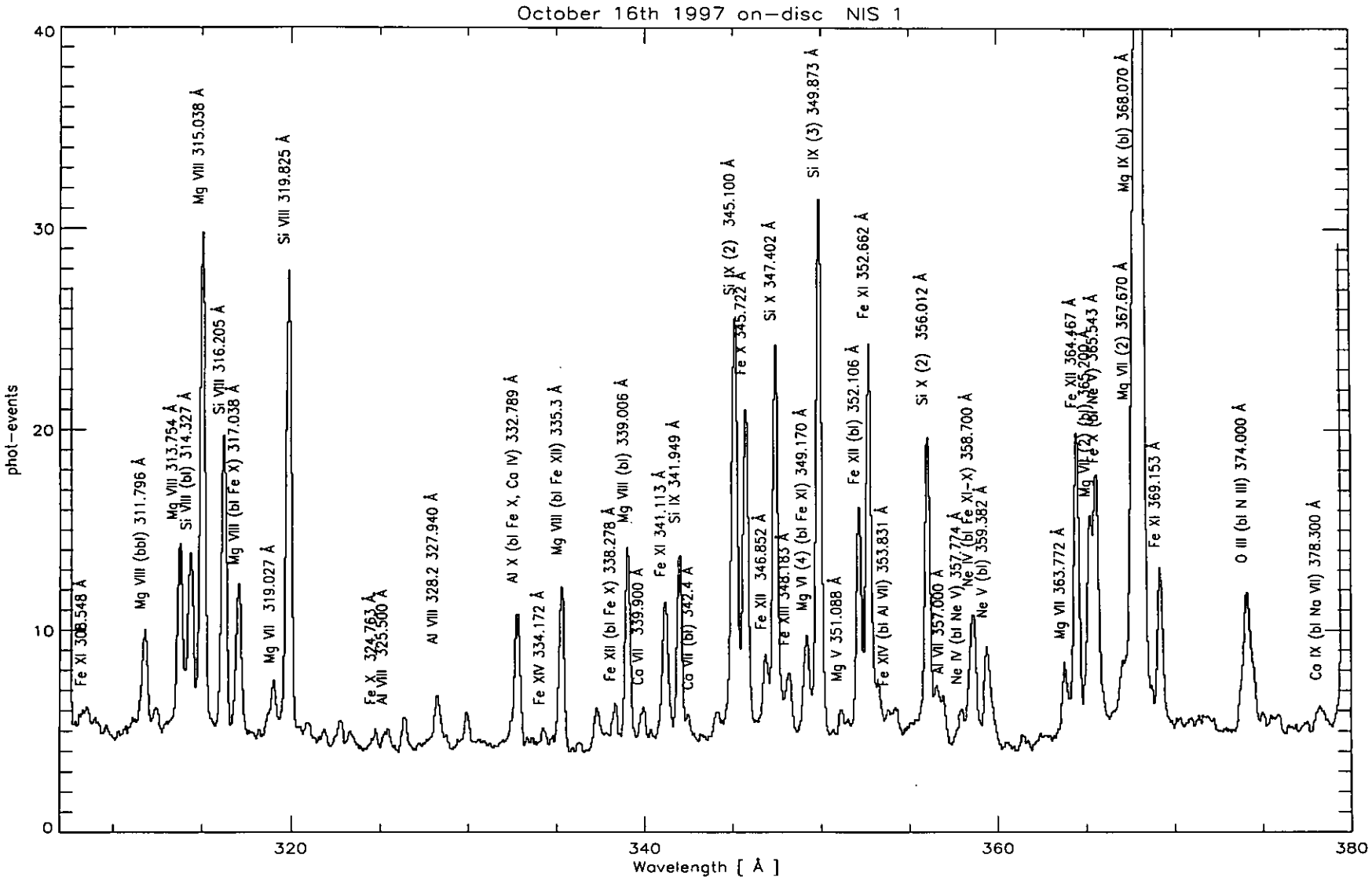

Figure C.11: *The NIS 1 averaged spectra of an area of the on-disc quiet sun observation of October 16th 1997.*

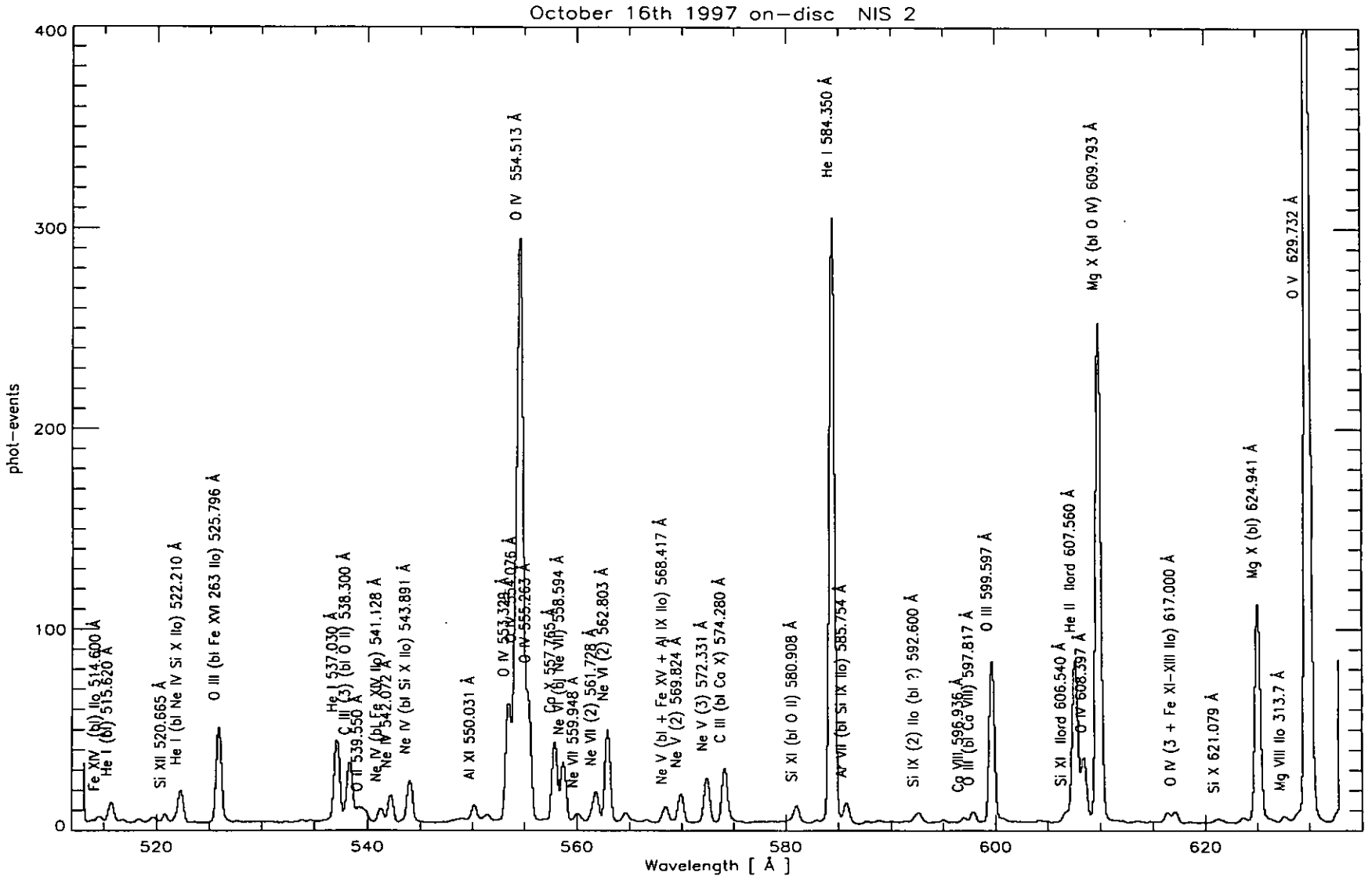

Figure C.12: *The NIS 2 averaged spectra of an area of the on-disc quiet sun observation of October 16th 1997.*

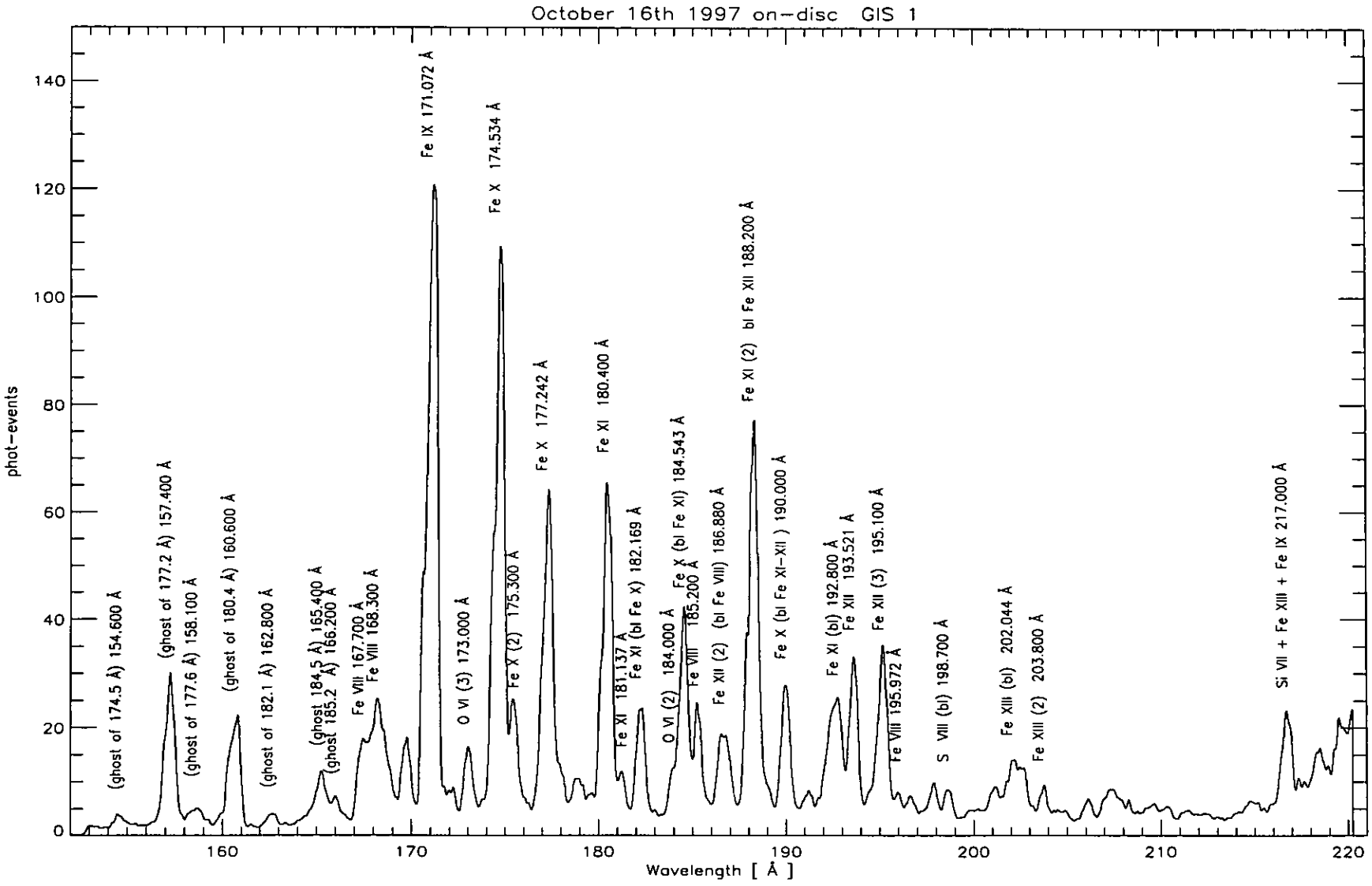

Figure C.13: *The GIS 1 averaged spectra of an area of the on-disc quiet sun observation of October 16th 1997.*

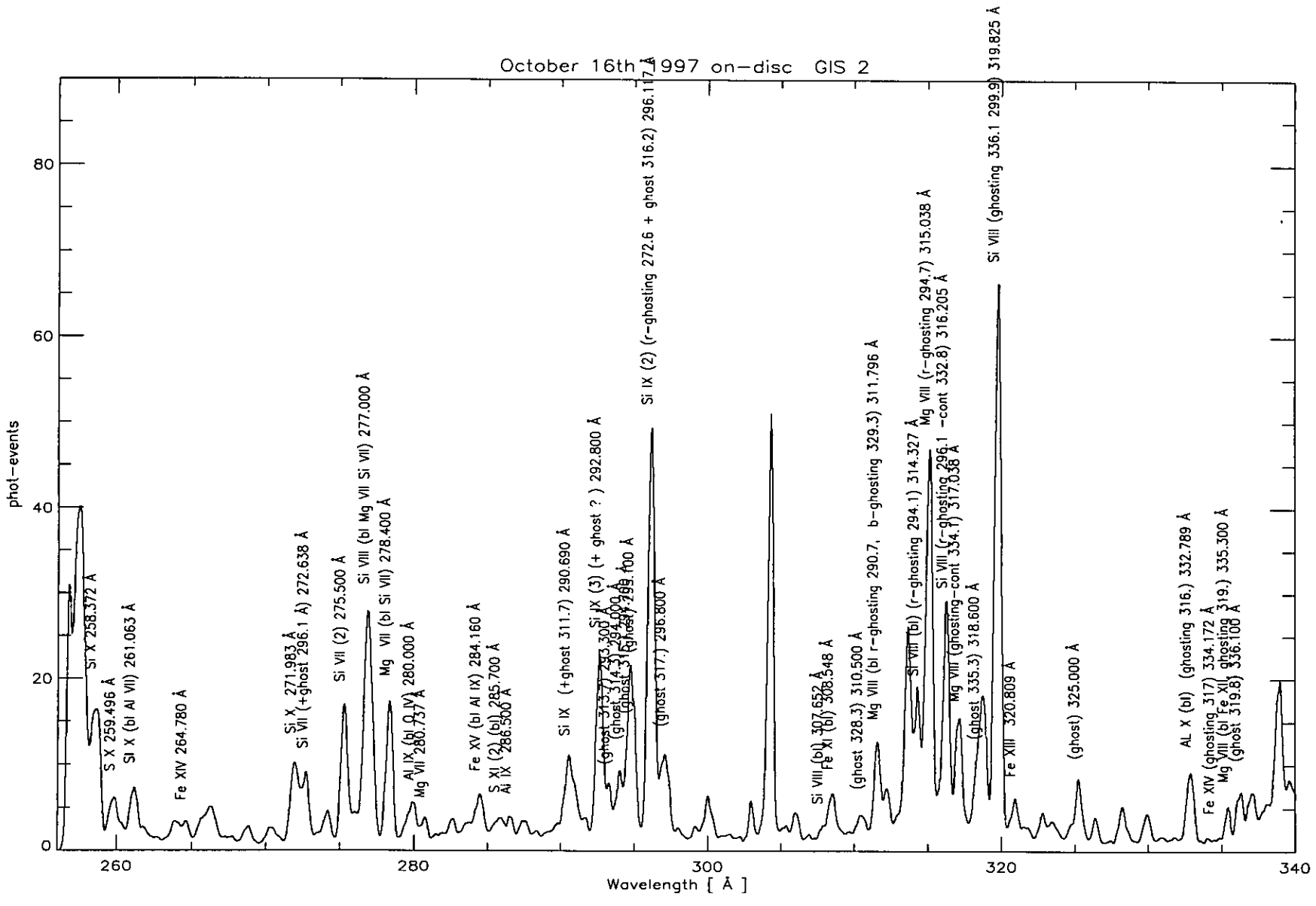

Figure C.14: *The GIS 2 averaged spectra of an area of the on-disc quiet sun observation of October 16th 1997.*

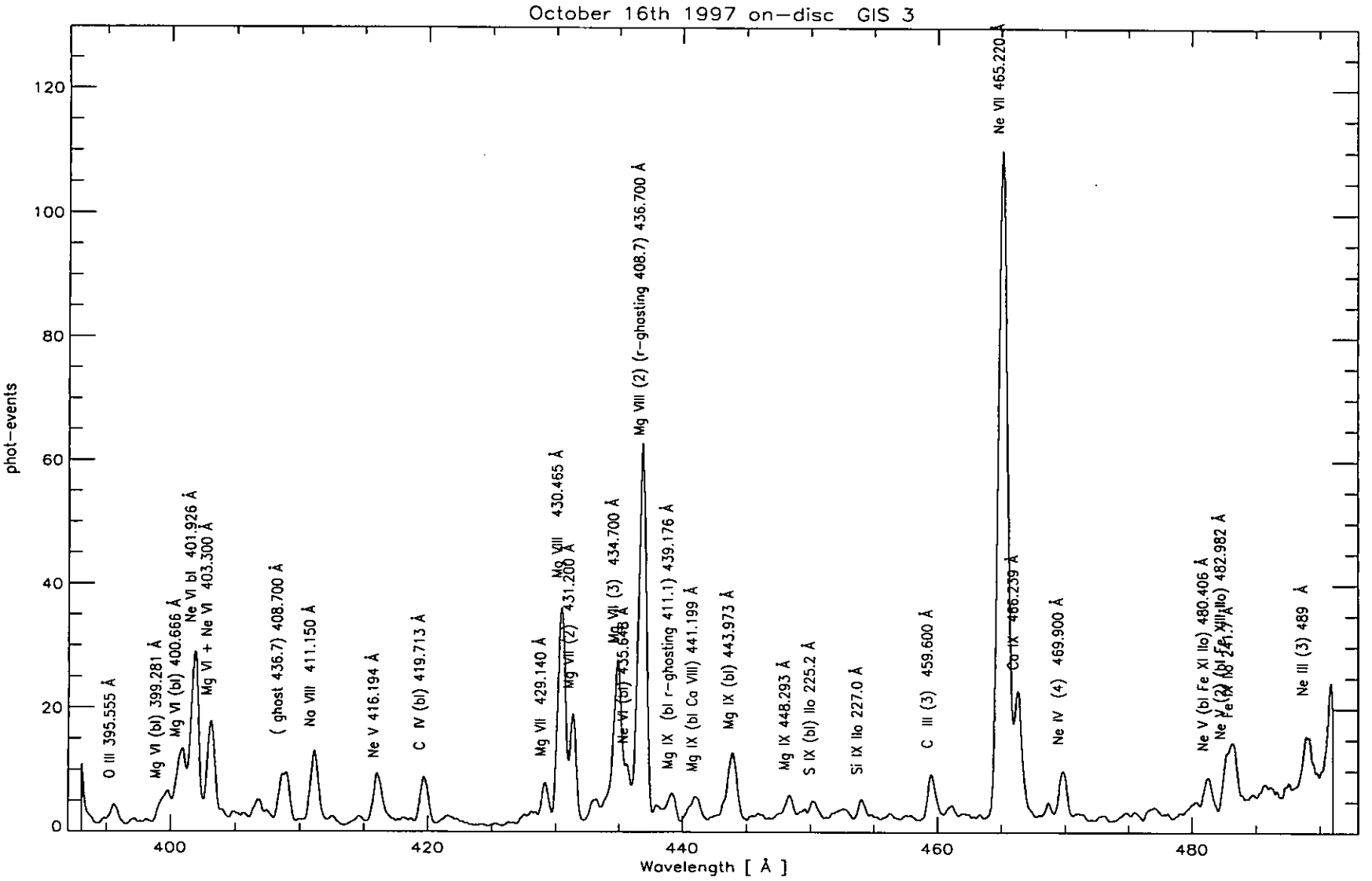

Figure C.15: *The GIS 3 averaged spectra of an area of the on-disc quiet sun observation of October 16th 1997.*

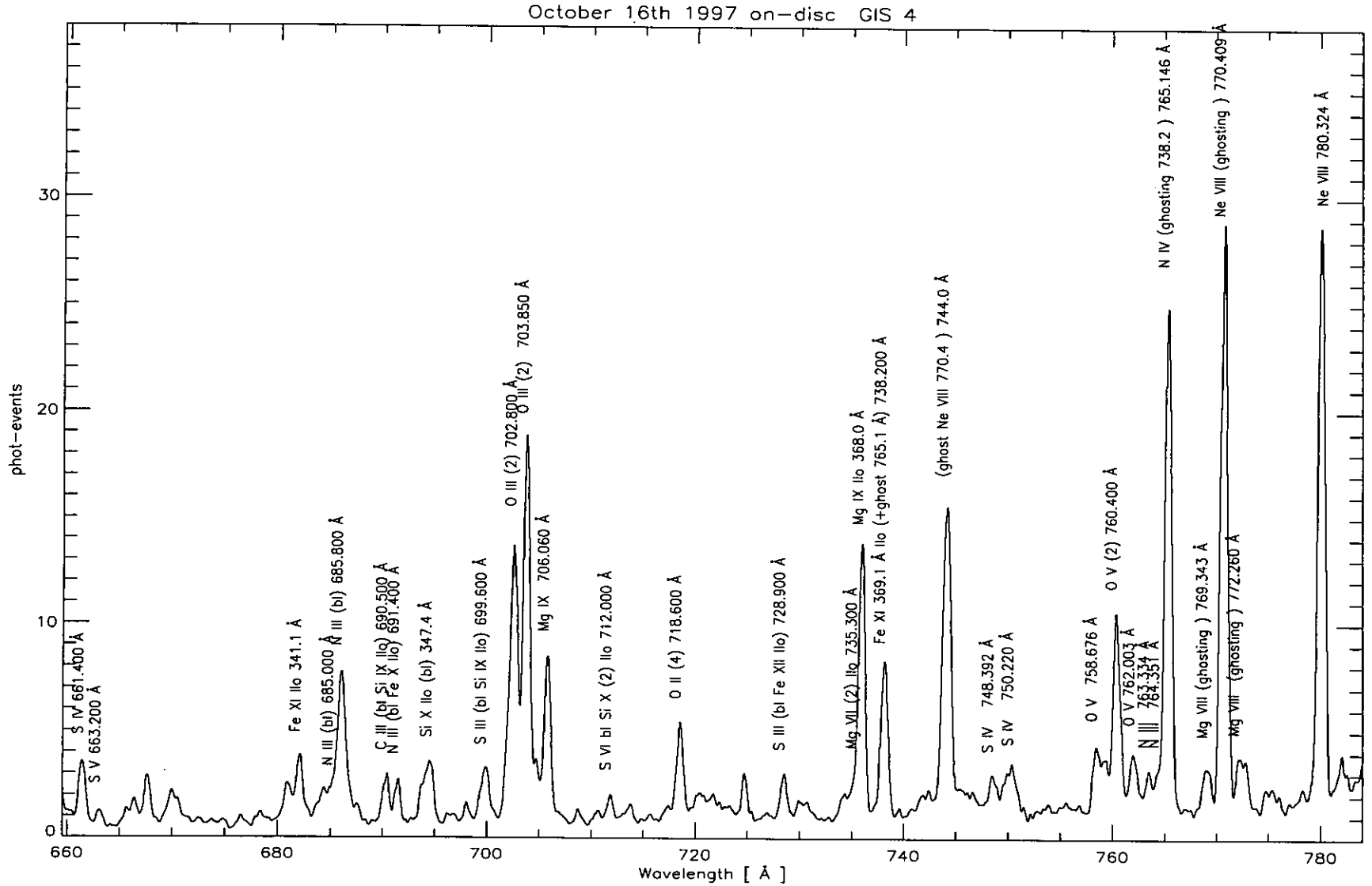

Figure C.16: *The GIS 4 averaged spectra of an area of the on-disc quiet sun observation of October 16th 1997.*

Table C.4: *Line List for the on-disc quiet sun observation of October 16th 1997.*

Ion	λ_{th} (Å)	λ_{ob} (Å)	Transition	I_{ob}	I_{th}/I_{ob}	+/-	Det	log T_{eff}	log T_{max}	frac	
Fe XI	308.548	308.4	3s2.3p4 $^1D_2$ - 3s.3p5 $^1P_1$	39.2	0.43	0.08	N 1	6.02	6.10		
Mg VIII	311.796	311.8	2p $^2P_{1/2}$ - 2s.2p2 $^2P_{3/2}$	144.5	0.71	0.08	N 1	5.96	5.91		
C IV	312.42	312.4	1s2 2s $^2S_{1/2}$ - 1s2 3p $^2P_{3/2}$	40.8	0.30	0.06	N 1	5.82	5.09	0.49	
C IV	312.451		1s2 2s $^2S_{1/2}$ - 1s2 3p $^2P_{1/2}$						5.09	0.25	
Al VI	312.236		2p4 $^3P_1$ - 2s.2p5 $^3P_2$						5.62	0.12	
Fe XII	312.262		3s2.3p3 $^2P_{1/2}$ - 3s.3p4 $^2P_{1/2}$						6.16	0.11	
Fe XIII	312.872	313.0	3s2 3p2 $^3P_1$ - 3s 3p3 $^3P_0$	22.6	0.17	0.05	N 1	6.07	6.20	0.79	
P X	312.981		2s22p2 $^3P_1$ - 2s2p3 $^3D_2$						6.15	0.21	
Mg VIII	313.754	313.8	2p $^2P_{1/2}$ - 2s.2p2 $^2P_{1/2}$	243.3	0.82	0.09	N 1	5.96	5.92		
Si VIII	314.327	314.4	2s22p3 $^4S_{3/2}$ - 2s2p4 $^4P_{1/2}$	241.4	0.88	0.09	N 1	5.98	5.91		
Mg VIII	315.039	315.0	2p $^2P_{3/2}$ - 2s.2p2 $^2P_{3/2}$	578.6	0.90	0.09	N 1	5.96	5.91		
Si VIII	316.205	316.2	2s22p3 $^4S_{3/2}$ - 2s2p4 $^4P_{3/2}$	341.1	1.18	0.12	N 1	5.98	5.91		
Mg VIII	317.039	317.1	2p $^2P_{3/2}$ - 2s.2p2 $^2P_{1/2}$	188.4	0.75	0.08	N 1	5.97	5.92		
Mg VII	319.027	319.1	2s22p2 $^1D_2$ - 2s2p3 $^1D_2$	68.0	0.52	0.11	N 1	5.91	5.78		
Si VIII	319.826	319.9	2s22p3 $^4S_{3/2}$ - 2s2p4 $^4P_{5/2}$	517.4	1.19	0.12	N 1	5.98	5.91		
Fe X	321.732	321.8	3s2.3p4(3p).3d $^4D_{5/2}$ - 3s.3p5(3p*).3d $^4F_{7/2}$	10.2	0.68	0.31	N 1	6.03	6.03	0.70	[51]
Fe X	321.804		3s2.3p4(3p).3d $^4D_{7/2}$ - 3s.3p5(3p*).3d $^4F_{7/2}$						6.03	0.29	
Fe X	324.763	324.7	3s2.3p4(3p).3d $^4D_{7/2}$ - 3s.3p5(3p*).3d $^4F_{9/2}$	21.4	0.67	0.18	N 1	6.03	6.03		[52]
Al VIII	325.276	325.4	2p2 $^3P_1$ - 2s.2p3 $^3P_0$	28.4	1.39	0.29	N 1	5.98	5.92	0.37	[53]
Al VIII	325.292		2p2 $^3P_1$ - 2s.2p3 $^3P_2$						5.92	0.34	
Al VIII	325.338		2p2 $^3P_1$ - 2s.2p3 $^3P_1$						5.92	0.29	
Al VIII	328.185	328.2	2p2 $^3P_2$ - 2s.2p3 $^3P_2$	50.6	1.29	1.00	N 1	5.99	5.92	0.73	[54]
Al VIII	328.232		2p2 $^3P_2$ - 2s.2p3 $^3P_1$						5.92	0.23	
Al X	332.789	332.8	2s2 $^1S_0$ - 2s.2p $^1P_1$	139.9	1.23	0.14	N 1	6.04	6.10		
Fe XIV	334.172	334.3	3s2 3p $^2P_{1/2}$ - 3s 3p2 $^2D_{3/2}$	22.1	0.65	0.16	N 1	6.09	6.24		
Mg VIII	335.253	335.3	2p $^2P_{1/2}$ - 2s.2p2 $^2S_{1/2}$	144.1	0.67	0.07	N 1	5.97	5.92		
Fe XII	338.278	338.3	3s2.3p3 $^2D_{5/2}$ - 3s.3p4 $^2D_{5/2}$	39.3	0.26	0.04	N 1	6.06	6.15		
Mg VIII	339.006	339.0	2p $^2P_{3/2}$ - 2s.2p2 $^2S_{1/2}$	150.8	0.82	0.09	N 1	5.96	5.92		
Ca VII	339.966	339.9		31.9	0.64	0.10	N 1	5.74	5.67		[55]AC
Fe XI	341.113	341.2	3s2.3p4 $^3P_2$ - 3s.3p5 $^3P_1$	96.9	0.55	0.06	N 1	6.05	6.11		
Si IX	341.949	342.0	2s22p2 $^3P_0$ - 2s2p3 $^3D_1$	109.0	1.15	0.12	N 1	6.03	6.04		
Ca VII	342.395	342.5		10.6	2.48	0.46	N 1	5.70	5.67	0.87	[56]AC
Ca IV	342.449								5.29	0.13	AC
Si IX	345.124	345.1	2s22p2 $^3P_1$ - 2s2p3 $^3D_2$	285.8	1.08	0.11	N 1	6.03	6.03	0.76	
Si IX	344.951		2s22p2 $^3P_1$ - 2s2p3 $^3D_1$						6.04	0.23	
Fe X	345.723	345.8	3s2.3p5 $^2P_{3/2}$ - 3s.3p6 $^2S_{1/2}$	187.5	1.06	0.11	N 1	6.03	6.04		
Fe XII	346.852	346.9	3s2.3p3 $^4S_{3/2}$ - 3s.3p4 $^4P_{1/2}$	52.9	0.97	0.12	N 1	6.01	6.16		
Si X	347.403	347.4	2p $^2P_{1/2}$ - 2s.2p2 $^2D_{3/2}$	210.9	1.14	0.11	N 1	6.05	6.14		
Ca VII	347.972	347.8		14.8	0.48	0.08	N 1	5.92	5.67	0.52	AC
Si X	347.741		2s.2p2 $^2D_{5/2}$ - 2p3 $^2D_{5/2}$						6.13	0.21	
Si X	347.729		2s.2p2 $^2D_{3/2}$ - 2p3 $^2D_{3/2}$						6.14	0.21	
Fe XIII	348.183	348.2	3s2 3p2 $^3P_0$ - 3s 3p3 $^3D_1$	39.4	1.11	0.12	N 1	6.07	6.21		
Mg VI	349.163	349.2	2s2.2p3 $^2D_{5/2}$ - 2s.2p4 $^2D_{5/2}$	67.0	0.71	0.07	N 1	5.86	5.65	0.45	
Mg VI	349.124		2s2.2p3 $^2D_{3/2}$ - 2s.2p4 $^2D_{3/2}$						5.65	0.34	
Si IX	349.873	349.9	2s22p2 $^3P_2$ - 2s2p3 $^3D_3$	295.9	0.98	0.10	N 1	6.03	6.02	0.84	
Si IX	349.794		2s22p2 $^3P_2$ - 2s2p3 $^3D_2$						6.03	0.16	
Na VII	350.645	350.6	2p $^2P_{1/2}$ - 2s.2p2 $^2P_{3/2}$	6.8	0.29	0.09	N 1	5.89	5.78		
Mg V	351.088	351.1	2p4 $^3P_2$ - 2s.2p5 $^3P_1$	15.7	0.21	0.02	N 1	5.57	5.46		
Fe XII	352.106	352.1	3s2.3p3 $^4S_{3/2}$ - 3s.3p4 $^4P_{3/2}$	127.8	0.88	0.09	N 1	6.03	6.16	0.80	
Al VII	352.149		2s22p3 $^4S_{3/2}$ - 2s2p4 $^4P_{1/2}$						5.78	0.12	
Fe XI	352.662	352.7	3s2.3p4 $^3P_2$ - 3s.3p5 $^3P_2$	209.2	1.05	0.11	N 1	6.05	6.11		
Mg V	353.092	353.1	2p4 $^3P_2$ - 2s.2p5 $^3P_2$	22.7	0.43	0.05	N 1	5.56	5.47		
Na VII	353.296	353.3	2p $^2P_{3/2}$ - 2s.2p2 $^2P_{3/2}$	14.2	0.83	0.11	N 1	5.85	5.78	0.84	
Mg V	353.3		2p4 $^3P_1$ - 2s.2p5 $^3P_1$						5.46	0.16	
Al VII	353.769	353.8	2s22p3 $^4S_{3/2}$ - 2s2p4 $^4P_{3/2}$	18.8	1.61	0.23	N 1	5.96	5.78	0.84	
Fe XIV	353.831		3s2 3p $^2P_{3/2}$ - 3s 3p2 $^2D_{5/2}$						6.24	0.15	
Mg V	354.225	354.2	2p4 $^3P_0$ - 2s.2p5 $^3P_1$	21.1	0.12	0.02	N 1	5.56	5.46		
Fe XIII	355.066		3s2 3p2 $^1D_2$ - 3s 3p3 $^3P_1$						6.21	0.17	
Mg V	355.329	355.3	2p4 $^3P_1$ - 2s.2p5 $^3P_2$	6.3	0.51	0.14	N 1	5.56	5.47		
Fe XI	355.837	355.7	3s2.3p4 $^1S_0$ - 3s.3p5 $^1P_1$	19.3	0.02	0.00	N 1	6.05	6.10		
Si X	356.012	356.1	2p $^2P_{3/2}$ - 2s.2p2 $^2D_{5/2}$	154.3	0.96	0.10	N 1	6.05	6.12	0.76	
Si X	356.05		2p $^2P_{3/2}$ - 2s.2p2 $^2D_{3/2}$						6.14	0.23	

[51] First identification (?)
[52] First identification
[53] First identification (?)
[54] First identification (?)
[55] First identification (?)
[56] First identification (?)

Table C.4: *(continued)*

Ion	λ_{th} (Å)	λ_{ob} (Å)	Transition	I_{ob}	I_{th}/I_{ob}	+/-	Det	log T_{eff}	log T_{max}	frac	
Fe XI	356.519	356.6	3s2.3p4 $^3P_1$ - 3s.3p5 $^3P_1$	32.0	0.85	0.10	N 1	6.05	6.11		
Al VII	356.888	356.9	2s22p3 $^4S_{3/2}$ - 2s2p4 $^4P_{5/2}$	21.1	1.83	0.23	N 1	5.93	5.78		
Ne IV	357.832	358.0	2s2 2p3 $^2D_{3/2}$ - 2s 2p4 $^2P_{1/2}$	20.6	0.90	0.12	N 1	5.41	5.30	0.64	
Ne V	357.954		2s22p2 $^3P_0$ - 2s2p3 $^3S_1$						5.49	0.36	
Fe XI	358.621	358.6	3s2.3p4 $^3P_0$ - 3s.3p5 $^3P_1$	92.9	0.97	0.10	N 1	5.84	6.11	0.38	
Ne IV	358.686		2s2 2p3 $^2D_{5/2}$ - 2s 2p4 $^2P_{3/2}$						5.30	0.24	
Ne V	358.484		2s22p2 $^3P_1$ - 2s2p3 $^3S_1$						5.49	0.22	
Fe X	358.413		3s2.3p4(3p).3d $^4F_{9/2}$ - 3s.3p5(3p*).3d $^4F_{9/2}$						6.03	0.13	
Ne V	359.382	359.4	2s22p2 $^3P_2$ - 2s2p3 $^3S_1$	37.4	0.90	0.10	N 1	5.52	5.49		
Fe XIII	359.642	359.6	3s2 3p2 $^3P_1$ - 3s 3p3 $^3D_2$	28.0	0.46	0.06	N 1	6.01	6.20	0.69	
Ca VIII	359.651								5.73	0.31	AC
Fe XVI	360.761	360.6	3s $^2S_{1/2}$ - 3p $^2P_{1/2}$	0.5	0.91	0.82	N 1	6.22	6.34		
Fe X	361.406	361.5	3s2.3p4(3p).3d $^4F_{7/2}$ - 3s.3p5(3p*).3d $^4F_{7/2}$	3.9	1.11	0.37	N 1	6.03	6.03	0.83	
Si XI	361.412		2s.2p $^3P_0$ - 2p2 $^3P_1$						6.19	0.16	
Mg VII	363.772	363.8	2s22p2 $^3P_0$ - 2s2p3 $^3P_1$	24.2	1.28	0.19	N 1	5.92	5.81		
Fe XII	364.467	364.5	3s2.3p3 $^4S_{3/2}$ - 3s.3p4 $^4P_{5/2}$	125.8	1.05	0.11	N 1	6.06	6.16		
Mg VII	365.234	365.2	2s22p2 $^3P_1$ - 2s2p3 $^3P_2$	103.7	0.95	0.10	N 1	5.92	5.81	0.37	
Mg VII	365.176		2s22p2 $^3P_1$ - 2s2p3 $^3P_0$						5.81	0.34	
Mg VII	365.243		2s22p2 $^3P_1$ - 2s2p3 $^3P_1$						5.81	0.27	
Fe X	365.543	365.6	3s2.3p5 $^2P_{1/2}$ - 3s.3p6 $^2S_{1/2}$	92.5	1.22	0.13	N 1	5.94	6.04	0.74	
Ne V	365.603		2s22p2 $^1D_2$ - 2s2p3 $^1P_1$						5.49	0.26	
Mg VII	367.674	367.7	2s22p2 $^3P_2$ - 2s2p3 $^3P_2$	191.4	0.84	0.09	N 1	5.92	5.81	0.77	
Mg VII	367.683		2s22p2 $^3P_2$ - 2s2p3 $^3P_1$						5.81	0.23	
Mg IX	368.07	368.1	2s2 $^1S_0$ - 2s.2p $^1P_1$	1383.6	0.96	0.10	N 1	6.01	5.98		
Fe XI	369.153	369.2	3s2.3p4 $^3P_1$ - 3s.3p5 $^3P_2$	54.7	1.20	0.13	N 1	6.05	6.11		
Si XI	371.503	371.7	2s.2p $^3P_2$ - 2p2 $^3P_1$	1.0	0.81	0.73	N 1	6.07	6.19		
Ca IX	371.882	371.8	3s.3p $^3P_0$ - 3s.3d $^3D_1$	0.9	0.44	0.40	N 1	5.90	5.78		
O III	374.075	374.1	2s22p2 $^3P_2$ - 2s22p3s $^3P_2$	54.2	0.92	0.17	N 1	5.15	5.11	0.33	
O III	373.805		2s22p2 $^3P_1$ - 2s22p3s $^3P_2$						5.11	0.11	
O III	374.435		2s22p2 $^3P_2$ - 2s22p3s $^3P_1$						5.11	0.11	
N III	374.434		2s2 2p $^2P_{3/2}$ - 2s2 3d $^2D_{5/2}$						5.09	0.10	
Ca IX	378.081	378.3	3s.3p $^3P_2$ - 3s.3d $^3D_3$	5.1	0.89	0.26	N 1	5.89	5.78	0.56	
Na VII	378.216		2p $^2P_{1/2}$ - 2s.2p2 $^2S_{1/2}$						5.78	0.38	
He I	515.617	515.7		14.3	0.54	0.06	N 2	5.02	4.53		AC
Si X	258.372	516.8	2p $^2P_{3/2}$ - 2s.2p2 $^2P_{3/2}$	522.5	0.57	0.10	N 2	6.05	6.13		
O VI	519.61	519.3	1s2 3d $^2D_{3/2}$ - 1s2 4f $^2F_{5/2}$	1.2	0.86	0.40	N 2	5.96	5.53	0.76	
Ar VIII	519.44		3p $^2P_{1/2}$ - 3d $^2D_{3/2}$						5.58	0.24	
O VI	519.722	519.7	1s2 3d $^2D_{5/2}$ - 1s2 4f $^2F_{7/2}$	3.8	0.60	0.11	N 2	5.97	5.53	0.50	
O VI	519.61		1s2 3d $^2D_{3/2}$ - 1s2 4f $^2F_{5/2}$						5.53	0.35	
Ar VIII	519.44		3p $^2P_{1/2}$ - 3d $^2D_{3/2}$						5.58	0.11	
Si XII	520.665	520.8	1s2.2s $^2S_{1/2}$ - 1s2.2p $^2P_{1/2}$	5.6	1.19	0.14	N 2	6.09	6.26		
He I	522.213	522.2		25.9	0.64	0.07	N 2	4.66	4.53		AC
O III	525.796	525.9	2s22p2 $^1D_2$ - 2s2p3 $^1P_1$	70.8	1.14	0.11	N 2	5.07	5.07		
He I	537.03	537.1		69.6	0.72	0.07	N 2	4.56	4.52		AC
C III	538.31	538.3	2s2p $^3P_2$ - 2s3s $^3S_1$	56.0	0.78	0.08	N 2	4.85	4.96	0.52	
C III	538.147		2s2p $^3P_1$ - 2s3s $^3S_1$						4.96	0.31	
C III	538.078		2s2p $^3P_0$ - 2s3s $^3S_1$						4.96	0.10	
Ca VII	539.395	539.5		3.1	1.18	0.34	N 2	5.76	5.67		AC
Ne IV	541.128	541.2	2s2 2p3 $^4S_{3/2}$ - 2s 2p4 $^4P_{1/2}$	12.4	1.11	0.12	N 2	5.29	5.27		
Ne IV	542.073	542.2	2s2 2p3 $^4S_{3/2}$ - 2s 2p4 $^4P_{3/2}$	22.9	1.21	0.12	N 2	5.30	5.27		
Ne IV	543.892	544.0	2s2 2p3 $^4S_{3/2}$ - 2s 2p4 $^4P_{5/2}$	38.7	1.15	0.12	N 2	5.35	5.27		
Al XI	550.031	550.2	1s2.(1s).2s $^2S_{1/2}$ - 1s2.(1s).2p $^2P_{3/2}$	17.4	1.84	0.20	N 2	6.06	6.16		
O IV	553.329	553.5	2s2 2p $^2P_{1/2}$ - 2s 2p2 $^2P_{3/2}$	107.9	1.05	0.11	N 2	5.27	5.27		
O IV	554.076	554.1	2s2 2p $^2P_{1/2}$ - 2s 2p2 $^2P_{1/2}$	124.6	1.81	0.19	N 2	5.28	5.27		
O IV	554.513	554.6	2s2 2p $^2P_{3/2}$ - 2s 2p2 $^2P_{3/2}$	555.8	1.02	0.10	N 2	5.27	5.27		
O IV	555.263	555.4	2s2 2p $^2P_{3/2}$ - 2s 2p2 $^2P_{1/2}$	109.1	1.07	0.11	N 2	5.27	5.27		
Mg VII	278.402	556.7	2s22p2 $^3P_2$ - 2s2p3 $^3S_1$	276.0	0.65	0.11	N 2	5.92	5.81	0.72	
Si VII	278.443		2p4 $^3P_1$ - 2s.2p5 $^3P_2$						5.77	0.28	
Ca X	557.765	557.9	3s $^2S_{1/2}$ - 3p $^2P_{3/2}$	72.0	1.08	0.11	N 2	5.97	5.82		
Ne VI	558.594	558.7	2s2 2p $^2P_{1/2}$ - 2s 2p2 $^2D_{3/2}$	55.9	1.00	0.10	N 2	5.75	5.63	0.82	
Ne VII	558.609		2s2p $^3P_1$ - 2p2 $^3P_2$						5.72	0.18	
Ne VII	559.948	560.0	2s2p $^3P_0$ - 2p2 $^3P_1$	8.9	0.90	0.10	N 2	5.88	5.72		
Ne VII	561.728	561.7	2s2p $^3P_2$ - 2p2 $^3P_2$	30.0	0.99	0.10	N 2	5.88	5.72		
Ne VI	562.803	562.9	2s2 2p $^2P_{3/2}$ - 2s 2p2 $^2D_{5/2}$	79.1	1.13	0.11	N 2	5.72	5.63		
Ne VII	564.528	564.5	2s2p $^3P_2$ - 2p2 $^3P_1$	8.9	1.08	0.12	N 2	5.88	5.72		
Si III	566.613	566.6	3s2 $^1S_0$ - 3s.4p $^1P_1$	2.5	0.46	0.08	N 2	5.19	4.81	0.87	
S VII	566.572		2p5.3s $^3P_1$ - 2p5.3p $^1S_0$						5.79	0.13	
Ne V	568.417	568.5	2s22p2 $^3P_0$ - 2s2p3 $^3D_1$	10.2	1.04	0.13	N 2	5.50	5.47		
Ne V	569.824	569.9	2s22p2 $^3P_1$ - 2s2p3 $^3D_2$	25.3	1.20	0.12	N 2	5.50	5.47	0.76	
Ne V	569.753		2s22p2 $^3P_1$ - 2s2p3 $^3D_1$						5.47	0.24	

Table C.4: *(continued)*

Ion	λ_{th} (Å)	λ_{ob} (Å)	Transition	I_{ob}	I_{th}/I_{ob}	+/-	Det	log T_{eff}	log T_{max}	frac	
Ne V	572.331	572.4	$2s22p2\ ^3P_2$ - $2s2p3\ ^3D_3$	38.8	1.22	0.12	N 2	5.50	5.47	0.86	
Ne V	572.098		$2s22p2\ ^3P_2$ - $2s2p3\ ^3D_2$						5.47	0.14	
Ca X	574.01	574.1	$3s\ ^2S_{1/2}$ - $3p\ ^2P_{1/2}$	46.1	0.98	0.10	N 2	5.90	5.82	0.85	
C III	574.279		$2s2p\ ^1P_1$ - $2s3d\ ^1D_2$						4.98	0.12	
O II	580.404	580.4	$2s22p3\ ^2P_{3/2}$ - $2s2p4\ ^2P_{1/2}$	2.5	1.38	0.34	N 2	4.78	4.87	0.63	
O II	580.41		$2s22p3\ ^2P_{1/2}$ - $2s2p4\ ^2P_{1/2}$						4.87	0.37	
O II	580.978	581.0	$2s22p3\ ^2P_{1/2}$ - $2s2p4\ ^2P_{3/2}$	12.5	1.00	0.12	N 2	5.70	4.87	0.49	
Si XI	580.907		$2s2\ ^1S_0$ - $2s.2p\ ^3P_1$						6.19	0.40	
O II	580.971		$2s22p3\ ^2P_{3/2}$ - $2s2p4\ ^2P_{3/2}$						4.87	0.10	
Si IX	290.69	581.3	$2s22p2\ ^3P_0$ - $2s2p3\ ^3P_1$	179.7	0.49	0.22	N 2	6.03	6.04		
He I	584.334	584.4		528.5	0.72	0.07	N 2	4.54	4.51		AC
Ar VII	585.754	585.7	$3s2\ ^1S_0$ - $3s.(2s).3p\ ^1P_1$	20.7	0.32	0.03	N 2	5.57	5.51		[57]
Si IX	296.117	592.6	$2s22p2\ ^3P_2$ - $2s2p3\ ^3P_2$	1037.9	0.37	0.04	N 2	6.03	6.03	0.73	[58]
Si IX	296.213		$2s22p2\ ^3P_2$ - $2s2p3\ ^3P_1$						6.04	0.27	
Ca VIII	596.936	597.0		5.1	0.92	0.13	N 2	5.84	5.73		AC
O III	597.817	597.9	$2s22p2\ ^1S_0$ - $2s2p3\ ^1P_1$	11.9	0.95	0.10	N 2	5.15	5.07		
O III	599.597	599.7	$2s22p2\ ^1D_2$ - $2s2p3\ ^1D_2$	160.5	1.15	0.12	N 2	5.04	5.06		
Si XI	604.147	604.3	$2s.2p\ ^1P_1$ - $2p2\ ^1D_2$	3.2	0.11	0.02	N 2	6.07	6.20		
Si XI	303.324	606.7	$2s2\ ^1S_0$ - $2s.2p\ ^1P_1$	764.6	0.29	0.03	N 2	6.06	6.20		
He II	303.78	607.6	$1s\ ^2S_{1/2}$ - $2p\ ^2P_{3/2}$	10255.6	0.09	0.01	N 2	5.48	4.92	0.66	
He II	303.786		$1s\ ^2S_{1/2}$ - $2p\ ^2P_{1/2}$						4.92	0.33	
O IV	608.397	608.4	$2s2\ 2p\ ^2P_{1/2}$ - $2s\ 2p2\ ^2S_{1/2}$	78.7	1.08	0.11	N 2	5.28	5.27		
Mg X	609.793	609.9	$1s2.(1s).2s\ ^2S_{1/2}$ - $1s2.(1s).2p\ ^2P_{3/2}$	538.3	1.53	0.15	N 2	5.96	6.04	0.80	
O IV	609.829		$2s2\ 2p\ ^2P_{3/2}$ - $2s\ 2p2\ ^2S_{1/2}$						5.27	0.19	
O IV	616.952	617.1	$2s\ 2p2\ ^2D_{5/2}$ - $2p3\ ^2P_{3/2}$	12.1	0.46	0.05	N 2	5.29	5.30	0.60	
O IV	617.036		$2s\ 2p2\ ^2D_{3/2}$ - $2p3\ ^2P_{1/2}$						5.30	0.33	
Si X	621.079	621.3	$2p\ ^2P_{1/2}$ - $2s.2p2\ ^4P_{1/2}$	4.8	0.74	0.09	N 2	6.04	6.12	0.85	
K IX	621.455		$3s\ ^2S_{1/2}$ - $3p\ ^2P_{3/2}$						5.74	0.15	
Mg X	624.941	625.0	$1s2.(1s).2s\ ^2S_{1/2}$ - $1s2.(1s).2p\ ^2P_{1/2}$	216.7	1.52	0.15	N 2	6.04	6.04		
O IV	625.853	625.8	$2s\ 2p2\ ^4P_{5/2}$ - $2p3\ ^4S_{3/2}$	4.9	0.41	0.05	N 2	5.25	5.24		
Mg VIII	313.754	627.6	$2p\ ^2P_{1/2}$ - $2s.2p2\ ^2P_{1/2}$	335.6	0.60	0.07	N 2	5.96	5.92		
Si VIII	314.327	628.6	$2s22p3\ ^4S_{3/2}$ - $2s2p4\ ^4P_{1/2}$	277.1	0.76	0.09	N 2	5.98	5.91		
O V	629.73	629.9	$2s2\ ^1S_0$ - $2s.2p\ ^1P_1$	1164.0	1.03	0.10	N 2	5.40	5.39		
		154.6	ghost of 174.5 Å				G 1				
		157.2	ghost of 177.2 Å				G 1				
		158.5	ghost of 178.0 Å				G 1				
		160.6	ghost of 180.4 Å				G 1				
		162.6	ghost of 182.1 Å				G 1				
		164.8	ghost ?								
		165.3	ghost of 184.5 Å				G 1				
		166.0	ghost of 185.2 Å				G 1				
Fe VIII	167.486	167.5		709.9	0.27	0.04	G 1	5.91	5.65		AC
Fe VIII	168.545	168.2		995.9	0.45	0.07	G 1	5.92	5.65	0.50	AC
Fe VIII	168.17								5.65	0.40	AC
Fe VIII	168.93	168.8		342.2	1.41	0.37	G 1	5.92	5.65	0.52	AC
Fe VIII	168.545								5.65	0.47	AC
Fe IX	171.073	171.1	$3p6\ ^1S_0$ - $3p5.3d\ ^1P_1$	4967.2	1.21	0.12	G 1	6.00	5.96		
O VI	173.079	173.0	$1s2\ 2p\ ^2P_{3/2}$ - $1s2\ 3d\ ^2D_{5/2}$	449.8	0.33	0.04	G 1	5.97	5.51	0.60	
O VI	172.935		$1s2\ 2p\ ^2P_{1/2}$ - $1s2\ 3d\ ^2D_{3/2}$						5.51	0.33	
Fe X	174.534	174.7	$3s2.3p5\ ^2P_{3/2}$ - $3s2.3p4(3p).3d\ ^2D_{5/2}$	3647.5	1.02	0.11	G 1	6.03	6.05		
Fe X	175.443	175.6	$3s2.3p5\ ^2P_{3/2}$ - $3s2.3p4(3p).3d\ ^2P_{1/2}$	489.3	0.17	0.02	G 1	6.03	6.04		
Fe X	177.243	177.2	$3s2.3p5\ ^2P_{3/2}$ - $3s2.3p4(3p).3d\ ^2P_{3/2}$	2224.3	0.97	0.11	G 1	6.03	6.05		
Fe XI	178.06	178.0	$3s2.3p4\ ^3P_2$ - $3s2.3p3(4s^*).3d\ ^3D_2$	214.8	0.35	0.08	G 1	6.05	6.11		
Fe XI	180.408	180.5	$3s2.3p4\ ^3P_2$ - $3s2.3p3(4s^*).3d\ ^3D_3$	2167.4	1.11	0.12	G 1	6.05	6.11		
Fe XI	181.137	181.3	$3s2.3p4\ ^3P_0$ - $3s2.3p3(4s^*).3d\ ^3D_1$	161.5	0.64	0.12	G 1	6.05	6.11		
Fe XI	182.169	182.2	$3s2.3p4\ ^3P_1$ - $3s2.3p3(4s^*).3d\ ^3D_2$	532.6	0.60	0.07	G 1	6.05	6.11	0.83	
Fe X	182.31		$3s2.3p5\ ^2P_{1/2}$ - $3s2.3p4(3p).3d\ ^2P_{3/2}$						6.05	0.17	
O VI	184.117	184.0	$1s2\ 2p\ ^2P_{3/2}$ - $1s2\ 3s\ ^2S_{1/2}$	185.2	0.44	0.09	G 1	5.96	5.51	0.66	
O VI	183.937		$1s2\ 2p\ ^2P_{1/2}$ - $1s2\ 3s\ ^2S_{1/2}$						5.51	0.33	
Fe X	184.543	184.5	$3s2.3p5\ ^2P_{3/2}$ - $3s2.3p4(1d).3d\ ^2S_{1/2}$	851.4	0.95	0.12	G 1	6.03	6.05		
Fe VIII	185.213	185.3		508.2	0.40	0.05	G 1	5.92	5.64		
Fe VIII	186.599	186.7		371.5	0.94	0.12	G 1	5.98	5.64	0.61	
Fe XII	186.884		$3s2.3p3\ ^2D_{5/2}$ - $3s2.3p2(3p).3d\ ^2F_{7/2}$						6.15	0.29	
Fe XI	188.232	188.2	$3s2.3p4\ ^3P_2$ - $3s2.3p3(2d^*).3d\ ^3P_2$	1513.5	0.88	0.09	G 1	6.05	6.11	0.73	
Fe XI	188.299		$3s2.3p4\ ^3P_2$ - $3s2.3p3(2d^*).3d\ ^1P_1$						6.11	0.27	
Fe XI	189.129	189.1	$3s2.3p4\ ^3P_1$ - $3s2.3p3(2d^*).3d\ ^3P_1$	72.8	0.52	0.15	G 1	6.05	6.11		
Fe X	190.043	190.0	$3s2.3p5\ ^2P_{1/2}$ - $3s2.3p4(1d).3d\ ^2S_{1/2}$	482.2	0.65	0.08	G 1	6.04	6.05		

[57] bl Si IX IIo

[58] bl unidentified line

Table C.4: *(continued)*

Ion	λ_{th} (Å)	λ_{ob} (Å)	Transition	I_{ob}	I_{th}/I_{ob}	+/-	Det	log T_{eff}	log T_{max}	frac
S XI	191.266	191.1	2s22p2 $^3P_2$ - 2s2p3 $^3S_1$	90.0	0.30	0.13	G 1	6.06	6.24	0.58
Fe XI	190.888		3s2.3p4 $^1D_2$ - 3s2.3p3(4s*).3d $^3D_2$						6.11	0.19
Fe XII	191.053		3s2.3p3 $^2P_{3/2}$ - 3s2.3p2(3p).3d $^2D_{5/2}$						6.16	0.16
S XI	191.266	191.3	2s22p2 $^3P_2$ - 2s2p3 $^3S_1$	13.9	1.15	1.04	G 1	6.07	6.24	
Fe XII	192.393	192.1	3s2.3p3 $^4S_{3/2}$ - 3s2.3p2(3p).3d $^4P_{1/2}$	222.9	1.04	0.31	G 1	6.06	6.16	
Fe XII	192.393	192.4	3s2.3p3 $^4S_{3/2}$ - 3s2.3p2(3p).3d $^4P_{1/2}$	81.8	2.83	2.06	G 1	6.06	6.16	
Fe XI	192.83	192.8	3s2.3p4 $^3P_1$ - 3s2.3p3(2d*).3d $^3P_2$	636.0	0.38	0.06	G 1	6.02	6.11	
Fe XII	193.521	193.6	3s2.3p3 $^4S_{3/2}$ - 3s2.3p2(3p).3d $^4P_{3/2}$	768.8	0.92	0.11	G 1	6.06	6.16	
Fe XII	194.911		3s2.3p3 $^2D_{3/2}$ - 3s2.3p2(1d).3d $^2D_{5/2}$						6.15	0.12
Fe XII	195.118	195.2	3s2.3p3 $^4S_{3/2}$ - 3s2.3p2(3p).3d $^4P_{5/2}$	947.9	1.15	0.14	G 1	6.06	6.16	
Fe XII	196.648	196.6	3s2.3p3 $^2D_{5/2}$ - 3s2.3p2(1d).3d $^2D_{5/2}$	120.2	0.44	0.15	G 1	6.06	6.15	
S VIII	198.553	198.6	2s2.2p5 $^2P_{3/2}$ - 2s.2p6 $^2S_{1/2}$	143.1	0.96	0.15	G 1	5.99	5.88	0.77
Fe XI	198.545		3s2.3p4 $^1D_2$ - 3s2.3p3(2d*).3d $^3P_1$						6.11	0.22
Fe XIII	200.022	200.1	3s2 3p2 $^3P_1$ - 3s2 3p 3d $^3D_2$	50.5	0.30	0.11	G 1	6.07	6.20	
Fe XIII	201.128	201.1	3s2 3p2 $^3P_1$ - 3s2 3p 3d $^3D_1$	202.1	0.19	0.03	G 1	6.07	6.20	
Fe XIII	202.044	202.1	3s2 3p2 $^3P_0$ - 3s2 3p 3d $^3P_1$	372.1	0.99	0.13	G 1	6.07	6.21	
Fe XI	202.706	202.7	3s2.3p4 $^1D_2$ - 3s2.3p3(2d*).3d $^1P_1$	271.5	0.92	0.13	G 1	6.03	6.11	0.52
Fe XI	202.448		3s2.3p4 $^3P_2$ - 3s2.3p3(2p*).3d $^3D_2$						6.11	0.22
S VIII	202.61		2s2.2p5 $^2P_{1/2}$ - 2s.2p6 $^2S_{1/2}$						5.88	0.19
Fe XII	203.272	203.2	3s2.3p3 $^2D_{5/2}$ - 3s2.3p2(1s).3d $^2D_{5/2}$	25.7	1.60	1.11	G 1	6.06	6.16	0.79
Fe XIII	203.163		3s2 3p2 $^3P_1$ - 3s2 3p 3d $^3P_0$						6.20	0.21
Fe XIII	203.828	203.7	3s2 3p2 $^3P_2$ - 3s2 3p 3d $^3D_3$	139.0	0.53	0.09	G 1	6.07	6.20	0.73
Fe XIII	203.797		3s2 3p2 $^3P_2$ - 3s2 3p 3d $^3D_2$						6.20	0.26
Fe XIII	204.263	204.4	3s2 3p2 $^3P_1$ - 3s2 3p 3d $^1D_2$	29.4	0.53	0.29	G 1	6.06	6.20	0.61
Fe XI	204.343		3s2.3p4 $^3P_2$ - 3s2.3p3(2p*).3d $^3F_3$						6.11	0.39
Fe XIV	211.32	211.4	3s2 3p $^2P_{1/2}$ - 3s2 3d $^2D_{3/2}$	20.4	1.62	1.10	G 1	6.09	6.25	
Fe XII	214.398	214.3	3s2.3p3 $^2D_{5/2}$ - 3s2.3p2(3p).3d $^4P_{5/2}$	16.3	0.98	0.89	G 1	6.02	6.16	0.87
O IV	214.152		2s2 2p $^2P_{3/2}$ - 2s.2p.(3p*).3p $^2P_{3/2}$						5.35	0.10
Si X	258.372	258.5	2p $^2P_{3/2}$ - 2s.2p2 $^2P_{3/2}$	305.2	0.99	0.11	G 2	6.05	6.13	
Si X	261.063	261.2	2p $^2P_{3/2}$ - 2s.2p2 $^2P_{1/2}$	90.3	1.72	0.24	G 2	6.05	6.14	
Fe XIV	264.78	264.6	3s2 3p $^2P_{3/2}$ - 3s 3p2 $^2P_{3/2}$	14.1	0.90	0.43	G 2	6.09	6.25	
Si X	271.983	272.0	2p $^2P_{1/2}$ - 2s.2p2 $^2S_{1/2}$	110.6	1.07	0.13	G 2	6.05	6.14	
Si VII	272.638	272.7	2p4 $^3P_2$ - 2s.2p5 $^3P_1$	78.5	0.48	0.07	G 2	5.92	5.77	
Si VII	275.353	275.3	2p4 $^3P_2$ - 2s.2p5 $^3P_2$	158.9	1.12	0.13	G 2	5.92	5.77	0.88
Si VII	275.667		2p4 $^3P_1$ - 2s.2p5 $^3P_1$						5.77	0.12
Mg VII	276.154	276.0	2s22p2 $^3P_0$ - 2s2p3 $^3S_1$	28.0	0.92	0.25	G 2	5.92	5.81	
Si VIII	277.054	276.9	2s22p3 $^2D_{5/2}$ - 2s2p4 $^2D_{5/2}$	359.4	0.82	0.09	G 2	5.96	5.90	0.41
Mg VII	277		2s22p2 $^3P_1$ - 2s2p3 $^3S_1$						5.81	0.26
Si VIII	276.838		2s22p3 $^2D_{3/2}$ - 2s2p4 $^2D_{3/2}$						5.89	0.20
Mg VII	278.402	278.4	2s22p2 $^3P_2$ - 2s2p3 $^3S_1$	163.9	1.10	0.12	G 2	5.92	5.81	0.72
Si VII	278.443		2p4 $^3P_1$ - 2s.2p5 $^3P_2$						5.77	0.28
Al IX	280.151	280.0	2s2.2p $^2P_{1/2}$ - 2s.2p2 $^2P_{3/2}$	36.4	0.86	0.17	G 2	5.89	6.03	0.66
O IV	279.933		2S2 2P 2P1.5 - 2s2.3s 2S0.5						5.32	0.17
O IV	279.933		2S2 2P 2P1.5 - 2s2.3s 2S0.5						5.32	0.17
Mg VII	280.737	280.7	2s22p2 $^1D_2$ - 2s2p3 $^1P_1$	14.7	1.16	0.41	G 2	5.91	5.79	
Al IX	284.042	284.4	2s2.2p $^2P_{3/2}$ - 2s.2p2 $^2P_{3/2}$	61.0	1.96	0.29	G 2	6.04	6.03	0.90
Fe XV	284.16		3s2 $^1S_0$ - 3s3p $^1P_1$						6.29	0.10
S XI	285.587	285.8	2s22p2 $^3P_1$ - 2s2p3 $^3D_1$	32.8	0.80	0.17	G 2	6.02	6.25	0.38
S XI	285.822		2s22p2 $^3P_1$ - 2s2p3 $^3D_2$						6.23	0.31
Al VIII	285.469		2p2 $^1D_2$ - 2s.2p3 $^1D_2$						5.89	0.22
Al IX	286.377	286.6	2s2.2p $^2P_{3/2}$ - 2s.2p2 $^2P_{1/2}$	20.0	1.74	0.46	G 2	6.02	6.03	
Si IX	290.69	290.6	2s22p2 $^3P_0$ - 2s2p3 $^3P_1$	91.0	0.97	0.13	G 2	6.03	6.04	
Fe XII	291.053	291.1	3s2.3p3 $^2D_{5/2}$ - 3s.3p4 $^2P_{3/2}$	24.9	0.65	0.19	G 2	6.06	6.16	
S XI	291.577	291.7	2s22p2 $^3P_2$ - 2s2p3 $^3D_3$	6.0	0.97	0.80	G 2	6.01	6.22	0.46
Mg VI	291.455		2s2.2p3 $^2P_{3/2}$ - 2s.2p4 $^2P_{1/2}$						5.66	0.30
S XI	291.81		2s22p2 $^3P_2$ - 2s2p3 $^3D_2$						6.23	0.19
Si IX	292.8	292.7	2s22p2 $^3P_1$ - 2s2p3 $^3P_0$	197.0	1.33	0.15	G 2	6.03	6.04	0.40
Si IX	292.856		2s22p2 $^3P_1$ - 2s2p3 $^3P_1$						6.04	0.32
Si IX	292.763		2s22p2 $^3P_1$ - 2s2p3 $^3P_2$						6.03	0.28
Si IX	296.117	296.2	2s22p2 $^3P_2$ - 2s2p3 $^3P_2$	448.2	0.85	0.09	G 2	6.03	6.03	0.73
Si IX	296.213		2s22p2 $^3P_2$ - 2s2p3 $^3P_1$						6.04	0.27
Si VIII	307.652	307.8	2s22p3 $^2P_{1/2}$ - 2s2p4 $^2D_{3/2}$	10.5	0.66	0.24	G 2	5.97	5.89	
Si VIII	308.195	308.5	2s22p3 $^2P_{3/2}$ - 2s2p4 $^2D_{5/2}$	55.1	0.69	0.10	G 2	6.00	5.90	0.54
Fe XI	308.548		3s2.3p4 $^1D_2$ - 3s.3p5 $^1P_1$						6.10	0.40
Al VI	309.595	309.5	2p4 $^3P_2$ - 2s.2p5 $^3P_2$	9.9	0.54	0.22	G 2	5.88	5.62	0.84
P X	309.2		2s22p2 $^3P_0$ - 2s2p3 $^3D_1$						6.17	0.16
Mg VIII	311.796	311.6	2p $^2P_{1/2}$ - 2s.2p2 $^2P_{3/2}$	92.0	1.12	0.14	G 2	5.96	5.91	
Fe XIII	312.109	312.2	3s2 3p2 $^3P_1$ - 3s 3p3 $^3P_1$	46.9	0.66	0.10	G 2	5.99	6.21	0.61
C IV	312.42		1s2 2s $^2S_{1/2}$ - 1s2 3p $^2P_{3/2}$						5.09	0.20
Fe XIII	312.872	313.0	3s2 3p2 $^3P_1$ - 3s 3p3 $^3P_0$	28.1	0.15	0.04	G 2	6.07	6.20	0.70

Table C.4: *(continued)*

Ion	λ_{th} (Å)	λ_{ob} (Å)	Transition	I_{ob}	I_{th}/I_{ob}	+/-	Det	log T_{eff}	log T_{max}	frac	
P X	312.981		2s22p2 $^3P_1$ - 2s2p3 $^3D_2$						6.15	0.19	
P X	312.77		2s22p2 $^3P_1$ - 2s2p3 $^3D_1$						6.17	0.10	
Mg VIII	313.754	313.7	2p $^2P_{1/2}$ - 2s.2p2 $^2P_{1/2}$	185.9	1.08	0.12	G 2	5.96	5.92		
Si VIII	314.327	314.3	2s22p3 $^4S_{3/2}$ - 2s2p4 $^4P_{1/2}$	180.5	1.18	0.14	G 2	5.98	5.91		
Mg VIII	315.039	315.1	2p $^2P_{3/2}$ - 2s.2p2 $^2P_{3/2}$	425.2	1.23	0.13	G 2	5.96	5.91		
Si VIII	316.205	316.3	2s22p3 $^4S_{3/2}$ - 2s2p4 $^4P_{3/2}$	194.4	2.06	0.22	G 2	5.98	5.91		
Mg VIII	317.039	317.1	2p $^2P_{3/2}$ - 2s.2p2 $^2P_{1/2}$	173.4	0.82	0.09	G 2	5.97	5.92		
Mg VIII	317.039	317.3	2p $^2P_{3/2}$ - 2s.2p2 $^2P_{1/2}$	21.9	6.50	2.02	G 2	5.96	5.92		
Si VIII	319.826	319.8	2s22p3 $^4S_{3/2}$ - 2s2p4 $^4P_{5/2}$	479.6	1.28	0.13	G 2	5.98	5.91		
O III	320.976	320.9	2s22p2 $^1D_2$ - 2s22p3d $^1F_3$	34.6	0.65	0.10	G 2	5.75	5.14	0.41	
Fe XIII	320.809		3s2 3p2 $^3P_2$ - 3s 3p3 $^3P_2$						6.20	0.38	
Mg IV	320.994		2p5 $^2P_{3/2}$ - 2s.2p6 $^2S_{1/2}$						5.30	0.19	
Fe X	321.732	321.7	3s2.3p4(3p).3d $^4D_{5/2}$ - 3s.3p5(3p*).3d $^4F_{7/2}$	11.3	0.61	0.18	G 2	6.03	6.03	0.70	
Fe X	321.804		3s2.3p4(3p).3d $^4D_{7/2}$ - 3s.3p5(3p*).3d $^4F_{7/2}$						6.03	0.29	
Al VIII	323.538	323.5	2p2 $^3P_0$ - 2s.2p3 $^3P_1$	16.8	0.95	0.24	G 2	5.94	5.92	0.80	
Mg IV	323.306		2p5 $^2P_{1/2}$ - 2s.2p6 $^2S_{1/2}$						5.30	0.13	
Al VIII	325.276	325.3	2p2 $^3P_1$ - 2s.2p3 $^3P_0$	41.3	0.95	0.10	G 2	5.98	5.92	0.37	
Al VIII	325.292		2p2 $^3P_1$ - 2s.2p3 $^3P_2$						5.92	0.34	
Al VIII	325.338		2p2 $^3P_1$ - 2s.2p3 $^3P_1$						5.92	0.29	
Al X	332.789	332.9	2s2 $^1S_0$ - 2s.2p $^1P_1$	46.8	3.66	0.39	G 2	6.04	6.10		
Mg VIII	335.253	335.4	2p $^2P_{1/2}$ - 2s.2p2 $^2S_{1/2}$	85.1	1.13	0.16	G 2	5.97	5.92		
Fe XII	338.278	338.0	3s2.3p3 $^2D_{5/2}$ - 3s.3p4 $^2D_{5/2}$	29.5	0.35	0.04	G 2	6.06	6.15		
O III	395.555	395.6	2s22p2 $^1D_2$ - 2s22p3s $^1P_1$	9.0	0.74	0.15	G 3	5.39	5.11		
Ne VI	399.821	399.8	2s2 2p $^2P_{1/2}$ - 2s 2p2 $^2P_{3/2}$	18.0	1.36	0.23	G 3	5.73	5.64		
Mg VI	400.662	400.7	2s2.2p3 $^4S_{3/2}$ - 2s.2p4 $^4P_{3/2}$	35.6	1.12	0.15	G 3	5.85	5.65		
Ne VI	401.926	401.9	2s2 2p $^2P_{3/2}$ - 2s 2p2 $^2P_{3/2}$	105.4	1.18	0.13	G 3	5.73	5.64		
Mg VI	403.307	403.1	2s2.2p3 $^4S_{3/2}$ - 2s.2p4 $^4P_{5/2}$	66.5	1.28	0.14	G 3	5.82	5.65	0.67	
Ne VI	403.255		2s2 2p $^2P_{3/2}$ - 2s 2p2 $^2P_{1/2}$						5.64	0.33	
Na VIII	411.166	411.1	2s2 $^1S_0$ - 2s.2p $^1P_1$	50.9	0.85	0.10	G 3	5.93	5.86		
Ne V	416.194	416.1	2s22p2 $^1D_2$ - 2s2p3 $^1D_2$	28.2	1.96	0.30	G 3	5.51	5.48		
Ne V	416.843	416.6	2s22p2 $^1S_0$ - 2s2p3 $^1P_1$	4.5	1.21	0.48	G 3	5.51	5.49		
Ne V	416.843	417.1	2s22p2 $^1S_0$ - 2s2p3 $^1P_1$	1.9	3.13	2.83	G 3	5.60	5.49		
C IV	419.713	419.7	1s2 2p $^2P_{3/2}$ - 1s2 3s $^2S_{1/2}$	36.0	0.40	0.05	G 3	5.81	5.08	0.40	
Ca X	419.754		3p $^2P_{3/2}$ - 3d $^2D_{5/2}$						5.82	0.39	
C IV	419.525		1s2 2p $^2P_{1/2}$ - 1s2 3s $^2S_{1/2}$						5.08	0.20	
Na VI	421.463		2s.2p3 $^3P_2$ - 2p4 $^3P_1$						5.67	0.42	
Mg VII	429.14	429.2	2s22p2 $^3P_0$ - 2s2p3 $^3D_1$	30.7	1.07	0.20	G 3	5.92	5.81		
Mg VIII	430.465	430.5	2p $^2P_{1/2}$ - 2s.2p2 $^2D_{3/2}$	196.8	1.00	0.11	G 3	5.96	5.91		
Mg VII	431.313	431.4	2s22p2 $^3P_1$ - 2s2p3 $^3D_2$	78.2	1.23	0.17	G 3	5.92	5.81	0.78	
Mg VII	431.188		2s22p2 $^3P_1$ - 2s2p3 $^3D_1$						5.81	0.22	
Si VIII	216.915	433.9	2s22p3 $^2D_{5/2}$ - 2s2p4 $^2P_{3/2}$	130.8	1.04	0.80	G 3	5.98	5.90		
Mg VII	434.72	434.4	2s22p2 $^3P_2$ - 2s2p3 $^3D_2$	25.1	0.78	0.42	G 3	5.91	5.81		
Mg VII	434.917	434.9	2s22p2 $^3P_2$ - 2s2p3 $^3D_3$	134.5	1.09	0.16	G 3	5.91	5.81	0.86	
Mg VII	434.72		2s22p2 $^3P_2$ - 2s2p3 $^3D_2$						5.81	0.13	
Ne VI	435.648	435.7	2s2 2p $^2P_{3/2}$ - 2s 2p2 $^2S_{1/2}$	45.0	0.78	0.20	G 3	5.73	5.64		
Mg VIII	436.672	436.5	2p $^2P_{3/2}$ - 2s.2p2 $^2D_{3/2}$	70.9	0.49	0.11	G 3	5.97	5.91		
Mg VIII	436.735	436.9	2p $^2P_{3/2}$ - 2s.2p2 $^2D_{5/2}$	352.0	0.93	0.10	G 3	5.96	5.91	0.90	
Mg VIII	436.672		2p $^2P_{3/2}$ - 2s.2p2 $^2D_{3/2}$						5.91	0.10	
Mg IX	441.198	441.1	2s.2p $^3P_0$ - 2p2 $^3P_1$	23.5	0.70	0.12	G 3	5.95	5.98	0.62	
Ca VIII	441.096								5.73	0.35	? (AC)
Mg IX	443.402	443.4	2s.2p $^3P_1$ - 2p2 $^3P_1$	17.2	0.44	0.10	G 3	6.01	5.98		
Mg IX	443.972	444.0	2s.2p $^3P_2$ - 2p2 $^3P_2$	66.1	0.55	0.07	G 3	6.01	5.98		
Mg IX	448.293	448.4	2s.2p $^3P_2$ - 2p2 $^3P_1$	25.8	0.46	0.07	G 3	6.01	5.98		
S IX	224.725	449.4	2s2.2p4 $^3P_2$ - 2s.2p5 $^3P_2$	178.0	1.52	0.41	G 3	6.02	6.00		
Si IX	225.024	450.3	2s22p2 $^3P_1$ - 2s2p3 $^3S_1$	331.4	0.91	0.16	G 3	6.03	6.04	0.68	
Fe X	225.161		3s2.3p5 $^2P_{3/2}$ - 3s2.3p4(1d).3d $^2D_{5/2}$						6.04	0.20	
S IX	225.22		2s2.2p4 $^3P_1$ - 2s.2p5 $^3P_1$						6.00	0.11	
N III	452.227	451.9	2s2 2p $^2P_{3/2}$ - 2s2 3s $^2S_{1/2}$	9.5	0.60	0.18	G 3	5.00	5.05	0.66	
N III	451.871		2s2 2p $^2P_{1/2}$ - 2s2 3s $^2S_{1/2}$						5.05	0.33	
Si IX	227	454.0	2s22p2 $^3P_2$ - 2s2p3 $^3S_1$	382.0	0.91	0.16	G 3	6.03	6.04		
C III	459.626	459.6	2s2p $^3P_2$ - 2s3d $^3D_3$	40.5	0.86	0.12	G 3	4.90	4.97	0.46	
C III	459.513		2s2p $^3P_1$ - 2s3d $^3D_2$						4.97	0.25	
C III	459.465		2s2p $^3P_0$ - 2s3d $^3D_1$						4.97	0.11	
Ne VII	465.22	465.1	2s2 $^1S_0$ - 2s2p $^1P_1$	709.7	1.11	0.11	G 3	5.88	5.72		
Ca IX	466.239	466.3	3s2 $^1S_0$ - 3s.3p $^1P_1$	116.8	0.62	0.07	G 3	5.90	5.78		
Ne IV	469.823	469.8	2s2 2p3 $^2D_{5/2}$ - 2s 2p4 $^2D_{5/2}$	47.0	1.10	0.14	G 3	5.31	5.28	0.56	
Ne IV	469.875		2s2 2p3 $^2D_{3/2}$ - 2s 2p4 $^2D_{3/2}$						5.28	0.37	
Ne V	481.36	481.3	2S22P2 3P1.0 - 2S2P3 3P2.0	26.0	0.95	0.77	G 3	5.51	5.47	0.40	
Ne V	481.276		2s22p2 $^3P_1$ - 2s2p3 $^3P_0$						5.47	0.34	
Ne V	481.36		2S22P2 3P1.0 - 2S2P3 3P1.0						5.47	0.26	

Table C.4: *(continued)*

Ion	λ_{th} (Å)	λ_{ob} (Å)	Transition	I_{ob}	I_{th}/I_{ob}	+/-	Det	log T_{eff}	log T_{max}	frac	
Ne III	489.495	489.0	2s2 2p4 $^3P_2$ - 2s 2p5 $^3P_2$	47.4	0.98	0.19	G 3	5.04	5.06	0.68	
Ne III	488.851		2s2 2p4 $^3P_1$ - 2s 2p5 $^3P_0$						5.06	0.18	
Ne III	489.629		2s2 2p4 $^3P_1$ - 2s 2p5 $^3P_1$						5.06	0.14	
S IV	661.395	661.4	3s2.3p $^2P_{3/2}$ - 3s2.(1s).3d $^2D_{5/2}$	33.6	0.57	0.13	G 4	5.05	5.10		
S V	663.126	663.1	3s.3p $^3P_2$ - 3s.3d $^3D_3$	8.4	0.25	0.14	G 4	5.22	5.20		
Al X	332.789	665.6	2s2 $^1S_0$ - 2s.2p $^1P_1$	282.1	0.61	0.47	G 4	6.04	6.10		
N III	684.998	685.2	2s2 2p $^2P_{1/2}$ - 2s 2p2 $^2P_{3/2}$	14.9	1.04	0.74	G 4	4.92	5.02		
N III	685.817	686.0	2s2 2p $^2P_{3/2}$ - 2s 2p2 $^2P_{3/2}$	92.3	1.01	0.21	G 4	4.92	5.02	0.83	
N III	686.336		2s2 2p $^2P_{3/2}$ - 2s 2p2 $^2P_{1/2}$						5.02	0.17	
Si X	347.403	694.6	2p $^2P_{1/2}$ - 2s.2p2 $^2D_{3/2}$	400.9	0.60	0.23	G 4	6.05	6.14		
O III	702.332	702.1	2s22p2 $^3P_0$ - 2s2p3 $^3P_1$	48.4	0.94	0.33	G 4	5.00	5.04		
O III	702.897	702.6	2s22p2 $^3P_1$ - 2s2p3 $^3P_2$	123.6	1.08	0.21	G 4	5.00	5.04	0.42	
O III	702.821		2s22p2 $^3P_1$ - 2s2p3 $^3P_0$						5.04	0.32	
O III	702.891		2s22p2 $^3P_1$ - 2s2p3 $^3P_1$						5.04	0.26	
O III	703.854	703.7	2s22p2 $^3P_2$ - 2s2p3 $^3P_2$	185.2	1.24	0.20	G 4	5.04	5.04	0.74	
O III	703.848		2s22p2 $^3P_2$ - 2s2p3 $^3P_1$						5.04	0.25	
Fe XI	352.662	705.2	3s2.3p4 $^3P_2$ - 3s.3p5 $^3P_2$	190.6	1.15	1.04	G 4	6.05	6.11		
Mg IX	706.058	705.8	2s2 $^1S_0$ - 2s.2p $^3P_1$	75.5	0.43	0.09	G 4	6.01	5.98		
Mg VII	367.674	735.4	2s22p2 $^3P_2$ - 2s2p3 $^3P_2$	187.1	0.86	0.54	G 4	5.92	5.81	0.77	
Mg VII	367.683		2s22p2 $^3P_2$ - 2s2p3 $^3P_1$						5.81	0.23	
Mg IX	368.07	736.0	2s2 $^1S_0$ - 2s.2p $^1P_1$	1347.2	0.98	0.17	G 4	6.01	5.98		
Fe XI	369.153	738.1	3s2.3p4 $^3P_1$ - 3s.3p5 $^3P_2$	781.1	0.08	0.01	G 4	6.05	6.11		[59]
N II	746.984	746.7	2s2 2p2 $^1D_2$ - 2s2 2p 3s $^1P_1$	10.9	0.80	0.44	G 4	4.80	4.77		
S IV	748.392	748.5	3s2.3p $^2P_{1/2}$ - 3s.3p2 $^2P_{1/2}$	18.3	0.46	0.17	G 4	5.00	5.09		
Mg IX	749.55	749.6	2s.2p $^1P_1$ - 2p2 $^1D_2$	13.9	0.24	0.15	G 4	6.01	5.99		
S IV	750.22	750.4	3s2.3p $^2P_{3/2}$ - 3s.3p2 $^2P_{3/2}$	21.0	1.07	0.42	G 4	5.03	5.09		
S IV	753.759	753.9	3s2.3p $^2P_{3/2}$ - 3s.3p2 $^2P_{1/2}$	5.9	0.67	0.57	G 4	5.02	5.09		
O V	758.675	758.5	2s.2p $^3P_1$ - 2p2 $^3P_2$	26.4	0.87	0.18	G 4	5.39	5.39		
O V	759.439	759.3	2s.2p $^3P_0$ - 2p2 $^3P_1$	21.6	0.80	0.20	G 4	5.39	5.39		
O V	760.444	760.4	2s.2p $^3P_2$ - 2p2 $^3P_2$	80.3	1.01	0.13	G 4	5.39	5.39	0.84	
O V	760.225		2s.2p $^3P_1$ - 2p2 $^3P_1$						5.39	0.16	
O V	761.126	761.0	2s.2p $^3P_1$ - 2p2 $^3P_0$	10.4	0.11	0.05	G 4	5.38	5.38		
O V	762.002	762.1	2s.2p $^3P_2$ - 2p2 $^3P_1$	24.6	0.87	0.18	G 4	5.39	5.39		
N III	763.334	763.5	2s2 2p $^2P_{1/2}$ - 2s 2p2 $^2S_{1/2}$	15.8	0.89	0.25	G 4	4.90	5.01		
N III	764.351	764.4	2s2 2p $^2P_{3/2}$ - 2s 2p2 $^2S_{1/2}$	15.8	1.73	0.58	G 4	4.90	5.01		
N IV	765.147	765.4	2s2 $^1S_0$ - 2s 2p $^1P_1$	210.0	0.88	0.10	G 4	5.18	5.18		
Mg VIII	769.343	769.1	2p $^2P_{1/2}$ - 2s.2p2 $^4P_{1/2}$	30.4	0.10	0.03	G 4	5.96	5.90		
Ne VIII	770.409	770.7	1s2 2s $^2S_{1/2}$ - 1s2 2p $^2P_{3/2}$	425.1	4.11	0.44	G 4	5.96	5.79		
Mg VIII	772.26	772.1	2p $^2P_{3/2}$ - 2s.2p2 $^4P_{5/2}$	30.7	0.70	0.19	G 4	5.85	5.90	0.77	
N III	772.385		2s 2p2 $^4P_{5/2}$ - 2p3 $^4S_{3/2}$						4.99	0.14	
Ne VIII	780.324	780.1	1s2 2s $^2S_{1/2}$ - 1s2 2p $^2P_{1/2}$	237.4	3.74	0.40	G 4	5.95	5.79		
Mg VIII	782.338	781.6	2p $^2P_{3/2}$ - 2s.2p2 $^4P_{3/2}$	14.4	0.71	0.22	G 4	5.96	5.90		

[59] bl ghost 765.4 Å

Table C.5: *Some of the ghosting reconstruction applied to the on-disc GIS spectra of October 16th, 1997. The averaged positions of the ghost and parent (i.e. ghosting) lines are indicated in columns (1) and (3). The ratio of the intensity of the ghost with that one of the ghosting line (in counts) is presented in column (2), while the intensity of the ghosting line (in counts), is shown in column (4). Note that the correction for ghosting is important for many lines, and that some lines have been corrected twice, for both the red- and blue-shifted ghosts.*

λ_{ob} (Å) (ghost)	ratio (counts)	λ_{ob} (Å) (parent)	I (counts) (parent)
154.628	0.02	174.689	1907.14
157.219	0.72	177.233	768.747
160.618	0.45	180.516	951.649
197.357	0.02	180.516	1382.59
197.876	0.05	180.516	1404.44
162.643	0.14	182.243	341.319
165.274	0.24	184.54	551.356
166.01	0.33	185.272	314.798
330.918	0.00	313.656	299.731
294.037	0.36	314.315	218.247
294.636	0.17	315.092	598.012
332.5	0.01	315.092	701.926
297.056	0.83	317.067	164.668
299.5	0.00	319.75	812.992
336.214	0.08	319.75	812.993
269.2	0.00	292.654	264.952
318.215	1.58	335.397	35.1732
318.429	0.89	335.397	90.808
408.58	0.12	436.921	747.661
409.04	0.08	436.921	836.852
704.656	0.16	736.002	142.054
742.581	0.54	769.107	25.4608
744.129	0.70	770.741	321.928
745.571	0.81	772.144	21.9378

C.3.1 The GIS ghosts for the on-disc observation – October 16th 1997

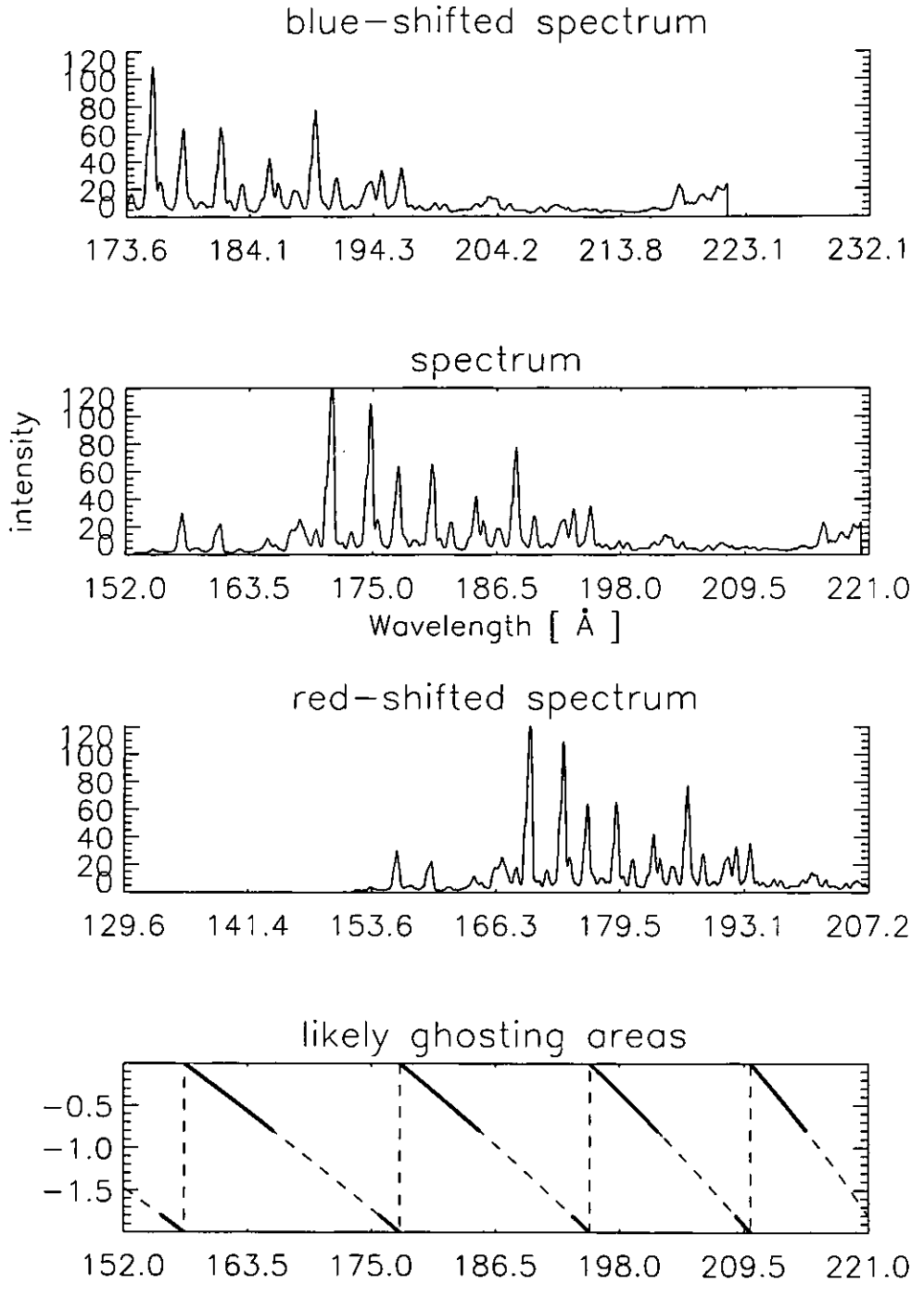

Figure C.17: *The GIS 1 spectrum of October 16th, 1997, on-disc (middle), with the blue- and red-shifted and the likely ghosting areas.*

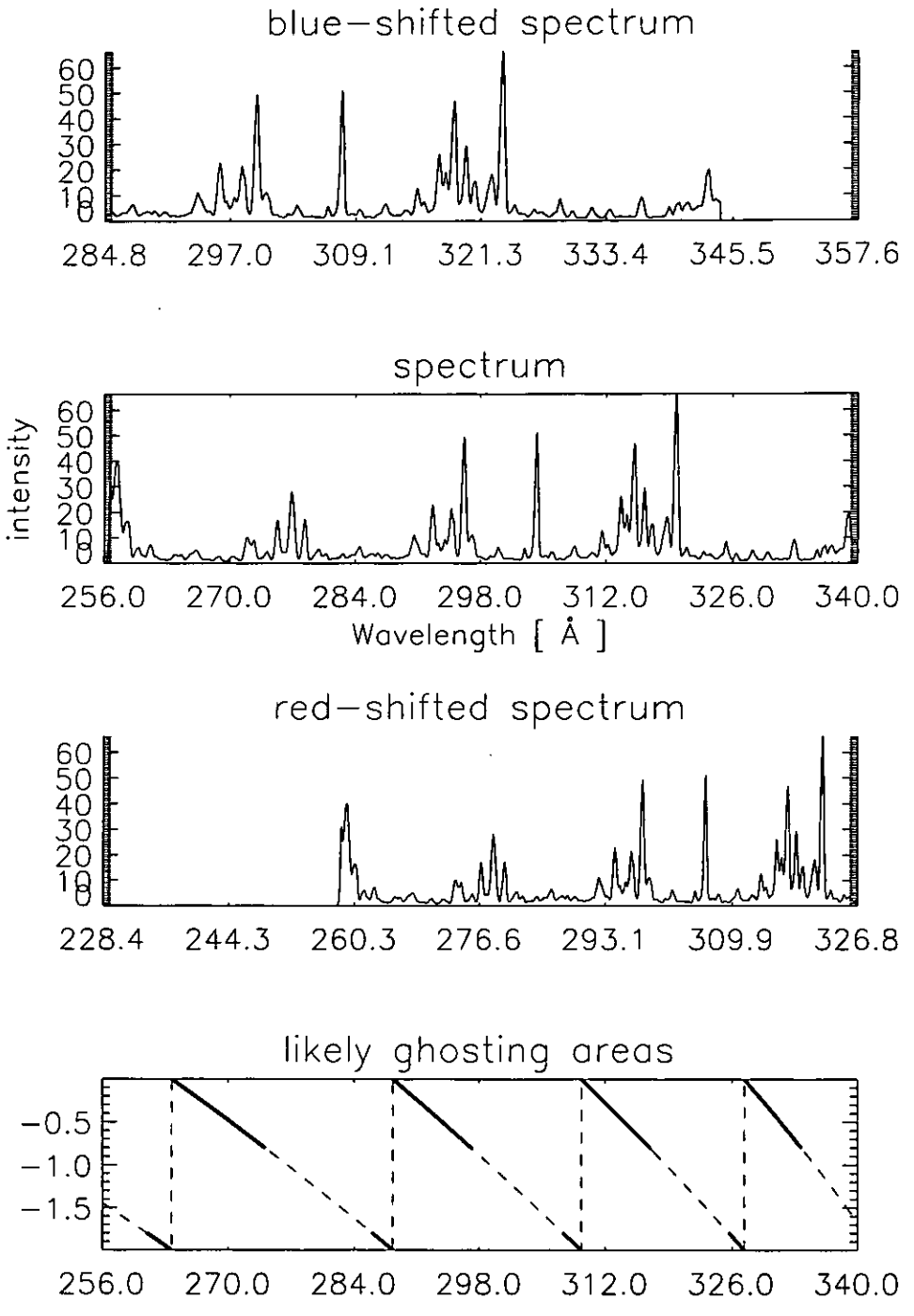

Figure C.18: *The GIS 2 spectrum of October 16th, 1997, on-disc (middle), with the blue- and red-shifted and the likely ghosting areas.*

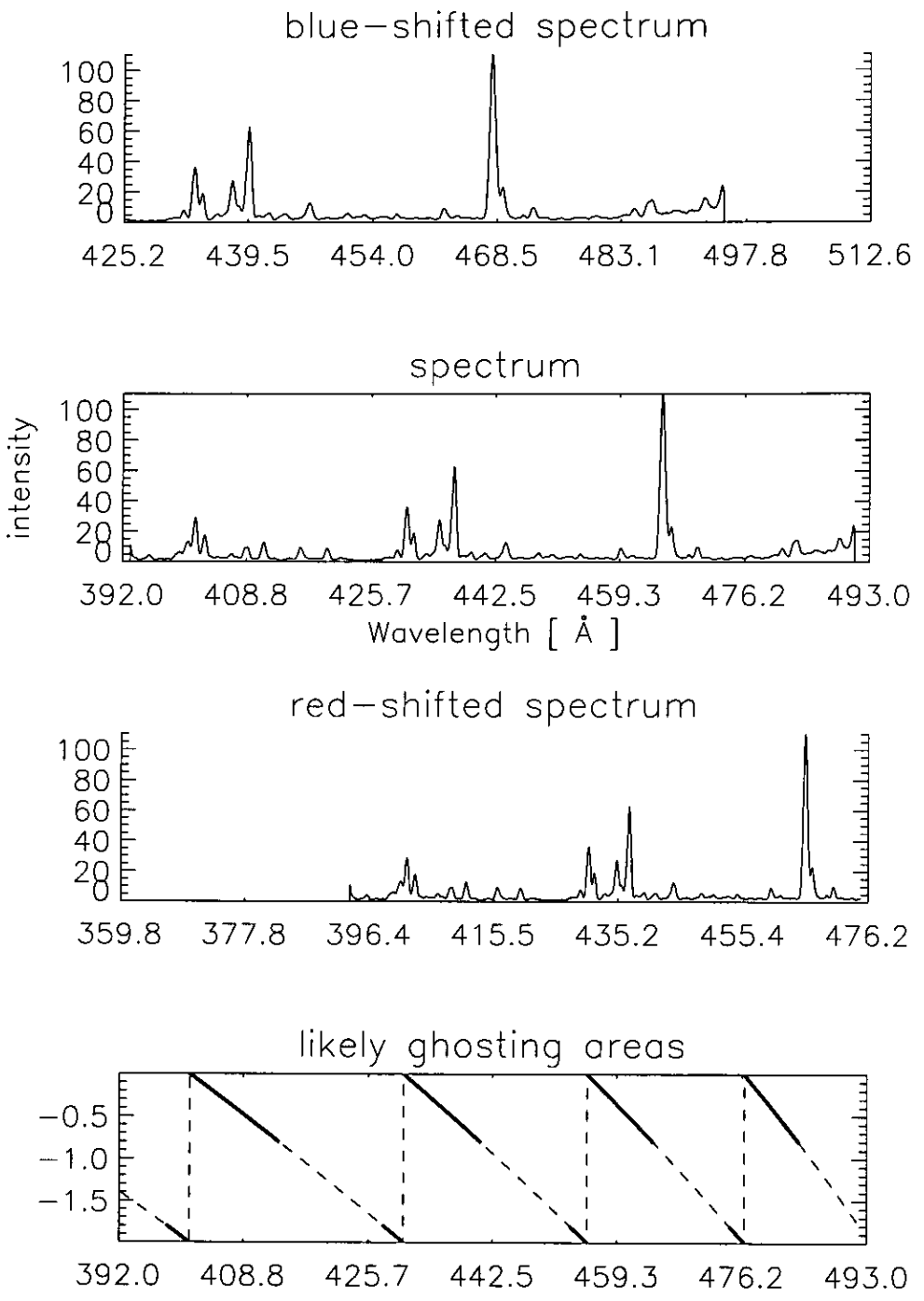

Figure C.19: *The GIS 3 spectrum of October 16th, 1997, on-disc (middle), with the blue- and red-shifted and the likely ghosting areas.*

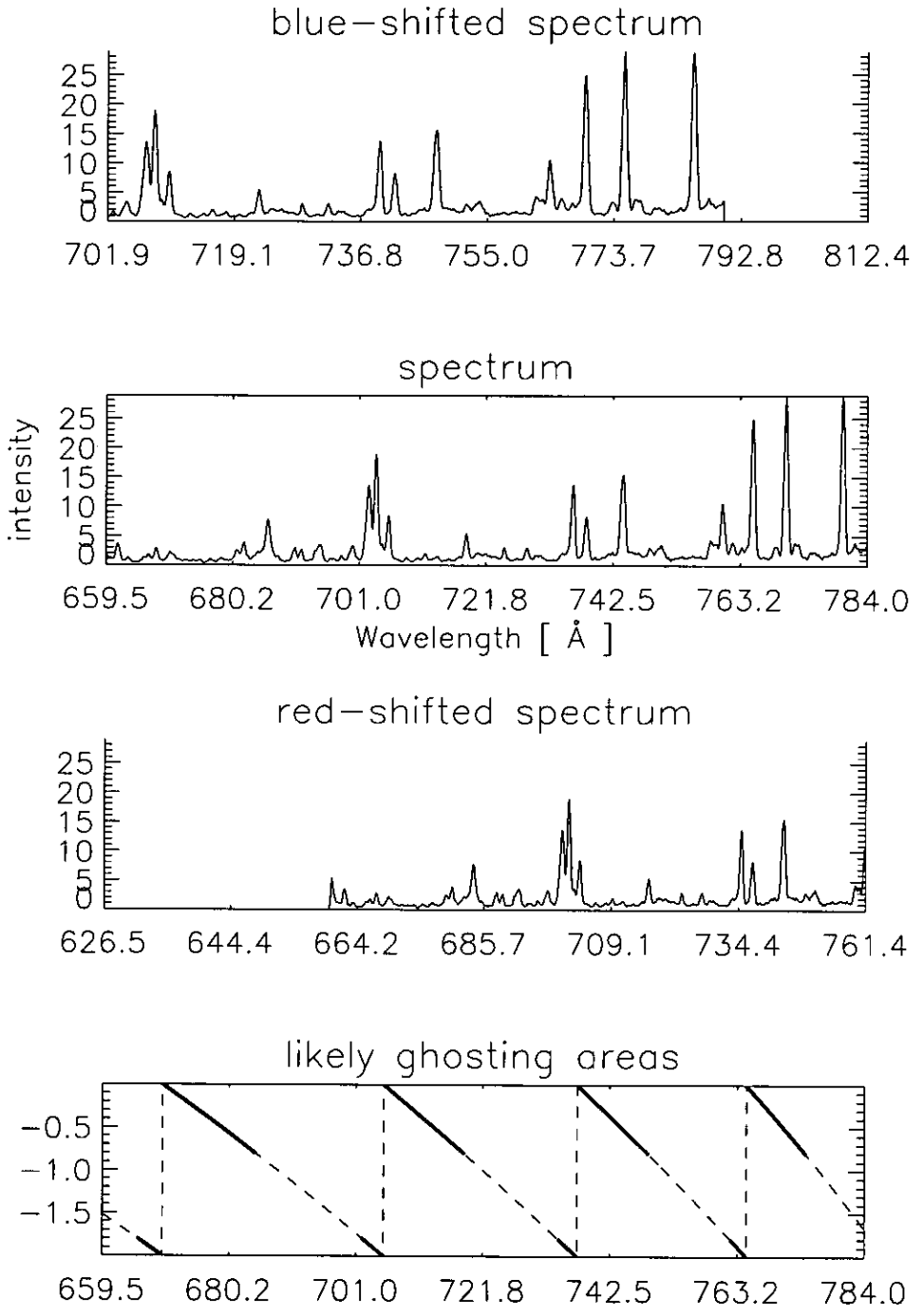

Figure C.20: *The GIS 4 spectrum of October 16th, 1997, on-disc (middle), with the blue- and red-shifted and the likely ghosting areas.*

Appendix D

Appendix to Chapter 5. CDS spectra of the Elephant's Trunk coronal hole

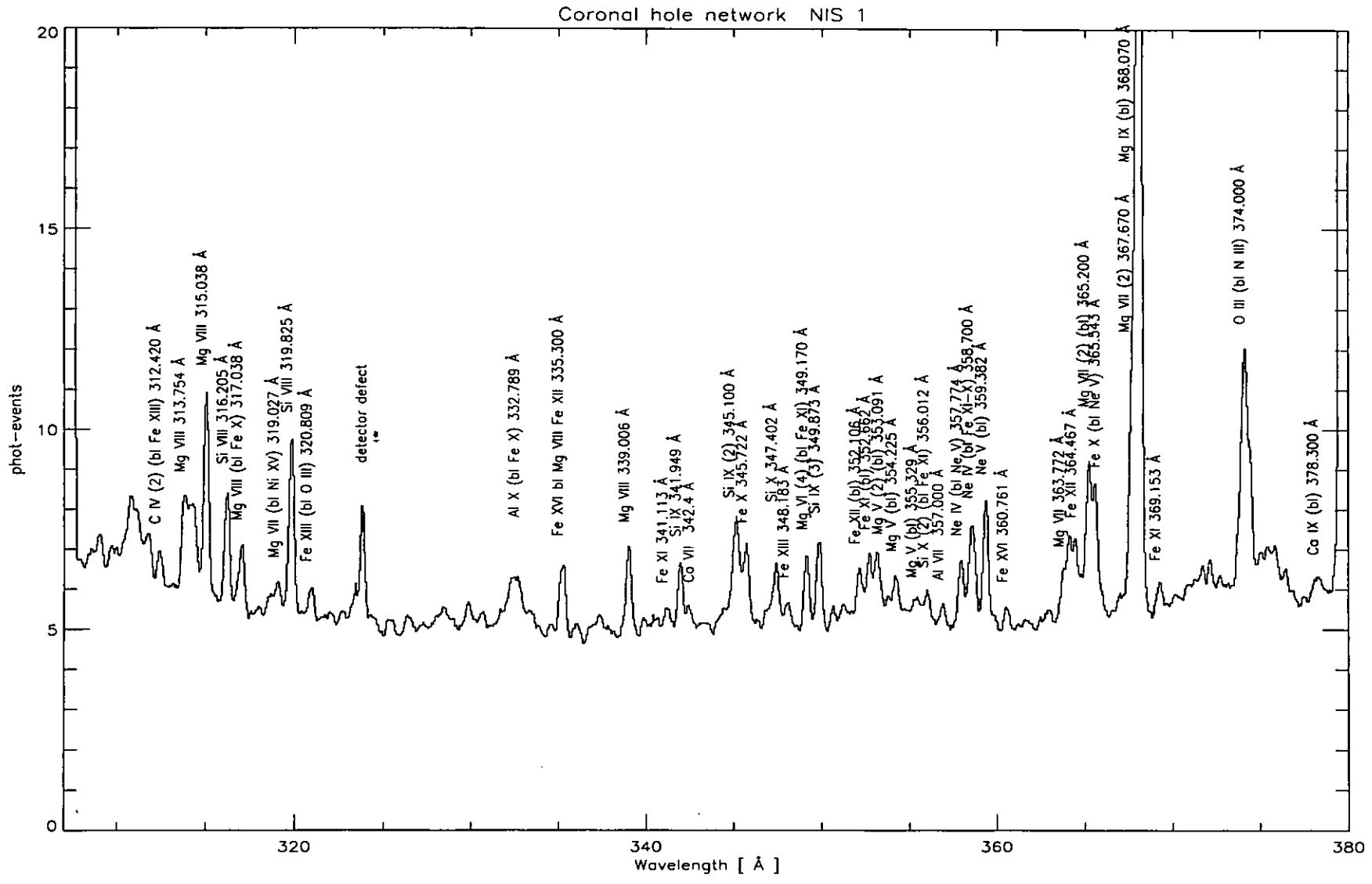

Figure D.1: *The NIS 1 averaged spectra of a network area of the Elephant's Trunk coronal hole – 27th August 1996. Note the high level of the scattered light and the low signal in all the coronal lines.*

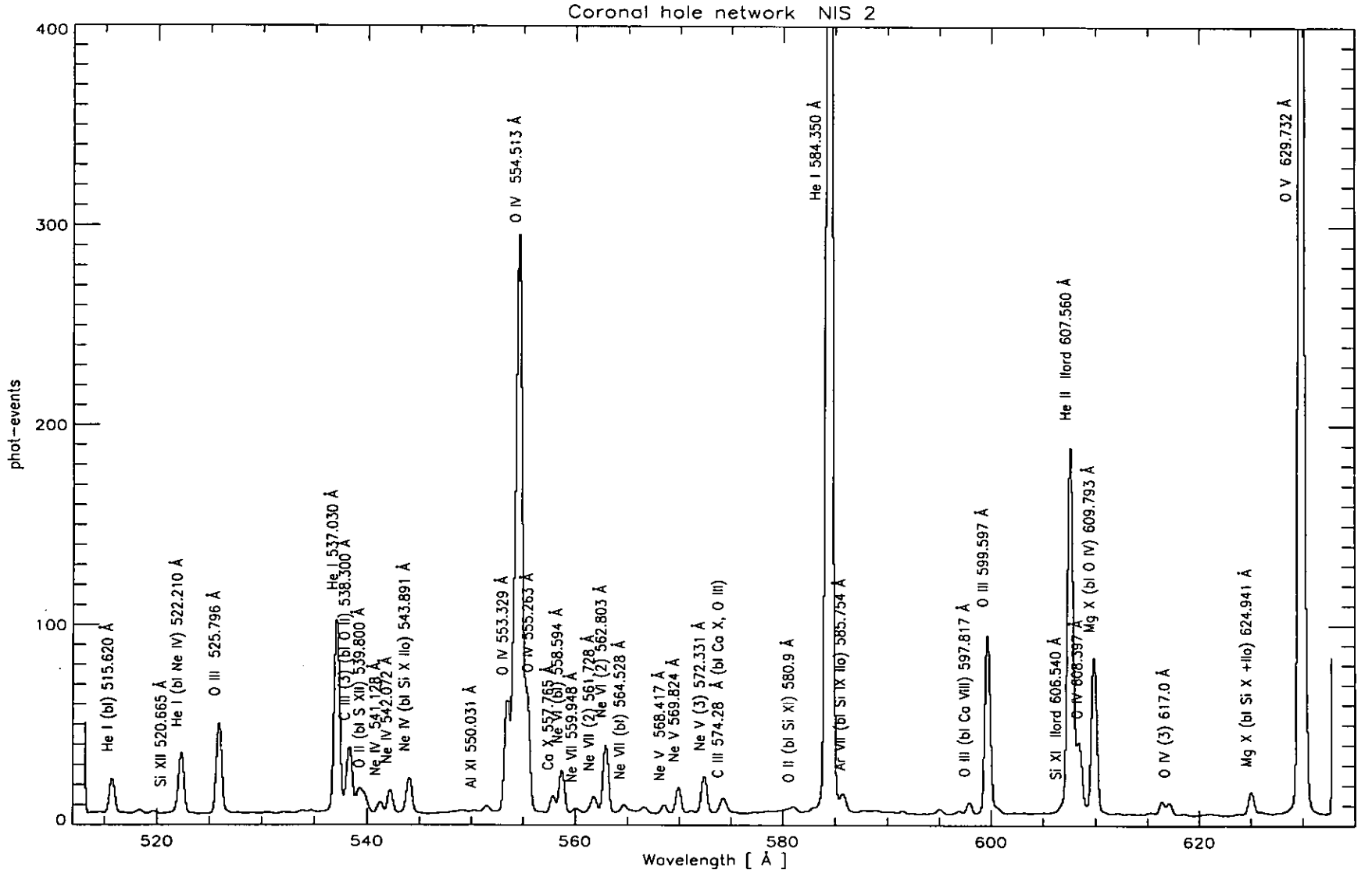

Figure D.2: *The NIS 2 averaged spectra of a network area of the Elephant's Trunk coronal hole – 27th August 1996. Note the low signal in all the coronal lines.*

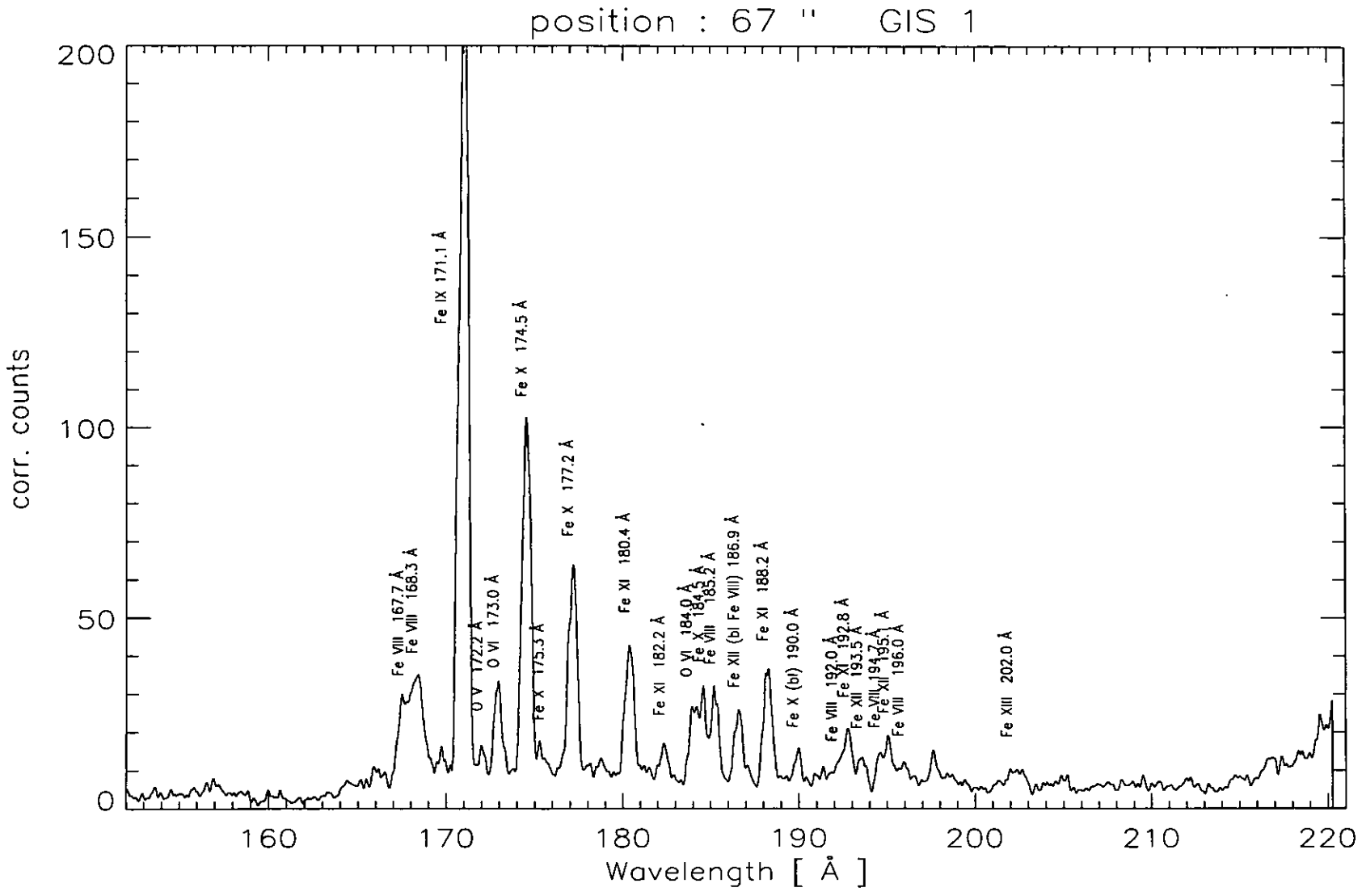

Figure D.3: *The GIS 1 spectrum of the coronal hole network region on August 27, 1996.*

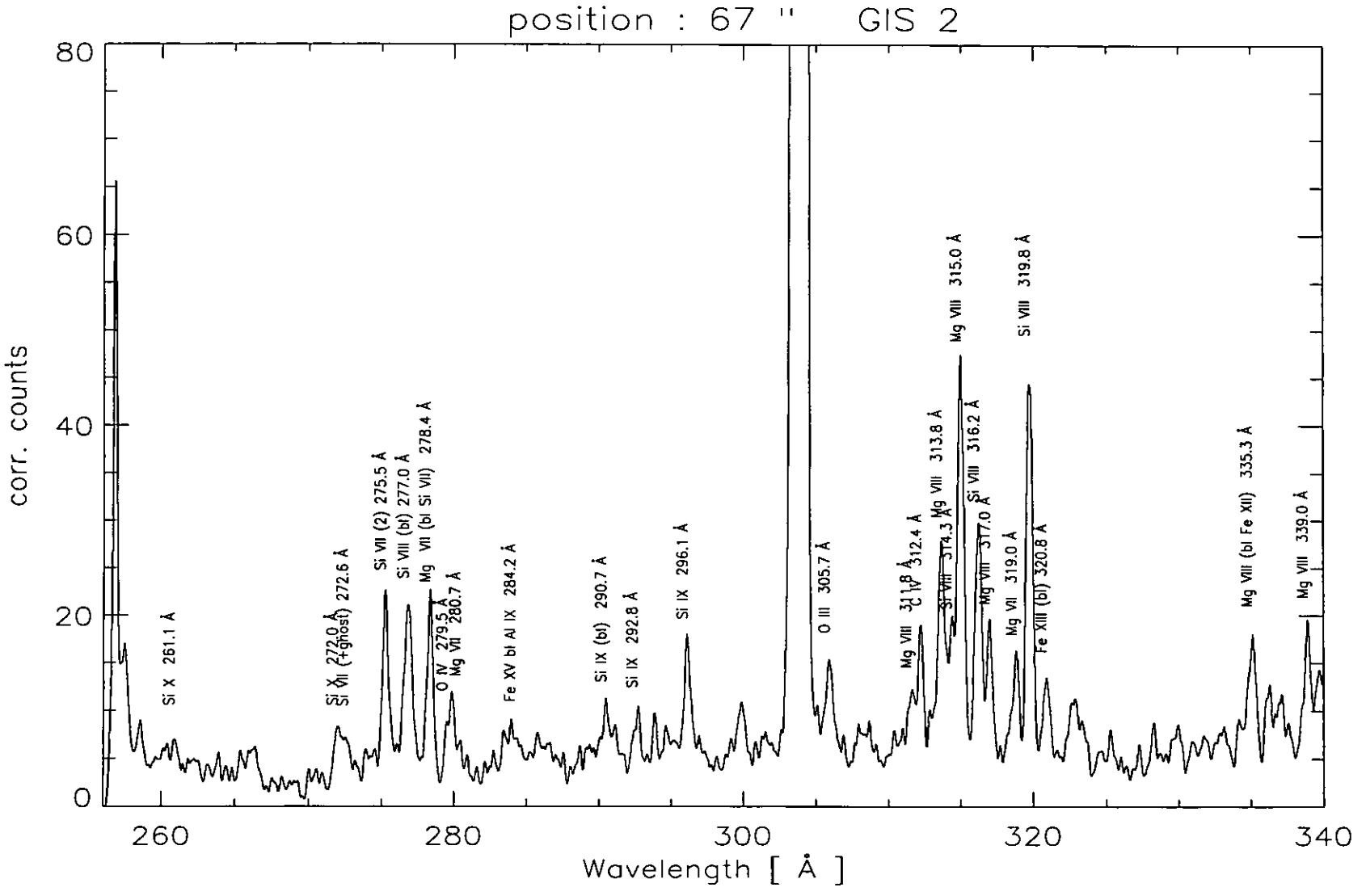

Figure D.4: *The GIS 2 spectrum of the coronal hole network region on August 27, 1996.*

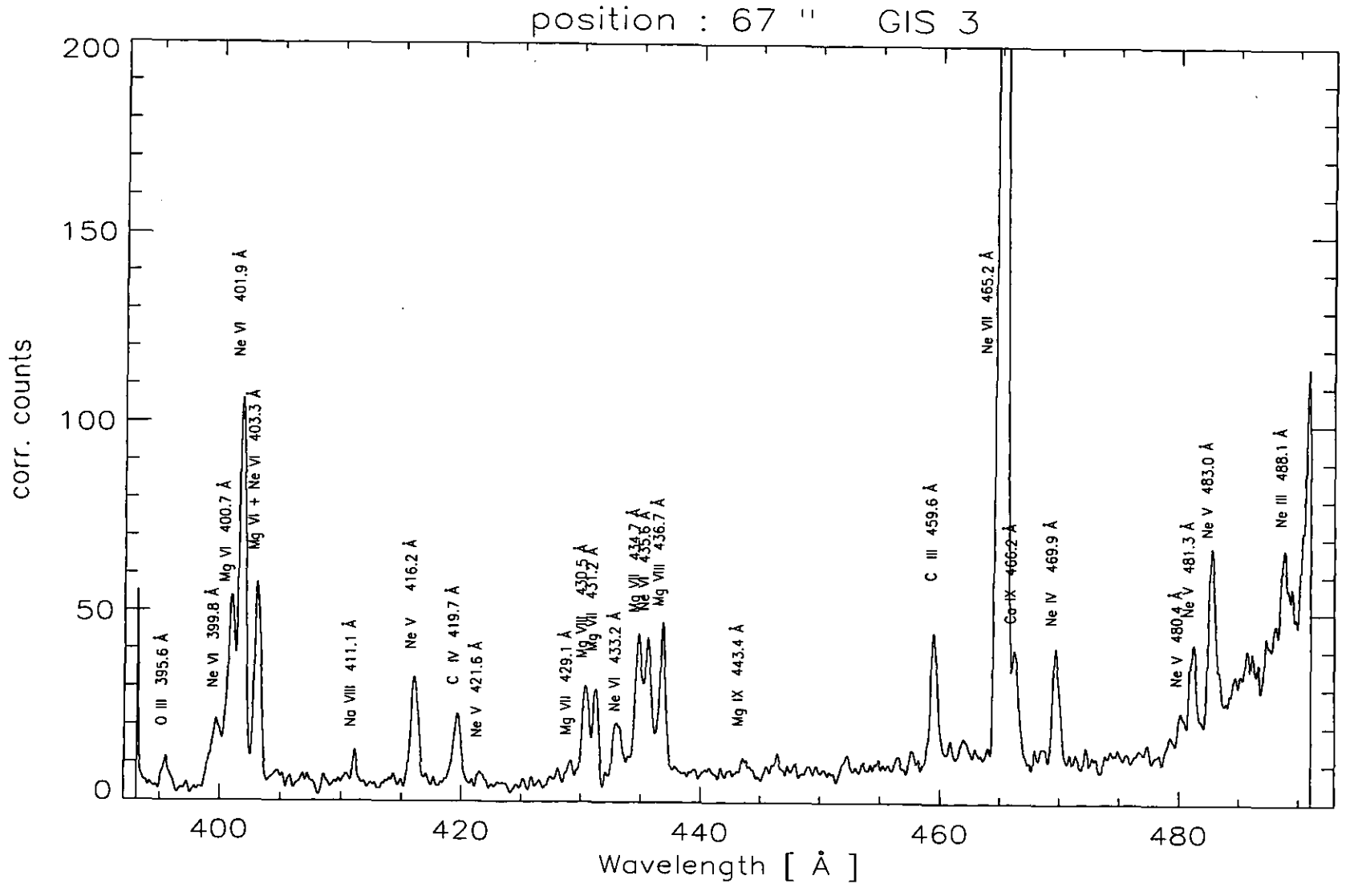

Figure D.5: *The GIS 3 spectrum of the coronal hole network region on August 27, 1996.*

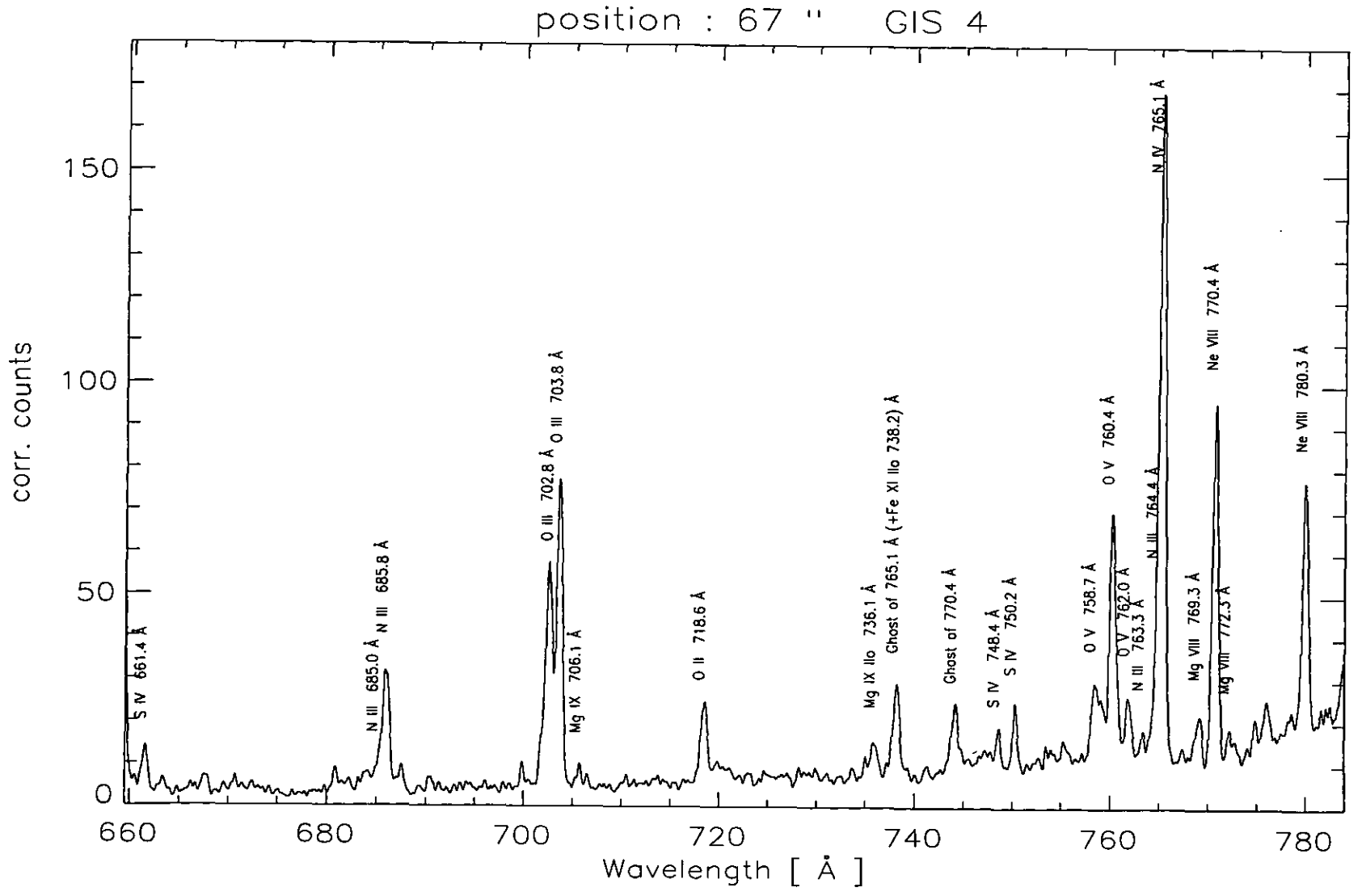

Figure D.6: *The GIS 4 spectrum of the coronal hole network region on August 27, 1996.*

Appendix E

Appendix to Chapter 6

E.1 Spectra and line identifications – plume observation – October 11th 1997

Table E.1: *Results for the 1997 October 11 GIS and NIS observation of a polar coronal hole plume.*

Ion	λ_{th} (Å)	λ_{ob} (Å)	Transition	I_{ob}	I_{th}/I_{ob}	+/-	Det	log T_{eff}	log T_{max}	frac	
HE I	537.03	537.1		37.0	0.64	0.07	N 2	4.54	4.52		AC
HE I	522.213	522.2		10.7	0.72	0.11	N 2	4.61	4.53		AC
	781	781.0	continuum	9.2	0.98	0.31	G 4	4.72	4.34		
	750	750.0	continuum	7.8	0.88	0.28	G 4	4.81	4.39		
C III	538.31	538.3	2s2p $^3P_2$ - 2s3s $^3S_1$	35.2	0.91	0.11	N 2	4.86	4.96	0.35	
O II	538.32		2s22p3 $^2D_{3/2}$ - 2s2p4 $^2P_{3/2}$						4.87	0.33	
C III	538.147		2s2p $^3P_1$ - 2s3s $^3S_1$						4.96	0.21	
	718	718.0	continuum	5.7	0.91	0.29	G 4	4.92	4.45		
C III	459.626	459.8	2s2p $^3P_2$ - 2s3d $^3D_3$	17.8	1.03	0.11	G 3	4.93	4.97	0.46	
C III	459.513		2s2p $^3P_1$ - 2s3d $^3D_2$						4.97	0.25	
C III	459.465		2s2p $^3P_0$ - 2s3d $^3D_1$						4.97	0.11	
N III	764.351	764.7	2s2 2p $^2P_{3/2}$ - 2s 2p2 $^2S_{1/2}$	10.4	1.24	0.20	G 4	4.94	5.01		
N III	763.334	763.5	2s2 2p $^2P_{1/2}$ - 2s 2p2 $^2S_{1/2}$	5.5	1.22	0.29	G 4	4.94	5.01		
N III	685.817	685.8	2s2 2p $^2P_{3/2}$ - 2s 2p2 $^2P_{3/2}$	49.4	1.07	0.12	G 4	4.96	5.02	0.72	
N III	685.515		2s2 2p $^2P_{1/2}$ - 2s 2p2 $^2P_{1/2}$						5.01	0.28	
N III	684.998	684.8	2s2 2p $^2P_{1/2}$ - 2s 2p2 $^2P_{3/2}$	7.8	0.97	0.20	G 4	4.96	5.02		
O III	702.897	702.7	2s22p2 $^3P_1$ - 2s2p3 $^3P_2$	64.5	1.09	0.11	G 4	5.03	5.04	0.42	
O III	702.821		2s22p2 $^3P_1$ - 2s2p3 $^3P_0$						5.04	0.32	
O III	702.891		2s22p2 $^3P_1$ - 2s2p3 $^3P_1$						5.04	0.26	
O III	703.854	703.7	2s22p2 $^3P_2$ - 2s2p3 $^3P_2$	112.4	1.06	0.11	G 4	5.03	5.04	0.75	
O III	703.848		2s22p2 $^3P_2$ - 2s2p3 $^3P_1$						5.04	0.25	
S IV	748.392	748.9	3s2.3p $^2P_{1/2}$ - 3s.3p2 $^2P_{1/2}$	9.0	0.99	0.17	G 4	5.04	5.09		
S IV	753.759	753.9	3s2.3p $^2P_{3/2}$ - 3s.3p2 $^2P_{1/2}$	4.4	1.00	0.29	G 4	5.04	5.09		
S IV	661.395	661.8	3s2.3p $^2P_{3/2}$ - 3s2.(1s).3d $^2D_{5/2}$	20.6	1.05	0.14	G 4	5.06	5.10		
O III	525.796	525.9	2s22p2 $^1D_2$ - 2s2p3 $^1P_1$	43.5	1.04	0.12	N 2	5.08	5.07		
Ne III	489.495	489.1	2s2 2p4 $^3P_2$ - 2s 2p5 $^3P_2$	14.0	0.84	0.10	G 3	5.11	5.06	0.66	
Ne III	488.851		2s2 2p4 $^3P_1$ - 2s 2p5 $^3P_0$						5.06	0.18	
Ne III	489.629		2s2 2p4 $^3P_1$ - 2s 2p5 $^3P_1$						5.06	0.13	
N IV	765.147	765.3	2s2 $^1S_0$ - 2s 2p $^1P_1$	97.4	1.17	0.12	G 4	5.17	5.18		
S V	663.126	663.3	3s.3p $^3P_2$ - 3s.3d $^3D_3$	2.4	1.05	0.54	G 4	5.21	5.20		
O IV	554.513	554.6	2s2 2p $^2P_{3/2}$ - 2s 2p2 $^2P_{3/2}$	290.5	1.08	0.11	N 2	5.26	5.27		
O IV	553.329	553.4	2s2 2p $^2P_{1/2}$ - 2s 2p2 $^2P_{3/2}$	55.0	1.14	0.13	N 2	5.26	5.27		
O IV	555.263	555.4	2s2 2p $^2P_{3/2}$ - 2s 2p2 $^2P_{1/2}$	59.5	1.08	0.12	N 2	5.26	5.27		
O IV	608.397	608.4	2s2 2p $^2P_{1/2}$ - 2s 2p2 $^2S_{1/2}$	42.8	1.11	0.13	N 2	5.26	5.27		
Ne IV	542.073	542.2	2s2 2p3 $^4S_{3/2}$ - 2s 2p4 $^4P_{3/2}$	6.0	1.12	0.23	N 2	5.27	5.27		
Ne IV	541.128	541.2	2s2 2p3 $^4S_{3/2}$ - 2s 2p4 $^4P_{1/2}$	2.5	1.32	0.52	N 2	5.28	5.27		
Ne IV	469.823	470.1	2s2 2p3 $^2D_{5/2}$ - 2s 2p4 $^2D_{5/2}$	9.5	1.21	0.14	G 3	5.28	5.28	0.58	

Table E.1: *(continued)*

Ion	λ_{th} (Å)	λ_{ob} (Å)	Transition	I_{ob}	I_{th}/I_{ob}	+/-	Det	log T_{eff}	log T_{max}	frac	
Ne IV	469.875		2s2 2p3 $^2D_{3/2}$ - 2s 2p4 $^2D_{3/2}$						5.28	0.38	
Ne IV	543.892	544.0	2s2 2p3 $^4S_{3/2}$ - 2s 2p4 $^4P_{5/2}$	10.8	1.01	0.16	N 2	5.34	5.27		
O V	760.444	760.5	2s.2p $^3P_2$ - 2p2 $^3P_2$	30.8	1.22	0.14	G 4	5.37	5.39	0.84	
O V	760.225		2s.2p $^3P_1$ - 2p2 $^3P_1$						5.39	0.16	
O V	758.675	758.6	2s.2p $^3P_1$ - 2p2 $^3P_2$	11.6	0.92	0.14	G 4	5.37	5.39		
O V	759.439	759.5	2s.2p $^3P_0$ - 2p2 $^3P_1$	9.6	0.83	0.14	G 4	5.37	5.39		
O V	762.002	762.1	2s.2p $^3P_2$ - 2p2 $^3P_1$	10.5	0.94	0.15	G 4	5.37	5.39		
O V	629.73	629.8	2s2 $^1S_0$ - 2s.2p $^1P_1$	662.9	0.84	0.08	N 2	5.37	5.39		
Ne V	569.824	569.9	2s22p2 $^3P_1$ - 2s2p3 $^3D_2$	5.0	1.05	0.24	N 2	5.49	5.47	0.76	
Ne V	569.753		2s22p2 $^3P_1$ - 2s2p3 $^3D_1$						5.47	0.24	
Ne V	416.194	416.1	2s22p2 $^1D_2$ - 2s2p3 $^1D_2$	7.1	1.24	0.15	G 3	5.51	5.48		
C IV	419.713	419.9	1s2 2p $^2P_{3/2}$ - 1s2 3s $^2S_{1/2}$	12.6	0.45	0.05	G 3	5.51	5.08	0.58	
C IV	419.525		1s2 2p $^2P_{1/2}$ - 1s2 3s $^2S_{1/2}$						5.08	0.29	
Ca X	419.754		3p $^2P_{3/2}$ - 3d $^2D_{5/2}$						5.82	0.13	
Mg V	351.088	351.0	2p4 $^3P_2$ - 2s.2p5 $^3P_1$	5.1	0.33	0.30	N 1	5.57	5.47		
Mg V	353.092	353.1	2p4 $^3P_2$ - 2s.2p5 $^3P_2$	17.3	0.31	0.11	N 1	5.58	5.47		
O IV	609.829	609.8	2s2 2p $^2P_{3/2}$ - 2s 2p2 $^2S_{1/2}$	82.7	1.64	0.18	N 2	5.72	5.27	0.65	
Mg X	609.793		1s2.(1s).2s $^2S_{1/2}$ - 1s2.(1s).2p $^2P_{3/2}$						6.04	0.34	
Ne VI	562.803	562.9	2s2 2p $^2P_{3/2}$ - 2s 2p2 $^2D_{5/2}$	20.4	0.94	0.12	N 2	5.76	5.63		
Ne VI	401.926	402.1	2s2 2p $^2P_{3/2}$ - 2s 2p2 $^2P_{3/2}$	25.6	1.07	0.11	G 3	5.77	5.64		
Ne VI	399.821	399.8	2s2 2p $^2P_{1/2}$ - 2s 2p2 $^2P_{3/2}$	6.8	0.79	0.09	G 3	5.77	5.64		
Ne VI	401.136	401.1	2s2 2p $^2P_{1/2}$ - 2s 2p2 $^2P_{1/2}$	11.7	0.90	0.10	G 3	5.77	5.64		
Ne VI	558.594	558.7	2s2 2p $^2P_{1/2}$ - 2s 2p2 $^2D_{3/2}$	14.7	0.83	0.12	N 2	5.77	5.63	0.81	
Ne VII	558.609		2s2p $^3P_1$ - 2p2 $^3P_2$						5.72	0.19	
Na VI	415.584	415.7	2p2 $^3P_1$ - 2s.2p3 $^3P_2$	1.0	0.96	0.31	G 3	5.81	5.66	0.39	
Na VI	415.504		2p2 $^3P_1$ - 2s.2p3 $^3P_0$						5.66	0.34	
Na VI	415.578		2p2 $^3P_1$ - 2s.2p3 $^3P_1$						5.66	0.27	
Mg VI	403.307	403.3	2s2.2p3 $^4S_{3/2}$ - 2s.2p4 $^4P_{5/2}$	38.5	1.07	0.11	G 3	5.81	5.65	0.85	
Ne VI	403.255		2s2 2p $^2P_{3/2}$ - 2s 2p2 $^2P_{1/2}$						5.64	0.15	
Mg VI	349.163	349.2	2s2.2p3 $^2D_{5/2}$ - 2s.2p4 $^2D_{5/2}$	23.0	1.05	0.33	N 1	5.82	5.65	0.50	
Mg VI	349.124		2s2.2p3 $^2D_{3/2}$ - 2s.2p4 $^2D_{3/2}$						5.65	0.38	
Ne VII	564.528	564.7	2s2p $^3P_2$ - 2p2 $^3P_1$	2.5	0.87	0.36	N 2	5.83	5.72		
Ne VII	561.728	561.7	2s2p $^3P_2$ - 2p2 $^3P_2$	6.9	0.98	0.20	N 2	5.83	5.72		
Ne VII	465.22	465.4	2s2 $^1S_0$ - 2s2p $^1P_1$	179.0	1.00	0.10	G 3	5.83	5.72		
Ca IX	466.239	466.5	3s2 $^1S_0$ - 3s.3p $^1P_1$	62.5	0.38	0.04	G 3	5.84	5.78		
Mg VII	434.917	434.9	2s22p2 $^3P_2$ - 2s2p3 $^3D_3$	78.4	0.76	0.08	G 3	5.85	5.80	0.84	
Mg VII	434.72		2s22p2 $^3P_2$ - 2s2p3 $^3D_2$						5.81	0.13	
Fe VIII	167.486	167.5		281.2	0.31	0.03	G 1	5.85	5.65		AC
Fe VIII	168.545	168.3		474.6	0.44	0.05	G 1	5.85	5.65	0.50	AC
Fe VIII	168.17								5.65	0.40	AC
Fe VIII	185.213	185.3		181.4	0.53	0.05	G 1	5.85	5.64		AC
Si VII	275.353	275.4	2p4 $^3P_2$ - 2s.2p5 $^3P_2$	79.8	0.64	0.07	G 2	5.85	5.77		
Mg VII	367.674	367.7	2s22p2 $^3P_2$ - 2s2p3 $^3P_2$	55.0	1.17	0.18	N 1	5.85	5.81	0.76	
Mg VII	367.683		2s22p2 $^3P_2$ - 2s2p3 $^3P_1$						5.81	0.23	
Mg VII	431.313	431.3	2s22p2 $^3P_1$ - 2s2p3 $^3D_2$	46.9	0.84	0.09	G 3	5.85	5.81	0.78	
Mg VII	431.188		2s22p2 $^3P_1$ - 2s2p3 $^3D_1$						5.81	0.22	
Mg VII	429.14	429.1	2s22p2 $^3P_0$ - 2s2p3 $^3D_1$	17.5	0.76	0.08	G 3	5.85	5.81		
Mg VII	363.772	363.8	2s22p2 $^3P_0$ - 2s2p3 $^3P_1$	14.6	0.85	0.34	N 1	5.85	5.81		
Mg VII	365.234	365.2	2s22p2 $^3P_1$ - 2s2p3 $^3P_2$	39.5	0.98	0.19	N 1	5.86	5.81	0.37	
Mg VII	365.176		2s22p2 $^3P_1$ - 2s2p3 $^3P_0$						5.81	0.35	
Mg VII	365.243		2s22p2 $^3P_1$ - 2s2p3 $^3P_1$						5.81	0.27	
Mg VII	276.154	276.1	2s22p2 $^3P_0$ - 2s2p3 $^3S_1$	16.8	0.60	0.07	G 2	5.86	5.81		
Al VII	356.888	357.0	2s22p3 $^4S_{3/2}$ - 2s2p4 $^4P_{5/2}$	7.2	0.83	0.60	N 1	5.86	5.78		
Mg VII	278.402	278.3	2s22p2 $^3P_2$ - 2s2p3 $^3S_1$	81.7	0.82	0.08	G 2	5.86	5.81	0.76	
Si VII	278.443		2p4 $^3P_1$ - 2s.2p5 $^3P_2$						5.77	0.24	
Na VIII	411.166	411.2	2s2 $^1S_0$ - 2s.2p $^1P_1$	19.9	0.86	0.09	G 3	5.87	5.86		
Ne VIII	780.324	779.5	1s2 2s $^2S_{1/2}$ - 1s2 2p $^2P_{1/2}$	46.7	2.20	0.24	G 4	5.87	5.79		
Fe X	365.543	365.6	3s2.3p5 $^2P_{1/2}$ - 3s.3p6 $^2S_{1/2}$	9.2	1.38	0.70	N 1	5.87	6.04	0.64	
Ne V	365.603		2s22p2 $^1D_2$ - 2s2p3 $^1P_1$						5.48	0.36	
O VI	184.117	184.0	1s2 2p $^2P_{3/2}$ - 1s2 3s $^2S_{1/2}$	33.6	0.47	0.06	G 1	5.87	5.51	0.65	
O VI	183.937		1s2 2p $^2P_{1/2}$ - 1s2 3s $^2S_{1/2}$						5.51	0.32	

Table E.1: *(continued)*

Ion	λ_{th} (Å)	λ_{ob} (Å)	Transition	I_{ob}	I_{th}/I_{ob}	+/-	Det	log T_{eff}	log T_{max}	frac	
Ca X	557.765	557.8	3s $^2S_{1/2}$ - 3p $^2P_{3/2}$	12.8	0.88	0.13	N 2	5.87	5.82		
Mg VII	277	276.9	2s22p2 $^3P_1$ - 2s2p3 $^3S_1$	92.8	0.69	0.07	G 2	5.87	5.81	0.47	
Si VIII	277.054		2s22p3 $^2D_{5/2}$ - 2s2p4 $^2D_{5/2}$						5.90	0.27	
Si VII	276.839		2p4 $^3P_0$ - 2s.2p5 $^3P_1$						5.77	0.13	
Si VIII	276.838		2s22p3 $^2D_{3/2}$ - 2s2p4 $^2D_{3/2}$						5.88	0.11	
Ne VIII	770.409	770.5	1s2 2s $^2S_{1/2}$ - 1s2 2p $^2P_{3/2}$	76.0	2.61	0.27	G 4	5.88	5.79		
O VI	173.079	173.1	1s2 2p $^2P_{3/2}$ - 1s2 3d $^2D_{5/2}$	122.5	0.22	0.02	G 1	5.88	5.51	0.60	
O VI	172.935		1s2 2p $^2P_{1/2}$ - 1s2 3d $^2D_{3/2}$						5.51	0.33	
Fe VIII	195.972	196.0	3p6.(1s).3d $^2D_{3/2}$ - 3p6.(1s).4p $^2P_{1/2}$	35.9	0.12	0.02	G 1	5.89	5.85		
Fe VIII	186.599	186.6		104.7	1.06	0.11	G 1	5.89	5.64		AC
Mg VIII	436.735	436.9	2p $^2P_{3/2}$ - 2s.2p2 $^2D_{5/2}$	93.1	0.69	0.07	G 3	5.89	5.91	0.89	
Mg VIII	436.672		2p $^2P_{3/2}$ - 2s.2p2 $^2D_{3/2}$						5.92	0.11	
Mg VIII	315.039	315.0	2p $^2P_{3/2}$ - 2s.2p2 $^2P_{3/2}$	129.7	0.78	0.13	N 1	5.90	5.91		
Mg VIII	315.039	315.2	2p $^2P_{3/2}$ - 2s.2p2 $^2P_{3/2}$	132.8	0.77	0.08	G 2	5.90	5.91		
Si VIII	319.826	319.9	2s22p3 $^4S_{3/2}$ - 2s2p4 $^4P_{5/2}$	115.6	0.79	0.08	G 2	5.90	5.91		
Mg VIII	339.006	339.0	2p $^2P_{3/2}$ - 2s.2p2 $^2S_{1/2}$	33.5	0.73	0.20	N 1	5.90	5.92		
Mg VIII	430.465	430.4	2p $^2P_{1/2}$ - 2s.2p2 $^2D_{3/2}$	62.2	0.67	0.07	G 3	5.90	5.92		
Si VIII	319.826	319.9	2s22p3 $^4S_{3/2}$ - 2s2p4 $^4P_{5/2}$	110.2	0.83	0.15	N 1	5.90	5.91		
Fe IX	171.073	171.1	3p6 $^1S_0$ - 3p5.3d $^1P_1$	1454.8	0.70	0.07	G 1	5.93	5.96		
Na IX	681.721	681.6	1s2.2s $^2S_{1/2}$ - 1s2.2p $^2P_{3/2}$	4.9	1.37	0.39	G 4	5.95	5.92		
Si IX	345.124	345.1	2s22p2 $^3P_1$ - 2s2p3 $^3D_2$	26.5	0.84	0.27	N 1	5.96	6.03	0.69	
Si IX	344.951		2s22p2 $^3P_1$ - 2s2p3 $^3D_1$						6.04	0.24	
Mg IX	368.07	368.1	2s2 $^1S_0$ - 2s.2p $^1P_1$	134.1	1.01	0.12	N 1	5.96	5.98		
Fe VIII	194.661	194.7	3p6.(1s).3d $^2D_{5/2}$ - 3p6.(1s).4p $^2P_{3/2}$	48.4	0.05	0.01	G 1	5.98	5.86	0.67	
Fe XII	194.609		3s2.3p3 $^4S_{3/2}$ - 3s2.3p2(3p).3d $^2P_{1/2}$						6.17	0.32	
Si IX	349.873	349.8	2s22p2 $^3P_2$ - 2s2p3 $^3D_3$	15.5	1.03	0.41	N 1	5.98	6.02	0.81	
Si IX	349.794		2s22p2 $^3P_2$ - 2s2p3 $^3D_2$						6.03	0.19	
Fe X	345.723	345.7	3s2.3p5 $^2P_{3/2}$ - 3s.3p6 $^2S_{1/2}$	18.2	1.07	0.41	N 1	5.99	6.04		
Fe X	184.543	184.5	3s2.3p5 $^2P_{3/2}$ - 3s2.3p4(1d).3d $^2S_{1/2}$	99.5	0.76	0.08	G 1	5.99	6.05		
Fe X	177.243	177.3	3s2.3p5 $^2P_{3/2}$ - 3s2.3p4(3p).3d $^2P_{3/2}$	420.9	0.48	0.06	G 1	5.99	6.05		
Fe X	174.534	174.7	3s2.3p5 $^2P_{3/2}$ - 3s2.3p4(3p).3d $^2D_{5/2}$	479.4	0.73	0.07	G 1	5.99	6.05		
Fe X	190.043	190.0	3s2.3p5 $^2P_{1/2}$ - 3s2.3p4(1d).3d $^2S_{1/2}$	38.7	0.66	0.08	G 1	6.00	6.05		
Fe XI	180.408	180.5	3s2.3p4 $^3P_2$ - 3s2.3p3(4s*).3d $^3D_3$	157.8	1.14	0.12	G 1	6.04	6.11	0.84	
Fe X	180.407		3s2.3p5 $^2P_{1/2}$ - 3s2.3p4(3p).3d $^2P_{1/2}$						6.04	0.12	
Fe XI	369.153	369.3	3s2.3p4 $^3P_1$ - 3s.3p5 $^3P_2$	4.5	1.09	0.86	N 1	6.04	6.11		
Fe XI	352.662	352.7	3s2.3p4 $^3P_2$ - 3s.3p5 $^3P_2$	12.1	1.37	0.64	N 1	6.04	6.11		
Fe XI	188.232	188.4	3s2.3p4 $^3P_2$ - 3s2.3p3(2d*).3d $^3P_2$	113.4	0.88	0.09	G 1	6.05	6.11	0.71	
Fe XI	188.299		3s2.3p4 $^3P_2$ - 3s2.3p3(2d*).3d $^1P_1$						6.11	0.26	
Mg X	624.941	625.0	1s2.(1s).2s $^2S_{1/2}$ - 1s2.(1s).2p $^2P_{1/2}$	9.1	2.61	0.49	N 2	6.07	6.04		
Al VII	353.769	353.7	2s22p3 $^4S_{3/2}$ - 2s2p4 $^4P_{3/2}$	9.0	0.78	0.47	N 1	6.09	5.78	0.56	
Fe XIV	353.831		3s2 3p $^2P_{3/2}$ - 3s 3p2 $^2D_{5/2}$						6.24	0.44	
Fe XII	193.521	193.6	3s2.3p3 $^4S_{3/2}$ - 3s2.3p2(3p).3d $^4P_{3/2}$	51.9	1.12	0.13	G 1	6.12	6.16		
Fe XII	364.467	364.5	3s2.3p3 $^4S_{3/2}$ - 3s.3p4 $^4P_{5/2}$	7.8	1.37	0.97	N 1	6.12	6.16		
Fe XII	195.118	195.3	3s2.3p3 $^4S_{3/2}$ - 3s2.3p2(3p).3d $^4P_{5/2}$	79.0	1.15	0.13	G 1	6.12	6.16		
Fe XIII	348.183	348.2	3s2 3p2 $^3P_0$ - 3s 3p3 $^3D_1$	10.4	0.85	0.52	N 1	6.21	6.20		
Fe XIV	274.2	274.2	3s2 3p $^2P_{1/2}$ - 3s 3p2 $^2S_{1/2}$	31.0	0.73	0.08	G 2	6.21	6.25	0.76	
Si VII	274.174		2p4 $^3P_1$ - 2s.2p5 $^3P_0$						5.76	0.23	
Fe XIII	202.044	202.2	3s2 3p2 $^3P_0$ - 3s2 3p 3d $^3P_1$	104.5	0.77	0.08	G 1	6.22	6.21		
Fe XIV	211.32	211.3	3s2 3p $^2P_{1/2}$ - 3s2 3d $^2D_{3/2}$	33.2	0.92	0.13	G 1	6.28	6.25		
Fe XV	284.16	284.5	3s2 $^1S_0$ - 3s3p $^1P_1$	100.1	0.88	0.09	G 2	6.33	6.29		
Fe XV	417.258	417.2	3s2 $^1S_0$ - 3s3p $^3P_1$	4.7	0.56	0.07	G 3	6.34	6.29		
Si XII	520.665	520.8	1s2.2s $^2S_{1/2}$ - 1s2.2p $^2P_{1/2}$	4.2	1.56	0.36	N 2	6.37	6.26		

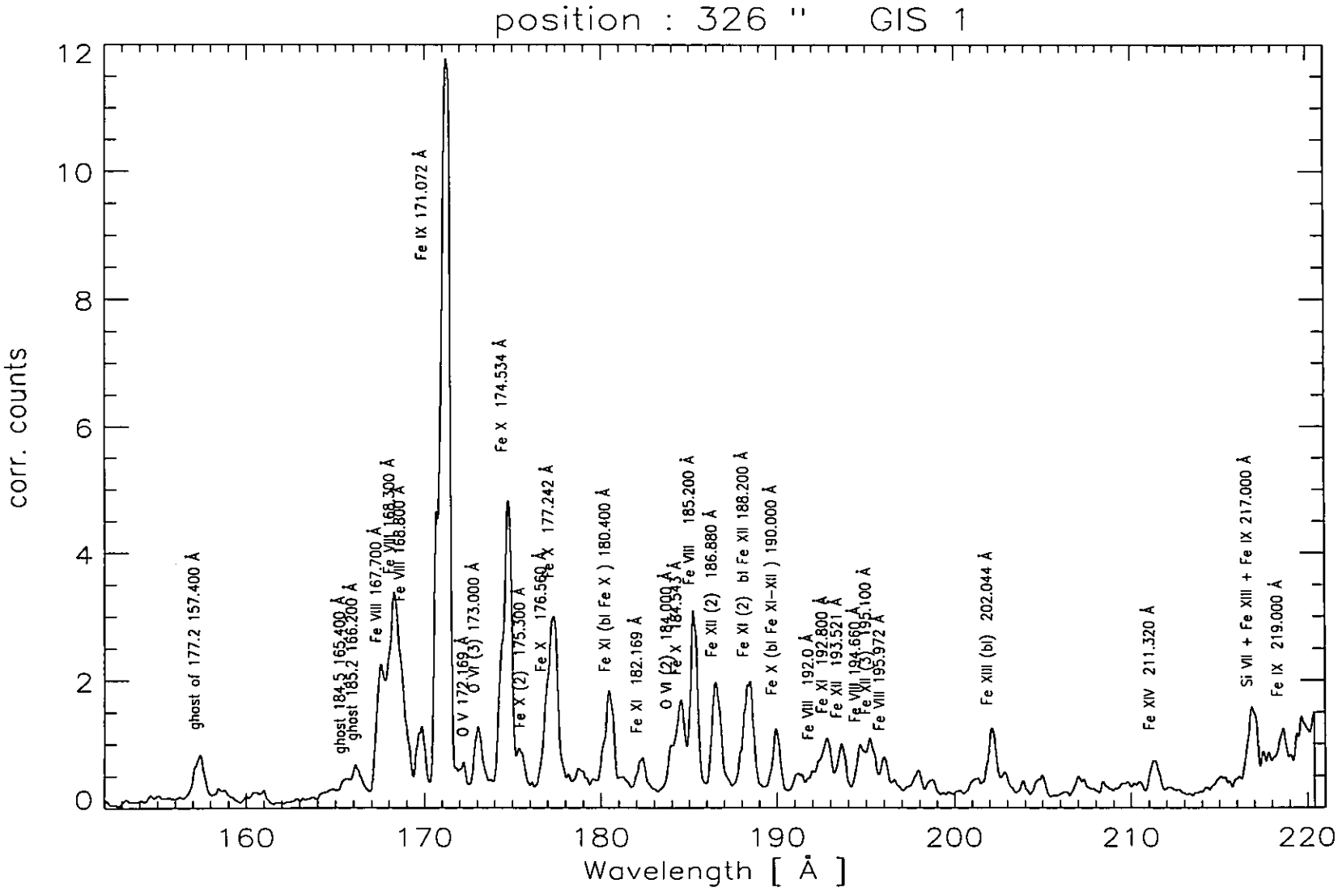

Figure E.1: *The GIS 1 spectrum of the plume – 11th October 1997.*

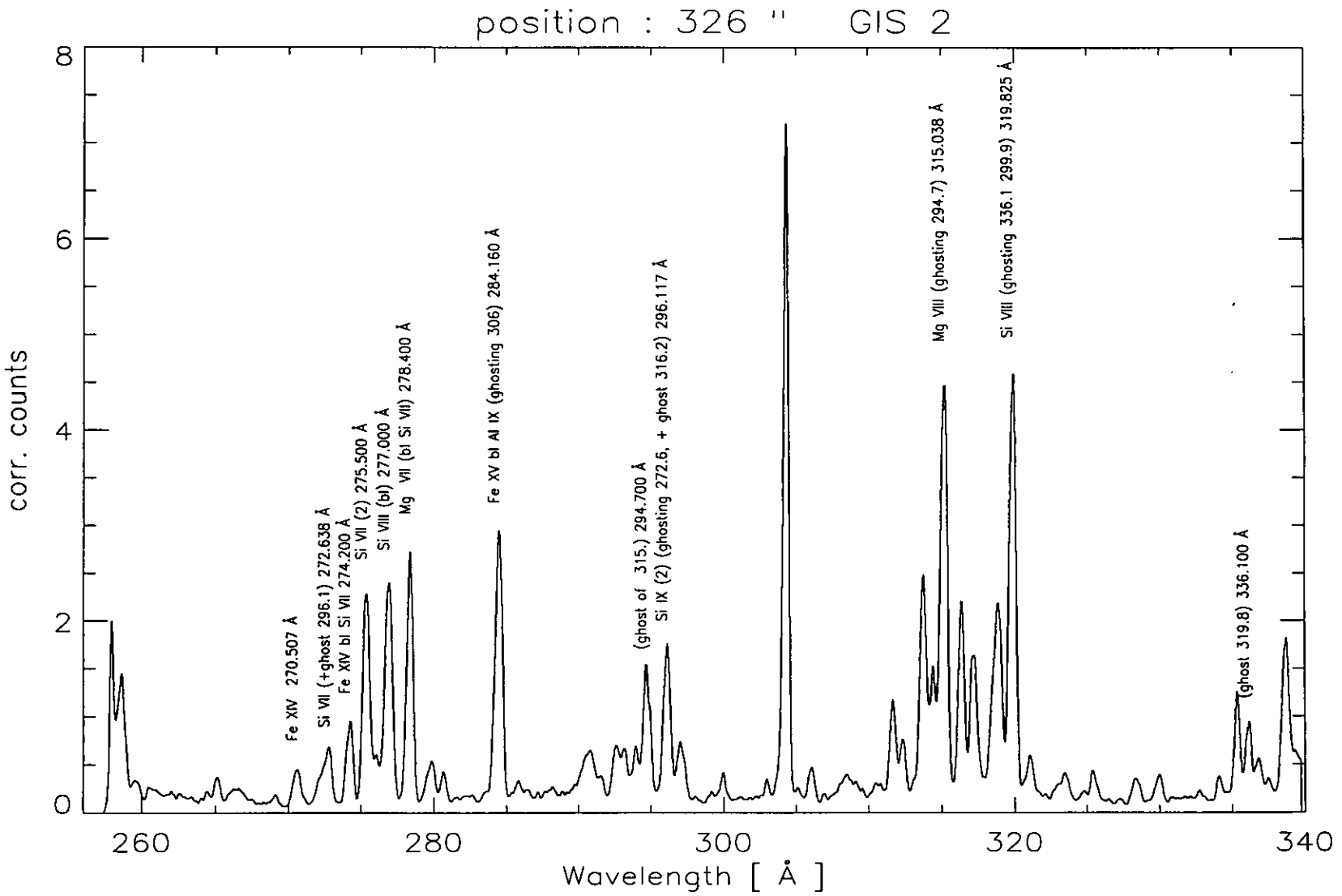

Figure E.2: *The GIS 2 spectrum of the plume – 11th October 1997.*

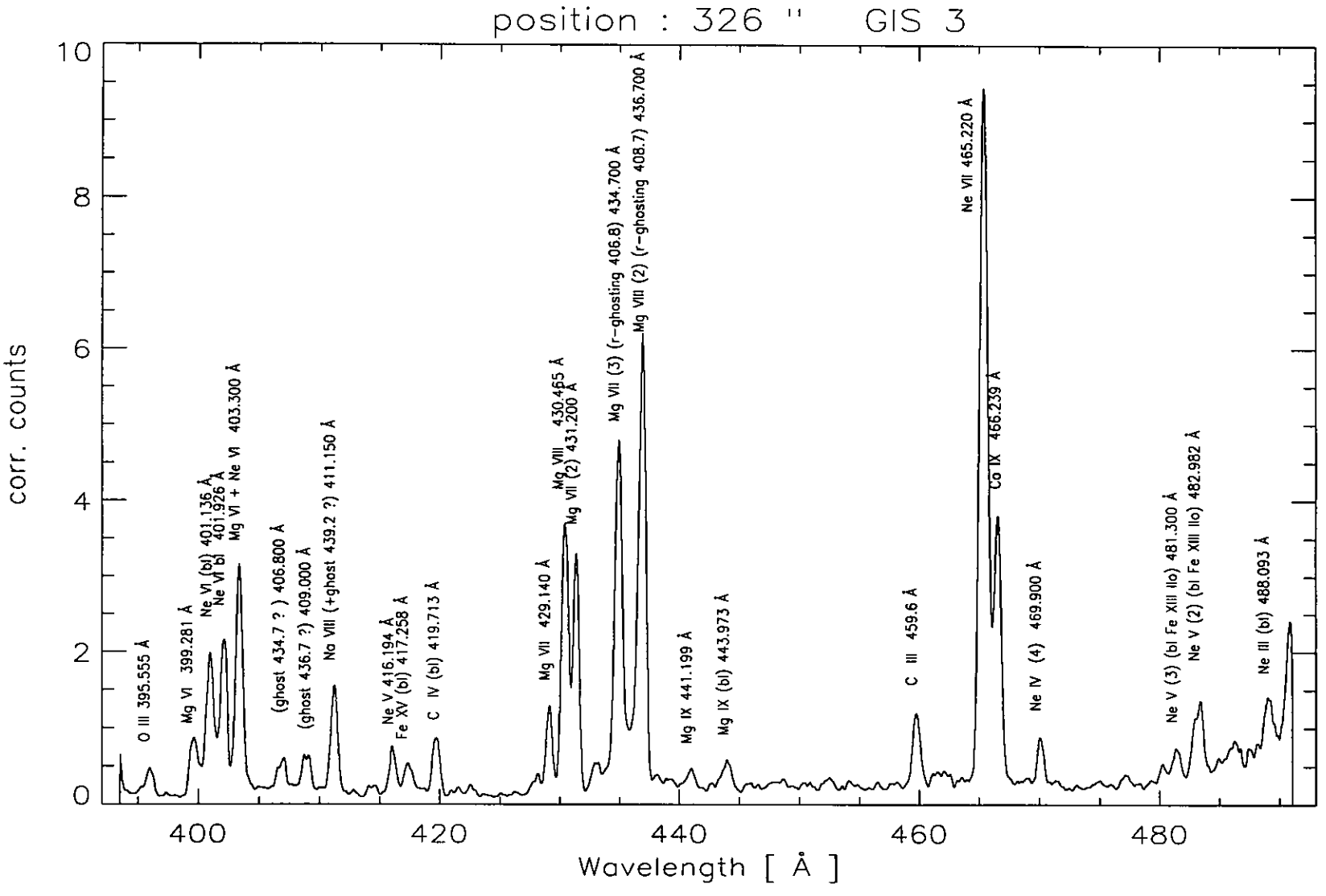

Figure E.3: *The GIS 3 spectrum of the plume – 11th October 1997.*

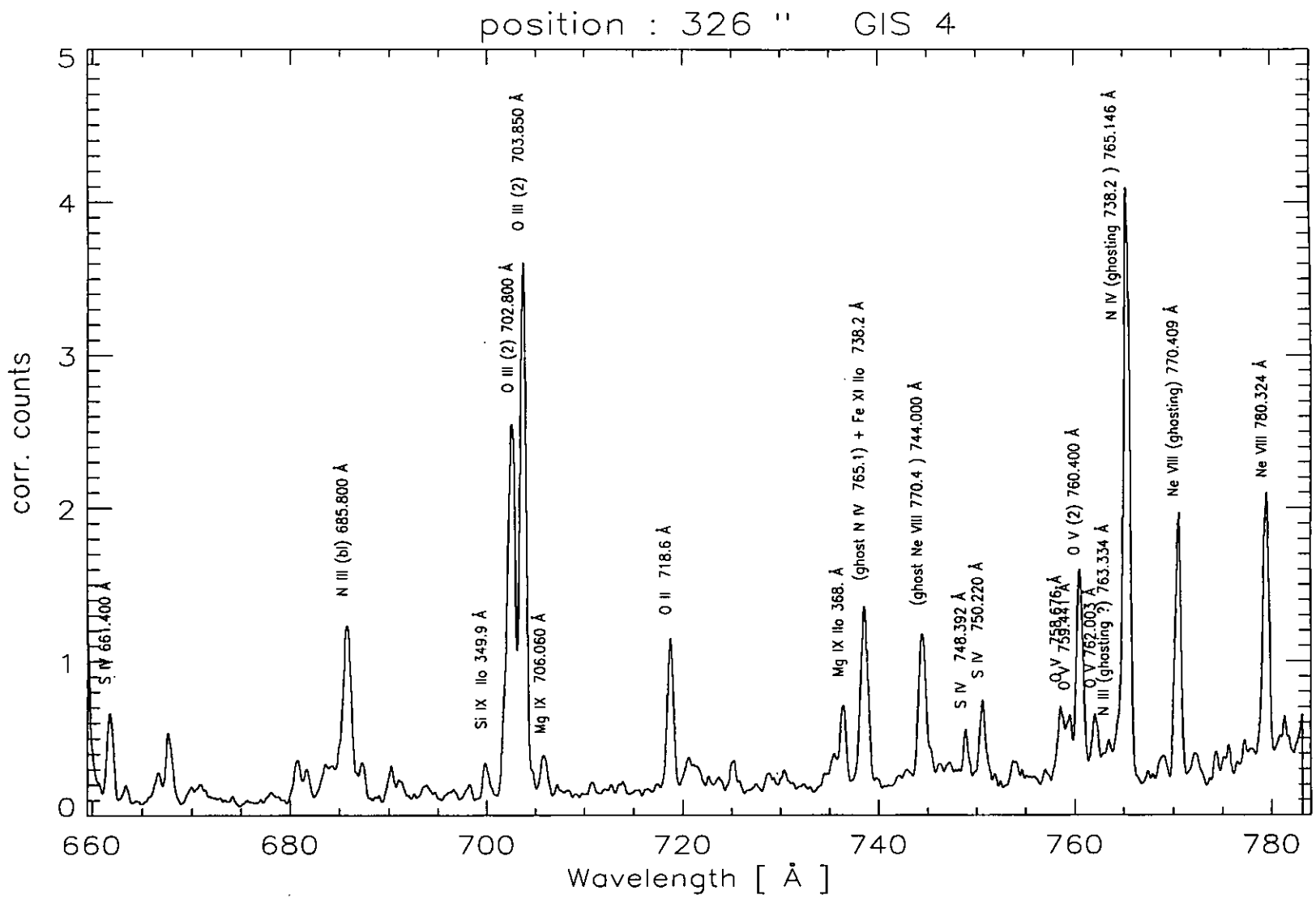

Figure E.4: *The GIS 4 spectrum of the plume – 11th October 1997.*